High Voltage Photovoltaic Devices for Autonomous Solar-to-Fuel Applications

Important note
To cite this publication, please use the final published version (if applicable).
Please check the document version above.

High Voltage Photovoltaic Devices for Autonomous Solar-to-Fuel Applications

Thierry de Vrijer

High Voltage Photovoltaic Devices for Autonomous Solar-to-Fuel Applications

Proefschrift

ter verkrijging van de graad van doctor
aan de Technische Universiteit Delft,
op gezag van de Rector Magnificus Prof. dr. ir. T.H.J.J. van der Hagen,
voorzitter van het College voor Promoties,
in het openbaar te verdedigen op
vrijdag 1 juli 2022

door

Thierry DE VRIJER

Master of Science in Sustainable Energy Technology, TU Delft, The Netherlands
geboren te Rotterdam, Nederland

This dissertation has been approved by the promotor:
Prof.Dr.Ir. A.H.M. Smets

Composition of the doctoral committee:

Rector Magnificus	Chairperson
Prof.Dr.Ir A.H.M. Smets	Delft University of Technology, promotor

Independent members:

Prof.Dr. A.W. Weeber	TNO / Delft University of Technology
Dr. T.J. Savenije	Delft University of Technology
Prof.Dr.Ir. R.A.J. Janssen	Eindhoven University of Technology
Prof.Dr. P. Roca i Cabarrocas	IPVF / Ecole polytechnique
Dr. S. Guha	former president United Solar
Dr. H. Sai	AIST
Prof.Dr. O. Isabella	Delft University of Technology (reserve member)

T̃UDelft

Delft University of Technology

"We have come as far as we have because we are the cleverest creatures to have ever lived on Earth. But if we are to continue to exist, we will require more than intelligence. We will require wisdom."

— David Attenborough, A Life on Our Planet: My Witness Statement

"Kein geloel, fußbal spielen!"
— Ernst Happel

Contents

Contents

Summary

In this dissertation, a framework is presented for the development of high voltage multijunction photovoltaic (PV) devices. Specifically, wireless silicon-based monolithically integrated 2-terminal multijuction PV devices are investigated. Such devices can be used in autonomous solar-to-fuel synthesis systems, as well as other innovative approaches in which the multijunction solar cell is used not only as a photovoltaic current-voltage generator, but also as an ion-exchange membrane, electrochemical catalysts and/or optical transmittance filter. The framework presented in this dissertation encompasses all investigations performed in answering this thesis' central question: *To what extent can fundamental insight and device engineering reduce the opto-electrical losses in a hybrid wafer-based and thin film photovoltaic multijunction device, based on group IV elements?* The answer to this central question is provided in three parts, focusing on **I.** textures, photovoltaic materials and single junction solar cells, **II.** a low bandgap-energy hydrogenated (:H) germanium(tin) (Ge(Sn)) absorber and **III.** multijunction PV and photoelectrochemical (PEC) devices.

In **Part I**, the trade-offs between i) chemical stability and performance and ii) optical performance and electrical performance are explored. In **Ch.2** the chemical instability upon ambient exposure of p-type (p-) nano-crystalline (nc-) silicon-oxide (SiO_x) films and devices with integrated p-nc-SiO_x layers is demonstrated. The instability can be resolved by processing at elevated deposition pressure, at the cost of (initial) conversion efficiency. Moreover, the trade-offs between optical and electrical characteristics for doped nc-silicon (Si) and nc-SiO_x films are demonstrated through variations in the relative precursor gas flow rates.

In **Ch.3** several novel texturing approaches for mono crystalline silicon are presented. A wide range of surface features are demonstrated as a function of the texturing approach and processing conditions. The trade-off between the optical behaviour (light in-coupling, wide angle scattering) and resulting potential gain in current generation on device level, on one hand and the roughness-induced electrical device losses (passivation behaviour, ability to facilitate crack-free nano- to poly-crystalline growth) on the other hand are characterized.

In **Ch.4** an expedient semi-empirical approach for the optimal bandgap profiling of alloyed absorbers is presented. Amorphous (a-) SiGe:H is used as a model, where changes in the bandgap energy (E_G) are realized through variations in the Ge-fraction. The trade-offs between the short-circuit current density (J_{sc}) and the product of the open circuit voltage and fill factor ($V_{oc}*FF$) of single junction devices as a function of i) the absorber thickness, ii) minimum bandgap energy and iii) the introduction of a plateau at the minimum bandgap energy are characterized.

In **Part II** the plasma enhanced chemical vapour deposition (PECVD) of a group IV, low bandgap, intrinsic and stable material based Ge(Sn):H is explored. In **Ch.5** the processing window for Ge:H films is identified by performing a full exploration of the processing conditions (precursor gas flow rates, temperature, pressure, power) and a strong correlation

was established between i) the density, ii) post-deposition oxidation behaviour and iii) opto-electrical properties of a/nc-Ge:H. Additionally, a processing window was identified where a/nc-Ge:H films are processed with the highest refractive indices and lowest dark conductivity values reported in literature for chemical vapour deposited Ge:H.

In **Ch.6** the structural and opto-electrical properties of Ge(Sn):H are compared to those of other group IV alloys. A unique and comprehensive overview is developed for the identification of oxide and hydride peaks across the group IV elements C, Si and Ge materials. Moreover, the first ever evidence of artificial (photo)synthesis in PECVD processed Ge:H films is presented. Infrared analysis indicates a two-step process resulting in the catalytic reduction of CO_2 in Ge:H films to products like CO, formic acid and formaldehyde. Finally, an optical-E_G range of over 1.3eV is presented using over 400 PECVD processed group IV alloys. Based on these results the fundamental relations between the material density, resulting from material stoichiometry, void fraction and crystalline phase fraction, and E_G are discussed. Moreover, the relation between the E_G and electrical material characteristics are revealed.

In **Ch.7** the first steps towards the PECVD processing of a GeSn:H alloy are presented, using a tetramethyltin ($Sn(CH_3)_4$) precursor. It is demonstrated that managing the C and Sn integration into the material is crucial, as large CH_3 fluxes results in porous and chemically unstable films and high atomic fractions of Sn are essential for achieving low-E_G. A number of nc-GeSn(C):H films with a crystallinity of $\approx$50% are processed with a highly heterogeneous nature, consisting of GeSn crystals with 15.5-17.5% Sn embedded in an a-GeC:H phase in which almost no Sn is present.

In **Part III** the focus is on the performance of multijunction PV devices and their use in photo-electrochemical applications. In **Ch.8** the influence of the p-nc-Si(O_X) layer in the tunnel recombination junction (TRJ) of silicon based multijunction devices is explored. By performing structural variations in the p-layer thickness and design in a unique set of devices (four types based on four different PV materials), the qualitative fundamental working principles of TRJs based on p- and n-doped Si(O_X) alloys are revealed. These insights result in the formulation of design rules for the integration of Si(O_X) based TRJs. Moreover, different current matching approaches are explored. The influence of the thickness of different intermediate reflective layers (IRL), based on n-type SiO_X, various transparent conductive oxides and Ag, is compared to the influence of absorber thickness variations on tandem silicon-heterojunction (SHJ)/nc-Si:H and triple junction SHJ/nc-Si:H/a-Si:H device performance. Understanding of the reflective/absorptive behaviour (J_{oc} gain), as well as the resistive behaviour ($V_{oc}*FF$ loss), of the different current matching approaches is essential for optimal device performance. Additionally, a $V_{oc} \approx$2V and $\eta \approx$15% are reported for a triple junction SHJ/nc-Si:H/a-Si:H device , which is the highest reported conversion efficiency for an all-silicon solar cell that generates at least 1V.

In **Ch.9**, in addition to an optimization of the p-type front contact and intrinsic (i-) nc-Si:H absorber, the flexible application of earth abundant and chemically inert Si and SiGe alloys is demonstrated in a large number of 2-terminal monolithically integrated multijunction devices. Two distinct device architectures, on different substrate morphologies, are used for these multijunction devices, combining up to 4 different junctions, yielding a V_{oc}-range of 0.5V to 2.8V. This range of V_{oc}s demonstrates the potential of all-silicon

multijunction devices for facilitating a range of prospective electrochemical (EC) reduction reactions and electrocatalysts in autonomous and wireless PEC devices.

Finally, in **Ch.10** the design, optimization and processing of electrocatalytically active contacts and micropores through the PV device, steps required for converting a multijunction PV device into a PEC device, are investigated. The trade-off between PV and EC performance as a function of micropore size and distribution is demonstrated and the successful processing of Pt microdots with a 2μm diameter and 5% surface coverage is shown.

Foreword

Look, we all know the deal. We're at a pivotal point in human history. The scientific community plays, we play, an instrumental role in this. Our role is two-fold. On one hand, we should teach and preach. Educate the next generation of engineers and preach the gospel of sustainable energy technology so that the public and policy makers can make better choices, informed choices. On the other hand, the community should continue to strive to improve renewable technologies. Continue to make it cheaper, more reliable and more efficient, so that only a fool would opt for the non-sustainable option. Neither role should be frowned upon and excellence in either role should be valued and celebrated.

I started this thesis with a quote from Sir David Attenborough, from his heartbreaking short: "A Life on Our Planet: My Witness Statement". I hope, that a number of decades from now you and I will be able to give a witness statement; a statement about how we dodged a bullet and managed to once again create a society that lives in harmony with nature. I hope this work is a small step in that direction. I hope..

1

Introduction

1.1 The problem

The world is facing a crisis. That crisis is overpopulation. Overpopulation has birthed a number of separate crises, including limited access to food, clean water and medicine in certain parts of the world. Moreover, the last century has seen a depletion of natural resources, amongst which an unprecedented reduction of the expanse and diversity of flora and fauna on land and in the sea. However, potentially the most devastating overpopulation-induced crisis is global warming. Global warming is the consequence of a drastic increase in global greenhouse gas (GHG) emissions in combination with equally drastic reduction of earths capacity, through deforestation and urbanisation, to process these gasses. In our fossil-powered societies GHG emissions are directly proportional to the energy demand.

There is no humane solution to overpopulation that will have a significant effect in this century. Laudable efforts are undertaken to globally improve equality and access to food, water, health care and education, as reflected in the UN's sustainable development goals [1]. A comparison of the birth rate statistics in the western world to the Arabic, African and Southern Asian nations [2], shows that improving these living standards is the most effective approach to reduce the population. However, improving living standards in the developing world will initially, inevitably, lead to an increase of the level of electrification before a population reduction is realized. Since the energy demand is roughly a function of population and level of electrification, expecting a decrease of the global energy demand in the next couple of decades is not realistic. The solution then should be found in the energy supply, by unmaking the centuries-old correlation between energy generation and GHG emissions.

Sustainable Energy
Enter stage, Sustainable Energy technologies. The world is full of abundantly available, clean and renewable sources of energy. According to several reports, a 100% renewable energy society by 2050 is not only technically feasible, but also cost competitive [3]–[5]. In these reports, renewable energy conversion is largely achieved by solar energy, wind energy and hydro power, with the exact mixture depending on location. In all these future energy scenarios, solar photovoltaic (PV) energy conversion plays an important role. Rapidly declining PV costs in combination with its modular nature, small unit

size and low unit investment allow for rapid expansion. In fact, PV energy provides the cheapest electricity in many parts of the world [6], [7]. The share of PV in the global energy mixture is projected to increase from the 2.8%[8] in 2019 to 40-60% in 2050 in certain scenarios[3]–[5]. However, some barriers exist related to the perception of PV and intermittent and decentralized nature of PV energy conversion.

PV energy

Due to the modular nature of PV systems, PV energy conversion occurs spatially diffuse, or decentralized. This is unlike conventional power generation where centrally generated power flows uni-directionally to the consumers. Consequently, the existing electricity grid needs adjustments to facilitate the large-scale integration of decentralized power generation. Improper understanding of the required changes also results in a perception barrier for PV. Policy makers and leading advisory agencies, such as the Intergovernmental Panel on Climate Change and the European Commission, tend to use improper grid integration assumptions and outdated cost assumptions in their models, resulting in a systematic underestimation of the PV potential [9]–[11].

Additionally, there is the intermittent nature of PV power conversion to consider. PV modules only generate electricity when there is light to convert to electricity, just as wind turbine generators do not generate electricity on a breezeless day. This intermittent nature of PV results in a mismatch between energy generation and consumption. To overcome this mismatch, energy storage is required. Besting any of these barriers to large scale PV integration, be it perceptional or related to the intermittent or decentralized generation, requires research and attention. In this dissertation we address the intermittency using PV energy conversion and storage.

Energy storage technologies

There is a range of energy storage technologies available. Thermal energy storage and pumped hydropower are excellent energy storage options, but their application is very limited due to geographical and minimum capacity-related restrictions. The most logical option for short-term energy storage, such as day-night cycles, are batteries. The dominant battery technology, Li-ion, is a mature technology with an excellent round trip efficiency of 90-93%[12]–[14]. Especially for the large fraction of the world population living in the Sun Belt, where seasonal variation is low [11], batteries are an excellent option.

However, batteries are not suited for seasonal, long-term, energy storage due to the relatively high self-discharge rate of up to 25% a year [15]. Moreover, up-scaling Li-battery technology to the capacity required to compensate for season fluctuations is not feasible considering factors like system costs and competition with rapidly growing markets like the electric automotive industry and mobile device industry. Additionally, the reliability of lithium supply will be tested in the next decades as demand increases and recycling practices are not well established [16], [17].

Chemical fuels

The best option for long term and large-scale energy storage are chemical fuels. Human kind has been optimizing means of storing gaseous and liquid hydrocarbons for a century in the form of gasoline and natural gas. For fuels, the issue of scale is easily solved through

larger containers or more containers. Moreover, once stored self-discharge as a function of time is negligible.

In terms of sustainable chemical fuels, molecular hydrogen is the natural option, as industrial scale electrolysers are commercially available. Electrolysers use electrical energy, preferentially surplus electrical energy from renewable sources, to split water into molecular hydrogen and oxygen. The hydrogen can be stored and converted back to electrical energy in winter using a fuel cell. This process is clean, renewable, and readily available, which is why it is often used in the modelling of 100% renewable [3]–[5] and carbon neutral [18] power systems. Drawbacks of this technology are that it is still relatively expensive, partly because the technology is not yet widely applied and partly because of the relatively low round trip efficiency of 40-50%. An additional challenge is the low volumetric energy density of hydrogen gas. This means that hydrogen has to be compressed and stored in reinforced containers at very high pressures of up to 800 bars, adding complexity and costs to this storage solution.

The question of what the best fuel is for our future energy system is therefore subject of debate. A number of carbon-based fuels are considered that can be produced through the electrochemical (EC) reduction of CO_2 with water. These fuels are CO (syngas), formic acid, formaldehyde, methanol and methane [19]–[22]. Which of these compounds is formed depends on the applied EC potential. The technology required for the direct EC reduction of CO_2 with water has a lower technology readiness level and is inherently more challenging, but these carbon based fuels are easier to store as they have a much higher volumetric energy density than H_2. Moreover, carbon-based fuels have the added benefit that the GHG CO_2, which in the future will have to be captured and stored [23], [24], is used as a feedstock. Regardless of the fuel of choice, efforts have to be made to improve availability and applicability of the devices and technology required to sustainably produce fuels through an EC reaction.

1.2 One way to do it

From a device architecture point of view, there are a number of ways in which sunlight can be used to drive the EC reduction of a molecule like water or CO_2. Different device configurations that can yield such a reaction, ranging from the most integrated approach **A** to the most decoupled approach **E**, are shown in Fig.1.1 borrowed from [25]. Each of these approaches, each level of integration, has its respective advantages and limitations. With each next level of integration, additional functionalities of the chosen semiconductor have to be balanced, resulting in an increasingly complex optimization. For the most decoupled approach **E**, for instance, the PV module only has to be optimized in terms of photovoltaic conversion efficiency and the EC device only for its Faradaic efficiency. The converter ensures that both components can operate at their separate optimal J-V conditions. The ease of optimization for this decoupled approach, combined with the fact that all these technologies are relatively mature, result in a reported solar-to-hydrogen (STH) efficiency of 20.6% and a simulated theoretical limit of 26.5% [26].

For the most integrated approach **A** the band gap energy of the semiconductor has to be chosen such that it can generate a potential large enough to drive the photo-electrochemical (PEC) reaction. This large bandgap energy fundamentally limits the cur-
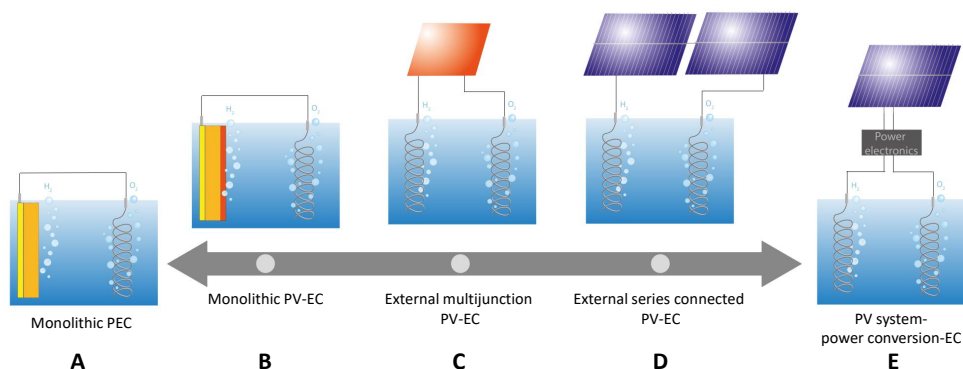
Figure 1.1: Device architectures that use sunlight to drive an EC reaction. The different approaches are ordered from the most integrated approach on the left, the photo-electrochemical device indicated by **A**, to the fully decoupled approach on the right **E**. In between are a range of semi-integrated approaches, where **B** indicates a monolithically integrated PV-EC device, and two external PV-EC devices where a multijunction PV device **C** and series connected single junction PV devices **D** are used. Figure is borrowed from [25].

rent density it can generate under the solar spectrum, without concentration approaches. Moreover, the conduction- and valence band edges have to be aligned with the PEC reaction energy levels and the semiconductor has to be stable in an aqueous environment. An optimization combining all these challenging functionalities often results in trade-offs and compromises that yield lower device STH conversion efficiencies. However, the more integrated approaches allow for the development of compact, easily produced, potentially cheaper units that have less wiring and fewer parts. Consequently, a fully integrated approach could facilitate ease of installation and has excellent scalability. It therefore makes sense to explore the approaches in between fully decoupled and fully integrated.

Semi-integrated architectures

Semi-integrated Solar-to-Fuel approaches are indicated by **B**, **C** and **D** in Fig.1.1. These approaches have in common that the PV and EC operation are directly connected. This means that the PV component has to generate sufficient voltage to drive the EC reaction. This voltage is larger than a conventional single junction solar cell can generate. The operating voltage for water splitting devices, for instance, is generally over 1.8V [27], [28], and even larger for the various CO_2 reduction pathways discussed earlier. In approach **D**, generating the required voltage is achieved by series connecting several single junction solar cells, while in **C** the voltage is generated by a multijunction PV device. The multijunction approach has a few benefits. Firstly, multijunction devices can generally achieve better spectral utilization and higher fill factors. Secondly, the cumulative J-V characteristics of the series connected single junction cells is an integer product of the single junction J-V characteristics. This means that for certain EC reactions the series connected devices could supply a substantial overpotential and consequently sub-optimal current density. Multijunction design allows for more flexibility, such that an optimal division of current and voltage at the maximum achievable power density can be achieved. Finally, the wiring

used for the series connection in approach **D** excludes the fabrication of autonomous solar-to-fuel synthesis systems. Such systems include the monolithic PEC **A** and PV-EC **B** applications, as well as other innovative approaches in which the multijunction solar cell is used not only as an photovoltaic current-voltage generator, but also as an ion-exchange membrane, electrochemical catalysts and/or optical transmittance filter.

Consequently, in this dissertation, we'll explore the opportunities and limitations of a high voltage multijunction device for PV-EC applications. In order to potentially demonstrate high conversion efficiencies and to retain the possibility of converting the PV stack to an PEC or monolithic PV-EC device, a high efficiency wafer-based silicon heterojunction (SHJ) solar cell is used as a substrate for the growth of the thin film junctions. Moreover, since the potential benefits of such a medium integrated approach involve potential low-cost and ease of production and scalability, we'll explore multijuction PV devices based on chemically stable and earth abundant elements.

The known unknowns
Within these boundaries, there are some key unknowns. The first was exposed by pioneering work on the processing of SHJ/thin-film silicon devices. An incompatibility between the conventional silicon texture and nano-crystalline silicon growth was revealed [29], [30]. Surface texturing is crucial for photovoltaic devices, as it results in an increase of the optical path length through a film without increasing the film thickness. A new texturing approach should therefore be developed.

Secondly, a fundamental understanding is required of the relation between plasma processing conditions, material growth and opto-electrical properties of a range of doped and undoped, amorphous and nano-crystalline, hydrogenated and oxygenated silicon layers. Only with such understanding can the effect of these layers in PV devices be explored across multijunction configurations and device architectures.

Thirdly, in an effort to produce a PV device that utilizes the lower energetic part of the solar spectrum, we intent to produce a low bandgap energy absorber material based on the group IV elements germanium and tin. Processing hydrogenated germanium through plasma enhanced chemical vapour deposition (PECVD) has proven challenging in the past and the last efforts date back almost a decade [31]–[33]. The PECVD processing of hydrogenated GeSn has not been attempted before.

Finally, while some PV-EC demonstrators have been reported [34], [35], a lot of unknowns regarding the losses and trade-offs in converting a PV device to an PV-EC device remain.

1.3 The question

The topic of this dissertation is high voltage multijunction PV devices. The focus however is not on optimizing a single device architecture. Rather, the intent is to provide a framework for optimal multijunction design that can result in a range of output voltages, for different EC applications. To produce this range of output voltages, different combinations of sub-cells are investigated, yielding a range of device architectures. The sub-cells include a silicon heterojunction with n-type emitter and thin film sub-cells with hydrogenated (:H) intrinsic absorbers based on nano-crystalline (nc-) silicon, amorphous silicon-germanium and amorphous (a-) silicon. These sub-cells, and the order in which

they are integrated in the multijunction device, are schematically shown in Fig.1.2. The figure additionally shows where a junction based on Ge(Sn):H would be integrated. The framework for optimizing this range of device architectures is to be obtained through the systematic optimization and characterization of PV materials and through a fundamental investigation and optimization of interfaces and trade-offs in multijunction PV devices based on group IV elements. The research question could therefore be stated as:

To what extent can fundamental insight and device engineering reduce the opto-electrical losses in a hybrid wafer-based and thin film photovoltaic multijunction device, based on group IV elements?

This research questions is broken down into the following three key questions:

- **I** How and to what extent can the processing conditions of individual layers and surfaces be tuned such that they result in desirable material properties for different functionalities for use in single junction photovoltaic devices?

- **II** Through a fundamental opto-electrical optimization, can an intrinsic low bandgap energy (0.5-0.8eV) plasma enhanced chemical vapour deposition processed hydrogenated germanium or germanium-tin alloy be developed for use in photovoltaic devices?

- **III** How do different materials, variations in material properties and different device configurations affect the performance of multijunction photovoltaic and photoelectrochemical devices?

1.4 Thesis outline

The outline of this thesis is visually presented in Fig.1.2. The three key questions stated above form the three main parts of this work, where each part is divided into three chapters. The visual shows how the different parts and chapters contribute to the optimization of the overall device. Each chapter consists of one or two journal articles.

Key question **I** forms the first part, titled ***Part I: Photovoltaic materials and single junction devices***. In this part the focus is on the characterization and optimization of individual layers and surfaces. This part consists of **Chapter 2**, which covers the optimization of doped silicon and silicon oxide layers. **Chapter 3** covers the texturization and passivation of the silicon wafer surface to facilitate the growth of nanocrystalline thin film junctions. **Chapter 4** covers the optimal bandgap profiling of stoichiometric absorbers, such as amorphous silicon germanium.

Key question **II** forms the second part, titled ***Part II: Development of a low bandgap Ge(Sn):H alloy***. In this part the focus is on the PECVD processing of a chemically stable and intrinsic hydrogenated germanium or germanium-tin alloy. This part consists of **Chapter 5**, which covers a full exploration of the processing window for Ge:H films. In **Chapter 6** elemental-, vibrational, optical- and electrical-analysis is performed on a range

Part I: Photovoltaic materials and single junction devices

Ch 2 Optimization of doped silicon layers

Ch 4 optimal bandgap profiling of stoichiometric absorbers

Ch 3 Texturization and passivation of silicon wafer surface

Part II: Development of a low bandgap Ge(Sn):H alloy

Ch 5 Optimization of Ge:H films

Ch 6 Development of GeSn:H films

Ch 7 *Analysis of Ge(Sn):H in reference to other hydrogenated group IV alloys

*(i)-a-Si:H

*(i)-a-SiGe:H

*(i)-nc-Si:H

(n)-c-Si

*(i)-a-Ge(Sn):H
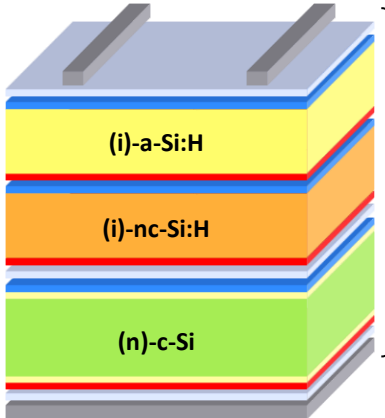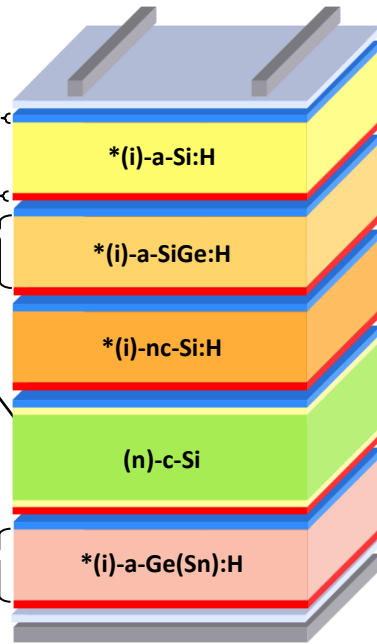
Part III: Multijunction photovoltaic devices

Ch 8 Tunnel recombination junctions and intermediate reflective layers

Ch 9 Silicon alloys in multijunction devices

(i)-a-Si:H
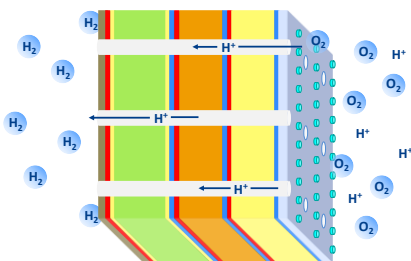
(i)-nc-Si:H

(n)-c-Si

Ch 10 From photovoltaic to photo-electrochemical device

Figure 1.2: Thesis outline

of group IV alloys, including GeSn:H, GeC:H, GeO:H, a/nc-Ge:H, a/nc-SiGe:H, a/nc-Si:H, SiC:H and SiO:H. Based on this study, the band gap and conductive properties of the films in relation to the lattice characteristics such as material density, stoichiometry, void fraction and crystalline phase fraction are discussed. Finally, in **Chapter 7** the development of GeSn:H films is covered.

Key question **III** forms the third part, titled ***Part III: Multijunction photovoltaic devices***. In this part the focus is on understanding and optimizing interfaces and current-voltage trade-offs in multijunction PV devices. In **Chapter 8** tunnel recombination junctions and intermediate reflective layers are covered. In this chapter trends across device architectures of Si(O):H based tunnel recombination junctions are explored, as well as the effectiveness of transparent conductive oxides and metals between subcells. In **Chapter 9** the flexible application of silicon and silicon-germanium alloys is demonstrated in two distinct device architectures, combining up to 4 different junctions, yielding a V_{oc} range of 0.5V to 2.8V. Finally, in **Chapter 10**, the steps and optimization considerations required to convert a PV to a PEC device are covered.
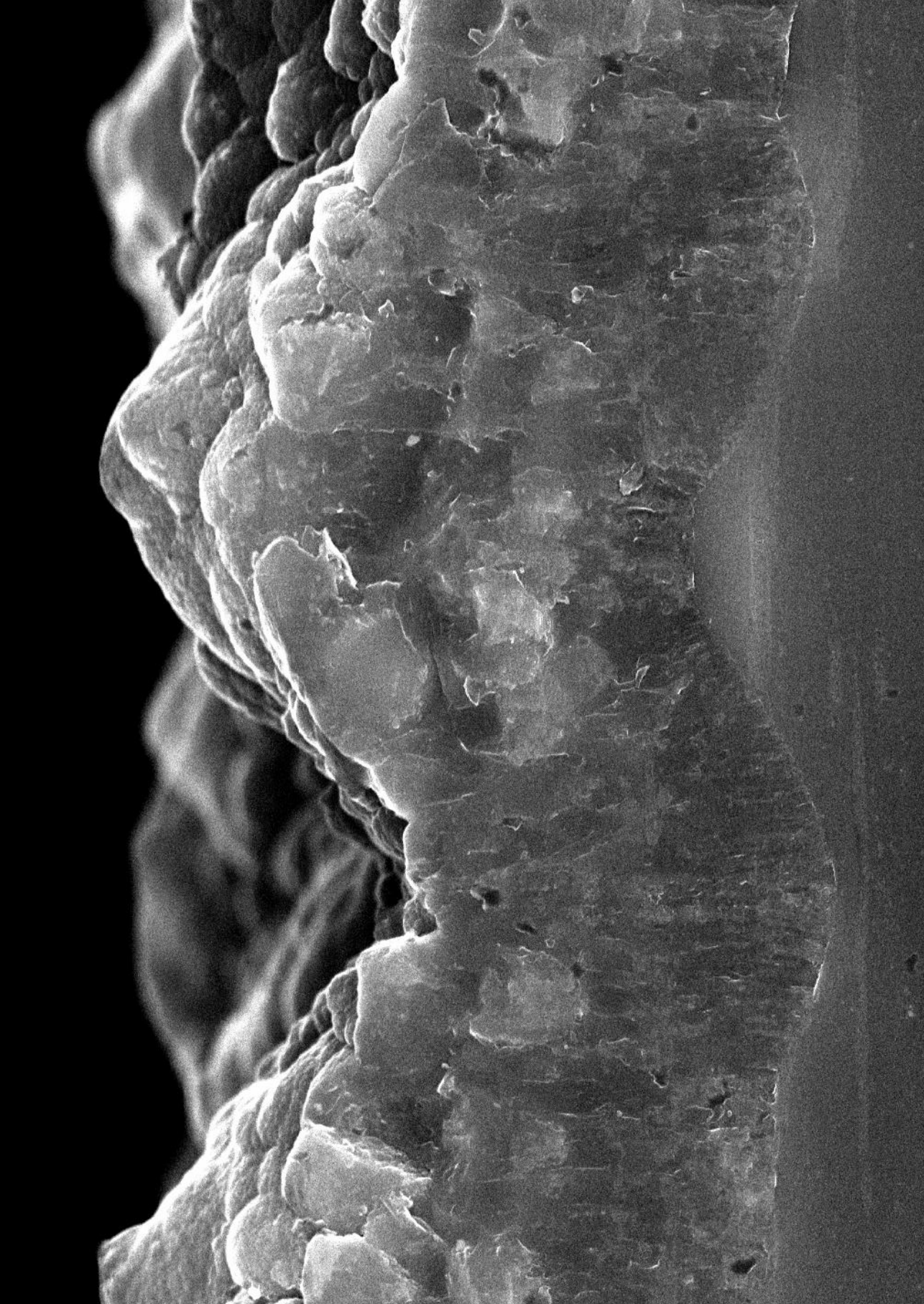
Part I:
Photovoltaic materials and single junction devices

A photovoltaic device consists of a series of layers, doped and intrinsic, and the interfaces between these layers. Different functionalities, different opto-electrical properties, are required of each of these layers. Balancing different functionalities often involves trade-offs. The particular opto-electrical properties that should be prioritized depends on the device architecture and the position of a layer in the device. Consequently, optimizing doped and intrinsic layers for a range of device architectures requires fundamental insight into the processing of these layers. In Part I, therefore, we focus on keyquestion **I**:

How and to what extent can the processing conditions of individual layers and surfaces be tuned such that they result in desirable material properties for different functionalities for use in single junction photovoltaic devices?

The hybrid multijunction device that is the intended end-product of this dissertation is schematically shown in Fig.1.3. This hybrid multijunction consists of a silicon heterojunction solar cell that is combined with thin film silicon junctions with nano-crystalline, amorphous silicon and/or silicon-germanium absorber layers. If we only consider the photo-active stack, excluding the transparent conductive oxides and metallization, the materials used in this device can be divided into three groups: the silicon wafer, the intrinsic thin film absorbers and the doped layers. Each of these groups is covered in a separate chapter in Part I.

Part I: Photovoltaic materials and single junction devices

Ch 2 Optimization of doped silicon layers

**Ch 4** optimal bandgap profiling of stoichiometric absorbers

Ch 3 Texturization and passivation of silicon wafer surface

(i)-a-Si:H

(i)-a-SiGe:H

(i)-nc-Si:H

(n)-c-Si

(i)-a-Ge(Sn):H
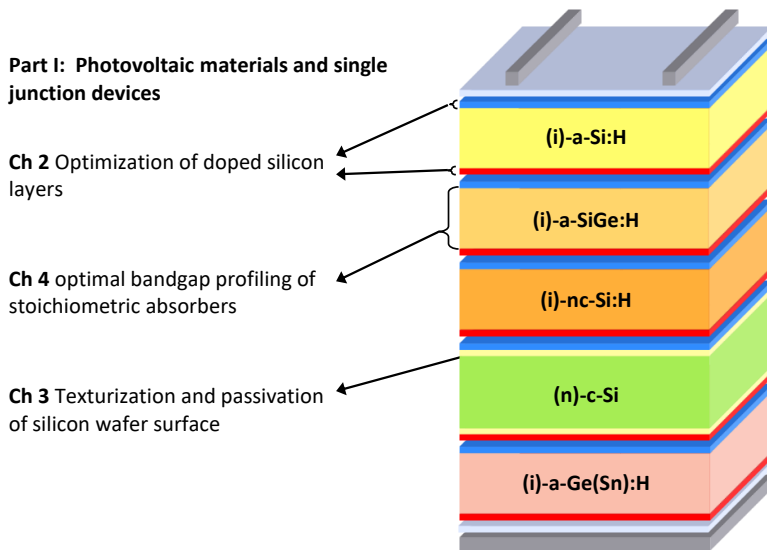
Figure 1.3: Outline Part I

Chapter 2 *Optimization of doped silicon layers*

In this chapter doped nanocrystalline silicon and silicon-oxide films are discussed. The opto-electrical properties of doped silicon films are the result of different material phases, the quality of these phases and the dopant concentration. Changes in material phases can be realized through adjustments in the plasma processing conditions. As a result of the heterogeneous nature of the material, doped hydrogenated amorphous/nanocrystalline silicon-oxide (a/nc-SiO$_{X \geq 0}$:H) is highly versatile. As a result of this versatility, a/nc-SiO$_{X \geq 0}$:H has received a lot of attention in the last decade or so [36]–[61]. Understandably, in these works, the films are often optimized with a single application in mind.

The different material phases in a/nc-SiO$_{X \geq 0}$:H provide versatility, but also an inherent trade-off between the optical and electrical properties. In the multijunction device presented in Fig.1.3, the doped a/nc-SiO$_{X \geq 0}$:H films are integrated at multiple positions in the device. Which particular opto-electrical property should be prioritized depends on the position at which the layer is integrated. High optical transparency, for example, is of great importance at the front of the device, but at the back of the device electrical conductivity can be prioritized. Moreover, for certain applications, other properties have to be considered, such as the refractive index for use as an intermediate reflective layer.

The focus in this chapter is therefore on characterizing the trade-offs between the opto-electrical properties in doped a/nc-SiO$_{X \geq 0}$:H films. In **Chapter 2.1**, the chemical stability of the doped a/nc-SiO$_X$:H films and their influence on device performance and stability is explored. In **Chapter 2.2**, the relation between the precursor gas flows, the material phase fractions and opto-electrical properties of doped a/nc-SiO$_{X \geq 0}$:H films are investigated, as well as the development of the material phase fractions in the growth direction.

15

Chapter 3 *Texturization and passivation of the silicon wafer surface*
Surface texturing is of great importance in photovoltaics, as it is a means of increasing the optical path-length, without increasing the absorber thickness. This is especially important for thin film silicon alloys, which are relatively defective by nature and therefore increasingly suffer from electrical losses as the absorber thickness is increased. Conventionally, a pyramidal surface texture is used in silicon photovoltaics, as these features are effective at reducing front reflection and are relatively easy and cheap to produce. There is an inherent issue however with the use of these features in multijunction devices. The pyramidal surface texture can be incompatible with the crystalline phase in the nc-Si:H absorber, as well as absorbers based on poly-si, perovskite and C(I)GS materials. This incompatability is the result of both issues with conformal growth and the formation of cracks [62]–[64] in the valleys between sharp features. A texturing method should therefore be developed that results in smooth surface features. These features should support the growth of a crack-free nano- to poly-crystalline layer. Additionally, the features should effectively scatter light into wide angles and be passivated with relative ease.

To that end, four different unconventional texturing approaches are explored and optimized. In **Chapter 3.1** three texturing approaches are introduced, based on different combinations of alkaline and acidic etchants, as well as the use of the sacrifical poly-Si layer. The influence of the etching time on the geometry and optical behavior was characterized and the ease of passivation was tested using different processing conditions for the a-Si:H passivation layer. In **Chapter 3.2**, the deposition conditions of the poly-Si sacrificial layer are optimized and an additional texturing approach is explored, based on the use of a photo-lithographic mask. Moreover, the use of the 3 most promising surface textures are compared in photovoltaic devices.

Chapter 4 *Optimal bandgap profiling of stoichiometric absorbers*
In this chapter we consider the thin film silicon absorbers. The processing of a/nc-Si:H is well understood and well established in the collective work of my predecessors in the PVMD group [65]–[74]. The focus in this chapter is therefore on the amorphous silicon germanium absorber. In particular, in the spirit of providing a framework for a range of optimal multijunction device architectures, the focus is on the flexible use of SiGe:H.

To that end, the effects of various deposition conditions are characterized on the opto-electrical properties of a-SiGe:H. This characterization is then used to realize a bandgap gradient in single junction a-SiGe:H solar cells. By comparing different bandgap grading techniques, a set of semi-empirical relations is then developed to achieve optimal bandgap profiling of stoichiometric absorbers, such as amorphous silicon germanium, for a range of device architectures.

2

Optimization of doped silicon layers

2.1 Chemical stability and performance of doped silicon oxide layers for use in thin film silicon solar cells

This section was published in *IEEE Journal of Photovoltaics**

Abstract

Doped hydrogenated silicon oxide layers (SiO_X:H) have recently successfully integrated as front window layer, back reflector layer, intermediate reflector layer, passivation layer and junction layer in thin film silicon solar cells. Depending on the deposition conditions of the SiO_X:H layers, some devices suffer from a degradation in performance in time. In this paper we demonstrate the responsible mechanism involved. It is demonstrated that oxidation of the p-type doped (p-)SiO_X:H with a high crystallinity and therefore poor passivation of crystalline grains is responsible for this degradation. The oxidation of p-SiO_X:H is caused by the in-diffusion of water vapor from the ambient air. Stable p-SiO_X:H can be obtained if the material is processed at higher pressure. In addition, the degradation can be prevented if the cell is well encapsulated, like using dense n-type (n-)SiO_X:H in the back reflector of the cell.

2.1.1 Introduction

Doped hydrogenated silicon oxide (SiO$_X$:H) has received much attention due to its versatile applicability in photovoltaic (PV) technologies [36]–[42]. Material properties like the crystallinity, activation energy (E$_{act}$), optical bandgap energy (E$_{04}$) and refractive index (n) of doped SiO$_X$:H films are highly tunable through adjustment of the deposition conditions [43]–[47]. SiO$_X$:H has various multifunctional applications in photovoltaic devices. The optical functionalities include integration into the front window layer, intermediate reflective layer (IRL) in multijunction devices [48]–[51] and as part of the back-reflector [51], [53]. Electrical functionalities include passivation [52], wide gap emitter layer for hetero SiO$_X$:H-crystalline silicon (c-Si) junction [53], doped layer functionality to form a p-i-n junction and doped SiO$_X$:H for excellent tunnel recombination junctions [54]. Finally, intrinsic SiO$_X$:H can act as a high-bandgap photovoltaic absorber in triple- and quadruple multijunction devices [55]. SiO$_X$:H material has played a crucial role as a doped layer and IRL in micromorph solar cells [46], [47], to reach record initial [54] and stabilized [48] efficiencies. In addition, SiO$_X$:H played an important role as tunnel recombination junction in novel hybrid micromorph and heterojunction PV devices for water splitting [56] and hybrid amorphous silicon/CIGS tandem devices [75]. While much attention has been devoted to this versatile material, the attention has been primarily focused on the initial performance of thin film silicon solar cells (TFSSC) which include doped SiO$_X$:H layers. It has however been observed within our lab that the performance of these cells, for certain deposition conditions, degrades over time. The degradation of TFSSC incorporating doped SiO$_X$:H layers has been observed to occur even in the absence of light, suggesting the involvement of other environmental factors. In this study we investigate the stability of doped SiO$_X$:H and look into the mechanisms governing its degradation. It has been reported that in order to prevent post-deposition oxidation of hydrogenated nanocrystalline silicon (nc-Si:H), which causes the material to degrade, a critical minimum deposition pressure is required [69]. This study therefore focuses on the influence of the deposition pressure on the performance and stability of p-type (p-)SiO$_X$:H and n-type (n-)SiO$_X$:H films, as well as single junction thin film a-Si:H cells incorporating p-SiO$_X$:H and n-SiO$_X$:H layers.

2.1.2 Experimental Details

In order to investigate the influence of the deposition pressure on the material properties of the doped SiO$_X$:H films, a series of p-SiO$_X$:H and a series of n-SiO$_X$:H films were deposited. The films have a thickness of around 100nm and are deposited on Corning Eagle XG glass. Using a Radiofrequency plasma enhanced chemical vapor deposition cluster tool, operating at a frequency of 13.56MHz.

In our lab recipes were developed for the doped SiO$_X$:H layers such that the films provide excellent initial performance in terms of both their optical and electrical performance. These recipes are presented in Table 2.1, which shows the full set of relevant deposition conditions used for all doped SiO$_X$:H films presented in this paper. The gas flow rates (F(gas)) are expressed as a ratio with respect to the silane flow rate. The used silane flow rate is equal to 0.8 sccm for p-SiO$_X$:H films and 1 sccm for n-SiO$_X$:H films, while the deposition pressure is 2.2 mbar for p-SiO$_X$:H and 1.5 mbar for n-SiO$_X$:H films. Consequently,

Table 2.1: Typical deposition condition for doped SiO_X:H films. A $F(SiH_4)$ of 0.8 was used for the deposition of the p-SiO_X:H films, while a $F(SiH_4)$ of 1 sccm was used for the n-SiO_X:H films

	p-SiO_X:H	n-SiO_X:H
$F(CO_2)/F(SiH_4)$	2.75	1.6
$F(H_2)/F(SiH_4)$	212.5	100
$F(B_2H_6)/F(SiH_4)$	0.004	-
$F(PH_3)/F(SiH_4)$	-	1.2
Pressure (mbar)	2.2	1.5
RF power (mW·cm^{-2})	90.3	69.4
Temperature (°C)	180	180

these deposition pressures are used both as a starting point and as reference throughout this paper. Parallel electrodes consisting of 500nm-thick Aluminium bars were deposited onto the films to perform dark conductivity measurements. These measurements were performed by measuring the current conducted between two electrodes at a fixed voltage and temperature in a dark environment. By repeating this measurement at 5°C intervals the activation energy (E_{act}) can be calculated using Arrhenius equation:

$$k_B T = -E_{act} \, ln \left(\frac{\sigma}{\sigma_0} \right) \tag{2.1}$$

Here σ is the conductivity, σ_0 is the material dependent conductivity constant, k_B is Boltzmann's constant and T is the temperature in Kelvin. Spectroscopic ellipsometry (SE) was used to determine the refractive index and the optical bandgap (E_{04}). The SE measurements were fitted to an effective medium model. SiO_X:H is an heterogeneous material consisting of an amorphous structure of hydrogenated amorphous silicon (a-Si:H) and silicon-oxide and crystalline grains. Therefore, the material properties of SiO_2 and a-Si:H are used to mimic the a-SiO_X:H tissue and polycrystalline silicon is used to mimic the crystalline grains. Consequently, the model uses the material properties of SiO_2, a-Si:H and polycrystalline silicon to approximate the optical properties of doped SiO_X:H material. The E_{04} was determined by calculating the photon energy level at which the absorption coefficient equals 10^4 cm^{-1} [39], [49], [50]. The SiO_2 content in each film, as determined by the effective medium model, is used as indicator for the oxygen fraction in the films. Throughout this paper the SiO_2 percentage is referred to when the oxygen fraction is discussed. Finally, the real part of the refractive index was extracted from the SE model, which is presented in this paper at a wavelength of 600nm. The crystallinity of the films was measured by Raman spectroscopy with a 514nm laser. The spectra are fitted with a Gaussian peak around 520 cm^{-1} corresponding to the crystalline silicon phase and Gaussians peaks at 160 cm^{-1}, 320 cm^{-1}, 390 cm^{-1} and 480 cm^{-1} corresponding to amorphous silicon and silicon-oxide matrix. The crystallinity (χ_C) in this paper is defined by:

$$\chi_C = \frac{I_{c\text{-Si}}}{I_{c\text{-Si}} + \gamma \cdot I_{a\text{-Si}}} \tag{2.2}$$

Here $I_{c\text{-Si}}$ is the integrated area under the Gaussian peak corresponding to the crystalline silicon phase and $I_{a\text{-Si}}$ for the peaks corresponding to the amorphous phase. γ
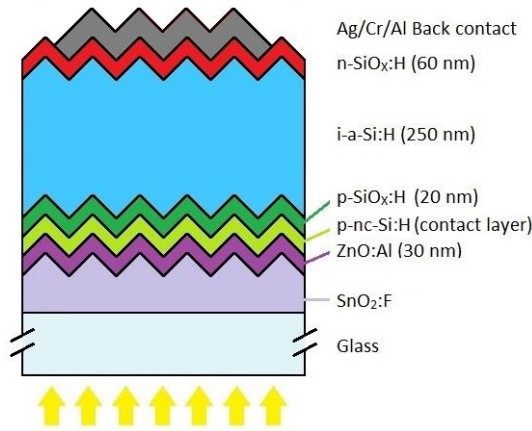
Figure 2.1: Schematic representation of the a-Si:H p-i-n cell

is a correction factor for the difference in cross section for phonon excitation of c-Si with respect to a-Si and equals 0.8. For the fabrication of the superstrate p-i-n cells, schematically presented in Fig.2.1, model type Asahi VU substrates were used. These substrates consist of glass with a thin textured Fluor-doped tin-oxide (SnO:F) TCO layer on top. A 20nm aluminium-doped zinc oxide (AZO) layer was sputtered to protect the TCO layer from the highly hydrogen diluted plasma conditions for the p-layer processing. The p-doped region of the device is based on two separate p-doped layers. First a very thin p-type nanocrystalline silicon (p-nc-Si:H) contact layer was deposited to ensure good ohmic contact with the front TCO, followed by a thicker 20nm p-SiO$_X$:H layer. The intrinsic (i)-a-Si:H absorber layer with thickness of 250nm was then deposited, using only a SiH$_4$ gas flow at a pressure of 0.7mbar and power density of $21.5\text{mW} \cdot \text{cm}^{-2}$, followed by the n-SiO$_X$:H layer with a thickness of 60nm. Finally, 30 back contacts were evaporated onto each fabricated substrate, defining 30 separate cells with a surface area of 16mm^2 each. Outside the active area of the solar cells an aluminium front contact was deposited.

The J-V measurements of the solar cells were conducted using an AM 1.5G solar simulator at an illumination of $100\text{mW} \cdot \text{cm}^{-2}$ under a controlled temperature of 25°C. The open-circuit voltage (V$_{OC}$) and fill factor (FF), used to calculate the conversion efficiency of the cells, were extracted from the J-V curves. The short-circuit current density (J$_{SC}$) was calculated from the external quantum efficiency (EQE) data, by weighing with the AM 1.5G spectrum. The presented solar cell performance data was obtained by measuring all 30 cells on each substrate and averaging the 12 best performing ones.

Results and Discussion

Influence of Deposition Pressure on Doped SiO$_X$:H Material Properties

Fig.2.2 presents the optical properties of the doped SiO$_X$:H films as a function of the deposition pressure. Increasing the deposition pressure from 1.5 to 8 mbar decreases the oxygen fraction in p-SiO$_X$:H from 73% to 31%. The decrease is even more significant in the n-SiO$_X$:H samples, where increasing the deposition pressure from 1.5 to 5 mbar
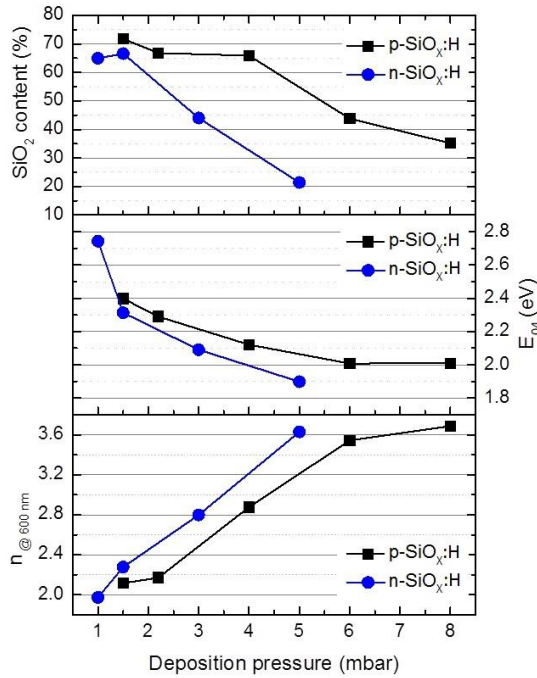
Figure 2.2: Optical bandgap energy, refractive index at 600nm and SiO$_2$ content of doped SiO$_X$:H films as a function of the deposition pressure

decreases the oxygen fraction from 68% to 23%. The lower oxygen fraction consequently leads to a higher refractive index. The refractive index of the p-SiO$_X$:H films increases from 2.1 at 2.2 mbar to 3.7 at 8 mbar. Consequently, the bandgap energy decreases from 2.3 eV to 2.0 eV for the same range of deposition pressures. The same trends were observed for the n-SiO$_X$:H samples. This relation between the oxygen fraction and the bandgap energy and refractive index of the SiO$_X$:H material are in line with earlier reports [39], [43], [44], [50], [76], [77].

The question is whether all these deposition conditions result in stable SiO$_X$:H layers and solar cells. First, the stability of the devices and p-SiO$_X$:H layers and its dependence on the deposition conditions are discussed. Fig.2.3 presents the electrical performance of the p-SiO$_X$:H films, as well as the performance of the cells with varying p-SiO$_X$:H deposition pressure, as a function of the time after deposition. The initial values for the E$_{act}$ of the films increase strongly with increasing deposition pressure from 406meV at 2.2mbar up to 735meV at 8mbar. This deterioration of the electrical performance with increasing deposition pressure is related to the crystallinity in the material, which decreases from 14% at 2.2mbar to 4% at 4mbar to fully amorphous at 8mbar. Crystalline tissue in p-SiO$_X$:H presents itself in the form of nanometer-wide branching filaments [36], [49]. As the crystalline tissue is much more conductive than the amorphous SiO$_X$:H tissue, these filaments form pathways for charge carrier conduction. Since the crystalline filaments are predominantly aligned in the growth direction of the doped SiO$_X$:H (top-to-
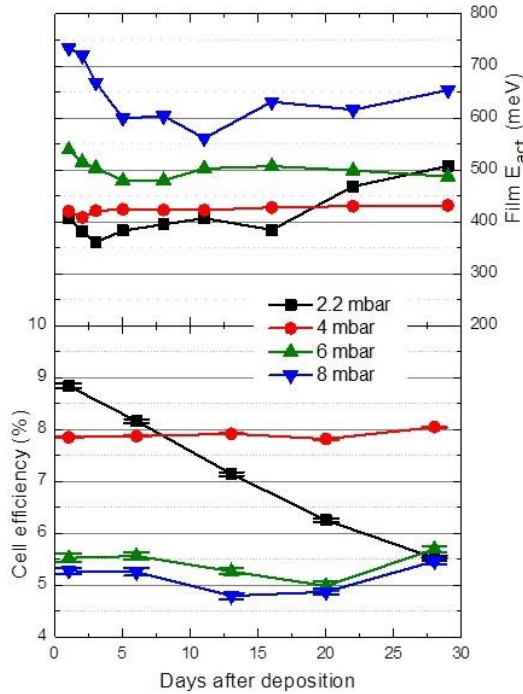
Figure 2.3: Activation energy of p-SiO$_X$:H films and conversion efficiency of cells with varying p-SiO$_X$:H layer deposition pressure, as a function of time

bottom direction of the cell), these filaments facilitate charge carrier movement through the doped SiO$_X$:H layer. As a result, a strong correlation between the crystallinity of the doped SiO$_X$:H and its activation energy and conductivity exists [36], [49], [59].

The film deposited at 2.2mbar has the best initial performance, but its activation energy showed a relative increase of 25% (+100meV) within the measured 28-day timeframe. However, the E$_{act}$ of the p-SiO$_X$:H film deposited at 4mbar remains stable, with a relative increase of 2% (+8meV), throughout the measured timeframe. The films deposited at 6 and 8 mbar also show no significant degradation over time. An interesting observation is that the evolution of the stability of the p-SiO$_X$:H layers in time are also apparent in the evolution of the performance of the cells in time. The cell with the 2.2mbar p-SiO$_X$:H layer has the highest initial conversion efficiency of 8.8%, but its performance degrades strongly over time, with a relative change of 49% (-4.3% absolute). The cell deposited under the same conditions, except for the p-SiO$_X$:H layer being deposited at 4mbar, has excellent stability over time with an efficiency of 7.9%. The cells with p-SiO$_X$:H layers deposited at 6 and 8 mbar also show no significant degradation over time. The degradation of the 2.2mbar reference cell was apparent in all of the external parameters. However, whereas the V$_{OC}$ and J$_{SC}$ only degrade by a small fraction, presenting a relative change of 2% (-20mV) and 7% (-1.03mA · cm^{-2}) respectively, the FF degraded most strongly with a relative decrease of 43% (31% absolute) from its initial value of 72.3%. The strong degradation of the FF is in line with a large increase of the series resistance, of relatively
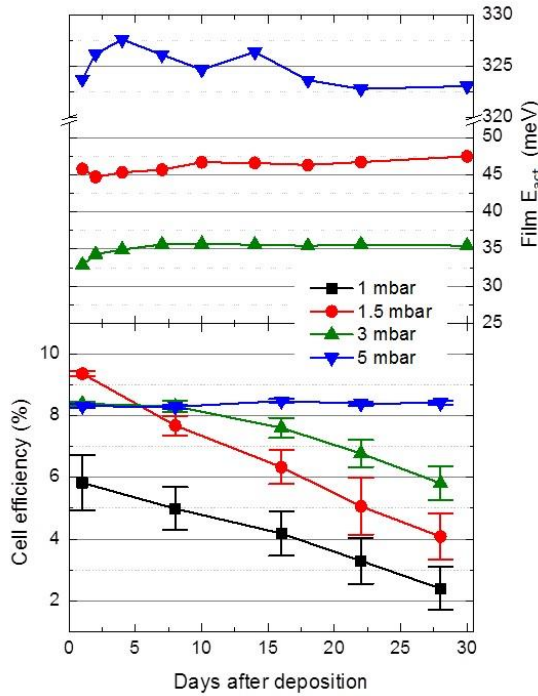
Figure 2.4: Activation energy of n-SiO$_X$:H films and conversion efficiency of cells with varying n-SiO$_X$:H layer deposition pressure, as a function of time

207% from the initial value of $4.6\Omega \cdot cm^2$, and a large decrease of the shunt resistance, which relatively decreased by 81% from its initial value of $748\Omega \cdot cm^2$. Interestingly, the stability of SiO$_X$:H is not unique for only the p-doped materials. The n-SiO$_X$:H layers have a similar dependence on the device performance. Fig.2.4 presents the E$_{act}$ of the n-SiO$_X$:H films and efficiency of the cells with varying n-SiO$_X$:H deposition pressure, as a function of time. The E$_{act}$ of the n-SiO$_X$:H films deposited at low pressures of 1.5 and 3 mbar increases only slightly over time, by 2-3meV. At 5mbar the E$_{act}$ no longer shows any significant degradation over the four-week timeframe. The 1mbar E$_{act}$ curve has been omitted since its conductivity was too poor for the measurement setup to get a reliable signal. Overall, the evolution of the E$_{act}$ of the n-SiO$_X$:H layers in time is insignificant compared to the evolution of E$_{act}$ of the p-SiO$_X$:H.

With the relative stability of the n-SiO$_X$:H films in mind, the evolution of the cell performance is rather striking. The cells with n-SiO$_X$:H layers processed at pressures of 1, 1.5 and 3 mbar degrade strongly over time, with a relative efficiency loss of between 45% and 63%. These results demonstrate that, similar to the p-SiO$_X$:H layers, increasing the deposition pressure has a positive effect on the stability of the solar cells. Note that no clear threshold value for the pressure above which stable solar cells are processed can be given. The threshold is determined by rather complex growth mechanism depending on the full set of deposition parameters. This is demonstrated by the fact that stable solar
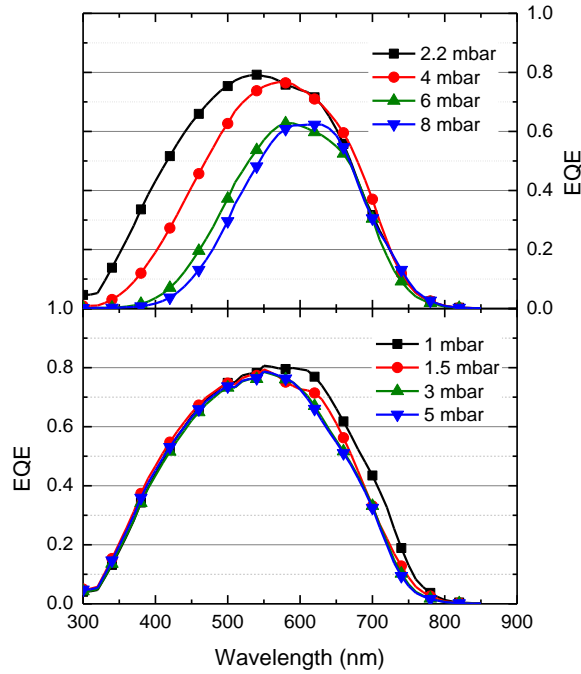
Figure 2.5: a (top): Shows the EQEs of cells with various deposition pressure for the p-SiO$_X$:H layer. The n-SiO$_X$:H is deposited at a pressure of 1.5mbar, Fig. 5b (bottom) shows the EQEs of cells with various deposition pressure for the n-SiO$_X$:H layer. The p-SiO$_X$:H is deposited at a pressure of 2.2mbar

cells can be achieved at a pressure of 4 mbar for the p-SiO$_X$:H layers and 5mbar for the n-SiO$_X$:H layers for the deposition conditions presented in Table 2.1. Fig.2.3 and Fig.2.4 show however that improving the stability of the doped SiO$_X$:H layers, by increasing the deposition pressure, comes at the price of a reduced conversion efficiency. Improving the stability of either the p-SiO$_X$:H layer or n-SiO$_X$:H layer leads to an absolute conversion efficiency loss of roughly 1% absolute. The cause of the initial performance loss is best demonstrated by the EQE curves of the cells, presented in Fig.2.5. Fig.2.5a shows the spectral response of cells with p-SiO$_X$:H deposited at various pressures, while Fig.2.5b shows those of cells with n-SiO$_X$:H layers deposited at various deposition pressure.

Fig.2.5a shows a decreased response in the short wavelength region with increasing deposition pressure for the p-SiO$_X$:H, shifting the EQE peak to the red region of the spectrum. The EQE decrease in the blue region indicates a loss of photons due to enhanced parasitic absorption in the p-SiO$_X$:H window layer of the cells. This enhanced parasitic absorption for p-SiO$_X$:H layers deposited at higher pressures is in line with the lower oxygen fraction and consequently lower values for E$_{04}$ of the p-SiO$_X$:H layer, as presented in Fig.2.2. The same reasoning can be applied to Fig.2.5b, where the EQE curves of the cells with n-SiO$_X$:H layers deposited at higher pressure have a lower spectral response just above the band gap of the a-Si:H absorber layer. Again, this can be attributed to enhanced parasitic absorption losses in the n-SiO$_X$:H layers deposited at higher pressure. A second
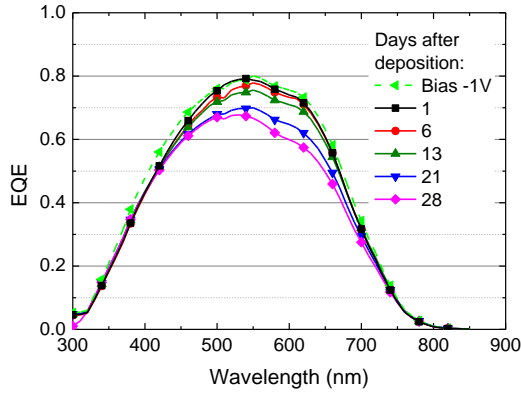
Figure 2.6: EQE curves of the standard cell (p-SiO$_X$:H and n-SiO$_X$:H deposited at 2.2mbar and 1.5mbar respectively) at different points in time over a four-week period. -1V bias voltage curve (green) measured 28 days after deposition.

noticeable effect in Fig.2.5a is the overall EQE decrease of the cells with p-SiO$_X$:H layers deposited at 6 and 8 mbar. This additional decrease is believed to be caused by enhanced reflection of the incident light at the front of the solar cell. The high pressure processing conditions result in relatively high refractive indices of around 3.6, at a wavelength of 600nm, which creates a large refractive index mismatch at the p-SiO$_X$:H/TCO interface. A relatively large fraction of the light is therefore reflected before reaching the absorber layer. The high refractive index of n-SiO$_X$:H deposited at 5mbar does not cause a likewise performance loss in p-i-n configuration, as the mismatch at the n-layer interfaces does not prevent any light from reaching the absorber layer.

Origin of the Degradation of TFSSC with Doped SiO$_X$:H Layers

In the previous section the relation between the deposition pressure and the stability of doped SiO$_X$:H has been discussed. The crucial question is what the physical origin of the instability is. Fig.2.6 shows the EQE curves of the reference p-i-n cell at 5 different measuring points over a period of 4 weeks

The area under the EQE curves continually decreases over time and the decrease appears to occur over the entire spectrum. Furthermore, a measurement with a -1V bias voltage, 13 days after deposition, recovers the EQE curve to its initial performance. The overall decrease of the area under the EQE curve, and the recovery of the performance under a bias voltage, indicates reduced charge carrier collection rather than an optical loss. This observation is in line with the strong degradation of the FF and the resistances discussed in the preceding chapter. Furthermore, similar trends were observed for the degradation of the activation energy for the corresponding 2.2mbar p-SiO$_X$:H film and 1.5mbar n-SiO$_X$:H film of Fig.2.3 and Fig.2.4. However, the absolute degradation was significantly larger for the p-SiO$_X$:H. From the previous results it can be concluded that we can use 4mbar conditions to process a stable p-SiO$_X$:H layer, 2.2mbar conditions to process an unstable p-SiO$_X$:H layer, 5mbar conditions to process a stable n-SiO$_X$:H layer
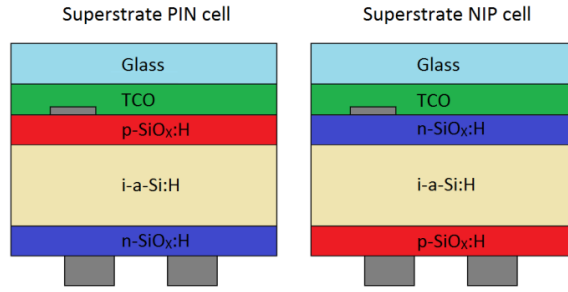
Figure 2.7: Simplified schematic representation of the superstrate p-i-n and n-i-p cell structures

Superstrate **p-i-n** configuration	Stable n-layer 5.0 mbar	Unstable n-layer 5.0 mbar
Stable p-layer 4.0 mbar	Stable	Stable
Unstable p-layer 2.2 mbar	Stable	Unstable

Superstrate **n-i-p** configuration	Stable n-layer 5.0 mbar	Unstable n-layer 5.0 mbar
Stable p-layer 4.0 mbar	Stable	Stable
Unstable p-layer 2.2 mbar	Unstable	Unstable

Figure 2.8: Stability of various device configurations in p-i-n (top) and n-i-p (bottom) structure. The green colour coding indicates a stable film and cell, while a red colour coding implies the unstable material.

and 1.5mbar to process an unstable n-SiO$_X$:H layer. Using these layers with different stability properties, we can look into the stability of cells with different device configurations. As we suspect that the observed doped SiO$_X$:H instability is not necessarily light induced, the cell stability might depend on the device structure as well as the stability properties of the integrated SiO$_X$:H layers. The device configurations were therefore deposited in a p-i-n sequence as well as a n-i-p sequence. A simplified schematic representation of these structures is shown in Fig.2.7.

Fig.2.8 presents the stability of the various stability configurations of the p-i-n and n-i-p cells, as gathered from Fig.2.3 and Fig.2.4. The figure demonstrates that the p-i-n cell is only unstable when both the integrated p-SiO$_X$:H and n-SiO$_X$:H layers are unstable. This means that the p-i-n cell is stable even when it contains a single unstable p-SiO$_X$:H or n-SiO$_X$:H layer. As conventionally an unstable material in a solar cell inevitably leads to an unstable solar cell, it is remarkable to find that in a superstrate p-i-n configuration an unstable doped p-SiO$_X$:H layer does not necessarily undermine the stability of its performance. Both n-i-p cells with an unstable p-SiO$_X$:H layer degrade strongly over time, showing a relative performance loss of 48-49% over a 24-day period. The cells with a stable p-SiO$_X$:H deposition pressure remain stable throughout the measured time-

frame. Moreover, the degradation, or lack thereof, occurs regardless of the stability of the n-SiO$_X$:H layer. The overviews provided in Fig.2.8 clearly demonstrate that two parameters determine whether the device configuration is stable. First, regardless of the device structure, a stable p-SiO$_X$:H layer will produce a stable cell. Secondly, regardless of the device structure, a stable n-SiO$_X$:H layer at the back side of the cell will produce a stable cell. The only configuration in which an unstable p-SiO$_X$:H layer resulted in stable device performance, is the configuration in which a dense n-type SiO$_X$:H is used in the back reflector of the cell. These results therefore demonstrate that the degradation of the p-SiO$_X$:H layer is responsible for the observed degradation of TFSSC with doped SiO$_X$:H layers and that the minor degradation observed in the n-SiO$_X$:H films does not significantly affect the performance of TFSSC. As to the cause of the degradation, the results implicate that multiple mechanisms are involved in the degradation of thin film silicon cells including doped SiO$_X$:H layers. First from these results it can be excluded that the observed degradation is light induced, since none of the four device configurations prevents the incident light from penetrating and reaching both doped SiO$_X$:H layers. In addition, the exposure of the doped layers to light does not differ between the four studied configurations, while the stability of the cells do. Secondly, illuminated cells do not show any enhanced degradation when operating under maximum power points, open circuit or short circuit conditions. This excludes field enhanced drift of ionic species or charged defects in the photovoltaic silicon layers.

Therefore, chemical instability, like oxidation of the crystalline silicon grains or filaments in the doped layers, is the most likely origin for degradation of the electrical performance of the cell. Oxidation at the surface of crystalline grains will increase the defects at grain interfaces and bulk of the doped SiO$_X$:H layers and enhance the charge carrier recombination. Similar oxidation has been studied for heterogeneous nanocrystalline silicon (nc-Si:H) alloys and the electrical quality and the performance of nc-Si:H solar cells [69], [74]. In particular, one study has demonstrated that water is predominantly involved in the oxidation of various orientations of hydrogenated crystalline silicon surface, whereas these surfaces are quite inert to the oxygen molecule [78]. We therefore suspect that the in-diffusion of water vapor from the ambient is responsible for the oxidation of the surface of the crystalline grains in the doped SiO$_X$:H material. In the case of oxidation, it matters where the SiO$_X$:H layer is positioned in reference to the backside of the solar cell, that is exposed to ambient air. The SiO$_X$:H layer at the back side is only partially protected from ambient air by the metal contact, as the metal contacts do not fully cover the back of the substrate. However, the SiO$_X$:H layer at the front window is better encapsulated by both the i-a-Si:H and the SiO$_X$:H layer in the back reflector of the cell. This additional encapsulation can function as a barrier against the in-diffusion of moisture from the ambient air. As such, a stable, dense n-SiO$_X$:H layer, or other type of encapsulant, prevents the degradation of the vulnerable p-SiO$_X$:H layer and effectively maintains the stability of the cell.

Relation Between Stability, Crystallinity and Thickness

We have made the point that the oxidation of the p-SiO$_X$:H layer, under influence of moisture present in the ambient air, is the cause of the poor stability of TFSSC with doped SiO$_X$:H layers. The remaining questions are: What is the exact degradation mechanism
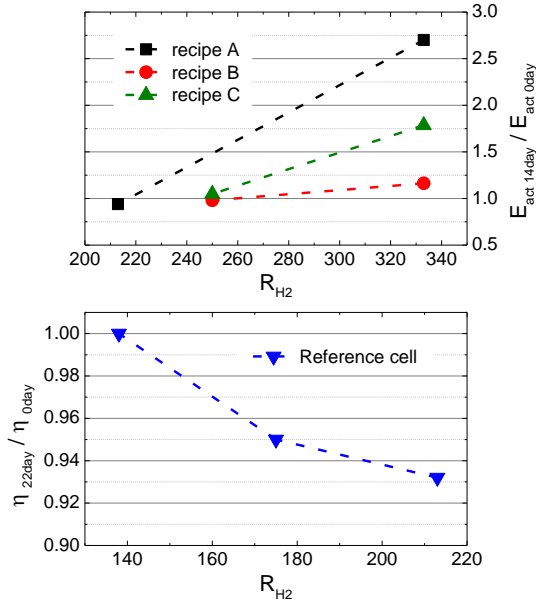
Figure 2.9: Relative performance loss of p-SiO$_X$:H films and cells as a function of the R$_{H_2}$. Dashed line indicates the use of a similar deposition recipe

Table 2.2: Deposition recipes of p-SiO$_X$:H films shown in Fig.2.9

	A	B	C
F(CO$_2$)/F(SiH$_4$)	4.0	4.2	4.7
F(H$_2$)/F(SiH$_4$)	213-333	250-333	250-333
F(B$_2$H$_6$)/F(SiH$_4$)	0.004	0.004	0.004
Pressure (mbar)	5	4	4
RF power (mW · cm^{-2})	90.3	125	111.1
Temperature (°C)	180	180	180

and why do p-SiO$_X$:H films deposited at higher pressures not suffer from degradation.

Fig.2.9 shows the degradation ratio, defined as the E$_{act}$ after 14days in reference to the E$_{act}$ after deposition (E$_{act\ 14day}$ / E$_{act\ 0day}$) for the p-SiO$_X$:H films and the efficiency after 22 days in reference to the initial efficiency (η_{22day} / η_{0day}) for the cells. There appears to be a strong relation between the R$_{H_2}$ value used for the deposition of p-SiO$_X$:H films and the rate of degradation of the corresponding films. We found that the R$_{H_2}$ slightly affects the refractive index and optical bandgap energy of the doped SiO$_X$:H. More importantly however is the strongly increasing crystallinity with increasing R$_{H_2}$ [36], [51]. The crystallinity of the presented deposition recipes A and B increased from 6-8% to 20-21% with a R$_{H_2}$ increase from 250 to 333, and for deposition recipe C a R$_{H_2}$ increase from 213 to 333 lead to a crystallinity increase from 0% to 24%. In line with these observations, we find similar trends for the deposition pressure, for which we demonstrated the correlation with the degradation rate of the doped SiO$_X$:H films. The crystallinity of the

doped SiO_X:H material is higher for films deposited at lower pressures. Even though the deposition pressure affects other material properties besides the crystallinity, the doped SiO_X:H films proved to be stable when the deposition pressure was increased, and the crystallinity decreased, to a certain degree.

The trends observed in the p-SiO_X:H films and cells however do not perfectly match. It was found that a stable p-SiO_X:H film does not necessarily produce a stable cell. Five separate deposition recipes that produced stable p-SiO_X:H films resulted in highly unstable p-i-n cells, for which relative efficiency losses between 73% and 92% were observed within a single day. There are two differences between the p-SiO_X:H film and the p-SiO_X:H layer in the cell, namely the substrate and the thickness of the layer. As mentioned in the experimental section, the films are deposited at a thickness of 100nm. The p-SiO_X:H layers in the cells have a thickness of 20nm. When the thickness of the p-SiO_X:H layer of the above mentioned highly unstable cell was increased to 100nm, to match the thickness of the stable p-SiO_X:H film, the resulting cell proved to have excellent stability within the measured timeframe.

However, the substrate type plays an important role as well. The p-SiO_X:H film is deposited directly on glass, while the p-SiO_X:H layer in the cell is deposited on top of a p-nc-Si:H seed layer. The more crystalline seed layer, with a crystallinity of roughly 30%, affects the initial growth of the much less crystalline p-SiO_X:H layer, with a crystallinity of about 4-5%. The seed layer therefore increases the crystallinity of the p-SiO_X:H layer with respect to the film that is deposited on top of a glass substrate. The initial growth of the p-SiO_X:H layer is strongly affected by the highly crystalline seed layer, but as the p-SiO_X:H growth continues, the crystallinity of the material decreases to a certain level, as dictated by the deposition recipe. This concept is illustrated in Fig.2.10**a**, in which the crystallinity is plotted as a function of the width of the cell. Two crystalline growth regimes in the p-SiO_X:H layer can be discerned in the figure. The initial regime is where the crystallinity is decreasing from the highly crystalline seed layer, which is followed by the second regime where the crystallinity remains stable at a level equal to that of the doped SiO_X:H films, as dictated by the deposition recipe. Therefore, if the p-SiO_X:H layer is thin enough to be located within the initial regime, it will experience an elevated level of crystallinity at the interface with the i-a-Si:H layer, as shown in Fig.2.10**b**.

It has been reported that post-deposition oxidation of nc-Si:H occurs if hydrogenated crystalline grain boundaries in the bulk are observed [69], [78], [79]. In device grade, stable, nc-Si:H films the grain boundaries are passivated by amorphous tissue rather than by hydrogen atoms. The amorphous tissue is necessary to fill the voids between the grains [80]. Lack of amorphous tissue allows the diffusion of H_2O in the cracks between the crystalline grains [69]. This leads to oxidation of the hydrogenated crystalline surfaces. We believe that a similar mechanism occurs in doped SiO_X:H material. The a-SiO_X:H tissue has the same functionality as a-Si:H tissue in nc-Si:H, i.e. it passivates the surface of the crystalline grains. If the crystallinity is too high, so the fraction of a-SiO_X:H (or a-Si:H) tissue with respect to c-Si tissue is too low, the silicon grains in the doped SiO_X:H suffer from post deposition oxidation. In other words, the fraction of a-Si:H and a-SiO_X:H tissue in the doped SiO_X:H material is insufficient to passivate the crystalline grains in films with a high crystallinity. This crystalline tissue passivation is not to be confused
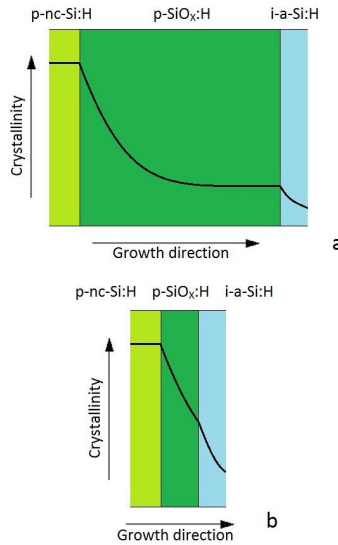
Figure 2.10: Schematic representation of the development of the crystallinity in the growth direction of a p-i-n cell. **b** shows a cell with a relatively thin p-SiO$_X$:H layer

with dangling bond passivation, which would also affect the initial performance. Poorly passivated crystalline silicon grains at the p-layer interface leaves the p-SiO$_X$:H layer vulnerable to degradation. Moisture in the ambient air has the ability to diffuse through the TFSSC and oxidize the poorly passivated crystalline grains at the p-layer interface. This results in the degradation of the electrical properties and p-doped nature of the p-SiO$_X$:H layer. At high deposition pressure, or low H$_2$ flow rate, the overall crystallinity of the deposited p-SiO$_X$:H layer is relatively low and the crystalline grains are properly passivated by a-Si:H and a-SiO$_X$:H tissue. With proper passivation, the p-SiO$_X$:H layer is protected from degradation similar to chemically stable nc-Si:H [69] and the resulting TFSSC remains stable throughout the measured timeframe.

Conclusion

In this paper we demonstrate the responsible mechanism involved in the degradation of a-Si:H solar cells, in which doped SiO$_X$:H films are integrated. It was demonstrated that the p-SiO$_X$:H layer is responsible for the degradation of single junction TFSSC. The influence of the deposition pressure on the material properties and stability of doped SiO$_X$:H films has been investigated. Increasing the deposition pressure of doped SiO$_X$:H films increases its stability. However, the optical and electrical properties of the films deteriorate when SiO$_X$:H films are deposited at higher pressures. This leads to a loss in the initial conversion efficiency when these doped SiO$_X$:H layers with improved stability are used in p-i-n cells. Furthermore, it was shown that for materials with lower crystallinity the rate of degradation is significantly reduced. We argue that at low deposition pressures the crystallinity in the p-SiO$_X$:H layer is relatively high and the fraction of a-Si:H and a-SiO$_X$:H tissue is insufficient to properly passivate the crystalline grains in the p-SiO$_X$:H material. These

unpassivated crystalline grains at the p-layer interfaces leaves the p-SiO$_X$:H vulnerable to the in-diffusion of H$_2$O present in the ambient air. Water vapor penetrates through the material and oxidizes the crystalline grains in the p-SiO$_X$:H layer, degrading its electrical properties over time. When well passivated at sufficiently high deposition pressure, or sufficiently low R$_{H_2}$, this degradation of the p-SiO$_X$:H layer does not occur. Alternatively, it was shown that an encapsulant can prevent the in-diffusion of water vapor altogether, protecting the p-layer from oxidation even at high crystallinity values. The n-SiO$_X$:H layer can act as such a barrier against water vapor penetration at sufficiently low crystallinity.

2.2 The relation between precursor gas flows, thickness dependent material phases and opto-electrical properties of doped a/nc-SiO$_{X \geq 0}$:H films

This section was published in *IEEE Journal of Photovoltaics*[†]

Abstract

Doped layers are a determining factor for the performance of photovoltaic devices such as silicon heterojunction and thin film silicon solar cells. The material properties of doped hydrogenated amorphous/nanocrystalline silicon-oxide (a/nc-SiO$_{X \geq 0}$:H) films processed by plasma-enhanced chemical vapor deposition generally exhibit a trade-off between optical and electrical performance. The opto-electrical properties are the result of different material phases in these heterogeneous films, such as hydrogenated amorphous silicon and silicon-oxide tissue, nanocrystalline silicon grains, their corresponding fractions and extent of doping. In this work, all the precursor gas flows are varied to achieve a wide range of doped a/nc-SiO$_{X \geq 0}$:H phases. A material phase diagram is introduced to clarify the complex interplay between processing conditions, dominant growth mechanisms, a/nc-SiO$_{X \geq 0}$:H phases and the resulting opto-electrical properties. In addition, it is discussed that material properties are strongly dependent on the thickness of the films, as the mix of different material phases is not uniform along the growth direction

2.2.1 Introduction

The efficiency of photovoltaic devices in which thin film silicon layers are integrated is strongly influenced by the properties of the doped layers. Such devices include silicon heterojunction solar cells [37], [81], [82], hybrid amorphous silicon/CIGS tandem devices [75], micromorph solar cells [40], [46], [83] and hybrid perovskite/c-Si tandem devices [84]. The doped silicon layers have a variety of multifunctional applications in these devices. Generally, the functionalities require optically transparent doped layers with high transverse conductivity. There exists a trade-off however between the optical and electrical properties of the layers [57]–[59]. Which particular property should be prioritized, such as a high optical bandgap for a window layer, the refractive index for an intermediate reflective layer, or the transverse conductivity in a tunnel recombination junction, depends on the particular application. It was previously demonstrated that the opto-electrical trade-off in doped silicon-based films results from an interplay between the development of a crystalline phase and oxygen integration in the amorphous phase [60], [61], as well as the density of the amorphous phase [71], [85]. An in-depth understanding of the material growth of the doped layers is therefore crucial for the production of an optimal device. In this paper we have investigated the influence of the precursor gas flow rates and thickness on the properties of p- and n-doped hydrogenated amorphous and nano-crystalline silicon and silicon-oxide (a/nc-SiO$_{X \geq 0}$:H) films.

2.2.2 Experimental Details

The doped films are deposited on Corning Eagle XG glass, cut in 10cm x 2.5cm strips. For processing, a RF plasma enhanced chemical vapor deposition cluster tool, operating at a frequency of 13.56MHz is used. In this cluster tool p-doped films and n-doped films are processed in separate dedicated chambers. Recipes were developed earlier for the doped hydrogenated silicon oxide (SiO$_X$:H) layers such that the films provide adequate initial performance in terms of both their optical and electrical performance for window layer applications in thin film solar cells [85], [86]. Based on this, in this work the material properties of the doped films are further characterized within a relatively small optimal range. The deposition parameters of the doped silicon layers and the ranges used for the precursor gas flow rates are reported in Table 2.3. The reported films have a thickness of 60-80nm, unless specifically mentioned otherwise. The deposition rates reported in Table 2.3 are the result of the full set of deposition conditions and indicates the range of deposition rates for all p-doped and n–doped films presented in this work. The diborane (B$_2$H$_6$) and phosphine (PH$_3$) precursors are diluted in H$_2$, such that the reported B$_2$H$_6$ gas flow rate consists of 0.02% diborane and the PH$_3$ flow rate consist of 2% phosphine. Incorporation of oxygen happens during processing through addition of a CO$_2$ precursor gas, and is not a result of a post-deposition oxidation process. Energy-dispersive X-ray spectroscopy measurements of a few p-doped SiO$_X$:H (p-SiO$_X$:H) samples indicated an atomic fraction of carbon in the films of below 1% , as a result of the CO$_2$ precursor. It is therefore assumed that carbon integration does not play a significant role in the presented results.

To perform dark conductivity measurements, parallel electrodes consisting of 500-nm-

Table 2.3: deposition parameters of the doped films. For the gas flow rates the range investigated in his work is indicated. The deposition rates are a result of the deposition conditions and indicate the highest and lowest deposition rate for the p-doped and n-doped samples presented in this work, respectively.

	p-SiO$_X$:H	n-SiO$_X$:H
SiH$_4$ (sccm)	0.6-1	1
H$_2$ (sccm)	170-200	100-120
CO$_2$ (sccm)	0-2.3	0-2.4
B$_2$H$_6$ (200ppm) (sccm)	10-40	-
PH$_3$ (0.2%) (sccm)	-	1.2-3.6
T$_S$ (°)	180	180
P$_{RF}$ (mW $\cdot$ cm^{-2})	90.3	69.4
p (mbar)	2.2	1.5
Dep. rate (nm $\cdot$ s^{-1})	0.015-0.047	0.011-0.019
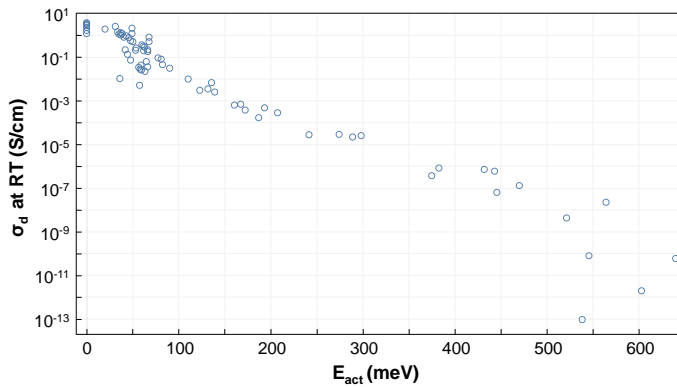
Figure 2.11: Dark conductivity (σ_d) at room temperature plotted as a function of activation Energy (E$_\mathrm{act}$) on a semi-logarithmic plot, for all processed samples.

thick aluminium bars were deposited onto the films using electron beam evaporation. These measurements were performed by measuring the current conducted between two electrodes at a fixed voltage of 10V and temperature in a dark environment. By repeating this measurement at 5°C intervals, from 130°C to 60°C, the activation energy (E_{act}) and dark conductivity at room temperature can be calculated using the Arrhenius equation:

$$k_{\mathrm{B}}T = -E_{\mathrm{act}}\ln\left(\frac{\sigma_0}{\sigma}\right) \qquad (2.3)$$

Here σ is the conductivity, σ_0 is the material dependent conductivity constant, k_{B} is Boltzmann's constant and T is the temperature in Kelvin. The E_{act} and dark conductivity at room temperature (σ_{d}) showed very similar trends, with high σ_{d}'s at low E_{act}'s. This is shown in Fig.2.11, where the σ_{d} of all measured samples is plotted as a function of the E_{act}. The E_{act} is therefore used in this work as a metric for the electrical performance of the doped a/nc-SiO$_{X \geq 0}$:H films.

A J.A. Woollam spectroscopic ellipsometer was used to determine the refractive index and the optical bandgap (E_{04}). The spectroscopic ellipsometry (SE) measurements were fitted to an effective medium model using the Bruggeman analysis mode. a/nc-SiO$_{X \geq 0}$:H is a heterogeneous material consisting of an amorphous structure of hydrogenated amorphous silicon (a-Si:H), amorphous silicon-oxide (a-SiO$_X$:H) and crystalline grains. Therefore, the material properties of SiO$_2$ and a-Si:H are used to mimic the a-SiO$_X$:H and a-Si:H tissue and polycrystalline silicon is used to mimic the crystalline grains. Consequently, the model uses the material properties of SiO$_2$, obtained from [87], a-Si:H, obtained from in-house measurements (Cody-Lorentz oscillator: Amp=122. Br=2.55, E_0=3.59, E_G=1.62, E_p=1.94, E_t=0.00, E_u=0.5), polycrystalline silicon (poly-Si_g2) obtained from the Woollam material library, to approximate the optical properties of doped a/nc-SiO$_{X \geq 0}$:H material. This is approach is similar to [88] and to [40], where the fraction (R_{SiOx}) is obtained indirectly. In [88] the oxygen content obtained through this approach was found to be consistent with the content deduced from X-ray photoelectron spectroscopy. In this work the observed trends in R_{SiOx}, as a function of deposition conditions, were found to be consistent with trends observed in the peak intensity of the stretching modes related to silicon-oxide bonds obtained from Raman spectroscopy measurements.

In this work, the E_{04} optical bandgap is used to describe trends in the optical absorption of the films. The different phases in the heterogeneous a/nc-SiO$_{X \geq 0}$:H material each retain their own respective electrical bandgap energy. The E_{04} can therefore be considered an effective optical bandgap, reflecting variations in the material phase fractions and quality of the amorphous phase. This definition is often used for heterogeneous mixed phase materials [58], [85], [39], [43], [88], for which determining a single electrical bandgap energy is non-trivial and often arbitrary. The E_{04} was determined by calculating the photon energy level at which the absorption coefficient equals 10^4 cm^{-1}. Additional structural analysis was performed through Raman spectroscopy, using an inVia confocal Raman microscope with a laser operating at a wavelength of 514nm. The crystallinity of the films was obtained from these measurements by fitting a Gaussian distribution with a peak at a Raman shift of 520 cm^{-1} corresponding to the crystalline silicon phase and by fitting Gaussians at 160 cm^{-1}, 320 cm^{-1}, 390 cm^{-1} and 480 cm^{-1} corresponding to transverse

acoustic, longitudinal acoustic, longitudinal optic and transverse optic amorphous silicon phonon modes, respectively. The crystallinity (χ_C) in this paper is defined by:

$$\chi_C = \frac{I_{\text{c-Si}}}{I_{\text{c-Si}} + \gamma \cdot I_{\text{a-Si}}} \tag{2.4}$$

Here $I_{\text{c-Si}}$ is the integrated area under the Gaussian distribution at 520cm^{-1} corresponding to the crystalline silicon phase and $I_{\text{a-Si}}$ for the peak at 480cm^{-1} corresponding to the amorphous phase. γ is a correction factor for the difference in cross section for phonon excitation of c-Si with respect to a-Si and equals 0.8, similar to [89], [90]. Consequently, the χ_C indicates the crystalline fraction of the silicon phase and does not take the amorphous silicon-oxide phase into account. This means that the total fraction of the doped a/nc-SiO$_{X\geq0}$:H material that is crystalline, so the crystalline phase fraction ($R_{\text{c-Si}}$) is equal to:

$$R_{\text{c-Si}} = \chi_C(1 - R_{\text{SiOx}}) \tag{2.5}$$

Regarding experimental error. The thickness, R_{SiOx} and E_{04} are extracted from SE measurements. All model fits have a mean square error between 2 and 7. For these fits, the thickness has an error margin between 0.1-0.9%, the SiO$_2$, a-Si:H and poly-Si material fractions have an relative error margin of 0.1-2%. For a number of selected samples 5 points were measured on a single film. Based on these measurements a maximum error margin of ±0.02eV can be reported for the E_{04}, ±2.2nm for the thickness and $\pm0.15\%$ absolute for the SiO$_2$ material fraction. Similarly, multiple Raman measurements on a single sample showed an error margin of 3.13% absolute for the crystallinity values reported in this work. A similar procedure was performed for the dark conductivity measurements, for 4 different sets of contacts on a single film. The resulting E_{act} values showed an maximum error margin of ±7meV. These reported values give insight into the combined error introduced by the measurement setups, model fits and sample uniformity. As to error in reproducibility, although each sample with its unique combination of deposition conditions and deposition time was produced only once, the very large sample size of over 75 films is a testament to the reproducibility and validity of the reported trends.

2.2.3 Results and Discussion

Influence of precursor gas flow rates

We start with the influence of the precursor gasses on the properties of p-doped silicon films. All precursor gas flow rates are reported relative to the silane flow rate ($F_{\text{gas/SiH4}}$). Changes in the deposition parameters of the films, such as the relative precursor gas flow rates, influence the plasma conditions. The plasma conditions in turn affect the growth of the doped a/nc-SiO$_{X\geq0}$:H material. This becomes apparent through changes in properties such as the crystallinity, the active dopant concentration, the density of the amorphous silicon phase and the oxygenation of the amorphous phase. The material growth in turn influences the opto-electrical behavior of the doped films. Therefore, to properly understand the complex influence of the relative precursor gas flow rates, we first look at the grown material. Using the the silicon-oxide phase fraction (R_{SiOx}), obtained from SE measurements, and the crystalline phase fraction ($R_{\text{c-Si}}$), obtained from Raman measurements, of the films, material phase plots are developed and presented in Fig.2.12,

to qualitatively visualize the effects of the relative gas flow rates on the a/nc-SiO$_{X \geq 0}$:H material growth. Even though the extent of oxidation of the a-SiO$_X$:H can vary, the a-Si and a-SiO$_X$:H are shown as separate material phase fractions as these phases can coexist in the heterogenous material [60], [61]. Moreover, it supports visualization of both the level of oxidation and the transition from an a/nc-Si:H to an a/nc-SiO$_X$:H material.

Fig.2.12 shows that, as a function of the precursor gas flow rates, the a-Si:H, a-SiO$_X$:H and crystalline silicon phase fractions present in the material can change significantly. The middle plot for instance shows that when $F_{H2/SiH4}$ is decreased and $F_{CO2/SiH4}$ is increased, the material changes from high crystallinity nanocrystalline silicon to predominantly amorphous silicon oxide. If we look at the effect of $F_{CO2/SiH4}$ in particular, in Fig.2.12 (middle, bottom), we see that an increase of $F_{CO2/SiH4}$ results in an increase of the R_{SiOx}, while crystalline growth is suppressed. For instance, when $F_{CO2/SiH4}$ is increased from 0 to 2.3 R_{SiOx} is increased from 15-28% to 41-52%, depending on $F_{B2H6/SiH4}$ and $F_{H2/SiH4}$. An increase of $F_{H2/SiH4}$, on the other hand, generally results in a higher crystallinity, which can also be observed in Fig.2.12 (top, middle). This relation between the H$_2$ flow rate and crystallinity will be discussed in more detail later.

The effect of the relative dopant flow rate $F_{B2H6/SiH4}$ is rather more complex, as observed in Fig.2.12 (Top, bottom). For one, the dopant precursor suppresses crystalline growth [60], [91], [92]. Raman measurements show that the crystallinity continually decreases with increasing $F_{B2H6/SiH4}$. At $F_{H2/SiH4}$ of 170 for instance, depending on the relative CO$_2$ flow rate, the $R_{c\text{-}Si}$ of the silicon phase decreases 18-20% when $F_{B2H6/SiH4}$ is increased from 10 to 40. Increasing the $F_{B2H6/SiH4}$ also leads to a decrease of the relative a-SiO$_X$:H material phase. The R_{SiOx} of the films with $F_{CO2/SiH4} \approx 1.4$ and $F_{H2/SiH4} = 170$, for instance, decreases from 46% to 17% when $F_{B2H6/SiH4}$ is increased from 10 to 40.

We have briefly discussed the effect of changes in the plasma conditions, through variations in the precursor gas flow rates, on the material phases in the doped a/nc-SiO$_{X \geq 0}$:H films. We can now consider the effect these material phase changes have on the optoelectrical properties. These effects can be observed in Fig.2.13. The material growth is a result of the delicate interplay between the different precursor gas flows. For that reason a single plot has been developed for the E_{act} and for the E_{04}, to visualize a large number of data points, rather than a large number of plots with fewer data points. The various data points are the result of variations in the relative B$_2$H$_6$, H$_2$, and CO$_2$ flow rates. Variations in the B$_2$H$_6$ are indicated by the depth of color, variations in the H$_2$ flow rate are indicated by the icon size and open/closed symbol nature, while the relative CO$_2$ flow rate is plotted on the x-axis. This means that the effect of varying a single deposition parameter can be observed by considering symbols of a certain size/color at a fixed x-axis position. As a visual aid, arrows of different styles have been introduced in the figure to describe different trends. Please note that the arrow style and fill used for certain $F_{gas/SiH4}$ in Fig.2.12 match those used in Figs.2.13, 2.14 and 2.15.

First, an increase of $F_{CO2/SiH4}$ increases both the E_{act} (Fig.2.13 ↑1) and the E_{04} (Fig.2.13 ↑2) of the doped layers. The increase of the E_{04} is clearly visible for each combination of gas flow rates. The increase of E_{04} with increasing R_{SiOx} has been widely reported [39], [43], [61], [76], [85], [93]. The influence of $F_{CO2/SiH4}$ on the electrical properties is less pronounced, though still significant at relatively high H$_2$ flow rates. The p-doped hydrogenated nanocrystalline silicon (p-nc-Si:H) samples for instance, deposited without
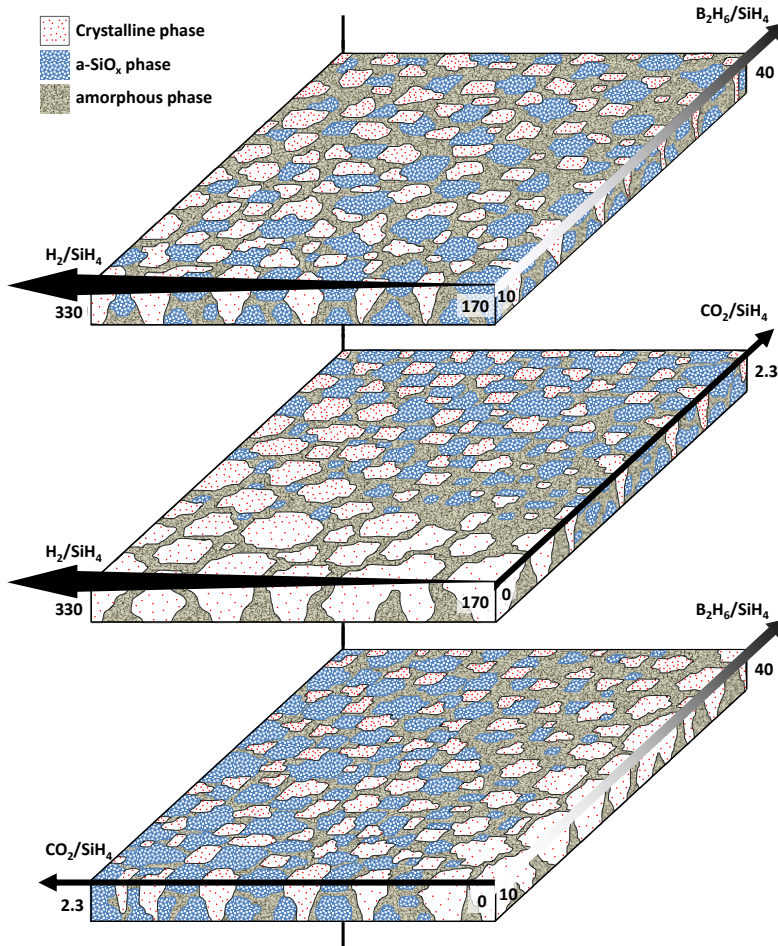
Figure 2.12: Material phase diagrams of p-doped silicon materials as a function of the relative H_2 and B_2H_6 flow rates (top), CO_2 and H_2 flow rates (middle), and CO_2 and B_2H_6 flow rates (bottom). The blue/white areas indicate an amorphous silicon oxide phase. The grey areas indicate an amorphous silicon phase. The white areas with red dots indicate a crystalline silicon phase. The plain arrow with solid fill indicates direction of increasing $F_{CO2/SiH4}$. The plain arrow with gradient fill indicates effect of increasing $F_{B2H6/SiH4}$. The widening arrow with solid fill indicates the effect of increasing $F_{H2/SiH4}$. These conventions are similar to those in Figs.2.132.142.15. Each plot is the result of connecting 12 parts, a 4x3 matrix. For each part the R_{SiOx} obtained from SE measurements was used to determine the a-SiO_X phase, while the R_{c-Si}, obtained from Raman measurements, was used to determine the c-Si phase. The red dots in the crystalline phase represent the dopants, while the density of red dots indicates the active dopant concentration. The active dopant concentration is not obtained from direct measurement, but rather indicates an educated guess of the active dopant concentration relative to the other processed samples. This estimation is based on trends in the dark conductivity measurements and R_{c-Si}, operating under the assumption that the measured dark conductivity is a function of the R_{c-Si} and active dopant concentration. The potential effect crystalline grain connectivity and grain passivation are consequently not considered.

CO_2 precursor, have an E_{act} of around 35meV, which is increased to around 60meV at $F_{CO2/SiH4} \approx 1.7$ and between 80-160meV for $F_{CO2/SiH4} = 2.33$. These trends are the result of an increase of the R_{SiOx} and decrease of the R_{c-Si}.

An increase of the hydrogen flow rate generally results in a lower E_{act} (Fig.2.13 ↑3), which is a consequence of the increasing R_{c-Si}. A higher R_{c-Si} likely indicates an improvement of the macroscopic conductive properties of the film as a results of more or larger crystalline grains with better grain-interconnectivity. This is in line with reports from [94] and [50]. The influence of $F_{H2/SiH4}$ on E_{04} is not conclusive from the presented results.

$F_{B2H6/SiH4}$ significantly affects the material growth. For the electrical properties, two different trends are visible. Increasing the doping flow rate significantly increases the E_{act} of the films (Fig.2.13 ↑4). The E_{act} increases from 110meV to 443meV at $F_{CO2/SiH4}=1.4$ and from 173meV to 470meV at $F_{CO2/SiH4}=2.2$ when $F_{B2H6/SiH4}$ is increased from 10 to 40. However, in the deposition regime where a relatively high CO_2 and H_2 flow rate are used (Fig.2.13 ↑5), a higher $F_{B2H6/SiH4}$ actually leads to a decrease of the E_{act}. We believe that the doping flow rate has two competing effects. For one, the dopant precursor suppresses crystalline growth. If, on the other hand, the films are relatively crystalline, an increase of $F_{B2H6/SiH4}$ can lead to a more conductive film through a larger active dopant concentration.

Understanding this requires some insight into the integration and ionization behavior of boron in a mixed phase material. For one, the doping efficiency in the amorphous phase is very low, since no substitutional doping occurs in a material lacking long range order [95], [96]. Instead, a small fraction of dopants in an amorphous network result in ionized defects, as a consequence of induced structural disorder [97], [98]. In the crystalline phase, a boron atom is much more likely to be active, as it substitutes a silicon atom in the lattice. It has been reported however that boron preferentially resides at the boundary of crystalline grains in an amorphous matrix, where it is predominantly inactive [99], [100]. At higher crystalline fractions, both the ratio of the crystalline to amorphous phase as well as the crystalline grain bulk versus grain surface ratio are increased. We speculate that this larger fraction of crystalline silicon sites, with respect to c-Si grain boundaries and amorphous sites, makes it more likely that boron integrated in the mixed phase growth results in an active dopant. For most films an increase of $F_{B2H6/SiH4}$ suppresses crystalline growth, thereby deteriorating the macroscopic conductive properties of the films and hardly increasing the active dopant concentration in the largely amorphous films. A decreased E_{act} with an increased $F_{B2H6/SiH4}$ is therefore only observed for the films with a high $F_{H2/SiH4}$. For these films the nucleation suppressive behavior of the dopant gas is compensated by the nucleation promoting behavior of the hydrogen. The macroscopic conductive properties are hardly affected and the active dopant concentration in these relatively crystalline films is increased. Finally, an increase of $F_{B2H6/SiH4}$ decreases the E_{04} (Fig.2.13↑6), regardless of the other precursor gasses. Increasing $F_{B2H6/SiH4}$ from 10 to 40, for example, decreases the E_{04} from 2.03eV to 1.95eV at $F_{CO2/SiH4} \approx 1.8$ and from 2.25eV to 2.10 eV at $F_{CO2/SiH4} \approx 2.3$. This is most likely a result of the decreased oxygenation of the material with increasing $F_{B2H6/SiH4}$. However, a decrease of E_{04} as a result of a decreasing hydrogen concentration with increasing $F_{B2H6/SiH4}$, as observed in p-doped amorphous silicon in [101], [102], cannot be excluded.
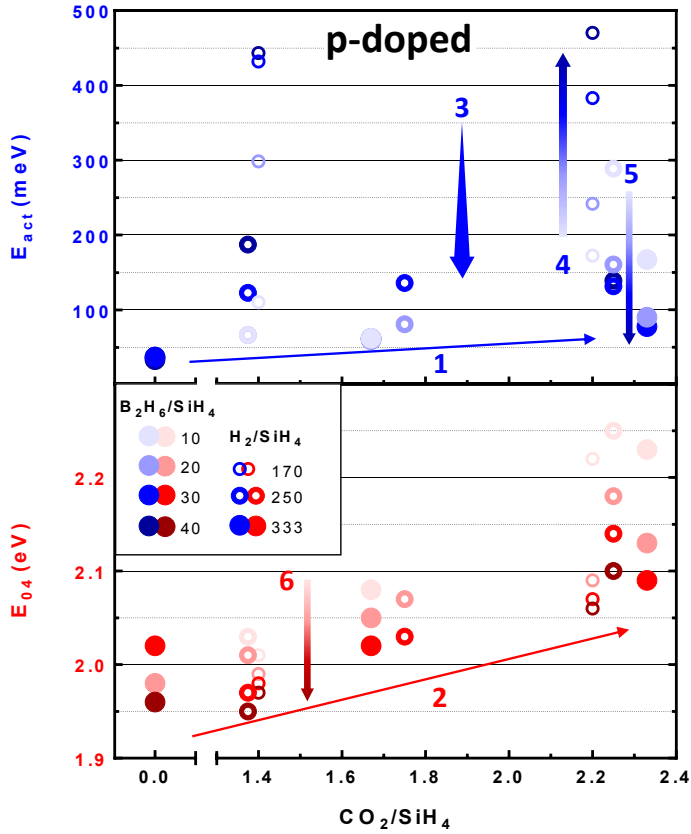
Figure 2.13: E_{act} (top) and E_{04} (bottom) of p-doped a/nc-SiO$_{X \geq 0}$:H films a function of the relative CO$_2$ flow rate ($F_{CO2/SiH4}$). The brightness/depth of color of the markers indicates the relative doping flow rate ($F_{B2H6/SiH4}$) while the size of the markers and their open/closed nature indicates the relative hydrogen flow rate ($F_{H2/SiH4}$). Arrows, added to indicate trends in the data, are referenced in the text. ↑1-2 indicate the influence of $F_{CO2/SiH4}$. ↑3 indicates the influence of $F_{H2/SiH4}$. ↑4-6 indicate the influence of $F_{B2H6/SiH4}$.
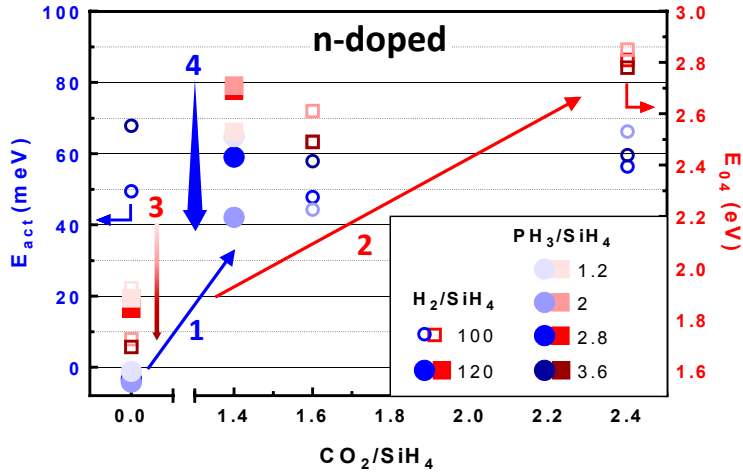
Figure 2.14: E_{act} (left, circles) and E_{04} (right, squares) n-doped a/nc-SiO$_{X \geq 0}$:H films as a function of $F_{CO2/SiH4}$. The brightness/depth of color of the markers indicates the $F_{PH3/SiH4}$ while the size of the markers and their open/closed nature indicates $F_{H2/SiH4}$. Arrows, added to indicate trends in the data, are referenced in the text. ↑1-2 indicate the influence of $F_{CO2/SiH4}$. ↑3 indicates the influence of $F_{PH3/SiH4}$. ↑4 indicates the influence of $F_{H2/SiH4}$.
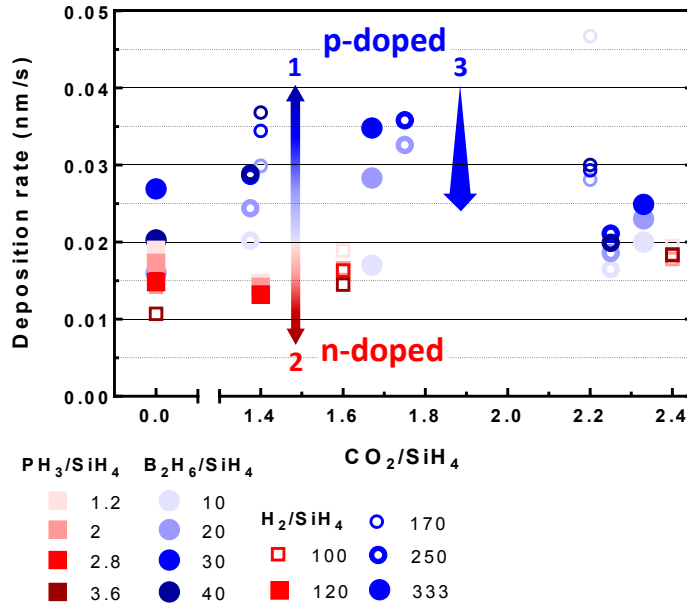
Figure 2.15: Deposition rate of n-doped (red, squares) and p-doped (blue, circles) a/nc-SiO$_{X \geq 0}$:H films, as a function of $F_{CO2/SiH4}$. The brightness/depth of color of the markers indicates the $F_{PH3/SiH4}$ while the size of the markers and their open/closed nature indicates the $F_{H2/SiH4}$. Arrows, added to indicate trends in the data, are referenced in the text. ↑1-2 indicate the influence of $F_{B2H6/SiH4}$ and $F_{PH3/SiH4}$. ↑3 indicates the influence of $F_{H2/SiH4}$.

The n-doped films generally show the same trends, although higher optical bandgaps and lower activation energies are achieved. For the samples with a relatively high $F_{H2/SiH4}$ the E_{act} increases significantly by about 40-60meV when CO_2 is introduced during deposition (Fig.2.14↑1). The E_{act} of the films deposited at lower $F_{H2/SiH4}$ ratio are not significantly influenced by the $F_{CO2/SiH4}$. The E_{04} increases with increasing $F_{CO2/SiH4}$ (Fig.2.14↑2) as expected. As with the p-doped films, an increase of the relative doping flow rate decreases the E_{04} of the films (Fig.2.14↑3). An increase of $F_{H2/SiH4}$, finally, significantly decreases the E_{act} of the nc-Si:H films (Fig.2.14↑4), within a certain range. It should be noted that at a relative flow rate of $F_{H2/SiH4}=140$ the films became highly transparent with activation energies of 500meV and higher.

The precursor gas flow rates also influence the deposition rate of the doped films. An increase of the diborane gas flow rate, for instance, strongly increases the deposition rate (Fig.2.15 ↑1), which is in line with earlier reports [86], [103], [104]. Diborane easily dissociates. Created radicals could have two possible effects resulting in the deposition rate increase. 1. Enhance the dissociation of silane in the plasma, thereby increasing the flux of SiH_X radicals to the surface. 2. Increase the dangling bond density at the surface, thereby increasing the amount of growth sites for silicon radicals. It has been proposed that the increased dangling bond density at the surface is a result of the ability of Hydroboron BH_3 radicals, that are readily formed in the plasma from the B_2H_6 precursor, to strip the surface of hydrogen through the formation of metastable BH_5 reactive intermediates [105], [106]. This increases the SiH_3 adsorption rate and therefore the silicon growth flux. An increase of the relative phosphine flow has the opposite effect (Fig.2.15 ↑2). The mechanism behind this is unclear.
An increase of the relative H_2 flow rate decreases the growth rate (Fig.2.15 ↑3). This is most likely a result of atomic hydrogen induced etching, which is enhanced with respect to the silicon growth flux under higher hydrogen dilution conditions. Indeed it has been reported for p-type a-Si:H films the void fraction decreases with increasing $F_{H2/SiH4}$ [103]. Moreover, since the low growth rate conditions are accompanied by a larger atomic hydrogen flux to the substrate, the crystallization of the silicon phase is enhanced. This explains the nucleation promoting behavior of an increased relative H_2 flow rate.

Manipulation of doped silicon material growth is achieved through the relative gas flow rates. Naturally, the extent of manipulation is limited. In Fig.2.16 (bottom) the trade-off between the E_{act} and E_{04} of all doped films is shown. A few things are apparent from this figure. 1. The lowest activation energies are achieved for the doped nc-Si:H samples. For $R_{SiOx} \geq 0$ both E_{act} and E_{04} increase. This is directly related to $R_{c\text{-}Si}$, which is indicated in Fig.2.16 (bottom) through icon size and color. 2. Although they have similar $F_{CO2/SiH4}$, the E_{04} of n-doped samples is higher than that of their p-doped counterparts. This is a result of higher R_{SiOx} with respect to the p-doped samples. The mechanism behind this is unclear. 3. Despite the high R_{SiOx} and E_{04} of the n-doped SiO_X:H samples, they retain relatively low E_{act}. This is unlike the p-doped samples where small changes have a strong effect on the opto-electrical performance. We can therefore reflect that the nature of the a/nc-$SiO_{X>0}$:H material is such that it favours n-type doping. This could be result of the fact that undoped amorphous silicon tissue by itself is slightly n-type and becomes more n-type when oxygen is introduced [107], [108]. Alternatively, it could be

Table 2.4: precursor gas flow rates of films used in Fig 7

	p-SiO$_X$:H	p-SiO$_X$:H 2	p-nc-Si:H	p-nc-Si:H
SiH$_4$	0.8	0.8	0.8	0.6
B$_2$H$_6$ (200ppm)	10	10	20	32
H$_2$	170	170	170	200
CO$_2$	2.3	2	-	-

the result of the deposition-rate-decreasing effect of phosphine with respect to diborane, as shown in Fig.2.15, resulting in a denser, less defective material. Or perhaps that phosphine favourably resides inside crystalline grains, as reported in [99], as opposed to near the grain boundaries or in the amorphous phase, resulting in a higher doping efficiency. Regardless of the reason, the results show that optimization of the p-doped layer, often crucial for device performance due to its placement between the absorber layer and incident light, is challenging. For this reason, Fig.2.16 (top) shows the p-doped samples in particular, with the additional information of the R$_{SiOx}$.

From Fig.2.16 (top) it is again clear that increased oxygenation inevitably leads to higher activation energies. The lowest E$_{act}$ are achieved by the p-nc-Si:H samples, which also have the lowest E$_{04}$, ranging from 1.96-2.06 eV. This range of optical bandgap energies is likely because in the spectral range where the E$_{04}$ is determined, the absorption is dominated by the amorphous phase in the doped a/nc-SiO$_{X \geq 0}$:H material. The E$_{04}$ therefore provides information on the quality of the amorphous tissue between the nanocrystalline phase. The band gap of this amorphous tissue is determined by two factors. First, the optical bandgap energy will increase with increased porosity of amorphous phase. Second, the optical gap will increase with increased oxygenation. This is demonstrated in Fig.2.16, since E$_{04}$ is only increased above 2.1eV when the amorphous phase becomes increasingly oxygenated.

Investigation of thickness

We have described the complex interplay between crystalline growth, oxygenation and dopant integration in the doped a/nc-SiO$_{X \geq 0}$:H films. The material properties of the doped films, when integrated in devices, does not exclusively depend on the deposition conditions, however. The opto-electrical properties of the doped layers are not uniform in the growth direction.

Fig.2.17 (left) shows the E$_{act}$ and E$_{04}$ of p-nc-Si:H and p-SiO$_X$:H films deposited at different thicknesses and two sets of deposition conditions. The deposition conditions are reported in Table.2.4. It can be observed that the E$_{act}$ decreases with increasing film thickness for both the oxygenated and oxygen-free doped silicon films. This is directly related to the crystallinity. The Raman shift of the p-doped films is plotted in Fig.2.17. There are four amorphous silicon peaks indicated, corresponding to the transverse acoustic (TA) mode at 160cm^{-1}, the longitudinal acoustic (LA) mode at 320cm^{-1}, the longitudinal optic (LO) mode at 390cm^{-1} and the transverse optic (TO) mode at 320cm^{-1}. It can be seen that with increasing thickness, the intensity of the Raman shift peak at 520cm^{-1},
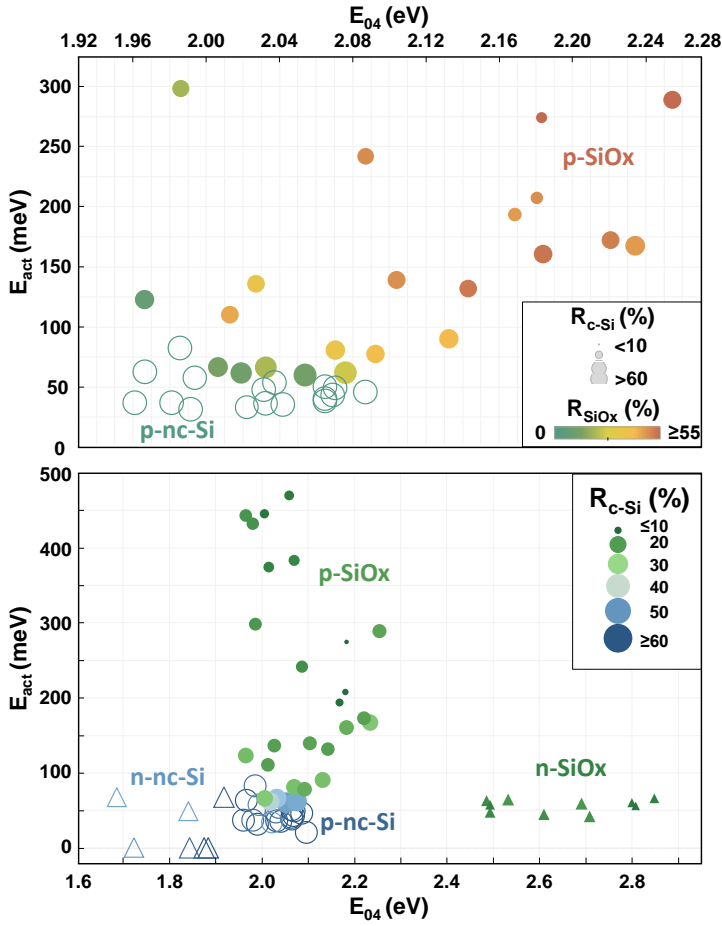
Figure 2.16: E_{act} as a function of E_{04} for all doped a/nc-SiO$_{X \geq 0}$:H samples (bottom) and exclusively p-type a/nc-SiO$_{X \geq 0}$:H samples (top). nc-Si:H samples are represented by open symbols, while SiO$_X$:H samples are represented by closed symbols. p-doped samples are represented by circles, while n-doped symbols (bottom plot) are represented by triangles. In the top plot, the color and brightness of the symbols indicates R_{SiOx}, while the size of the symbols indicates $R_{c\text{-}Si}$. In the bottom plot both symbol color/brightness and size indicate $R_{c\text{-}Si}$.
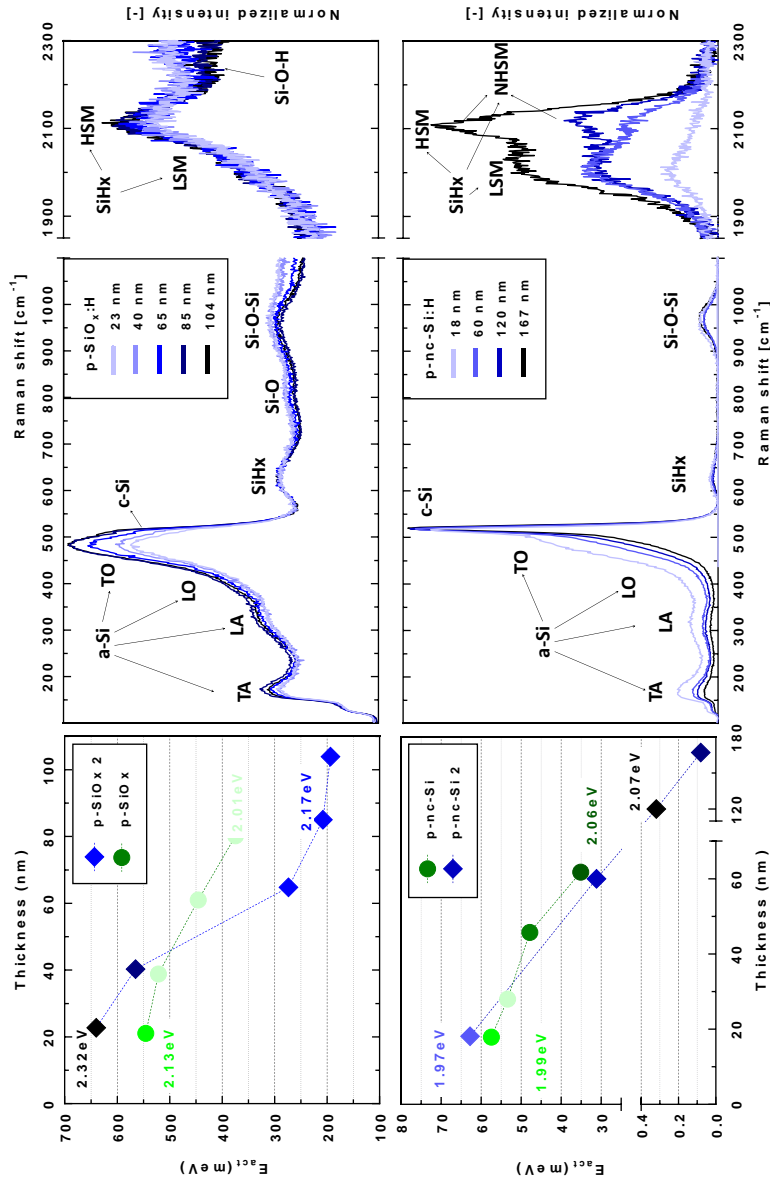
Figure 2.17: Material properties as a function of thickness. The plot on the left shows E$_{act}$ as a function of thickness for two sets of p-SiO$_X$:H films (left, top) and two sets of p-nc-Si:H films (left, bottom). The brightness of color of the icons indicates the E$_{04}$ from lowest (bright) to highest (dark) value within the series. The lowest and highest E$_{04}$ values are indicated in text in the plots. Structural analysis of these samples is shown in the plots on the right. These plots show the normalized count rate as a function of Raman shift for the p-SiO$_X$ 2 samples (right, top) and the p-nc-Si 2 samples (right, bottom) processed at different thicknesses, as indicated in the legend. Suspected identification of the observed peaks is indicated in the graphs. For the p-nc-Si:H samples the background was subtracted manually.

which corresponds to the crystalline silicon phase, increases with respect to the amorphous silicon peaks. This observation, the increased crystallinity in the growth direction, is in line with earlier reports, where development of crystalline filaments in the growth direction was demonstrated [36], [59], [61], [109].

The thickness of the films also influences the optical bandgap energy. For the p-SiO$_X$:H films the E$_{04}$ decreases with increasing thickness. This is likely the results of a decreased silicon-oxide phase fraction. The R$_{SiOx}$ obtained from SE measurements decreased from 64% to at 23nm to 47% at 104nm. This decrease of the R$_{SiOx}$ can also be observed in Fig.2.17 (top, right), by a decrease of the silicon-oxygen bond related Raman shift peaks. These peaks are the Raman shift peak at 795cm^{-1} related to Si-O stretching [110], the broad peak at roughly 900-1100cm^{-1} related to Si-O-Si stretching modes [69], [79] and the peak at 2250cm^{-1}, related to the Si-O-H stretching modes [69], [111]. All these SiO$_X$ related Raman peak intensities decrease with increasing thickness, while the amorphous silicon peaks increase. It should be noted that some influence of the glass substrates on the Raman spectra cannot be excluded. This said, the trends are confirmed with SE measurements where the influence of the substrate is excluded.

The E$_{04}$ of the p-nc-Si:H samples on the other hand increases with increasing thickness. This is likely the result of the amorphous phase growing more porous along the growth direction. More precisely, the density of the amorphous phase is related to the organization of the silicon-hydrides in the amorphous network. When distributed monohydrides are increasingly organized in multi-vacancies and small voids, the density of the network decreases and the optical bandgap increases [73], [112]. This can be corroborated by a distinct signature in the Raman spectrum in the 1800-2200cm^{-1} range. This range, related to the silicon-hydride stretching modes, can be simplified into a low stretching mode (LSM) peak at roughly 2000cm^{-1} and a high stretching mode peak (HSM) at roughly 2100cm^{-1} [69]. The LSM corresponds to mono- configurations, while the HSM corresponds to silicon-hydrides and di-hydrides organized in small vacancies and voids [66], [67]. In addition in the 2100-2103cm^{-1} range a narrow signature of the extreme high stretching modes (NHSM) [69]. These stretching modes reflect the mono- and di-hydrides on the surface of crystalline silicon grains. Fig.2.17 (bottom, right) shows that with increasing p-nc-Si:H thickness the NHSM peak strongly increases with respect to the LSM peak, indicating an increase of hydrogenated c-Si grain boundaries not passivated by a-Si:H tissue. Subsequently the amorphous tissue between the grains becomes more porous. This increased porosity of the amorphous phase along the growth direction is similar to the development of a-Si bulk properties in the growth direction [113].

2.2.4 Conclusion

In this work we have investigated how the opto-electrical properties of doped silicon films are determined by the different phases, and their relative fractions, present in the doped heterogeneous a/nc-SiO$_{X\geq0}$:H material. Using a material phase diagram, we have visualized how the relative nanocrystalline silicon, amorphous silicon and amorphous silicon-oxide fractions can be manipulated through changes in the precursor gas flow rates. Moreover, we discussed how these material phases, in combination with the density of the a-SiO$_X$:H phase and the extent of doping, influence the opto-electrical properties of the

processed films.

An increase of the relative CO_2 flow rate leads to increased oxygenation of the amorphous phase, which predominantly results in a higher optical bandgap. An increase of doping gas flow rate suppresses crystalline growth, decreases the oxygen content and, if the material is sufficiently crystalline, increases the active doping concentration. Sufficient crystallinity can be achieved by increasing the relative hydrogen flow rate, which decreases the deposition rate, resulting in denser and more crystalline material growth. However, if the relative hydrogen flow rate exceeds a certain threshold, the balance between the silicon growth flux an atomic hydrogen etching is upset, resulting in poor electrical properties with activation energies of 500meV and up.

We also demonstrate that the opto-electrical properties are not uniform along the growth direction. For p-doped a/nc-SiO$_{X \geq 0}$:H films the activation energy decreases with increasing film thickness, as a function of the crystalline fraction. The optical bandgap energy of p-SiO$_X$:H films decreases with thickness, as a results of decreased oxygenation of amorphous phase. The optical bandgap energy of the p-nc-Si:H films increases with thickness due to increased porosity of the amorphous phase along the growth direction.

3

Texturization and passivation of silicon substrates

3.1 Advanced textured monocrystalline silicon substrates with high optical scattering yields and low electrical recombination losses for supporting crack-free nano- to poly-crystalline film growth

This section was published in *Energy Science & Engineering**

Abstract

Crystalline silicon tandem devices with perovskites, CIGS and nano-crystalline silicon, as well as the TOPCon design are incompatible with the conventional pyramidal surface texture of silicon. This is a result of crack formation in nano- to poly-crystalline growth on large sharp surface features. In this work three texturing approaches are investigated, using alkaline and/or acidic wet chemical etches, that can lead to the crack-free growth of a nano- to poly-crystalline materials on textured surfaces. In this work we show that without acidic smoothening, the fraction of <111> pyramidal surface coverage has to remain relatively small to prevent crack formation during crystalline growth on these surfaces. Applying an acidic etch as a function of time continuously smoothens surface features. This shifts the reflection to wider scattering angles and results in higher total reflected intensity with respect to the conventional texture, making it an interesting option for a wide variety of tandem pv applications. Finally we demonstrate crater like features on a <100> monocrystalline silicon surface using an etching process including a sacrificial layer. These craters increases light scattering into wider angles, but to a lesser extent than the former approach.

In terms of passivation, we demonstrate the positive effect of a post deposition hydrogen treatment. Initial dilution of the silane plasma improves passivation on a <111> surface, but is detrimental to passivation on a <100> surface, likely because the hydrogen dilution results in epitaxial growth at the c-Si/a-Si:H hetero-interface. A minority carrier lifetime of over 3ms has been achieved for all texturing approaches, after deposition of a 15nm a-Si:H layer on both sides of the wafer, for different a-Si:H deposition and annealing schemes.

3.1.1 Introduction

With the relative price of crystalline silicon modules dropping faster than the balance of systems costs for a PV system, increasing the efficiency of PV devices at low production costs is crucial. As such, much attention is devoted to the TOPCon design. TOPCon devices can be upgraded from PERC and PERT devices with relative ease through addition of an ultra-thin SiO_2 layer and a doped poly-Si layer. Moreover, TOPCon is easily adapted for IBC [114] and bifacial use [115]. Alternatively, tandem PV devices are receiving increased attention, where a crystalline silicon (c-Si) bottom cell is to be combined with a perovskite [116]–[118], C(I)GS [119] or nano-c-Si top cell [29], [30]. These approaches all have a major challenge in common. The <111> crystal orientation, the pyramidal surface texture that is the standard for industry and the scientific community, is crucial for light management but incompatible with the crystalline phase in the nano/poly-si, perovskite and C(I)GS materials [75], [120], [121]. Not only is conformal growth challenging on the sharp pyramidal features, the crystalline phase tends to form cracks [62], or low-density defective regions [63], [64]. These cracks are located in the valley between sharp features, or in other words the focal point of perpendicular growth on steep features. Developing surface features on mono crystalline silicon through a wet chemical treatment requires anisotropic etching behavior.

One approach, widely used industry, is the use of an KOH-, NaOH- or TMAH alkaline etch [122], [123]. Alkaline solutions preferentially etch crystal orientations with lower activation energies for the etching reactions. The bonds of the <111> crystal orientation for instance are much stronger, and therefore harder to break, than the <100> orientation. Consequently, the preferential etching of the <100> plane results in a square based pyramidal <111> plane. Alternatively, the <110> orientation is also preferentially etched, but results in perpendicular trenches with <111> side walls that are less attractive for pv applications [124].

Applying an acidic etch, such as a combination of hydrofluoric acid (HF) and nitric acid (HNO_3), on a polished monocrystalline silicon results in isotropic etching. Some non-uniformity is required to develop features on a mono c-Si surface. Saw damaged wafers exhibit such non-uniformity, but the optical effectiveness of features resulting from the chemical polish of the saw damaged is limited, due to a lack of tunability [123], [125]. Alternatively, with the use of photolithography some parts of the surface can be masked, resulting in anisotropic etching of the surface. This has proven successful [126], [127], but such an expensive approach would limit the wide scale application.

In this work we explore 3 alternative wet chemical etching approaches on polished n-type monocrystalline silicon wafers with <100> crystal orientation. The aim is to develop a texture that does not negatively affect the quality of the crystalline phase processed on top of the wafer surface and provide efficient light scattering. Moreover, for use in photovoltaic devices, it is important that the developed surface can be passivated with relative ease to ensure sufficently high charge carrier lifetimes. Passivation can be complicated if multiple crystal orientations are exposed on the wafer surface. In Texturing approach 1 (T1) and texturing approach 2 (T2), anisotropic etching is achieved through an alkaline TMAH etch. In T1 however, the process is interrupted before the surface is fully covered. In T2, the alkaline etch is followed by an acidic HF/HNO_3 poly-etch step, which etches
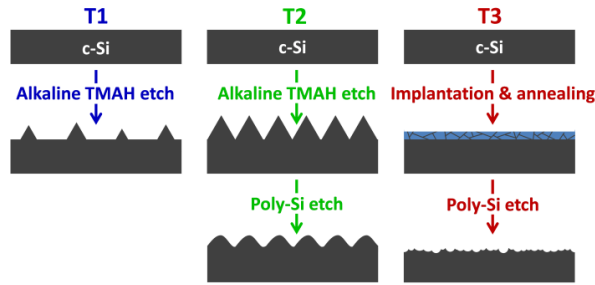
Figure 3.1: Simplified flowchart of texturing approaches T1-T3

isotropically, resulting in the smoothening of the sharp pyramidal features. In texturing approach 3 (T3), a sacrificial boron implanted poly-Si layer is first processed to create anisotropic etching behavior, as the grain boundaries in the poly-Si layer are favorably etched with respect to the crystalline phase. This sacrificial layer is then fully etched away using poly-etch. Simplified flowcharts of the three approaches are shown in Fig.3.1. For all 3 approaches the influence of the etching time on the surface features and optical behavior was characterized and the passivation quality of a range of amorphous silicon layers was investigated.

3.1.2 Experimental Details

Texturing approaches   In this work, polished Topsil Floatzone n-type <100> monocrystalline silicon wafers were used with a thickness of 300μm, unless mentioned otherwise. These wafers were used for three texturing approaches. For T1 an alkaline Tetramethylammonium hydroxide (TMAH) (25% wt. in $H_2$0) etch solution is used at a temperature of 80°C, followed by a 3 minute rinse in deionized (DI) water. For T2 a 10 minute TMAH etch and rinse was followed by an acidic poly-etch, consisting of 1 part HF (40% wt. in H_2O), 6 parts HNO_3 (69.5% wt. in H_2O) and 3 parts H_2O. For T3 a 2nm SiO_2 layer is first is grown on the wafer through a nitric acid oxidation cycle (NAOC), which is described elsewhere [128]. On top of this an amorphous silicon layer of 250nm is processed, using a Tempress low pressure chemical vapour deposition (LPCVD) tube furnance. This layer is then implanted with boron ions and annealed at high temperature to active the dopants and crystallize the amorphous layer. For the boron implantation a Varian Implanter E500HP is used with an energy of 5 keV and a dose of 10^{16}cm^{-2}. Next, a Tempress tube furnace is used for annealing in an N_2 atmosphere at 950°C. The ramping rate for heating or cooling is 10°C/min. The poly-si sacrificial layer is then fully etched away using a different acidic poly etch solution with respect to T2, consisting of 1 part HF (40% wt. in H_2O), 35 parts HNO_3 (69.5% wt. in H_2O) and 14 parts H_2O.

Roughness and optical measurements   The SEM analysis was performed on a FEI Nova NanoSEM 450, using an immersion detector at an acceleration voltage of 10kV. The AFM analysis was performed on an Bruker AFM FastScan. Using a Fastscan closed loop scanner head a 20μm by 20μm area was measured. The RMS roughness (Sq),

maximum peak height (Sz) and mean slope (Sdq) were extracted using the NanoScope Analysis software from Bruker. The reflectance measurements were performed using a LAMBDA 1050+ UV/Vis/NIR Spectrophotometer with 150mm integrating sphere and InGaAs detector from PerkinElmer. For the angular distribution of the reflectance the 180mm automated reflectance/transmittance analyzer (ARTA [129]) accessory is used on a similar, LAMBDA 950 PerkinElmer base unit.

Wafer passivation Between the texturization process and the amorphous silicon deposition the wafers were cleaned through 3 consecutive NAOC cycles. The amorphous silicon layers used for passivation were grown using a radiofrequency plasma enhanced chemical vapor deposition cluster tool, operating at a frequency of 13.56 MHz. The deposition conditions are indicated in table3.1. The nc-Si:H film was grown in a separate reactor in the same cluster tool, at very high frequency (40MHz), a substrate temperature of $180°C$, a pressure of 4mbar and forward power of 278 mW $\cdot$ cm^{-2}. The H$_2$ flow is set at 120 standard cubic centimeters per minute (sccm), while the initial SiH$_4$ flow of 1.2sccm is increased to 3.5sccm after about 50nm of deposition for the remainder of the growth The lifetime measurements were performed on a Sinton WCT-120 under Transient photo-conductance decay (Transient PCD) mode. The reported lifetimes are at a minority carrier density of 1e15 cm^{-3}. The wafers were annealed in a Thermo Scientific Heratherm in an ambient atmosphere.

3.1.3 Results and discussion

Influence of texturing approaches on surfaces and optical behaviour

The three texturing approaches result in different textures, as shown in Fig.3.2. For T1 the surface is transformed from the flat <100> to a pyramidal <111> surface with increasing etching time. The RMS roughness (Sq), maximum peak height (Sz) and mean slope (Sdq), resulting from the AFM analysis, are plotted in Fig.3.3. For T1, increasing the etching time from 30s to 4mins leads to an increase of the RMS roughness from about 9nm to 360nm while the maximum peak height increases from about 210nm to 1.9μm. After about 5 mins the surface is fully covered with pyramids. At this point the mean slope of about 45 degrees no longer increases. The RMS roughness and max peak height keep steadily increasing to about 480nm and 2.8 microns at 9 mins, our last measured data point. This has a large impact on the spectral reflected intensity, as shown in Fig.3.4. While the shape of the reflectance does not change, the reflectance at a wavelength of 600nm is decreased from about 35% to 12% when the etch time is increased from 30s to 9 minutes.

For T2 the pyramidal <111> features are smoothened using an acidic etch. The etching time was varied from 30s to 30 minutes. The SEM images in Fig.3.2. show how the pyramidal features are smoothened with increasing etch time. The RMS roughness is decreased from about 630nm after 30s to about 530nm after 3mins and down to 290nm after 10mins. The maximum peak height is decreased from 3.8μm to 2.1μm in that same period of time, while the mean slope is decreased from about 45 degrees, to 22 degrees. As shown in Fig.3.4, as a result of the decreasing roughness and peak height, the reflected intensity is increased from 22% to 34% when the etch time is increased from
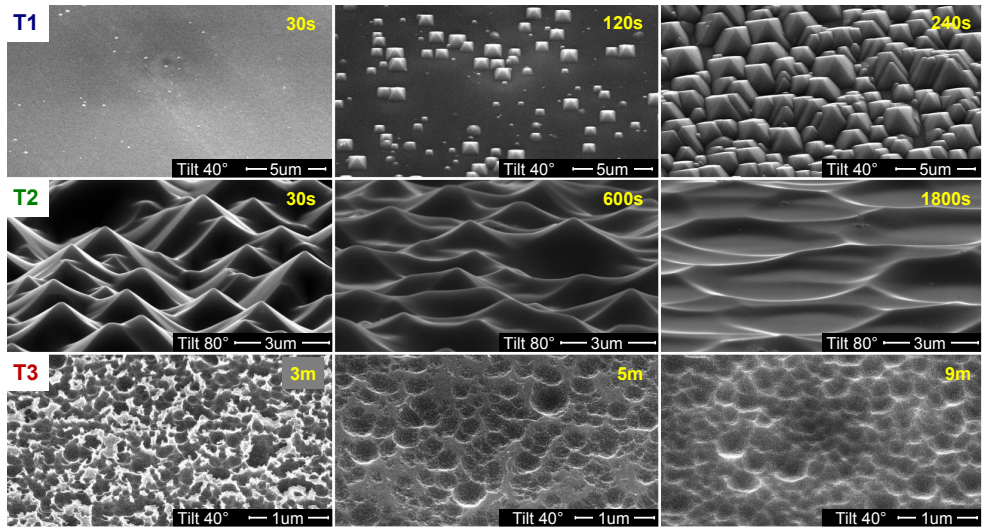
Figure 3.2: Scanning Electron Microscopy images of the T1 (top), T2 (middle) and T3 (bottom) textures as a function of etching time of the final step in the texturing process. Sample tilt and scale are indicated in the images

30s to 10 min. For T3 a 250nm sacrificial poly-si layer is etched using a poly etch. As Fig.3.2 shows, getting the timing of the etching process right is important to obtain the desired crater like features. At 3 minutes the poly-si layer is removed, but some of the SiO_2, which has a much lower etching rate than Si, remains. At 5 minutes the crater like features are apparent. The features are rather small with a RMS roughness of about 25nm, a maximum peak height of about 210nm and a mean slope of about 17 degrees, as reported in Fig.3.3. Since the features are relatively small the reflectance is about 32% at 600nm, almost similar to that of a flat surface. When the etching time is further increased, the roughness, peak height and reflectance do not change much for the observed etching times. The features are eventually smoothened again, as the poly etch has an isotropic etching behavior on mono c-Si.

For single junction solar cells, the features on the silicon wafer surface will be positioned at the front of the device. In this case, minimal reflectance, so maximal light in- coupling is desirable. However, for tandem PV applications in which c- Si operates as the bottom cell, the surface features will be located at the interface between two junctions. In this case, wide angle light scattering is potentially more critical than light in- coupling. To investigate the light-scattering efficiency of the surfaces, the angular distribution of the reflected intensity at a wavelength of 600nm is shown in Fig.3.5. For T1, the shape of the angular reflection changes as the surface is transformed from predominantly flat, to pyramidal. For a polished surface (0m), the reflection is in the direction normal to the surface. Since the incident light has a certain spot size, a very small angular distribution is observed. A fully pyramidal surface also reflects mainly in the normal direction. The pyramids have a mean slope of 45 degrees. A fraction of the light, under normal incidence, is reflected off this slope parallel to the surface. When it encounters a second slope, a
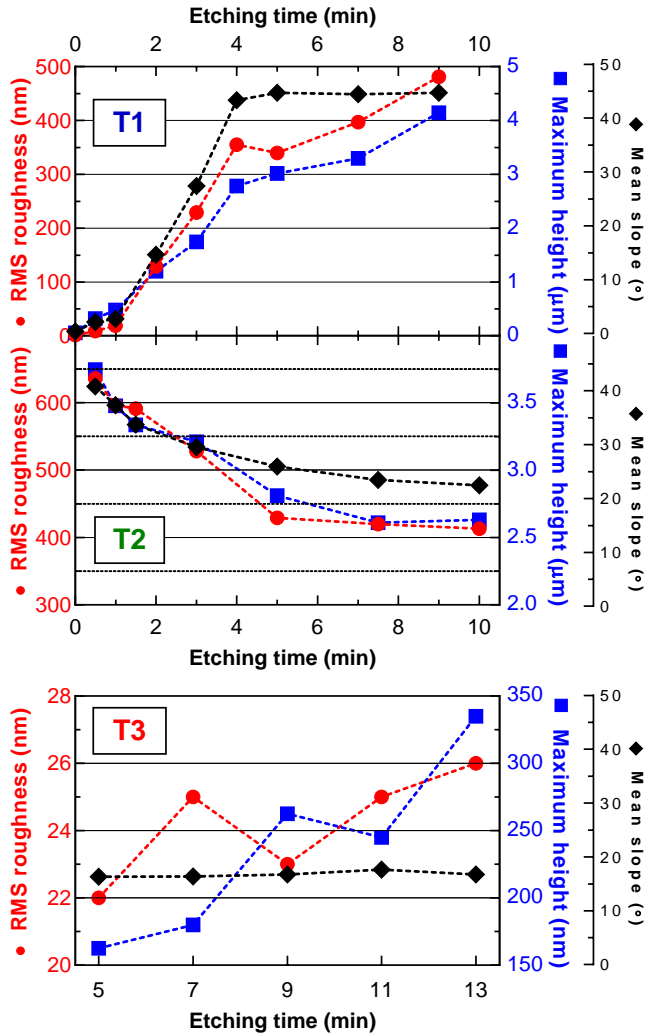
Figure 3.3: RMS roughness (red circles), Means slope (black diamonds) and maximum feature height (blue squares) as a function of etching time of the T1 (top), T2 (middle) and T3 (bottom) texturing approaches. T1 0min. represents a polished wafer.
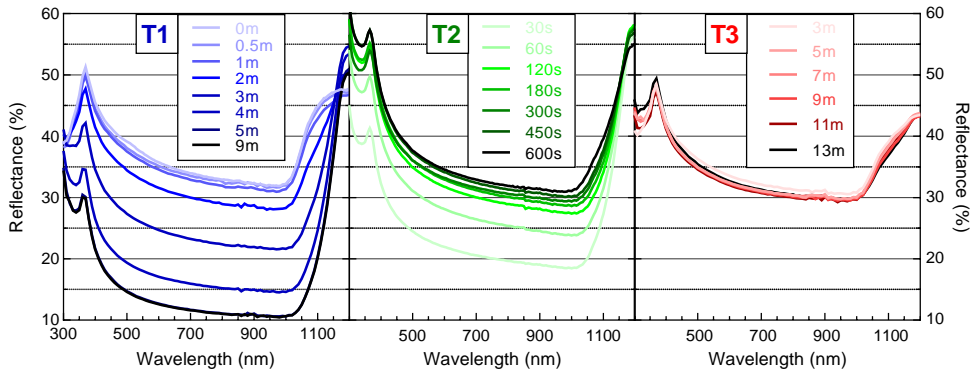
Figure 3.4: Spectral reflectance measurements as a function of etching time for T1 (left, blue), T2 (middle, green) and T3 (right, red). T1 0min. represents a polished wafer.

fraction is reflected back perpendicular to the surface, as schematically shown in Fig.3.6. Since there is a distribution in the slope and size of the pyramids, we observe an increased reflection in the 30 to 80 and -30 to -80 degree angle range with increasing pyramidal coverage. For T2 we observe a shift of the angle of maximum intensity with increasing etching time. This is because the average slope of the pyramids decreases from about 45 degrees to about 30 degrees, as shown in Fig.3.3. As the average slope is decreased, the earlier mentioned double reflection events become increasingly rare. This leads to an increase of the total reflected intensity with etching time, as observed in Fig.3.4, and a shift to scattering angles equal to twice the angle of the slope of the pyramids. This is demonstrated by the observation that for T2 the angle of maximum reflected intensity is about 0 degrees for a mean slope of 42 degrees at 30s. At 60s the means slope is about 30-35 degrees and maximum reflected intensity is about 70 degrees and it is further shifted to about 50 degrees at 5 mins etch time and a mean slope of 25 degrees.
For T3 the etching time does not significantly affect the angular reflection distribution. Light is scattered in wider angles than for flat surfaces, but due to the relatively small features, light is still mainly reflected in the perpendicular direction.

Passivation of textured surfaces

An important criteria for wafers with texture resulting from T1-T3 is that they should be relatively easy to passivate. In order to test the passivation quality, we processed a 15nm amorphous silicon layer on both sides of the textured wafers and measured the minority carrier lifetime. For good passivation, in the order of several milliseconds, a thin uniform amorphous silicon layer is desirable. Initial experiments showed that the growth of such a layer is not only a function of the deposition conditions. A recipe optimized for the passivation of a c-Si surface with pyramidal <111> features, referred to as a-Si:H-2 in table3.1, resulted in very low lifetimes of several tens of microseconds on a polished <100> surface. The lifetime decreased even further upon low temperature annealing, at 180°C, potentially indicating epitaxial growth [130]. Epitaxial crystalline growth through the amorphous silicon passivation layer is detrimental to the passivation quality [130]–
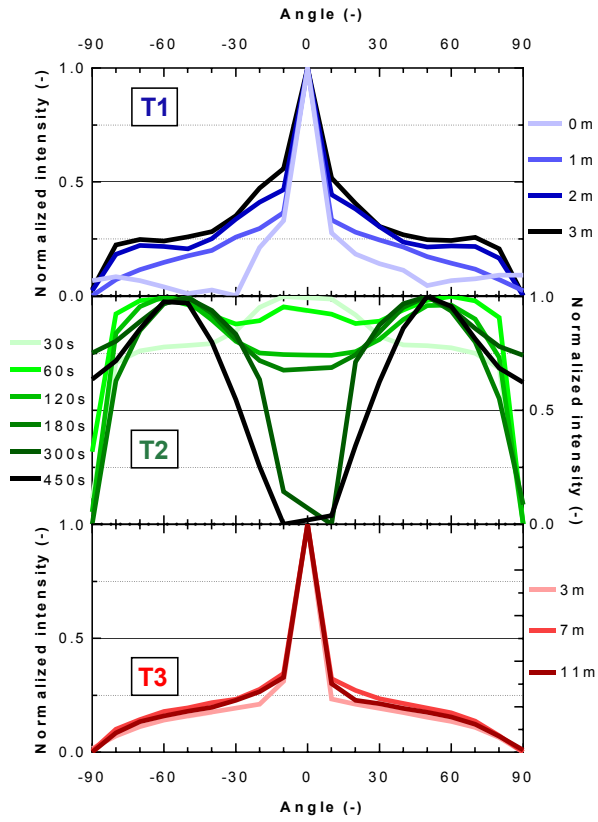
Figure 3.5: Normalized intensity of T1 (top, blue), T2 (middle, green) and T3, (bottom, red) as a function scattering angle, for different etching times. Normalization is performed with respect to the maximum intensity. T1 0min. represents a polished wafer.
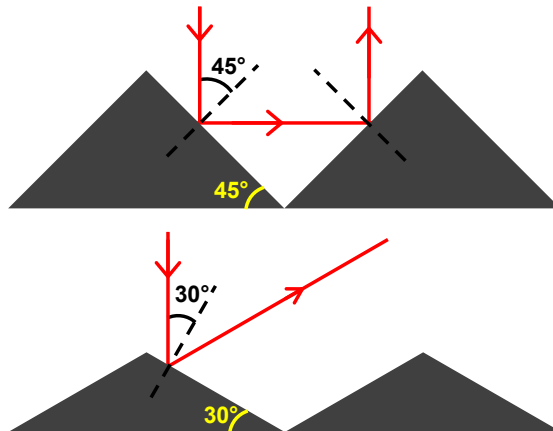
Figure 3.6: Simplified visual of light (red) reflected of a surface with a 45 degree slope (top) and 30 degree slope (bottom), respectively.
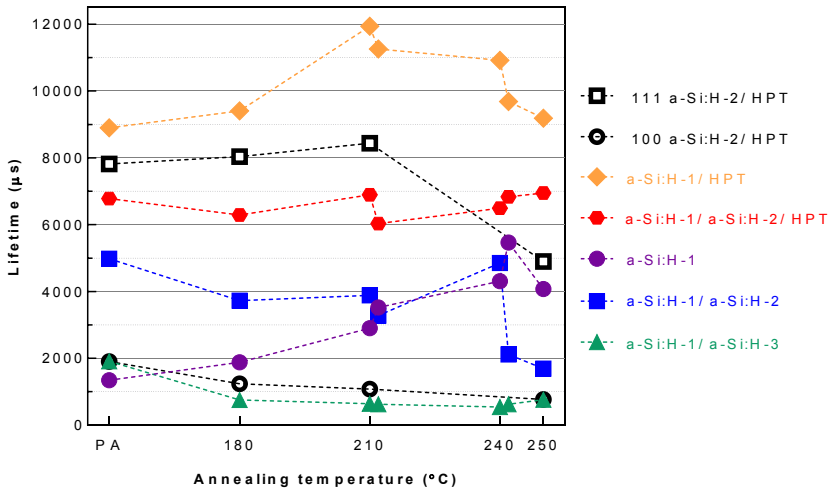
Figure 3.7: Lifetimes of passivated wafers as a function of annealing temperature. The legend indicates the various amorphous silicon conditions used for passivation. These conditions can be found in table 3.1. PA indicates wafer passivation pre-annealing. Multiple datapoints at the same temperature indicates the lifetime of wafers annealed at 10mins followed by an additional 20mins.

[133].

   To distinguish between the effect of the surface roughness and the crystal orientation on the amorphous silicon growth, the experiment was repeated on a flat, polished $<111>$ and $<100>$ surface. The results are shown in Fig.3.7, indicated by the black curves with open symbols. This time, the a-Si:H-2 deposition was followed by a hydrogen plasma treatment (HPT). The results show that a $<100>$ surface is more challenging to passivate than an $<111>$ surface, which is in line with earlier reports [132], [134], [135]. This is likely because at the surface, a $<111>$ crystal orientation only has a single dangling bond per surface atom that requires passivation, while the $<100>$ surface has two dangling bonds per surface atom. This is illustrated in Fig.3.8, where the red lines indicates dangling bonds at the surface of the silicon crystal in case of a flat $<111>$ and $<100>$ crystal orientation. Apart from the overall higher lifetimes of the $<111>$ wafers, the results show that if the silane precursor is diluted in hydrogen, poor minority carrier lifetimes are very likely to occur on a $<100>$ surface. The lifetimes further decrease upon annealing, potentially indicating epitaxial growth. On the other hand, hydrogen diluted silane plasmas lead to decent passivation on a $<111>$ surface in this work and in others [134], [136].

Introducing hydrogen in the plasma has two effects on etching and growth of the amorphous and crystalline phase. Firstly, introducing hydrogen causes competition between the silicon growth flux and atomic hydrogen etching [69], [137]. The atomic hydrogen more efficiently etches weaker bonds. Consequently, it selectively etches the amorphous over the crystalline phase [138], [139]. Secondly, the initial growth is determined by the availability of SiH_x precursors at the surface. For dense material growth, or indeed for
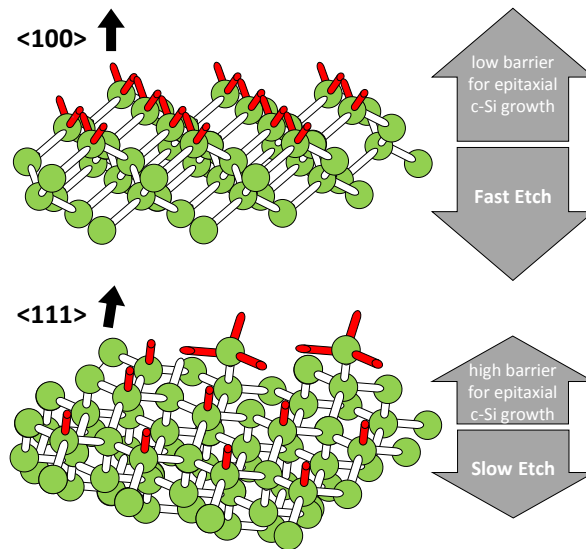
Figure 3.8: <100> (top) and <111> (bottom) orientations at the surface of a silicon crystal. Green circles represent silicon atoms, white lines represent covalent silicon bonds, red lines represent the dangling bonds at the surface.

crystalline growth, sufficient mobility of SiH_X precursors on the surface is required. The atomic hydrogen flux to the substrate surface in a hydrogen diluted plasma is believed to enhance the mobility and increase the diffusion of SiH_X precursor on the surface [140], [141]. The main difference between the two crystal orientations is the additional terminated silicon bond per surface atom available on the <100> surface.

In addition, the crystalline orientation plays a crucial role in etching and growth as well. A c-Si surface with <100> orientation etches faster than a <111> orientation. A <100> surface atom has only two back bonds that needs to be simultaneously broken by hydrogen atoms or other etchants, whereas the <111> surface has alternately a full monolayer that requires three back bonds to be simultaneously broken. This relative stable monolayer acts as a barrier for fast etching in the <111> direction. It requires more effort and consequently more energy to etch the <111> surface. The opposite is also true: since its costs less energy to remove <100> surface atoms it also requires less energy to form crystalline layers on top in the <100> direction. In addition a <100> surface atom has no rotational freedom, a condition which benefits crystalline growth. The <111> surface has alternately a monolayer of single back bonded atoms with rotational freedom. This will hinder crystalline growth and it becomes more likely to facilitate the growth of amorphous tissue on top. Consequently, a hydrogen diluted silane plasma results easily in epitaxial growth on top of the <100> oriented silicon surface in reference to a <100> oriented silicon surface.

To prevent epitaxial growth, an amorphous silicon layer was grown on a polished <100> surface using only SiH_4 as a precursor, indicated by a-Si:H-1. As Fig.3.7 shows, this leads

Table 3.1: Conditions used for processing the different a-Si:H passivation layers and hydrogen plasma treatment

	a-Si:H-1	a-Si:H-2	a-Si:H-3	HPT
SiH_4 (sccm)	40	10	2	0
H_2 (sccm)	0	30	200	200
T_{sub} (°C)	180	180	130	180
P_{rf} (mW·cm^{-2})	19.4	20.8	62.5	20.8
p (mbar)	0.7	1.4	10	2.2

to a minority carrier lifetime of about 1.2ms in the as deposited, or pre-anneal (PA) state. The lifetime is further increased to a maximum of over 5ms when annealed for 30mins at 240°C. When hydrogen is introduced post a-Si:H deposition, the lifetime can be further increased. Hydrogen was introduced through a hydrogen plasma treatment, or by growing amorphous bilayers, were the a-Si:H-1 deposition was followed by a hydrogen diluted silane plasma (a-Si:H-2 or a-Si:H-3) deposition. For the latter, the combined thickness was kept constant at about 15nm and both layers were of roughly equal thickness. The deposition conditions used for these layers are shown in table3.1. The lifetimes of these passivated wafers are shown in Fig.3.7, as a function of annealing temperature. Pre-anneal, for all samples the lifetime is increased when hydrogen is introduced in some form. The combination with a-Si:H-3 seems to lead to epitaxial growth, since the lifetime drops significantly when annealed. The highest lifetimes are obtained when an a-Si:H-1 layer or a-Si:H-1/a-Si:H-2 bilayer is followed by a HPT. Lifetimes between 7-9ms are obtained pre-anneal, and for the best sample this is increased to 12ms when annealed for 10 mins at 210°C. This is on par with $>$ 8ms lifetimes reported by Mews et al. for a similar a-Si:H layer and HPT on <100> polished wafers [112]. For higher annealing temperatures the lifetime drops. During regular processing of a SHJ device however substrate temperatures are generally kept below 200°C, so this should be no obstacle.

This demonstrates that integration of hydrogen in the amorphous silicon is crucial for high quality passivation, but dilution of silane in hydrogen during initial growth can lead to undesired epitaxial growth on <100> surfaces. This means that passivating the T1-T3 surface can be challenging since different crystal orientations are exposed and different roughness's are obtained as a function of etching time. To get an indication of the passivation effectiveness, 15nm of a-Si:H-1 followed by HPT was processed on each texturing approach. The lifetimes are shown in Fig.3.9. The figure shows that decent lifetimes of 3ms and up can be achieved for all texturing approaches. However, T1 and T3 require annealing at relatively high temperatures, 240-250°C, for 30 mins to achieve these lifetimes. A strong increase of the lifetime from the μs to ms range has been reported earlier, especially when hydrogen diluted amorphous silicon is used [136]. It is understood that the increase of the passivation quality upon annealing is mainly a result of hydrogen moving to the c-Si/a-Si:H interface, reducing the interface defect density [142], [143]. For longer annealing times, the passivation quality can be further increased as a results of hydrogen induced reorganization of the amorphous silicon bulk [112], [142], [144]. For T2 lifetimes of 4-7ms are achieved already pre-anneal. The passivation remains stable
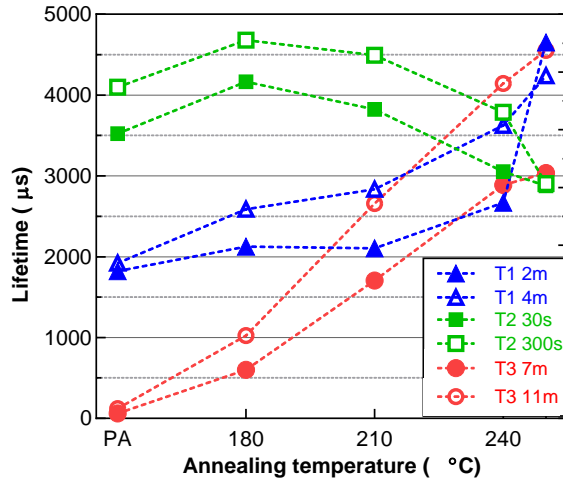
Figure 3.9: Lifetimes of textured wafers passivated by a 15nm a-Si:H-1+HPT layer, as a function of annealing temperature. Lifetimes are reported at a minority carrier density of 1e15 cm^{-3}. Lifetimes are reported for two different etching times for T1 (blue), T2 (green) and T3 (red), respectively.

up to 180°C, after which the quality slightly deteriorates at higher annealing temperatures. The reason why the observed lifetime decrease as a function annealing temperature occurs exclusively for T2 is unclear. It is most likely a result of the relatively large geometry of the T2 pyramidal features, which can potentially cause some non-uniformity in thin films in terms of thickness and porosity, in combination with the relative large fraction of <100> surface orientations.

Growth of device quality nano-crystalline silicon absorber

Finally, we consider the quality of the nc-Si:H processed on the 3 textures. Cross sectional SEM images of these films are shown in Fig.3.10. Feature sharpness determines whether cracks appear. Where along the growth position the cracks appear depends on the focal point of the features, which is a function of the feature size and depth. In Fig.3.10 about 3μm of nc-Si:H was grown on the different textures, which is representative for a nc-Si:H absorber in a multijunction device [72], [145], and much thicker than the poly-Si layer in a TOPcon device [146], [147] and the required absorber thickness of a perovskites [148] or C(I)GS top cell [149]. The images show crack-free, device quality nc-Si:H growth on T2 that was smoothened for 300s and T3 that was etched for 5 minutes. Only T1, etched for 3 minutes, clearly shows cracks through the nc-Si:H film, meaning that yet shorter etching times are required for the growth of a device quality film.
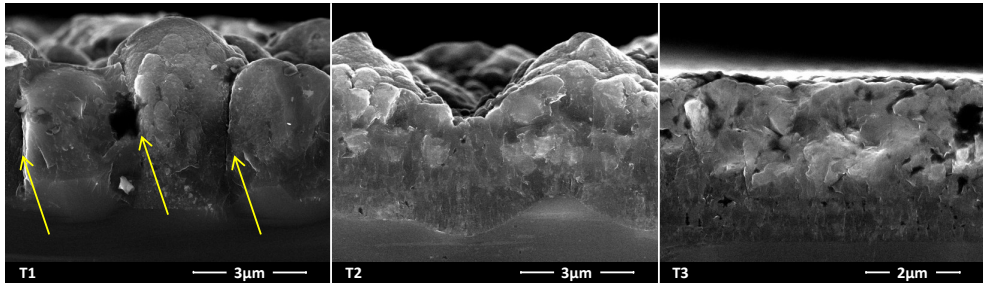
Figure 3.10: Cross sectional SEM images of a 3micron nc-Si:H layer grown on top of a textured c-Si wafers. T1 is shown left, T2 in the centre, T3 on the right. Yellow arrows indicate cracks in the grown material.

3.1.4 Conclusion

We have performed a study on the surface of mono crystalline silicon wafers, following the application of three novel wet chemical texturing approaches that are designed to support the processing of device quality nano- to poly-crystalline materials. Specifically, we characterized the influence of etching time, of the final processing step, on the surface features, optical behavior and passivation quality of the three texturing approaches. The development of small and dispersed pyramids (T1) does not seem very promising for pv applications. The fraction of pyramidal surface coverage has to remain small for crack-free nanocrystalline material growth, at which point the optical behavior is close to that of a flat surface. The surface features, and resulting optical behavior, of the smoothening of a surface fully covered by square based pyramidal <111> features (T2), show a strong etch-time dependence. The roughness, peak height and the average slope of pyramids decrease with etch time. These changes lead to a shift to wider scattering angles and higher total reflected intensity, which makes for an interesting texture for tandem pv applications. The processing of a crack-free device quality 3μm nc-Si:H layers has been demonstrated at an etch time of 300s. The etch time could potentially be further reduced, especially for thinner films, without damaging the integrity of the nano- or poly crystalline film.

The use of a sacrificial layer to create anisotropic etching behavior with an acidic etch is potentially very promising. We have demonstrated that crater like features can be produced on a <100> monocrystalline silicon surface. These features decrease the reflected intensity by 3-5% with respect to flat wafers and increase the reflection into wider angles, albeit not as efficiently as T2. This texturing approach could benefit from further optimization of the sacrificial layer.

The passivation quality showed a strong dependence on the crystal orientation at the wafer surface, in combination with the amorphous silicon deposition conditions. Post deposition treatment of the a-Si:H passivation layer with hydrogen, either through a hydrogen plasma or a bilayer configuration with hydrogen diluted a-Si, strongly improves passivation quality. Dilution of the plasma with hydrogen during initial growth increases passivation quality on a <111> surface, likely as a results of densification of amorphous phase. On a <100> surface however, hydrogen dilution leads to very poor lifetimes, as it increases the probability of epitaxial growth at the at the c-Si/a-Si:H hetero-interface, which is detrimental to the passivation quality.

Different a-Si:H deposition conditions were used on the 3 texturing approaches, which have multiple crystal orientation at the c-Si/a-Si:H interface. A minority carrier lifetime of over 3ms has been achieved for all texturing approaches after deposition of a 15nm a-Si:H layer on both sides of the wafer.

3.2 The optical performance of random and periodic textured crystalline silicon surfaces for photovoltaic applications

This section is under review in *EPJ Photovoltaics*[†]

Abstract

Surface textures that result in high optical yields are crucial for high efficiency photovoltaic (PV) devices. A next route for PV are multijunction solar cells, in which c-Si is combined with nano-crystalline silicon, perovskites or C(I)GS materials. These nano- to poly-crystalline materials are incompatible with the relatively steep slopes of the conventional <111> crystal orientation of the dominant mono crystalline-silicon (c-Si) technology.
In this conceptual work three different texturing approaches are presented that result in smooth concave structures devoid of sharp features. For T_{sac}, a sacrificial implanted poly-c-Si layer is used to develop a random surface texture. The influence of the processing conditions, such as layer thickness, implantation energy, dose and ion type, annealing time and temperature, of the sacrificial layer on the developed surface features is investigated. Additionally, a photolithographically developed honeycomb texture (T_{honey}) is presented. The influence of mask design on the honeycomb features is discussed and a relation is established between the honeycomb period and crack formation in nano-crystalline silicon layers. The reflective properties (spectral reflection, haze in reflection and angular intensity distribution) of these approaches are characterized and compared to a third texturing approach, T_{sp}, the result of chemically smoothened pyramidal <111> features. It was demonstrated that high optical scattering yields can be achieved for both T_{honey} and T_{sp}. Additionally, the performance of a-Si/nc-Si tandem devices processed onto the different textures is compared using both optical device simulations and real device measurements. Simulations demonstrate strong improvements in J_{sc}-sum ($\approx$45%), in reference to a flat surface, and high $V_{oc}*FF$ of over 1V are demonstrated for T_{sp}.

3.2.1 Introduction

Surface textures that result in high optical yields are crucial for high efficiency photovoltaic (PV) devices. The technology that dominates the PV market, the mono crystalline-silicon (c-Si) solar cell [150], predominantly of PERC design [151], uses the pyramidal <111> silicon crystal orientation as a front surface texture. This texture is very easy to process through a single chemical etching step, and very efficient at light in-coupling.

A next route for photovoltaics, potentially offering higher yields at low production costs, are multijunction PV devices. In these devices, a crystalline silicon junction is combined with additional junction(s) based on different PV technologies. However, many of these technologies, including nano-crystalline silicon [29], [30], [152], perovskites and C(I)GS materials [75], [120], [121], contain a crystalline phase which is incompatible with the relatively steep slopes of the conventional <111> crystal orientation. The formation of defective regions, or cracks, in the crystalline phase has been reported to occur in the focal point of perpendicular growth on steep features [62]–[64]. These defective regions are detrimental to solar cell performance.

Consequently, in this conceptual work, two alternative texturing approaches are presented. The aim of these approaches is to produce smooth concave structures devoid of sharp features, that result in high optical scattering yields. Both approaches involve the use of a temporary layer, or sacrificial layer, to achieve the desired anisotropic etching of a mono-crystalline silicon surface. For the first texturing approach, presented in section3.2.3, a sacrificial poly-c-Si layer is used to develop a random surface texture. This approach is similar to the one presented in our earlier work [153], for which no optimization was performed on the poly-Si layer processing conditions. In section3.2.3, using a photolithographically developed SiO_2 mask, a periodic texturing approach is presented, resulting in a honeycomb structure. In section 3.2.3, the optical scattering yields of these two approaches are compared to a third texturing approach, the result of consecutive alkaline and acidic etching steps, producing random, smooth and concave structures [153]. Additionally, the performance of multijunction devices processed on the different textured substrates is optically simulated. Finally, in section 3.2.3, the performance of the three textures integrated in thin film multijunction PV devices are compared.

3.2.2 Experimental Details

Three different texturing approaches are presented in this work. 300μm n-type polished crystalline silicon wafers from Topsil are used for all three approaches. T_{sp} is the result of consecutive alkaline and acidic etching steps. The influence of these etchings steps on the surface features, as well as the exact solutions and etching conditions, can be found in [153].

A flowchart is presented in Fig.3.11 for the steps resulting in honeycomb textured surface (T_{honey}). The honeycomb textures (T_{honey}) are obtained using an approach similar to [154]. A flowchart of this approach is presented in Fig.3.11. In step 1, a 300nm SiO_2 layer is grown on the silicon wafer using a $1100°$C wet oxidation process. After SiO_2 deposition, the wafer is consecutively coated with an adhesive, hexamethyl disilizane, using nitrogen as a carrier gas. In step 2, spin coating is used to apply a 1.4μm Shipley SPR3012 positive
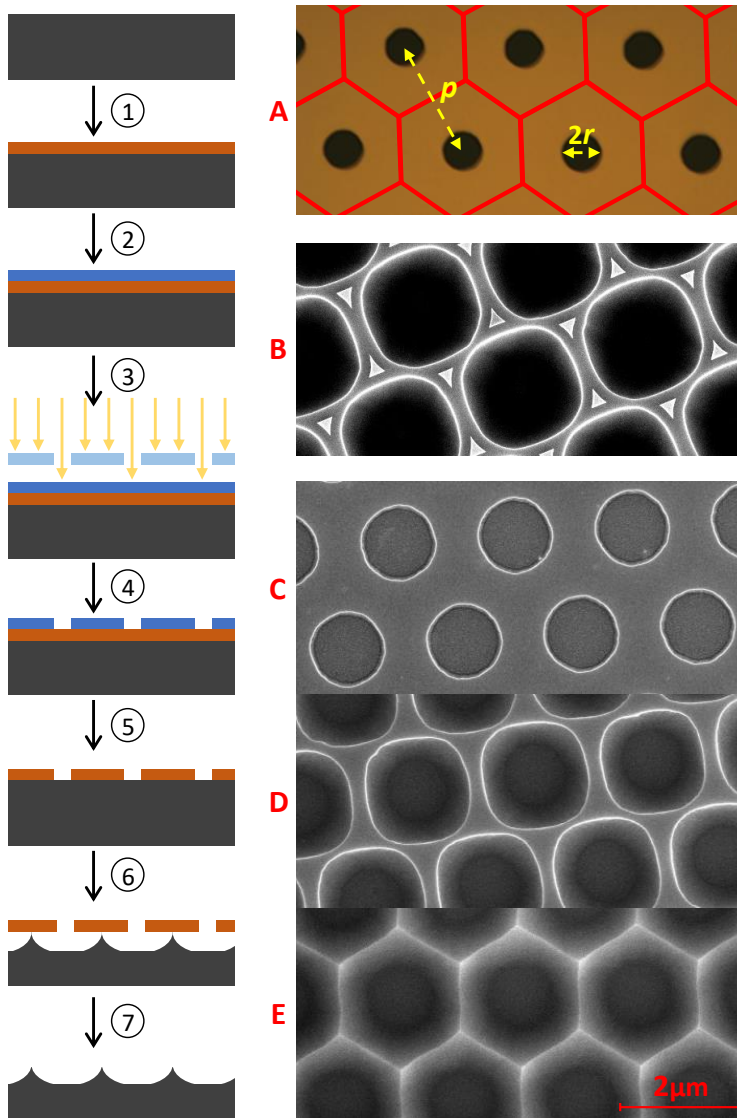
Figure 3.11: Flowchart of the honeycomb texturing approach. A schematic representation of the silicon surface and additional layers phase is presented on the left. Processing steps 1-7 are referenced in the text. Visual **A**. is optical microscope image of the mask used for exposure. Red lines are added to indicate the honeycomb structure resulting from the used mask. Visual **B**-**E** are SEM images at 0 degrees tilt, Visual **B** indicates the effect of under-etching at step 4. Visuals **C**-**E** indicate the effect of etching time during step 6.
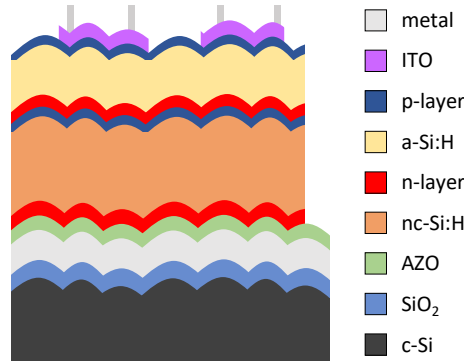
Figure 3.12: Schematic structure of the solar cells

photoresist. An annealing step is then performed, at 95°C for 90 seconds, followed by lithographic exposure during step 3, at at 140 mJ · cm^{-2}, and another anneal for 90s at 115°C. An optical microscope image of the mask used for exposure is indicated by **A**. In this image, the red honeycomb structure is added to indicate the eventual formation in reference to the position of the holes. Step 4 is the development phase, during which the areas of the photoresist that were irradiated are removed. This involves coating the wafer with the developer, followed by an anneal at 100°C for 90 seconds. During step 5 the pattern is transferred from the mask to the SiO$_2$ layer through a 4 minute dip in a bath of commercially available buffered oxide etch (7:1). Afterwards, the acid is removed by rinsing with DI water and the remaining photoresist is removed in a bath of acetone at 40°C. In step 6 the wafer is exposed to a poly-etch to etch the silicon wafer. The etching time should be optimized such that the etched hexagonal areas underneath the holes come into contact with one another. The evolution of the surface as a function of etching time is presented through visuals **C**-**E**. If the SiO$_2$ is not fully etched during this step 5, the poly-etch will first have to etch through the remaining SiO$_2$, resulting in longer required etching times for honeycomb completion and the SiO$_2$ triangles that are observed in visual **B**. Finally, in step 7, the remaining SiO$_2$ mask is removed using another HF etching step.

A schematic representation of the solar cell device architecture is shown in Fig.3.12. For this conceptual research, the Si wafer is not part of the photoactive stack but exclusively acts as a textured substrate. For the solar cell depositions, a 300nm SiO$_2$ layer was processed first, using a 1100°C wet oxidation process, to electrically isolate the textured wafer from the photo-active stack. Next, a 500nm silver layer was evaporated on the SiO$_2$ layer, followed by a 90nm sputtered aluminum doped zinc-oxide (AZO) layer. The photoactive stack is processed in n-i-p substrate configuration, using plasma enhanced chemical vapour deposition (PECVD). The deposition conditions of the intrinsic and n-type (n-) PECVD processed layers can be found in [155]. For the p-type (p-)layers, two consecutively processed p- nano-crystalline (nc-) hydrogenated (:H) siliconoxide (SiO$_X$) layers are used, with the diborane gas flow rate set at 10sccm 0.02%B$_2$H$_6$ in H$_2$ for the initial 12nm, and 50sccm for the final 4nm. The other p-layer deposition conditions are

similar to those reported in [156]. Following deposition of the photoactive stack, a 70nm indium-doped tin-oxide (ITO) is sputtered and a 500nm Al metal front grid is evaporated. Details regarding the used scanning electron microscope (SEM) and atomic force microscope (AFM) are reported in [153]. A Lambda 950 Spectrophotometer was used to determine the angular intensity distribution (AID) of the reflectance. A Lambda 1050 Spectrophotometer was used for spectral reflectance and Haze measurements. The haze in reflection (H_{R}) is defined as the ratio of diffuse to the total reflection:

$$H_{\mathrm{R}}(\lambda) = \frac{R_{\mathrm{dif}}(\lambda)}{R_{\mathrm{tot}}(\lambda)} \tag{3.1}$$

More information about the haze and AID measurements can be found in [129], [157], [158].

Raman spectroscopy, using an inVia confocal Raman microscope with a laser operating at a wavelength of 514nm, was performed to determine the crystallinity of a few selected layers. The method for obtaining the crystallinity is reported elsewhere [159]. The external quantum efficiency (EQE) was obtained using an in-house EQE setup. The EQE of an individual junction in a multijunction device was obtained by saturating the other junction(s) with bias light. By weighing the EQE spectra with the AM1.5$_{\mathrm{G}}$ solar spectrum, the short-circuit current density (J_{sc}) of the individual junctions was obtained. EQE measurements are performed without bias voltage, unless mentioned otherwise. The J-V curves of the devices are measured at 25°C using an AM1.5$_{\mathrm{G}}$ solar simulator. The open circuit voltage (V_{oc}), fill factor (FF), series resistance (R_{s}) and shunt resistance (R_{sh}) are obtained from these J-V curves. On each sample, 24 individual 16mm^2 cells are processed. All 24 cells are measured and the results presented in this work are the average of the five best cells. More detailed descriptions of these measurements can be found in [155].

3.2.3 Results and discussion

Random texturing using a sacrificial layer

A random surface texture can be developed using a heterogeneous sacrificial layer. The purpose of the heterogeneity is to achieve anisotropic etching of the sacrificial layer. As a result of this anisotropic etching, the etchant will reach the silicon surface, having locally etched through the sacrificial layer, at different points in time, spatially. Consequently, when the sacrificial layer is fully etched over the entire sample, the silicon surface will have been exposed to the etchant for a non-uniform period of time, resulting in a random surface texture. The heterogeneity of the sacrificial layer can be the result of factors like material stoichiometry, different material phases or pinholes. In this section a sacrificial poly-crystalline silicon film is used, where the porous grain boundaries in reference to the dense c-Si grains result in the desired anisotropic etching behaviour. This texturing approach (T_{sac}) has been presented before in our earlier work [153], where it was concluded that the surface features were too small to yield the desired optical behaviour. In this section an optimisation of the sacrificial layer is performed to achieve larger surface features, which would result in lower reflectance and better wide-angle scattering.

A flowchart of the processing method is presented in Fig.3.13. The figure additionally in-
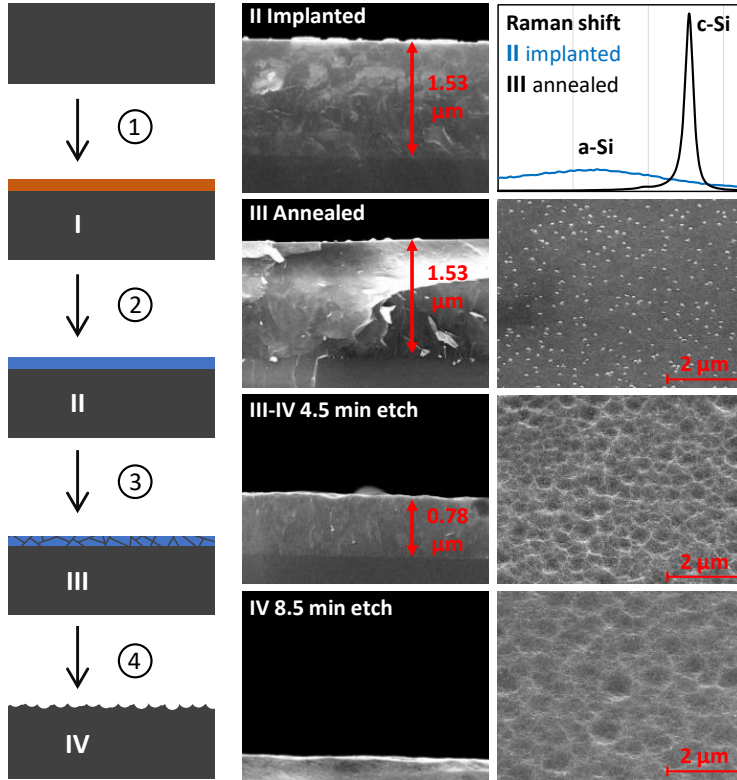
Figure 3.13: Flowchart of the sacrificial-layer texturing approach (T_{sac}). A schematic representation of the sacrificial layer and silicon surface at each phase (phase I-IV) is presented on the left. Processing steps 1-4 are referenced in the text. A cross-sectional SEM image of the silicon surface and sacrificial layer at phase II is presented in the centre, following implantation in an approximately 1.5μm a-Si layer. Raman spectroscopy measurements of the sacrificial layer at phase II and phase III are presented in the top right plot, where the peak referred to as c-Si is positioned at 520cm^{-1} and the peak referred to a-Si at around 480cm^{-1}. SEM images of the cross-section and surface of the substrates at a 40 degrees tilt, at phase III and IV and at some point between these phases are presented as well.
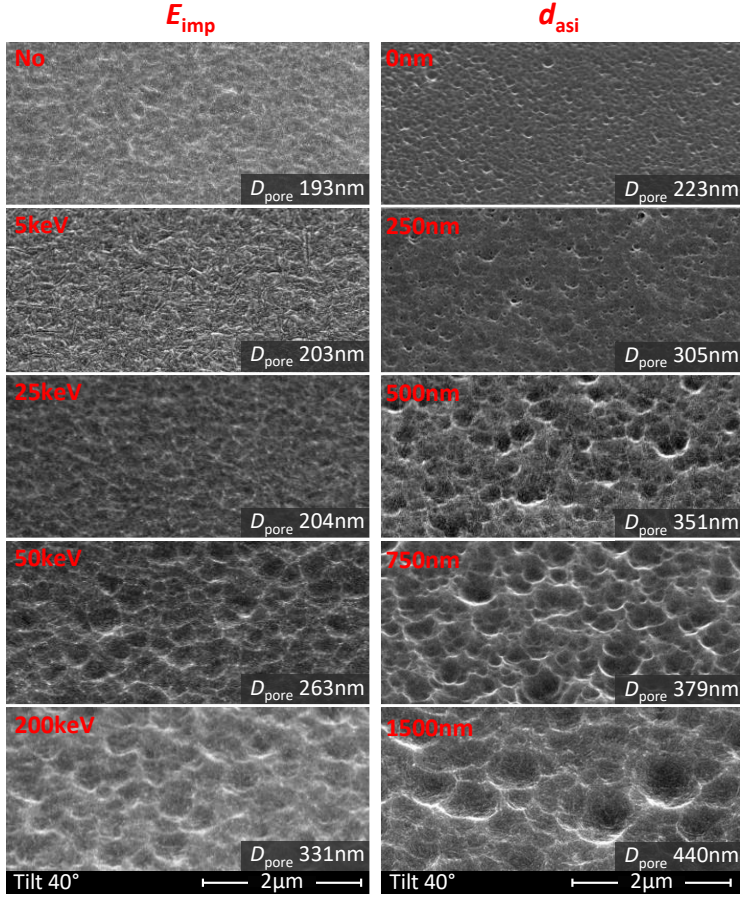
Figure 3.14: SEM images and D_{pore} values of two argon implanted series of samples. Samples on the left are processed with increasing E_{imp} and d_{aSi}=1um. Samples on the right are processed with increasing d_{aSi} and E_{imp}=250keV. All samples implanted with δ_{imp}=1e16cm^{-2}. No implantation occurred for the top-left sample, while the implantation was performed without amorphous silicon layer for the top-right sample.

cludes SEM images to visualize the state of the substrate along the process. Starting with a c-Si wafer that is stripped of the native oxide layer, an amorphous silicon (a-Si) layer is grown in step 1 using a Tempress low pressure chemical vapour deposition tube furnace. In step 2, ion implantation of the a-Si layer is performed with a Varian Implanter. At this point the sacrificial layer is amorphous and the surface is relatively flat. The substrate is then subjected to a high temperature thermal anneal in an N_2 atmosphere in step 3. At this point, the surface and cross-section appear largely unchanged, but the Raman plots demonstrate that the sacrificial layer is now poly-crystalline. Finally, in step 4, the sacrificial layer is etched in a poly-etch solution. After etching for 4.5min, just over half of the poly-Si sacrificial layer is etched and the crater-like surface features are present. When the sacrificial layer is fully etched, the silicon surface is exposed with craters up to 600nm in diameter.

All four steps can influence the features formed on the c-Si surface. In earlier work it was observed that the etching time of step 4 should be chosen such that sacrificial layer has just been fully etched [153]. Prolonged exposure to the etchant results in smoothening of the craters and a decrease of surface roughness. In this section, the conditions used for steps 1-3 are characterized. These include the a-Si sacrificial layer thickness (d_{aSi}) developed in step 1, the implantation conditions used in step 2, which include the implantation dose (δ_{imp}), implantation energy (E_{imp}) and ion type used for implantation, and finally the annealing time and temperature in step 3. Of these conditions, only the annealing time and temperature did not significantly affect the size of the craters. For the crater size, the mean pore diameter (D_{pore}) is used as a metric, as obtained from AFM measurements. For a series of samples annealed at both 950°C and 1050°C, for 15-30-60-90mins, the D_{pore} was observed to increase slightly from 370-380nm to 385-395nm when the annealing time was increased from 15mins to 30mins. A further increase of annealing time, for either temperature, did not result in a significant change of D_{pore}. The discussion will therefore focus on the influence of d_{aSi} and conditions used for ion implantation. All following samples are annealed for 20mins at 1050°.

SEM images and D_{pore} of the silicon surfaces as a function of E_{imp} and d_{aSi} are shown in Fig.3.14. Additionally, in the top left of the figure, a sample is included for which step 2 of Fig.3.13 was omitted, so where no implantation occurred. The SEM image shows that implantation is essential for the formation of large craters. In Fig.3.15, the influence of δ_{imp} is shown in some more detail. For the P-implanted samples shown in the inset, D_{pore} is observed to increase continuously with increasing δ_{imp}. Raman measurements performed on an additional set of Ar-implanted samples with varying δ_{imp} indicate a direct relation between δ_{imp} and the crystallinity of the sacrificial layer. The crystallinity is observed to continuously decrease with increasing δ_{imp}, and is highest for the sample for which no implantation occurred. A decrease of the crystallinity in these poly-Si layers is consistent with the formation of larger grains, as larger grains can result in a larger fraction of amorphous tissue in between grains. Moreover, an increase of the average grain size in poly-Si layers with increased δ_{imp} is in line with earlier reports [160]–[162]. While no grain size measurements are performed in this work, reportedly the Si self-diffusion coefficient during anneal can be improved through impurity doping, which facilitates the merger of small grains during anneal and consequently results in an increase of the average grain size [161], [162]. We suspect therefore that the D_{pore} scales with the average grain size
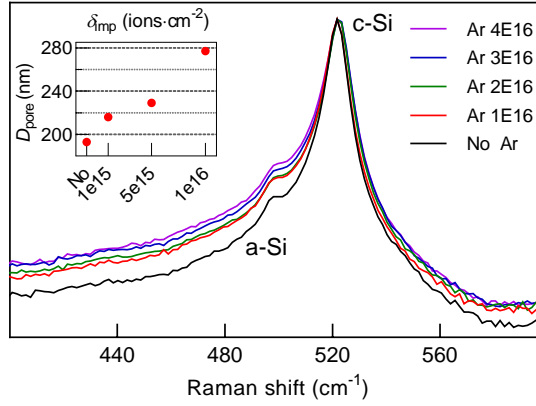
Figure 3.15: Raman measurements of Ar implanted poly-Si sacrificial layers at phase 3 (post-anneal) at different δ_{imp}. Samples are processed with d_{aSi}=1.5μm and E_{imp}=250keV. Raman measurements are normalized using the highest count and plotted on a semi-logarithmic scale. The inset show D_{pore} as a function of δ_{imp} for P implanted sacrificial layers, with E_{imp}=5keV and d_{aSi}=1μm.
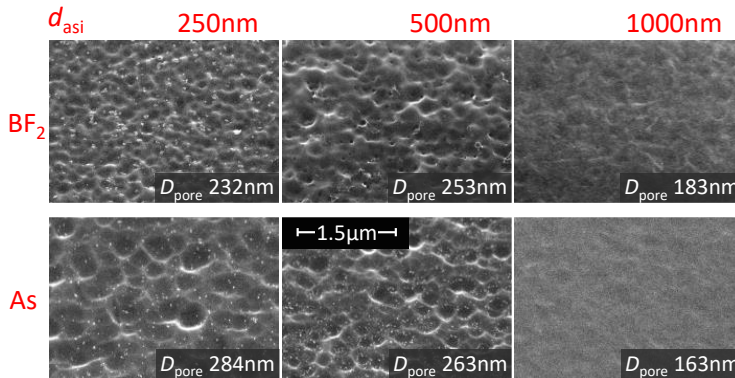
Figure 3.16: SEM images and D_{pore} values of sacrificial layers implanted with BF$_2$ and As, with d_{aSi} varied between 250-500-1000nm . Implantation occurred at δ_{imp}=1e16cm^{-2} and E_{imp}=250keV.
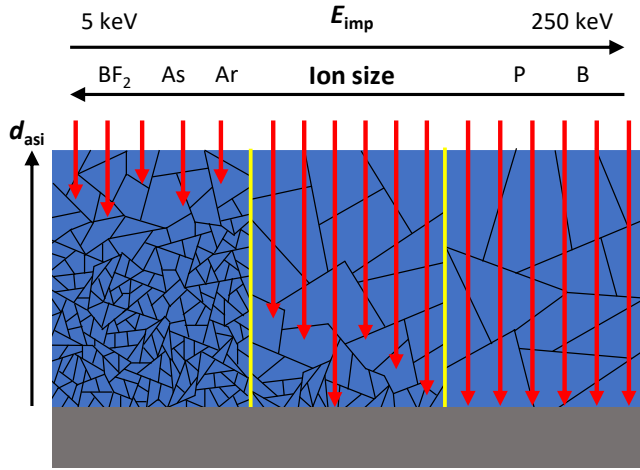
Figure 3.17: Simplified schematic representation of the grain size development as a function of the ion distribution (red arrows) in reference tot the silicon surface (grey rectangle), as a function of d_{aSi}, the ion type and E_{imp}.

in the sacrificial poly-Si layer and that the development of the grain size is influenced by the presence and dose of implanted ions.

Grain formation is not exclusively affected by δ_{imp}. Fig.3.14 shows that the crater size increases with both E_{imp} and d_{aSi}, for the selected conditions. For $d_{\mathrm{aSi}}=1\mu$m, increasing E_{imp} of the Ar implanted samples from 5keV to 200keV results in an increase of D_{pore} from about 200nm to over 330nm. Similarly, increasing d_{aSi} from 250nm to 1500nm, for an Ar implantation energy of 250keV, results in an increase of D_{pore} from about 300nm to 440nm. Fig.3.14 shows that: i) if no implantation takes place, no craters are formed. ii) The surface of a no-implantation sample strongly resembles the surface of a low energetic implantation sample and iii) if no a-Si layer is used for the implantation, craters are still formed, but with a very small D_{pore}. This is not unexpected, since Raman measurements show that the energetic ion bombardment during implantation amorphizes a thin top region of the silicon wafer, which will recrystallize to form a poly-Si layer upon annealing.

These combined observations lead to suspect that the development of the grain size, for a given δ_{imp}, is the result of an interplay between d_{aSi} and E_{imp}. The profile of implanted ions can be approximated by a gaussian distribution [163], [164]. Note that the ions will no longer have a ioninc nature following implantation. With increasing E_{imp}, the width of the gaussian widens and the peak is positioned further away from the surface. This means that with a low E_{imp}, the ions will be predominantly implanted near the surface of the a-Si layer and will not affect grain formation, upon thermal anneal, close to the silicon wafer surface. With higher E_{imp}, more energetic implantation occurs and the ions are implanted deeper into the amorphous silicon layer. Consequently, for the 1000nm Ar implanted a-Si layer of Fig.3.14, a larger fraction of ions will be positioned close to the silicon surface, facilitating the formation of large grains near the silicon surface and

consequently the formation of large craters on the silicon surface. Similarly, for the 250keV Ar implanted a-Si layers, D_{pore} can be observed to increase with d_{aSi}. Experiments with much thicker d_{aSi} of 3μm and 4μm again showed a strong decrease of D_{pore} and RMS roughness.

The implantation profile is not exclusively a function of E_{imp} however. For similar E_{imp}, larger, heavier ions are implanted closer to the surface. This effect is shown in Fig.3.16, Where it can be observed that, for a given δ_{imp} and E_{imp}, the largest D_{pore} are realized in thinner a-Si layers with increasing ion size. This interplay between d_{aSi}, E_{imp} and the used ion type is schematically shown in Fig.3.17. This schematic visualizes how the grain size near the silicon surface will vary as a function of these parameters. This means that for a given ion type, E_{imp} and d_{aSi} should be optimized in tandem for the development of large crystal grains.

In addition to the interplay between these three parameters, Fig.3.17 and Fig.3.16 indicate that, if E_{imp} and ion type are chosen such that ions are implant close to the c-Si surface, the largest D_{pore} are achieved for relatively thick a-Si layers. For similar δ_{imp}, the largest D_{pore} of the Ar implanted sacrificial layers is 440nm, while that of the BF$_2$ and As implanted sacrificial layers is 253nm and 284nm, respectively. This observation seems to suggest that the formation of larger grains is impeded in thin films, or conversely that thicker films facilitate the formation of larger grains.

Periodic honeycomb texturing

A flowchart of all steps involved in developing the periodic honeycomb features is presented in section 3.2.2. When all steps are optimized, the developed honeycomb texture is determined by the mask used during step 3. The formed honeycomb structure is a function of two parameters, which are the the period (p), defined as the distance between the centre of two hexagons, and the height difference (h) between the corner of the hexagon and the centre. As an isotropic etchant is used, the texture depth is equal to the distance between edge of a hole in the mask and nearest corner of the hexagon. Consequently, h will be equal to the distance from the centre of the hexagon to the corner, which is equal to $\frac{p}{\sqrt{3}}$, minus the radius (r) of the hole, or:

$$r = \frac{p}{\sqrt{3}} - h \tag{3.2}$$

The ratio of h over p is referred to as the aspect ratio. For use in thin film silicon solar cells, the aspect ratio of the honeycomb texture should be around 0.25 [165]. Moreover, it was concluded in earlier work that maximum photo-currents are realized in nano-crystalline silicon (nc-Si) solar cells when p is about 0.5μm larger than the film thickness [166]. Taking into account this desired aspect ratio of 0.25 and p=3μm, a mask is used in this work with $r \approx 1\mu$m, in accordance with Eq.8.3. If the texture is used in combination with a different PV absorber material, with a different bandgap energy and absorption coefficient, different reflective behaviour might be preferred. In order to characterise the change in optical behaviour as a function of p, a second mask is used with r=1μm and p=2μm. The resulting surface textures are presented in Fig.3.18.

Finally, in addition to improving the optical behaviour of the silicon surface, the honeycomb texture should facilitate the growth of crack-free nano- to poly-crystalline growth.
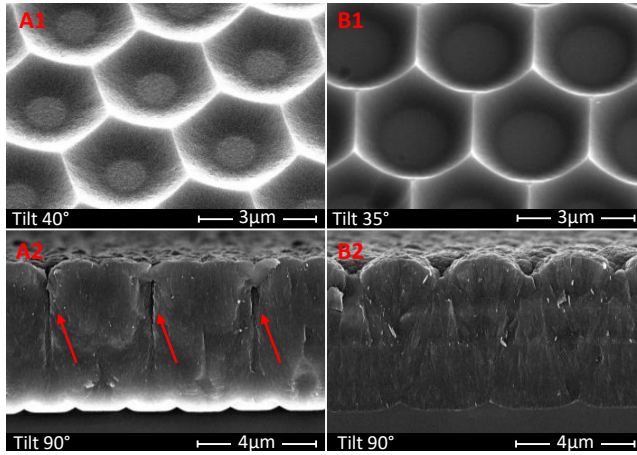
Figure 3.18: SEM images of honeycomb structures. **A1-2** have a honeycomb periodicity of 2μm, while **B1-2** have a periodicity of 3μm. **A1** and **B1** are surface images at 35-40 degrees tilt. **A2-B2** are cross-sectional images of a c-Si honeycomb surface structure on top of which a 5μm nc-Si layer is grown. Red arrows in image **A2** indicate cracks formed in the nc-Si phase as a result of the honeycomb surface texture.

The growth of a crystalline phase on sharp surface features can result in the formation of cracks [63], [64], which is detrimental to solar cell performance [29], [62]. SEMS **A2** and **B2** in Fig.3.18 demonstrate that the formation of cracks is a function of both p and the thickness of nc-Si film. The texture with $p=3\mu$m can facilitate the growth of a 5μm crack free nc-Si film, while the texture with $p=2\mu$m can only facilitate very thin nc-Si films before significant crack formation occurs. For that reason, the devices presented in section 3.2.3 are exclusively processed on the larger honeycomb textures with $p=3\mu$m.

Optical performance of surface textures

To determine the optical behaviour of the different surface textures, the spectral reflectance (R) and haze in reflection (H_{R}), as well as the angular intensity distribution (AID) are measured. This comparison is performed between the texture using a sacrificial layer (T_{sac}) developed in section 3.2.3, the honeycomb textured (T_{honey}) developed in section 3.2.3 and the texture with chemically smoothened pyramidal features (T_{sp}) developed in [153]. SEM images for each texture are shown in Fig.3.20

The reflective behaviour of the different bare silicon surfaces is shown in Fig.3.19. R provides information on the light in-coupling effectiveness of the textured surface. Light in-coupling is predominantly related to the probability of multiple reflection events. The probability of such an event taking place decreases when the mean slope of surface features decreases. A decrease of the mean slope with increasing etching time is the cause of the decrease in R over the entire spectral range observed for T_{sp}, which is in line with [153]. The low probability of multiple reflection events for T_{sp}, especially for 9.5-11mins etching time, result in R-values that are not much different from that of a flat surface, as can be observed in the T_{sac} R spectra. It should be noted that the change in reflectance
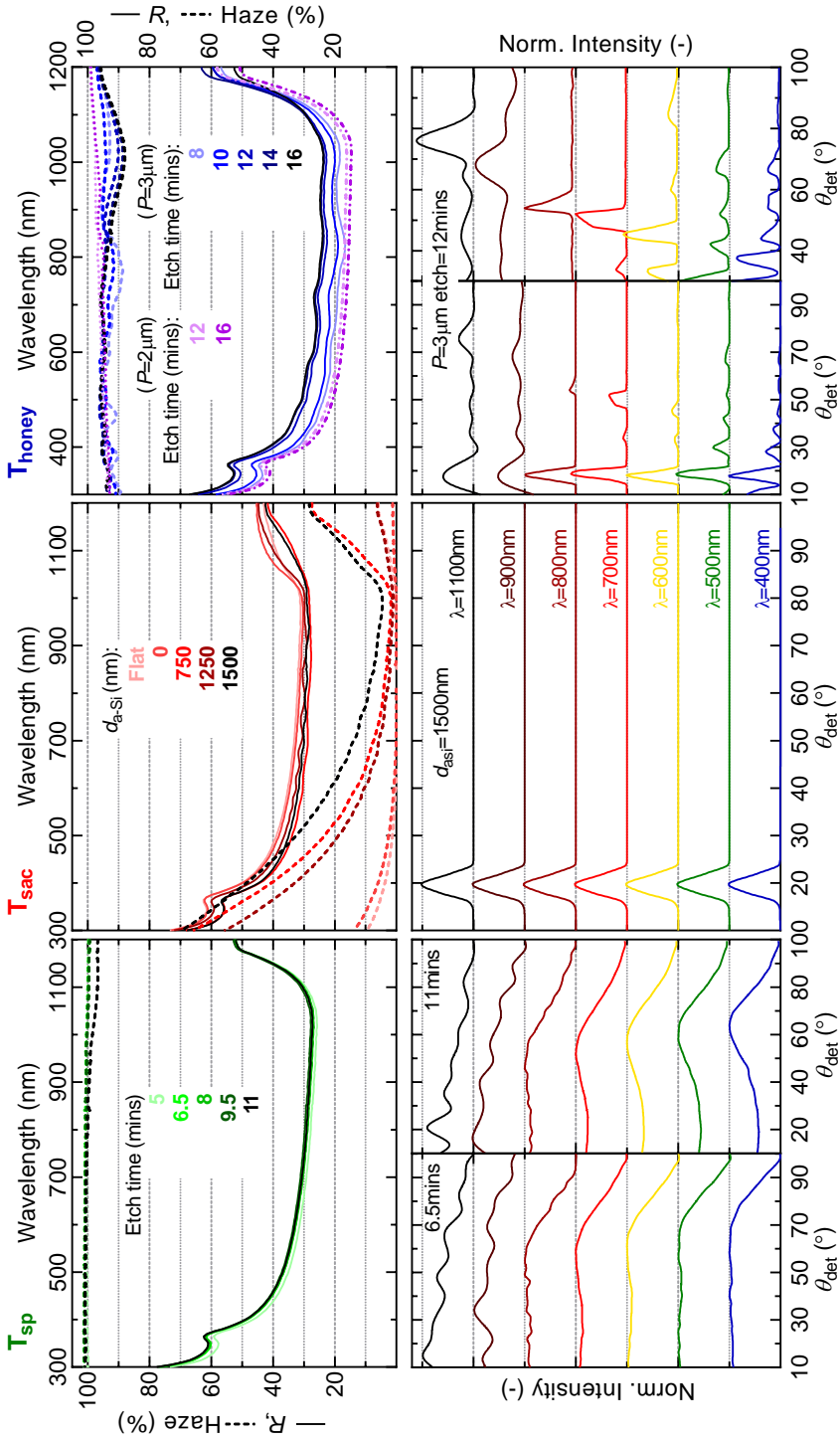
Figure 3.19: caption on next page

Figure 3.19: Reflective behaviour of T_{sp} (green, left), T_{sac} (red, centre) and T_{honey} (blue, right). Presented are R (top, solid lines) and H_R (top, dashed lines) and AID (bottom). AID measurements show normalized intensity (normalized to max value) as a function of detector angle (θ_{det}) in reference to the incident light, with the sample positioned at a 10 degree angle, for different wavelengths (λ). For T_{sp}, R and H_R are shown as a function of etching time and AID measurements are shown for samples etched at 6.5mins (left) and 11mins (right). For T_{sac}, R and H_R are shown as a function of d_{aSi}. R and H_R of a flat, polished wafer is included as reference. AID measurements are shown for the sample with d_{aSi}=1500nm. For T_{honey}, R and H_R are shown as a function of etching time (step 4) for honeycombs with p=2μm (R=dashed/dotted, H_R=dotted) and p=3μm (R=solid, H_R=dashed). AID measurements are shown for samples with p=3μm etched for 12mins, with right image showing AID normalized to max value in θ_{det}=30°-90° range.

due to a mean slope related change in the average angle of incidence, following from the Fresnel equations, is minimal in the $\leq$45° mean slope range, and would be opposite in trend.

The use of the T_{sac} approach results in only a marginal R decreases, by about 0-5%. While the influence on light in-coupling is minimal, application of T_{sp} or T_{sac} changes the scattering behaviour significantly in reference to a flat surface. The H_R of T_{sac} is observed to increase from a few percent to 5-60% with increasing d_{aSi}, depending on the spectral range. Nevertheless, the small R-decrease and H_R $\leq$30% for wavelengths (λ)>500nm indicate that the T_{sac} approach might have limited effectiveness for light in coupling and/or scattering applications, presumably as a result of the limited depth of the formed craters. The relatively poor scattering nature is confirmed by the AID measurements of the d_{aSi}=1500nm sample. Note that the slope distribution, height profile and additional surface parameters of T_{sac}, T_{sp} and T_{honey} are available in the supplementary information.

On the other hand, the H_R of T_{sp} is close to 100% over the entire spectral range for all etching times, indicating that no specular component remains to the reflection. While the R and H_R measurements show a minimal etching time dependence, the AID shows a subtle yet significant change in reflective behaviour. At 6.5mins the reflected intensity in the θ_{det}=10-65° range is roughly equally distributed. However, when the etching time is increased to 11mins, the mean slope is decreased to approximately 30° and light in the visible range (λ=400-700nm) is predominantly scattered into wide 60° angles.

The application of T_{honey} appears more effective at light in-coupling then T_{sp} and T_{sac}, especially at smaller p where width-to-depth ratios are larger and slopes are steeper. As with T_{sp}, the reflectance of T_{honey} increases with etching time. For p=3μm, at an etch time of 8mins, the different holes have barely reached one another (Fig.3.11 between **D** and **E**) and the slopes are relatively steep, resulting in effective light in-coupling. With increasing etching time, steep features are smoothened and reflection increases. H_R of the T_{honey} is in the 88-100% range, owing to the full surface coverage of concave features. The periodic nature of the T_{honey} is also apparent in the reflective behaviour. Constructive and destructive interference effects can be observed over the H_R and R spectral range. The interference behaviour, can clearly be observed in the AID spectra. On the bottom right the AID spectrum normalized in the θ_{det}=30-100° range of the p=3μm (12mins) sample is presented. The maximum reflection, so the peak of constructive interference, is observed to shift to larger θ_{det} with increasing λ. Additionally, an increase of $\Delta\theta_{det}$

between peaks of constructive interference can be observed with increasing λ, so that at larger wavelengths fewer inference peaks are present. The left figure of T_{honey} AID shows however that the largest fraction of the reflected light still occurs in the normal direction. This is likely a result of the relatively flat areas at the bottom of the honeycomb structure positioned underneath the hole in the SiO_2 mask.
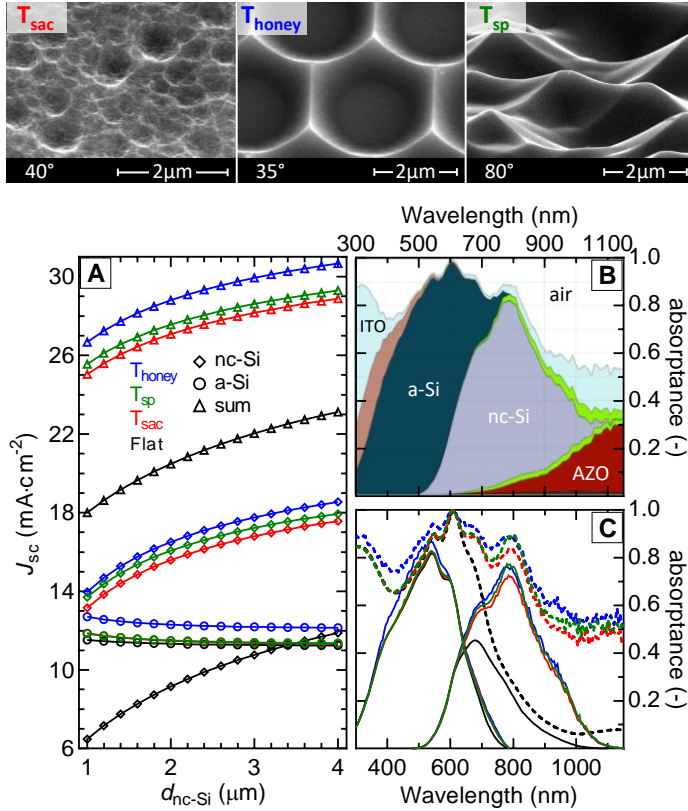
Figure 3.20: Simulated performance of a-Si/nc-Si tandem devices on flat substrates and substrates with T_{sac} (red), T_{sp} (green) and T_{honey} (blue) textures. SEM images (top) show surface morphology T_{sac}, T_{sp} and T_{honey}. **A)** shows the J_{sc} of the a-Si junction, nc-Si junction and the sum of both junctions for the different substrate types, as a function of nc-Si absorber thickness ($d_{nc\text{-}Si}$). **B)** shows the spectral absorptance in each of the layer of the tandem device on T_{honey}. In addition to the layers indicated in the plot (air, ITO, a-Si, nc-Si, AZO) absorptance in the p-nc-SiO_x:H layer (brown), n-nc-SiO_x:H layers (green) and Ag layer (dark grey) are indicated. **C)** shows the a-Si and nc-Si absorptance curves and 1-R curves for the different substrate types, for tandem device with $d_{a\text{-}Si}$=300nm and $d_{nc\text{-}Si}$=1.2μm.

Next we compare the light management effectiveness of the various textured substrates when integrated in a PV device, using the GenPro4 optical model [167]. GenPro4 gives the spectral reflectance and absorptance of each layer in a PV device and allows for the use of AFM scans to simulate the texture. Using the multijunction a-Si/nc-Si tandem device schematically shown in Fig.3.12 as a model, and various AFM scans, current gen-

eration in the different absorbers as a function of surface texture was simulated. Fig.3.20 shows the J_{sc} generated in an 250nm a-Si absorber and nc-Si absorber, with a thickness varied from 1-4μm, for a device with flat interfaces as well as T_{sp} (6.5 and 11mins), T_{sac} (d_{aSi}=1500nm), and T_{honey} (12mins) textured interfaces.

The figure demonstrates that the J_{sc}-sum is strongly increased for all three textured surfaces in reference to a flat surface. The J_{sc} difference mainly originates from the nc-Si bottom junction, as the a-Si-J_{sc} values are not much different. This is not unexpected since i) a relatively thick a-Si absorber thickness (d_{aSi}) of 250nm is used, ii) the absorption probability of light with λ=300-600nm in the direct-bandgap a-Si junction is relatively high and iii) the light in-coupling effectiveness between the different junctions does not differ much, as shown in Fig.3.19. T_{honey} achieves better light in-coupling than the other textures, as indicated by the lower R-values in Fig.3.19, which is reflected in the higher J_{sc} values of the a-Si junction.

The main difference is achieved in the nc-Si junction, which has a lower absorption probability and therefore benefits more from the increased optical pathlengths, and the potential for total internal reflection events, achieved with textures that scatter light effectively. This is demonstrated in Fig.3.20**C**, where a strong increases in the λ=700-1100nm region can be observed for the different textures in reference to the flat surface, for which the optical path length is just two times d_{ncSi} before light is lost in air (1-R). The effect of the increased scattering efficiency, as represented by H_R, of T_{honey} and T_{sp} in reference to T_{sac} is mainly observed in the λ=700-950nm region.

According to the simulations, J_{sc}-sum of T_{sp} and T_{sac}, in reference to a flat surface, is increased by about 7-7.5mA · cm^{-2} and that of T_{honey} by about 8.5 mA · cm^{-2}, which represents an increase of over 45%. No current matched situations are presented in Fig.3.20**A**. Additional simulations show that current matching can be achieved at d_{aSi}=310nm and d_{aSi}=1um for T_{sac} (12.61mA · cm^{-2}) and T_{honey} (13.41mA · cm^{-2}). Achieving current matching of T_{sp} at d_{aSi}=1um requires a d_{aSi}=350nm (12.98mA · cm^{-2}).

Additionally, Fig.3.20**B** shows that the difference between 1-R and the summed absorptance in the a-Si and nc-Si absorbers is mainly due to parasitic absorption in the TCOs positioned at the front (ITO) and back (AZO) of the device and some minor absorption in the p- and n-doped SiO$_x$:H layers.

Influence of textures on solar cell performance

Finally, the performance of n-i-p a-Si/nc-Si tandem devices processed on silicon wafers that are textured using T_{sac} (6.5mins), T_{sac} (12mins) and T_{sac} (d_{aSi}=1500nm) is compared. The device structure is schematically shown in Fig.3.12. Two sets of devices are processed; one with a high bandgap energy (E_G) a-Si absorber (a-Si(H)) with $E_{G\ a-Si(H)}$ ≈1.7eV, developed in [73], and the other with a low-E_G a-Si absorber (a-Si(L)), with $E_{G\ a-Si(L)}$ ≈1.6eV. Deposition conditions for both can be found in [168]. The difference between the a-Si(L) and a-Si(H) absorber can be observed in Fig.3.21**A**, where the absorption onset is observably shifted from about λ=730 to λ=780nm. As a consequence, use of the a-Si(H) absorber results in increased absorption in the nc-Si absorber.

From the J-V characteristics of the tandem devices presented in Fig.3.22, a number of observations can be made.

i) The highest J_{sc}-sum is achieved with T_{sp}, which is unlike in the optical simulations
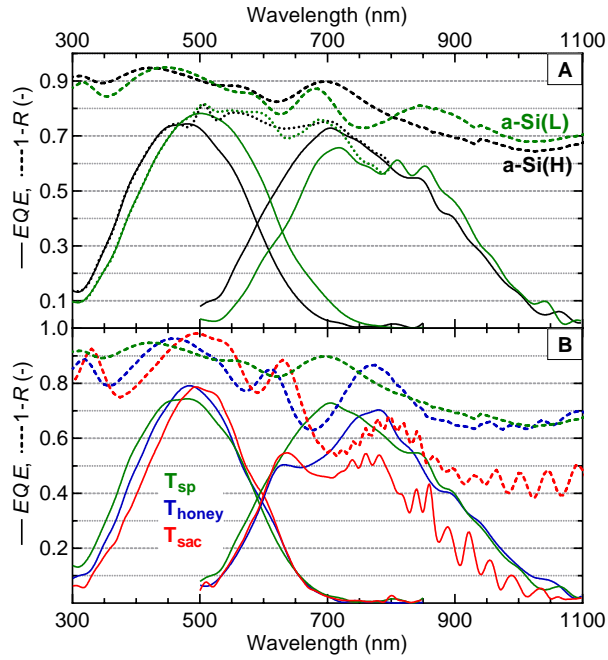
Figure 3.21: EQE and 1-R spectra as a function of wavelength. **A** shows the spectra of tandem devices with a-Si(H) and a-Si(L) absorber on T_{sp} (6.5mins) textured substrate, with dotted line indicating EQE-sum. **B** shows the spectra of tandem devices with a-Si(H) absorbers on T_{sac} (6.5mins), T_{sac} (12mins) and T_{sac} (d_{aSi}=1500nm) textured substrates.
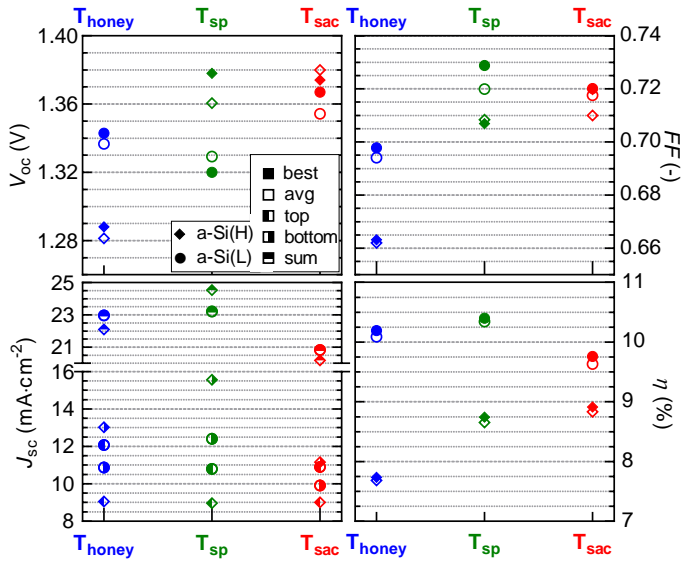
Figure 3.22: caption on next page

Figure 3.22: Solar cell characteristics of a-Si/nc-Si tandem devices as a function of substrate texture. Symbols indicate the characteristics of the best (closed) and average of best 5 (open) cells on a substrate, based on conversion efficiency. Symbol type indicates results of devices with high-E_G a-Si (diamond) and low-E_G a-Si (circle). J_{sc} is obtained from EQE-measurements and is presented separately for the bottom nc-Si junction, top a-Si junction and sum of both junctions.

presented in the preceding section. The J_{sc}-sum is especially high for the a-Si(H) samples, while for the a-Si(L) samples it is not much different from the T_{honey}. The high J_{sc}-sum of T_{sp} is mainly a result of generation in the bottom junction, which is considerably higher in reference to T_{sac} and T_{honey}. The EQE-curve in Fig.3.21**B** shows that is mostly due to a large interference fringe with high reflectance for T_{honey} in the λ=600-800nm range. The presence of the interference peak likely results from the bottom of the honeycomb, which appears optically flat, as indicated by the relatively large specular component in the AID measurements of T_{honey}. A spectral shift of the interference fringes has been demonstrated, for instance, as a function of the thickness of a n-nc-SiO$_x$:H layers positioned between two junctions [152]. The difference between simulated and experimental results is therefore likely due to a difference in layer thicknesses.

ii) The J_{sc}-sum of T_{sac} is 2-4mA $\cdot$ cm^{-2} lower than T_{sp} and T_{honey} due to the relatively low roughness of the surface. The interference fringes that can be expected from an optically flat surface with a large specular component to the reflection (no anti-reflection coating, refractive index grading and/or nanoscale-roughness at the front of the devices), and with thin layers in the 10-250nm wavelength range, can be observed in the Fig.3.21**B** for λ >700nm. T_{sac} also has the highest V_{oc}'s. The relation between substrate roughness and V_{oc} is well documented [62], [63], [157], [169], [170] and is especially relevant for the growth of nano- to poly-crystalline materials. This J_{sc}-V_{oc} trade-off as a function of substrate roughness demonstrates well the challenges in developing the right texture of optimal device performance.

iii) The highest efficiencies are achieved on the T_{sp}, with T_{honey} (a-Si(L)) a close second. The V_{oc}*FF of T_{honey} suffers, presumably due stress induced in the nc-Si layer due to the relative steepness and periodic nature of the honeycomb slopes. More detailed research is being performed on the relation between 1. the honeycomb design (r and p of the mask and etching time), 2. the nc-Si properties (d_{ncsi} and processing conditions) and 3. the external PV device characteristics.

iv) The EQE of T_{honey} in Fig.3.21**B** also demonstrates the attractiveness of this periodic texture, as the highest response in the infrared (λ >1000nm) is achieved using this periodic texture, which is in line with the constructive interference peaks observed in the AID measurements in this spectral range. This feature makes it of potential interest in multijunction silicon devices such as the one in [54], [171]–[173], where high (infra)red response is essential for achieving high conversion efficiencies.

3.2.4 Conclusion

In this work, the optimization of two texturing approaches are presented that results in smooth, concave surface features on monocrystalline silicon. For T_{sac}, a sacrificial implanted poly-c-Si layer is used to develop a random surface texture. The influence of the

processing conditions (layer thickness, implantation energy, dose and ion type, annealing time and temperature) of the sacrificial layer on the developed surface features is investigated. A relation is established between the implantation energy and ion type and the a-Si layer thickness. Additionally it was found that the largest features are formed at high implantation dose and relatively thick a-Si layers.

Additionally, a photolithographically developed honeycomb texture (T_{honey}) is presented. The influence of mask design on the honeycomb features is discussed and a relation is established between the honeycomb period and crack formation in nano-crystalline silicon layers.

The reflective properties of a number of T_{honey} and T_{sac} surfaces are characterized and compared to a third texturing approach, consisting of chemically smoothened pyramidal $<111>$ feature (T_{sp}). It was demonstrated that high optical scattering yields can be achieved for both T_{honey} and T_{sp}. The angular intensity distribution of the period honeycomb texture shows a strong wavelength dependence, that should be tunable through photolithographic mask design.

Finally, the performance of the different textures integrated in a-Si/nc-Si tandem devices is compared using both optical device simulations and real device measurements. Simulations demonstrate strong improvements in J_{sc}-sum ($\approx$45%), in reference to a flat surface, for T_{honey} and T_{sp} and high $V_{oc}*FF$ of over 1V are demonstrated for T_{sp}.

4

Optimal bandgap profiling of stoichiometric absorbers

4.1 An expedient semi-empirical modelling approach for optimal bandgap profiling of stoichiometric absorbers: a case study of thin film amorphous silicon germanium for use in multijunction photovoltaic devices

This section was published in *Solar Energy Materials & Solar Cells**

Abstract

Bandgap energy profiling is applied in a variety of materials for photovoltaic technologies, such as chalcogenides, III-V materials and perovskites. Bandgap profiling of the absorber layer is used to fight the fundamental loss mechanisms imposed by the bandgap energy of the absorber for the maximum voltage and current that a photovoltaic device can generate. The bandgap profile can be affected by a number of profiling strategies, such as the difference between the maximum and minimum bandgap energy, the position of the minimum bandgap energy, the width over which this minimum bandgap energy occurs and the total absorber width. These parameters have a complex effect on output characteristics of a photovoltaic device. Varying multiple parameters at once further increases the complexity, limiting the effectiveness of rigorous physical opto-electrical modeling. In this work we therefore present an expedient semi-empirical approach for the optimal bandgap profiling of stoichiometric absorbers.

Using PECVD processed amorphous silicon germanium as a model, we present a unique set of semi-empirical relations that simulate the V_{OC} and J_{SC} of solar cells as a function of the bandgap energy profile. For this model, the influence of deposition conditions such as the relative germane flow rate, the deposition power and substrate temperature on the opto-electrical properties of a-SiGe:H films is first characterized. Opting for the relative germane flow rate to control the bandgap profiling, the experimental results of a large number of solar cells with profiled a-SiGe:H absorber are presented, varying: 1. the absorber thickness, 2. the peak germane flow rate, so minimum bandgap energy, and 3. the introduction of a plateau at the minimum bandgap energy. Using this experimental data and optical simulations, the expedience and effectiveness of the semi-empirical approach is demonstrated.

4.1.1 Introduction

The bandgap energy of the absorber layer of a photovoltaic (PV) device introduces limits for the maximum voltage and current that the device can generate. Bandgap energy profiling of the absorber layer is an interesting technique to stretch these limits. Through profiling a bandgap energy gradient can be introduced along the growth direction of the absorber layer. Bandgap profiling is applied in a variety of materials for PV technologies, such as chalcogenide materials like $Cu_2Sn_{1-x}Ge_xS_3$ [174], $Cu_2ZnSn(S,Se)_4$ [175] and CIGS [176], III-V materials like AlGaS [177], [178] and perovskites [179]–[181]. The bandgap profile can be affected by a number of parameters, such as the difference between the maximum and minimum bandgap energy, the position of the minimum bandgap energy, the width over which this minimum bandgap energy occurs and the total absorber width. Each of these parameters have a complex effect on output characteristics of a PV device, such as the open-circuit voltage (V_{OC}) and the short-circuit current density (J_{SC}). The complexity is further increased when multiple parameters are varied at once.
This complexity makes rigorous physical opto-electrical modeling to predict output characteristics of a PV device with a profiled absorber layer an arbitrary and rather futile endeavour. For that reason, based on a combination of experimental data and optical simulations, we present in this work a unique and expedient semi-empirical approach to simulate the V_{OC} and J_{SC} for stoichiometric absorbers to achieve optimum bandgap profiling.

For the development of the semi-empirical approach hydrogenated amorphous silicon germanium (a-SiGe:H) is used. a-SiGe:H is processed using plasma enhanced chemical vapour deposition (PECVD), which is a mature process that provides excellent control over processing conditions and consequently material growth and produces reliable devices. The opto-electrical properties of a-SiGe:H strongly depend on the germanium (Ge) fraction. By controlling the Ge fraction PV devices with profiled a-SiGe:H absorbers can be processed with a range of V_{OC}'s and J_{SC}'s. Using the semi-empirical relations presented in this work the absorber profiles can be predicted that result in the highest $V_{OC}*J_{SC}$ product. Alternatively, the highest V_{OC} can be found for a given J_{SC} or the highest $V_{OC}*J_{SC}$ can be found for a given minimum bandgap energy.

The latter two are of particular importance for multijunction PV devices, since for optimal operation of a 2-terminal monolithically integrated multijunction device the photo-generated current in each junction should be similar. The transmission and absorption in all individual sub-cells combined with current matched operation conditions have a complex interplay that depends on the multi-junction design. a-SiGe:H for instance has been used in a range of device configurations, such as triple junction amorphous silicon (a-Si:H)/ a-SiGe:H/ nanocrystalline silicon (nc-Si:H) [182], proto-Si/ a-SiGe:H/ nc-Si:H [183] and a-Si:H/ a-SiGe:H/ a-SiGe:H [184] devices, as well as quadruple junction a-Si:H/ a-SiGe:H/ nc-Si:H/ nc-Si:H [173], a-Si:H/ a-Si:H/ a-SiGe:H/ nc-Si:H [55] and a-SiO$_x$:H/ a-SiGe:H/ nc-Si:H/ nc-SiGe:H [185] devices. The combination of available solar spectrum, spectral range of absorption and required photo-generated current of the a-SiGe:H junction is different for each of these configurations. The semi-empirical model presented in this work allows for a quick and expedient optimization of the profiled a-SiGe:H ab-

	P_{RF} (mW · cm^{-2})	p (mbar)	T_{S} (°C)	SiH$_4$ (sccm)	GeH$_4$ (sccm)	H$_2$ (sccm)	CO$_2$ (sccm)	B$_2$H$_6$ (200ppm) (sccm)	PH$_3$ (0.2%) (sccm)
i-a-SiGe:H	27.8	3.6	180	30	0.4-5.3	200	-	-	-
p-SiO$_X$:H	83.3	2.2	180	0.8	-	170	2.3	20	-
p-nc-Si:H	83.3	2.2	180	0.8	-	170	-	20	-
n-SiO$_X$:H	76.4	1.5	180	1	-	120	1.6	-	2
n-nc-Si:H	76.4	1.5	180	1	-	120	-	-	3
n-a-Si:H	27.8	0.6	180	40	-	-	-	-	11

Table 4.1: Conditions used for the various PECVD processed layers
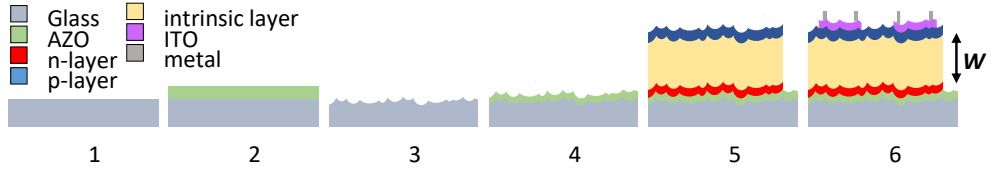
Figure 4.1: Processing flow chart for the n-i-p substrate solar cells presented in this work.

sorber for each of these architectures, without the need to process a large number of multijunction devices.

In the first section we will investigate the influence of deposition conditions on the stoichiometry and opto-electrical properties of a-SiGe:H films. In the second section we will investigate the effect of the Ge fraction, thickness and grading profile in single junction a-SiGe:H solar cells. Finally, based on these experimental results, we introduce a set of unique semi-empirical relations for the J_{SC} and V_{OC} as a function of the peak germane flow rate, absorber thickness and plateau fraction of the profiled a-SiGe:H absorber.

4.1.2 Experimental section

The films and devices presented in this work are processed on Corning Eagle XG glass, using a radiofrequency plasma enhanced chemical vapor deposition cluster tool. The deposition conditions of the a-SiGe:H absorber materials and doped layers are indicated in Table4.1.

Films

All a-SiGe:H films are processed with the conditions reported in Table4.1, unless specifically mentioned otherwise. The thickness, real part of the refractive index and optical bandgap energies were determined through Spectroscopic Ellipsometry (SE). The SE measurements were fitted using a Cody-Lorentz model. The E_{04} was determined by calculating the photon energy at which the absorption coefficient equals 10^4cm^{-1}. Raman measurements were performed using a Renishaw inVia Raman Microscope, using an Argon laser with an operational wavelength of 514.5nm. The Raman plots shown in this work were normalized using the total number of counts in the reported range.

To perform dark conductivity measurements, 500nm Aluminium parallel electrodes were
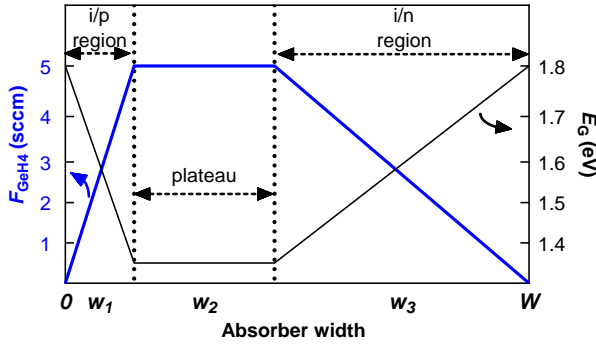
Figure 4.2: Schematic representation of bandgap profiling in an a-SiGe:H absorber layer. The F_{GeH4} and approximate E_{G} are visualized as a function of the position in the absorber layer. In this work the i/p-interface is located at position 0 and the i-n interface is located at position W. W indicates the total absorber width, while w_1, w_2 and w_3 indicate i/p-region width, plateau region width and i/n-region width, respectively. The ratio of the i/p-region width to the i/n-region width is indicated by $r_{\mathrm{w}} = w_1/w_3$. The plateau fraction is defined as $f_{\Delta\mathrm{W}} = w_2/W$. A V-shaped absorber profile occurs when $w_2 = 0$, while a U-shaped profile occurs when $w_2 > 0$.

evaporated onto the processed films. The current conducted between the two electrodes was then measured at a fixed temperature and voltage of 10V. By repeating this measurement at 5°C intervals, from 130°C to 60°C, the dark conductivity at room temperature (σ_{d}) and the activation energy (E_{act}) can be calculated using the Arrhenius equation. Regarding error, the E_{04} is extracted from SE measurements. Based on mean square error analysis, the E_{04} has an error margin of ± 0.001eV. For a number of selected samples 5 points were measured on a single film. Based on these measurements a maximum error margin of $\pm$ 0.01eV can be reported for the E_{04}. Similarly, for the dark conductivity measurements, 4 different sets of contacts were measured on a single film. The resulting dark conductivity values showed an maximum error margin of $\pm$ 20%.

Cells

The solar cells were processed in n-i-p substrate configuration. Solar cell processing consists of a number of steps, as schematically shown in Fig.4.1. The process starts with Corning glass that is cleaned in consecutive ultrasonic baths of acetone and isopropanol. In step 2 a sacrificial 700nm aluminum-doped zinc oxide (AZO) layer is sputtered on the glass. In step 3 the AZO layer is completely etched away in a 1:3:6 HF (40%):HNO$_3$ (69%):H$_2$O solution, resulting in textured glass. This approach was first developed by [186] and [72]. Then, in step 4, again a 700nm AZO layer is sputtered onto the glass, in an Argon atmosphere at 400°C. This AZO layer serves as the back contact. A transparent back contact is used, without a back reflector. This situation with minimal back reflection provides the most straightforward relation between the variations in a-SiGe:H profiling and the generated J_{SC} and V_{OC}. Moreover, it better represents the light absorption performance of the a-SiGe:H cell used in a multijunction configuration. In step 5 the photo-active stack is processed on the AZO layer. A strip of AZO on either end of the substrate is masked during deposition. Finally, in step 6, a 70 nm ITO layer is sputtered on
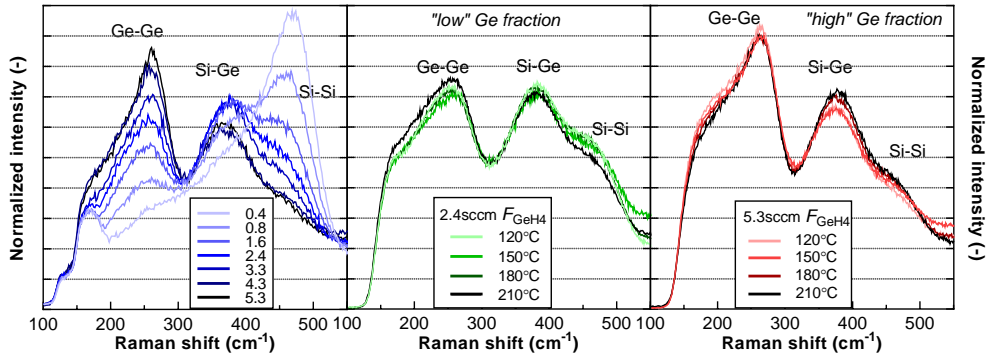
Figure 4.3: Normalized peak intensity as a function of Raman shift for samples processed at 180°C and different F_{GeH4} (left) and different substrate temperatures at 2.4sccm F_{GeH4} (centre) and at 5.3sccm F_{GeH4} (right). Measurements are normalized using the total count in the reported range. Identification of peaks are indicated in the plots. Ge-Ge, Si-Ge and Si-Si indicate the collective Ge-Ge, Si-Ge and Si-Si stretching modes in an amorphous state

top of the photo-active stack, followed by the thermal evaporation of a 500nm Aluminum grid. A mask is used during these two steps to develop 20 separate 16mm^2 cells on each substrate. The photoactive stack consist of a number of layers, which are in processing order: 6nm n-nc-Si:H/ 30nm n-SiO$_X$:H/ 5nm n-a-Si:H/ 4nm i-a-Si:H / 150nm i-a-SiGe:H / 3nm i-nc-Si:H/ 12nm p-SiO$_X$:H / 3nm p-nc-Si:H.

The profiled a-SiGe:H absorbers were obtained by gradually changing the germane gas flow rate F_{GeH4}, while the other deposition conditions are kept constant. This is schematically shown in Fig.4.2, where it can be seen that the F_{GeH4} is initially ramped up in the i/p-region (w_1), then kept constant in the plateau region (w_2) and finally ramped down in the i/n-region (w_3). The total absorber width is indicated by (W). The profiling in the i/p- and i/n-regions was accomplished by dividing the regions in small sections with a fixed thickness, each with a different F_{GeH4}. The F_{GeH4} dependent deposition rate, determined from film measurements, was then used to calculate a deposition time for each separate section.

The J-V measurements of the solar cells were performed using an AM1.5$_G$ solar simulator, illuminated from the p-side, at an illumination of 100 mW $\cdot$ cm^{-2} under a controlled temperature of 25°C. The V_{OC} and fill factor (FF), used to calculate the conversion efficiency of the cells, were extracted from the J-V curves. The J_{SC} was calculated from the external quantum efficiency (EQE) data, by weighing with the AM1.5$_G$ spectrum. The presented solar cell performance data was obtained by measuring 20 cells on each substrate and averaging the 5 best performing ones.

4.1.3 Results and Discussion

Material

With the intent to develop an absorber layer with a profiled bandgap energy, we consider two ways to realize a change in bandgap energy in a-SiGe:H. The first is through varia-
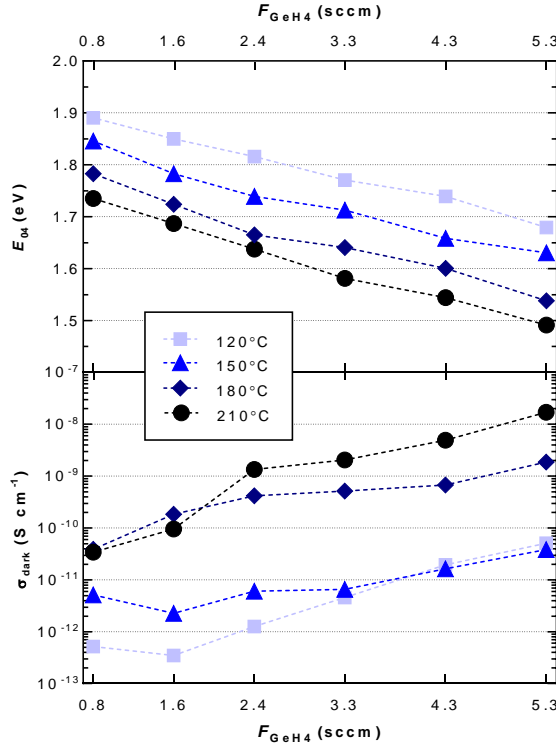
Figure 4.4: Optical bandgap energy (E_{04}) (top) and dark conductivity at room temperature (σ_d) (bottom) as a function of F_{GeH4}. SiH$_4$ and H$_2$ flow rates were kept constant. Samples were processed at 4 different substrate temperatures, as indicated by the legend.

tions in the material stoichiometry, the second is through densification of the amorphous phase. In this section we report how deposition conditions influence the material density and stoichiometry and consequently the opto-electrical properties.

First we discuss the effect of the relative Germane flow rate (F_{GeH4}). A number of samples were processed at a F_{GeH4} ranging from 0.4 to 5.3sccm. For these samples the SiH$_4$ and H$_2$ flows are kept constant at 30sccm and 200sccm. Structural analysis of these samples is presented in Fig.4.3(left). As expected, with an increase of F_{GeH4} the peaks in the 170-280cm^{-1} range, associated with the amorphous germanium (Ge)-Ge LA- (177cm^{-1}), LO- (230cm^{-1}), and TO- (278cm^{-1}) modes, continuously increase with respect to the amorphous silicon (Si)-Si TO-mode at (480cm^{-1}). The peak at 380-390cm^{-1} is a superimposition of peaks related to amorphous silicon LO mode and Si-Ge stretching modes. With increasing Si-Ge bonding, the peak intensity is seen to increase and is shifted downward. Finally, for the 0.8-1.6sccm F_{GeH4} samples the amorphous Si-Si TA mode is visible at 160cm^{-1}, but this peak is "absorbed" in the larger a-Ge:H peaks as the Ge fraction increases.

Fig.4.3 shows that the effect of the substrate temperature during deposition T_S on the Ge-fraction seems to be dissimilar for different F_{GeH4}. For the 2.4sccm Fig.4.3(centre) sample the fraction of Ge-Ge bonds slightly increases with respect to the fraction of Si-Si bonds, with increasing T_S. However, the 5.3sccm F_{GeH4} sample series Fig.4.3(right) shows the opposite effect. The reason for this is unclear. Regardless, the effect of F_{GeH4} on the Ge-fraction is much stronger than that of T_S.

In Fig.4.4 the E_{04} and σ_d of the films are plotted as a function of the F_{GeH4}, for different substrate temperatures. The figure shows that, within the measured range, E_{04} decreases linearly with increasing F_{GeH4}, owing to the change in the Ge-fraction. For all measured substrate temperatures (T_S), the E_{04} decreases with about 0.21-0.24eV when F_{GeH4} is increased from 0.8 to 5.3sccm. Both the decreasing bandgap energy with increasing Ge-fraction [187]–[198] and linear relation [188], [190], are in line with earlier reports.
A decrease of the T_S also leads to an approximately linear increase of E_{04}. For all measured F_{GeH4} the E_{04} decreases about 0.16-0.2eV when temperature is increased from 120°C to 210°C. This occurs despite the fact that the T_S has no clear continuous effect on the Ge-fraction. This indicates that the band gap shift as a function of T_S occurs primarily due to densification of the films, which is supported by the refractive index (n) of the films. At 2.4 sccm, for instance, n at a wavelength of 600nm increases from 3.91 to 4.70 when T_S is increased from 120°C to 210°C. At 5.3sccm n increases from 4.39 to 4.93 in the same range.

Next we evaluate the electrical properties of the films, by considering the dark conductivity at room temperature (σ_d). The σ_d increases strongly with increasing F_{GeH4}. Depending on the T_S, σ_d increases between 1-3 orders of magnitude. Part of this increase can be attributed to the bandgap narrowing. For example, increasing the F_{GeH4} from 0.8sccm to 5.3sccm for the 150°C samples decrease the bandgap energy by about 0.22eV, and the E_{act} by about 0.12eV. The increased σ_d is likely also a consequence of an increased disorder in the material. a-Si:H disordered materials have already a complex nature. The addition of Ge makes it even more complex [195], specifically when the material is changed from a-Si:H to a-Si$_{0.5}$Ge$_{0.5}$:H [189], [199].
The increased disorder can be a result of a few properties of germanium: I. The difference between the average Si-Si and Ge-Ge bond length puts strain on the amorphous network, resulting in disordered material growth. II Ge is heavier than Si. The influence of ion impact of the heavier GeH$_X$ radicals, can results in more ion induced lattice amorphisation. Moreover, the heavier GeH$_X$ radicals have lower mobility on the growing surface for similar temperatures [196]. Both these effects can result in a higher deposition rate and more porous growth. III The preferential bonding of atomic hydrogen to silicon, resulting in a reduced hydrogen content and increased unpassivated dangling bond density with increasing Ge fraction [189], [199], [200]. The increase in disorder results in an increased defect density. Moreover, the dominant defect type in a-Ge:H has energy levels close to the conduction band [201]. This results in a more n-type material, causing an increase of the dark conductivity and strongly reduces the minority carrier lifetimes [187]. The dark conductivity also shows a clear increase with increasing T_S, which is in line with [202]. This is most likely related to a continuous decrease of the hydrogen fraction in the
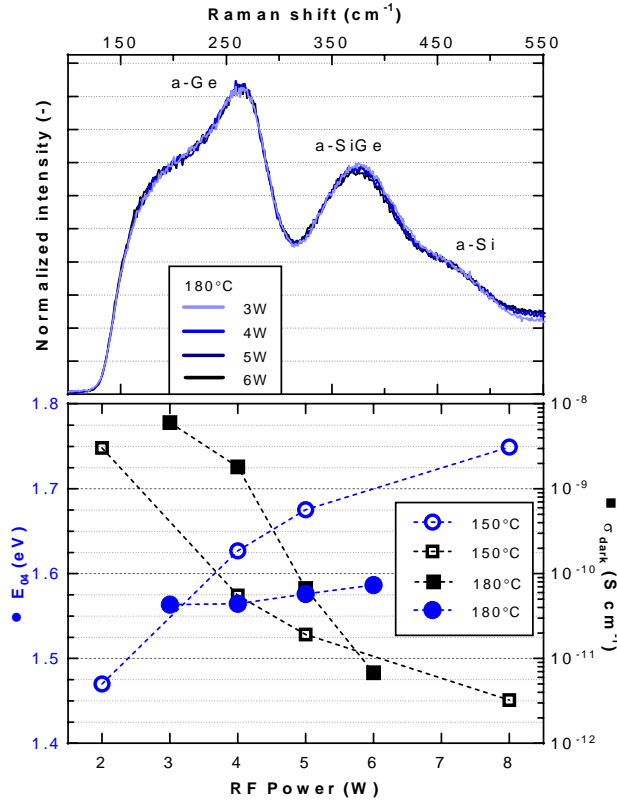
Figure 4.5: Structural and opto-electrical properties of a-SiGe:H films as a function of P_{RF}. Top plot shows normalized intensity as a function Raman shift for different powers, processed at a substrate temperature of 180°C. Bottom plot shows E_{04} (left axis) and σ_{d} (right axis) as a function of P_{RF}, processed at a substrate temperature of 150°C (open symbols) and 180°C (closed symbols). All samples are processed at 4.3sccm F_{GeH4}

material, that reportedly occurs with an increase of T_{S} [195], [202], [203].

Finally, we consider the influence of the RF power $\left(P_{\mathrm{RF}}\right)$. Fig.4.5(top) shows that the P_{RF} does not seem to significantly affect the Ge fraction and Si-Ge bonding in the films. However, the E_{04} increases and σ_{d} decreases continuously within the measured range, as shown in Fig.4.5(bottom). This decrease in σ_{d} is likely the result of a decrease of defective regions in the amorphous network with more energetic ion bombardment. There are 3 possible mechanisms that could accomplish this: I Densification of the already grown a-SiGe:H tissue, due to the impact of heavy Ge ions [32]. II Increased surface diffusion of high energy GeH$_{\mathrm{X}}$ species [199]. III Enhanced generation of atomic hydrogen, resulting in increased preferential surface etching of weakly bonded GeH$_{\mathrm{X}}$ and SiH$_{\mathrm{X}}$ radicals. Regardless of the underlying mechanisms, we consider the relative F_{GeH4} to be the most straightforward way to control the bandgap energy of the a-SiGe:H material, which has a more predictable linear dependence.
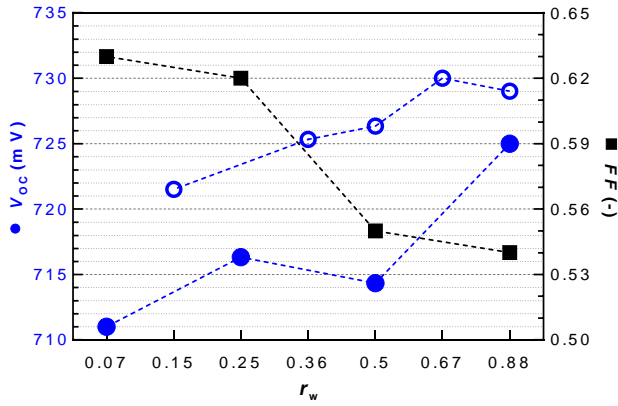
Figure 4.6: The V_{OC} (left axes, blue circles) and FF (right axis, black squares) as a function of r_{w}. $r_{\mathrm{w}} = w_1/w_3$, indicating the position of lowest bandgap energy with respect to the i/p-interface. Open and closed symbols represent two separate series of cells with different front contacts. a-SiGe:H absorbers were processed with a V-shaped bandgap profile ($w_2 = 0$) and constant absorber thickness of $W = 150$nm.

Single junction

After characterization of the a-SiGe:H films, a number of single junction solar cells were processed. These solar cells are initially processed with a V-profile, which means the plateau region width w_2, as indicated in Fig.4.2, is equal to 0. For the development of the semi-empirical relations, we first determined the effect of the position of $F_{\mathrm{GeH4\ peak}}$ on the V_{OC} and FF of the devices. This is accomplished by varying the ratio of the i/p-region width w_1 to the i/n-region width w_3, indicated by $r_{\mathrm{w}} = w_1/w_3$, while keeping the absorber thickness W constant at 150nm. Fig.4.6 demonstrates that the V_{OC} continuously increases with increasing r_{w}, while the FF decreases. This observation is in line with earlier reports [204]–[206].

The V_{OC} increase with increasing r_{w} can be intuitively understood as the position of lowest bandgap is moved away from the doped layer interface. More specifically, the V_{OC} increase can be understood to be a result of a decrease of the defect density near the i/p-interface with an increased i/p-region width, or r_{w}, since the defect density is lowest for low Ge-fractions. Note that in this series of cells $r_{\mathrm{w}} \leq 1$, so the the i/p-region width remained below half the width of the absorber. The increase of FF with decreasing i/p-region width has been reported in earlier work [204] where the FF was shown to increase in U-shaped a-SiGe:H cells independently with both an increase of the i/n-region width and a decrease of the i/p-region width.

We then experimentally determined the effect of three profiling strategies for stoichiometric absorbers on the $J\text{-}V$ characteristics of single junction solar cells. These are the maximum bandgap energy difference in the absorber, the shape of the bandgap profile and the absorber thickness. More specifically, we adjusted I. the peak germane flow rate $F_{\mathrm{GeH4\ peak}}$, so minimum bandgap energy, for V-shape profile and fixed 175nm thickness
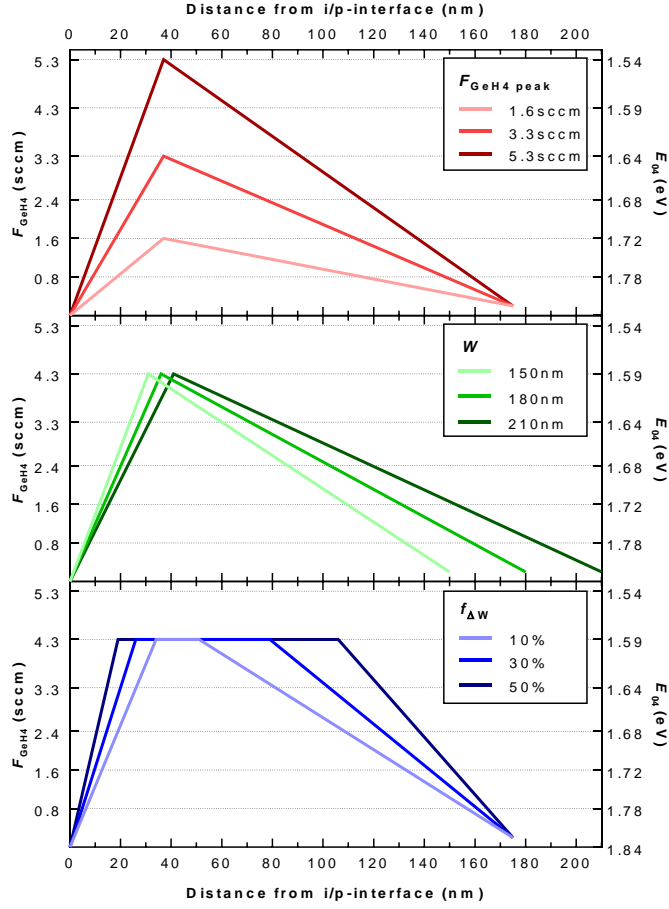
Figure 4.7: Visualization of the different bandgap profiles. Vertical axes show the F_{GeH4} and corresponding E_{04} values, as measured in Section 4.1.3, as a function of distance from the i/p-interface. For each profiling strategy 3 different bandgap profiles are plotted, visualizing the effect of varying $F_{\mathrm{GeH4\,peak}}$ (top, red), W (middle, green) and $f_{\Delta\mathrm{W}}$ (bottom, blue).
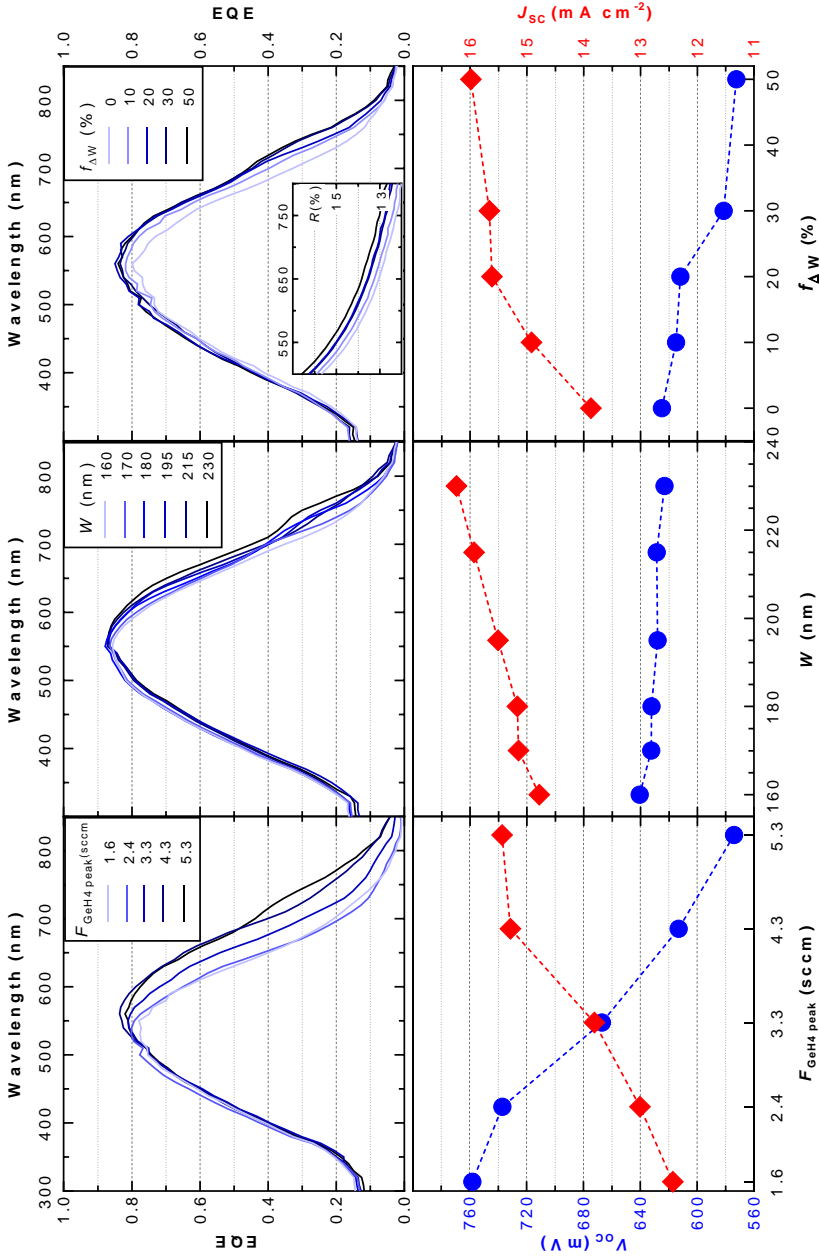
Figure 4.8: Solar cell performance as a function of different bandgap profiling strategies. Top plots show EQE as a function of wavelength, for different values of $F_{\mathrm{GeH4\ peak}}$ (left), W (centre), and $f_{\Delta W}$ (right). In the bottom plots, J_{SC} (bottom, red diamonds) and V_{OC} (bottom, blue circles) are plotted as a function of $F_{\mathrm{GeH4\ peak}}$ (left), W (centre) and $f_{\Delta W}$ (right). When not varied, the cells were processed at a thickness (W) of 175nm, a $F_{\mathrm{GeH4\ peak}}$ of 4.3sccm and a $f_{\Delta W}$ of 0%. Inset in top right plot shows reflectance as a function of wavelength for various plateau fractions.

and r_w (Fig.4.7-top, red), II. The total thickness W of the absorber for a V-shaped profile with a fixed r_w (Fig.4.7-middle, green) and III. Shifting from a V- to a U-shape profile, through the introduction of a plateau at $F_\mathrm{GeH4\ peak}$, with a fixed r_w and W=175nm (Fig.4.7-bottom, blue). The ratio of the plateau region width w_2 with respect to W is indicated by the plateau fraction ($f_\mathrm{\Delta W}$).

The effect of the profiling strategies on the V_OC, J_SC and EQE of the cells are shown in Fig.4.8. For all strategies there is a clear trade-off between the V_OC and J_SC. An increase of $F_\mathrm{GeH4\ peak}$ affects the V_OC and J_SC most drastically of the three profiling strategies. An increase of the $F_\mathrm{GeH4\ peak}$ from 1.6 to 5.3 sccm leads to a V_OC drop of over 180mV, while the J_SC increases by 3 mA $\cdot$ cm^{-2}. This trade-off is in line with earlier reports [173]. The EQE curves show that the onset of absorption in the lower infrared region is shifted to higher wavelengths. This is the result of a decreased E_G over the entire width of the absorber layer with increasing $F_\mathrm{GeH4\ peak}$. This additionally results in an absorption increase over a larger spectral range, which is apparent from around a wavelength of 500nm, since for shorter wavelengths the absorption probability is already near unity.

Considering the effect of thickness, Fig.4.8 shows that an increase from 160 to 230nm leads to the expected absorption increase in the red and near-infrared part of the spectrum. The V_OC is decreased. Interestingly, the penalty in V_OC is less then 20mV, for an increase in J_SC of almost 1.5 mA $\cdot$ cm^{-2}. The V_OC decrease can intuitively understood to be a result of a weakening of the electric field across the absorber width with increasing intrinsic layer thickness. More specifically, the V_OC decrease is a result of increased recombination, since a fraction of generated carriers has to traverse a larger distance across the absorber to either contact, increasing the recombination probability. It should be noted that the V_OC decrease occurs despite the small increase that could be expected from the increase in J_SC, since $V_\mathrm{OC} \sim \ln J_\mathrm{ph}$.

Finally, an increase of the $f_\mathrm{\Delta W}$ has a similar trade-off. An increasing $f_\mathrm{\Delta W}$ leads to a decrease of the average bandgap energy of the absorber, increasing the J_SC. At the same time the V_OC of the absorber is decreased as the average bandgap energy is decreased and both the i/p- and i/n-region width are decreased with increasing plateau fraction. The effect of plateau fraction seems to have two regions however. Increasing $f_\mathrm{\Delta W}$ from 0% to 20% results in an additional 1.7 mA $\cdot$ cm^{-2} at the cost of only 13mV. If $f_\mathrm{\Delta W}$ is increased further, the penalty to V_OC becomes more severe and the gain in J_SC is significantly reduced.

It should be noted that the J_SC gain with plateau increase occurs despite an increase of reflection from the front of the device. This is demonstrated by the inset in the rightmost EQE plot, where the reflectance is plotted as a function of wavelength, for the different $f_\mathrm{\Delta W}$ values. A similar effect was observed with increasing $F_\mathrm{GeH4\ peak}$. The change in reflectance is likely the result of an increased refractive index mismatch. At a wavelength of 650nm the refractive index of a-SiGe:H is increased from 4.26 at 1.6sccm to 4.45 at 5.3sccm, increasing the mismatch with the a-Si:H buffer (4.20) at the i/p-interface. With increasing $f_\mathrm{\Delta W}$ the width over which the mismatch occurs is decreased, thereby increasing reflection.

The findings presented in the this section result in some design rules for optimal device

performance with an profiled stoichiometric absorber. Considering the large trade-off between the V_{OC} and J_{SC} as a function of $F_{\mathrm{GeH4\ peak}}$, this profiling strategy should mainly be used to tune the region in which a-SiGe:H layer is absorbing. When the absorption occurs in the desired spectral range, a higher current density can be realized by plateau introduction and by increasing the W, which both have their respective influence on the V_{OC}.

Semi-empirical simulations

The information presented in the preceding section can be used to find the optimal bandgap profile for a range of device architectures. To that end, using a combination of experimental data and optical simulations, we developed a set of semi-empirical relations that includes the effect of all three profiling strategies. The goal of these relations is not to present a rigorous physical study such as those performed in [205]–[207]. Instead, the emphasis is on the development of an expedient, semi-empirical approach, based on physical relations, to achieve optimum bandgap profiling. This approach has some important applications. For instance, if a specific J_{SC} is required, the combination of W, $F_{\mathrm{GeH4\ peak}}$ and $f_{\Delta W}$ resulting in the highest V_{OC} can be found. Alternatively, for a certain $F_{\mathrm{GeH4\ peak}}$, so spectral range of absorption, the combination of W and $f_{\Delta W}$ can be found that results in the highest V_{OC}-J_{SC} product. It should be noted that the FF is not considered in this study as it is too heavily dependent on series- and shunt-resistance fluctuations that originate from influences outside of the profiled absorber layer.

Parameter input and accuracy.   Several assumptions were made to obtain the semi-empirical relations. In section 4.1.3 the processing conditions of the doped layers were kept constant. Consequently, the impact of the doped layers and the doped layer/absorber-interfaces were not taken into account in the simulations. The continuous nature of the germanium distribution in the absorber was simplified, instead using an average Ge fraction for different parts of the absorber. Moreover, the constants in the equations were fitted to the experimental data presented in this work. Fitting the same set of equations to different experiments would yield different constants. Something relatively simple as introducing a back reflector, for instance, would already significantly change the absolute J_{SC} values. As such, the absolute values of the J_{SC} and V_{OC} are not as important as the approach itself and the trends in these values in response to changes in the bandgap profile.

For the development of the semi-empirical relations it is important that the thickness of the absorber layer is determined accurately. In most works concerning the use of thin films in device applications, a reported thickness is actually an estimated or intended thickness. The estimated layer thickness is often based on the deposition rate of a film processed under the same conditions. There are however a number of factors that can result in a mismatch between the intended and actual thickness of a layer in a device. Such factors include: 1. A difference in substrate texture. The film measurements are performed on flat substrates, whereas the devices are processed on textured substrates. 2. A difference in substrate material. The material phase of the substrate can affect the growth and growth rate of a thin film. 3. Experimental error in the measurements used to determine the deposition rates. 4. For chemical vapour deposition of stoichiometric

profiled absorbers, the influence of the precursor gas residence time on Ge profiling can influence the growth rate. In the case of our a-SiGe:H processing for instance, discrete steps are used in the F_{GeH4} profiling. Deposition rate differences as a function of F_{GeH4} are accounted for in the F_{GeH4} deposition profiles, as detailed in section 4.1.2. However, in reality the precursor gas availability is not discrete, due to the gas-residence time. 5. Atomic hydrogen etching during the next deposition. Some material could be removed by the subsequent processing of layer using the H_2-rich plasma. 6. The assumption of a linear deposition rate as a function of time.

As there are a number of reasons for a potential deviation between the intended and actual absorber thickness, optical simulations of the cells were performed using GENPRO4 [167]. For the optical simulations, in addition to the nk data of the a-SiGe:H films, the nk data of all other layers in the devices was obtained through SE measurements. Moreover, the surface roughness of the textured glass was measured using atomic force microscopy, in order to accurately simulate the texture, and thereby the refractive and diffractive light scattering, at the interfaces between different layers. Using this data, we successfully replicated the EQE curves of all 3 experimental series shown in Fig.4.8, by only changing the relevant variable (i.e., $f_{\Delta W}$, W, or $F_{\text{GeH4 peak}}$). Not only the shape of the EQE's was accurately matched, the deviation between the measured and simulated J_{SC} was only 1.7% on average with a maximum of 3.2%. The thickness values from the optical simulations are therefore reported in this work and used for the following semi-empirical relations.

J_{SC} **relations.** We first consider the J_{SC}. As observed in Fig.4.8, the three profiling strategies have two distinct effects. The $F_{\text{GeH4 peak}}$ changes the spectral range of absorption, while W and $f_{\Delta W}$ affect the fraction of light that is absorbed, according to the Lambert-Beer law. For the low light trapping, single pass conditions considered in this work the generated photo-current can intuitively be expressed as:

$$J_{ph} \approx K_1 \left(1 - \exp[- \int \alpha(\lambda)\mathrm{d}\lambda \; W] \right), \tag{4.1}$$

Here K_1 is a constant that is a function of the absorption onset. In cells with profiled a-SiGe:H absorbers, the absorption coefficient changes along the width of the absorber. Consequently, Eq.4.1 cannot be directly applied in this case. To simplify analysis, the a-SiGe:H absorber is split-up into w_1, w_2, and w_3, as indicated in Fig.4.2. For simplicity, an average absorption coefficient is assumed for each of the regions, indicated by $\alpha_1, \alpha_2, \alpha_3$. The total photo-current generated in the absorber can be calculated by simply adding up the generated photo-currents of each part. Therefore:

$$J_{\text{ph}} \approx K_1 \{1 - \exp(-\alpha_1 w_1 - \alpha_2 w_2 - \alpha_3 w_3)\} \tag{4.2}$$

Now, if we rearrange the terms in Eq.4.2 and keep r_{w}, the ratio of w_1 to w_3, constant, we arrive at:

$$J_{\text{ph}} \approx K_1 \left[1 - \exp \left\{ -\frac{\alpha_1 r_{\text{w}} + \alpha_3}{1 + r_{\text{w}}} W - \left(\alpha_2 - \frac{\alpha_1 r_{\text{w}} + \alpha_3}{1 + r_{\text{w}}} \right) W f_{\Delta W} \right\} \right] \tag{4.3}$$

The terms highlighted in blue can be considered constant for this study. In the ideal case, the J_{ph} is equal to the J_{SC}. However, the experimental results seem to indicate that
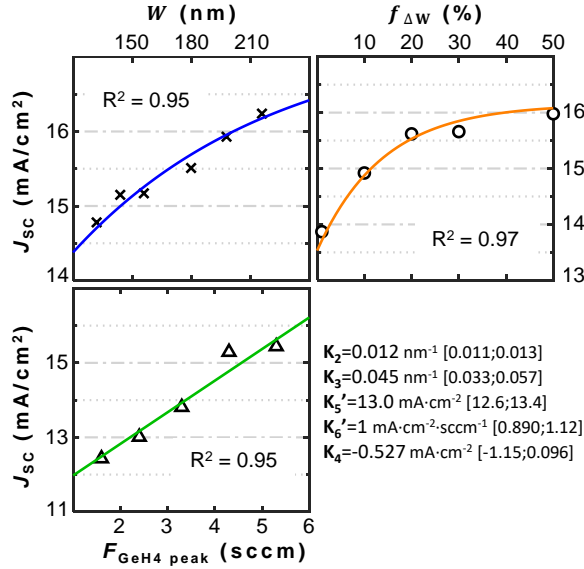
Figure 4.9: The results of fitting the semi-empirical relation described in Eq.**??** to the experimentally obtained J_{SC}'s from the $F_{GeH4\,peak}$ series, the thickness series and the plateau fraction series. R-square values indicate the goodness of fit. The values obtained for the fitting constants are indicated in the figure with their respective 95% confidence intervals between brackets.

the collection efficiency cannot be neglected. In particular, the small overall increase of the EQE's in Fig.4.8 with increasing $f_{\Delta W}$ seems to indicate the presence of a barrier against charge carrier collection. Therefore a separate term must be introduced to account for the collection efficiency of generated charge carriers. If we substitute the first constant term in blue by K_2 and the second term by K_3, the expression for J_{SC} then becomes:

$$J_{SC} \approx K_1\{1 - \exp(-K_2 W - K_3 W \Delta w)\} - K_4 \tag{4.4}$$

Here K_4 is a constant term representing the collection efficiency. Equation 4.4 is intuitively appealing. If the $f_{\Delta W}$ is kept constant, the J_{SC} increases exponentially with W following the Lambert-Beer law. If W is kept constant and the $f_{\Delta W}$ is increased, the J_{SC} increases because a larger fraction of the device has a higher absorption coefficient. If W is increased to infinity, the J_{SC} becomes equal to K_1. K_1 is therefore logically a function of the minimum bandgap energy.

The next step is to express the relation between K_1 and the minimum bandgap energy (E_{min}). For this we consider the number of additional photons available in the AM1.5$_G$ spectrum by a ΔE shift in E_{min}. For cells with an a-SiGe:H absorber, the relevant spectral range over which E_{min} may shift is about 1.3-1.8eV. In this spectral range, the AM1.5$_G$ spectrum can be approximated with relative accuracy as a linear function of $\frac{1}{E_{min}}$. This relation was chosen for its simplicity: it is physically equivalent to assuming that the spectral power density decays linearly with increasing wavelength. This means that the magnitude of increase in K_1 decreases inversely with an increase in E_{min}. In other terms:
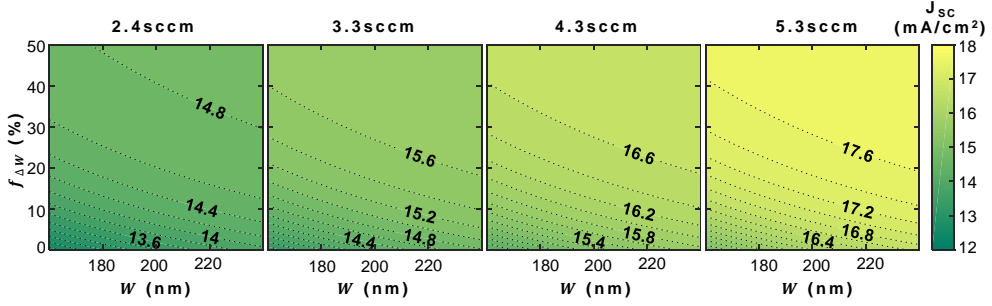
Figure 4.10: The combined effect of varying the $F_{\text{GeH4 peak}}$, thickness and the plateau fraction. Contour plot indicate J_{SC} as a function of plateau fraction and thickness, at $F_{\text{GeH4 peak}}$=2.4 (left), 3.3 (centre,left), 4.3 (centre, right), 5.3 (right). Values are obtained using using Eq.4.8 and the constants presented in Fig.4.9.

$$\frac{dK_1}{dE_{\min}} = K_5 \frac{1}{E_{\min}} + K_6 \tag{4.5}$$

Here K_5 and K_6 are constants. We have established in section 4.1.3 that E_{04} approximately linearly depends on F_{GeH4}. Using this relation, and the experimental data presented in Fig.4.4, the $E_{\min}$ can be expressed as a function of $F_{\text{GeH4 peak}}$, according to:

$$E_{\min} = 1.86 - 0.0773\, F_{\text{GeH4 peak}} \tag{4.6}$$

We would like to point out that while the relation between $F_{\text{GeH4 peak}}$ and $E_{\min}$ is fundamental, the constants presented in Eq.4.6 are specific to our processing chamber. We also recognize that the E_{04} is not equal to the electrical bandgap energy of the material. However, due to the nature of the presented relations, we make the assumption that a change in E_{04} is approximately equal to a change in the electrical bandgap energy. Using Eq.4.6 parameter K_1 can be reduced to a function of the relative $F_{\text{GeH4 peak}}$. Integrating Eq.4.5 and using Eq.4.6, we obtain:

$$K_1 \approx \frac{K_5}{1.86^2 \left(1 - \frac{0.0773\, F_{\text{GeH4 peak}}}{1.86}\right)^2} + \frac{K_6}{1.86 \left(1 - \frac{0.0773\, F_{\text{GeH4 peak}}}{1.86}\right)} + K_7 \tag{4.7}$$

The short-circuit current density can now be expressed entirely in terms of W, $f_{\Delta\text{W}}$, and $F_{\text{GeH4 peak}}$. Collectively, these variables define the bandgap profile. Moreover, since $\frac{0.0773\, F_{\text{GeH4 peak}}}{1.86}$ is always less than 1 for the range of germane flow rates used in this study, the term K_1 can be assumed to have a linear dependence on the $F_{\text{GeH4 peak}}$. Eq.4.7 can therefore be simplified and the complete expression for J_{SC} now becomes:

$$J_{\text{SC}} \approx \left(K_5' + K_6'\, F_{\text{GeH4 peak}}\right)\left\{1 - \exp(-K_2 W - K_3 W f_{\Delta\text{W}})\right\} - K_4 \tag{4.8}$$

There are 5 constants in this equation: K_2, K_3, K_5', K_6' and K_4. These constants were determined with the experimental data presented in Fig. 4.8. The fact that the

experimental data consists of three separate series, in which a single parameter is varied, simplifies the process of curve fitting. For instance, when only thickness is varied, the equation reduces to a relatively simple Lambert-Beer law expression. Similarly, when only the $F_{\text{GeH4 peak}}$ is varied, the exponential term in the equation can be considered constant and the equation assumes a linear form. As such, the task of fitting a complicated equation was performed by simultaneously fitting three relatively simple equations to the experimental series. In this way, the constants K_2, K_3, K_5', K_6' were evaluated for all 3 experimental series while a separate value of K_4 was determined for each experimental series.

The results of the fitting procedure, including the coefficient of determination (R^2) and the values obtained for the different fitting constants, are presented in Fig.4.9. Using these values and Eq.4.8, the contour plots of Fig.4.10 are obtained. As before, the strong effect of the $F_{\text{GeH4 peak}}$ is very clear. For a certain combination of W and $f_{\Delta W}$, the J_{SC} can be increased by several mA $\cdot$ cm^{-2} when $F_{\text{GeH4 peak}}$ is increased. Moreover, the effect of thickness and plateau fraction are insightfully visualized and provide an expedient tool for device design. If for example, given a certain device architecture, the J_{SC} generated by the a-SiGe:H junction should be increased without changing the absorption onset. For instance from 15.4mA $\cdot$ cm^{-2} to 16.4mA $\cdot$ cm^{-2} at a 4.3sccm $F_{\text{GeH4 peak}}$, the plots show that this could be achieved by changing $f_{\Delta W}$ from 10% to 30%, by changing the thickness from 160nm to 240nm, or a combination of the two. Naturally, the best solution depends on the V_{OC} generated as a result of each solution.

V_{OC} relations   Next we focus on the development of a set of semi-empirical relations for the V_{OC} of the cells. Determining the V_{OC} of a p-i-n device with a profiled stoichiometric absorber like a-SiGe:H is a complex process. Nonetheless, a good starting point is the following expression:

$$V_{\text{OC}} \approx \frac{nk_{\text{B}}T}{q}\ln\left(\frac{J_{\text{SC}}}{J_0}\right) = \frac{nk_{\text{B}}T}{q}\{\ln(J_{\text{SC}}) - \ln(J_0)\} \tag{4.9}$$

where n is the ideality factor of the device, k_{B} is the Boltzmann constant, and T is the absolute temperature. J_0 is the saturation current density and is a measure of the recombination in the device. The effect of the absorber profile on J_{SC} has been determined in section 4.1.3. Therefore, in order to study the effect of bandgap profile on V_{OC}, the relation between bandgap profile and J_0 must be described. To this end, we can use the expression from [208]:

$$J_0 = BT^{\gamma}\exp\left(\frac{-E_{\text{G}}}{k_{\text{B}}T}\right) \tag{4.10}$$

Here B is a constant that represents material dependent recombination. γ is another material property which describes the temperature dependence of J_0. In this study we only consider device performance at constant temperature, so this term can be considered constant. Moreover, for profiled absorber layers, the bandgap energy varies along the width of the absorber. We therefore consider an averaged bandgap energy $\overline{E_{\text{G}}}$ instead. Replacing E_{G} by E_{04}, the averaged bandgap energy can be calculated from the average F_{GeH4}. The F_{GeH4} varies linearly in the i/p- and i/n-regions, and remains constant in the plateau region. Using $F_{\text{GeH4 peak}}$ and assuming a minimum F_{GeH4} of 0, the $\overline{E_{04}}$ can be

integrated over the different regions of the absorber. The expression for averaged F_{GeH4} is then:

$$\overline{F_{\text{GeH4}}} = \frac{1}{W} \int_W F_{\text{GeH4}} \mathrm{d}x = \frac{F_{\text{GeH4 peak}}}{2} (1 + f_{\Delta \text{W}}) \tag{4.11}$$

By combining Eq.4.9, Eq.4.10 and Eq.4.11, we obtain:

$$V_{\text{OC}} \approx \frac{nk_{\text{B}}T}{q} \left\{ \ln(J_{\text{SC}}) - \ln(B) - \gamma \ln(T) + \frac{E_{04}}{k_B T} \right\}$$

$$\text{where} \quad \frac{E_{04}}{k_{\text{B}}T} = \frac{1.86}{k_{\text{B}}T} - \frac{0.0773}{2k_{\text{B}}T} F_{\text{GeH4 peak}} (1 + f_{\Delta \text{W}}) \tag{4.12}$$

As to the parameter B, from equation 4.10 it can be seen that larger values of B means more recombination. It is quite challenging to accurately model recombination in thin film solar cells. We have established however, in section 4.1.3 and [201], that the defect density in the amorphous germanium phase is much larger than in the amorphous silicon phase. The defect density and consequently the recombination therefore scale in direct proportion to the germanium fraction. This fraction can be approximately represented by the integral of the F_{GeH4} over W.

The equations up to this point are derived from Eq.4.9. The complex p-i-n junctions with profiled stoichiometric absorbers considered in this study require two additional terms to be added to Eq.4.9. The first term is the results of the i/p-region width. Where Eq.4.9 describes a balance between the J_{SC} and J_0, where an increase in J_0 results in a decrease of both V_{OC} and FF of a device, the experimental results in Fig.4.6 instead shows a trade-off between V_{OC} and FF as a function of the i/p-region width. In fact, from these results we can determine that the V_{OC} varies approximately linearly as a function of the i/p-region width.

The second term is related to the fact that the minimum bandgap energy inside the a-SiGe:H absorber can constrain the extent to which the quasi-Fermi levels can split across the device. In effect, E_{min} places an upper limit on the built-in voltage, which in turn can be considered the upper limit of the V_{OC}. In equation 4.9, E_{min} is only relevant to the extent that it increases the J_{SC}. E_{min} can be expressed as a function of the $F_{\text{GeH4 peak}}$ according to Eq.4.6. If we combine Eq.4.12 with Eq.4.6 and add the two additional terms, we obtain Eq.4.13.

$$V_{\text{OC}} \approx \frac{nk_{\text{B}}T}{q} \ln \left\{ \frac{J_{\text{SC}}}{\kappa_1 W \, F_{\text{GeH4 peak}}(1 + f_{\Delta \text{W}})} \right\} - \frac{0.0773 n}{2q} F_{\text{GeH4 peak}}(1 + f_{\Delta \text{W}}) +$$

$$+ \kappa_2 F_{\text{GeH4 peak}} + \kappa_3 W(1 - f_{\Delta \text{W}}) + \frac{nk_{\text{B}}T}{q} \left\{ \frac{1.86}{k_{\text{B}}T} - \gamma \ln(T) \right\} \tag{4.13}$$

$$V_{\text{OC}} \approx A \ln \left\{ \frac{J_{\text{SC}}}{\kappa_1 W \, F_{\text{GeH4 peak}}(1 + f_{\Delta \text{W}})} \right\} + B \, F_{\text{GeH4 peak}}(1 + f_{\Delta \text{W}}) +$$

$$C \, F_{\text{GeH4 peak}} + D \, W(1 - f_{\Delta \text{W}}) + E \tag{4.14}$$
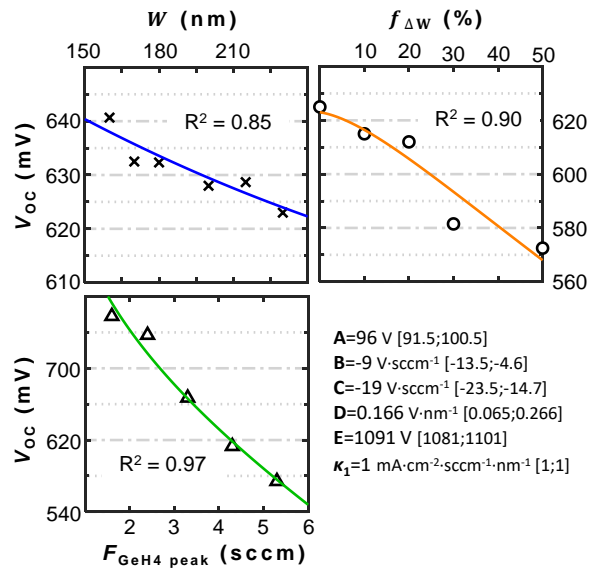
Figure 4.11: The results of fitting the semi-empirical relation described in Eq.4.14 to the experimentally obtained V_{OC}'s from the $F_{GeH4\ peak}$ series, the thickness series and the plateau fraction series. R-square values indicate the goodness of fit. The values obtained for the fitting constants are indicated in the figure with their respective 95% confidence intervals between brackets.

The terms highlighted in blue in Eq.4.13 are considered constant for the purposes for this study. Therefore, the influence of bandgap profile on V_{OC} may be more simply expressed by Eq.4.14, where A, B, C, D, E are constants. Each term represents a different effect on the V_{OC}. The first term consists of two parts, namely the J_{SC} (numerator, violet) and the effect on J_0 as a results of disorder (denominator, red) introduced by germanium. The non-linear dependence of V_{OC} on the amount of disorder in the material, as a function of the relative germanium fraction, is in agreement with the dark conductivity trends presented in Fig.4.4. The second term (orange) describes the effect of the average bandgap energy on J_0. The third term (green) accounts for the limits to which the quasi-Fermi levels can split across the device as a result of the minimum bandgap energy in the profiled absorber. The fourth term (light blue) represents the influence of the i/p-region width. Finally, the constant E is allowed to vary between the different series and accounts for small experimental differences which can occur from one deposition series to the next. κ_1 is introduced to achieve unit matching, and is set to 1. D is determined first by fitting to the data presented Fig.4.6. The remaining 4 constants are then fit to the data from the thickness-, plateau-, and $F_{\mathrm{GeH4\ peak}}$ series presented in Fig.4.8.

The results of the fitting procedure, including the mean square error (R^2) and the values obtained for the different fitting constants, are presented in Fig.4.11. Using these values, and equation Eq.4.14 for V_{OC} that incorporates the effects of all three profiling strategies, the contour plots of Fig.4.12(top) are obtained. The plots show that the effects of varying the $f_{\Delta W}$ and W, to achieve a certain current density change, are not quite similar in the studied ranges. For an 1mA $\cdot$ cm^{-2} increase, the example given in section 4.1.3, the penalty to V_{OC} is about 20mV if only W is changed and slightly higher if only $f_{\Delta W}$ is changed. The relative V_{OC} decrease becomes larger though for large plateau fractions.

Finally, we consider the combined effect on the V_{OC} and J_{SC}, by the three profiling strategies. To this end V_{OC}*J_{SC}, is presented in Fig.4.12(bottom). The combined results provide some interesting insights. 1. The highest V_{OC}*J_{SC} values are obtained for relatively low germanium fractions, which means that the loss in V_{OC} with increasing $F_{\mathrm{GeH4\ peak}}$ outweighs the gain in J_{SC}. Consequently, for optimal device performance, the $F_{\mathrm{GeH4\ peak}}$ should only be increased to change the $E_{\min}$ and thereby the absorption onset. 2. The $f_{\Delta W}$ has an optimum value, which shifts as a function of thickness. This implies that the absolute width of the plateau region can only be increased to some extent, before the loss in V_{OC} outweighs the gain in J_{SC}. If we consider the product of the $f_{\Delta W}$ and W, the optimal width of the plateau region is in the range of 25-40nm. 3. For the ranges considered in this study, the thickness resulting the highest V_{OC}*J_{SC} is a function of the $f_{\Delta W}$. However, if we consider a V-shaped profile (0% $f_{\Delta W}$), relatively thick a-SiGe:H absorbers exceeding 240nm by several tens of nanometers can be realized before the loss in V_{OC} starts to outweigh the gain in J_{SC}.
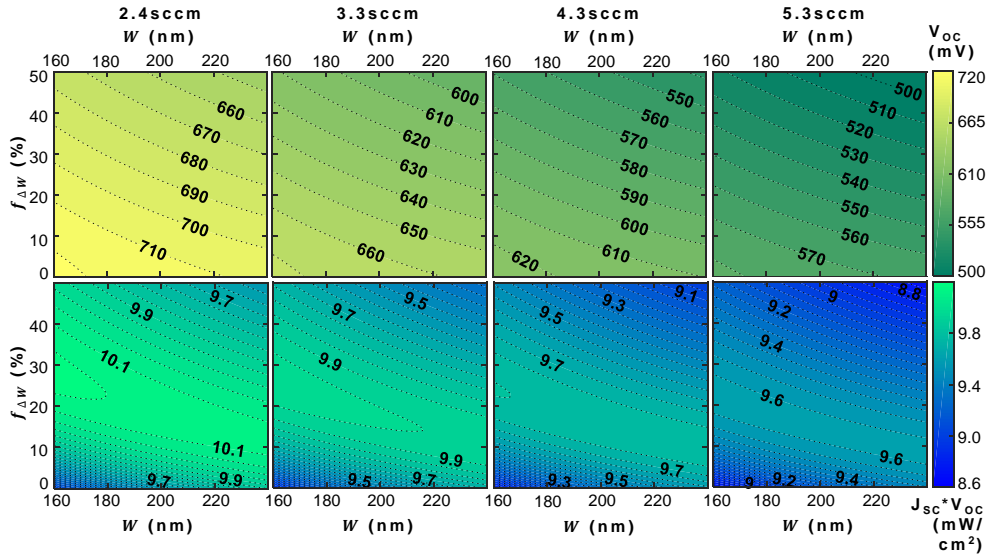
Figure 4.12: The combined effect of varying the $F_{\text{GeH4 peak}}$, W and the $f_{\Delta W}$. Contour plots indicate V_{OC} (top row) and $V_{\text{OC}}*J_{\text{SC}}$ (bottom row) as a function of $f_{\Delta W}$ and thickness, at $F_{\text{GeH4 peak}}$=2.4 (left), 3.3 (centre,left), 4.3 (centre, right), 5.3 (right). V_{OC} values are obtained using using Eq.4.14 and the constants presented in Fig.4.11. $V_{\text{OC}}*J_{\text{SC}}$ is the product of V_{OC} and the J_{SC} results presented in Fig.4.10.

4.1.4 Conclusion

In this work we present an expedient semi-empirical approach for the optimal bandgap profiling of stoichiometric absorbers. Using a-SiGe:H as a model, in three sections we present a unique set of semi-empirical relations that simulate the J_{SC} and V_{OC} of cells as a function of the bandgap energy profile, based on optical simulations and extensive experimental research both on material and device level.

In the first section the influence of deposition conditions such as the relative germane flow rate, the deposition power and temperature on the opto-electrical properties of a-SiGe:H is characterized. An increase of the deposition power and a decrease of the deposition temperature and relative germane flow rate all result in a decrease of the optical bandgap energy and an increase of the dark conductivity. We demonstrate that the most straightforward way to tune the bandgap energy of a-SiGe:H is through the relative germane flow rate, which continuously changes the germanium fraction of the material.

In the second section the experimental results of a large number of solar cells with profiled a-SiGe:H absorbers are presented. We demonstrate the effect of three separate profiling strategies to tune the bandgap profile. These are 1. the absorber thickness, 2. the peak germane flow rate, so minimum bandgap energy, and 3. The introduction of a plateau at the minimum bandgap energy, equivalent to gradually changing the V-shaped profile to a U-shaped profile. These findings results in some design rules for optimal device performance. Considering the large V_{OC} drop with J_{SC} gain for an increase of $F_{\text{GeH4 peak}}$,

this profiling strategy should mainly be used to tune the region in which a-SiGe:H layer is absorbing. Subsequently, a higher current density can be realized by increasing the plateau fraction and by increasing the thickness, which both have their respective penalties on the V_{OC}. Additionally, we demonstrate the trade-off between V_{OC} and FF as a function of i/p-region width, for an otherwise constant bandgap profile.

In the final section a set of unique semi-empirical equations, based on physical relations, for the J_{SC} and V_{OC} as a function of the minimum bandgap energy, thickness and plateau fraction of the profiled absorber is introduced. To demonstrate the effectiveness of this expedient approach, these equations are fitted to the large experimental data set presented in the first two sections. This semi-empirical approach has several important applications. Using these relations the combination of thickness, minimum bandgap energy and plateau fraction resulting in the highest V_{OC}-J_{SC} product can be found. Additionally, for a certain required J_{SC}, or alternatively for a certain spectral range of absorption, the bandgap profile resulting in the highest V_{OC} can be found, which is particularly useful for multijunction applications.
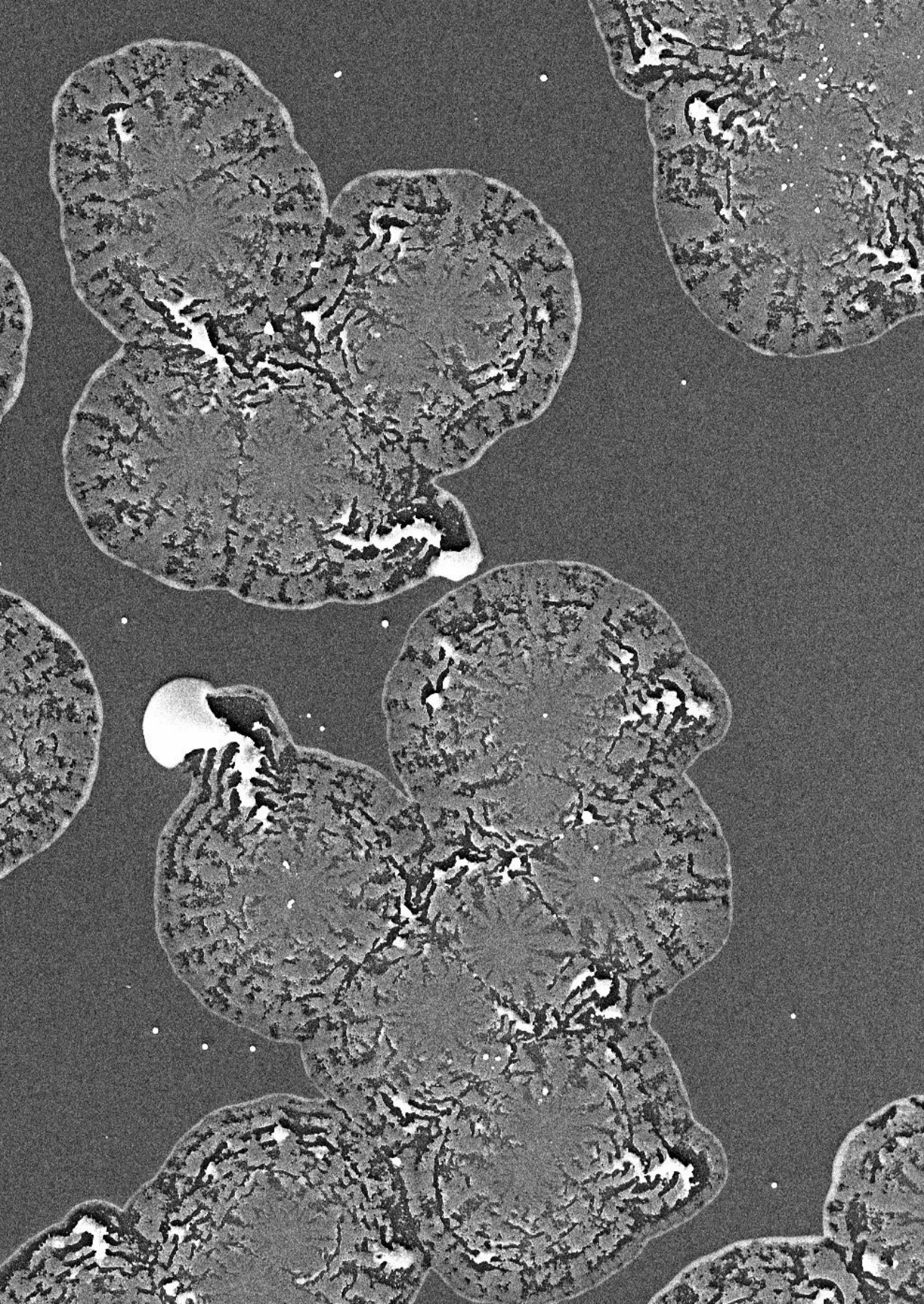
Part II:
Development of a low bandgap Ge(Sn):H alloy

In photovoltaic devices, thermalization and non-absorption losses fundamentally limit the spectral utilization of a semiconductor with a given bandgap energy. By using more than one junction, more than one bandgap energy, spectral utilization can be improved. The PV industry is predominantly silicon based. In order for the PV industry to consider multijuction PV devices for mainstream use, improved spectral utilization should be realized while maintaining low production costs. Moreover, the additional junction should not compromise the excellent stability and longetivity of silicon PV.

Considerable effort is being devoted to develop a high bandgap PV junction to pair with c-Si. These efforts include perovskites [117], III-V's [209], CZTS [210], or a-Si:H/nc-Si:H junctions, such as the one developed in this dissertation (Fig.4.13). Notably, photons with an energy below 1.1eV are utilized in none of these approaches.

In the solar spectrum, over 17 mA $\cdot$ cm^{-2} is available in the 0.5-1.1eV spectral range. A fraction of this current density would be large enough to not be current-limiting in the monolithically integrated 2-terminal multijunction device developed, as well as other silicon based multijunction devices [30], [55], [145], [172], [173], [211]. Adding a junction with a low bandgap energy material could potentially provide a low-cost boost in conversion efficiency. Additionally, in the spirit of providing a framework for a range of optimal multijunction device architectures, a low-bandgap energy material provides additional flexibility.

In the search for a stable, earth-abundant and cheap low-bandgap energy material, germanium is an excellent option. Germanium is silicon's group IV neighbour. Like silicon, germanium can be PECVD processed using a X-H$_4$ precursor and can be expected to have an inherent chemical stability. By alloying germanium with tin, the bandgap energy could be even further reduced. In Part II, therefore, we focus on keyquestion **II**:

Through a fundamental opto-electrical optimization, can an intrinsic low bandgap energy (0.5-0.8eV) plasma enhanced chemical vapour deposition processed hydrogenated germanium or germanium-tin alloy be developed for use in photovoltaic devices?

Part II is divided into three chapters. The optimization of Ge:H and GeSn:H films is covered in Chapters 5 and 7, respectively. In Chapter 6 a reflection on the processing and properties of Ge(Sn):H films in reference to other group IV alloys is covered.

Part II: Development of a low bandgap Ge(Sn):H alloy

Ch 5 Optimization of Ge:H films

Ch 6 Development of GeSn:H films

Ch 7 *Analysis of Ge(Sn):H in reference to other hydrogenated group IV alloys

*(i)-a-Si:H

*(i)-a-SiGe:H

*(i)-nc-Si:H

(n)-c-Si

*(i)-a-Ge(Sn):H
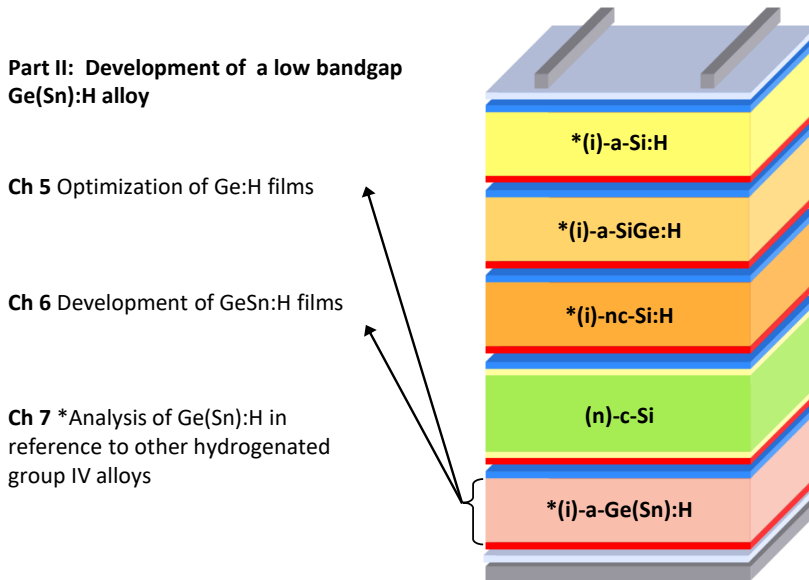
Figure 4.13: Outline Part II

Chapter 5 *Optimization of Ge:H films*

The processing of a group IV, low bandgap, intrinsic and stable material starts with the processing of Ge:H. PECVD processing of Ge:H has not been performed for almost a decade [31]–[33] and has not before been processed in our research group. In **Chapter 5.1**, a full exploration of the processing window in our reactor is therefore performed and the influence of deposition conditions such as temperature, power, pressure, and the relative gas flow rates on a/nc-Ge:H are characterized. Moreover, the relation between processing conditions, post-deposition oxidation and opto-electrical properties of the films is investigated. Learning from this initial exploration, improved PECVD processed a/nc-Ge:H films are presented in **Chapter 5.2**. In this chapter, the temperature induced densification of Ge:H films is discussed.

Chapter 6 *Analysis of Ge(Sn):H in reference to other hydrogenated group IV alloys*

In this dissertation, a range of undoped hydrogenated materials are processed based on group IV elements. A number of SiO:H films are processed in Ch.5.1, Si:H films are processed in Ch.3.1 and SiGe:H films in Ch.4. In Ch.5 Ge:H films are processed and in Ch.7 GeSn:H films. For many of these, both amorphous and nano-crystalline films were processed. Additionally, for the purpose of this chapter, a number of SiC:H, GeC:H and GeO:H films were fabricated. This range of a/nc-Si$_{X\geq0}$Ge$_{Y\geq0}$(O,C,Sn):H films provides insight into the processing, material characteristics and opto-electrical properties of hydrogenated group IV alloys.

In **Chapter 6.1**, vibrational and elemental analysis is performed on all of the aforementioned alloys. The presence and position of peaks in the infrared and Raman spectra of the different alloys are compared, identified and analyzed. Moreover, the evolution of the different spectra is monitored over time for samples stored under different conditions.

In **Chapter 6.2**, evidence of a post-deposition carbisation reaction in Ge:H films is presented using infrared analysis. This carbisation reaction, which most likely involves the electrochemical reduction of CO_2, occurs following the oxidation of Ge:H films. Physical and chemical pathways for the CO_2 reduction reaction in porous Ge:H films are presented.

In **Chapter 6.3**, the opto-electrical properties of all of the aforementioned alloys are presented and compared. Using a large dataset of over 500 films based on eight different alloys of group IV elements, the inherent challenges of processing Ge(Sn):H films are identified and communicated. Finally, potential solutions to these inherent challenges are presented.

Chapter 7 *Development of GeSn:H films*

Following the development of a dense and stable Ge:H film, in this chapter the first ever PECVD processed hydrogenated germanium-tin films are reported. The influence of tetra-methyl-tin concentration, the tin precursor, and other processing conditions on amorphous and nano-crystalline GeSn:H films is characterized. The dominant influence of carbon (from methyl) and tin incorporation on the stability and opto-electrical properties is discussed, as well as the intriguing role the crystalline phase fraction plays in the processing of nc-GeSn:H.

5

The optimization of hydrogenated germanium films

5.1 The impact of processing conditions and post-deposition oxidation on the opto-electrical properties of hydrogenated amorphous and nano-crystalline Germanium films

This section was published in *Journal of Non-Crystalline Solids** [†]

Abstract

Low-cost multijunction photovoltaic devices are the next step in the solar energy revolution. Adding a bottom junction with a low bandgap energy material through plasma enhanced chemical vapor deposition (PECVD) processing could potentially provide a low-cost boost in conversion efficiency. A logical candidate for such a PECVD-processed narrow bandgap material is germanium.

In this work we investigate the growth of PECVD processed hydrogenated amorphous/nano-crystalline germanium (a/nc-Ge:H), by characterizing over 100 samples, processed with a wide range of deposition pressures, powers, temperatures and GeH_4 dilution in hydrogen, using elemental analysis, vibrational analysis and analysis of the opto-electrical properties. We have identified a small processing window in which nc-Ge:H films are processed reproducibly. We also report on the strong correlation between the refractive index of the films and the presence- and extent of post-deposition oxidation. Notably, the oxidation generally increased the photoresponse of the films, as it results in a decrease of room temperature σ_d by 1-3 orders of magnitude. However, oxidation results in an increase of the bandgap energy and therefore impedes the development of a low bandgap material. The lowest E_{04} we report is about 1.1eV, with an E_{Tauc} of 0.9eV and an $\sigma_{\mathrm{ph}}/\sigma_d$ of 3.4.

5.1.1 Introduction

In 2015, for the first time in the history of photovoltaics, the PV module cost was no longer the dominant factor in the cumulative costs of installing a PV system [212]. This makes it even more crucial to increase the efficiency of PV devices, while maintaining low production costs. To that end a lot of effort is being devoted to the development of a high bandgap energy absorber, often to partner with a crystalline silicon (c-Si) solar cell, the industry's workhorse. Examples of these are perovskite/c-Si tandems [117], GaAsP/c-Si tandems [209] and CZTS/c-Si tandems [210]. What these approaches have in common is that photons with an energy below 1.1eV are not utilized. A path to yet higher conversion efficiencies would be the utilization of these low energy photons. For the AM1.5$_G$ solar spectrum, a total of about $9.92 \cdot 10^{20}$ s^{-1} $\cdot$ m^{-2} photons are available in the 0.7eV-1.1eV spectral range, which equals a current density of 15.9 mA $\cdot$ cm^{-2}. For the 0.5-1.1eV spectral range the available current density is equal to 17.1 mA $\cdot$ cm^{-2}. A fraction of this current density would be large enough to not limit the output current of monolithically integrated 2-terminal multijunction devices such as an amorphous silicon/ nano-crystalline silicon/ crystalline silicon hybrid device [30], thin film silicon triple and quadruple junction devices [55], [172], [173], [213] and the commercially available micromorph modules by [145] and [211]. All these devices are processed using plasma enhanced chemical vapor deposition (PECVD). Consequently, adding a bottom junction with a low bandgap energy material through PECVD processing, could potentially provide a low-cost boost in conversion efficiency.

A logical candidate for a PECVD processed low bandgap material is the group IV element germanium. Being larger and heavier than silicon, with its valence shell further removed from the nucleus, germanium forms weaker covalent bonds, resulting in a lower bandgap energy. In the past, attention has been devoted to processing hydrogenated amorphous germanium (a-Ge:H) through RF [214] and DC magnetron sputtering [215], [216] thermal evaporation [217], and glow discharge chemical vapor deposition [31], [218]–[226]. Limited work has been performed however on RF PECVD processing of thin film germanium [32], [227]. In this work we investigate the growth of hydrogenated amorphous germanium and nanocrystalline germanium (nc-Ge:H), by performing a full characterization of the parameter space of processing conditions. To that end, well over 100 a/nc-Ge:H films are processed to characterize the influence of deposition temperature, power, pressure and GeH$_4$ dilution in hydrogen, using elemental analysis, vibrational analysis and analysis of the opto-electrical properties.

5.1.2 Experimental section

Here, all reported films have a thickness of about 80-120nm. The films are simultaneously processed on 4 inch, n-type Cz 500μm thick polished monocrystalline silicon wafers cut in quarters for Fourier Transform Infrared (FTIR) spectroscopy measurements, on 2cm × 1cm quartz substrates for Photothermal Deflection Spectroscopy (PDS) measurements and on 10cm × 2.5cm Corning Eagle XG glass for all other measurements. The films were processed in the Cascade RF-PECVD reactor, which has a circular electrode with a diameter of 160mm and an electrode spacing of 20mm. Cascade is a laminar flow reactor, where germane (GeH$_4$) and molecular hydrogen are used as precursor gasses.
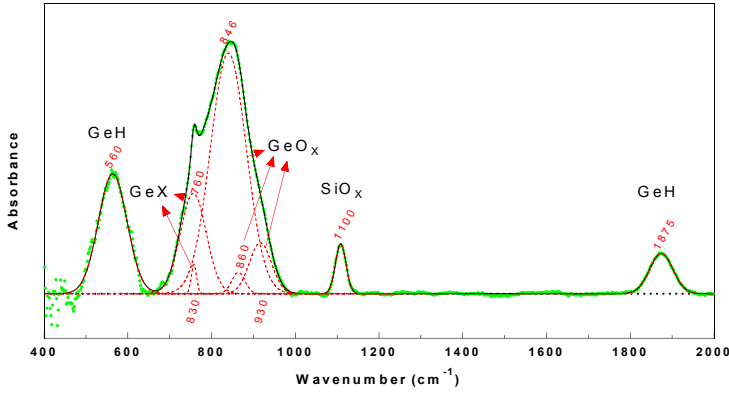
Figure 5.1: Example of the fitted FTIR absorbance spectrum of a typical Ge:H film after oxidation. Green symbols indicate measured data after background correction. Black solid curve indicates fitted spectrum. Red curves indicate the individual fitted Gaussians. The centre wavenumbers of fitted Gaussians are indicated in red below/above the curves. The authors' identification of the fitted peaks are indicated in black above the fitted curves.

FTIR spectra were obtained using a Thermo Fisher Nicolet 5700 spectrometer. The FTIR spectra were fitted using the Fityk freeware [228]. The background was subtracted manually. Fig.5.1. Shows an example of a fitted FTIR spectrum. From the fitted spectra two material characteristics were determined. To facilitate extraction of these characteristics the absorbance spectrum was obtained from the transmission data using:

$$A_{\mathrm{abs}}(\lambda) = \alpha(\lambda)d = \frac{T(\lambda)}{I_0(\lambda)} \tag{5.1}$$

Where A_{abs} is the absorbance, α is the material specific absorption coefficient, d is the thickness, T is the transmittance, and I_0 is the incident intensity. This simplification ignores the exponential decay of light through an absorptive medium. We argue this to be a valid assumption since $\alpha d < 0.01$.

The hydrogen concentration (C_{H}) was determined using the area of the Ge-H absorbance peak at 560cm⁻¹, using the following equation:

$$C_{\mathrm{H}} = \frac{\rho_{\mathrm{Ge}}}{\rho_{\mathrm{H}}} \cdot \left(A \cdot \frac{A_{\mathrm{abs}}(\omega)}{d} ln(10) \cdot \omega^{-1} \right) \tag{5.2}$$

where the part between brackets represents the hydrogen content N_{H}. C_{H} is calculated from N_{H}, through division of the hydrogen content by the atomic density of Hydrogen ρ_{H} over that of germanium ρ_{Ge}. Here ω is the wavenumber, d the thickness of the films, A_{abs} the area of the Gaussian measured around 560cm⁻¹. A is a proportionally constant which is amongst other things a function of the dipole mass, frequency and effective charge [67]. In this work, a value of $1.3 \cdot 10^{19}$cm⁻¹ is used for A, which was determined by [229] and is in the same order as the value of $1.1 \cdot 10^{19}$cm⁻¹ used by [230].

To quantitatively express the GeO$_X$ peak intensity, as measured by FTIR, the absorption
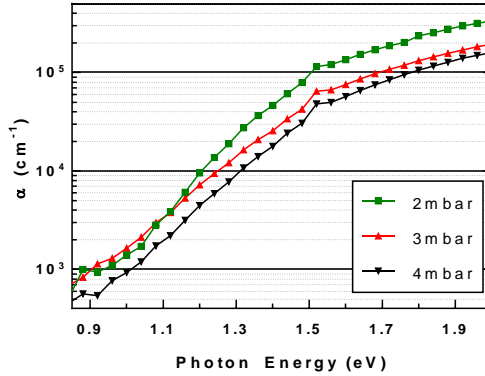
Figure 5.2: Absorption coefficient as a function of photon energy for a few selected a-Ge:H films. Spectra are obtained from Photothermal Deflection Spectroscopy measurements. The films are processed at different pressures and at a $F(H_2)/F(GeH_4)$ of 400, 20W and 200°C.

coefficient of the GeO$_X$ peaks is used. This is done because multiple Gaussians are fitted in the 800-1050cm^{-1} range, with peak centres at roughly 846cm^{-1}, 860cm^{-1}, 930cm^{-1} and 1000cm^{-1}, likely corresponding to different GeO$_X$ bonding configurations. These different bonding configurations make determining a single proportionally constant rather arbitrary. Therefore, the absorption coefficient of the summed GeO$_X$ peaks ($\alpha_{\mathrm{GeO_X}}$) is used in this work as a thickness independent metric for sum of the relative GeO$_X$ peak intensities. This metric is calculated by:

$$\alpha_{\mathrm{GeO_X}} = d^{-1} \cdot ln(10) \cdot \sum \left(A_{\mathrm{abs\ GeO_X}}(\omega) \cdot \omega^{-1} \right) \tag{5.3}$$

It should also be noted that the GeO$_X$ peaks in our samples are often, but not always, accompanied by absorbance peaks with a centre wavenumber of around 760cm^{-1} and 830cm^{-1}. These unidentified peaks are designated Ge$_X$ in Fig.5.1. The peak at 1100cm^{-1} is related to SiO$_X$ bonds present on the surface of the silicon substrates.

The thickness, real part of the refractive index and optical bandgap energies were determined through Spectroscopic Ellipsometry (SE). The SE measurements were fitted using a Cody-Lorentz model. The E_{04} was determined by calculating the photon energy at which the absorption coefficient equals 10^4cm^{-1}. The E_{04} can therefore be considered an effective optical bandgap. The Tauc bandgap energy (E_{Tauc}) is reported at certain points in this work. The E_{Tauc} is closer to the electrical bandgap of the material and is obtained directly from the fitted model. The spectral absorption coefficient, as obtained from Photothermal Deflection Spectroscopy, of a few selected Ge:H films is shown in Fig.5.2, so that the position of E_{04} with respect to the absorption curves can be determined.

Raman measurements were performed using a Renishaw inVia Raman Microscope, using an Argon laser with an operational wavelength of 514.5nm. The spectra are then fitted using Gaussian distributions at Raman shifts of 177 cm^{-1}, 230 cm^{-1} and 278 cm^{-1} for the LA, LO and TO amorphous germanium stretching modes [231], [232] and an additional Gaussian distribution for the crystalline germanium peak at 300cm^{-1} [233], [234]. No

Gaussian was added for the a-Ge TA mode, as its Raman shift of about 80cm^{-1} is located outside of the measured range. The crystallinity (X_C) in this work is defined as:

$$X_C = \frac{I_{\text{c-Ge}}}{I_{\text{c-Ge}} + \gamma \cdot I_{\text{a-Ge}}} \tag{5.4}$$

Where $I_{\text{c-Ge}}$ is the integrated area of the Gaussian corresponding to crystalline germanium and $I_{\text{a-Ge}}$ is the area of the Gaussian of the a-Ge TO mode, the largest of a-Ge stretching modes. γ is a correction factor for the difference in cross section for phonon excitation of c-Ge with respect to a-Ge. In this work a value of 0.85 is used.

For the dark- and photo-conductivity measurements parallel electrodes consisting of 500nm-thick aluminum bars were evaporated onto the films. The dark conductivity at room temperature (σ_d), was determined by measuring the current at a fixed voltage of 10V for at different temperatures, ranging from 130°C to 60°C in 5°C increments, in a dark environment. From this measurement the activation energy (E_{act}) and pre-exponential factor σ_0 of the films was also calculated, using the Arrhenius equation:

$$\sigma_d = \sigma_0 \exp\left(\frac{-E_{\text{act}}}{k_b T}\right) \tag{5.5}$$

The photoconductivity (σ_{ph}) was calculated by measuring the current at a fixed voltage of 10V, using an AM1.5G solar simulator at an illumination of 100mW $\cdot$ cm^{-2} and a controlled temperature of 25°C. Finally, the setup used to obtain the PDS measurements is described in detail elsewhere [235].

5.1.3 Results and Discussion

The processing window

In this work we explore the full processing window for Ge:H thin films in our reactor, for a fixed electrode gap. The extent of this processing window is indicated in Fig.5.3, where the crystallinity of the grown films is plotted as a function of the deposition pressure and power. The plotted powers and pressures represent the extent of the processing window, at a 20mm electrode gap. Dust formation occurred for samples processed at pressure above 5-6mbar and powers above 25-30W, as indicated in Fig.5.3. For conditions below 5W and 0.5-0.8mbar a stable plasma could no longer be ignited. In Fig.5.3 all processed samples are plotted. The size and colors of the symbols indicate the development of a crystalline germanium phase. A crystalline phase was only observed for certain samples processed at 200°C and at the highest F(H$_2$)/F(GeH$_4$) of 400.

At power conditions of 20 W and 25 W and with increasing pressures, the material phase of the Ge:H films changes from amorphous to nanocrystalline at 2-3 mbar and from nanocrystalline back to amorphous at pressures above 4 mbar. This material phase dependence on pressure is qualitatively similar to what has been observed for Si:H alloys processed with a diluted silane plasma [69]. Although power densities in Ref. [69] are higher (due to higher dissociation energies for silane molecules in reference to the germane molecules) the dominant growth mechanisms are the same. At lower pressures the ion
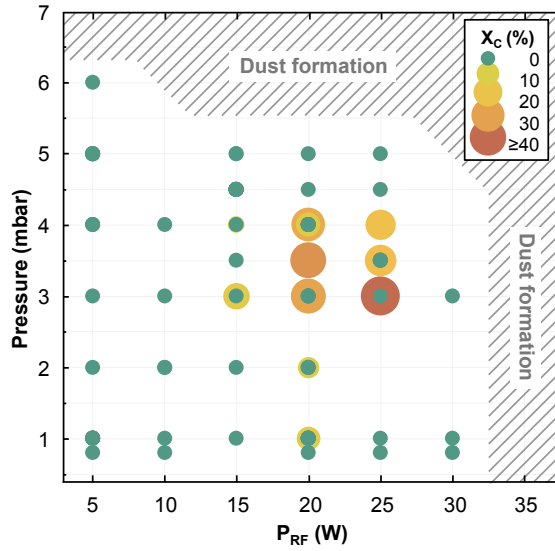
Figure 5.3: Pressure plotted as a function of Power, for all processed Ge:H films. Crystallinity of films indicated by both the icon size and color. The shaded area indicates the boundaries of the processing window, where dust formation occurred.

bombardment energy is too high and ion induced atom bulk displacement [66] results in an amorphous structure. At a critical pressure the number of ion-neutral collisions in the plasma sheath are sufficient to reduce the ion energy below the threshold of ion-bulk displacement. At higher pressures the secondary reaction with atomic hydrogen H in the plasma bulk reduces the total H flux to the growth surface leading to amorphous growth again.

The influence of deposition temperature

Having determined the processing window, we consider the effect of varying a single deposition parameter. We start with the effect of the substrate temperature (T_S) on the measured film characteristics, as presented in Fig.5.4. In the case of silicon, processing conditions close to the amorphous-to-nanocrystalline transition regime produces the best quality amorphous material. For that reason, two sets of conditions are chosen that result in amorphous Ge:H films, but are close to the nc-Ge:H regime.

The first characteristic that grabs the attention is the relatively high deposition rate, of several nanometers per second. This is 1-2 orders of magnitude higher than that of amorphous silicon in a similar PECVD reactor in our lab. The deposition rate slightly increases when T_S is increased, for the samples processed at 4.5mbar/15W. The samples processed at a lower pressure/power ratio do not show the same trend however. For both series, the refractive index $(n_{@600nm})$ steadily increases with temperature, while the hydrogen concentration (C_H) and the optical bandgap energy (E_{04}) steadily decrease. In fact, the E_{04} and $n_{@600nm}$ seem to linearly depend on the C_H, which is in line with earlier reports [219]. The E_{04}, $n_{@600nm}$ and C_H trends indicate the growth of a less porous material

with increasing T_S.

More information is provided by the presence of absorbance peaks in the FTIR spectra in the 850-1050cm^{-1} range. We suspect that the multiple peaks in this broad spectral range originate from GeO$_X$ stretching modes, as a similar absorbance signature has been widely reported in oxygenated silicon samples [69], [79], [196], [227], [236]. With respect to the SiO$_X$ stretching modes, the GeO$_X$ peaks are shifted down by about 100-150cm^{-1}. This is in line with expectations since several Ge-H stretching modes are also shifted down with respect to their silicon counterparts. As to the origin of the GeO$_X$ peaks, a large fraction Ge:H films do not have an GeO$_X$ signature. It is therefore likely that the GeO$_X$ bonds are formed during a post-deposition oxidation process. It should also be noted that the GeO$_X$ peaks in our samples are often, but not always, accompanied by absorbance peaks with a centre frequency of around 760cm^{-1} and 830cm^{-1}. These peaks reportedly appear in environmentally unstable films hydrogenated germanium films [32]. The nature of these peaks are discussed in more detail in section 6.1.

The absorption coefficient of the GeO$_X$ peaks ($\alpha_{\mathrm{GeO_x}}$) has a maximum between a deposition temperature of 250°C and 300°C, which allows for the division into a low and high temperature region. In the lower temperature region, $\alpha_{\mathrm{GeO_x}}$ steadily increases with deposition temperature. The underlying mechanism for this increase is not clear.
In the high temperature region, the GeO$_X$ peak intensity decreases. This is likely related to a reduction in the void density of the material, which reportedly occurs from a certain threshold temperature [222] and is in line with the increasing refractive index. We believe that the underlying cause of the decreasing void density is not the lack of dissociation of larger Ge$_2$H$_6$ and Ge$_3$H$_8$ plasma phase polymers as described elsewhere [220]. Rather, the temperature dependence of void integration is surface diffusion controlled, as has been observed in amorphous silicon [66], [67]. With respect to silicon, germanium is a relatively large and heavy atom, forming weaker chemical bonds. Consequently, germane dissociates more readily than silane [218], [224], [237], leading to a relatively large flux of Ge-radicals to the growing surface. Moreover, the Ge-radicals have much higher reactivity, so lower mobility, on the growing surface [199]. The large growth flux in combination with low surface diffusion result in a porous material with a relatively large void density.
For the Ge-radicals incident on the growing surface to reach and fill a site that would result in a void, a certain activation energy is required. It is likely that, from a certain threshold temperature, small voids are filled. This results in a dense film that is resistant to post-oxidation of the bulk. The surface mobility of Ge-radicals and densification of the Ge:H tissue is further increased with increasing temperature, resulting in the total absence of a GeO$_X$ signature for the higher pressure/power sample at 350°C. The surface-diffusion-controlled void incorporation is a function of the growth flux [66], which explains the different position of the threshold temperature for the 2 series in Fig.5.4.

$\alpha_{\mathrm{GeO_x}}$ has a strong correlation with the electrical properties of the a-Ge:H films. The films with a strong GeO$_X$ signature have a relatively low activation energy (E_{act}) of 50-75meV. It has been reported that oxygen contamination of Ge films creates defects with energy levels close to the conduction band [33], [215]. We have confirmed with Hall measurements that the samples are indeed n-type. In the high temperature regime, where
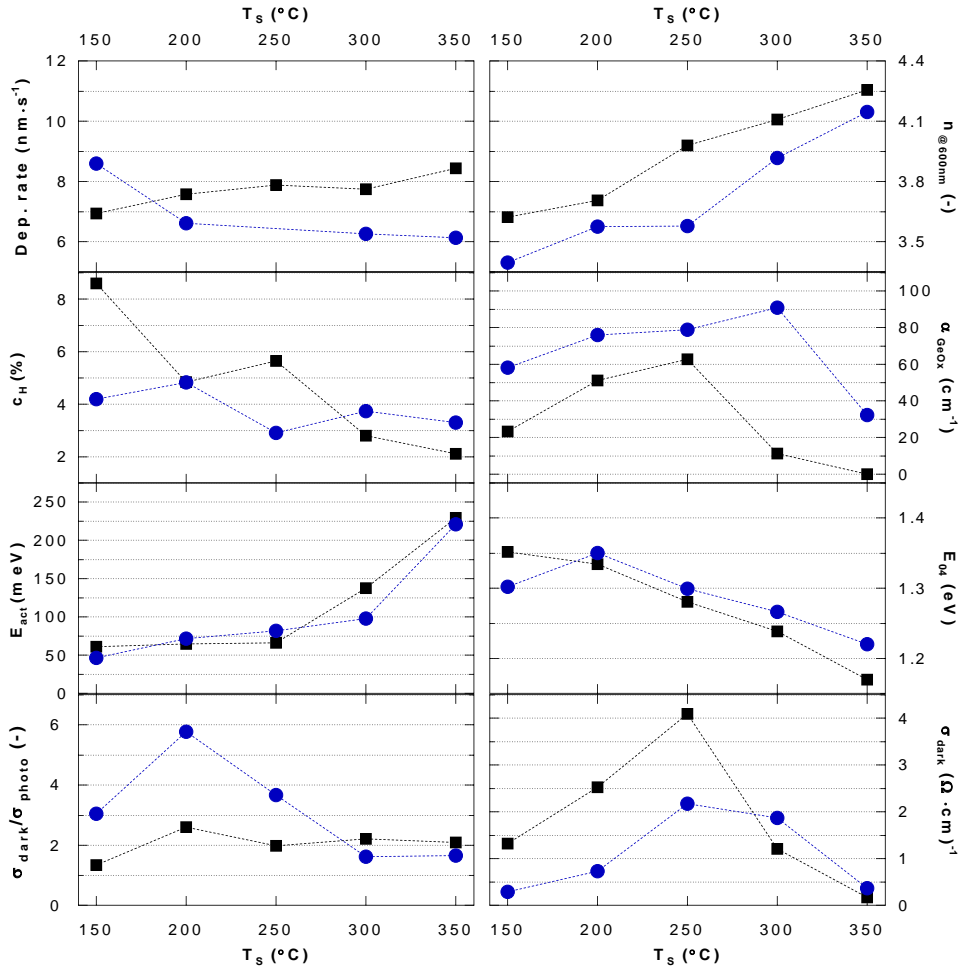
Figure 5.4: The effect of substrate temperature on material properties. The samples represented by the blue circles are processed at 3.5mbar, 25W and a $F(H_2)/F(GeH_4)$ of 400. The dep.rate at 250°C for these samples has been omitted due to an error in recording the deposition time. Samples represented by black squares processed at 4.5mbar, 15W and a $F(H_2)/F(GeH_4)$ of 350.
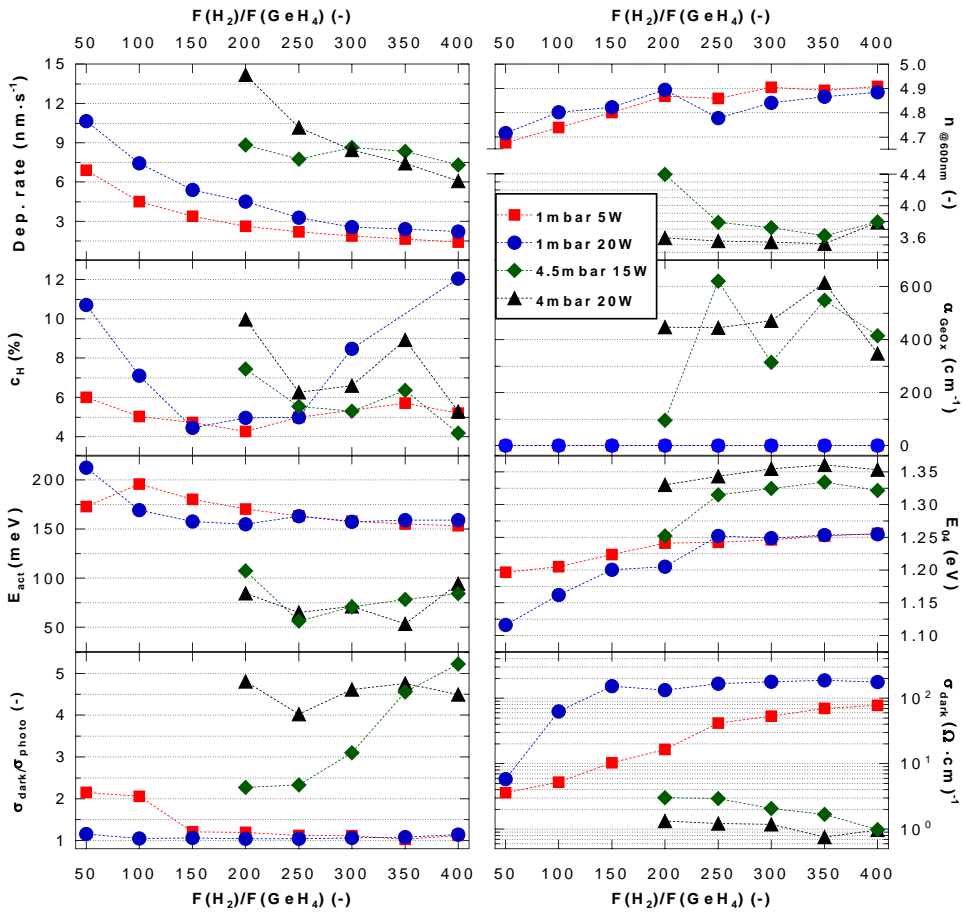
Figure 5.5: Effect of hydrogen dilution on the measured material properties. The films are processed at 200°C. Deposition power and pressure are indicated in the legend.

$\alpha_{\mathrm{GeO_x}}$ is strongly reduced, E_{act} increases to about 250meV. This value is still significantly less than half the bandgap energy, with a Tauc bandgap energy (E_{Tauc}) of around 1eV. In fact, none of the samples processed in this work, a large fraction of which had no FTIR peaks other than those related to Ge-H stretching, had an activation energy of over 280meV. This shows that the dominant defect type present in the amorphous germanium films have energy levels relatively close to the conduction band edge, which corroborates the conclusion of earlier work on glow-discharge a-Ge:H films [223]. The dark conductivity (σ_{d}) evolution as a function of T_{S} shows a strong correlation with the $\alpha_{\mathrm{GeO_x}}$ trend. σ_{d} is highest for the samples with the strongest oxygen contamination. The dark conductivity for all these samples is relatively high, resulting in relatively poor photo/dark conductivity ratios ($\sigma_{\mathrm{ph}}/\sigma_{\mathrm{d}}$) of no more than 5-6. This relatively poor photoresponse of a/nc-Ge:H tissue, with respect to a/nc-Si:H, is in line with earlier reports [238], [239].

In order to process device quality films, an effort should be made to decrease the deposition rate of the Ge:H films. This could potentially be achieved by changing I. the power and pressure at which the samples are processed, or II. by changing the dilution of the GeH$_4$ precursor in H$_2$. We start with an investigation of the latter.

The influence of GeH_4 dilution in H_2

Plotted in Fig.5.5 are 2 curves processed at relatively low pressure and 2 curves processed at relatively high pressure. None of the samples processed in this series had a significant crystalline fraction. The deposition rate for all samples decreases with increasing F(H$_2$)/F(GeH$_4$). This could be a result of increased atomic hydrogen etching with respect to the Ge growth flux. Alternatively, it could be a result of decreased availability of Ge-radicals in the plasma, or a combination of both. A slight deviation from the trends visible in some of the plots between a F(H$_2$)/F(GeH$_4$) of 200 and 250 is likely a result of a change in absolute flow rate around that point, as H$_2$/GeH$_4$ is changed from 200sccm/1sccm to 125sccm/0.5sccm. For the low pressure samples, when F(H$_2$)/F(GeH$_4$) is increased from 50 to about 200-250 the C_{H} and E_{act} decrease, while E_{04}, $n_{\mathrm{@600nm}}$ and σ_{d} increase. $\alpha_{\mathrm{GeO_x}}$ shows that none of the low-pressure samples are oxygen contaminated. As to the underlying mechanism, apparently the complex environment created by increased atomic hydrogen etching, reduced availability of Ge-radicals and less energetic ion bombardment creates conditions in which the void fraction decreases, making the material less porous. Moreover, in this environment C_{H} decreases, resulting in a decreased passivation fraction of Ge dangling bonds, thereby increasing the defect density in the material. As Ge defect states have energy levels closer to the conduction band [223], the material becomes slightly more n-type, resulting in a lower E_{act} and higher σ_{d}. The increased defect density also increases E_{04}, as defect related sub-bandgap absorption is increased.

The high pressure samples largely show the same trends. However, the higher pressure results in more porous films, with lower $n_{\mathrm{@600nm}}$ and a significant GeO$_{\mathrm{X}}$ signature. The presence of oxygen results in a lower E_{act}, higher E_{04}, and higher $\sigma_{\mathrm{ph}}/\sigma_{\mathrm{d}}$. Surprisingly, the presence of oxygen results in much lower σ_{d}, despite the much lower E_{act} of these samples. We'll discuss this in more detail later.
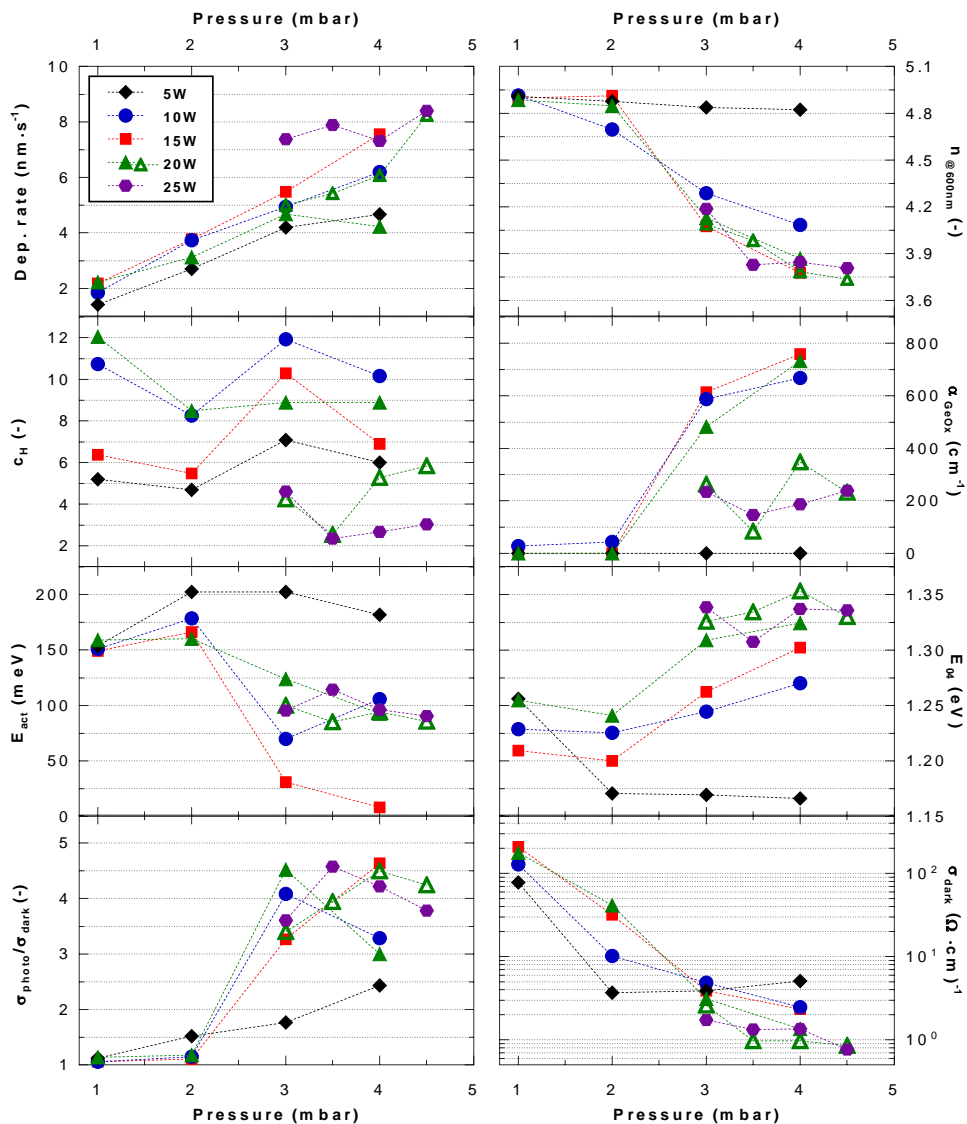
Figure 5.6: Effect of deposition pressure and power on the material properties. The films are processed at 200°C and a $F(H_2)/F(GeH_4)$ of 400.

The influence of deposition pressure and power

In Fig.5.6 the same material characteristics are plotted, for a range of powers, as a function of pressure. For all reported powers, the deposition rate increases as a function of pressure. This results in more porous material growth, as indicated by a decrease of $n_{@600nm}$. It should be noted that the $n_{@600nm}$ of the samples processed at 5W and 10W decrease linearly with increasing pressure, while the $n_{@600nm}$ drops significantly between 2 and 3 mbar. This is because the samples processed at $\leq$15W start to develop a crystalline phase, as shown in Fig.5.3. The crystallinity of the Ge films influence the opto-electrical properties to a certain degree. The maximal σ_{ph}/σ_d, for instance, roughly coincide with the highest crystallinity fractions. However, the material properties are more strongly affected by the degree of oxidation. The σ_d, E_{04} and E_{act} all follow the α_{GeO_X} trend. Notably, E_{04} initially decreases between 1-2 mbar, when α_{GeO_X} is minimal, following the linear relation between $n_{@600nm}$, C_H and E_{04} as was observed in the temperature series.

The effect of post-deposition oxidation

The results from the previous sections seem to indicate that there is a strong correlation between the α_{GeO_X} and the opto-electrical properties. To gain some more insight into the nature of this effect the E_{04} and σ_{ph}/σ_d are plotted as a function of $n_{@600nm}$ in Fig.5.7. The α_{GeO_X} is indicated through the color and size of the icons. From this visual it is clear that with increasing GeO$_X$ signature, both the E_{04} and σ_{ph}/σ_d are increased. In fact, E_{04} values of over 1.25eV and σ_{ph}/σ_d ratios of over 3.4 are only reached for samples with a significant GeO$_X$ signature.

This raises 3 questions: I. Why does oxidation occur for some samples but not others? II. Why does oxidation lead to the increase of the E_{04}? III. And why does oxidation lead to an increase of the σ_{ph}/σ_d?

To gain some more insight into the first two questions, we consider the strong correlation between the E_{04} and $n_{@600nm}$. If the refractive index of the films decreases, the E_{04} is generally higher. Moreover, as the $n_{@600nm}$ decreases, both the fraction of films with $\alpha_{GeO_X} > 0$ and the absolute value of α_{GeO_X} increases. In other words, the films without GeO$_X$ signature are the films with a high refractive index. This means that films with a high density do not undergo post-deposition oxidation.

As to the underlying cause, there are two plausible explanations. First, a decrease of the refractive index indicates an increase of the porosity and consequently the void density in the material. It might be that the defects present at the void surfaces are energetically well aligned with the reaction potential for the reaction resulting in GeO$_X$ formation. This would mean that with increasing void density, the number of potential reaction sites for the GeO$_X$ formation would increase. Increased porosity would thereby consequently lead to an increased α_{GeO_X}. However, in this case you might expect to see a more continuous increase of α_{GeO_X} with decreasing $n_{@600nm}$ than presented in this work. The oxidation as a function of $n_{@600nm}$ is near discrete. The second explanation is therefore more likely. For this we consider that the species responsible for the oxidation cannot diffuse into the material bulk when the Ge:H is too dense. The average Ge-Ge bond length in a relatively dense amorphous germanium film is about 2.46Å [240], while the diameter of an H$_2$O molecule is about 2.75Å [241]. Therefore, in a relatively dense a-Ge:H film, water vapor
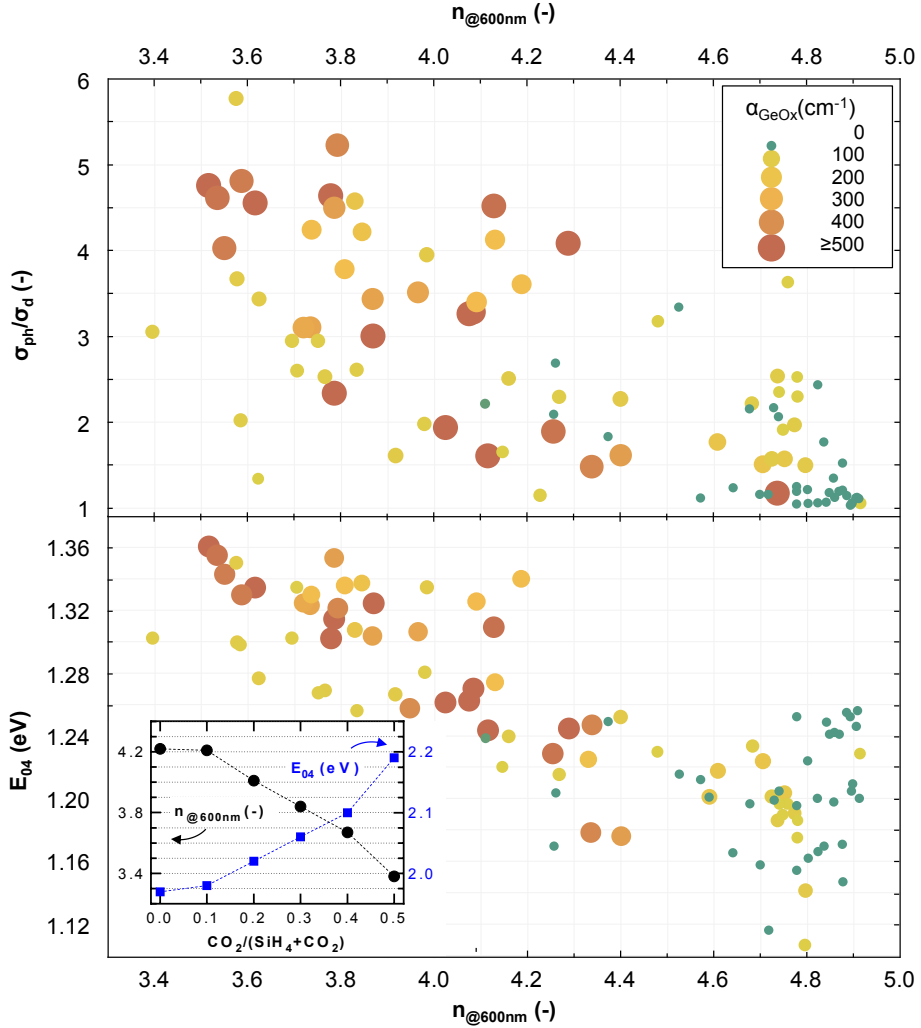
Figure 5.7: $\sigma_{\mathrm{ph}}/\sigma_{\mathrm{d}}$ (Top) and E_{04} (Bottom) plotted as a function of $n_{@600\mathrm{nm}}$. $\alpha_{\mathrm{GeO_X}}$ is indicated by the size and color of the icons. The small green symbols represent films for which no GeO$_X$ signature was detected. Inset shows $n_{@600\mathrm{nm}}$ (black circles) on the left y-axis and E_{04} (blue squares) on the right y-axis of intrinsic silicon oxide films as a function of the relative CO$_2$ flow rate (CO$_2$/(SiH$_4$+ CO$_2$))

from the ambient would not be able to penetrate. If enough Ge atoms are missing from the amorphous lattice, so with a high enough void fraction, water vapor would be able to diffuse into the porous lattice. The in-diffusion of water molecules into the porous bulk would result in the observed oxidation of the a-Ge:H bulk. Besides this microscopic sensitivity to water induced oxidation, a similar effect can occur in the case of macroscopic cracks in the grown films, which is especially likely to occur in films with a relatively high crystalline fraction.

It is hard to make an assumption with respect to the causality of the relation between the level of oxidation and the $n_{@600nm}$. It is likely that more porous films will oxidize more strongly during the limited exposure time. On the other hand, increasing the level of oxidation of an amorphous material also generally results in a lower refractive index. An experiment with intrinsic amorphous silicon oxide, for instance, showed a strong decrease of the $n_{@600nm}$ with increasing CO_2 precursor gas flow rate during PECVD deposition, as shown in the inset in Fig.5.7. This effect, a decrease of $n_{@600nm}$ with increased oxidation, has been reported earlier, both for intrinsic a-SiO$_X$:H [76] and a-GeO$_X$:H [215]. The fact that $n_{@600nm}$ does not scale linearly with α_{GeO_X} suggests that it might be a combination of both porosity facilitated oxidation and oxidation induced porosification.

To answer the third question, related to the origin of the σ_{ph}/σ_d increase with α_{GeO_X}, the E_{act}, pre-exponential factor (σ_0), σ_{ph} and σ_{ph}/σ_d are plotted as a function σ_d in Fig.5.8, on semi-log and log-log axes. The σ_d, σ_0 and E_{act} are related according to Eq. 4. The E_{act} represents the difference between the Fermi level and the nearest band edge, which is the conduction band edge for a-Ge:H. Eq. 4 shows that there are two effects that influence σ_d. **I**. An increase of E_{act} decreases σ_d. **II**. an increase of σ_0 increases σ_d. The first effect is visible for the samples without GeO$_X$ signature (green icons) with an E_{act} in the 150-250meV range (Fig.5.8, left). For these samples, the σ_d clearly decreases with increasing E_{act}. The effect E_{act} has on the σ_d is minor however with respect to the increase of σ_0, that dominates the strong increase in σ_d. For the samples without GeO$_X$ signature and σ_d above 10^{-2}, the increase in σ_{ph} is directly proportional to the increase in σ_d (Fig.5.8, centre right), resulting in a constant σ_{ph}/σ_d of 1.

The largest σ_{ph}/σ_d are achieved for the samples with GeO$_X$ signature. With respect to the samples without oxidation, they have an σ_d that is 1-3 orders of magnitude lower, despite much lower activation energies. The effect of the decreased σ_0 on the σ_d is much stronger than the σ_d increase resulting from the E_{act} decrease. Given that oxidation results in a decrease of σ_0 by 1-5 orders of magnitude, and the highest σ_{ph} are achieved by the un-oxidized samples, the improved σ_{ph}/σ_d ratios are clearly a result of a decreased σ_d rather than an increased σ_{ph}.

The question is why oxidation strongly decreases σ_0 in our Ge:H samples. Conductivity is a function of carrier density and mobility. The proportional increase of the σ_{ph} with the σ_d, in combination with the lack of additional photo-generated charge carriers upon external illumination, seems to indicate that high σ_d of the samples without GeO$_X$ signature is the result of a high carrier density rather than high carrier mobility. The high carrier density is likely the result of a very high defect density. Upon oxidation both σ_0, indicative of the defect density, and E_{act}, indicative of the relative energy level of the dominant defect type(s), are decreased. The decrease of both metrics seems to suggest
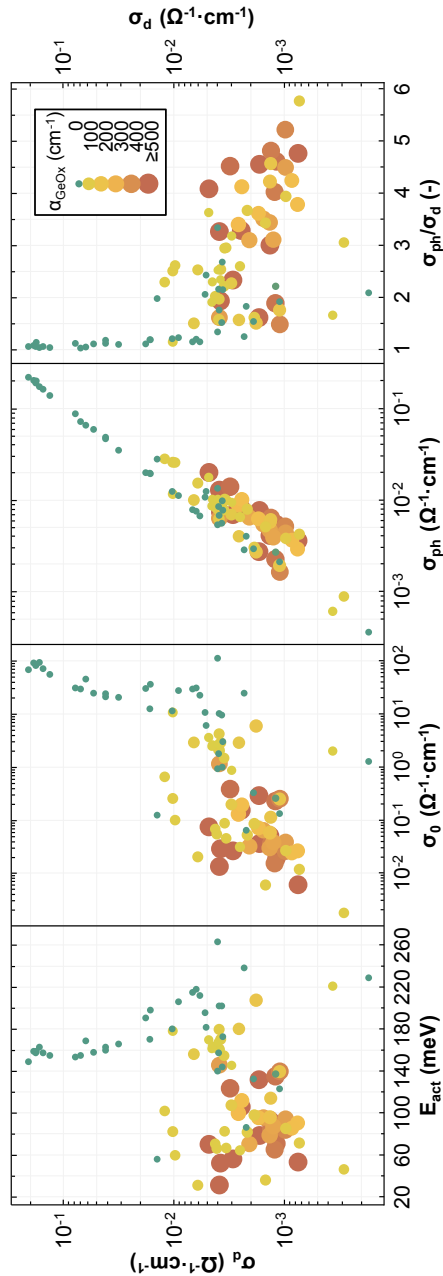
Figure 5.8: The E_{act} (left, semi-log plot), σ_0 (centre left, log-log plot), σ_{ph} (centre right, log-log plot) and σ_{ph}/σ_d (right, semi-log plot) plotted as a function of σ_d. α_{GeO_X} is indicated by the size and color of the icons. The small green symbols represent films for which no GeO$_X$ signature was detected
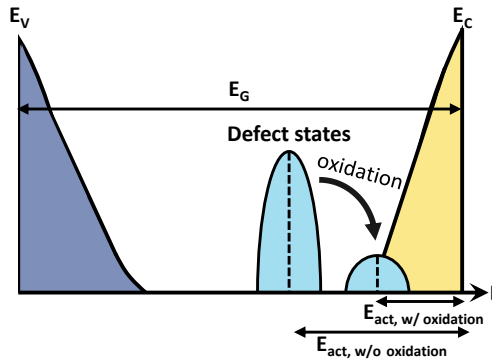
Figure 5.9: Simplified density of states diagram showing the effect of oxidation on the Ge:H material. The blue area (left) and yellow area (right) represent the valence and conduction band tails, respectively. The light blue areas (centre) represent the defect states with and without oxidation. E_V is the valence band edge, E_C the conduction band edge, E_G the mobility gap of the Ge:H material.

that the oxygen passivates the defects in a/nc-Ge:H, decreasing the defect density and consequently the σ_0 and σ_d. A simplified density of states diagram is presented in Fig.5.9 as a visual aid for the effect of oxidation on the defect density and average energy level. The formed GeO$_X$ complexes have an energy level much closer to the conduction band, thereby shifting the Fermi level closer to the band edge and decreasing the E_{act}. In other words, a large density of defects with energy levels around 150-250meV from the conduction band edge is replaced by a much smaller defect density, closer the band edge.

5.1.4 Conclusion

In this work we investigate the influence of deposition temperature, power, pressure and the dilution of GeH$_4$ in H$_2$ on the material properties of well over a 100 PECVD processed a/nc-Ge:H films. We identified the processing window for Ge:H films in our reactor, with an electrode gap of 20mm. This window ranges from about 1-5mbar and 5-30W. nc-Ge:H films, with a crystallinity up to 54%, were obtained in the 15-25W range at 3-4mbar, 200°C, under the highest hydrogen dilution of F(H$_2$)/F(GeH$_4$)=400.

We found that there is a strong correlation between the refractive index and the presence of a GeO$_X$ signature. We speculate that a high refractive index indicates a dense a-Ge:H network with a low void density, which prevents the in-diffusion of water from the ambient. This water vapour is responsible for the post-deposition oxidation of the Ge:H bulk. The oxidation has a very strong effect on the electrical properties of the films, as E_{act} is decreased, while σ_0 is strongly reduced. The decrease of σ_0 outweighs the increase of E_{act}, resulting in a decrease of σ_d by 1-3 orders of magnitude. We believe the oxygen has a passivating effect, decreasing the Ge-dangling bond related defect density in the bulk. The highest σ_{ph}/σ_d ratios of 5-6 are realized by Ge:H films with a GeO$_X$ signature.

We've observed that the oxidation results in an increase of E_{04}. It therefore impedes the development of a low bandgap material. The lowest E_{04} we report is about 1.1eV, with an E_{Tauc} of 0.9eV and an σ_{ph}/σ_d of 3.4

5.2 Improved PECVD processed hydrogenated germanium films through temperature induced densification

This section was published in *Materials Science in Semiconductor Processing*[‡]

Abstract

Amorphous and nano-crystalline germanium is of potential interest for a wide range of electronic, optical, opto-electronic and photovoltaic applications. In this work the influence of deposition temperature on hydrogenated germanium (Ge:H) films was characterized, using over 200 Ge:H and over 70 SiGe:H films. The demonstrated temperature-induced densification of Ge:H films resulted in more stable films with a lower bandgap energy and dark conductivity and higher activation energy.

	P_{RF} (mW · cm^{-2})	p (mbar)	T_S (°C)	e_d (mm)	SiH$_4$ (sccm)	GeH$_4$ (sccm)	H$_2$ (sccm)	Thickness (nm)
Ge:H *Fig.5.11*	12.4-49.7	4-5	200-275	10	-	0.5	200	70-200
Ge:H *Fig.5.12*	12.4-248.7	0.5-6	200-350	10-20	-	0.5-2	100-200	40-350
SiGe:H *Fig.5.13*	13.9-56	2-6	150-210	10	30	0.4-5.3	150-200	40-500

Table 5.1: deposition conditions and thickness range of (Si)Ge:H films presented in this work

5.2.1 Introduction

Amorphous (a-) and nano-crystalline (nc-) germanium (Ge) is of potential interest for a wide range of applications. The use of a/nc-Ge has been investigated for thin film transistors [242] and novel complementary metal-oxide semiconductor devices [243]. It has been considered a promising material for sensitive detectors for near infrared light [244], gamma radiation [245] and infrared sensing in microbolometers [33]. More generally, it is of potential use as a low dielectric constant material for the micro-electronics industry [246]. Additionally, it has been investigated as a low bandgap material for photovoltaic applications [31], [32], [239].

The processing of device quality germanium is not without challenges. In earlier work, a full exploration of the processing window for plasma enhanced chemical vapour deposition (PECVD) processed hydrogenated (:H) Ge films at an electrode gap of 20mm was performed [201]. It was observed that the occurrence and level of post-deposition oxidation had a dominant influence on the opto-electrical properties of the films. Consequently, the performed exploration of individual deposition conditions, such as the RF power, reactor pressure, substrate temperature and the dilution of the germane (GeH$_4$) gas flow rate in molecular hydrogen (H$_2$) largely reflected on the relation between the deposition conditions on degree post-deposition oxidation. In an effort to produce films that are more resistant again post-deposition oxidation, a processing window with a reduced electrode gap of 10mm is explored. A reduced electrode gap could reportedly yield an improvement of film quality [32]. A reduced electrode gap allows for the processing at higher pressure. This results in reduced ion bombardment energy of the growth surface due to more ion-neutral collisions in the plasma sheet. This processing regime is sometimes referred to as the high pressure depletion regime [69].

5.2.2 Experimental section

The Si(Ge):H films are PECVD processed on c-Si substrates for optical and vibrational analysis as well as on glass substrates for electrical analysis. The PECVD processing conditions and film thickness ranges are listed in table 5.1. A list with the full set of deposition conditions used for each individual film can be found in the supplementary information. The Ge:H and SiGe:H films are processed in two separate radiofrequency PECVD reactors. More information about the specific reactor design used for processing Ge:H films can be found in [201] and for SiGe:H processing can be found in [156].

The methods for obtaining the activation energy (E_{act}), the dark conductivity at room temperature σ_d and photoconductivity σ_{ph} are similar to those used in earlier work [201]. Spectroscopic Ellipsometry (SE) was used to determine the refractive index at a wave-
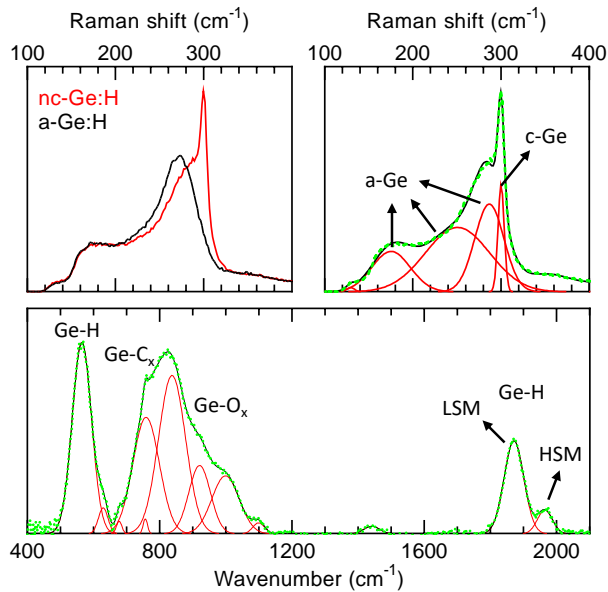
Figure 5.10: Typical Raman and FTIR spectra of Ge:H films post-oxidation. On the top left typical Raman spectra of an amorphous and nano-crystalline Ge:H film is shown. For the Raman spectrum (top right) and FTIR spectrum (bottom) the individual fitted Gaussian's (red), sum of the fitted Gaussian's (black) and measurements after background subtraction (green, dashed) are shown. The amorphous and crystalline Ge vibrational modes are indicated in the Raman plot, while the Ge-H wagging mode at $560 cm^{-1}$, Ge-H low stretching mode (LSM) and high stretching mode (HSM) and the broad collection of Ge-C_x and Ge-O_x vibrations in the 650-$1100 cm^{-1}$ range are indicated in the FTIR plot.

length of 600nm ($n_{@600nm}$), as well as the thickness and optical bandgap energy E_{04}, which is the energy at which the absorption coefficient of the film equals 10^4cm^{-1}. The SE measurements were fitted using a Cody-Lorentz model. Typical examples of the imaginary pseudo dielectric function of stable a-Ge:H, porous a-Ge:H and and nc-Ge:H films resulting from these fits, as well as selected fitting parameters, can be found in the supplementary information.

A Thermo Fisher Nicolet 5700 spectrometer and an inVia confocal Raman microscope were used to obtain the Fourier-transform infrared spectroscopy (FTIR) spectra and Raman spectra. The spectra were fitted using the Fityk freeware [228]. The background was subtracted manually. Examples of typical Raman and FTIR spectra, including the identification of peaks relevant for the characterisation performed in this work, are presented in Fig.7.1. The Raman spectroscopy measurements were used to determine the crystallinity. The method for determining crystallinity is reported elsewhere [201].

Two material characteristics were determined from the fitted FTIR spectra. The first metric is related to the Ge-C_x and Ge-O_x vibrations that have peaks in the 600-1100cm^{-1} wavenumber range. These vibrations are the results of post-deposition oxidation and carbisation of the films, and are therefore indicative of a chemically unstable material. To quantitatively express the cumulative peak intensity in this range, the absorption coefficient of the sum of the Ge-O and Ge-C vibrational peaks (α_{tot}) is used. This approach to obtain a thickness independent metric for the chemical stability of the Ge:H films is similar to the one used in [201], except that the Ge-C vibrations at 760cm^{-1} and 830cm^{-1} are now added to the summation as well. Consequently, α_{tot} is determined by:

$$\alpha_{tot} = d^{-1} \cdot ln(10) \cdot \sum \left(A_{\text{abs Ge-O+Ge-C}}(\omega) \cdot \omega^{-1} \right) \tag{5.6}$$

The second metric obtained from the FTIR spectra is related to the area under the Gaussian distributions fitted to the Ge-H peak at 1980cm^{-1}, referred to as the high stretching mode (HSM), and to the area of the Ge-H peak at 1875cm^{-1}, referred to as the low stretching mode (LSM). The ratio of HSM area to the LSM is referred to as the microstructural parameter R.

5.2.3 Results and Discussion

Effect of T_S at a small electrode gap

In an effort to produce stable, intrinsic films with a low bandgap energy and good electrical properties, deposition conditions were varied at the smallest possible electrode gap, for our reactor, of 10mm. These conditions include the RF power (P_{RF}), pressure (p) and germane flow rate F_{GeH4} at a constant hydrogen flow rate (F_{H2}) of 200sccm. The explored ranges are presented in Table 5.1. The resulting combinations of depositions conditions were processed both at a substrate temperature (T_S) of 200°C and 275°C. Additionally, two sets of conditions were chosen, one resulting in the growth of an a-Ge:H film, the other in the growth of an nc-Ge:H film. These films were then exposed to a post-deposition hydrogen plasma treatment, for which power and duration were varied. With all these variations, a single dominant parameter becomes apparent, namely the influence
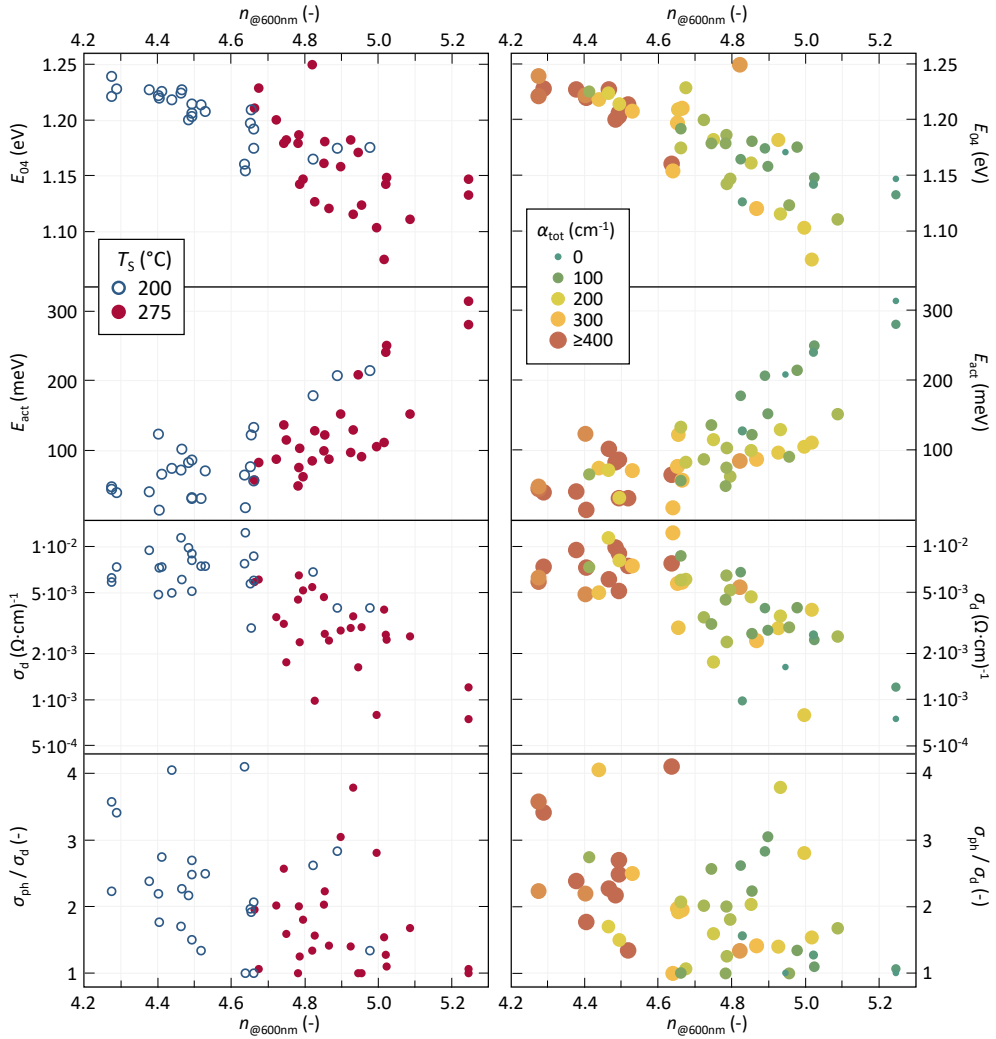
Figure 5.11: Selected opto-electrical properties as a function of the $n_{@600\text{nm}}$ of the initial sample set processed at an e_{d} of 10mm. In the left column icon colour and fill indicate T_{S}. In the right column icon colour and size indicate α_{tot} and small green symbols represent films for which no significant Ge-O or Ge-C signature was detected. The full range of deposition conditions of samples in this figure can be found in Table 5.1. No significant thickness dependence is evident in the 70-200nm thickness ranges presented in this figure. An additional plot indicating the thickness of each sample is presented in the supplementary information.

of T_S on the processed films. This effect is visualized in Fig.5.11, where the optical bandgap energy E_{04}, E_{act}, σ_d and the ratio of the photo-conductivity to σ_d ($\sigma_{\mathrm{ph}}/\sigma_d$) are plotted as a function of $n_{@600\mathrm{nm}}$. These metrics are plotted twice, with the icon fill and colour indicating the T_S in the left column and α_{tot}, the selected metric for instability, in the right column.

The figure shows that the full set of conditions results in the growth of Ge:H films with a $n_{@600\mathrm{nm}}$ ranging from about 4.2 to over 5.2. However, for this particular processing window, none of the films processed at a temperature of 200°C has an $n_{@600\mathrm{nm}}$ over 5 and none of the film processed at 275°C has an $n_{@600\mathrm{nm}}$ below 4.65. This means that irrespective of deposition power, pressure, dilution and post-deposition treatment, the films with the highest refractive index are processed at a temperature of 275°C. If we consider the opto-electrical properties as a function of $n_{@600\mathrm{nm}}$, a direct relation is apparent. The refractive index can be considered a metric for material density, with higher $n_{@600\mathrm{nm}}$ indicating higher material density. This relationship as has been established in a wide range of materials including inorganic solids [247], SiO_2 [248], [249] and other thin evaporated glass films [250] and most importantly in hydrogenated silicon [65], [251]. With increased material density a decrease of E_{04} and increase of the E_{act} can be observed. The E_{act} indicates the difference between the Fermi energy level and the nearest band edge, which is the conduction band edge for these Ge:H films. The decrease of E_{04} in combination with the increase in E_{act} therefore indicates that the E_{act} is shifted towards that of an intrinsic film, for which $E_{\mathrm{act}}=0.5E_G$.

Additionally, it should be noted that the $n_{@600\mathrm{nm}}$ values achieved at the reduced electrode gap are considerably higher than the maximum 4.9 achieved in our earlier work [159], where T_S of 300°C and up were also used. This suggest that the reduced electrode gap allows for the processing of denser materials. In tandem with the increased density, the E_{04} of 1.07eV and E_{act} of over 300meV are also improvements over the values achieved at the larger electrode gap.

Considering the conductivity of the films, σ_d is also lowest for the samples with a high $n_{@600\mathrm{nm}}$, processed at elevated T_S. It should be mentioned that the lowest σ_d values presented in this work are 1-5 orders of magnitude lower than those reported for all other known a/nc-Ge:H films, processed by chemical vapour deposition techniques, to best of the authors knowledge [33], [218], [219], [239], [252], [253]. Remarkably, the increased intrinsicity and decreased σ_d of the material do not result in improved photoresponse $\sigma_{\mathrm{ph}}/\sigma_d$. If we consider the stability of the Ge:H films, with small, green icons representing a stable film in the right column in Fig.5.11, its clear that denser films are generally more stable. Moreover, opto-electrical properties such as the E_{04}, E_{act} and σ_d show a near linear relation to the level of oxidation and carbisation, as previously reported [201].

The effect of T_S on Ge:H and SiGe:H

For the parameter space detailed Table 5.1, temperature emerges as a dominant parameter for the deposition of dense Ge:H films. This observation raises two questions: 1. is this observation limited to this particular parameter space and 2. is this observation also valid for Ge:H alloys, such as SiGe:H. We'll first consider whether the dominant influence of T_S holds when the processing range of the used deposition parameters is widened. In Fig.5.12, the E_{04} of over 250 Ge:H films processed in our reactor are plotted as a function
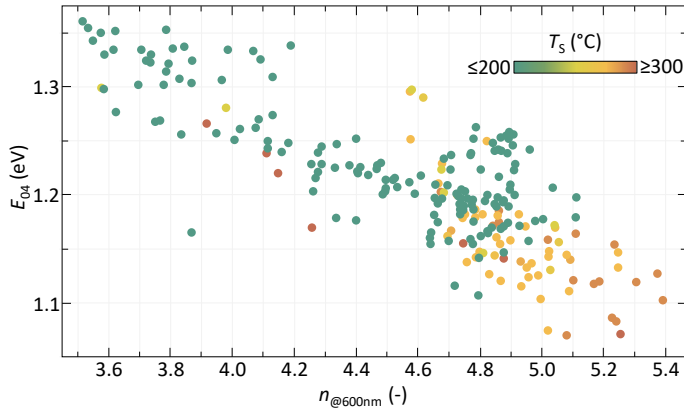
Figure 5.12: The E_{04} plotted as a function of $n_{@600nm}$ for all Ge:H samples processed in our reactor. T_S is indicated by the color of the icons. The full range of deposition conditions of samples in this figure can be found in Table 5.1.

of $n_{@600nm}$, with temperature indicated by the icon colour. The range of used deposition parameters is reported in Table 5.1. Its clear that while films grown at elevated temperature do not necessarily have a high $n_{@600nm}$, without elevated temperature $n_{@600nm}$ values over 5.2 are not achieved. Moreover, a near linear relation between $n_{@600nm}$ and E_{04} is clearly evident. The only films with a $E_{04} \leq 1.1$eV are those with $n_{@600nm} \geq 5$, indicating that the processing of dense films is a prerequisite for obtaining a low bandgap energy film.

The second question is whether this observation is limited to the PECVD processing of Ge:H films, or whether it extends to Ge:H alloys as well. For that reason, over 70 SiGe:H films were processed. The E_{04} as a function of $n_{@600nm}$ of these films is plotted in Fig.5.13. For these films a range of deposition conditions were varied, including P_{RF}, p, T_S and the ratio of F_{SiH4} to F_{GeH4}, as indicated in Table 5.1. The ratio of precursor gasses has a strong effect on the optical bandgap energy, as reported in [156]. The F_{GeH4} is therefore indicated by the icon size in Fig.5.13, while F_{SiH4} is kept constant at 30sccm. The icon colour indicates T_S. For the SiGe:H films, as with Ge:H, irrespective of power, pressure and even stoichiometry the densest films with lowest E_{04} are processed at elevated temperatures. Also in the SiGe:H films this is likely the result of densification, as T_S did not have a significant effect on the material stoichiometry [156].

Detailed effect of T_S on a/nc-Ge:H films

To characterise the effect of T_S in more detail, and investigate the mechanism involved in the temperature induced densification of the films, 3 series of films were processed in the 250-300°C T_S range. The results are shown in Fig.5.14, with the exact deposition conditions indicated in the caption. The first series of films was processed at conditions resulting in porous nc-Ge:H films (red squares), another resulting in dense nc-Ge:H films (blue triangles) and the third series results in dense a-Ge:H films (black circles).
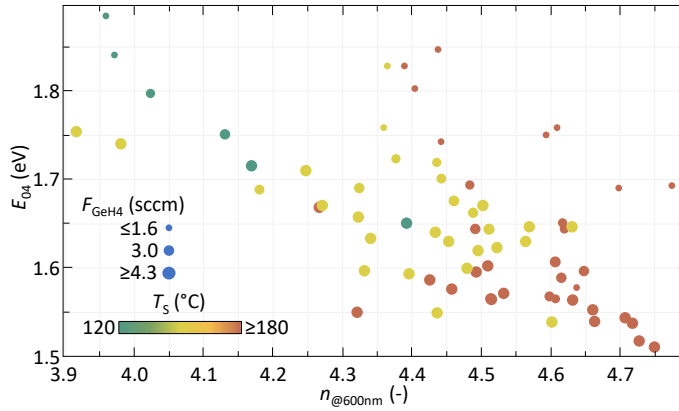
Figure 5.13: The E_{04} plotted as a function of $n_{@600nm}$ for a large set of SiGe:H samples. T_S is indicated by the color of the icons. Icon size indicates the F_{GeH4} flow during deposition. F_{SiH4} is kept constant at 30sccm. The full range of deposition conditions of the samples in this figure can be found in Table 5.1.

The nc-Ge:H films are considered first. For both series, the $n_{@600nm}$ increases with increasing T_S, indicating a densification of the films. This densification is accompanied by an increase of the crystallinity of the films. The crystalline phase is much denser than the amorphous phase, so this correlation is not unexpected. The increased densification results in a decrease of the E_{04}. For the dense nc-Ge:H films this is likely a results of the decreased amorphous phase fraction. For the porous nc-Ge:H films it could additionally be the result of a decreased a-GeO or a-GeC phase fraction, as indicated by the decrease of α_{tot}. The decreased α_{tot} also results in a decrease of the σ_d and increase of the E_{act}, as the dominant defect type in Ge:H is positioned further from the conduction band edge in reference to the GeO:H or GeC:H phase [33], [201], [215].

For the dense nc-Ge:H films the E_{act} and σ_d remain relatively unchanged as a function of T_S. This seems to indicate that there are no significant changes in the defect density and dominant defect type, despite changes in the crystallinity and a slight increase of α_{tot} for the samples processed above 280°C. The α_{tot} increase is somewhat surprising, as we've generally observed an increase in stability with increasing T_S. The low values for α_{tot} seem to indicate however that the oxidation does not reach into the bulk. Rather it is likely that the oxidation is limited to the surface of crystalline grain boundaries on or near the surface. It has been observed in the processing of nc-Si:H that the crystalline phase fraction increases with thickness [36], [61], [109], [159]. Moreover, for very high crystallinity values the amorphous phase fraction, or density of the amorphous phase, is insufficient to properly passivate the crystalline grain boundaries [85]. It is therefore likely that the slight increase of α_{tot} is the result of the oxidation of crystalline grains on and near the surface of the films. For certain applications, such as for a p-i-n photovoltaic device architecture, the nc-Ge:H layer would be positioned between doped films, and likely encapsulated. Therefore, the slight increase of α_{tot} does not necessarily eliminate this high temperature deposition regime, where the lowest bandgap energies are achieved.

Also for the a-Ge:H films an overall increase of $n_{@600nm}$ with increasing T_S can be ob-
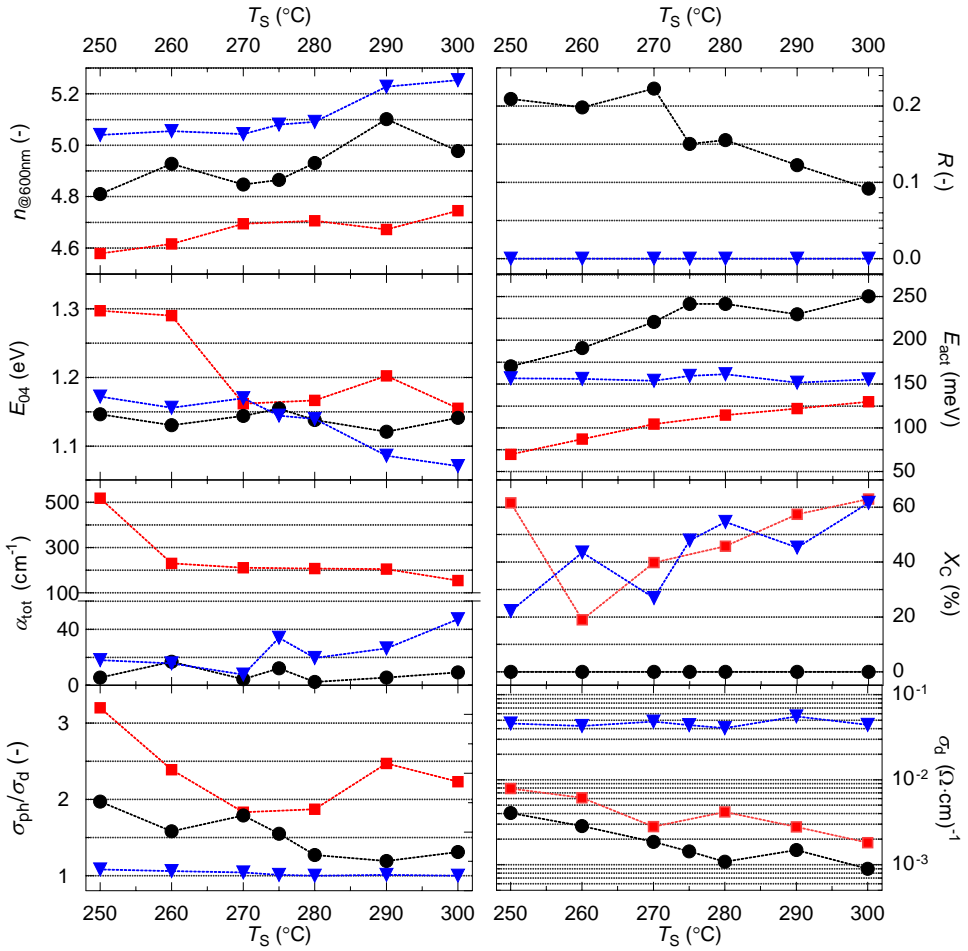
Figure 5.14: The effect of substrate temperature on selected material properties. Porous nc-Ge:H samples (red squares) are processed at F_{GeH4}=0.5sccm, 5mbar and 49.7mW · cm⁻². Dense nc-Ge:H films (blue triangles) are processed at F_{GeH4}=1sccm, 1mbar and 24.9mW · cm⁻². Dense a-Ge:H samples (black circles) are processed at F_{GeH4}=2sccm, 4mbar and 14.9mW · cm⁻². F_{H2} is maximum for all samples at 200sccm.

served. This increased densification is not the result of any changes in the oxidation or crystallinity, as can be deduced from α_{tot} and X_{c}. The only parameter that continuously decreases with T_{S} is the micro-structural parameter R. R is a metric for the ratio of high stretching mode Ge-H vibrations in the FTIR spectra, positioned at 1980cm^{-1} to the low stretching mode Ge-H vibrations positioned at 1875cm^{-1}, as indicated in Fig.7.1. Drawing a parallel to silicon processing [65], [67], low stretching mode Ge-H vibrations are the result of hydrogen atoms positioned in small volume deficiencies at sizes of vacancies with one or two Ge atoms absent from the lattice. High stretching mode vibrations on the other hand are related to hydrogen bonded to germanium in a more porous material phase. The hydrogen resides as the surface of larger nano-sized voids. A decrease of R therefore indicates a decrease of nano-sized void fraction. This decrease of the void fraction with increasing T_{S} is in line with earlier reports [219], [222]. The increase in $n_{\text{@600nm}}$ is therefore not the result of a change in material phase fractions, but rather of a densification of the amorphous germanium phase. It should be noted that for this particular series, the hydrogen concentration also decreases with increasing temperature, which could also contribute to he observed changes. Notably, the nc-Ge:H films do not exhibit this HSM, resulting in a constant R value of 0. This indicates that the nc-Ge:H films are free of nano-sized voids. As with the porous nc-Ge:H films, the densification results in an increased E_{act} and decreased σ_{d} .

This behaviour provides some insight. The photoresponse $\sigma_{\text{ph}}/\sigma_{\text{d}}$ doesn't change significantly. As argued before [201], as the large flux of photo-generated charge carriers does not result in an increase of the measured photo-current, the carrier mobility must be relatively poor. Considering the n-type nature of the Ge:H material [201], [219], [223], hole mobility is likely limiting. The poor mobility is the result of defect-facilitated Shockley-Read-Hall recombination, which indicates that the overall defect density is still significant. However, with T_{S}, the defect density, or the concentration of different types of defects, does change. The E_{act} increases while the E_{04} does not, so the density of defects with n-type nature decreases. This increase of E_{act} results in the observed σ_{d} decrease, according to:

$$\sigma_{\text{d}} = \sigma_0 \exp\left(\frac{-E_{\text{act}}}{k_{\text{b}}T}\right) \tag{5.7}$$

Moreover, R continuously decreases as E_{act} continuously increases. This indicates that the density of n-type defects is related to the concentration of nano-sized voids in the Ge:H material. If we extrapolate the trend in R, and further reduce R to 0, an E_{act} of about 350meV could potentially be achieved for the a-Ge:H films. This means that most dense a-Ge:H films, the E_{act} remains well below half of the bandgap energy. The same is true for the E_{act} of the nc-Ge:H films. Assuming that the crystalline phase is predominantly responsible for conduction in the high crystallinity Ge:H films, an E_{act} of about 330meV, half the the bandgap energy of c-Ge, could be expected. This indicates that the presence of a certain n-type defect persists. As to the nature of this defect, whether some interaction of hydrogen with Ge, or a certain Ge-defect results in the observed donor behaviour, remains unsure.
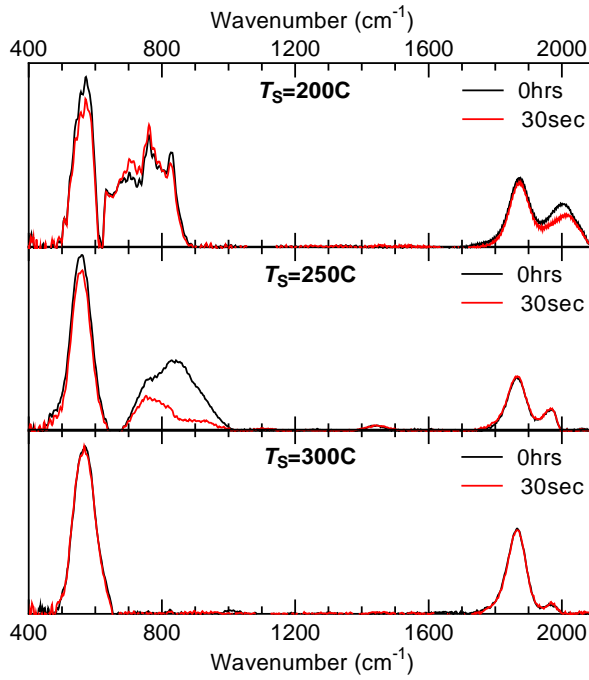
Figure 5.15: FTIR spectra of 3 Ge:H samples, processed at $T_S=200°$C (top), $T_S=250°$C (middle) and $T_S=300°$C (bottom). Samples are measured before (black curve) and after 30s dip in de-ionized water (red curve).

Temperature induced densification

Finally, we reflect on the underlying mechanism of the temperature induced densification of the Ge:H films. There are roughly two ways in which deposition conditions can result in changes in the grown material. The first is by affecting changes in the plasma that result in changes in the growth flux composition. A straightforward example of this is varying the precursor gas flow ratios. It's been speculated that an increase of temperature could alter the flux composition through the dissociation of larger Ge_2H_6 and Ge_3H_8 plasma phase polymers at elevated temperature [220].

Alternatively, under influence of plasma exposure a restructuring of the grown, or growing, surface can occur. The growing surface, or sub-surface, region undergoing restructuring upon continued plasma exposure has been referred to as the growth zone [139], [254]. An example of this is the densification of the growth zone under the influence of physical ion bombardment. A more relevant mechanism is the temperature dependent void integration, which has been observed in amorphous silicon [66], [67] and which we discussed previously [201]. This mechanisms involves the restructuring and densification of the amorphous network, resulting in the virtual movement of small voids towards the surface. This process requires energy, that is increasingly available when the deposition temperature is increased. This means that at elevated temperatures, under influence of the plasma, small voids can diffuse out of the growth zone.

There is a distinction between the temperature facilitated densification of the films through compositional changes in the growth flux on the one hand, and retroactive restructuring of the growth zone the other hand. This distinction is that from the former a certain material uniformity in the growth direction can be expected, while the latter could potentially result in the formation of two distinct regions. A porous top region on top of a dense bulk region could occur for a certain temperature range, since when the RF generator is turned of, the growth zone will not have had the time required for the densification process.

Lacking in-situ measurements to evaluate the composition of the plasma or growing surface, some post-deposition measurements have been performed. We reasoned earlier [201] that water is responsible for the observed post-deposition oxidation of the Ge:H films. The oxidation is resisted in dense Ge:H but occurs readily in porous Ge:H, as water can penetrate into the bulk. A number of samples, processed at different temperatures, were placed in de-ionized (DI) water for 30 seconds. FTIR measurements were performed before and after the exposure to DI water. The plots of three of the samples are shown in Fig.5.15. It can be observed that the sample processed at 300°C does not show any significant changes, while the sample processed at 200°C shows the changes that can be expected of a sample undergoing oxidation. These are a decrease of the Ge:H phase, indicated by Ge-H wagging vibrations are 560cm^{-1} and the LSM at 1875cm^{-1} and HSM at 1980cm^{-1} and an increase of the Ge-O$_x$ related vibrations in the 600-900cm^{-1} region. Particularly, a strong decrease of the HSM can be observed, as the porous regions that facilitate the in-diffusion of water oxidize first. It should be noted that all samples had an initial thickness of 150-200nm and that the 200°C sample was fully etched away after 3 hours in DI water.

The sample processed at 250°C shows a different effect however. After 30s in water, the Ge-O$_x$ related vibrations are strongly reduced, while the Ge-H wagging mode is reduced only slightly and the LSM and HSM are unchanged. This suggests that the film initially consists of a porous top region, that readily oxidizes after deposition, on top of a dense bulk region. The oxidized region is consecutively etched away when exposed to DI water. This observed oxidation and etching behaviour, and the presence of two distinct regions it indicates, are in support of the retroactive restructuring and densification mechanism. This process is likely to occur with increasing effectiveness as temperature is increased, resulting in the fully dense and stable film processed at 300°C in Fig.5.15.

5.2.4 Conclusion

In this work the effect of processing hydrogenated amorphous and nano-crystalline germanium films at a reduced electrode gap is explored. It has been observed that a smaller electrode gap facilitates the processing of denser films, indicated by a higher refractive index, with lower E_{04} and higher E_{act} in reference to the best values obtained at a larger electrode gap.

Moreover, it was observed that the deposition temperature has a dominant effect on the material properties. Consequently, in the first two sections the effect of deposition temperature is demonstrated irrespective of other deposition conditions, such as power, pressure, electrode gap and the precursor gas flow ratios, using over 200 Ge:H and over 70 SiGe:H films.

A closer inspection of the 250-300°C temperature range yields some differences between amorphous and nano-crystalline germanium samples. The crystalline fraction of the nc-Ge:H samples increased with increasing T_{S}, resulting in lower bandgap energies and denser films, but no significant changes in the E_{act} and σ_{d}. In the stable a-Ge:H films the nano-sized void fraction, absent in the nc-Ge:H samples, decreases with T_{S}. This void and vacancy decrease results in an increased E_{act} and decreased σ_{d}.

Additionally, a change in post-deposition oxidation and etching behaviour in de-ionized water was observed as a function of deposition temperature. This behaviour indicates an Ge:H growth mechanism that involves the retroactive restructuring and densification during material growth, under influence of a high temperature plasma.

The temperature-induced densification of Ge:H films was demonstrated that resulted in more intrinsic and stable films with a lower bandgap energy and dark conductivity. These developments improve the attractiveness of a/nc-Ge:H for a variety of electronic, optical, opto-electronic and photovoltaic devices.

6

Analysis of Ge(Sn):H in reference to other hydrogenated group IV alloys

6.1 Spectroscopic review of hydrogenated, carbonated and oxygenated group IV alloys

This section is published in *Vibrational Spectroscopy* *

Abstract

Semiconductors based on group IV elements are widely used in the fields of micro-electronics, optics and photonics. The group IV alloys are processed using plasma enhanced chemical vapour deposition and its opto-electrical properties are a result of the material composition and structure. Infrared and Raman spectroscopy are complementary and powerful tools for providing these essential material characteristics. In this work, the vibrational modes present in hydrogenated, oxygenated and carbonated group IV alloys are investigated in a unique range of amorphous and nano-crystalline $Si_{X \geq 0}Ge_{1-X}$:H films and their alloys with C, O and Sn. Measurements are performed both post-deposition and following extended exposure to the ambient and de-ionized water. This comprehensive review is of value in the fields of material science and engineering as a single work of reference for group IV peak identification.

Additionally, the effect of electrical screening, the influence of the dielectric medium on the peak frequency of a vibrational mode, is illustrated using the experimentally observed frequency shifts of X-O and X-H (X=C, Si, Ge) vibrational modes. All experimentally observed centre frequencies of silicon hydride stretching modes in silicon solids and corresponding silicon-hydride configurations are identified using a straightforward Lorentz-Lorenz model approximation and considering all potential hydrogenated volume deficiencies within a tetrahedrally coordinated amorphous and nanocrystalline lattice. It shows that the stretching mode signature can reveal detailed information on the volume deficiencies in IV-valence alloys.

6.1.1 Introduction

Semiconductors based on group IV elements like silicon, carbon, and germanium are widely used in the fields of micro-electronics, optics and photonics, for a range of applications including transistors, detectors, displays and photovoltaics. The performance of devices in which group IV semiconductors are applied, is a result of the opto-electrical properties and chemical stability of group IV alloys, which in turn are a direct result of the chemical composition and structural characteristics of the material. Understanding of these material properties is therefore crucial for optimization of hydrogenated group IV alloys. Vibrational spectroscopy has proven an important means of providing essential information related to the material stoichiometry [198], [255]–[257], concentration of elements like hydrogen [70], [222], [258]–[260], the void fraction and porosity [65], [67], [113], [196], [261], the preferential bonding of elements in stoichiometric films [199], [215], [220], the chemical stability of films [78], [79], [159] and the amorphous and crystalline material phase fractions [141], [159], [262], [263].

While Fourier-transform infrared spectroscopy (FTIR) and Raman Spectroscopy (Raman) are often used tools in material characterization, works combining results of these complementary techniques for group IV alloys are scarce, as are works presenting more than a single alloy of varying stoichiometry. Such a comprehensive review of group IV alloys is of great value as a reference for peak identification. Additionally, trends across the centre frequencies of vibrational groups in group IV alloys, as a function of the period and group of an element, can provide insight for the identification of peaks during the development of novel alloys.

For that reason, in this work, a range of group IV amorphous (a-) and nano-crystalline (nc-), unalloyed and alloyed, hydrogenated (:H) materials are processed of varying elemental composition. FTIR and Raman spectroscopy measurements and energy dispersive X-Ray (EDX) compositional analysis are performed on these plasma enhanced chemical vapour deposition (PECVD) processed undoped films. Vibrational spectroscopy is based on measuring the vibrational modes of single or group of chemical bonds in molecules up to solids. FTIR and Raman analysis are complementary vibrational techniques. In infrared absorption the absorbed photon matches the energy differences between the vibrational energy states. FTIR detects bonded atoms with a strong dipole moment that undergo a photo-induced change in dipole moment. Raman spectroscopy is based on the inelastic scattering of photons in which the shifts of the photon energy reflects the energy difference between the vibrational modes. Raman detects bonded atoms with a weak dipole moment that exhibit a photo-induced change in polarization. Here, these measurements are performed before and after the films are subjected to different degradation conditions in the dark and under light, in the ambient and in de-ionized (DI) water. This extensive experimental design provides the opportunity to compare vibrational spectra in 3 unique ways: 1. a comparison between homogeneous and heterogeneous materials with different material phases, 2. a comparison of the presence and peak frequency of oxide and hydride vibrational modes across the group IV elements carbon, silicon and germanium and 3. a comparison of the vibrational spectra between the state immediately after deposition and following exposure to different ambient and illumination conditions.

The purpose of this work is twofold. For one, the added value of this unique experimental design, for the fields of material science and engineering, is in providing a comprehensive overview of the vibrational spectra of group IV alloys. In addition to providing a single work of reference for peak identification, a fundamental perspective is presented on the peak frequencies as a function of the material structure and elemental composition. Moreover, throughout this work examples are provided of the applications of vibrational spectroscopy for relating material characteristics to opto-electrical properties, chemical stability and/or device performance.

The discussion section of this work consists of four main parts. In the first part of the discussion, part 6.1.3, the as-deposited FTIR spectra of the a/nc-Si$_{X\geq0}$Ge$_{1-X}$:H films and their alloys with C, O and Sn are characterized. This section includes descriptions of the hydrides, oxide and carbide peak frequencies as well as a discussion of the potential applications of hydride identification. Following these descriptive sections, a reflection on the relation between subtle shifts of FTIR vibrational frequencies and the physical and chemical nature of the local environment of vibrational excited chemical bonds in a solid is presented in 6.1.4. In part 6.1.5, the Raman spectra are analyzed, with a focus on the amorphous and crystalline (c-) peaks, followed by the hydride-, oxide- and carbide-bonds. Finally, in part 6.1.6, a reflection is presented on the potential subjective nature of the peak fitting process in heterogeneous, chemically complex group IV alloys.

6.1.2 Experimental section

Film processing

The films presented in this work are processed on 4 inch, n-type Cz 500μm thick polished monocrystalline silicon wafers. The a/nc-Ge:H and a-GeCSn:H films were processed in the Cascade radio-frequency (RF) PECVD reactor, which has a circular electrode with a diameter of 160mm and an electrode spacing of 20mm. Cascade is a laminar flow reactor, where germane (GeH$_4$) and molecular hydrogen are used as precursor gasses. Additionally, for the GeCSn:H depositions, tetramethyltin (TMT) (Sn(CH$_3$)$_4$) is used as a precursor. Injection of TMT into the reactor is controlled through a valve, for which the open and close time can be controlled. The ratio of the close time to the open time is referred to as the duty cycle in table 6.1. More information can be found in [264]. All other films were processed in a different RF-PECVD cluster tool. In this cluster tool the intrinsic (i-) a-Si:H, i-nc-Si:H and remaining films (i-a/nc-SiGe:H, a-GeO:H, nc-SiO:H, a-GeC:H, nc-SiC:H) films are processed in separate dedicated chambers, each with a flat 12cmx12cm shower-head electrode. The deposition conditions of the processed films, including deposition times and thickness, are reported in Table.6.1.

After deposition the wafers were cut in quarter pieces to measure the evolution of the vibrational spectra and opto-electrical parameters over time, as a function of degradation condition. Of each processed film, three quarters were stored in a temperature controlled room. One quarter was stored in the dark under ambient conditions. A second quarter was stored in an in-house light soaking setup, under ambient conditions. A third quarter was stored in the dark in a container filled with DI water. The vibrational and electrical parameters of these films were then measured at approximately 10 hours, 100 hours and 1000 hours after deposition, with an additional measurement performed at 1hr after

Table 6.1: Deposition conditions of the films presented in this work. Precursor gas flow rates indicated in standard cubic centimeters (sccm). nc-Si:H processed at 40MHz. a-GeCSn:H processed with $Sn(CH_3)_4$ duty cycle of 2857

	P_{RF}	p	T_S	SiH_4	GeH_4	CH_4	H_2	CO_2	Dep. time	Thickness
	$(mW \cdot cm^{-2})$	(mbar)	(°C)	(sccm)	(sccm)	(sccm)	(sccm)	(sccm)	(s)	(nm)
a-Si:H	19.4	0.7	180	40					1100	177
nc-Si:H*	277.8	4	180	3.3			120		900	45.9
a-SiGe:H	20.8	3.6	180	30	5.3		200		2800	292.2
nc-SiGe:H	20.8	3.6	180	30	0.4		200		1100	148.1
nc-Ge:H	99.5	3.5	200		0.5		200		1680	222.6
a-Ge:H	24.9	4	200		0.5		200		2100	182.6
a-GeO:H	20.8	3.6	180		2		200	20	850	173.8
a-GeC:H	20.8	3.6	180		2	15	200		800	170.6
nc-SiC:H	20.8	3.6	180	5		10	200		1848	213.4
nc-SiO:H	20.8	3.6	180	5			200	5	1861	164.9
a-GeCSn:H	14.9	4	230		1.5		200		570	91.0

deposition for the samples stored in water.

Vibrational and elemental analysis

FTIR spectra were obtained using a Thermo Fisher Nicolet 5700 spectrometer. The Raman spectra were obtained using an inVia confocal Raman microscope with a laser operating at a wavelength of 514nm. The EDX analysis was performed on a FEI Nova NanoSEM 450, using an acceleration voltage of 3kV. The elemental composition was obtained by comparing the area of fitted gaussian distributions after background subtraction. As such, the elemental fractions represent atomic fractions rather than weight fractions. For the GeCSn:H sample an acceleration voltage of 5kV was used, to include the main Sn electron transmission at around 3.44 keV in addition to the one at 0.69 keV. While this peak is not included in Fig. 6.1 for visualisation purposes, it is included for determining the atomic fraction.

Fitting vibrational spectra

The spectra were fitted using the Fityk freeware [228]. The background was subtracted manually. Gaussian distributions were added manually. For each sample, the minimum number of Gaussians are used to accurately match the shape of the measured data. The process of determining the number of Gaussians is based on the experience of fitting and re-fitting the hundreds of intrinsic group IV alloys, presented in [156], [168], [201], [262], [264], [265]. Following the manual fit, an autofit option was used to minimize the error between the measured data and the sum of the Gaussian distributions by determining the exact peak frequency, width and height of the Gaussian distributions. For bonding configurations with multiple hydrides, or other atoms or groups, the convention -X_n is used in this work. A reflection on the fitting process is presented in section 6.1.6.

6.1.3 FTIR spectra of hydrogenated a/nc-Si$_{X \geq 0}$Ge$_{1-X}$:H and their alloys with Sn, C and O

The vibrational spectra and elemental analysis of a number of amorphous and nano-crystalline group IV materials and their alloys with carbon and oxygen are shown in Fig. 6.1. The measured curves are indicated in green, while the Gaussian distributions fitted to reproduce the curves are indicated in red. The sum of the fitted Gaussians is represented by the black curve. The peak frequencies of the fitted Gaussians are indicated in the spectra and an overview of the observed peaks is presented in Table 6.2, including the most likely origin of the vibrational modes. It should be noted that C and O fractions in the Ge(C,O):H and Si(C,O):H alloys are intentionally added during deposition using CO_2 and CH_4 precursor gasses, while C and O fractions in the a/nc-Si$_{X \geq 0}$Ge$_{1-X}$:H films are the results of post-deposition oxidation and carbisation reactions.

C,Si,Ge-hydrides

The hydrogen vibrational modes are often used as a tool for determining the hydrogen concentration in thin films, a relevant metric for relating structural characteristics to electrical material properties such as the bandgap energy and degree of electrical passivisation [136]. Moreover the specific configuration of the hydrogen stretching modes (SM) have proven an important tool for thin film analyses. The ratio between the low SM (LSM) and high SM (HSM), visualized for Si-H stretching in Fig. 6.4, are used as a metric for determining void fraction and material density in thin a-Si:H [65], [67], [113], [261], a-SiGe:H [196] and a-Ge:H [262], [265] films. Moreover, in nc-Si:H, the specific SM signature is used to optimize the growth of device quality films photovoltaic applications [69].

None of the a/nc-Si:H and a/nc-SiGe:H (a/nc-SiGe$_{X \geq 0}$:H) show significant traces of oxygen or carbon contamination according to EDX, which aids in the identification of hydride vibrational modes in these samples. The a/nc-SiGe$_{X \geq 0}$:H spectra appear quite similar, which is not unexpected, since Si-Ge bonds are not FTIR active and hydrogen is reported to favourable bond with silicon in PECVD processed a-SiGe:H alloys [189], [199], [200]. The peaks in the a/nc-SiGe$_{X \geq 0}$:H FTIR spectra are therefore expected to be silicon hydrides with a small fraction of germanium hydrides in the SiGe:H samples. In the four a/nc-SiGe$_{X \geq 0}$:H samples two peaks are observed in the 500-800cm^{-1} range which are related to Si-H wagging modes [79], [194], [260], [266]. The peak observed at around 870-881cm^{-1} is likely related to Si-H$_n$ bending [69], [79], [194], [230], [260]. In the nc-SiC:H films, Si-H$_n$ bending is slightly shifted to higher wavenumbers, likely due to the presence of carbon in the local environment. The four a/nc-SiGe$_{X \geq 0}$:H samples all exhibit several peaks in the 1850-2200cm^{-1} range, which are related to Si-H$_n$ stretching modes [69], [79], [267]. A detailed description of the exact identification and frequency of the different Si-H SM's in this range is presented in section 6.1.4. There seems to be no significant Si-H$_3$ SM, which would reportedly result in a vibrational mode at 2140cm^{-1} [69], [254].
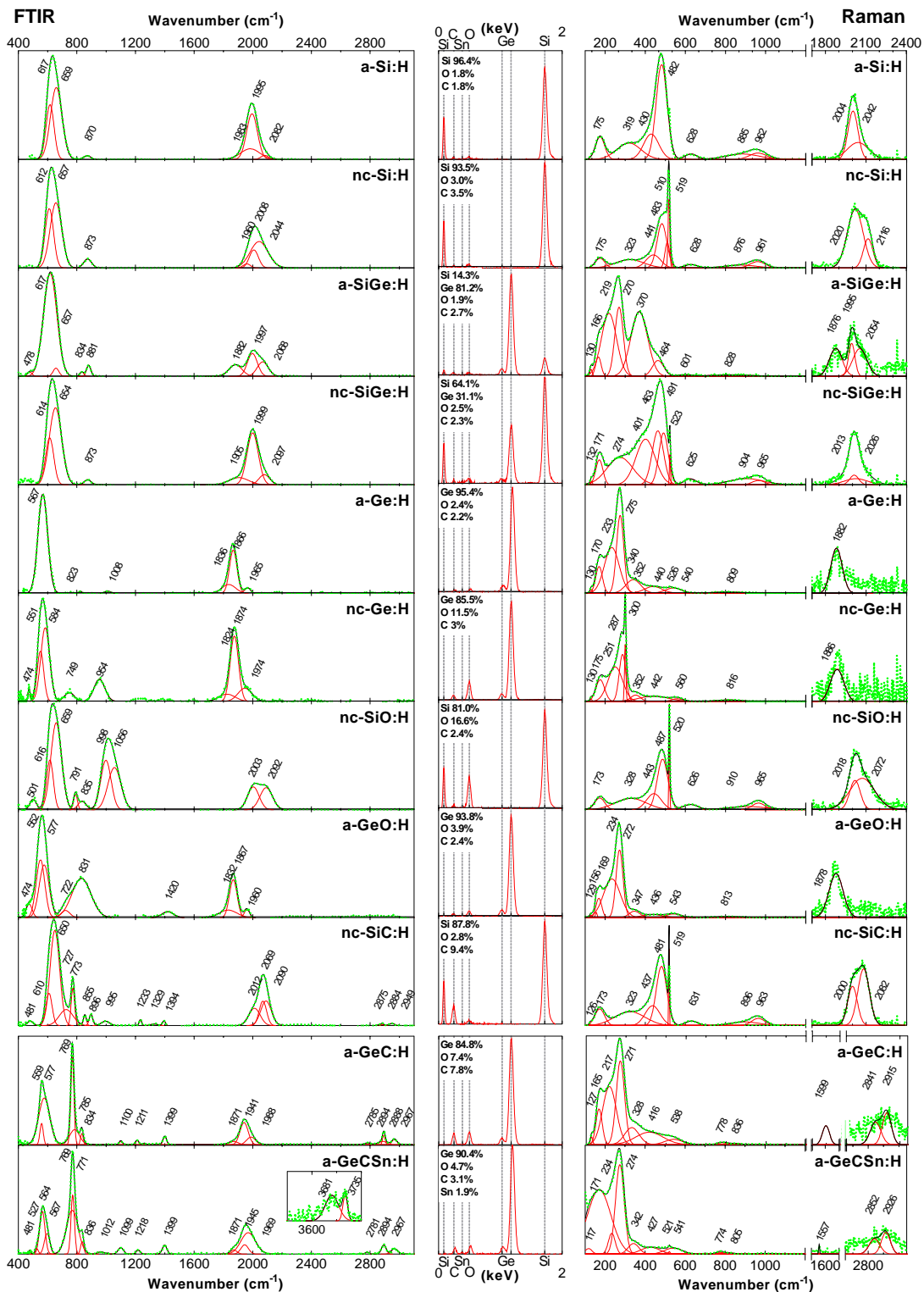
FTIR

Raman

Figure 6.1: Vibrational spectra of group IV elements. FTIR spectra (left) and Raman spectra (right) plotted as a function of wavenumber, for a/nc-Si$_{X\geq0}$Ge$_{1-X}$:H and their alloys with C, O and Sn. The green dashed lines indicate the measured data after background subtraction. Gaussian distributions (red curves) are fitted to the experimental data. The black curves indicate the sum of the fitted Gaussian's. The wavenumber of the peak frequencies of the fitted Gaussian curves are indicated in the figures. The atomic fractions of the presented materials are indicated in the centre, as obtained by EDX analysis. Inset (bottom left) shows the 3500-3800cm^{-1} range of the a-GeCSn:H sample. Note that the horizontal axis of the bottom two Raman plots (a-GeC:H and a-GeCSn:H) deviates from the plots positioned above.

Table 6.2: List of FTIR peaks identified in samples processed in this work. Vibration types, rocking (Ro), wagging (W), bending (Be), stretching (St), indicated in table. Note that Both Ge-O$_x$ and Si-O$_x$ manifest as broad peaks, resulting from the superimposition of a range of X-O(H) vibrations, with the exact centre peak frequency depending on the ratio of the bonds.

Peak frequency (cm^{-1})	Suspected bond	vibration	Refs
480	C-O$_x$	W	[268], [269]
560-580	Ge-H$_n$	W	[32], [194], [196], [201], [230], [260], [270], [271]
610-660	Si-H$_n$	W	[79], [194], [260], [266]
630	Ge-C$_x$	St	
650-950	Ge-O$_x$	St	[32], [201], [255], [260], [272]
720-790	Si-C$_x$	St	[256], [260], [273]–[280]
750-760	Ge-H$_n$	Be	[32], [196], [230], [231]
770	C-H$_n$	Ro	[281]–[284]
830	C-H$_n$	Ro	[282], [283]
870-890	Si-H$_n$	Be	[69], [79], [194], [230], [260]
900-1200	Si-O$_x$	St	[69], [79], [196], [236], [266]
990-1020	C-H$_n$	W	[256], [266], [274]–[278], [280], [284]
1100	C-O$_x$	St	[268], [285], [286]
1210-1230	C-H$_n$	W	[274], [280], [285]
1400	C-H$_n$	Be	[268], [274], [286]–[288]
1430-1450	(O$_x$)C-H$_n$	Be	[268], [286], [289], [290]
1660	C=O$_x$	St	[285], [290], [291]
1740	H$_n$C-O$_x$	St	[292], [293]
1800-2050	Ge-H$_n$	St	[32], [194], [196], [201], [222], [230], [270], [294]
1850-2200	Si-H$_n$	St	[69], [79], [159], [267]
2800-3000	C-H$_n$	St	[256], [260], [274]–[277], [282], [284], [294]
3500-3800	O-H$_n$	St	[285]

In the a/nc-SiGe$_{X\geq0}$:H samples an additional peak appears, located at around 1875 cm^{-1}, that coincides with peaks in the a-Ge:H and nc-Ge:H spectra. This peak is related to Ge-H$_n$ SM's [32], [194], [196], [201], [222], [230], [270], [294]. The a/nc-Ge:H FTIR spectra look very similar to the a/nc-Si:H spectra, except that the all peak frequency are shifted to lower wavenumbers. Ge-H$_n$ wagging occurs at around 560-580cm^{-1} [32], [194], [196], [201], [230], [260], [270], [271], and Ge-H$_n$ bending at about 750-760cm^{-1} [32], [196], [230], [231] and the Ge-H SM at 1875cm^{-1} is accompanied by a Ge-H$_n$ SM at approximately 1970cm^{-1} [32], [196], [222], [230], [270], [294].

Additionally, we consider the carbon hydrides, which can be found in the SiC:H and GeC(Sn):H spectra. Carbon hydride SMs appear in the 2800-3000cm^{-1} wavenumber region [256], [260], [274]–[277], [282], [294]. C-H$_n$ SMs manifest as three distinct peaks, with peak frequencies at around 2790cm^{-1}, 2890cm^{-1} and 2970cm^{-1}. These peaks can also be observed in the GeC:H spectra in Fig.6.2, where they are seen to increase with increasing CH$_4$ flow rate during deposition. In tandem with the C-H$_n$ stretching, C-H$_n$ rocking

vibrations at 770 cm^{-1} and 830cm^{-1} increase with CH_4 flow rate. Moreover, vibrations appear in the nc-SiC:H spectrum in Fig. 6.1 and the GeC:H spectrum in Fig.6.2 that are most likely the results of C-H$_n$ wagging, in the 1020cm^{-1} [256], [266], [274]–[278], [280], [284] and 1210-1230 range [274], [280], [285] and C-H$_n$ bending at 1400-1450cm^{-1} range [196], [268], [274], [286]–[290].

Finally, O-H$_n$ SMs can be observed in the inset in the GeCSn:H FTIR spectrum in Fig. 6.1. The O-H$_n$ SMs appear up-shifted with respect to the group IV hydride SMs, approximately to the 3600-3800cm^{-1} range [285]. Oxygen incorporation in the porous GeCSn:H film is the results of a post-deposition oxidation that occurs during the 1-2 minute ambient exposure during the transfer from the PECVD reactor to the FTIR measurement setup. Interestingly, O-H$_n$ incorporation is only observed in Ge-based alloys, whereas in porous Si-based alloys post-deposition oxidation only occurs due by oxygen incorporation in the Si-Si back bond resulting in Si-O-Si [265].

Si,Ge-oxides and carbides

The appearance of O-H$_n$ SMs are a demonstration of the porous nature of a film, in which oxidation occurs readily. The monitoring of oxidation behaviour is relevant for optimization towards a chemically stable, device quality material. Examples of FTIR analyses of the oxidation behaviour of thin films include nc-Si:H [69], [79], nc-SiGe:H [80] and a/nc-Ge:H [201], [262], [265]. In these works, the FTIR measurements do not only provide information on degree of oxidation and/or carbisation. Monitoring of the vibrational modes over time provides information on the type of chemical reaction that takes place and the local environment in which the degradation reaction occurs. Moreover, for samples in which O or C are intentionally added, vibrational spectroscopy can provide information on the material stoichiometry.

Considering the identification of oxide and carbide bonds in the group IV alloys presented in Fig. 6.1. Silicon-oxygen vibrations can be observed in the nc-SiO:H films, and to a lesser extent in the nc-SiC:H film, as a wide peak in the 900-1200cm^{-1} range [69], [79], [236], [266]. The peaks can be best approximated by two Gaussian distribution with centre peak frequencies at around 990-1000cm^{-1} and 1050cm^{-1}. The exact type of Si-O vibrations is unclear, which is indicated in this work by the subscript "x". With respect to the Si-O$_x$ vibrations, the Ge-O$_x$ vibrations are down-shifted to about 650-1000cm^{-1}, which is in line with our earlier work [201], [262], [265] and that of others [32], [260], [272]. Reports identify various Ge-O related vibrational modes in this range, such as the Ge-O-H mode with a peak frequency of 670cm^{-1} [255], Ge-O-Ge at 750cm^{-1} [32], [196], [220], [255], [260], [272] and at 860cm^{-1} [196], [220]. Some Ge-O$_x$ vibration is also likely the origin of the peak in the nc-Ge:H spectrum at 954cm^{-1}.

It should be noted, considering the small carbon fraction in the a-GeO:H samples, that the presence of Ge-C related vibrations in the 650-1000cm^{-1} range cannot be excluded. To facilitate identification of the Ge-O$_x$ and Ge-C$_x$ peaks, a number of GeO:H and GeC:H samples were processed, as shown in Fig.6.2. For these samples, the CO_2 and CH_4 gas flow rates during deposition, the precursor gasses for oxygen and carbon integration, were varied. A few things can be observed from these spectra. First, with increasing CO_2 flow rate, the band of vibrations in the 650-1000cm^{-1} range show an overall increase with respect to the Ge-H$_n$ wagging vibrations, and are likely related to Ge-O$_x$ vibrations.
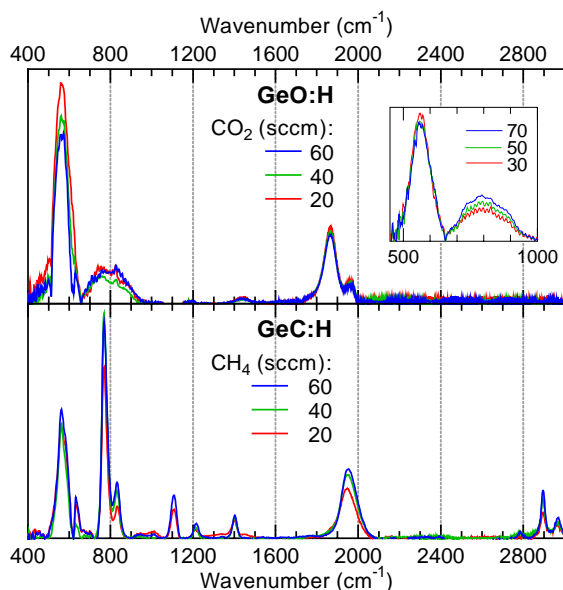
Figure 6.2: FTIR spectra of a-GeO (top) and a-GeC samples (bottom) process at different CH_4 and CO_2 precursor gas flow rates. In the inset a second set of a-GeO samples is presented, processed at varying CO_2 flow rates.

The distinct peaks at 770cm^{-1} and 830cm^{-1} are confidently assigned to C-H$_n$ wagging vibrations, in line with earlier reports [256], [260], [274]–[280]. Similarly, the peak at approximately 1000cm^{-1} is confidently assigned to C-H$_n$ bending vibrations, in line with [256], [266], [274]–[278], [280], [284]. Both assignments are made considering the peak frequency in reference to Ge-H and Si-H wagging vibrations, the increase of peak intensity with CH_4 flow rate and the fact that these peaks appear in both the SiC:H and GeC:H FTIR spectra. It should be noted however that a number of different vibrations have been reported in this wavenumber range. At 770cm^{-1} Ge-H vibrations have been reported [32], [196], [230], [231], as well as Ge-O$_x$ vibrations [196], [255]. Similarly, the peak at 830cm^{-1} has been attributed to Ge-O$_x$ [32], [272], [295], [296] and Ge-H vibrations [196], [230], [231], [284]. Similarly, for the peak at around 1000cm^{-1} Ge-C-C vibrations are reported [282], [283], as well as C-O vibrations [297], [298]. In section 6.1.6 we reflect on the multitude of peaks identified int his range.

Additionally, a small distinct peak appears at 620 cm^{-1} for higher CO_2 flow rates. This peak is matched by a stronger peak in the GeC:H spectra, and is therefore likely related to a Ge-C$_x$ vibration, which reportedly occurs in this range [279], [284], [288], [295], [299], [300]. A similar vibration, Si-C$_x$ stretching, can be observed in the nc-SiC:H spectrum, where a peak is positioned in between those of the Si-H$_n$ and C-H$_n$ wagging vibrations. The exact peak frequency is a function of the local environment and assumptions during the fitting procedure, and consequently ranges from about 710-760cm^{-1} in earlier reports [256], [260], [273]–[280].

Besides the Ge-H and C-H vibrations, two more peaks are present in the GeC:H spectra in Fig.6.2. These peaks occur at 480cm^{-1} and 1100cm^{-1}. Considering that i) matching peaks, though small, can be observed in the GeO:H and nc-SiC:H spectra and ii) the frequency of the peaks in reference to the Ge-O$_x$ and Si-O$_x$ SMs, the latter is likely the result of C-O$_x$ stretching [268], [285], [286] while the former is the result of C-O$_x$ wagging [268], [269].

FTIR-spectra after degradation

To better understand the vibrational modes in the group IV alloys presented in this work, the samples were stored under different conditions and the vibrational spectra were monitored over time. The FTIR and Raman spectra measured after a 1000hrs of storage, unless indicated otherwise in the plots, are presented in Fig. 6.3.

A strong effect can be observed in the a/nc-Ge:H and a-GeO:H vibrational spectra. For the samples stored in water, the various Ge-H vibrational modes decrease over time. At the same time, the amorphous germanium Raman modes (100-300cm^{-1}) disappear as well, exclusively leaving a c-Si peak at 520cm^{-1} and a peak related to Si-O vibrations in the 900-1050cm^{-1} range. This means that at this point the c-Si wafer and oxidized wafer surface are being measured, which indicates that Ge:H reacts strongly with the DI water, a reaction in which the Ge:H tissue is consumed. Note that these Raman modes will be discussed in more detail in section 6.1.5. The consumption of the Ge:H film was confirmed by spectroscopic ellipsometry measurements, where a decreased film thickness was observed as a function of time.

During this consumption of Ge:H, additional vibrational modes appear over time that assist in the identification of peaks in the FTIR fingerprint region ($\omega \lesssim 1500$cm^{-1}). These modes are the result of different bonding configurations between carbon, hydrogen and oxygen. In the a-GeO:H, a/nc-Ge:H and a/nc-SiGe:H spectra peaks appear at 1660cm^{-1}, related to the C=O [285], [291] or C-O vibration [290], and at 1740cm^{-1}, related to either an H$_3$CO [292] or H$_2$CO [293] vibration. Additionally, in the a/nc-Ge(O):H spectra vibrational modes appear at around 1440cm^{-1}, also present in the GeO:H spectra of Fig.6.2, related to (O$_x$)C-H$_n$ bending [268], [286], [289], [290]. This post-deposition process during which carbon is integrated in the germanium alloys is discussed in detail elsewhere [265].

Finally, it is noteworthy that the monitoring of the vibrational modes in the a/nc-Ge(O,C):H films provides information on the resilience against water induced degradation. The resilience against oxidation is increased in the a-GeC:H samples, where CH$_4$ is added during deposition. Not only is the rate of film consumption decreased, the inherent stability of the GeC$_x$ phase can also be observed in the 650-1000cm^{-1} range in the a-Ge(O):H spectra. For the samples stored in water, unlike the samples stored in the ambient, the dominant vibration shifts over time, towards a peak frequency of 770cm^{-1}, which is associated to Ge-C$_x$ vibrations.

FTIR

Raman

a-Si:H

nc-Si:H

a-SiGe:H

nc-SiGe:H

a-Ge:H

nc-Ge:H

nc-SiO:H

a-GeO:H

nc-SiC:H

a-GeC:H
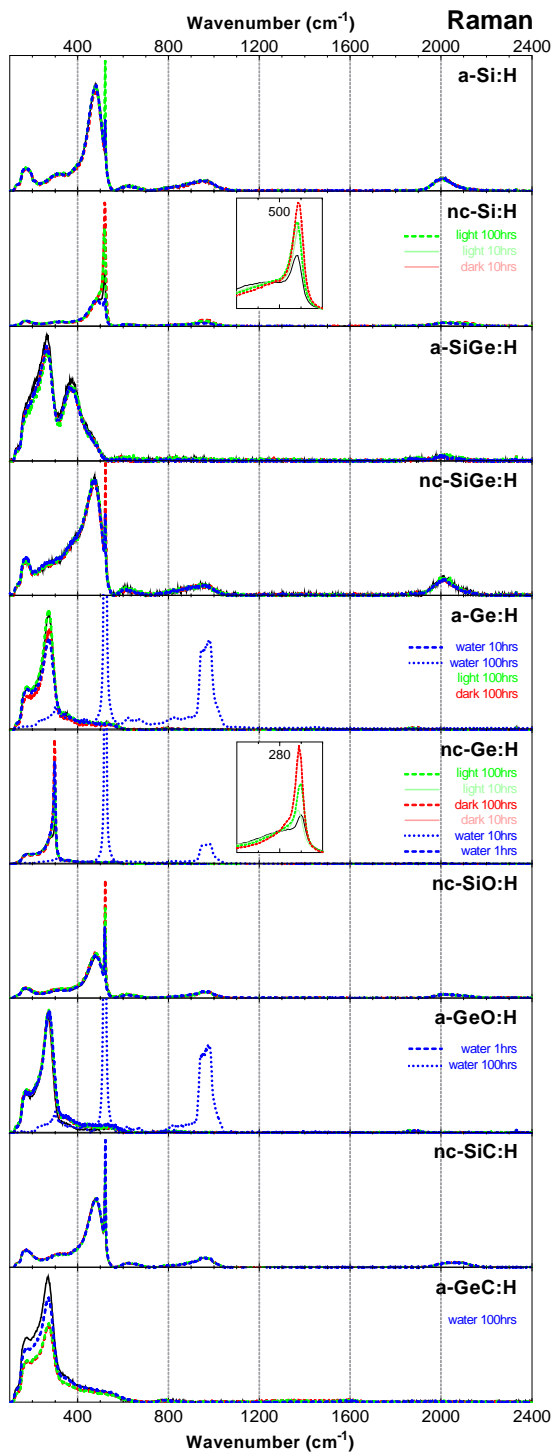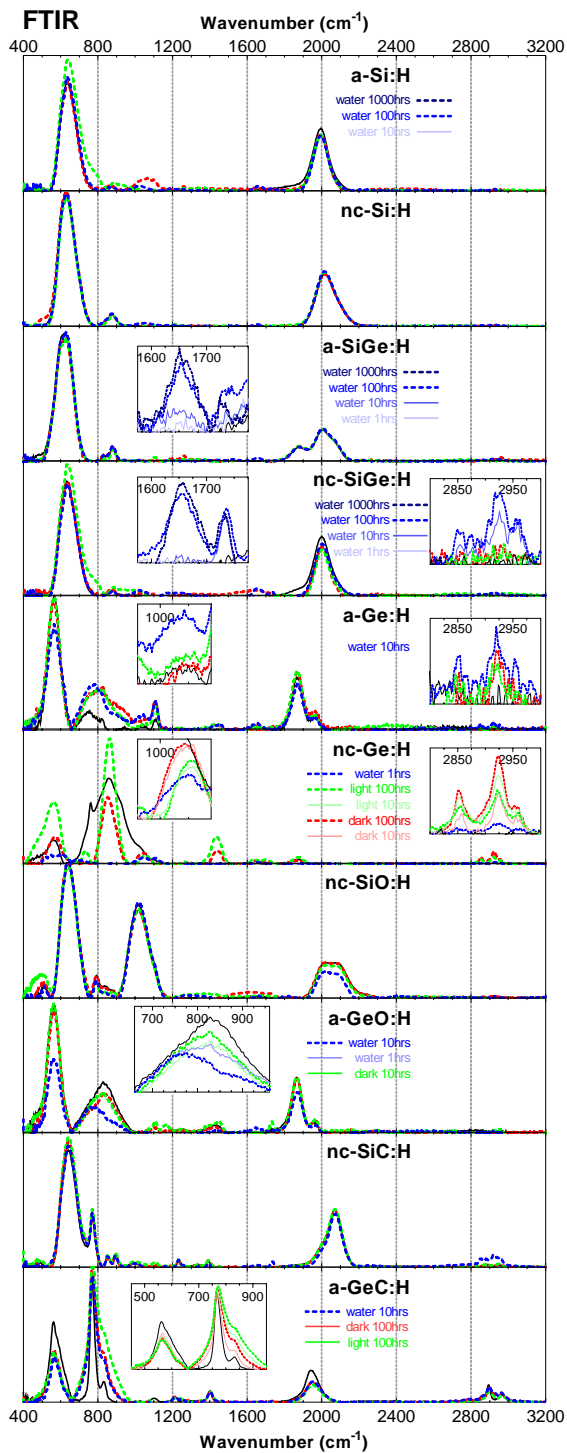
Figure 6.3: Vibrational spectra of group IV elements. FTIR spectra (left) and Raman spectra (right) plotted as a function of wavenumber, for a/nc-Si$_{X>0}$Ge$_{1-X}$ and their alloys with C, O and Sn. All curves are presented after background subtraction. The black solid curves represent measurements at 0hrs. The dashed green curves indicate measurements after degradation in the light under ambient conditions. The dashed red curves indicate measurements after degradation in the dark under ambient conditions. The dashed blue curves indicate measurements after degradation in the dark in de-ionized water. The number of hours after degradation is indicated in the plots. Note that the insets are zoom-ins; the same data presented on a decreased vertical axis range for a selected wavenumber range.

6.1.4 Physical relation between local environment and peak frequencies

The identification of the observed vibrational modes across the different group IV alloys allows for a reflection on the physical relation between the peak position and local environment. The vibrating valence bonds like C-H$_n$, Ge-H$_n$, and Si-H$_n$ are physically described as dipole vibrations. The effective charge of a vibrating mono-hydride X-H (X=C, Si, Ge, Sn) is determined by valence electrons that make the valence Si-H bond, whereas the effective mass of the vibrating system is mainly determined by the mass of the hydrogen atom, assuming that the position of the X atom is static due to the back bonds with three neighboring X atoms. Interestingly, the peak frequency of these vibration modes reveal lots of physical and chemical detail of the local environment of the excited dipole X-H vibration.

Here we will shortly elaborate on this using the most extensive studied X-H vibration in literature, i.e. the silicon-hydrides in molecules, at surfaces of a-Si:H and c-Si:H, and in the bulk of a-Si:H, nc-Si:H and hydrogen implanted c-Si [303] as shown in Fig.6.4**A**. The dielectric nature of a medium of vibrating dipoles can be described by the superposition of Lorentz-Lorenz dipole oscillators [67]:

$$10^{-4} \sum_j N_j \frac{q_{0,j}^2 \Omega_j^2}{4\pi^2 c^2 m_j \epsilon_0} \left(\frac{1}{\omega^2 - \omega_{0,j}^2 + 2i\delta_j\omega} \right) = 3\frac{\epsilon(\omega) - 1}{\epsilon(\omega) + 2} \tag{6.1}$$

With $\epsilon(\omega)$ the dielectric function of the medium of vibrating dipoles. Every type of X-H vibration has it own eigenfrequency (ω_0) depending on the effective charge (q_0)(unscreened), effective dipole mass (m) and screening of its surrounding, as described by Ω. The X-H vibrations in a free molecule can be considered as 'unscreened' dipole vibrations and reside in molecules like silane (SiH$_4$) and polysilane (Si$_n$H$_{2n+2}$). The 'unscreened' frequency is determined by the hydride nature, i.e. mono-, di-, tri-, and tetra-hydrides as shown in Fig.6.4**B**. From Eq.8.1 it can be derived that subtle frequency shifts ($\Delta\omega$) in reference to the 'unscreened' eigenfrequency are given by:

$$\Delta\omega_j = -\frac{10^{-4}}{24\pi^2 c^2 m_j \omega_{0,j} \epsilon_0} \frac{K_j q_{0,j}^2 \Omega_j^2}{V_{Si}} \tag{6.2}$$

Where parameter K is the nano-structure parameter reflecting the averaged number of Si-H dipoles per volume unit V of one missing Si in the Si:H network [67], [73]. It are these subtle frequency shifts that can reveal the physical nature of the dipole vibrations.
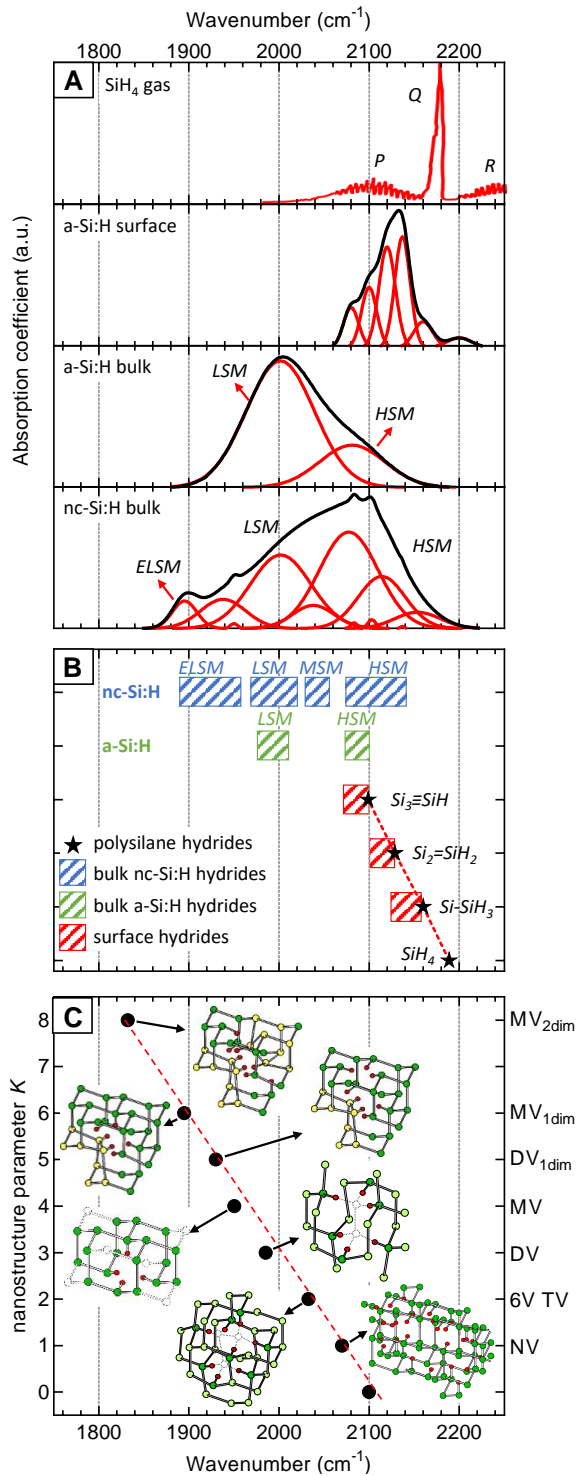
Figure 6.4: caption on next page

Figure 6.4: **A)** Typical IR absorption spectra for SMs of hydrides in silane gas [301], on an a-Si:H surface and in the a-Si:H bulk and nc-Si:H bulk [69], [302]. The absorption spectrum in the silane gas includes the typical P, Q and R-branches due to the rotational-vibrational coupled transitions of the molecule. The SM frequencies of the surface and bulk broaden and shift to lower values. **B)** The experimentally observed spectral ranges of Si-H SMs observed in (poly-)silane molecules, a-Si:H and nc-Si:H including the typical nomenclature adopted in this paper; extreme-low SM (ELSM), low SM (LSM), medium SM (MSM), high SM (HSM). Note that **B)** only has a horizontal axis, the vertical offset is applied for visualisation purposes. Fig. **C)** all experimentally observed SMs in a-Si:H, nc-Si:H and hydrogen implanted c-Si versus the K parameter including the corresponding type of hydrogenated volume deficiency.

First, the effect of electrical screening is illustrated in Fig.**A-B**. The eigenfrequency of 'un-screened' silicon hydrides shifts from larger frequencies in (poly-)silane molecules to lower frequencies when the hydride types are bonded to a surface. Here the dipole vibration experiences an electrical screening by the dielectric nature of the sub-surface solid. Screening means that the effective charge of the dipole is altered due the dielectric medium around it in reference to the unscreened dipole (ω_0 ~3020 cm^{-1}, ~2189 cm^{-1}, ~2110 cm^{-1} and ~1908 cm^{-1} for CH_4, SiH_4, GeH_4 and SnH_4). Maximum screening is obtained when the dipole vibration is incorporated in the bulk with locally a high dielectric constant. This is demonstrated by the Ge-based alloys in Fig.6.5. In this figure, the frequency ranges are visualized of all carbon, silicon and germanium hydride and oxide vibrational modes observed in this work. Fig.6.5 shows that Ge:H has the lowest wavenumber for the hydride wagging, bending and stretching modes, as well as oxide stretching modes, and the largest shifts $\Delta\omega$ in reference to the unscreened ω_0. The C-(O,H) SMs appear up-shifted in reference to Si-(O,H) SMs, which appear up-shifted in reference to Ge-(O,H), which is in line with the fact that Ge:H has the highest dielectric constant of all IV-valence alloys studied in this paper.

The typical tetrahedral coordination of IV-valence alloys basically defines the K-values of the various hydrogenated volume deficiencies. A monovacancy is in theory a vacancy in which 4 hydrogen atoms can be incorporated and replace one silicon atom ($V H_4$ where 'V' is the missing Si atom monohydride density of $K{=}4$). The monohydride can be incorporated in polyvacancies as well. For these small polymer-like shaped vacancies the general relation is valid that in an m-vacancy, m silicons are replaced by 2m+2 hydrogen atoms ($V_m H_{2m+2}$). For poly-vacancies with m$\geq$3 the centered V positions accommodate two hydrogens instead of the three hydrogens as at the polyvacancy ends. For a divacancy, the local monohydride densities are represented by $K{=}3$ and for a trivacancy by both $K{=}3$ and $K{=}2$ ($H_3 V$-$(V H_2)_{m\text{-}2}$-$V H_3$). Experimental evidence exists that deficiencies with equivalent sizes to divacancies exist in a-Si:H. Nuclear magnetic resonance spectroscopy [304], small-angle neutron scattering [305], positron annihilation studies [306], [307] as well as density analysis [65] have shown that hydrogen is predominantly clustered together with 6 H atoms in dense a-Si:H. If the vacancy becomes larger than a polymer-chain of missing silicon atoms, we define the 'hole' in the matrix as a nanosized void. Small-angle X-ray scattering measurements on a-Si:H films deposited with several techniques show that mainly nanosized voids with a typical diameters of 2-4nm are present in the a-Si:H network [305], [308]. These observations are corroborated by positron lifetime measurements [309] and density measurements [65]. In view of the typical defect densities in a-Si:H (10^{15}-
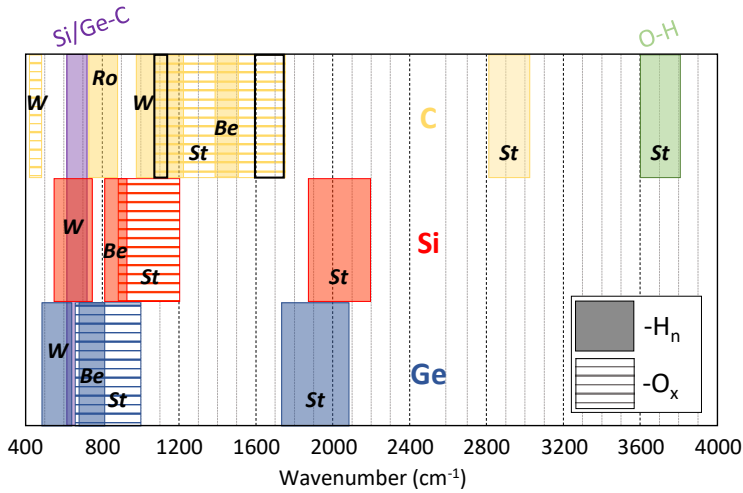
Figure 6.5: Schematic representation of the vibrations observed in this work. Colored areas indicate width of observed vibrations, while black text indicates vibration type: rocking (*Ro*), wagging (*W*), bending (*Be*), stretching (*St*). Visual indicates O-H_n vibrations (top,green), C-(O_x,H_n) (top, yellow) vibrations, Si-(O_x,H_n) (centre, red) and Ge-(O_x,H_n) vibrations (bottom, blue). Dashed area indicates range of O_x vibrations while even coloured areas indicates range of H_n vibrations. Purple area indicates range of Si-C and Ge-C vibrations. Black squares present in yellow dashed range of C-O_x vibrations indicates specific C-O_x vibrations observed in this work.

10^{17} cm^{-3}), the surface has to be considered as almost fully hydrogen passivated and several hundreds of hydrogen atoms must be bonded to such an internal void surface. Consequently, the void surface can be interpreted as a normal a-Si:H surface. On these surfaces, similar to hydrogen passivated c-Si and a-Si surfaces, monohyrides and dihydrides are present.

All configurations discussed above, are based upon a network of tetrahedral silicon sites, which reside in rings of 6 sites. However, just like on a crystalline or amorphous surface, the Si atoms at the edge of a vacancy can form or reconstruct to dimer configurations, i.e. the silicon atoms reside in a ring of 5 atoms. A monovacancy ($X_{1.1}H_6$) and divacancy (H_3X-$X_{1.1}H_5$) with a dimer reconstruction are shown in Fig.6.4**C**. We have to note here, that the volume in the lattice of the Si atoms in a 5-ring is ~20 percent larger, since the 5-ring resides in a volume at which 6 silicon atoms can reside. Two silicon dimers share a quarter of their volume with the vacancy site, which makes the volume of this vacancy site 10 percent larger relative to a vacancy site without a dimer. These configurations reflect the most compact way to incorporate Si-H bonds into a silicon matrix and are only obtained by either hydrogen implantation in c-Si or at the interface between a-Si:H tissue and crystalline silicon grains in the bulk of the densest nc-Si:H films.

Fig.6.4**C** shows on the horizontal axis all silicon-hydride SMs observed in a-Si:H, nc-Si:H and hydrogen implanted c-Si. All these frequencies can be plotted versus its parameter K (vertical axis) of its corresponding local silicon-hydride density in the hydrogenated volume deficiencies. Note, that the same effective charge of the Si-H dipole $q_0 = 0.40e$ has been used, and therefore Fig.6.4**C** clearly demonstrates the validity of Eq.8.2 for the

Table 6.3: List of Raman peaks identified in samples processed in this work. * No definitive assignment can be made based on FTIR, Raman and EDX data

Peak position (cm^{-1})	Suspected vibration	Refs
165-175	a-Si TA	[310]
170-180	a-Ge LA	[232], [271], [311]
230-250	a-Ge LO	[232], [271], [311]
270-280	a-Ge TO	[196], [232], [233], [271]
300	c-Ge	[233], [234], [296], [312], [313]
320	a-Si LA	[310]
330	O-Ge-O/Ge-O-Ge	[314]–[316]
370-410	Si-Ge	[156], [196], [232], [310], [311]
430-440	a-Si LO	[159], [259]
440	O-Ge-O/Ge-O-Ge	[314]–[316]
480	a-Si TO	[159], [196], [271], [310]
520	c-Si	[110], [159]
540-560 *	Ge-H	
	O-Ge-O	[314]–[316]
	Ge-C	[288], [295], [300], [317]
620-630	Si-H	[110]
800	Si-C TO	[318], [319]
870-900	Si-H$_n$	
960	Si-O-Si	[159]
970	Si-C LO	[318], [319]
1600	C-C (G-band)	[279], [284], [288], [319]–[322]
1870-1890	Ge-H $_n$	
1900-2100	Si-H$_n$	
2800-3000	C-H$_n$	

same type of silicon hydride. In addition, Fig.6.4 demonstrates in general the power of the infrared analyses: the various SM's directly reveal the type and densities of hydrogenated volume deficiencies in the material. It scales with the macroscopic density of the bulk material, but also reveals specific hydrogen passivations at the interface of a-Si:H tissue and reconstructed surfaces of nano-crystalline grains.

6.1.5 Raman spectra of a/nc-Si$_{X \geq 0}$Ge$_{1-X}$ and their alloys with C, O and Sn

Raman analysis of the films is presented in Fig. 6.1 and an overview of the observed peaks, and their suspected origin, is presented in Table6.3. A discussion of the amorphous and crystalline vibrational modes and the application of Raman analysis is presented first, before the Raman-active hydrides, oxides and carbides are considered.

Amorphous and crystalline C, Si and Ge

Crystalline bulk material exhibits a single vibrational Raman mode, while in amorphous bulk materials generally four distinct Raman vibrational modes are present; the transverse acoustic (TA), transverse optic (TA) longitudinal acoustic (LA) and longitudinal optic (LO) phonon modes. The Raman TO/LA peaks provide an important analytic tool for a range of thin film applications. These Raman modes are used to determine the stoichiometric nature of alloys such as a-SiGe:H [156], [189], [199]. The ratio between the TO/LA vibrational modes in reference to the crystalline mode is used to determine the crystallinity

in nc-Si:H [85], [90] and nc-Ge:H [201], [296] films. Additionally, for nano-crystalline materials, in which nano-size crystals are embedded in an amorphous phase, the centre peak frequency and width of the crystalline peak provides information used to determine the average size of silicon [266], [323] and germanium nanocrystals [233]. Moreover, for a crystalline alloy, the shift of the crystalline peak, in reference to an unalloyed crystal, can provide information about the stoichiometry of the crystalline phase, as demonstrated in experiments performed on SiGe [324] and GeSn crystals [264], [325]–[327].

The four amorphous silicon modes are clearly visible in the a-Si:H and nc-Si:H samples. The a-Si:H TA and LA modes appear at $160cm^{-1}$ and $320cm^{-1}$, as reported earlier [310]. As does the TO mode at $480cm^{-1}$ [159], [196], [271], [310]. The LO mode appears at about $440cm^{-1}$, which is unlike the traditionally reported $390cm^{-1}$ [310] frequency but in line with more recent reports like [159], [259]. Additionally, the peak related to the crystalline silicon phase, at $520cm^{-1}$ is apparent in the nc-Si(O,C):H samples [110], [159]. The Raman-active Ge vibrational modes are again shifted to lower wavenumbers with respect to their silicon counterparts. The amorphous germanium TA phonon mode at $80cm^{-1}$ is positioned outside the range presented in this work. The LA mode at $177cm^{-1}$, LO mode at $230cm^{-1}$ [232], [271], [311], and TO mode at $278cm^{-1}$ [196], [232], [233], [271] are clearly present in the measured a/nc-Ge:H spectra, in addition to the c-Ge peak at $300cm^{-1}$ present in the spectrum of the nc-Ge:H film. [233], [234], [296], [312], [313]. The a-SiGe:H and nc-SiGe:H spectra are approximately a combination of the a/nc-Si:H and a/nc-Ge:H spectra. In these, a broad signal is apparent in the 100-$550cm^{-1}$ range, that is the superimposition of the various amorphous silicon and germanium modes. In addition to these modes, specific Si-Ge vibrational modes are present that appear in the 370-$410cm^{-1}$ range [196], [232], [310], [311]. A visualisation of the evolution of the different a-Si, a-Ge and a-SiGe Raman peaks as a function of the Ge-fraction in a large number of a-SiGe:H samples can be found elsewhere [156].

Additionally, an unexpected observation from the evolution of the Raman spectra over time, in Fig. 6.3, should be discussed. The intensity of the c-Si peak at $520cm^{-1}$ in the nc-Si:H sample can be observed to increase over time. A similar intensification of the crystalline peak can be observed in the nc-Si(O):H sample and the nc-Ge:H sample, at $300cm^{-1}$. Although the cause of this post-deposition crystallization cannot be determined with any certainty, the most likely explanation is a thermally induced crystallization, resulting from conductivity measurements performed at $130°C$ at 10-100-1000hrs after deposition.

The behaviour of carbon is dissimilar to that of its group-IV kin Si and Ge, in that carbon has the tendency to form double and triple covalent bonds involving 4-6 valence electrons. These so-called sp and sp2 hybridizations are unstable in Si and Ge, where exclusively sp3 hybridization occurs. This makes the exact interpretation of Raman spectra of amorphous carbon films more complex than their other group IV counterparts. Carbon-carbon bonds are generally present in the 1200-$1650cm^{-1}$ range[288], [319]. More specifically, they appear as the diamond (D) bond with the peak frequency at ≈1320-$1360cm^{-1}$, graphite (G) band with the peak frequency ≈1565-$1590cm^{-1}$ [279], [284], [320]–[322] and two additional bands with peak frequencies at ≈1165-$1190cm^{-1}$ and ≈1485-1510 [319]–[321], where increased amorphization results in broadening of these bands. Of these bonds, only

the G-band weakly appears in the a-GeC(Sn):H spectra at around 1600cm^{-1}. The vibrations are accompanied by weak C-H$_n$ vibrations in the 2800-3000cm^{-1} range. Unlike the a-GeC:H spectrum, carbon-related vibrations do not seem to have a significant influence on the nc-SiC:H Raman spectrum. No features were apparent in the 1200-1650 a-C range or in the 2800-3000 C-H$_n$ range. Also at $\approx$800cm^{-1} and $\approx$970cm^{-1}, where the Si-C TO and LO mode reportedly appear [318], [319], the Raman spectra do not seem to differ significantly from the a/nc-Si:H and nc-SiO:H spectra.

hydrides, oxides and carbides in Raman spectra

The FTIR active Si-H vibrational bonds are also Raman active, albeit not as strongly. The Si-H SMs appear more or less at the same frequency in the Raman spectrum. In both the a-Si:H and nc-Si:H spectra the Si-H wagging modes appear at 628cm^{-1}, Si-H$_n$ bending at 876-885cm^{-1} and Si-H and Si-H$_2$ stretching in the 1900-2100cm^{-1} range. Apart from these modes, the Ge-H SMs that appeared in FTIR spectra are also present in a/nc-Ge:H Raman spectra with peak frequencies at 540-560cm^{-1} and 1880-1886cm^{-1}.
The peak at $\approx$960cm^{-1} is likely related to Si-O-Si stretching [159]. This Si-O-Si peak is present in all silicon rich samples (a/nc-Si:H, nc-SiGe:H, nc-SiO:H, nc-SiC:H) presented in this work.

Three more wide, overlapping peaks are present in the a/nc-Ge:H Raman spectra that also appear in the a-GeO:H and a-GeC(Sn):H spectra, with peak frequencies at $\approx$340-350cm^{-1}, $\approx$440cm^{-1} and $\approx$540-560cm^{-1}. While the latter is most likely the result of Ge-H wagging, it is challenging to determine the exact origin of former two peaks. Two of the peak frequencies roughly coincide with the amorphous silicon LA and LO modes. It cannot be excluded that during Ge:H plasma processing the heavy Ge-ion bombardment causes some amorphization of the silicon wafer, resulting a thin amorphous silicon layer. These silicon elements would not appear in the EDX measurements, since a low enough acceleration energy was used as to not probe the silicon surface. However, if they feature this strongly in the Raman spectra, Si-H$_n$ or Si-Ge vibrations would be expected in the FTIR and Raman spectra, respectively, but such vibrations are absent. Considering the EDX measurements, Ge-O related vibrations are a more likely origin of the these peaks. Little information is available regarding Raman vibrations in amorphous GeO$_x$. Research into the Raman spectra of quartz-like GeO$_x$ structures indicate that the twisting vibrations of O-Ge-O bonds and Ge-O-Ge bonds appear at 330, 440 and 530cm^{-1} [314]–[316], which coincide well with the peak frequencies in this work. It should be noted that with respect to the quartz-like GeO$_x$ structures, the peaks in this work are wider. This is in line with expectations, since in hydrogenated amorphous structures there is a much greater range of available back-bonded configurations. Another potential origin for the peak at $\approx$540cm^{-1} in the a-GeC(Sn):H Raman spectrum are Ge-C vibrations [288], [295], [300], [317]. The peaks at 1600cm^{-1} and 2800-3000cm^{-1} do in fact indicate the presence of small fractions of C-C and C-H$_n$ bonds in the a-GeC:H sample.

6.1.6 Reflection on the fitting process of heterogeneous group IV alloys

Finally, a reflection on the fitting of vibrational spectra. As discussed in section 6.1.4. the peak frequency is determined by the local X-H dipole density of its corresponding incorporation configuration. The width of the peak is determined by the local distortion in reference to a tetrahdrally coordinated nature of most IV-valence materials. Here we distinguish three possibilities: an amorphous matrix, a crystalline lattice and the interface between amorphous and crystalline phase. The peak widths corresponding to X-H within a fully crystalline nature are narrow (<5 cm^{-1} at full width at half maximum (FWHM)), like seen for the Si-H on hydrogenated crystalline grains, the so-called NHSMs. The X-H vibration modes in an amorphous local environment have the broadest width, for example the LSM and HSM for a-Si:H tissue ($\approx$58 cm^{-1} at FWHM). In between are the hydrogenated volume deficiencies at the border of the amorphous and crystalline phase, reflected by example by the ELSM ($\approx$24 cm^{-1} at FWHM). A consequence of this is that the widths of the peaks are limited to three typical widths corresponding to these three phases. This general guideline of three classes of peak widths is a helpful tool in the determination of the number of Gaussians to be chosen for fitting the spectrum with a physical relevant interpretation. Note, that two peaks for which the difference in their peak frequency is smaller than the width of the two peaks will not result a an unique fitting solution. If this would correspond to a physical reality it would mean that both corresponding dipole vibrations cannot be uniquely resolved. However, even with these specific guidelines, the fitting of vibrational spectra can be subjective, especially with increasing film heterogeneity, so with increasing chemical and structural complexity. This is exemplified by three observations from this work.

1. For the nc-Si:H samples in Fig.6.4**A** it is demonstrated, based on a large set of samples with a wide variety of Si:H phases, that a total of 11 Gaussians should be fitted to account for all potential Si-H stretching modes in the nc-Si:H bulk environment. In Fig. 6.1 a good fit was achieved for nc-Si:H with three Gaussian distributions and a decent fit could be achieved with only two Gaussians. Adding additional Gaussians to the fitting of the sample in Fig. 6.1 would be an arbitrary process, unless the exact number, centre frequency and width of the Gaussians are known. This requires intricate prior knowledge of the material that is to be fitted, which is often not available.

2. Even if extensive prior knowledge is available, simplification during the fitting procedure might be required. In the nc-Si:H Raman spectrum in Fig. 6.1 for instance, six peaks are fitted in the $<$530cm^{-1} wavenumber region; four peaks for the various amorphous phonon modes, a single peak for the c-Si vibrational mode and an additional peak at 510cm^{-1}. The 510cm^{-1} peak accounts for the fact that the exact peak position of a silicon crystal, on a nanometer scale, is crystal-size dependent. A fit true to nature would therefore require a very large number of narrow Gaussians, each representing a particular crystal size. In Fig. 6.1 a single Gaussian is added to compensate for the effect of frequency shift as a function of crystal size, since a single Gaussian (in addition to regular amorphous and crystalline modes) could accurately represent the measured data. However, compensating for this effect in the fitting process is inherently subjective.

3. In section 6.1.3 it was indicated that a large number of vibrations was reported in the 650-950cm^{-1} range in a/nc-Ge(O,C):H films. This multitude of vibrational modes

reported in this range is unsurprising. For these chemically complex alloys, the absorbance in this range is the result of the superimposition of a large number of vibrational modes resulting from different bonding configuration between Ge, C, O and H. This is evident considering, for instance, the vibrational spectra of a-GeO:H and a-GeC:H post deposition, in the insets in Fig. 6.3. In these insets the Gaussians widen and the centre peak frequency shifts under influence of post-deposition oxidation. The reported peak frequency for Ge samples with traces of oxygen, carbon and hydrogen, will therefore not only be a function of the ratio of different bonds present in the material, but also of the assumptions during the fitting procedure regarding baseline subtraction and the number of vibrational modes.

The three examples demonstrate that the fitting of vibrational spectra of chemically and/or structurally complex films can be a subjective process, in which assumptions, prior knowledge and the level of detail of the metrics one tries to obtain from the fitting process plays a role. If, for instance, the purpose is to identify the local configurations of hydrogen incorporation, the spectra need to be fitted with a limited number of Gaussians which all have a physical relevant fixed peak width corresponding to one of the three phases. However, if the purpose is to identify the chemical composition of the bulk, the fitting approach using the lowest number of Gaussians for a unique fit will be sufficient.

6.1.7 Conclusion

In this work, the vibrational modes present in hydrogenated, oxygenated and carbonated group IV alloys are investigated. Raman and infrared spectroscopy measurements are performed in combination with elemental analysis to identify vibrational modes in a unique range of amorphous and nano-crystalline $Si_{X \geq 0}Ge_{1-X}$:H films and their alloys with C, O and Sn. Measurements are performed both post-deposition and following extended exposure to the ambient and DI water. This comprehensive review is of value as a reference for group IV peak identification.

The effect of electrical screening, the influence of the dielectric medium on the peak frequency of a vibrational mode, is illustrated using the experimentally observed frequency shifts of bending, wagging and stretching vibrations of C-H in reference to Si-H, and Si-H in reference to Ge-H. Similar shifts are demonstrated for C-O stretching modes in reference to Si-O and Ge-O. Additionally, all experimentally observed frequency positions of silicon hydride stretching modes in silicon solids and corresponding silicon-hydride configurations are identified using a straightforward Lorentz-Lorenz model approximation and considering all potential hydrogenated volume deficiencies within tetrahedrally coordinated amorphous and nanocrystalline lattice. It shows that the stretching mode signature can reveal detailed information on the volume deficiencies in IV-valence alloys.

6.2 Infrared analysis of catalytic CO$_2$ reduction in hydrogenated germanium

This section is published in *Physical Chemistry Chemical Physics*[†]

Abstract

The oxidation and carbisation kinetics of porous amorphous and nano-crystalline hydrogenated germanium (a-Ge:H and nc-Ge:H) films exposed to ambient air and de-ionized water have been studied using vibration modes observed by infrared spectroscopy. Based on infrared analysis a two-step process of first oxidation by water and secondly carbisation by carbon-dioxide (CO$_2$) is proposed that partly mimics the (photo-)catalytic processes in artificial (photo)synthesis. It is shown that water acts like the precursor for oxidation of porous a-Ge:H and nc-Ge:H in the first step. The incorporation of oxygen in a-Ge:H and nc-Ge:H alloys occurs preferentially at Ge-dangling bonds and not in the Ge-Ge back bond like in hydrogenated silicon alloys (next of kin IV-valence element). The formation of germanium-oxide (GeO) tissue at void surfaces locally creates Ge-alloys with significant lower energy levels for the valence band that can align with the half reaction for water reduction. The heterogeneous nature of a-Ge:H and nc-Ge:H oxidation will result in local catalytic generation of electrons and protons. It is proposed that these charge carriers and ions act as precursors for the second-step reaction based on carbisation that includes both the adsorption of CO$_2$ and formation of CO and formaldehyde.

6.2.1 Introduction

The Intergovernmental Panel on Climate Change climate report 2021 shows that at the end of this century negative CO_2 emissions are required to limit the increase in global temperature to $1.5°C$ in reference to the 1850-1900 period [328]. The electrochemical reduction of CO_2 will likely play an essential role in achieving these negative emissions, as it allows for the synthesis of carbon-based fuels using clean renewable energy and the greenhouse gas CO_2 as feedstock. Where traditionally nano-structured metals are used to drive the CO_2 reduction reaction (CO_2RR)[329]. Recently considerable effort is devoted to the development of heterogeneous catalysts based on earth abundant materials [329]–[332].

The group IV element germanium is such an (relatively) earth abundant material. The elemental abundance of Ge is ≈ 1.8ppm in the earths crust [333], which makes it more abundant then known conventional catalyst materials (Au, Pt, Pd) and noble metal complex based molecular catalysts (Ru, Ir, Re) although not as abundant as elements used for novel metal complexes (Co, Ni, Fe, Mn, Cu) [330]. In this work infrared evidence is presented based on which the the electrochemical reduction of CO_2 to CO, formic acid and formaldehyde in hydrogenated (:H) germanium films is proposed. The Ge:H films are processed using plasma enhanced chemical vapour deposition (PECVD), a technique that is relatively fast, not energy intensive and compatible with processing of photovoltaic devices. This potentially facilitates the use of Ge:H as nano-particles in solutions, or as a photo-electrode in integrated photo-electrochemical or alternative photovoltaic-electrochemical applications [334]–[336].

The post-deposition oxidation by water, and carbisation by CO_2, of hydrogenated germanium films are characterized and potential pathways are proposed for the electrochemical reduction of CO_2 in Ge:H films. Fundamental insight into the reaction rate and type of reaction are provided by monitoring Fourier Transform Infrared Spectroscopy (FTIR) spectra of Ge:H films stored in the ambient and in de-ionized (DI) water, of amorphous (a-) and nano-crystalline (nc-) samples, of unalloyed and alloyed $Ge(Si_x,O_x)$:H samples and of Ge:H samples of different material porosity and chemical stability.

6.2.2 Experimental section

The films presented in this work are processed on 4 inch, n-type Cz 500μm thick monocrystalline silicon wafers. The a/nc-Ge:H films were processed in the Cascade radio-frequency PECVD reactor, which has a circular electrode with a diameter of 160mm and an electrode spacing of 20mm. Cascade is a laminar flow reactor, where germane (GeH_4) and molecular hydrogen are used as precursor gasses. The a/nc-Si_xGe:H and a-GeO_x:H films were processed in a different a radio-frequency PECVD cluster tool, with a flat 12cmx12cm shower-head electrode. The deposition conditions of the processed films, including deposition times and thickness, are reported in Table 6.4. After deposition the wafers were cut in quarter pieces to measure the FTIR spectra as the Ge:H films evolve over time under two storage conditions; in the dark and in DI water.

FTIR spectra were obtained using a Thermo Fisher Nicolet 5700 spectrometer. The spectra were fitted using the Fityk freeware [228]. The background was subtracted manually. In this work, the subscript "n" is used to indicate bonding configurations with 1,2 or 3

Table 6.4: Deposition conditions of the films presented in this work; radiofrequency power (P_{RF}), pressure (p), substrate temperature (T_S) and gas flow rates (F_{gas}). All samples are processed with $F_{H2}=200$ sccm

| | P_{RF} | p | T_S | CO_2-SiH_4 | GeH_4 | Thickness |
	(mW · cm⁻²)	(mbar)	(°C)	(sccm)	(sccm)	(nm)
a-Si$_x$Ge:H	20.8	3.6	180	30	5.3	292.2
nc-Si$_x$Ge:H	20.8	3.6	180	30	0.4	148.1
nc-Ge:H	99.5	3.5	200		0.5	222.6
a-Ge:H	24.9	4	200		0.5	182.6
a-GeO$_x$:H	20.8	3.6	180	20	2	173.8
a-Ge:H-1	49.8	5	280		0.5	121.4
a-Ge:H-2	49.8	5	250		0.5	85.5
a-Ge:H-3	14.9	4	290		2	174.5
a-Ge:H-4	49.8	5	275		1	185.6
a-Ge:H-5	74.6	4	200		0.5	201.2

Table 6.5: Assignment of FTIR peaks, including wagging (W), bending (Be), stretching (St) designation.

Peak position (cm⁻¹)	Suspected bond	vibration	Refs
560-580	Ge-H$_n$	W	[32], [201]
650-950	Ge-O$_x$	St	[201], [255]
1020	C-H$_n$	W	[278], [284]
1100	C-O$_x$	St	[285], [286]
1210-1230	C-H$_n$	W	[274], [280], [285]
1400	C-H$_n$	Be	[268], [274], [286]–[288]
1430-1450	(O$_x$)C-H$_n$	Be	[268], [286], [289], [290]
1660	C=O$_x$	St	[285], [290], [291]
1740	H$_n$C-O$_x$	St	[292], [293]
1875	Ge-H$_n$ **LSM**	St	[32], [201], [262]
1950-2000	Ge-H$_n$ **HSM**	St	[32], [201], [262]
2800-3000	C-H$_n$	St	[278], [284]

hydrides, while the subscript "x" is used to indicate non-stoichiometric materials with an unknown, or varying, material fraction x.

6.2.3 The oxidation and etching behaviour of Ge:H by water

For a full understanding of the oxidation and carbisation behaviour, the evolution of the a/nc-Ge(O$_x$,Si$_x$):H films over time are monitored. The results are presented in Fig.6.6. The vibrational spectra provide some remarkable insight into the chemical stability of the films. For all a/nc-Ge(O$_x$):H samples, independent of storage condition, several distinct vibrational modes appear post-deposition, among which a broad band of vibrations in the 650-1000cm⁻¹ range. This band of vibrations, not present in chemically stable a/nc-Ge:H films, are previously identified as a range of Ge-O and potentially Ge-C vibrations [32], [201].

Notably, while the evolution of the Ge-O vibrations is similar for both storage conditions, i.e. in the dark and in DI water, the evolution of the Ge-H vibrations in water and the ambient is dissimilar. For the samples stored in water, Ge-H wagging and stretching vibrations, at ≈560cm⁻¹ and 1870cm⁻¹, in the FTIR spectra of a/nc-Ge(O$_x$):H films, decrease over time. This indicates that the Ge:H phase is etched when submerged in water,
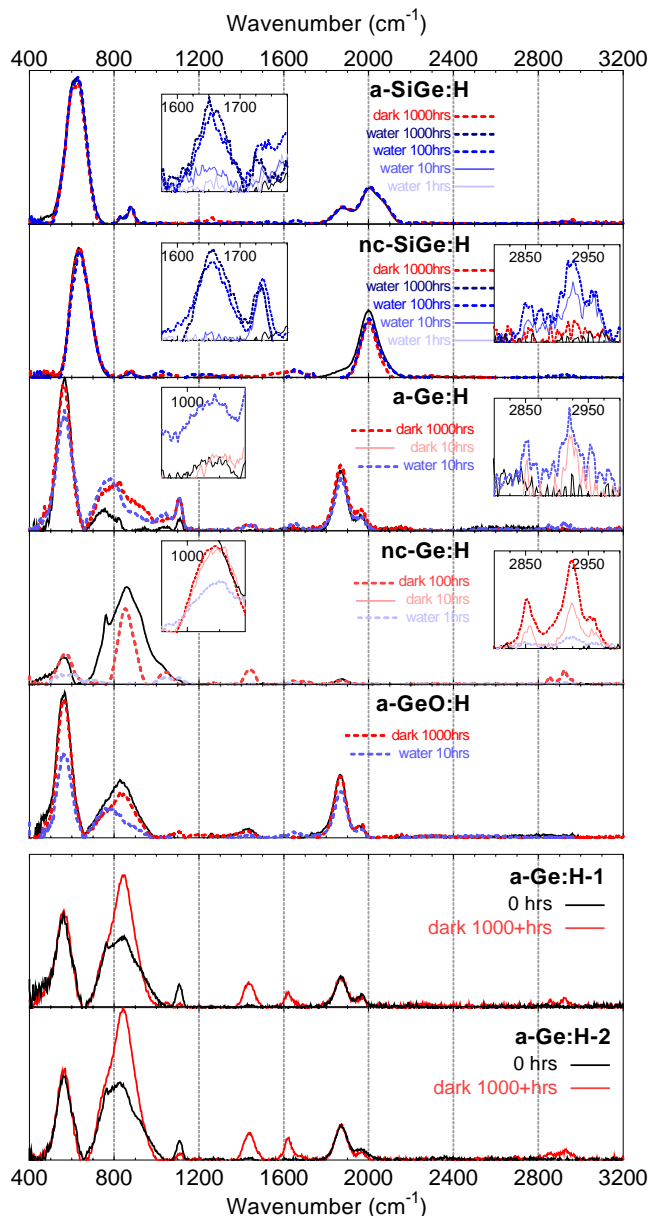
Figure 6.6: FTIR spectra of a/nc-Ge(O$_x$,Si$_x$):H alloys. All curves are presented after background subtraction. The black solid curves represent measurements at 0hrs. The red curves indicate measurements after exposure to the ambient and blue curves indicate measurements after exposure to DI water. Measurements are performed after 1000hrs exposure, unless otherwise indicated in the plot. Deposition conditions of the films are presented in table 6.4.
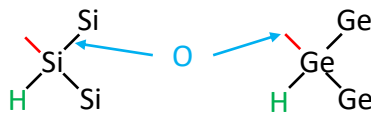
Figure 6.7: Simplified schematic of the favourable position of oxygen in an hydrogenated silicon and germanium structure. Red line represents a dangling bond.

assuming that the Ge-H bonds are to a certain extent homogeneously distributed over the film thickness. This etching of the Ge:H films in DI water, and the consequent reduction in film thickness, was confirmed by measurements using spectroscopic ellipsometry (SE). However, the Ge-H vibration intensity of samples stored in the ambient does not change significantly over the observed 1000+hour period. This can be observed in the FTIR spectra of a-Ge:H-1-2 in Fig.6.6, selected from amongst a dozen similar samples. Nor did SE measurements indicate a decrease in film thickness. This behaviour leads to two important observations.

The first observation is related to the interaction between water and Ge:H. Specifically, the position of the oxygen atom in the amorphous Ge:H phase. The Ge-O vibrations increase without a decrease of the Ge-H vibrations. This means that water will not react with Ge-H bonds and the oxygen atom will not position itself at a site occupied by hydrogen. It also appears unlikely that water will react with a Ge-Ge bond and position itself backbonded to two Ge-atoms, since Raman spectroscopy measurements did not indicate a significant decrease of Ge-Ge vibrations. Additionally, if we consider the oxidation of Si:H, where oxygen is favourably positioned back-bonded to two Si atoms, distinct SiH_2O_2 and $SiHO_3$ modes do appear upon the oxidation, positioned up shifted by about 50-250cm^{-1} with respect to the SiH_2 modes [69], [78], [79]. Similar O_2GeH_2 or O_3GeH stretching modes are not apparent in the FTIR spectra presented in this work. The absence of these modes and the lack of significant change in the observed Ge-Ge and Ge-H bond intensity,in combination with the relatively poor hydrogen passivisation efficiency of dangling bonds in Ge:H in reference to Si:H [199], [200], [337] and the relatively high dangling bond densities that are expected in these films [201], [262], likely indicate that water will react with the Ge-dangling bonds and oxygen will predominantly occupy the Ge-dangling bond position. The different positioning of O in Si:H and Ge:H is schematically shown in Fig.6.7. The favorable positioning of O at the Ge-dangling bond site explains the defect passivating behaviour of oxygen in a-Ge:H films that was observed in earlier work [201]. Additionally, it explains why in a-Ge:H, unlike in a-Si:H, H and O incorporation are reportedly competitive[215], [220].

The second important observation is related to the etching behaviour of Ge:H. The a/nc-Ge:H films of Fig.6.6 are consumed too fast to allow for a detailed investigation of the etching behaviour of Ge:H over time. For that reason, three additional a-Ge:H samples were processed and their degradation in DI water was monitored at much smaller time increments. In previous research it was observed that the degradation behaviour of Ge:H

samples is related to the material density [168], [201]. a-Ge:H-3-5 are therefore processed at conditions resulting in a-Ge:H films with varying porosity and expected chemical stability. The results are shown in Fig.6.8. The refractive index at a wavelength of 600nm ($n_{@600nm}$) is used as a metric for the material density, with a high $n_{@600nm}$ indicating a dense material.

The difference in degradation behaviour of the three a-Ge:H films is significant. The a-Ge:H film with the highest material density first shows a decrease of the Ge-H modes at 40 hours and the first Ge-O vibrations only appear at 100hrs. For the two more porous samples, post-deposition oxidation has already occurred during the 1-2 minute ambient exposure during the transfer from the PECVD reactor to the FTIR measurement setup. Notably, for the a-Ge:H sample with $n_{@600nm}$=4.85, the Ge-O vibrations are decreased after 30s of etching in DI water. This oxidation and etching behaviour indicates the presence of two distinction regions, a porous top region on top of a dense bulk region, for this particular sample. This observation, and the underlying mechanisms, are discussed in more detail elsewhere [262]. After the initial etching of the porous top region, the Ge-H vibrations gradually decrease with respect to the Ge-O vibrations, and after 25 hours only a fraction of the film thickness remained. It can be observed that the oxidation of the porous a-Ge:H film with $n_{@600nm}$=4.63 occurs at a much higher rate.

Fig.6.8 yields more insight into the mechanism involved in the porosity-facilitated etching behaviour. A clear trend is observed between the $n_{@600nm}$ of the a-Ge:H films and the intensity and centre position of the peak at around 1950-2100cm^{-1}. This peak is the result of Ge-H stretching and is referred to as the high stretching mode (HSM). The peak at 1875cm^{-1} is referred to as the Ge-H low stretching mode (LSM). The HSM is seen to increase with respect to the LSM for decreasing $n_{@600nm}$, which has been been reported in earlier work [262]. Compared to hydrogenated silicon alloys [65], [67], HSM vibrations are the result of hydrogen bonded to germanium at the surfaces of nanosized voids. A shift of the peak position towards higher wavenumbers, as observed in a-Ge:H-5 in reference to a-Ge:H-3 and a-Ge:H-4, indicates that the vibrating Ge-H reside at the surfaces of yet larger nanosized voids. Not only does the rate of oxidation increase with the HSM/LSM ratio, the HSM is also reduced much more strongly than other bonds. It is likely that when larger voids are present in the material, water can diffuse into the nano-sized voids present in the bulk. With this in-diffusion, the number of reaction sites that water can access are strongly increased. Consequently, the rate of oxidation, as well the etching rate, increases with increasing void fraction. The pores that facilitate the in-diffusion of water are oxidized first, as demonstrated by the strong decrease of the HSM in the first 30 minutes for sample a-Ge:H-5.

While the oxidation of Ge:H films is observed for both storage conditions, the question remains as to what causes the difference in etching behaviour between samples stored in the ambient and in water. This question has three potential answers. ***1.*** *a difference in reactive species.* In the ambient, O_2 could potentially be the source of oxygen, instead of water. This seems unlikely, since the observed relation between density and stability is likely macroscopic by nature. A dense material prevents the in-diffusion of water and thereby bulk oxidation. A dense Ge:H phase, unlike a porous Ge:H phase, has an average bond length small enough to prevent the in-diffusion of H_2O but not the in-diffusion of
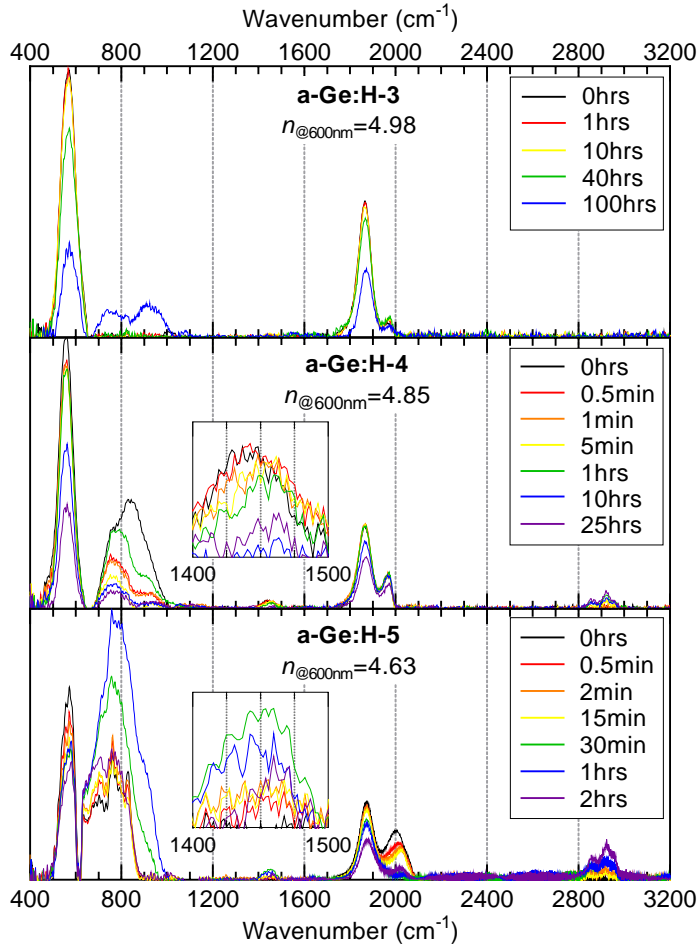
Figure 6.8: Evolution over time of three different a-Ge:H alloys stored in DI water. Samples have varying $n_{@600nm}$, where the high-$n_{@600nm}$ a-Ge:H-3 sample is most dense and the low-$n_{@600nm}$ a-Ge:H-5 sample is most porous. Deposition conditions of the a-Ge:H-3-5 films are reported in Table 6.4.

O_2 [201]. Moreover, if a different species was involved in the oxidation reaction, a more distinct difference between Ge-O signatures could be expected. **2.** *A difference in rate of oxidation*, due to a difference in the concentration of H_2O in the direct environment of the films. While this cannot be excluded, it seems unlikely to be a dominant factor considering that evidence of etching is observed in a-Ge:H-4-5 Fig.6.8 after seconds, while no such evidence is apparent in a-Ge:H-1-2 in Fig.6.6 after 1000+hrs. The most likely explanation then is **3.** *a difference in reaction type.* It is likely that the etching reaction is one requiring the simultaneous breaking of multiple Ge-bonds by H_2O. The multiple bonds should be broken in quick succession, since a competition will exist between the breaking and reconstruction, or cross-linking, of the Ge-bonds. As H_2O will favourable react with the Ge-dangling bond, the etching reaction is unlikely to occur in the absence of abundant water. Alternatively, etching could be the result of a multi-step reaction in which the secondary reaction step, or steps, are not energetically favoured with respect to the first and will therefore only occur if abundant water is present.

6.2.4 Carbisation of Ge:H by CO_2

In addition to the Ge-O vibrational modes, several distinct vibrations appear post-deposition in the Ge:H spectra. Considering a-Ge:H-4-5 in Fig.6.8, the oxidation is accompanied by the appearance, and continuous increase, of C-H_n stretching vibrations in the 2800-3000cm^{-1} range. In fact, the appearance of the C-H_n stretching modes can be observed in all films containing an hydrogenated germanium phase.

This observation indicates the occurrence of a post-deposition process during which carbon is absorbed in the germanium alloys. Additional information as to the nature of this process is provided by the appearance of several distinct vibrational modes. In Fig.6.6 peaks appear at at 1100cm^{-1}, 1230cm^{-1}, 1660cm^{-1} and 1740cm^{-1} in the a/nc-Ge(O_x,Si_x):H spectra. Insets are provided for the a/nc-Si_xGe:H samples in Fig.6.6, to demonstrate the evolution of the peaks as a function of time. After 10hrs the peak at 1740cm^{-1} appears, in concert with the C-H_n stretching modes at $\approx$2850cm^{-1} and 2930cm^{-1}. Following the appearance of these peaks, a vibration appears at 1660cm^{-1}. Additionally, in the a/nc-Ge(O_x):H spectra in Fig.6.6 and in spectra a-Ge:H-4 and a-Ge:H-5 in Fig.6.8, vibrational modes appear at 1020cm^{-1} and 1450cm^{-1} that increase over time in reference to the Ge-H modes.

All of these vibrational modes are the result of different bonding configurations between carbon, hydrogen and oxygen, as indicated in table 6.5. The peak at 1020cm^{-1} is reportedly the result of the C-H_n wagging vibration [278], [284], the peak at 1100cm^{-1} is the result of C-O_x stretching [285], [286], the peaks at 1230cm^{-1} and 1400cm^{-1} are likely the result of C-H_n wagging [274], [280], [285] and bending[268], [274], [286]–[288], respectively. The peak at 1430-1450cm^{-1} is the result of (O_x)C-H_n bending [268], [286], [289], [290], while the peaks at 1660cm^{-1} and 1740cm^{-1} are reportedly the result of different C-O_x [285], [290], [291] and H_nC-O_x [292], [293] stretching modes.

Since samples are stored inside an ISO7 cleanroom and exposed to no other source of carbon than the ambient, the most likely source of carbon in the post-deposition carbisation process is CO_2. All of the CH_yO_z vibrations listed above, where y and z are discrete numbers, can be attributed to the vibrations of CO, HCHO (formaldehyde), HCOOH
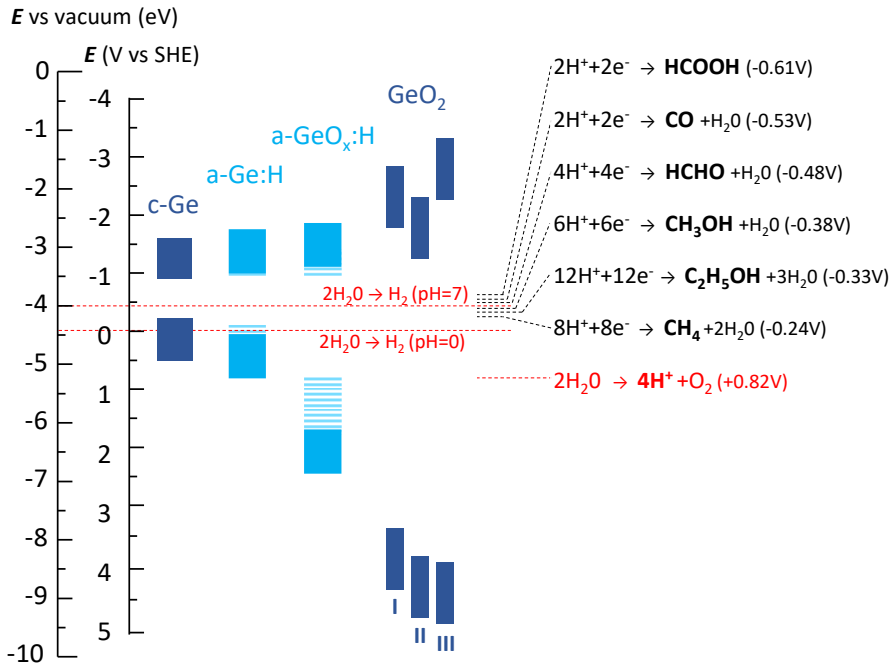
Figure 6.9: Conduction and valence band edges of Ge materials in reference to the vacuum level and standard hydrogen electrode (SHE). The vacuum level and SHE potential are aligned using the absolute chemical potential of electrons under SHE conditions, of -4.44eV [336], [338], [339]. Alignment with respect to the vacuum level of Ge based on [338], [340], GeO$_2$I based on [341], [342], GeO$_2$II on [341], [343], [344] and GeO$_2$III on [345]. Bandgap energy of a-Ge:H estimated to be in the range of 0.9-1.1eV [201]. a-GeO$_x$:H indicates suspected band alignment upon oxidation of a-Ge:H. Dashed areas of a-Ge(O$_x$):H materials indicate suspected band edge variations based on level of hydrogenation and oxidation. The water reduction half reaction at pH=0 and pH=7 are indicated by the red lines, as well as the water oxidation half reaction at pH=7. The electrochemical redox potentials of six different CO$_2$ reduction pathways, vs SHE at pH=7, are indicated by the dashed black lines, including the number protons and electrons required for the reaction [19]–[21], [334], [346].

(formic acid) and H$_3$COH (methanol). Based on these two observations we propose a post-deposition process involving the electrochemical reduction of CO$_2$. This proposition raises 3 main questions: 1. What is the sequence of events resulting the electrochemical reduction of CO$_2$ in Ge:H films? 2. What are the potential adsorption mechanisms for CO$_2$ onto Ge:H? and 3. What type of CO$_2$RR is taking place in the Ge:H films?

Regarding question 1; the sequence of events resulting in CO$_2$ reduction. From the FTIR spectra, especially those of a-Ge:H-1-2, it is apparent that the Ge-O vibrations appear before the numerous CH$_y$O$_z$ vibrations. The presence of the GeO$_x$:H phase in the heterogeneous a-GeO$_x$:H material is therefore likely a prerequisite for the CO$_2$RR. This prerequisite of the GeO$_x$:H phase could potentially be related to the CO$_2$ adsorption mechanisms, which will be considered in the next section. Alternatively, the requirement
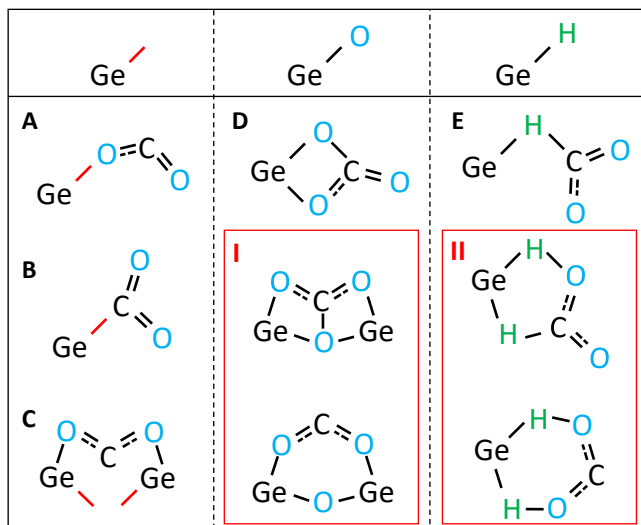
Figure 6.10: Simplified schematic representation of the potential CO2 adsorption mechanisms facilitated by a Ge-dangling bond (left), Ge-O bond (centre) and Ge-H bond (right). Red line represents a Ge-dangling bond. Red boxes **I** and **II** are unlikely routes and are referenced in the text.

of a GeO_x:H phase can be understood if we consider that water splitting potentially provides the necessary protons for the CO_2RR. Consequently, in order for the CO_2RR to occur, the valence band edge should be aligned with the potential for water oxidation and the conduction band edge should be well aligned with the potential for the CO_2RR to formaldehyde. For crystalline Ge, the conduction band edge is already well aligned with the CO_2RR, as can be observed in Fig.6.9. The valence band edge, however, is about 1eV removed from the potential for water oxidation. As it is unlikely that the valence band edge of Ge:H is positioned 1eV below that of the crystalline Ge, we propose that the observed CO_2RR is the result of a 2-step process. In the first step Ge:H oxidizes in a reaction with water, forming GeO_x:H. The bandgap energy of GeO_x:H increases with oxygen fraction. Several studies show that this difference is mainly caused by a downward shift of the valence band edge with respect to the vacuum level, rather than an upwards shift of the conduction band edge [341], [345], [347]. GeO_x:H, therefore, is energetically well suited for the oxidation of water and generation of protons. The second step then involves the adsorption and electrochemical reduction of CO_2. Notably, this process, in which the photo-catalytic oxidation of water provides the protons required for the reduction of CO_2, resulting in the formation of formaldehyde, or other CH_yO_z products, is comparable to photosynthesis and therefore often referred to as artificial photosynthesis [20], [334], [336].

Regarding question 2; the potential adsorption mechanisms for CO_2 onto Ge:H. If we consider the sequence of events, and the bonds present in the FTIR spectra prior to the appearance of the CH_yO_z vibrations, three types of Ge-bonds are available to facilitate CO_2 adsorption. These three bonds are the Ge-dangling bond, Ge-H bond and Ge-O bond. These bonds, and their potential role in facilitating CO_2 adsorption, are schematically shown in Fig.6.10. Of these potential adsorption mechanisms, those positioned in

the red boxes are less likely to occur for varying reasons. The adsorption mechanisms in box **I** requires O to back-bonded to two Ge-atoms, which is unlikely to be the case in a-Ge:H as established in the previous section. The adsorption mechanisms in box **II** requires H to be shared between Ge and O. Such a reaction would very likely result in a change in the Ge-H vibrational modes, a peak broadening or decrease of the peak intensity, that is not observed in the FTIR spectra. Each of the remaining mechanisms, labeled **A-E**, are plausible routes for the CO_2 adsorption in Ge:H, based on the experimental data presented in this work.

Regarding question 3; the type of CO_2RR occurring in Ge:H. There are 6 pathways for electrochemical CO_2 reduction, each resulting in a different reaction product [20], [335], [336], [348]. The different pathways require a different number of electrons and protons. The simplest reactions, the reduction of CO_2 to formic acid or CO, require 2 electrons and protons. Each successive pathway requires two additional electrons and protons, as indicated in Fig.6.9. These are, listed in order of increasing number of charge carriers required, reactions resulting in the formation of CO, formaldehyde, methanol, methane or ethanol.

The peaks observed in the FTIR spectra in this work appear predominantly the result of CO, HCHO and HCOOH vibrational modes. Selectivity for a certain reaction product can be the result of the specific energetic alignment of the conduction band edge with a certain reaction. However, in Ge:H this seems unlikely to play dominant role, since a well-aligned conduction band edge for CO_2 reduction to formic acid and CO should also facilitate the CO_2RR to methane and ethanol as can be observed in Fig.6.9. It is therefore more likely related to the probability of the occurrence of a certain pathway. This probability is directly related to the number of electrons and protons involved in the reaction. The reduction of CO_2 to, for example, ethanol, requires the simultaneous availability of 12 protons and 12 electrons. This reaction is therefore less likely to occur than the formation of formic acid, which only requires two of each charge carrier type. Consequently, we would expect the largest fraction of vibrations to be related to the "simplest" reaction pathways, resulting in CO, formic acid and formaldehyde.

6.2.5 Conclusion

In this work the first ever evidence of the post deposition appearance of CH_yO_z vibrational modes in PECVD processed hydrogenated germanium is presented. It is proposed that the observed carbisation reaction involves the catalytic reduction of CO_2 in Ge:H films to products like CO, formic acid and formaldehyde. A two-step process is proposed, in which the reduction of CO_2 follows the post-deposition chemical transformation of a-Ge:H to a-GeO$_x$:H upon reaction with water. The reaction rate is demonstrated to be a function of the material porosity.

A theory is presented in which the a-GeO$_x$:H phase is essential for energetic alignment of the valence band edge with the water oxidation reaction potential. Protons from water splitting are used for the catalytic CO_2 reduction reaction. Moreover, we demonstrate that the carbisation reaction does not results in the consumption of the catalyst material. However, etching of the Ge:H films does occur during the oxidation of Ge:H, only if the film is submerged in de-ionized water. Many questions remain as to the specific reactions

resulting in the etching of the Ge:H phase as well as the CO_2 adsorption reaction. The authors hope to inspire additional computational and experimental research to validate the theories proposed in this work.

Though many question remain, these findings demonstrate the potential use of a-Ge(O_x):H as an inexpensively processed, relatively earth abundant electro-catalyst or electrode material for photo(voltaic)-electrochemical device applications.

6.3 Opto-electrical properties of group IV elements: the challenges of processing hydrogenated germanium

This section is published in *Advanced Science*[‡]

Abstract

In this paper the opto-electrical nature of hydrogenated group IV alloys with optical bandgap energies ranging from 1.0 eV up to 2.3 eV are studied. The fundamental physical principles that determine the relation between the bandgap and the structural characteristics such as material density, elemental composition, void fraction and crystalline phase fraction are revealed. Next, the fundamental physical principles that determine the relation between the bandgap and electrical properties such as the dark conductivity, activation energy and photoresponse are discussed.

The unique wide range of IV valence alloys helps to understand the nature of a/nc-Ge:H films with respect to the intrinsicity, chemical stability and photoresponse. These insights resulted in the discovery of i) a processing window that results in chemically stable Ge:H films with the lowest reported dark conductivity of σ_d values down to $4.6 \cdot 10^{-4}$ $(\Omega \cdot \mathrm{cm})^{-1}$ for chemical vapour deposited Ge:H films, and ii) O, C and Sn alloying approaches to improve the photoresponse and chemical stability of the a/nc-Ge:H alloys.

6.3.1 Introduction

Semiconductors based on group IV elements are the workhorse of the modern electronics industry. Elements like silicon, carbon, and germanium are used for a range of applications in the fields of micro-electronics [349], optics [350], photonics [351], [352] and photovoltaics (PV).

There are some inherent advantages to the processing of group IV alloys. Group IV elements can form tetrahedral structures, with each valence electron covalently bonded, requiring no other element for the processing of neutral, intrinsic materials. This is unlike other major semiconductor technologies which require elements from different groups for intrinsic processing. Examples are semiconductors based on elements from group III and V and chalcogenides, which use elements from groups II-VI or I-III-VI. These elements have different properties; different radii, electronegativity and melting points, which inherently introduces complexity. This complexity is predominantly expressed in two ways.

First, processing chemically stable materials is fundamentally more challenging. The relation between the complexity of the global chemical system and chemical stability of chalcogenides, for example, has been well documented [353]–[356]. A similar struggle for chemical stability is ongoing in the relatively novel field of the chemically complex perovskites [357]–[360]. A result of the inherent chemical instability of these materials are either potential trade-offs between performance and stability, or more complex and expensive encapsulation on a device level.

Secondly, the inherent complexity is expressed in the processing of these materials. Processing is generally accomplished by exerting great control, using techniques such as molecular beam epitaxy or metal-organic chemical vapour deposition, used for the processing of III-V's, or atomic layer deposition which is used for the processing of certain layers in perovskite solar cells [361], [362]. Alternatively, if deposition techniques are used during which less control is exerted, such as the evaporation-based techniques or sputtering used for chalcogenides, a high temperature anneal step is often required for obtaining a device grade material [354], [355], [363], [364]. Either route can result in time and/or energy intensive, and therefore relatively expensive, processing.

Additionally, with the expected upscaling of certain semiconductor applications, such as PV, in mind, there is elemental abundance to consider. Si and C are among the 12 most abundant elements in the lithosphere, in terms of molar abundance, with Si ranked second [333]. Ge and Sn are also more abundant than elements used for alternative PV technologies, such as indium and arsenic used for III-V's, cadmium, tellurium and selenide used for chalcogenides and elements such as cesium, rubidium, iodine and bromine used for metal halide perovskites [358], [365], [366].

In light of the inherent advantages, a range of plasma enhanced chemical vapour deposition (PECVD) processed hydrogenated (:H) group IV alloys are presented in this work, demonstrating a wide range of bandgap energies. These alloys are based on carbon, silicon, germanium and tin and their alloys with oxygen. The fundamental relation between material elemental composition, density and the opto-electrical properties of the group IV alloys are discussed, based on the 400+ films presented in this work. In particular, the processing of a low bandgap group IV Ge:H material is discussed, in reference to other group IV alloys. Based on our experience processing over 230 Ge:H films, three main

Table 6.6: Deposition conditions of the films presented in this work

	P_{RF} (mW·cm^{-2})	p (mbar)	T_S (°C)	SiH_4 (sccm)	GeH_4 (sccm)	CH_4 (sccm)	$Sn(CH_3)_4$ (duty cycle (-))	H_2 (sccm)	CO_2 (sccm)
SiC:H	20.8	3.6	180	5		10		200	
SiO:H	20.8	3.6	180	5				200	5
a-Si:H-1*	69.3	9	130	1.5-5				200	
a-Si:H-2*	18-20.8	0.7	130-180	40					
nc-Si:H†	277.8	4	180	3.3				120	
SiGe:H	13.9-56	2-6	150-210	30	0.4-5.3			150-200	
GeO:H	20.8	3.6	180		2-4			200	20-70
GeC:H	20.8	3.6	180		2	20-60		200	
Ge:H	12.4-248.7	0.5-6	200-350		0.5-2			100-200	
GeCSn:H	14.9-29.8	1-5	210-290		1-2		20-12000	200	
best a-Ge:H	14.9	4	290		2			200	
best nc-Ge:H	24.8	1	290		1			200	

challenges are identified, related to the material intrinsicity, stability and photoresponse. Finally, two potential pathways are discussed for tackling these challenges.

6.3.2 Experimental section

The Ge:H and GeCSn:H films are simultaneously processed on 4 inch, n-type Cz 500μm thick polished monocrystalline silicon wafers cut in quarters for Fourier Transform Infrared (FTIR) spectroscopy measurements and on 10cm x 2.5cm Corning Eagle XG glass for all other measurements. The Ge:H and GeCSn:H films were processed in the Cascade RF-PECVD reactor, which has a circular electrode with a diameter of 160mm and an electrode spacing that is varied between 10-20mm. Cascade is a laminar flow reactor, where germane (GeH_4) and molecular hydrogen are used as precursor gasses. In addition to these precursors, tetramethyltin (TMT) ($Sn(CH_3)_4$) is used for the GeCSn:H depositions. The TMT, a liquid at room temperature, is evaporated in a separate canister at 70°C. For a fraction of the GeCSn:H samples the TMT flow was diluted in He. Injection of TMT into the reactor is controlled through a valve, similar to those used for atomic layer deposition. For the samples presented in this work, the open time of the valve was varied between 5-10ms while the close time was varied between 100ms and 60s. The ratio of the close time to the open time is referred to as the duty cycle. More detailed experimental information regarding the GeCSn:H films is reported elsewhere [264].

All other films are processed in a separate PECVD reactor, with a flat 12cmx12cm shower-head electrode, on 10cm x 2.5cm Corning Eagle XG glass. The films presented in this work have a thickness of 80-180nm. The deposition conditions of the processed films are reported in Table.6.6.

FTIR spectra were obtained using a Thermo Fisher Nicolet 5700 spectrometer. The FTIR spectra were fitted using the Fityk freeware [228]. The background was subtracted manually. The absorption coefficient of the summed Ge-O$_x$ and Ge-C$_x$ bonds in the 650-1000cm^{-1} wavenumber range (α_{tot}) is used in this work as a thickness independent metric for sum of the relative Ge-O and Ge-C peak intensities. The method for obtaining this metric, as well as examples of representative FTIR and Raman measurements, are reported elsewhere [262].

The thickness, real part of the refractive index at a wavelength of 600nm ($n_{@600nm}$) and optical bandgap energies were determined through spectroscopic ellipsometry (SE).
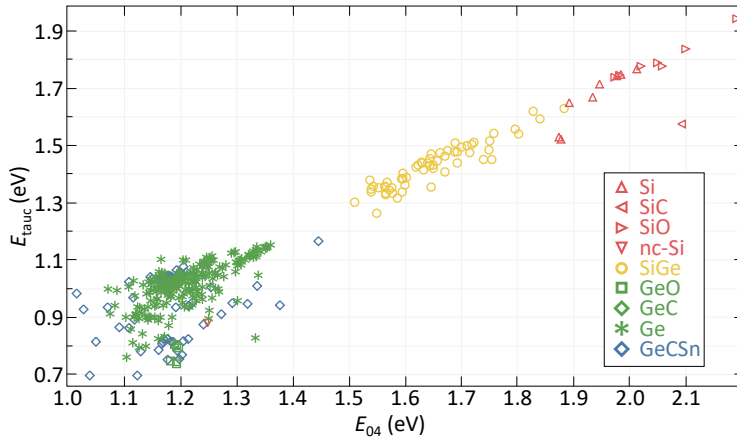
Figure 6.11: Tauc bandgap energy as a function of the E_{04} optical bandgap energy of a range of hydrogenated group IV alloys

The SE measurements were fitted using a Cody-Lorentz model. Determining the electrical bandgap energy of the amorphous and nano-crystalline stoichiometric and non-stoichiometric hydrogenated group IV alloys presented in this work is a non-trivial and potentially arbitrary process. For that reason, the E_{04} optical bandgap energy is used in this work to describe trends in the optical absorption of the films. E_{04} was determined by calculating the photon energy at which the absorption coefficient equals $10^4 \mathrm{cm}^{-1}$. Based on mean square error analysis, the E_{04} has an error margin of $\pm 0.004 \mathrm{eV}$. Additionally, the Cody-Lorentz optical bandgap energy ($E_{\mathrm{C\text{-}L}}$) was obtained from the fitted SE model. The relation between E_{04} and $E_{\mathrm{C\text{-}L}}$ is shown in Fig.6.11, from which it can be observed that the trend, as a function of elemental composition, is largely similar and that the $E_{\mathrm{C\text{-}L}}$ is roughly 0.2eV lower than E_{04}. The larger spread for the Ge:H films and alloys is likely a result of the large degree of heterogeneity between samples in terms of oxidation and carbisation states and amorphous and crystalline material phase fractions.

For the dark- and photo-conductivity measurements, parallel 500nm Al electrodes were evaporated onto the films. The dark conductivity at room temperature was determined by measuring the current at a fixed voltage of 10V, in a dark environment, at different temperatures ranging from 130°C to 60°C in 5°C decrements. From this measurement the activation energy of the films was also calculated, using the Arrhenius equation. The photoconductivity (σ_{ph}) was calculated by measuring the current at a fixed voltage of 10V, using an AM1.5G solar simulator at an illumination of $100 \mathrm{mW \cdot cm^{-2}}$ and a controlled temperature of 25°C. For the σ_{d} and σ_{ph} measurements, 4 different sets of contacts were measured on a single film. The resulting dark conductivity values showed a maximum error margin of about $\pm 11\%$, while the E_{act} values showed a maximum error margin of $\pm 9 \mathrm{meV}$.

6.3.3 Why different group IV alloys

With the hydrogenated group IV alloys presented in this work a wide range of E_{04} are achieved, ranging from about 0.9eV for the high $n_{@600nm}$ Ge:H films to about 2.2eV for the low $n_{@600nm}$ SiO:H film, as presented in Fig.6.12. The refractive index can be considered a metric for material density, as was previously demonstrated for hydrogenated silicon [65]. Consequently, the films with the highest density are those with the lowest bandgap energy.

The opto-electrical properties of hydrogenated group IV elements are the result of the structural characteristics of the films, which in turn are a result of the parameters like the substrate type used for deposition, deposition technique and deposition condition. In this section, the high level relations between the structural and opto-electrical characteristics are addressed. For the films presented in Fig.6.12 more information about the relation between the processing conditions and structural characteristics, as well as more detailed structural investigation of the films, is provided for GeCSn [264],Ge [201], [262], [265], [367], SiGe [156], [262], SiO [201].

From these collective works, three structural characteristics through which a change in density can be realized. For two of these mechanisms trendlines have been added in Fig.6.12. The first effect, indicated by trendline **I**, involves the elemental composition. The use of larger, higher-period elements will result in lower bandgap energies. This effect, long established in III-V semiconductors [368], [369], occurs because larger elements generally results in larger averaged bond lengths (lattice constants) resulting in smaller overlap of the orbital of the valence electrons. As a consequence, splitting of the sp3 anti-bonding and bonding level, the chemical origin of the bandgap, is reduced and bandgap energies are decreased. Considering group IV elements, it can be observed that the bandgap energy of SiC>Si>SiGe>Ge>GeCSn. Similar, more detailed, observations have been reported before in relation of the stoichiometry of two-element group IV alloys such as SiGe:H [156], [187], [189] and SiC:H [256], [273].

The second set, trendlines **II**, indicate a change in the $n_{@600nm}$ and E_{04} as a function of void fraction, or porosity. In these hydrogenated amorphous materials, nano-sized voids are present in the material at sites where multiple C, Si or Ge atoms are missing. We have reported before on the relation between void fraction and bandgap energy in Ge:H and SiGe:H [262] as well as in a-Si:H [70]. It should be noted that the relation between the void fraction, or porosity, and E_{04} in amorphous materials is often reported as a relationship between the hydrogen concentration and the bandgap energy. Indeed, the two properties are often related; as the void fraction is increased more dangling bond sites are available for hydrogen to attach to. Moreover, the void fraction is often determined using specific hydrogen vibrational modes as a metric [65], [189], [196], [222], [262]. However, using a-Si:H it was demonstrated [68] that for similar hydrogen concentration dissimilar void fractions, bandgap energies and absorptive behaviour can be realized. The volumetric compressive nature of the amorphous matrix as a function of the density, distribution and size of nano-sized voids determines the absorptive nature, and by extension the bandgap energy, of amorphous materials [70]. The fraction of dangling bonds occupied by hydrogen, and consequently the hydrogen concentration, will influence this compressive nature. The notion that trendlines **II** in Fig.6.12 is the result of a change in hydrogen concentration would therefore be an oversimplification.
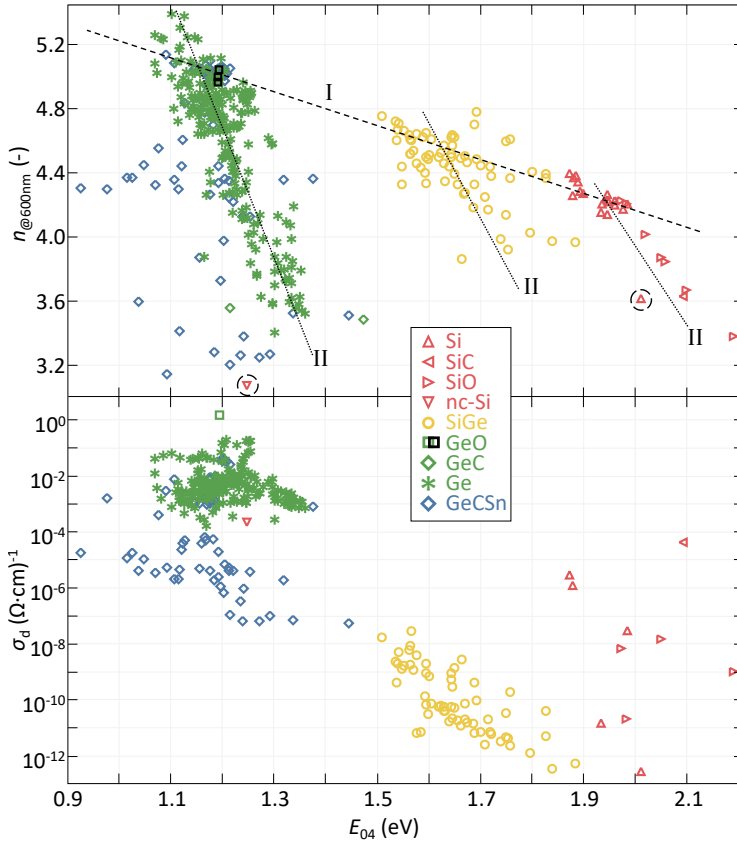
Figure 6.12: $n_{@600\mathrm{nm}}$ (top) and σ_{d} (bottom) as a function of the E_{04} optical bandgap energy of a range of hydrogenated group IV alloys. Trendlines **I** and **II** in top plot are referenced in text. GeO samples represented by black squares in top plot for improved identification.

Finally, the third mechanism for realizing a change in E_{04} involves the crystalline phase fraction. This is essentially an extension of the previous observation, as the crystalline phase is the most dense bonding configuration for atoms and consequently has the lowest bandgap energy. This can be observed considering the dashed circles in Fig.6.12(top), where the nc-Si sample at around 1.25eV has a bandgap energy of about 0.75eV below that of its porous a-Si:H counterpart. The presence of a crystalline phase results in a heterogeneous material in which the amorphous phase and crystalline phase each retain their respective opto-electrical properties, making interpretation more challenging.

In Fig.6.12 (bottom), the σ_{d} can be observed to decrease with increasing E_{04}. In fact, the σ_{d} of the most silicon rich SiGe:H samples and Si:H samples is about 10 orders of magnitude lower than that of most of the Ge:H samples. This relation is not unexpected. The σ_{d} is a result of the charge carrier concentration and mobility. At a given temperature, the intrinsic carrier density (n_{i}) will increase with decreasing E_{G}, as described in Eq.8.1. Low E_{G} materials will therefore have a higher σ_{d}. Alternatively, the relation
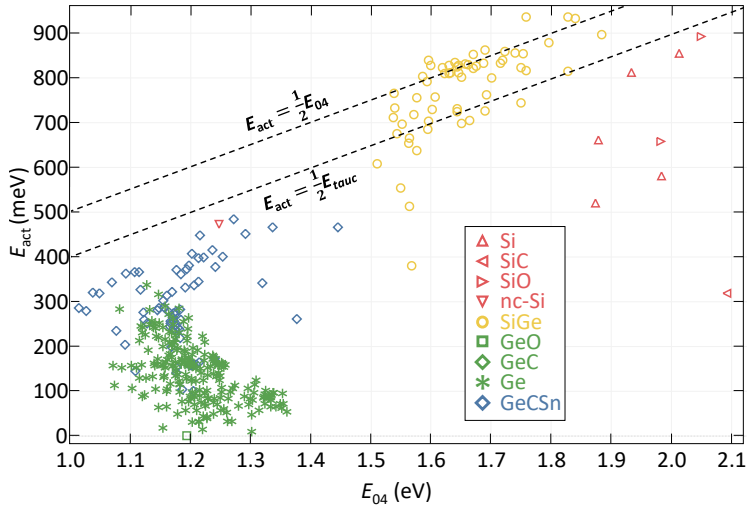
Figure 6.13: E_{act} as a function of the E_{04} of a range of hydrogenated group IV alloys. Trendlines are added to indicate an intrinsic material, based on the E_{04} and $E_{\text{C-L}}$. For the $E_{\text{C-L}}$ trendline the assumption $E_{\text{C-L}} = E_{04} - 0.2\text{eV}$ is used, based on data presented in Fig.6.11.

between the E_{G} and σ_{d} can be understood through Eq.8.2. For intrinsic materials, where $E_{\text{act}} \approx 0.5 E_{\text{G}}$, the σ_{d} will exhibit an exponential increase with decreasing E_{G}. Despite this inherent relation between E_{04} and σ_{d}, for the GeCSn:H films σ_{d} values are obtained that are 2-3 orders of magnitude below that of the Ge:H films, for similar E_{04}. Considering the Ge:H sample size and extent of variations in processing conditions, this indicates some inherent challenges in the processing of Ge:H films.

$$n_{\text{i}}^2 \sim \exp\left(\frac{-E_{\text{G}}}{k_{\text{b}}T}\right) \tag{6.3}$$

$$\sigma_{\text{d}} = \sigma_0 \exp\left(\frac{-E_{\text{act}}}{k_{\text{b}}T}\right) \tag{6.4}$$

6.3.4 The challenges of processing Ge:H

Intrinsicity of Ge:H

Ideally, group IV elements used as absorber materials in p-i-n or n-i-p junctions should be intrinsic. In intrinsic materials the concentration of electrons and holes are roughly equal. If the concentration of one charge carrier type exceeds the other, the recombination probability of minority charge carriers increases and consequently the probability of successful electron-hole pair collection decreases. It should be noted that for optimal operation, when used in a PV device, the absorber could be made slightly p-type to compensate for the lower hole mobility in reference to the electron mobility for these amorphous materials [370]. The activation energy (E_{act}) of the group IV alloys are shown in Fig.6.13. The E_{act} in this work is defined as the difference between the Fermi level and the nearest band edge. An intrinsic material is one where the Fermi level is positioned halfway the
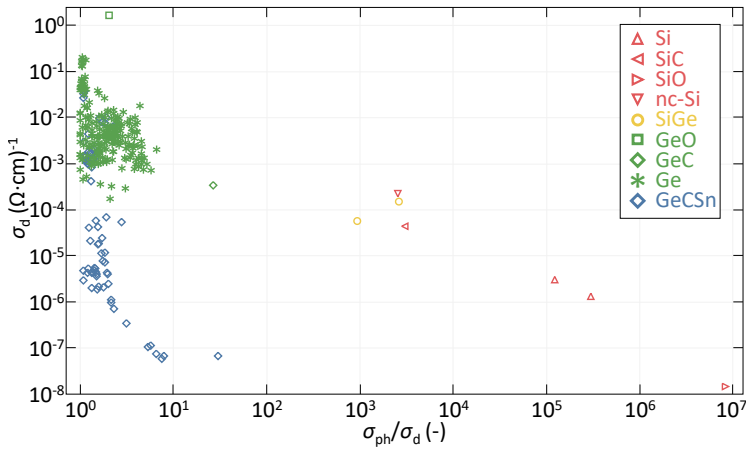
Figure 6.14: σ_{d} as a function of the $\sigma_{\mathrm{ph}}/\sigma_{\mathrm{d}}$ ratio, of a range of hydrogenated group IV alloys.

bandgap, so with $E_{\mathrm{act}} \approx 0.5 E_{\mathrm{G}}$. Two lines are plotted in Fig.6.13, indicating the E_{act} of an intrinsic film based on the E_{04} and $E_{\mathrm{C\text{-}L}}$. It can be observed that not all of the Si(Ge,O):H films are intrinsic. The non-intrinsic behaviour in these undoped films is the result of the energetic nature of the defects and has been linked to the fraction of nano-sized voids in the material and the hydrogen concentration [306], [371]. Additionally, the elemental composition of the alloys can influence the type and presence of majority charge carriers [196], [239]. Nonetheless, for all Si(Ge,O):H alloys, films are presented that either are intrinsic, or very close to intrinsic. This is unlike Ge:H. None of the 200+ Ge:H films, processed under a wide range of conditions, are intrinsic. Rather, the films have an n-type nature [201], [219], [223].

Photoresponse of Ge:H

An additional challenge is related to the low $\sigma_{\mathrm{ph}}/\sigma_{\mathrm{d}}$ of the Ge:H films in reference to the other group IV alloys. The $\sigma_{\mathrm{ph}}/\sigma_{\mathrm{d}}$ ratio of the Ge:H films does not exceed a value of 5, as can be observed in Fig.6.14. This is in line with the few other reports of CVD processed Ge:H films the authors are aware of, where the $\sigma_{\mathrm{ph}}/\sigma_{\mathrm{d}}$ ratio did not exceed 1.1 [32], [187].

The low $\sigma_{\mathrm{ph}}/\sigma_{\mathrm{d}}$ is largely a fundamental effect. As discussed earlier, upon a decrease of E_{G} the σ_{d} is increased exponentially. If we assume intrinsic materials with $E_{\mathrm{act}}=0.5 E_{\mathrm{G}}$ and $E_{\mathrm{G\,a\text{-}Si}}=1.8$, and $E_{\mathrm{G\,a\text{-}Ge}}=0.9$eV, the $\exp\left(\frac{-E_{\mathrm{act}}}{k_{\mathrm{b}}T}\right)$ term in Eq.8.2 would increase by 8 orders of magnitude. σ_{ph}, which is basically σ_{d} augmented by conductivity that is the result of photo-generated charge carriers, will undergo a similar increase. Additionally, when E_{G} is decreased, a larger fraction of photons can be absorbed from the solar spectrum, which affects the photoconductivity. This effect is less and less however, when the E_{G} is further decreased, since the solar spectral irradiance decreases exponentially for $E_{\mathrm{G}} \geq 1.82$eV, as described by Planck's law. If, for example, the E_{G} is decreased from that of a-Si:H to that of a-Ge:H, the photon flux available in the AM1.5g solar spectrum is increased from $1.3 \cdot 10^{21} \mathrm{s}^{-1} \cdot \mathrm{m}^{-2}$ to $3.3 \cdot 10^{21} \mathrm{s}^{-1} \cdot \mathrm{m}^{-2}$, by a factor of about 2.5. As the

exponential increase of both σ_{ph} and σ_{d} far exceeds the individual near-linear increase of σ_{ph} by orders of magnitude, the ratio of the σ_{ph} to σ_{d} will decrease strongly with decreasing E_{G}. The low $\sigma_{\mathrm{ph}}/\sigma_{\mathrm{d}}$ of Ge:H can fundamentally be understood to be lower than that of Si(Ge,C,O):H. It is unlikely however that $\sigma_{\mathrm{ph}}/\sigma_{\mathrm{d}}$ is fundamentally limited to the degree observed in Fig.6.14 and [32], [187]. Improvement could potentially be achieved through improved intrinsicity and decreased defect density, as will be discussed in section 6.3.5.

Stability of Ge:H

A final challenge is related to the chemical stability of the Ge:H films. It was demonstrated in earlier work that for the majority of the processed samples, for a very large part of the processing window, a signature in the FTIR spectra appeared within minutes after deposition, that is related to the post-deposition oxidation of the Ge:H films [201]. We argued that this post-deposition reaction is related to the microscopic properties of the Ge:H films. In subsequent work, we found that post-deposition not only an oxidation reaction occurred, but also a carbisation reaction [262], [367], which likely involves some form of catalytic CO_2 reduction. We demonstrated that the rate of oxidation is directly related to the density of the material and specifically the fraction of nano-sized voids in the material [265]. These collective works have also provided some insight into possible routes to processing stable Ge:H films with favourable opto-electrical properties.

6.3.5 Potential solutions for processing Ge:H

In processing over 230 Ge:H films, using the wide range of deposition conditions reported in table 6.6, three main challenges were identified. These challenges for processing device quality Ge:H are related to the intrinsicity, photoresponse and stability of the films. In this section, two potential pathways are considered to resolve these challenges. The first pathway concerns a very specific processing window, while the second involves alloying of Ge:H.

The right processing window

In Fig.6.15 the $n_{\mathrm{@600nm}}$ is plotted as a function of α_{tot}, the metric used to indicate chemical instability in the processed films. As expressed in section 6.3.2, α_{tot} is a film-thickness independent metric, obtained from infrared measurements, that indicates the absorption by oxide and carbide bonds that are formed post-deposition. The figure shows that with increasing $n_{\mathrm{@600nm}}$, with increasing material density, the stability of the material is increased, as reported earlier [201], [262], [265]. More importantly the figures show that a decrease of the electrode distance (e_{D}), an increase of T_{S} and a decrease of the P_{RF} each result in the processing of denser, and consequently more stable, films. Moreover, the most stable films, with $\alpha_{\mathrm{tot}} \approx 0$ and $n_{\mathrm{@600nm}} \geq 5.2$ are processed when all three conditions are met.

 The relation between increased deposition T_{S} and improved stability is one we reported on in more detail in earlier work [262]. In that work, a mechanism was proposed in which temperature induced densification is achieved through a process that involves the retroactive restructuring and densification of the (sub-)surface region during material growth.
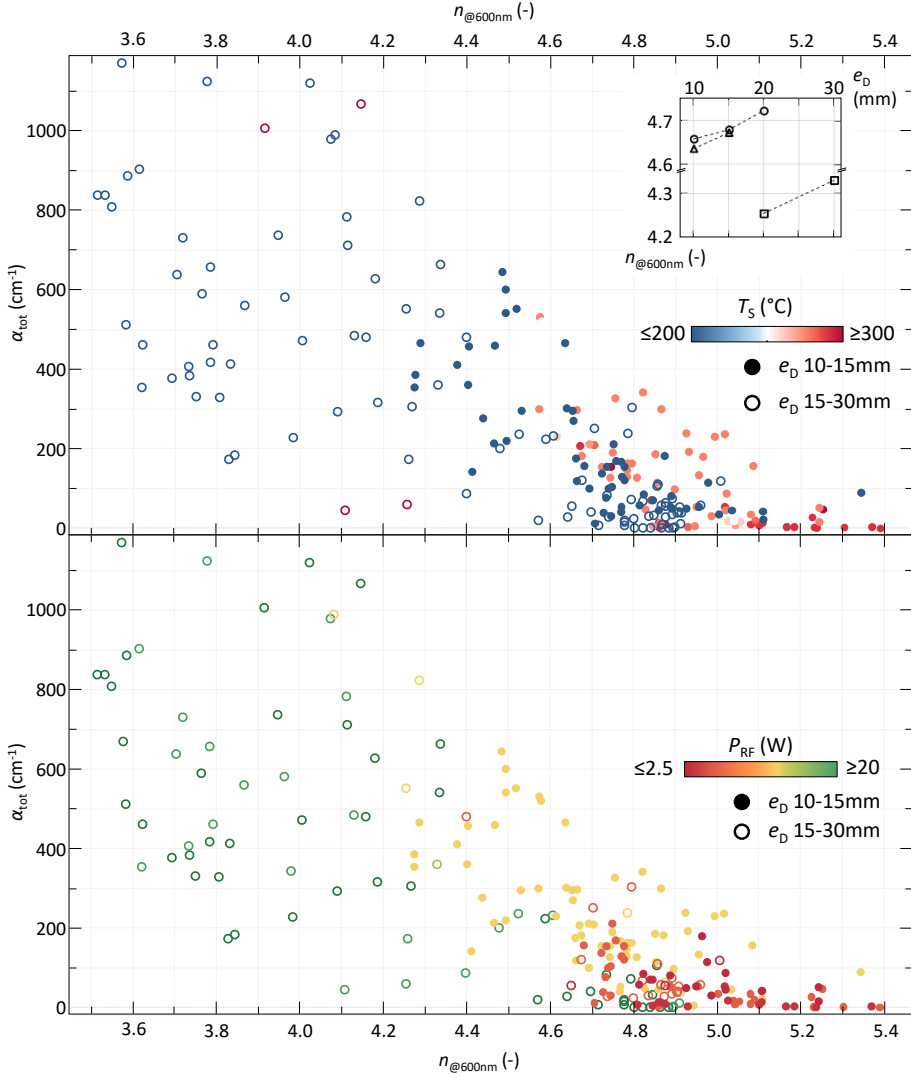
Figure 6.15: α_{tot} as a function of $n_{@600\text{nm}}$ for all Ge:H films. Closed icons and open icons indicate samples processed with $e_{\text{D}} \leq 15\text{mm}$ and $e_{\text{D}} > 15\text{mm}$, respectively. Colour indicates T_{S} (top) and P_{RF} (bottom). Inset shows $n_{@600\text{nm}}$ as a function of e_{D} for three sets of samples, processed under different conditions. Deposition conditions within each set, indicated by the dashed lines, are kept constant.

The region undergoing restructuring has been referred to as the growth zone [139], [254]. Growth zone densification is likely the result of the virtual movement of small voids towards the surface upon continued plasma exposure, and has earlier been observed amorphous silicon [66], [67].

A clear correlation can be observed between the e_D and the chemical stability. Two observations can be made in this regard. The first observation is related to the fraction of samples with $n_{@600nm} \leq 4.4$, which are predominantly samples processed at $e_D \geq 15$mm. This observation is likely related to the fact that a much larger deposition parameter space (eg. a wider range of P_{RF}, p and precursor gas flows) was explored at $e_D \geq 15$mm, resulting in a larger fraction of samples processed at sub-optimal conditions and more porous unstable films.

The second observation is related to the highest $n_{@600nm}$ values obtained for stable films, with α_{tot} roughly ≤ 50cm^{-1}, at $e_D \geq 15$mm with respect to those obtained at e_D¡15mm. The largest $n_{@600nm}$ at larger e_D is just over 4.9, while that of a smaller e_D is almost 5.4. This relation between α_{tot} and $n_{@600nm}$ will be addressed in more detail further along this section.

The relation between the e_D and increased $n_{@600nm}$ is an indirect one. For three sets of samples where e_D was decreased with all other conditions kept constant, instead of an increase, $n_{@600nm}$ was observed to decrease slightly with decreasing e_D, as can be observed in the inset in Fig.6.15(Top). Smaller e_D allows for processing at lower P_{RF} and higher pressure, in a regime referred to as the high pressure depletion regime [69]. It is apparent from Fig.6.15 that processing at relatively low power is a prerequisite for dense and stable Ge:H films.

As to the relation between P_{RF} and $n_{@600nm}$, there are three main ways in which P_{RF} can affect material growth. The first two are related to precursor gas dissociation. An increase of deposition power results in more effective precursor gas dissociation and consequently in a larger GeH$_x$ growth flux. This generally results in a higher deposition rate and more porous growth. Additionally, if more than one precursor gas is used, the balance of radicals in the growth flux could be upset by a change in deposition power. Stronger bonds require more energy for dissociation. As a consequence, with increasing P_{RF} the dissociation of stronger bonds is increased, in relative terms, in reference to the dissociation of weaker bonds. For Ge:H processing H$_2$ and GeH$_4$ are used. The former has a bond dissociation energy of 436 kJ/mol [372], while breaking the bond of a single hydrogen atom from the latter only takes about 340-360kJ/mol [373]–[375]. A relative increase of atomic hydrogen in the growth flux, in reference to GeH$_x$ radicals, can therefore be expected with increasing P_{RF}.

Both these mechanisms can also be realized through changes in other deposition conditions. An overall growth flux increase can be realized through an increase of p and changes in the growth flux composition can realized by varying the ratio of F_{GeH4} to F_{H2}. Both of these mechanisms undoubtedly play a role. Indeed in earlier work an improvement of the stability of Ge:H films was demonstrated by tuning the ratio of the precursor gasses F_{GeH4}/F_{H2}, and p [201]. However, the most dense and stable films in Fig.6.15, with $n_{@600nm} \geq 5$, are processed at a relatively large range of p, from 1-4mbar, and F_{GeH4}/F_{H2}, from 0.25%-1%. As these two conditions are not indicative of a dense film,
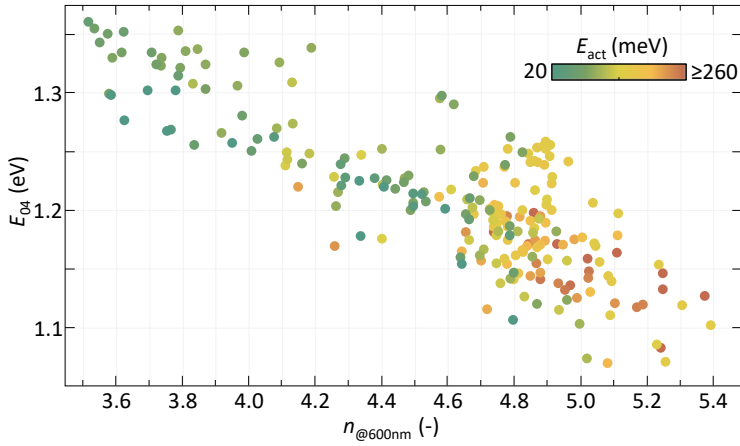
Figure 6.16: E_{04} as a function of $n_{@600nm}$ for all Ge:H films. Colour indicates E_{act}.

and P_{RF} is, the relevant mechanism in this range is likely energetic ion-bombardment. The processing of dense films under low-energetic ion-bombardment conditions is not in line with earlier reports on Ge:H[32] and SiGe:H [156] films, where the beneficial effect ion-bombardment induced densification was reported.

From this we conclude that the most dense Ge:H films are processed under conditions that result in low-energetic ion bombardment, where densification is achieved through temperature induced restructuring of the growth zone. These conditions are facilitated by a small electrode distance, as a power-threshold is required for a stable plasma and a smaller electrode facilitates a stable plasma at lower powers.

A relation has been established between the $n_{@600nm}$, and by extension the material density, and stability of Ge:H films. In addition to being stable, the films should be intrinsic and have a low E_G. In Fig.6.16 the relation between $n_{@600nm}$, E_{04} and E_{act} is presented for all Ge:H films. A decrease of E_{04} can be observed with increasing $n_{@600nm}$ for the Ge:H films, similar to the trend observed in Fig.6.12 for all hydrogenated group IV alloys. The E_{act} can be observed to generally increase with increasing $n_{@600nm}$. This trend is somewhat counter-intuitive, since the difference between an intrinsic Fermi energy level and the nearest band-edge logically decreases with decreasing E_G. The increasing E_{act} with increasing $n_{@600nm}$ is the result of two reactions. First, the activation energy of Ge:H films decreases upon post-deposition oxidation [201], as the GeO$_x$ has a strong n-type nature [215]. This effect is predominantly visible for samples with $n_{@600nm} \leq 4.9$. Additionally, in earlier work it was demonstrated that the n-type defect density, and consequently E_{act}, scales with the concentration of nano-sized voids in Ge:H [262]. A smaller concentration of nano-sized voids therefore results in denser films with higher E_{act}, despite lower E_{04}.

Only for samples with $n_{@600nm} \geq 5.2$, in the absence of the post-deposition oxidation and negligible void fractions, is the intuitively understood decrease of E_{act} with E_{04} reflected. The decrease of E_{04} in this range is predominantly the result of variations in the crystalline phase fractions, as discussed in more detail elsewhere [262].

The right processing conditions, reported in table 6.6, yield dense and stable a/nc-Ge:H films. Additionally, it can be observed that the σ_d generally decreases with decreasing P_{RF} and increasing T_S. This effect can predominantly be observed in the inset of Fig.6.17(top), in which unstable films are omitted. The dashed lines in Fig.6.17 indicate the position where $\sigma_{ph}/\sigma_d=1$. The conductivity values of most films are positioned near this line, indicating that σ_{ph} scales with σ_d. Surprisingly, the improved σ_d for the dense Ge:H films σ_d does not result in higher σ_{ph}/σ_d.

Low σ_d values are realized by stable as well as oxidized Ge:H films. Moreover, the largest σ_{ph}/σ_d ratios, those that deviate most from the dashed line, are achieved by oxidized Ge:H samples, as can be observed in the inset of Fig.6.17(bottom). The higher photoresponses, and relatively low σ_d for certain oxidized samples, are achieved despite much lower E_{act}.

The σ_d can be considered a function of the defect density, represented by the recombination parameter σ_0 in Eq.8.2, and the position of the defect energy levels with respect to the nearest band edge, represented by E_{act}. The fact that low σ_d values are achieved for oxidized Ge:H samples, with much lower E_{act} than the stable Ge:H samples, must mean that even the densest Ge:H samples have a relatively high defect density. A defect density that is much decreased in the oxidized Ge:H samples. This effect, a reaction in which oxygen introduced in the material post-deposition results in the passivation of defects, decreasing the defect density as well the E_{act}, has been discussed in more detail in earlier work [201].

A relatively large defect density in the Ge:H films would also explain the poor photoresponse of the Ge:H films and improvement of σ_{ph}/σ_d upon oxidation. The low photoresponse indicates that only a small fraction of photo-generated charge carriers are collected. This means that the carriers recombine between the generation and collection event. The recombination process is a defect-assisted recombination process, considering the amorphous nature of the materials. A decrease of the defect density would consequently facilitate an increase of the σ_{ph} with respect to the σ_d.

In amorphous silicon, hydrogen is responsible for the passivation of defects. The germanium films in this work are hydrogenated and the Ge:H films with $n_{@600nm} \geq 5.0$ have a hydrogen concentration in the range of 3-5%. This is in the same range as the hydrogen concentration in relatively dense Si:H films [65], [71]. If the concentration of hydrogen in both materials is similar, why then is the degree of defect passivation not? A potential explanation is provided by studies concerning the nature of defects in c-Ge and the behaviour of hydrogen in c-Ge. Several studies show that the dangling bonds in Ge, unlike in silicon, are exclusively negatively charged [243], [340]. Interstitial hydrogen in germanium is also exclusively negatively charged [243], [340], or at least never positively charged [337], which is also unlike silicon. As a consequence, hydrogen passivation of the germanium dangling bond is very ineffective. It should be noted that these studies are performed on c-Ge, not on a/nc-Ge:H. Nevertheless the described behaviour is in good agreement with the trends observed in this work, related to the hydrogen concentration and defect passivation behaviour of hydrogen in Ge:H inferred from the σ_d and σ_d trends. Additionally, the results suggest that oxygen, unlike hydrogen, readily passivates the Ge dangling bonds.
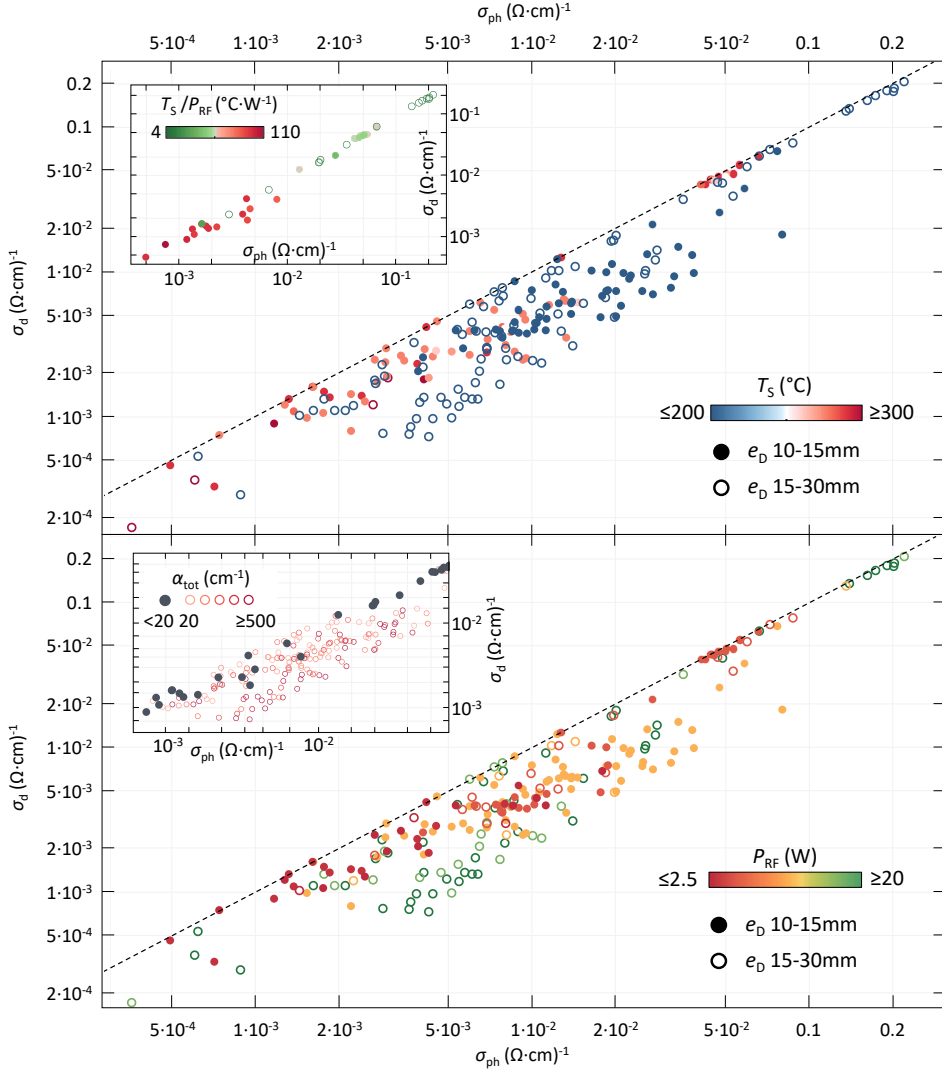
Figure 6.17: σ_{d} as a function of σ_{ph} for all Ge:H films. Closed icons and open icons indicate samples processed with $e_{\mathrm{D}} \leq 15$mm and $e_{\mathrm{D}} > 15$mm, respectively. Colour indicates T_{S} (top) and P_{RF} (bottom). The top inset exclusively shows stable films ($\alpha_{\mathrm{tot}} < 20$), while colours indicate $T_{\mathrm{S}}/P_{\mathrm{RF}}$. In bottom inset the colours and icon type indicate α_{tot}.
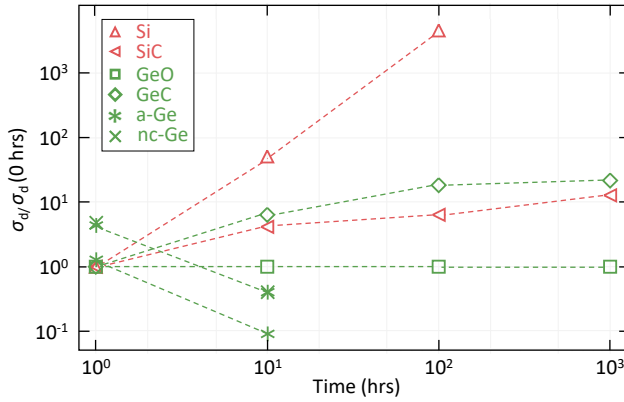
Figure 6.18: Development of the σ_d for a range of group IV alloys as a function of time stored in de-ionized water.

Considering i) the poor passivation behaviour of atomic hydrogen in Ge:H, ii) the observed change in conductive behaviour upon oxidation of Ge:H films and iii) the increase of E_{act} for denser Ge:H films, a decrease in defect density is the most likely cause for changes in σ_d in chemically stable a-Ge:H films. A low σ_d can therefore be considered indicative of good intrinsic a-Ge:H films. It should be noted that the lowest σ_d values reported in Fig.6.17 are 1-5 orders of magnitude lower than those reported for all other known a/nc-Ge:H films [33], [218], [219], [239], [252], [253], processed by chemical vapour deposition techniques, to the best of the authors knowledge.

GeX alloys

The notion that oxygen is able to passivate defects in Ge:H allows for another approach to tackling the intrinsicity, stability and photoresponse related challenges in the processing of Ge:H, namely alloying. The results of the preceding section indicate that through alloying, through the introduction of elements or compounds that can passivate Ge-defects, the photoresponse can be improved. Similar improvements to the photoresponse can be observed through alloying with carbon and silicon, although these effects can at least partly be ascribed to the relation between E_G, E_{act}, and σ_{ph}/σ_d, described in section 6.3.4, as alloying with O,C and Si inevitably results in an increase of E_G.

To investigate the influence of Ge:H alloying on the stability, a number of GeX:H and SiX:H alloys were stored in de-ionized (DI) water and the evolution of the opto-electrical properties were monitored over time. The electrical properties, which proved most sensitive to degradation, of the films are presented in Fig.6.18. The figure shows σ_d of the films, measured after 1-10-100-1000 hours in DI water, in reference to the initial measurement prior to water exposure. It can be observed that a decrease of the σ_d upon water exposure occurs exclusively for the a/nc-Ge:H samples. For Si:H and the different alloys σ_d increases over time. This indicates that exclusively for a/nc-Ge:H the oxidation improves the electrical characteristics of the films, as discussed in [201], [262]. Moreover, the a/nc-Ge:H films are fully etched in de-ionized water in the 10-100hrs period. The

reactions involved in the Ge:H consumption and the relation between material density, etch rate and type of reaction are discussed in detail elsewhere [265].

Fig.6.18 also shows that the stability of the Ge:H films is strongly improved when alloyed with O and C. A similar improvement of the stability of σ_d can be observed in the Si:H films, when alloyed with C. The Ge(C,O):H films are no longer consumed within the 1000hrs measured time-frame and σ_d. In fact, the σ_d of GeO:H remains very stable over time, while GeC:H continuously increases, with about an order of magnitude over the measured time-frame. While Ge(C,O):H alloys exhibit higher E_{04} than unalloyed Ge:H, a similar improvement in chemical stability could potentially be achieved in GeSn(C):H alloys, for which lower bandgap energies can potentially be realized. Consequently, potential pathways towards the successful processing of GeSn(C):H are currently being investigated [264].

6.3.6 Conclusion

In this work over 400 PECVD processed films are presented, based on hydrogenated group IV alloys, exhibiting an E_{04} range of over 1.3eV. Based on these results the fundamental relations between the material density, as a function of the elemental composition, void fraction and crystalline phase fraction, and bandgap energy are discussed. Moreover, the relation between the bandgap energy and electrical materials characteristics such as the dark conductivity, activation energy and photoresponse are considered.

Additionally, based on 230 a/nc-Ge:H films, 3 inherent challenges are identified related to the PECVD processing of hydrogenated germanium. These are related to the intrinsicity, chemical stability and photoresponse of the films. Two pathways for tackling these challenges are presented. The first involves a very specific processing window, at relatively high temperature and low RF power at a small electrode distance. Using this processing window chemically stable Ge:H films are processed with σ_d values down to $4.6 \cdot 10^{-4}$ $(\Omega \cdot cm)^{-1}$ and σ_{ph}/σ_d values up to 2.3, which are the best achieved for chemical vapour deposition processed Ge:H films, to the best of the author's knowledge. The second pathway involves the alloying of Ge:H. Improved chemical stability is demonstrated for Ge:H films alloyed with O and C. While these alloys exhibit higher E_{04} than unalloyed Ge:H, a similar improvement in chemical stability could be achieved in GeCSn:H alloys, for which E_{C-L} values as low as 0.7eV are demonstrated.

7

PECVD processing of GeSn:H films

7.1 PECVD processing of low bandgap-energy amorphous hydrogenated germanium-tin (a-GeSn:H) films for opto-electronic applications

This section was published in *Applied Materials Today**

Abstract

An alloy based on the group IV elements germanium and tin has the potential of yielding an earth-abundant low bandgap energy semiconductor material with applications in the fields of micro-electronics, optics, photonics and photovoltaics. In this work, the first steps towards the plasma enhanced chemical vapour deposition (PECVD) processing of a chemically stable, low bandgap energy and intrinsic GeSn:H alloy are presented. Using a tetramethyltin (TMT) precursor, over 70 PECVD processed films are presented. It was observed that the opto-electrical film properties are a result of the material phase fraction, void fraction, hydrogenation and the level of tin and carbon integration. In particular, managing the carbon integration from the TMT precursor into the material is crucial for obtaining low-bandgap and chemically stable materials. The collective findings from this work will aid in successfully identifying PECVD processing pathways for GeSn:H.

7.1.1 Introduction

An alloy based on the group IV elements germanium and tin has the potential of yielding a relatively earth-abundant and safe semiconductor material with a low bandgap energy. Such a GeSn alloy has potential applications in general CMOS compatible optical devices [352], for use in a mid-infrared laser [376] or light-emitting diodes [377], [378]. Alternatively, research is performed on (Si)GeSn to develop a lattice matched direct bandgap option for III-V semiconductor based photovoltaic multijunction devices [325], [379], [380]. The far majority of works consider the epitaxial growth of GeSn films. For epitaxial film growth, deposition techniques such as molecular beam epitaxy [327], [381]–[383], co-evaporation [384], and sputtering [385], [386] are used, as well as chemical vapour deposition (CVD) at reduced pressure [326], [377], [387], [388], low pressure [380] and ultra-high vacuum [378], [389], [390].

Only a small number of works have explored the use of amorphous (a-)GeSn. These a-GeSn films were sputtered [270], [391], [392] or evaporated [393], but the use of CVD for a-GeSn films has not yet been reported. Using a CVD processing technique, such as plasma-enhanced CVD (PECVD), would potentially allow for the relatively cheap and fast processing of a-GeSn films and is compatible with the conventional and mature processing techniques used for the processing of thin film silicon alloys for photovoltaic and display applications. For that reason, in this work, a first investigation is performed on the PECVD processing of hydrogenated (:H) a-GeSn. The purpose of such an amorphous hydrogenated alloy would not be to provide a cheaper alternative for the processing of expitaxially grown GeSn, but rather to explore a low-cost industry-compatible group IV alloy for PV applications, and potential additional applications in the fields of micro-electronics, optics and photonics. To successfully identify PECVD processing pathways for a-GeSn:H, the advantages, challenges and limitations are evaluated using vibrational- and elemental spectroscopy, spectroscopic ellipsometry and electrical characterization techniques.

7.1.2 Experimental section

For the development of the GeSn:H films, a tin precursor is added during the growth of the hydrogenated germanium films. The processing conditions of the Ge:H films were optimized in our earlier work [168], [201], [262]. The typical deposition conditions for nc-Ge:H and a-Ge:H films used in this work are presented in table **??**. Generally, for the PECVD processing of hydrogenated amorphous alloys, a precursor such as methane [CH_4], silane [SiH_4] or germane [GeH_4] is used, where the desired element is bonded to 4 hydrogen atoms. Such a SnH_4 precursor is not chemically stable however. Some works report the use of in-house developed deuter-ostannane [SnD_4] as a Sn-precursor [378], [390], which uses the hydrogen isotope deuterium to improve the stability of the precursor. Others report the use of the commercially available $SnCl_4$ [380], tetra-ethyltin [$Sn(C_2H_5)_4$] [394], [395] and tetra-methyltin [$Sn(CH_3)_4$] (TMT) [388]. In this work TMT is used, as it is the least complex, commercially available Sn-precursor that exclusively consists of group IV elements and hydrogen. A challenge with this precursor is that four CH_3 groups are introduced into the reactor with each Sn-atom. Carbon integration is generally undesirable, as it results in an increase of the bandgap energy [168], [279], [284], an effect opposite to that of Sn-integration.

Table 7.1: Deposition conditions of amorphous and nano-crystalline GeSn:H samples; radiofrequency power (P_{RF}), pressure (p), substrate temperature (T_{S}), germane flow rate (F_{GeH4}) and H_2 flow rate (F_{H2}). The TMT duty cycle (δ) is varied between 429 and 12000.

	$\mathbf{P_{RF}}$ (mW · cm^{-2})	$\mathbf{p}$ (mbar)	$\mathbf{T_S}$ (°C)	$\mathbf{GeH_4}$ (sccm)	$\mathbf{H_2}$ (sccm)
a-Ge:H	14.9	4	210-290	2	200
nc-Ge:H	24.8	1	210-290	1	200
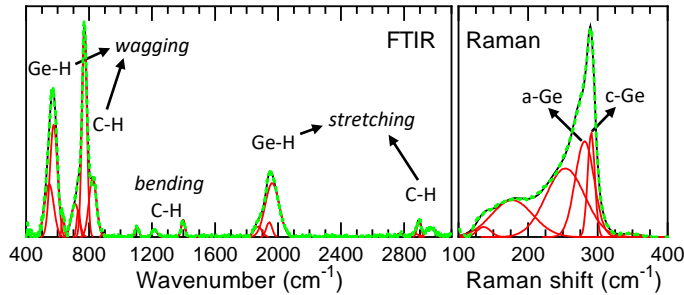
Figure 7.1: Typical FTIR (left) and Raman (right) spectra of un-oxidized GeSn:H films. Raman spectrum is of an nc-GeSn:H film. The individual fitted Gaussian's (red), sum of the fitted Gaussian's (black) and measurements after background subtraction (green, dashed) are shown. The amorphous and crystalline Ge vibrational modes are indicated in the Raman plot, while the Ge-H and C-H vibrational modes are indicated in the FTIR plot.

The GeSn:H films are batch-processed on different substrates simultaneously. Quartered n-type Cz 500μm polished monocrystalline silicon wafers of 4 inch size are used for Fourier Transform Infrared (FTIR) spectroscopy, Raman spectroscopy (Raman), Energy Dispersive X-Ray Spectroscopy (EDX) and Scanning Electron Microscopy (SEM) analysis. Corning Eagle XG glass substrates of 10cm x 2.5cm are used for all other measurements. The GeSn:H films were processed in the Cascade radiofrequency-PECVD reactor, which has a circular electrode with a diameter of 160mm. Cascade is a laminar flow reactor, where germane (GeH_4), molecular hydrogen and TMT are used as precursor gasses. The TMT, a liquid at room temperature, is evaporated in a separate canister at 70°C. Injection of TMT into the reactor is controlled through a valve, similar to those used for atomic layer deposition. For the samples presented in this work, the open time of the valve was varied between 5-10ms while the close time was varied between 100ms and 60s. The ratio of the close time to the open time is referred to as the duty cycle (δ). For a fraction of the GeSn:H samples the TMT flow from the canister, prior to injection into the reactor, was diluted in Helium. Considering the relatively high duty cycles used in this work, the impact of He dilution on the plasma is assumed to be minimal. He dilution mainly serves to decrease the TMT concentration introduced during each injection event.

It should be noted that for the samples with the largest duty cycles, the close time is expected to exceed the residence time of the injected TMT. The residence time (τ) can be calculated according to eq.7.1, where V_{R} is the reactor volume, p the pressure during deposition, T the temperature of the precursor gas. F_{gas} is the cumulative gas flow rate in sccm, p_0 the standard pressure of 1.01bar and T_0 the standard temperature of 273K.

With $V_\text{R} \approx$10L, $T \approx$300K, p=4mbar and $F_\text{gas} \approx$200sccm, the residence time is on the order of 10s, while the close time of the valve is increased up to 60s.

$$\tau = \frac{V_\text{R}\ p\ T_0}{F_\text{gas}\ p_0\ T} \tag{7.1}$$

The methods for obtaining the activation energy (E_act), the dark conductivity at room temperature σ_d and photoconductivity σ_ph are similar to those used in earlier work [201], [262]. Spectroscopic Ellipsometry (SE) was used to determine the refractive index at a wavelength of 600nm ($n_{@600\text{nm}}$), as well as the thickness and optical bandgap energy E_{04}, which is the energy at which the absorption coefficient of the film equals 10^4cm^{-1}. The SE measurements were fitted using a Cody-Lorentz model, which provides excellent representation of the processed materials.

A Thermo Fisher Nicolet 5700 spectrometer and an inVia confocal Raman microscope were used to obtain the FTIR- and Raman spectra. Additionally, SEM and EDX analysis was performed on a FEI Nova NanoSEM 450. SEM imaging was performed at an acceleration voltage of 10kV, while EDX measurements were performed at 5KV. The FTIR, Raman and EDX spectra were fitted using the Fityk freeware [228]. The background was subtracted manually. Examples of Raman and FTIR spectra, typical for chemically stable GeCSn:H samples with low oxygen content, including the identification of peaks relevant for the characterisation performed in this work, are presented in Fig.7.1. Peak identification is performed based on an extensive study of the vibrational spectra of hydrogenated group IV alloys presented in [367]. Additional FTIR spectra, typical for samples suffering from post-deposition oxidation, can be found in the supplementary information.

Examples of typical EDX spectra are provided in the main text. The elemental composition was obtained by comparing the area of fitted Gaussian distributions after background subtraction. As such, the elemental fractions represent atomic fractions ($at._\text{x}$) rather than weight fractions. Atomic fractions of oxygen present in the material are not intentionally added during deposition, but are the results of post-deposition oxidation and indicative of a chemically unstable material. The Raman spectroscopy measurements were used to determine the crystallinity (χ_c). The method for determining crystallinity is reported elsewhere [201].

In addition to the atomic fractions and the crystallinity, the relative number of hydrogen atoms (N_H) bonded to germanium and carbon was determined from the absorbance peaks in the FTIR spectra, using:

$$N_\text{H} = A \cdot \frac{A_\text{abs}(\omega)}{d} ln(10) \cdot \omega^{-1} \tag{7.2}$$

Here ω is the wavenumber, d the thickness of the films, A_abs the area of the Gaussian distribution corresponding do Ge-H or C-H vibrations, respectively. A is an empirically determined proportionally constant that is different for the C-H and Ge-H vibrations, as it is a function of the effective charge, mass and frequency of the dipole [67]. For determining the number of hydrogen atoms bonded to germanium ($N_\text{H-Ge}$), the Ge-H wagging modes, positioned at around 560cm^{-1}, are conventionally used, as the strength of the wagging modes is proportional to the hydrogen concentration, while the strength of the stretching modes is not [230]. For the Ge-H wagging mode, a proportionality constant

of $A=1.3\cdot10^{19}$cm^{-2} is used, as determined by [229] and in line with the $1.1\cdot10^{19}$cm^{-2} used by [230]. For determining the number of hydrogen atoms bonded to carbon ($N_{\text{H-C}}$). The C-H stretching modes are conventionally used [266], [274], [396], [397]. This is presumably because C-H wagging occurs in a region generally occupied by a large number of vibrational modes, as demonstrated in [367], making deconvolution of different absorbance-peaks challenging and arbitrary. For the C-H stretching modes, a proportionality constant of $A=1.35\cdot10^{21}$cm^{-2} is used, similar to [266], [396] and in the same order as the value of $1.7\cdot10^{21}$cm^{-1} used by [274], [397]. Finally, the ratio between the hydrogen atoms bonded to carbon and germanium ($R_{\text{CH/GeH}}$) was determined using:

$$R_{\text{CH/GeH}} = \frac{N_{\text{H-C}}}{N_{\text{H-C}} + N_{\text{H-Ge}}} \tag{7.3}$$

7.1.3 Results and Discussion

Introducing TMT

For a first experiment, TMT is injected into the reactor at various duty cycles during a-Ge:H deposition, using the conditions reported in table **??**. This initial exploration revealed certain inherent challenges to the processing of GeSn:H using TMT, specifically at relatively low duty cycles of approximately δ <1000. The first is indicated by the SEM images in Fig.7.2, where an inhomogeneous distribution of Sn can be observed at different magnifications. In the top left image, distribution of Sn across a diagonal over the sample surface can be observed, believed to be following a path from the TMT injector to the turbopump. An artifact therefore of the laminar-flow-design of the reactor. The second challenge can be observed in Fig.7.3, where in the top-left image the formation of Sn clusters on the sample surface can be observed. This observation is in line with earlier reports, where the clustering of Sn for epitaxially grown GeSn was observed for deposition temperatures over 200-230°C[381], [382].

In an attempt to prevent the clustering of Sn and distribute the TMT more evenly, the evaporated TMT was diluted in Helium in the canister prior to insertion into the reaction chamber. It can be observed, in the top-right image in Fig.7.3, that the He-dilution, for the very low $\delta=100$, does not prevent the clustering of Sn but rather results in a change of geometry of the Sn-clusters. The EDX plot in Fig.7.3 demonstrates that the formations on the sample surface are indeed Sn clusters. These two challenges, related to the inhomogeneous distribution of TMT in a laminar flow reactor and the clustering of Sn at elevated deposition temperature, were exclusively observed in SEM images for relatively low δ. As such, these challenges could be considered boundary conditions for the processing of GeSn with this particular Sn-precursors and reactor design.

Additionally, relatively high carbon and oxygen contents can be observed in the EDX plot of Fig.7.3, for the position on the surface measured next to the Sn cluster (blue circle). As indicated in section 7.1.2, with the TMT precursor four CH$_3$ groups are introduced for each Sn atom. Unlike C, atomic fractions of oxygen present in the material are not introduced during deposition, but are the results of post-deposition oxidation and indicative of a chemically unstable material. In our previous work, on a/nc-Ge:H, a relation was established between i) processing conditions, ii) material density/porosity and iii) the occurrence and degree of post-deposition oxidation [168], [201], [262], [265].
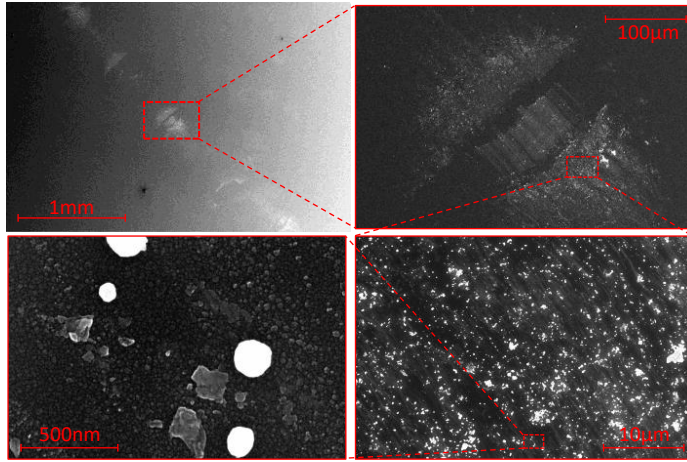
Figure 7.2: Four SEM images at different magnification of the surface of an a-GeSn:H sample with $\delta=100$ and $F_{\mathrm{He}}=0$sccm.

The relatively high carbon integration, in reference to that of Sn, introduces certain challenges to the processing of a chemically stable, low-bandgap energy, intrinsic ($E_{\mathrm{act}} \approx 0.5E_{04}$) Ge:H alloy. E_{04} generally increases with increasing $at._\mathrm{C}$, as can be observed in Fig.7.4**I-II**, especially in reference to the densest Ge:H films which have an E_{04} of $\approx$1.1eV. This is also owing to the increase of $at._\mathrm{O}$ in the films, which scales with the $at._\mathrm{C}$, as can be observed in Fig.7.4**IV**. This relation is not unexpected, as C-integration is predominantly expected to occur through the integration of CH$_n$ groups from the TMT precursors. The integration of CH$_n$ groups results in an increase of material porosity, which is reflected by the change in $n_{@600\mathrm{nm}}$ in Fig.7.4**II**, as a function of $at._\mathrm{C}$. This relation between CH$_n$ flux and porosity is in line with observations from the PECVD and glow-discharge CVD processing of SiC:H using a CH$_4$ precursor, where it was concluded that more CH$_n$ than atomic C was build into the material [273], resulting in a deposition rate increase [398] and increase of the H-concentration [399] with increasing CH$_4$ flow rate in reference to SiH$_4$. As a consequence, the mechanisms responsible for the increase in $at._\mathrm{C}$ will also result in an increase of material porosity, and consequently influence the oxidation behaviour [168], [201], [262], [265].

Notably, E_{04} is not increased for all samples, despite a decrease of $n_{@600\mathrm{nm}}$. If we consider the samples with $E_{04} \leq$1.1eV, it can be observed that they all have a relatively high Sn concentration in reference to carbon concentration, as indicated by the $at._\mathrm{Sn}/at._\mathrm{C}$ in Fig.7.4**III**. This indicates that through Sn-integration relatively low E_{04} values can be realized despite the presence of carbon.

The carbon integration does not exclusively have negative effects on the film properties however. Using GeSnC:H in p-i-n or n-i-p junctions, for instance for PV applications, requires the alloy to be (close to) intrinsic. In intrinsic materials the concentration of electrons and holes are roughly equal, with the Fermi level positioned halfway the bandgap, so with $E_{\mathrm{act}} \approx 0.5E_{\mathrm{G}}$. Earlier work resulted in the believe that the a/nc-Ge:H phase
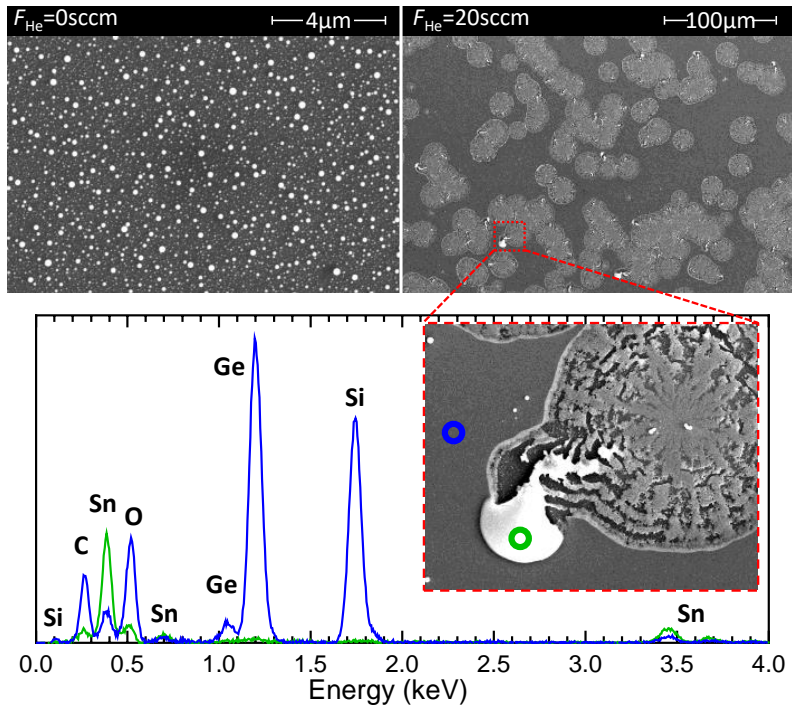
Figure 7.3: SEM (top) and EDX (bottom) measurements of the surface of a-GeSn:H samples with δ=100. SEM images are shown of samples with F_{He}=0sccm (top-left) and F_{He}=20sccm (top-right). EDX measurements shown after background subtraction of a position on a Sn cluster (green) and on the amorphous GeSn:H phase (blue), as indicated in the inset. Identification of the various peaks indicated in plot.
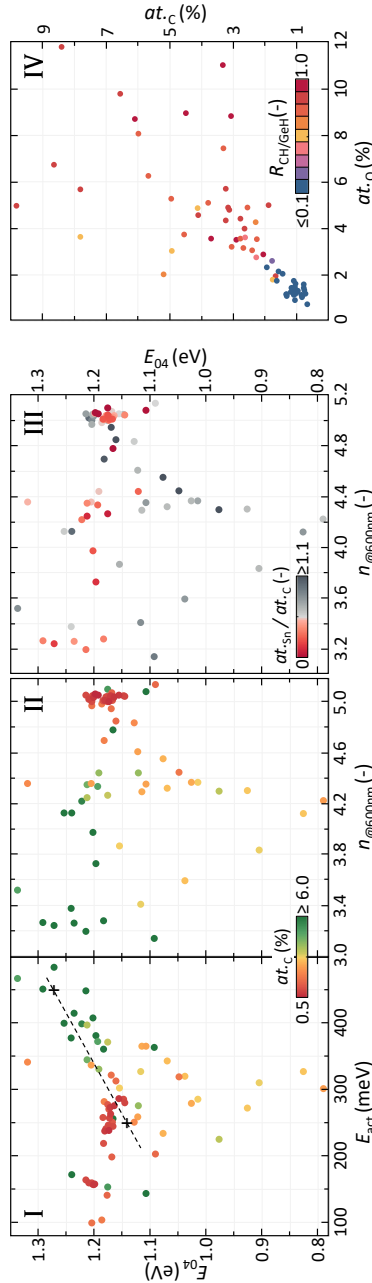
Figure 7.4: The influence of carbon on the opto-electrical properties of GeSn:H. **I** and **II** show E_{04} as a function of E_{act} and $n_{@600\mathrm{nm}}$, respectively, with colour indicating $at._{\mathrm{C}}$. In **III** E_{04} is plotted as a function of $n_{@600\mathrm{nm}}$, with colour indicating in $at._{\mathrm{Sn}}/at._{\mathrm{C}}$. In **IV** $at._{\mathrm{C}}$ is plotted as a function of $at._{\mathrm{C}}$, with colour indicating in $R_{\mathrm{CH/GeH}}$.

has a relatively high defect density, with an n-type nature, and $E_{\mathrm{act}} <<0.5E_{\mathrm{G}}$. This is likely related to the behaviour of hydrogen in germanium, as hydrogen does not readily passivate germanium dangling bonds [168], [201], [262]. The poor hydrogen passivating behaviour can also be observed by considering the icon colour in Fig.7.4**IV**, which shows that the number of hydrogen atoms bonded to C in reference to Ge is in the range of 60-80% at only an $at._{\mathrm{C}}$=2-8%.

It can be observed in Fig.7.4**I** that the E_{act} significantly increases with increasing $at._{\mathrm{C}}$. Qualitatively, the increases of E_{act} with $at._{\mathrm{C}}$ can be expected, as for an intrinsic material $E_{\mathrm{act}} \approx 0.5E_{04}$. Notably however, the increase in E_{act} exceeds that of E_{04}. Considering the trendline added to Fig.7.4**I**, an E_{04} increase of 150meV results in an 200meV increase of E_{act}. Based on Fig.7.4**I** we therefore speculate that carbon, or the CH_n groups dissociated from the TMT precursor, effectively passivate the Ge-dangling bonds and decrease the defect density in reference to an unalloyed a/nc-Ge:H phase. This defect passivating behaviour was previously suggested for oxygen, as a decrease of σ_{d} despite a decrease in E_{act} was observed in a/nc-Ge:H films upon post-deposition oxidation [201]. It should be noted that this increase of E_{act} in Fig.7.4**I** occurs despite the the fact that $at._{\mathrm{O}}$ scales with $at._{\mathrm{C}}$ (Fig.7.4**IV**) and that oxygen integration generally results in a strong decrease of E_{act}, as the GeO_x phase has a strong n-type nature [201], [262]. This demonstrates that the Ge-C bond has an energetic nature that is either p-type or close to intrinsic.

Next we consider the effect of δ in some more detail, as presented in Fig.7.5. For the two amorphous series (red and black icons) the observed trends as a function of δ match, while the trends for the series processed under nano-crystalline conditions (blue icons) is dissimilar for most measured metrics. For the series processed under amorphous conditions, the carbisation of the films appears to have a dominant influence on their respective opto-electrical properties. With increasing δ, $at._{\mathrm{C}}$ decreases, resulting in an increase of $n_{@600\mathrm{nm}}$ and decrease of $at._{\mathrm{O}}$ and E_{04}. As discussed before, E_{act} scales with $at._{\mathrm{C}}$, while σ_{d} decreases with increasing with E_{act}, as was observed before in Ge:H films [201], [262]. As a consequence the highest photoresponses ($\sigma_{\mathrm{ph}}/\sigma_{\mathrm{d}}$) are achieved at relatively low δ, so high $at._{\mathrm{C}}$ values.

The opto-electrical properties of the samples processed under nano-crystalline conditions show some deviating behaviour. Fig.7.5 (blue icons) shows that exclusively for the nano-crystalline samples a decrease of δ results in a decrease of E_{04}, an increase of E_{act} and decrease of σ_{d}. These samples have a relatively low $at._{\mathrm{O}}$ and $at._{\mathrm{C}}$, and a significantly higher $at._{\mathrm{Sn}}/at._{\mathrm{C}}$ than the amorphous samples.

In Fig.7.6 the $at._{\mathrm{Sn}}$ of all samples in which a crystalline peak was observed is presented as a function of the exact Raman shift of the crystalline Ge peak as well as the crystalline phase fraction. The figure not only shows that the $at._{\mathrm{Sn}}$ increases with the χ_{C}, it also shows that the c-Ge peak position is shifted downward with increasing $at._{\mathrm{Sn}}$ and χ_{C}. This observation is in line with earlier reports, where a decrease of the Raman-shift of the c-Ge peak was observed in epitaxially grown crystalline GeSn with increasing $at._{\mathrm{Sn}}$ [325], [326], [387], [389]. The relation between the χ_{C}, $at._{\mathrm{Sn}}$ and c-Ge peak position suggest that the crystalline phase in the heterogeneous nc-GeSn:H material is in fact a GeSn crystalline phase. Additionally, the relation between χ_{C}, $at._{\mathrm{Sn}}/at._{\mathrm{C}}$ and $at._{\mathrm{Sn}}$ suggests a growth mechanism in which Sn is favourably integrated in the crystalline phase in reference to the amorphous phase.

Figure 7.5: Influence of duty cycle on the elemental composition and opto-electrical properties of 4 different series of GeSn:H samples. All samples are processed at F_{He}=5sccm and amorphous conditions, with the exception of samples processed at T_{S}=290°C (blue), which are processed at nano-crystalline conditions (as indicated in table??). For all series the close time was varied at a fixed open time of 7ms.
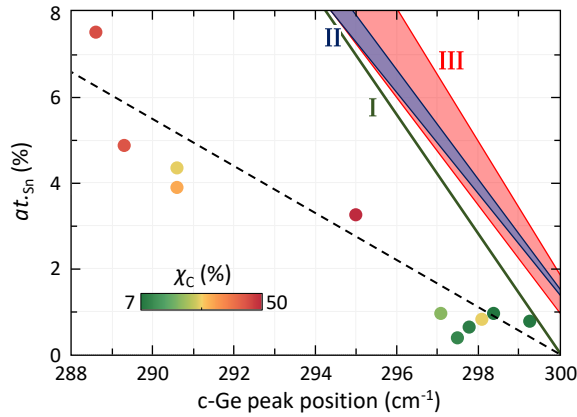
Figure 7.6: $at._{\mathrm{Sn}}$ as a function of the measured Raman shift of the c-Ge peak of all samples with χ_{c}. Colour indicates the χ_{c} of the samples. A trend-line (black, dashed) is added for the samples measured in this work. Additional lines and areas are present in the graph, indicating the relation between $at._{\mathrm{Sn}}$ and the Raman shift of the c-Ge peak for epitaxially grown c-GeSn films according to **I** (green) [389], **II** (blue) [395] and **III** (red) [326].

Moreover, if we consider the relation between the $at._{\mathrm{Sn}}$ and the Raman-shift of the crystalline GeSn peak reported in other works, as indicated by the coloured lines and areas in Fig.7.6, and compare it to the relation observed in our experimental data, it can be concluded the Sn concentration is likely much higher in the crystalline phase than in the amorphous phase. Extrapolating the data presented in Fig.7.6, an $at._{\mathrm{Sn}}$ of 15.5-17.5% could be expected for the nc-GeSnC:H sample with an 288.7cm^{-1} c-Ge peak position. Considering the χ_{C} of around 50% and the overall $at._{\mathrm{Sn}}$ of 7.8%, the amorphous phase is expected to have a very low $at._{\mathrm{Sn}}$ of 0-1.8%. This means that the nc-GeSnC:H samples have a strongly heterogeneous nature, consisting of GeSn crystals embedded in an predominantly amorphous germanium-carbide phase. Considering the relation between $at._{\mathrm{Sn}}$ and E_{G} presented in [392], [400], the GeSn crystals can be expected to have an E_{G} in the range of 0.5-0.55eV.

In determining the optimal processing regimes, it can be established that the lowest E_{04} are achieved for the nc-GeSn:H samples at low δ of $\lessgtr$2000. For moderate duty cycles, the a-GeSn:H samples processed at elevated temperature exhibit lower E_{04} values, as well as lower σ_{d} and higher $\sigma_{\mathrm{d}}/\sigma_{\mathrm{ph}}$ values. While both these series are processed at elevated temperature, the difference between these series is mainly the P_{RF} at which they are processed. In the next section we will therefore look at the effect of these two processing conditions in more detail.

Temperature

First we consider the influence of T_{S} on three sets of samples, with different F_{He} and δ. Two main observations can be made from Fig.7.7. Firstly, independent of the TMT dilution in F_{He}, processing stable, dense amorphous GeSn films with high $n_{@600\mathrm{nm}}$ and low E_{04} is very challenging for low δ-values. Even at elevated T_{S}, which generally results in dense material growth for Ge:H and SiGe:H films [262], porous material growth cannot
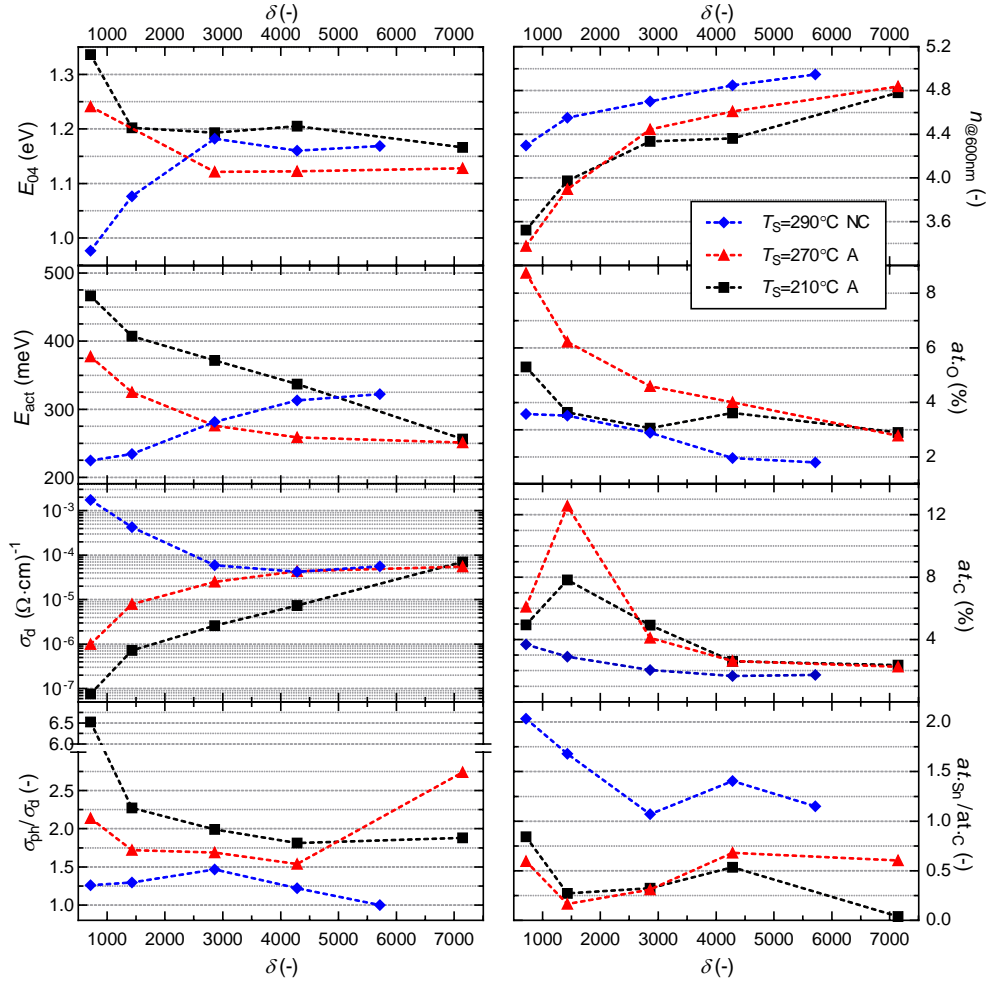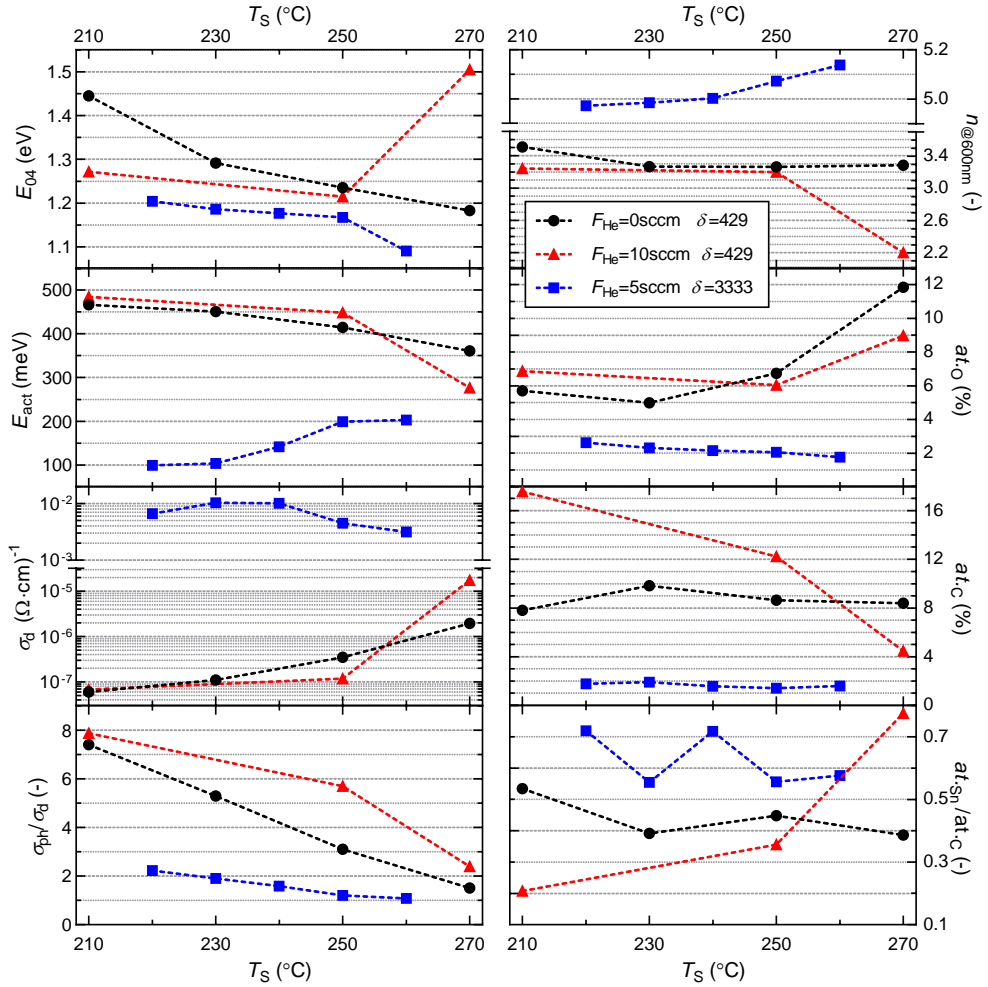
Figure 7.7: Influence of deposition temperature on the elemental composition and opto-electrical properties of 3 different series of GeSn:H samples. All samples are processed at amorphous conditions (as indicated in table **??**).

be avoided as indicated by the low $n_{@600nm}$-values. The highest $n_{@600nm}$ of the two series with δ=429, in reference to the series processed at δ=3333, is 1.5 lower. As a consequence the samples readily oxidize, as indicated by the high $at._O$. This oxidation behaviour makes the processing of chemically stable amorphous a-GeSn:H at relatively low δ not feasible.

The second observation is related to the electrical behaviour of the three series of samples. Consdidering the influence of T_S on the δ=3333 samples, it can be observed that with increasing T_S, $n_{@600nm}$ increases, further reducing oxidation and increasing E_{04}. $at._C$ and $at._{Sn}/at._C$ seem to remain relatively unchanged as a function of T_S. With the decrease of $at._O$, E_{act} is observed to increase and σ_{ph}/σ_d to decrease. This is in line with our earlier reports on the oxidation behaviour of hydrogenated germanium, where it was suggested that oxygen in germanium passivates defects, decreasing the defect density, but creating Ge-O$_x$ bonds with an n-type nature that decrease E_{act} [201].

The difference in electrical behaviour between the low-δ and δ=3333 samples seems to suggest that carbon, or potentially Sn, in addition to oxygen has the ability to passivate the Ge-defects. This can be concluded from the change in E_{act} in reference to the change in E_{04}. For an undoped material a change of ΔE_{act}=0.5ΔE_{04} can be expected. However, it can be observed in Fig.7.7 that the 200-300meV E_{act} difference between the low-δ and δ=3333 samples far exceeds the 100-150meV E_{04} difference, so $\Delta E_{act} \gg 0.5\Delta E_{04}$, which is similar to the observation indicated by the trendline in Fig.7.4**I-II**. As a result of the much higher E_{act}, σ_d is 5-3 orders of magnitude lower for the low-δ samples in reference to the δ=3333 samples and the σ_{ph}/σ_d is generally higher for the samples with high $at._C$. This indicates that without the presence of some element to passivate the germanium defects, other than hydrogen which is not very effective at doing so, it is challenging to achieve favourable electrical material characteristics.

Power

Next we consider the influence of power. Fig.7.8 shows that with increasing power, E_{04} continuously increases. While this increase can be ascribed to an increasing $at._O$ in the 6-10W range, the origin of this increase in the 2-6W range is unclear. With increasing P_{RF}, more energy is supplied to the plasma, more effectively dissociating the precursor gasses and resulting in a larger overall growth flux. As a consequence, the growth rate is continually increased from about 10nm/min at 3W to 21nm/min at 10W. More porous growth, that is more susceptible to oxidation, could be expected as a results of this growth-rate increase. While this could account for the increase of $at._O$ and E_{04} for $P_{RF} \geq$8W, a similar porosification and decrease of $n_{@600nm}$ are not observed at lower powers.

In addition to an overall growth flux increase, a change in P_{RF} can also change the growth flux composition. Stronger bonds require more energy for dissociation. At higher P_{RF}, more energy is supplied to the plasma. As a consequence, in relative terms, the dissociation of stronger bonds is increased at higher power in reference to the dissociation of weaker bonds. The fraction of compounds with high dissociation energy precursors in the growth flux composition will therefore increase with increasing P_{RF}.

Of the precursors introduced during deposition of GeSn:H, dissociation of a methyl group from the TMT precursors only requires 227 kJ/mol [401]. However, further dissociating
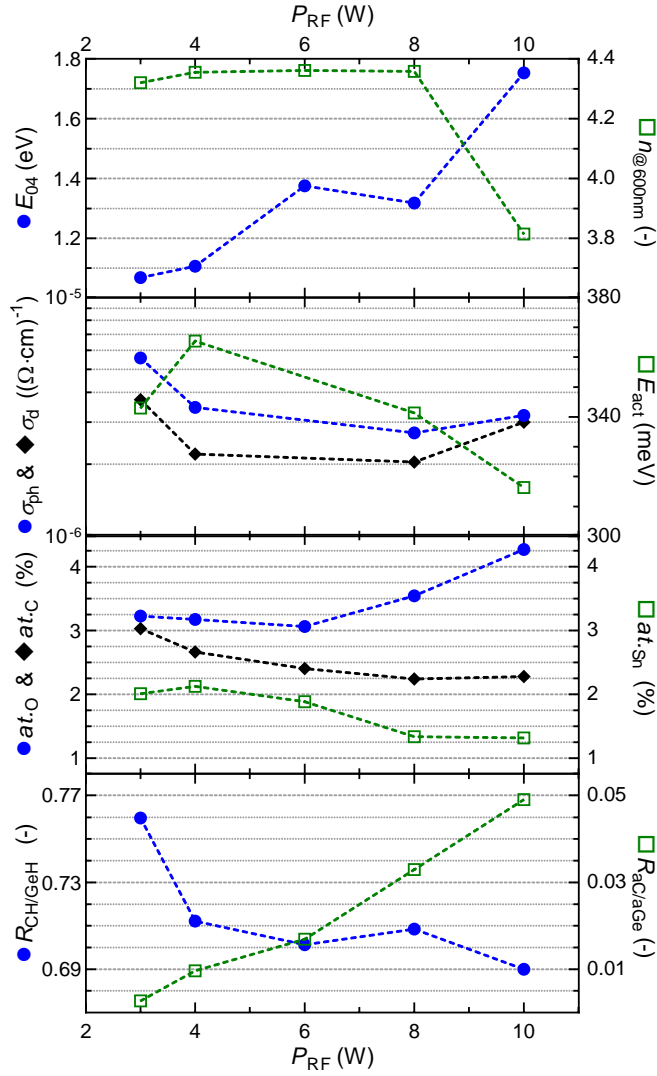
Figure 7.8: Influence of RF power on the elemental composition and opto-electrical properties of GeSn:H samples. Samples processed at amorphous conditions, with T_S=230°C, F_{He}=5sccm and δ=2857. The metrics represented by the different icon types are indicated on the respective vertical axes.

the methyl group itself requires a relatively large amount of energy, as the dissociation of a single hydrogen atom from CH_3 requires 457kJ/mol and dissociating a second hydrogen atom requires an additional 418 kJ/mol[402], which is similar to that of H_2 at 436kJ/mol. The dissociation of GeH_4, on the other hand, only requires about 350kJ/mol [373], [374]. This means that with increasing P_{RF}, in relative terms, the dissociation of H_2 and CH_{2-3} will increase in reference to GeH_4 dissociation, which in turn will increase in reference to dissociation of CH_3 from Sn.

The consequence of these growth-flux-composition effects as a function of P_{RF} can be observed in the vibrational spectroscopy and EDX spectroscopy measurements performed on the films. As shown in Fig.7.8, $at._{Sn}$ continuously decreases with increasing P_{RF} as the relative fraction of $Sn(CH_n)_n$ radicals in the growth flux is decreased.
Additionally, two effects occur: I. the dissociation of the neutral GeH_4 precursor to GeH_{1-3} neutral radicals and ions is increased in reference to the dissociation of CH_3 groups from TMT and II. in reference to GeH_4 dissociation, CH_3 dissociation is increased with increasing P_{RF} and the fraction of smaller CH_{1-2} radicals in the growth flux is increased. As a consequence, the ratio of the C-H bonds in reference to the Ge-H bonds observed in the infrared spectra generally decreases with increasing P_{RF}, as indicated by $R_{CH/GeH}$, and the fraction of amorphous C-C vibrations continuously increases, as indicated by $R_{aC/aGe}$. It should be noted that the increase of atomic hydrogen etching in reference to material growth, resulting from more effective CH_n and H_2 dissociation, could also play a role in the increase of $R_{aC/aGe}$ with P_{RF}.

The opto-electrical film properties, then, are a result of the material phase fraction, void fraction, hydrogenation and the level of tin and carbon integration. To achieve favourable film properties, sufficient control has to be exerted over the film growth. From the preceding results we can conclude that the growth flux composition can be controlled to some extent through the P_{RF}. With increasing P_{RF} the dissociation of methyl groups, and to a lesser extend germane, in reference to TMT is increased. This control is complicated however by an overall increase of the growth flux and consequently more porous growth, with increasing P_{RF}. The deposition temperature is a possible processing condition for controlling the void fraction. Material densification occurs with increasing T_S. Care has to be taken however considering the solubility of Sn. The void fraction can also be influenced through the duty cycle and potentially through the dilution of GeH_4 in H_2, as atomic hydrogen etching in reference to the growth flux is increased with increasing hydrogen dilution. Additionally, similar to the duty cycle, the F_{GeH4}/F_{H2} ratio upsets the balance between CH_n, $Sn(CH_n)_n$ and GeH_n in the growth flux. The experimental results of a series of samples for which F_{GeH4}/F_{H2} is varied is available in the supplementary information.

7.1.4 Conclusion

In this work, the first steps towards the PECVD processing of a chemically stable, low-E_G and intrinsic GeSn:H alloy are presented. The processing of such an alloy, using a TMT precursor, is a complicated process with a number of inherent challenges.

Among these is the relatively low melting point of Sn, resulting in the formation of Sn-clusters at high TMT injection levels. The Sn-clustering prevents the formation of a low-E_{G} GeSn:H phase and introduces a limit to the amount of TMT that can be injected into the plasma. An additional challenge is the TMT precursor itself, through which four CH_3 groups are introduced into the reactor for each Sn-atom. We demonstrate in this work that managing the carbon integration into the material is crucial for obtaining low-E_{G} and chemically stable materials.

As a result of large CH_n fluxes, the porosity is generally observed to increase with the carbon concentration, resulting in increased oxidation of the samples. Surprisingly however, some C-integration seems favourable from a defect engineering perspective. Strong increases of E_{act}, far exceeding the increase in E_{G}, has been observed in amorphous GeSnC:H films with $at._{\mathrm{Sn}}$ as lows as 3-6%. This suggest that C effectively passivates the dominant defect type in Ge:H, resulting in films with a Fermi level closer to that of an intrinsic material. Additionally, C readily reacts with H, with the fraction of C-H bonds far exceeding the fraction of Ge-H bonds already at carbon concentration of a few percent.

Considering the optical behaviour of the films, low E_{04} are only realized at relatively high Sn/C ratios. High Sn to C ratios are predominantly realized for samples with a relatively high crystallinity. In fact, we show that low duty cycles, so high levels of Sn and C integration, are only feasible for highly crystalline materials. nc-GeSn(C):H films with χ_{C}=50% are processed with a highly heterogeneous nature, consisting of GeSn crystals with 15.5-17.5% Sn embedded in an a-GeC:H phase in which almost no Sn is present. Such heterogeneous nc-GeSnC:H films could provide a potential route towards a low bandgap energy group IV alternative for photovoltaic multijunction applications.
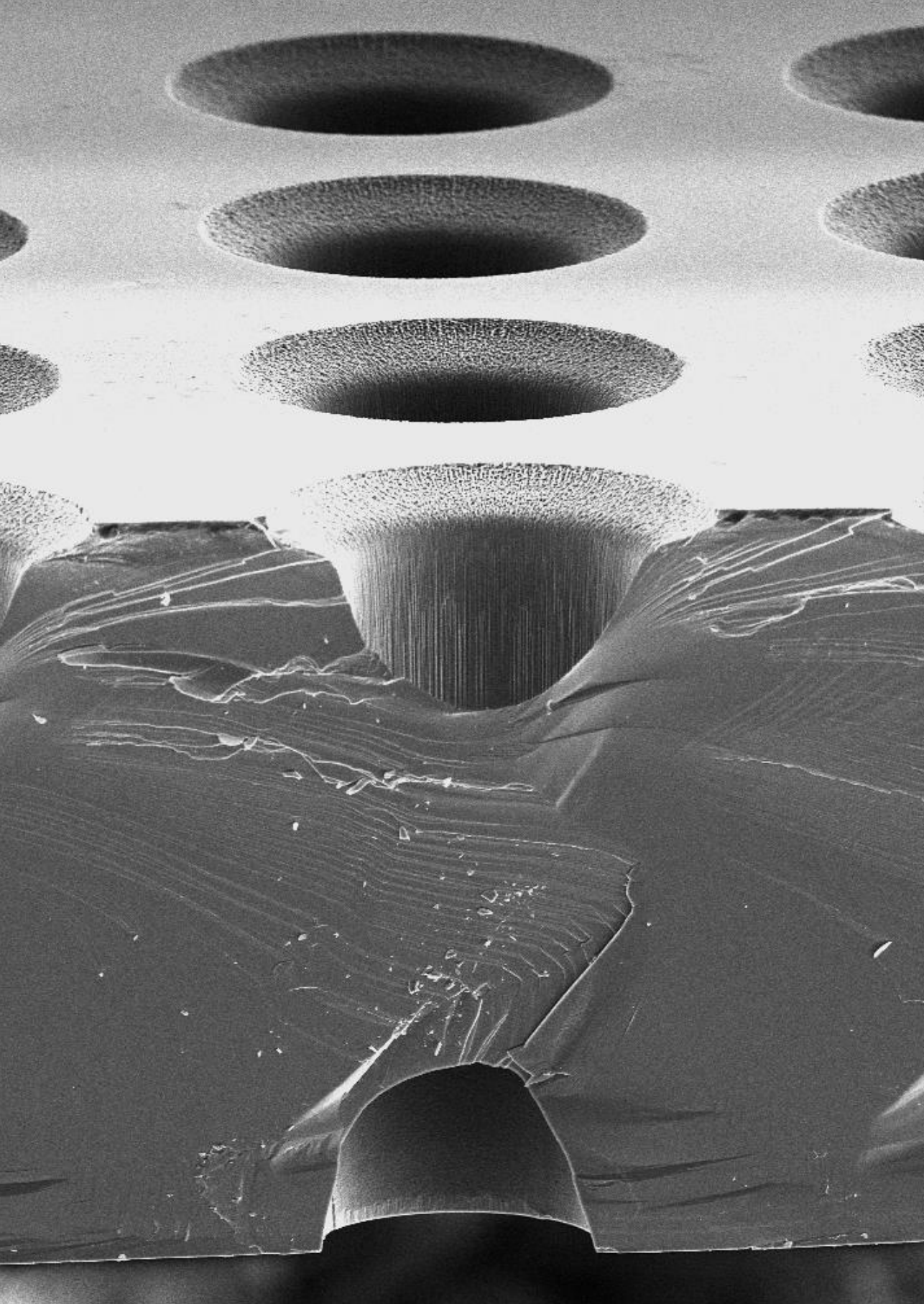
Part III:
Multijunction photovoltaic devices

The focus of this dissertation is to provide a framework for optimal multijunction design that can result in a range of output voltages. In Part I and Part II of this work a systematic optimization and characterization of PV materials and single junction PV devices is performed. In Part III, multijunction PV devices are considered.

There are some additional challenges in the processing of multijunction PV devices in reference to single junction devices. Charge carriers are photo-generated in each individual subcell. This introduces two additional design considerations. In the n-i-p substrate devices developed in this work, only holes in the top junction and electrons in the bottom junction are collected at the electrodes. For optimal operation, all other photo-generated charge carriers need to recombine at the interface between subcells, at the so-called tunnel recombination junction (TRJ). Additionally, for optimal operation, the photo-generated current in each subcell should be matched, as the output current of the overall multijunction device is limited by that of the subcell with the lowest photo-current.

These two additional design rules inherently introduce additional complexity. The intrinsic absorbers layers that in single junction PV devices are optimized to generate maximum power under the full solar spectrum, should now generate sufficient current under illumination conditions filtered by preceding subcells. Doped layers that were optimized to minimize parasitic absorption and recombination losses should now facilitate recombination between subcells and potentially provide increased reflection at the interface between subcells. These different functionalities introduce trade-offs in the design of a multijunction device. Trade-offs that can vary between different device architectures. In Part III, therefore, we focus on keyquestion **III**:

How do different materials, variations in material properties and different device configurations affect the performance of multijunction photovoltaic and photo-electrochemical devices

Part III is divided into three chapters. An optimization of the optical and electrical behaviour of the interface between subcells is presented in Ch.8. In Ch.9, the various optimizations performed in this dissertation are combined to process a range of silicon based multijunction PV devices. Finally, in Ch.10, the steps required to develop a photo-electrochemical device from a photovoltaic device are presented.
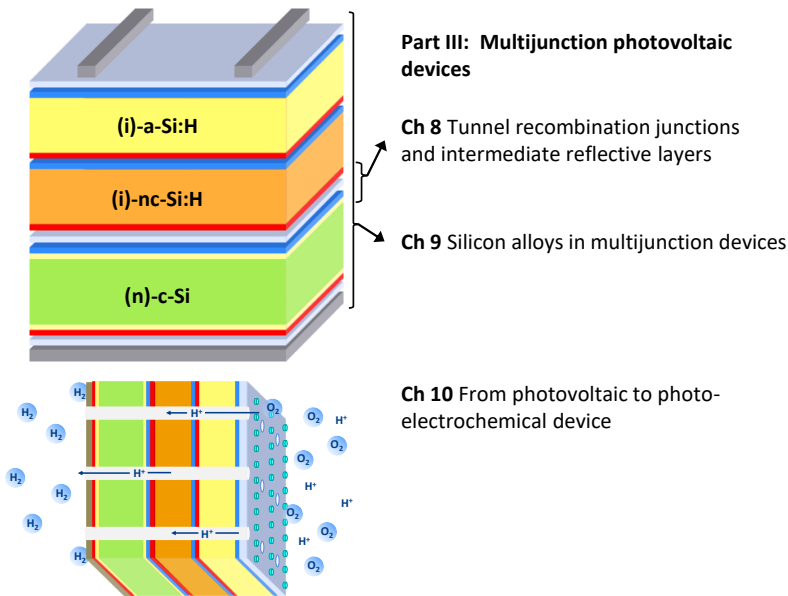
Figure 7.9: Outline Part III

Chapter 8 *Tunnel recombination junctions and intermediate reflective layers*

A lot is asked of the doped layers in a multijunction device. The doped layer should be an effective semi-permeable membrane for one type of charge carrier. Resistance against carrier movement through the layer should be minimal and the layer should be transparent to minimize parasitic absorption. Additionally, the layer should facilitate recombination of charge carriers when in contact with a doped layer of opposite charge. All this should be accomplished without exceeding the nanometer-length-scale. Combining these different functionalities is challenging. Especially considering that material growth can be dissimilar on different substrates with, for instance, different material phase fractions and textures. In **Chapter 8.1** therefore the TRJ operation is investigated by varying the deposition conditions, thickness and design of the p-layer across the different device architectures.

Apart from the electrical operation, optical absorption should be considered. For a given texture and front contact, current generation in a subcell can be changed through the thickness of the absorber or by changing the reflection at the interface between two subcells, using a so-called intermediate reflective layer. Consequently, in **Chapter 8.2** the trade-offs between J_{sc} and the $V_{\mathrm{oc}}*FF$ are characterized for both absorber thickness variations and variations in the IRL thickness and material type.

Chapter 9 *Silicon alloys in multijunction devices*

As stated in the introduction, the purpose of this dissertation is to provide a framework for optimal multijunction design that can result in a range output voltages, for different EC applications. In this chapter, using all the optimizations and characterizations performed in the previous chapters, the V_{oc} range that can be achieved by combing up

to four different junctions is investigated, based on various Si(Ge):H alloys, in both thin film silicon device architectures and hybrid crystalline silicon and thin film silicon device architectures, on silicon surfaces with varying textures.

Chapter 10 *From photovoltaic to photo-electrochemical device*
Finally, following the demonstration of a 2.3V $V_{\rm oc}$ range that can facilitate an array of electrochemical reduction reactions, the final steps for using a PV cell in an integrated autonomous solar-to-fuel synthesis system are considered. Converting a multijunction PV device into a PEC device capable of continuous, autonomous stand-alone operation, requires the use of electrocatalytically active contacts and the development of micropores through the PV device to prevent large pH-gradient related overpotentials. Additionally, the contacts at the front of the device should be patterned to facilitate light transmission into the device. In this chapter, the different considerations for the design and development of the micropores and electrocatalytic contacts for an all-silicon autonomous solar-to-fuel device are discussed.

8

Tunnel recombination junctions and intermediate reflective layers

8.1 The fundamental operation mechanisms of nc-SiO$_{X \geq 0}$:H based tunnel recombination junctions revealed

This section was published in *Solar Energy Materials and Solar Cells**

Abstract

Two terminal multi-junction (MJ) photovoltaic (PV) devices are well established concepts to increase the solar-to-electrical power conversion in reference to single PV junctions. In multi-junction PV devices two consecutive sub-cells are interconnected using a tunnel recombination junction (TRJ) in which the light excited holes of one sub-cell recombine with the light excited electrons of the other sub cell. An ideal TRJ is an ohmic contact with non-rectifying behaviour. TRJ's based on p- and n-doped silicon-oxides have been successfully applied in a variety of hybrid multi-junction PV devices in which tunnelling and trap-assisted tunnelling over width of 5-20 nm rules the TRJ's recombination kinetics. In this contribution the qualitative fundamental working principles of tunnel recombination junctions based on p- and n-doped silicon and silicon-oxide alloys are revealed using both electrical modelling and experiments based on a unique set of tandem lab cells (four types based on four different PV materials) combined with structural variations in TRJs architectures. The study results in design rules for the integration of silicon-oxide based TRJs and provides fundamental insights into the sensitivity of the electrical performance of the TRJ's to doping concentrations, to alignment of the conduction and valence bands of consecutive sub-cells, to the nature of interface defects, to the growth of amorphous and crystalline phases and its dependence on substrate or seed layers and to the nanoscale thicknesses of the TRJ layers.

8.1.1 Introduction

Multijunction photovoltaic (PV) devices are a logical next step for further reducing the cost price per Watt peak of PV, by increasing the yield per area. In particular, tandem PV devices with a crystalline silicon (c-Si) bottom cell are receiving increased attention. These c-Si bottom cells are combined with a range of PV technologies, such as perovskites [116]–[118], C(I)GS [119], III-V technologies such as GaInP/GaAs [403] and GaAsP [209] or nano-c-Si top cells [29], [30]. In multijunction devices charge carriers are photo-generated in each individual subcell. In two-terminal multijunction devices, in case of a p-type front contact, electrons generated in the top junction and holes generated in the bottom junction need to recombine at the interface between the two subcells, at the so-called tunnel recombination junction (TRJ). An ideal TRJ, one that facilitates this recombination between subcells, is an Ohmic contact with non-rectifying behaviour. When not properly engineered, the TRJ can act as a p-n junction with a reverse direction to that of the subcells.

In multijunction devices with a silicon-based bottom cell generally nanocrystalline silicon (nc-Si:H) or nanocrystalline silicon-oxide (nc-SiO$_X$:H) based TRJ's are used [40], [46], [48], [83], [84], [404], [405]. The performance of PV cells is very sensitive to the p-doped layer in particular, as achieving desirable doped layer properties such as low activation energy, high conductivity and optical transparency is inherently more challenging in p-doped layers in reference to n-doped layers [159], [406].

Moreover, interpreting the fundamental effect of changes to individual doped layers in the TRJ, based on device performance, is challenging. The p-doped (p-) layer determines the energetic alignment in, and thereby performance of, the subcell it is a part of. It also determines the electrical characteristics, and consequently the effectiveness, of the TRJ. Additionally, from a processing perspective, the p-layer can affect the subsequent growth of the n-layer just as the p-layer growth can be influenced by the preceding layer. To distinguish between these effect and functionalities, the investigated nc-Si(O$_X$):H based TRJ's should be integrated in different device architectures and multijunction configurations, including absorber layers with different crystalline phase fractions, band gap energies and stoichiometries. This allows for the isolation of the impact of the TRJ, from the opto-electrical nature of the subcells, on the device performance.

To achieve this isolation, and considering the sensitivity of device performance to the p-layer properties in particular, in this work, the effect of changes to the p-layer are investigated across four different multijunction PV device architectures. These are tandem devices consisting of a wafer-based silicon heterojunction (SHJ) subcell and subcells with hydrogenated nanocrystalline silicon absorbers, hydrogenated amorphous silicon germanium (a-SiGe:H) absorbers and hydrogenated amorphous silicon (a-Si:H) absorbers, in various configurations. The plasma enhanced chemical vapour deposition (PECVD) processed devices are schematically shown in Fig.8.1. TRJ operation is investigated by varying the deposition conditions, thickness and design of the p-layer of the bottom junction. Moreover, electrical simulations are performed to qualitatively support findings from the experimental results, in order to reveal the fundamental operation mechanisms that determine the performance of tunnel recombination junctions.

8.1.2 Experimental section

Processing tandem devices

Table 8.1: Conditions used for the various PECVD processed layers. i-nc-Si:H processed at 40MHz, all other layers at 13.56MHz

	P_{RF} (mW $\cdot$ cm^{-2})	p (mbar)	T_S (°C)	F_{SiH4} (sccm)	F_{GeH4} (sccm)	F_{H2} (sccm)	F_{CO2} (sccm)	F_{PH3} (2%) (sccm)
i-a-SiGe:H	27.8	3.6	180	30	0.4-5.3	200	-	-
i-a-Si:H (absorber)	62.5	10	120	2	-	200	-	-
i-a-Si:H (SHJ)	27.8	0.6	180	40	-	-	-	-
i-nc-Si:H	278	4	180	1.2/3.5	-	120	-	-
n-nc-SiO$_X$:H	76.4	1.5	180	1	-	120	1.6	2
n-nc-Si:H	76.4	1.5	180	1	-	120	-	3
n-a-Si:H	27.8	0.6	180	40	-	-	-	11

In this work the results of four different tandem device architectures are presented. These are tandem devices consisting of a SHJ subcell and a subcell with a nc-Si:H absorber, a nc-Si:H subcell combined with either an a-SiGe:H absorber or a-Si:H absorber and finally a tandem device consisting of an a-SiGe:H subcell and an a-Si:H subcell. The devices are processed using a radiofrequency PECVD cluster tool. The variations within experimental series are exclusively applied to the p-layer in the TRJ. As the 100+ tandem PV devices developed for this work are processed over a period of 2 years on a lab-scale PECVD tool, some variations to supporting layers exist between experimental series. These variations include absorber thickness variations, affecting which of the subcells is current limiting. Such variations do not exist within an experimental series, where "experimental series" in this work is defined as a set of devices processed at a given point in time, for which no variations exist in architecture and processing conditions other than the intended variations to the p-layer in the TRJ.

Precursor gas flow rates are indicated by (F_{gas}). Diborane (B$_2$H$_6$) is used as a precursor gas for boron doping. The reported diborane gas flow rates are 0.02% B$_2$H$_6$ in H$_2$. The reported phosphine (PH$_3$) flow rates, used as the precursor for phosphorus doping, are 2% PH$_3$ in H$_2$. Silane (SiH$_4$) and carbon-dioxide (CO$_2$) are used as silicon and oxygen precursors, respectively. The n-doped (n-) layer of the top junction, the n-layer that is part of the TRJ, consists of an n-nc-Si:H 5nm/ nc-SiO$_X$:H 15nm/ n-a-Si:H 5nm stack starting from the p-layer of the bottom junction. The deposition conditions of the absorber materials and doped layers are indicated in Table8.1. A schematic representation of the tandem devices is shown in Fig.8.1.

The three tandem devices that combine two thin film junctions (nc-Si:H, a-SiGe:H, a-Si:H) are processed in n-i-p/n-i-p substrate configuration on textured Corning Eagle XG glass. The texturing process was developed by [157] and [72] and is explained in more detail elsewhere [156]. A 700nm aluminum-doped zinc oxide (AZO) layer is sputtered onto the textured glass for use as a transparent back contact. No back reflector is used, as the situation with minimal back reflection provides the most straightforward comparison of variations in the TRJ and the generated J_{SC}, V_{OC} and FF. The front contact consists of transparent conductive oxide (TCO), a sputtered 75nm indium-doped tin oxide (ITO) layer, in combination with a 500nm aluminum front grid, which is deposited through thermal evaporation. The i-nc-Si:H absorber layer has a thickness of about 3μm, the
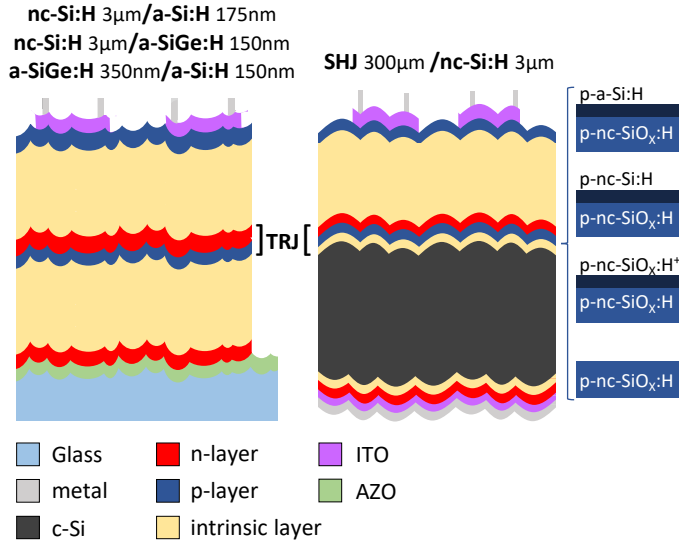
Figure 8.1: Schematical representation of the four different device architectures presented in this work. All devices are processed in n-i-p/n-i-p substrate configuration. Absorber layer thicknesses for thin film nc-Si:H/a-Si:H, nc-Si:H/a-SiGe:H and a-SiGe:H/a-Si:H devices (left) and SHJ/nc-Si:H (right) tandem devices are indicated above the structure. Small blue visuals on the right indicate the four different p-layer stacks used in this work.

i-a-Si:H absorber layer has a thickness of about 175nm. The i-a-SiGe:H absorber layers have a profiled bandgap energy across the absorber width. Bandgap profiling is achieved by varying the relative GeH_4 flow rate during deposition. The used absorber profile is different for the nc-Si:H/a-SiGe:H and a-SiGe:H/a-Si:H tandem devices. When used as the top junction in the tandem device (nc-Si:H/a-SiGe:H) a maximum GeH_4 flow rate of 3.3sccm with a plateau fraction of 0% (a V-shaped absorber profile), i/p-region width of 20nm and absorber thickness of 175nm is used. When used as the bottom junction (a-SiGe:H/a-Si:H) a maximum GeH_4 flow rate of 5.3sccm is used, with a plateau fraction of 30% (U-shaped profile), i/p-region width of 20nm and absorbed thickness of 350nm. More information about the used bandgap profiles can be found in [156].

For the SHJ processing, Topsil Floatzone n-type <100> polished mono-crystalline silicon wafers are used with a thickness of 300μm. These wafers are then textured using a two-step approach. First a 10 minute Tetramethylammoniumhydroxide etch and rinse was applied, followed by an acidic poly-etch, consisting of 1 part HF (40.5% wt. in H_2O), 6 parts HNO_3 (69.5% wt. in H_2O) and 3 parts H_2O. This results in smooth pyramidal surface features on both sides of the wafer. More information about the development, optical behaviour and surface passivation of this texturing approach can be found elsewhere [153]. The backside of the wafer is finished by subsequently processing 10nm i-a-Si:H layer and 10nm n-a-Si:H layer. This is followed by a full area 150nm sputtered ITO layer and an evaporated metal contact consisting of 300nm Ag/ 30nm Cr/ 800nm Al. On the front side of the wafer an i-a-Si:H layer is processed followed by a p-layer and the n-i-p junction with i-nc-Si:H absorber. The front contact, 75nm ITO and 500nm Al, is similar

to the other tandem devices.

Measuring tandem devices

The external quantum efficiency (EQE) was measured using an in-house EQE setup at TU Delft, consisting of a Xenon lamp and a monochromator for spectral data acquisition. To measure both junctions separately, bias light was used to saturate the top and bottom cell in turn. The top cell was saturated using light with wavelengths between 365nm and 530nm, while the bottom cell was saturated with light between 800nm and 950nm. The J-V measurements of the solar cells were conducted using an AM1.5$_G$ solar simulator at an illumination of 100mW $\cdot$ cm^{-2} under a controlled temperature of 25°C. The open-circuit voltage (V_{oc}) and fill factor (FF) were extracted from the J-V curves. Each tandem device consists of a single substrate, on which 24 individual cells with an area of 16mm^2 were processed. All 24 cells on the substrate were measured. The results presented in this work are the average of the 5 best performing cells on each substrate. For each of the four different tandem configurations, the J-V curves and external device characteristics of the cell with the highest conversion efficiency and the highest V_{oc}*FF product can be found in the supplementary information.

Electrical simulations

In this work energy band diagrams are presented of a range of TRJ's to qualitatively and visually support interpretation of the observed trends. The simulations were performed using TCAD Sentaurus [407]. For the simulations uniform materials were assumed with experimentally obtained bandgap and activation energies. To evaluate the energy alignment, Poisson equations were solved, assuming equipotential electrodes. The models and material related parameters used to simulate the device structures presented in this work are reported in [408]. The energy band diagrams are shown under equilibrium conditions, in the dark. The energy alignment is at the core of charge transport. Accordingly, band diagrams under equilibrium illustrate concisely and simply the fundamental mechanisms for charge transport. Adding operational conditions, such as light injection and an applied potential to the band diagrams add more complexity and would make the obtained diagrams less suited for the purpose of qualitatively supporting interpretation of experimentally observed trends.

8.1.3 Results and Discussion

Loss mechanisms in tandem devices

There are several ways in which the properties of the p-doped layer in a TRJ can result in losses to the V_{oc} and FF in a tandem device. Most straightforward, the material properties of the p-layer determine the performance of the bottom n(-i)-p junction. Fundamentally speaking, the active acceptor dopant concentration (N_A) can increase the built-in voltage (V_{bi}) across the i-layer in the bottom cell, since

$$V_{bi} \sim \ln \left(\frac{N_A}{n_i} \right) \tag{8.1}$$

where n_i is the intrinsic carrier concentration. The active dopant concentration, amongst other material properties such as the stoichiometry [156], material phase fractions in heterogeneous materials and the material density [159], can also influence the bandgap energy E_G and activation energy E_{act} of the the p-layer. This in turn influences the energetic band alignment at the i/p-interface of the bottom cell, which can significantly affect the V_{bi} in a drift device, according to [409]:

$$qV_{bi} = E_G - E_{Fn} - E_{Fp} \tag{8.2}$$

where E_G is the band gap energy of the intrinsic absorber layer and E_{Fn} and E_{Fp} are the Fermi energy levels in the n- and p-doped layer, respectively. With no significant variations in the work function of the p-layer, which we can assume according to [410], and with the i-layer and n-layer deposition conditions remaining constant, changes in E_G or E_{act} of the p-layer will have an effect on E_{Fp} and consequently on the built-in voltage in the device. The p-layer material properties do not only affect the device voltage directly. A variation in the optical transparency or refractive index of the p-layer in the TRJ can influence the transmission into the bottom cell. This results in changes in the generated photo-current density (J_{ph}), which influences the V_{oc} according to:

$$V_{oc} \sim \ln\left(\frac{J_{ph}}{J_0}\right) \tag{8.3}$$

While this effect is generally minor, variations in the recombination current density (J_0) are not. The J_0 is an indicator of the charge carrier recombination in a device, and the i/p-interface is well known for being a significant recombination site in thin film silicon devices, if not well-engineered [57], [58], [85].

All these effects influence the performance of the bottom cell in the device. If we consider the p-layer as part of TRJ in a multijunction device, additional complexity is added. As mentioned, in n-(i-)p/n-i-p tandem PV devices, the TRJ should facilitate the recombination of holes from the bottom cell with electrons from the top cell to prevent non-ohmic behaviour. As the FF is a measure of the resistive losses in a photovoltaic device, it will be affected by a p-layer that results in a poorly engineered TRJ or i/p-interface. Additionally, in tandem devices the FF is subject to the mismatch between the current density generated in the top and bottom cell [411], [412]. Variations in the refractive index or optical transparency of the p-layer can affect the current matching between both junctions[46], [48], [405], consequently affecting the FF. Moreover, the FF can vary depending on which of the subcells is current limiting. These combined effects can make pinpointing the origin of observed trends in tandem devices challenging. The latter two challenges are mitigated in this work, to a certain extent, by performing experiments across different device architectures with different current matching conditions and current limiting subcells.

Influence of p-nc-SiO$_X$:H deposition conditions on the performance of tandem a-Si:H/nc-Si:H solar cells

The influence of variations in the F_{B2H6} during deposition of the p-layer of the bottom junction in nc-Si:H/a-Si:H tandem devices are reported in Fig.8.2. A trade-off can be
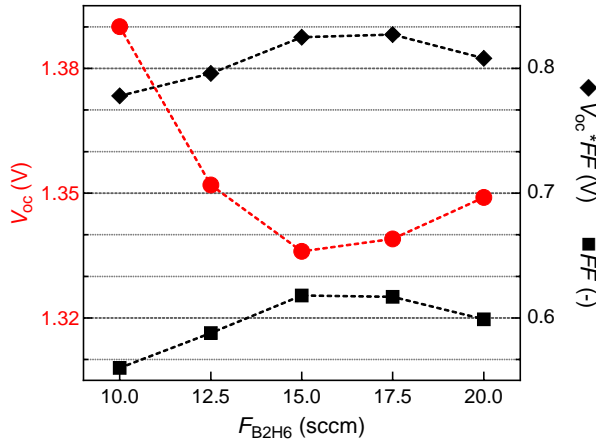
Figure 8.2: The V_{oc} (red circles, left y-axis), FF (black squares, right axis) and $V_{oc}*FF$ product (black diamonds, right axis) of nc-Si:H/a-Si:H tandem solar cells as a function of the diborane gas flow rate of the p-nc-SiO$_X$:H layer in the tunnel recombination junction. The p-layer stack consists of a single p-nc-SiO$_X$:H layer. All samples are processed at F_{H2}=170sccm and F_{CO2}=1.8sccm.

observed between the V_{oc} and FF as a function of F_{B2H6}. Increasing F_{B2H6} from 10 to 15sccm, for instance, increases the FF from 56% to 61.8%, while the V_{oc} is decreased by 54mV.

The opto-electrical properties of p-nc-SiO$_X$:H are a function of the relative a-SiO$_X$:H, nc-Si:H and a-Si:H material phase fractions, the density of the amorphous phase and the active dopant concentration [159]. An increase of F_{B2H6} can result in the suppression of crystalline growth, a decrease in a-SiO$_X$:H phase fraction and potentially in an increase of the active doping concentration [159].

It is difficult to determine which of these effects results in the observed V_{oc} and FF trends. A decrease of the a-SiO$_X$:H phase fraction results in a decrease of the bandgap energy near the i/p-interface, which can result in the observed V_{oc} decrease, according to Eq.8.2. At the same time, an increase of F_{B2H6} can results in an increase of the active dopant concentration, increasing V_{oc} according to Eq.8.1. A competition between these two effects could result in the observed V_{oc} trends as a function of F_{B2H6}.

The FF also exhibits an optimum in the investigated range. Crystalline tissue in p-nc-SiO$_X$:H grows in filaments [36], [61], [109]. These filaments are essential for transverse carrier transport through the p-layer. With increasing F_{B2H6} crystalline growth will be suppressed [60], [92], [159]. As a result, carrier transport might suffer, leading to additional resistive losses and a FF decrease. Additionally, sufficient amorphous tissue is required to passivate the crystalline grains and crystalline phase at the i/p-interface [85]. An increase of the amorphous phase faction could improve this passivation, improving the FF. This trade-off might result in the observed optimum of the FF.

Alternatively, as deposition time was kept constant, an increase of F_{B2H6} can result in an increase of the deposition rate [103], [137], [159], and consequently in thicker p-nc-SiO$_X$:H
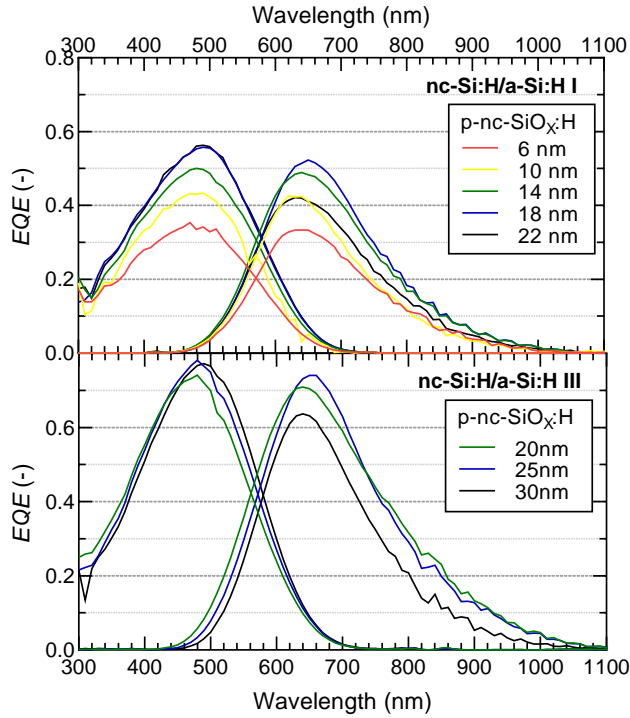
Figure 8.3: External Quantum Efficiency plots of the top and bottom junctions of two separate series of nc-Si:H/a-Si:H tandem devices. The thickness of the p-nc-SiO$_X$:H layer in the tunnel recombination junction of the tandems is varied. Experimental series **I** (top) is processed with a single p-nc-SiO$_X$:H layer while series **III** (bottom) is processed with a p-nc-SiO$_X$:H/p-nc-Si:H bi-layer configuration.

layers. This can impact the V_{oc} and FF of the tandem devices, as will be discussed in more detail in the next section.

The results presented in Fig.8.2 indicate that variations in F_{B2H6} largely results in trade-offs between V_{oc} and the FF. Four additional series of tandems devices, not presented here, in which the F_{H2} and F_{CO2} were varied for different F_{B2H6} values showed similar trade-offs without significant overall improvements in $V_{oc}*FF$. These combined results indicate that there is a limit to the gains than can be realized by exclusively changing the opto-electrical properties of the p-nc-SiO$_X$:H, using a single unprofiled p-nc-SiO$_X$:H layer.

Influence of p-nc-SiO$_X$:H thickness on the performance of tandem a-Si:H/nc-Si:H solar cells

Next, we investigate the influence of the thickness of the p-layer in the TRJ of tandem PV devices. The EQE curves in Fig.8.3(Top) show a significant increase of both the top and bottom cell, when the thickness of the p-doped layer is increased from 6nm to 18nm. Reflection measurements, presented in the supplementary information, show no
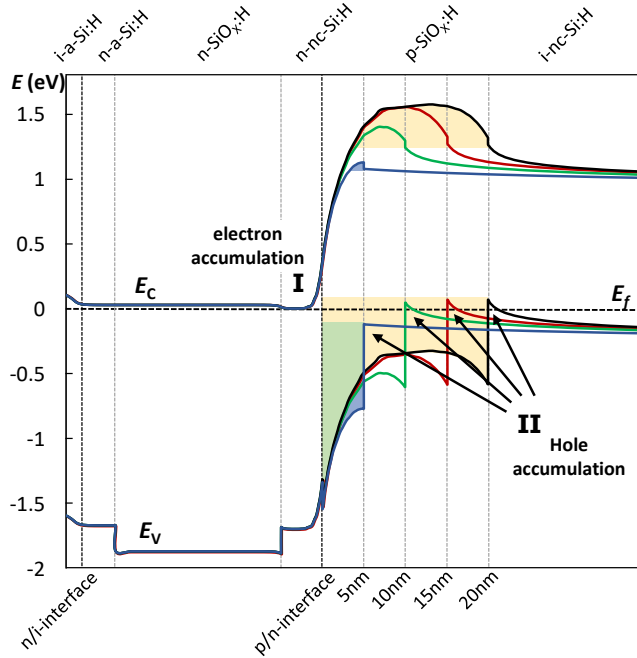
Figure 8.4: Electrical simulations of the TRJ under equilibrium conditions in the dark. The energy band diagrams are shown for a p-nc-SiO$_X$:H thickness of 5nm (blue), 10nm (green), 15nm (red) and 20nm (black). For all thicknesses the conduction band edge E_C and valence band edge E_V are shown. The energy levels of the band edges are indicated in reference to the Fermi energy level E_f, positioned at 0 eV. The materials presented in the plots are indicated on top of the band diagram. The n/i-interface and p/n-interfaces are indicated below the band diagram. Position I and II, the electron and hole accumulations sites, are referenced in the text. The coloured areas indicate the energy barriers for holes (bottom) and electrons (top), respectively. The blue areas indicated the barrier for a p-nc-SiO$_X$:H layer thickness of 5nm, while the yellow areas indicates the barriers for a 20nm p-nc-SiO$_X$:H layer. The green area indicates an overlap between the two barriers.

significant change in the front reflection of the devices, indicating an electrical rather than an optical effect. Both junctions are measured separately, while the opposite junction is saturated with bias light. As such, we can observe the effectiveness of generation and collection in each junction in turn. Both junctions, for thin p-layers, have a similar EQE limit. Moreover, the EQE increases to a similar degree with increasing p-layer thickness. This indicates that for a p-layer thickness below 18nm, collection in the tandem device is limited by the TRJ. From 18nm to 22nm the device no longer seems to be limited by the TRJ, as the EQE of the top cell only shows a minor increase, while the bottom cell EQE is decreased. This latter effect can also be observed in Fig.8.3(Bottom), where the EQE curves of another series of tandem nc-Si:H/a-Si:H devices are plotted. This is likely an optical effect as more light is reflected back into the top cell and less light transmitted into the bottom cell with increasing p-nc-SiO$_X$:H thickness, which is in line with earlier reports [46], [48], [50], [51], [413].

In order to analyze these effects, electrical simulations of the TRJ have been performed. A schematic band diagram of the TRJ as a function of the p-nc-SiO$_X$:H thickness is shown in Fig.8.4. The visual shows the energetic band alignment at the i/p-, p/n- and n/i-interfaces, for p-nc-SiO$_X$:H layers with a thickness of 5nm, 10nm, 15nm and 20nm and constant activation energy (E_{act}) and bandgap energy E_G. Considering that free electrons reside in the conduction band and move down slope, while holes move up-slope in the valence band, electrons photo-generated in the top junction will have a tendency to accumulate at the p/n-interface, at position **I**. Similarly, holes generated in the bottom junction will have a tendency to accumulate at the i/p-interface, at position **II**. Note that the desired recombination event is one in which an electron from the top junction, from position **I**, recombines with a hole from the bottom junction, at position **II**. This recombination event is most likely to occur through a defect assisted process, referred to as trap-assisted tunneling in several simulations studies involving tunneling junctions [410], [414].

In order for this tunneling event to take place, the holes need to overcome an energy barrier, indicated by the coloured areas in the valence band in Fig.8.4. As can be understood from this figure, the energy barrier consists of a spatial and energetic component; the best tunneling junction is one in which the position **I** and **II** are energetically aligned and spatially close. For efficient TRJ operation, apart from effectively directing holes towards p/n-interface, electrons from the bottom junction should be effectively shielded from the p/n-interface, lest they contribute to the accumulation of electrons at position **I** or increase SRH-recombination inside the p-layer. The energy barrier against electron movement to the tunneling junction is indicated by the coloured areas in the conduction band in Fig.8.4. Both ineffective hole transport and poor electron-shielding can result in the built-up of charge at position **I** and/or **II**, and the creation of a reverse electric field across the TRJ.

The visual provides excellent insight into the nature of the p-thickness related collection issue. It can be observed that at a p-nc-SiO$_X$:H layer thickness of 5nm (blue curves), there is a large energy barrier against hole movement, indicated by the blue/green area (bottom), and position **I** and **II** are energetically poorly aligned. Moreover, there is hardly an energy barrier, indicated by the blue area (top), against the movement of electrons from the bottom junction to the p-layer and even towards position **I**. When the thickness is increased, band-bending in the p-layer is shifted upwards. As a result, at a p-nc-SiO$_X$:H thickness of 10nm (green curve), position **I** and **II** are energetically well aligned, the hole barrier is decreased and the energy barrier against electron movement is significantly increased. When the thickness is further increased to 15nm (red curve), the conduction band edge in the p-layer is further shifted upwards. Consequently, the energy barrier against electron movement is further increased with respect the energetic barrier against hole movement, improving the TRJ recombination efficiency. Simply put, with the electrical properties of the p-nc-SiO$_X$:H layer being what they are, a minimum p-layer thickness is required for the p-doped layer to fulfill its function in the bottom junction as an electron shield a semi-permeable membrane for holes.

It should be noted that the assumption of a constant E_{act} and E_G as a function of thickness is potentially a simplification. The p-layer effectiveness as a function of thickness could additionally be improved as the E_G and E_{act} evolve along the growth direction [159].
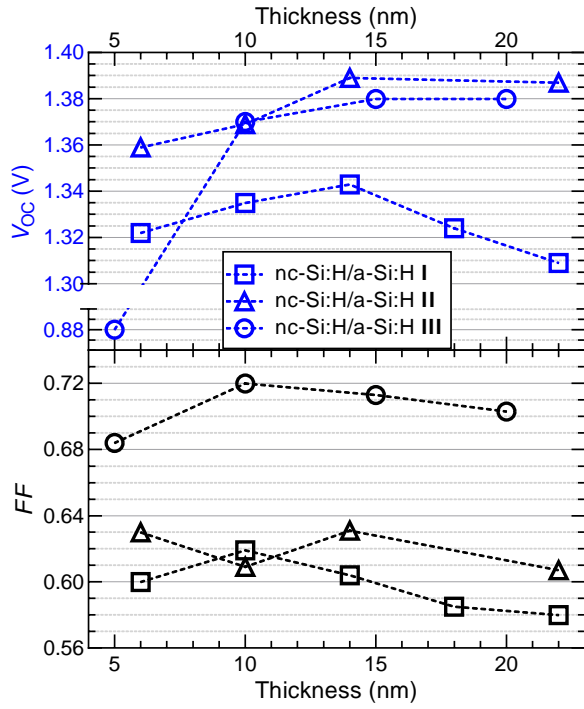
Figure 8.5: The V_{oc} (Top) and FF (bottom) of tandem nc-Si:H/a-Si:H devices as a function of p-nc-SiO$_X$:H thickness. The icons represent three separate experimental series, where the **I**(squares) and **II**(triangles) are processed with a single p-nc-SiO$_X$:H layer and series **III**(circles) is processed with a p-nc-SiO$_X$:H/p-nc-Si:H bi-layer configuration.

The influence of the p-nc-SiO$_X$:H thickness on the V_{oc} and FF of three separate series of tandem nc-Si:H/a-Si:H devices is plotted in Fig.8.5, where series **I** and **II** have a single p-nc-SiO$_X$:H layer (and different top junction design) and series **III** has a bi-layer configuration. The bi-layer is schematically visualized in Fig.8.1 with a p-nc-SiO$_X$:H layer and a thin 3-5nm p-nc-Si:H contact layer at the interface with the n-layer. A few things are apparent from these results. 1. the FF is rather sensitive to the p-layer thickness and has optimum in the range of 10-15nm. 2. An optimal V_{oc} is achieved for p-layer thicknesses in the range 15-20nm. For series **I** and **III** the V_{oc} decrease for a p-layer thicknesses exceeding 15nm is minimal within the reported range, which is unlike the trend for the FF. This seems to indicate that for an optimal V_{oc} a minimal rather than a specific optimal p-layer thickness is required, or at least that there is a greater range of optimal thicknesses. In terms of V_{oc}*FF product, optimal performance is realized for a thickness of about 15nm.

These trends in V_{oc} and FF can also be understood from the simulations shown in Fig.8.4. As the thickness is increased from 5nm to 15nm, the band bending at the i/p-interface changes. As a result, the difference between the Fermi level and the valence band edge

at the i/p-interface is decreased, and V_{bi} is increased according to Eq.8.2, resulting in the observed increase in V_{oc}. Fig.8.4 shows that this is no longer true if the thickness is further increased beyond 15nm; the V_{oc} improvement reaches an optimum. Further increasing the thickness beyond this point increases the distance a hole has to travel through the p-layer, increasing resistance against this movement, as the defect density in the p-nc-SiO$_{\mathrm{X}}$:H layer is assumed to be much higher than in the i-layer. Consequently, J_0 is increased, decreasing V_{oc} according to Eq.8.3. Alternatively, the V_{oc} increase of the tandem devices, with p-nc-SiO$_{\mathrm{X}}$:H thickness, can be understood to be the result of a decrease of the reverse electric field across the TRJ.

A similar effect results in the observed trend for the FF, although that is better explained in terms of resistances. From 5nm to 10-15nm, as a result of improved electron shielding, the shunt resistance is increased as the free movement from electrons from the bottom to the top junction is impeded. For series **I**, for instance, the measured shunt resistance more than doubled by increasing the p-nc-SiO$_{\mathrm{X}}$:H thickness from 5nm to 10nm, from $\approx 6300\Omega{\cdot}\mathrm{m}^2$ to $\approx 13600\Omega{\cdot}\mathrm{m}^2$. Further increasing the p-layer thickness results in increased recombination in the p-layer and at the i/p-interface, increasing the R_{S} and decreasing the FF.

Another important observation from the V_{oc} and FF of the devices is that the V_{oc}*FF product of the series with contact layer (series **III**) is significantly higher than that of the other two series. In fact, incorporating the contact layer results in a significant FF boost of about 9% absolute. This improvement is also apparent in Fig.8.3 , where the EQE's of series **III** are significantly higher than those of series **I**. Consequently, the next step is to investigate the influence of the contact layer properties.

Influence of the contact layer on the performance of tandem PV devices

To investigate the influence of the contact layer, the contact layer properties are varied, resulting in 7 different bi-layer configurations. A number of these bi-layer configuration variations were performed across four different tandem device architectures. The results are shown in Fig.8.6(Top) where the V_{oc}*FF product is plotted for samples with a 5nm p-type amorphous Si:H (p-a-Si:H) contact layer, no contact layer (ref) and 6 different 3-6nm p-nc-Si:H contact layers that are processed at different conditions (gas flow rates, power) but all designed to have a low E_{act} compared to the p-nc-SiO$_{\mathrm{X}}$:H layer. E_{act} determination is based on film measurements performed in earlier work [85], [159].

The results clearly show that including a thin p-a-Si:H, which has a relatively high E_{act}, is detrimental to device performance. On the other hand, for nearly all series the V_{oc}*FF product is improved when a p-nc-Si:H contact layers is added. This indicates that the exact deposition conditions, and resulting material properties, of the thin contact layer are relatively unimportant. As long as they result in a low activation energy film, the contact layer will provide a performance boost in reference to a single p-nc-SiO$_{\mathrm{X}}$:H layer. Fig.8.6(bottom) shows the relation between the series resistance (R_{S}) of the devices and the V_{oc}*FF product. By comparing the devices processed in a single series of experiments, so icons of similar type and colour, it can be observed that the V_{oc}*FF improvements are predominantly a results of the decreased R_{S}. A notable exception are the a-SiGe:H/a-Si:H tandem devices. For these devices, the addition of a contact layer leads to both a reduction of the R_{S} and an increase of the V_{oc}*FF product. Unlike the other tandems
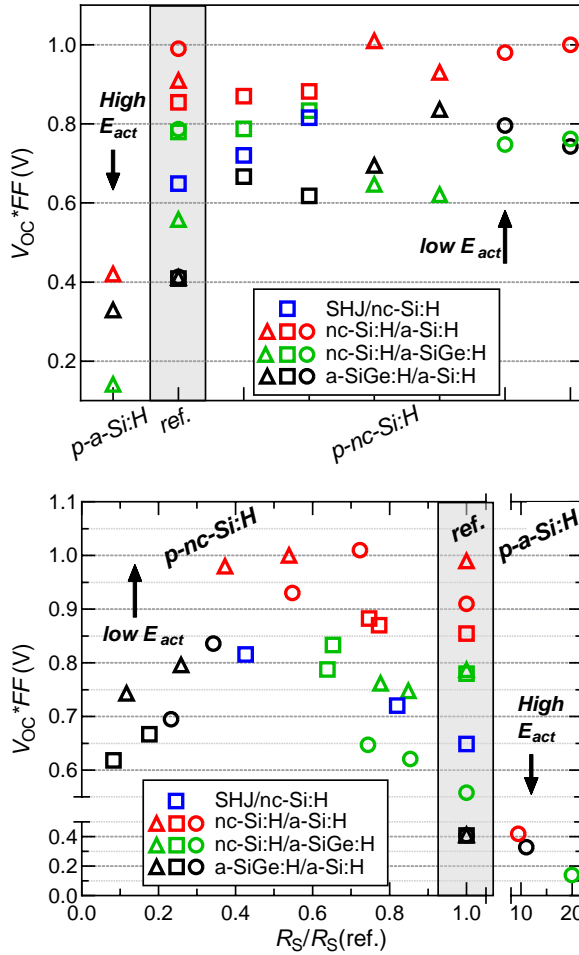
Figure 8.6: The V_{oc}-FF product plotted as a function of the different contact layers (Top) and V_{oc}-FF product plotted as a function of change in series resistance (R_s) with respect to the reference sample without contact layer (bottom). Contact layers are processed on top of a 15-20nm p-nc-SiO$_X$:H layer. Tick marks in top plot indicate samples with a 5nm p-a-Si:H contact layer, no contact layer (ref) and 6 different low E_{act} 3-6nm p-nc-Si:H contact layers, processed at different conditions (gas flow rates, power). The arrows and E_{act} designation indicate the E_{act} in reference to that of the single p-nc-SiO$_X$:H layer. The icons (triangle-square-circle) indicate series of samples processed at the same point in time with the exact same deposition conditions for all supporting layers. The colours indicates the multijunction architecture, namely SHJ/nc-Si:H (blue), nc-Si:H/a-Si:H (red), nc-Si:H/a-SiGe:H (green) and a-SiGe:H/a-Si:H (black).

Figure 8.7: Electrical simulations of the TRJ under equilibrium conditions in the dark. The energy band diagrams are shown for a single p-nc-SiO$_X$:H layer (blue), and two bi-layer configuration with a p-nc-Si:H contact layer with a low E_{act} of 250meV (red) and still lower E_{act} of 32meV (black). All p-layer stacks have a total thickness of 20nm, the contact layers have thickness of 5nm. For all configurations the conduction band edge E_C and valence band edge E_V are shown. The energy levels of the band edges are indicated in reference to the Fermi energy level E_f, positioned at 0 eV. The materials presented in the plots are indicated on top of the band diagram. The n/i-, p/n- and i/p-interfaces are indicated below the band diagram. The electron accumulation site at position **I**, and hole accumulation sites at positions **II** and **X** are referenced in the text. The coloured areas indicate the energy barriers for holes (bottom) and electrons (top), respectively. Blue areas indicate the barrier for a single p-nc-SiO$_X$:H layer, while the yellow areas indicate the barriers for the bi-layer configuration with the lowest E_{act} contact layer. The green area indicates an overlap between the two barriers.

however, the devices with the contact layer resulting in the lowest R_S decrease do not have the highest $V_{oc}*FF$ product. This is because for these tandems, which have two thin amorphous absorbers, the shunt resistance had a dominant influence on the FF.

The results provide some clues as to the dominant loss mechanism in the devices. The recombination efficiency at the p/n-interface does not seem to be a limiting factor. More specifically, the availability of defects, or traps, at the p/n-interface to facilitate tunneling is likely not limiting. In this case, trap-assisted tunneling would potentially be improved by the addition of a thin defect-rich p-a-Si:H layer. Rather, the availability of holes at the p/n-interface, or the hole transport towards the p/n-interface is likely limiting. Fig.8.7 shows how a low-E_{act} contact layer potentially improves hole availability. In the figure several band diagrams are schematically shown of the TRJ, visualizing the situation

without contact layer (blue curve) , with contact layer (red curve) and with a very low E_{act} contact layer (black curve). It can be observed that with decreasing E_{act}, the band bending changes such that the hole barrier is continuously decreased. Moreover, a position is created indicated position **X** in Fig.8.7, spatially close to the electron accumulation position **I**, where holes can accumulate. This means that the introduction of a low E_{act} contact layer not only reduces the overall hole barrier and increases the overall electron barrier. It also creates an additional "pathway", where the holes overcome two small energetic barriers, from position **II** to position **X** and subsequently to position **I**, rather than one large barrier. Consequently, with decreasing contact layer E_{act}, recombination occurs more efficiently at the TRJ as carriers are more effectively "directed" towards the p/n-interface, reducing the probability of recombination between generation and "desired" recombination at the p/n-interface.

Do we need p-nc-SiO$_X$:H?

The preceding section shows that devices with a p-nc-SiO$_X$:H/p-nc-Si:H bi-layer configuration have a much higher $V_{\mathrm{oc}}*FF$ product than devices without p-nc-Si:H layer. This begs the question: is the p-nc-SiO$_X$:H layer a requirement? In other words, would not a single 15-20nm p-nc-Si:H layer outperform the bi-layer configurations?

To answer this question, 6 different p-layer configurations are processed for 3 different tandem device architectures. The results are plotted in Fig.8.8, where the red open icons represent the samples without p-nc-SiO$_X$:H layer. The other samples are different p-nc-SiO$_X$:H/p-nc-Si:H or p-nc-SiO$_X$:H/p-nc-SiO$_X$:H$^+$ bi-layer configurations. p-nc-SiO$_X$:H$^+$ indicates that the p-nc-SiO$_X$:H contact layer is processed with a higher F_{B2H6} flow rate in reference to the initial layer.

It is apparent that the samples without p-nc-SiO$_X$:H layer are the worst in each series, with a single outlier, irrespective of device architecture. Clearly, the p-nc-SiO$_X$:H layer is a requirement for optimal tandem device performance. This is likely due to its high
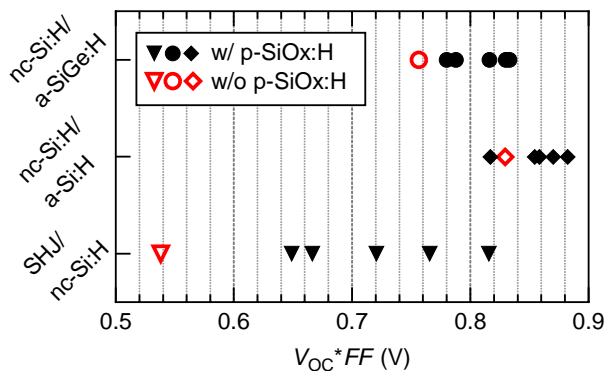
Figure 8.8: V_{oc}-FF product for 3 different tandem device architectures. Red icons indicate a single p-nc-Si:H layer in the TRJ. Black icons indicate 5 different bi-layer p-nc-SiO$_X$:H/p-nc-SiO$_X$:H$^+$ and p-nc-SiO$_X$:H/p-nc-Si:H bi-layer configurations.
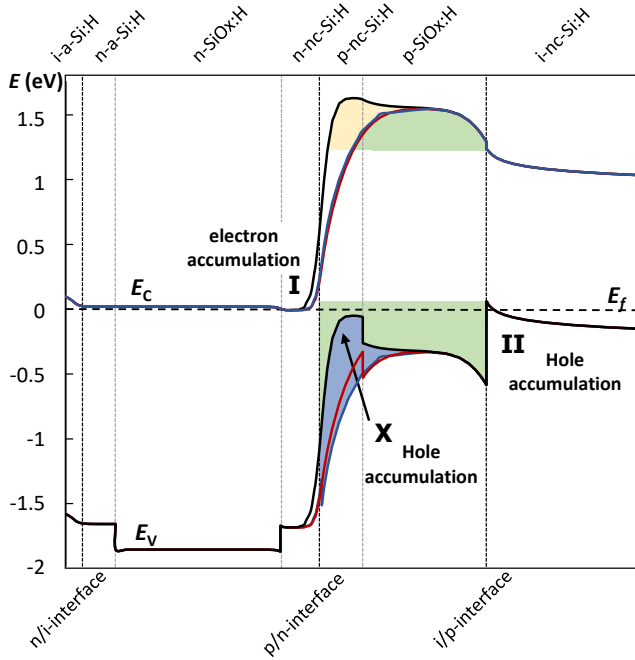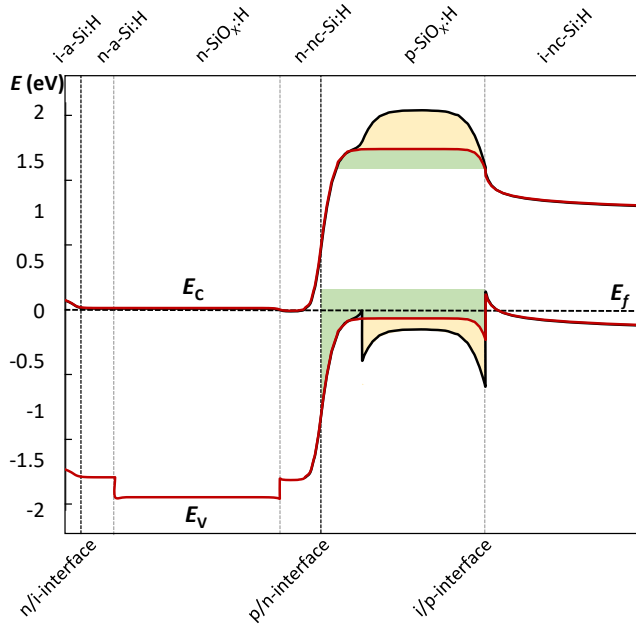
Figure 8.9: Electrical simulations of the TRJ under equilibrium conditions in the dark. The energy band diagrams are shown for a 15nm p-nc-SiO$_\text{X}$:H/ 5nm p-nc-Si:H bilayer configuration (black) and a 20nm p-nc-Si:H layer (red). For both p-layer stacks the E_C and valence band edge E_V are shown. The energy levels of the band edges are indicated in reference to the Fermi energy level E_f, positioned at 0 eV. The materials presented in the plots are indicated on top of the band diagram. The n/i-, p/n- and i/p-interfaces are indicated below the band diagram. The coloured areas indicate the energy barriers for holes (bottom) and electrons (top), respectively. The yellow area indicates the barrier for the bi-layer, while the blue areas indicates the barriers for the single p-nc-Si:H layer. The green area indicates an overlap between the two barriers.

bandgap nature. The combination of high bandgap energy and low activation for a well performing p-contact has previously been reported for SHJ devices, where the p-contact is in contact with an n-type TCO [415]. The band diagrams in Fig.8.9 show how the bi-layer configuration with p-nc-SiO$_X$:H can potentially improve performance with respect to a single p-nc-Si:H layer. Indicated in the visual is the situation where the E_G of the p-nc-SiO$_X$:H layer increases more strongly, with respect to the p-nc-Si:H layer, than the E_{act}. In this case, the electron barrier with respect to the hole barrier is increased. In both cases the p-nc-Si:H ensures good alignment at the p/n-interface. Alternatively, the high bandgap nature of the p-nc-SiO$_X$:H at the i/p-interface, or more specifically the larger difference between the conduction band edge and Fermi level in the p-layer, could decrease E_{Fp} and result in higher V_{bi} according to Eq.8.2. This is especially true for higher bandgap absorbers. Finally, it should also be noted that better passivation by the predominantly amorphous p-nc-SiO$_X$:H at the i/p-interface, with respect to p-nc-Si:H, could also potentially positively affect the $V_{oc}*FF$ product of the tandem devices.

p-nc-SiO$_X$:H$^+$ contact layer doping

So far, the highest $V_{oc}*FF$ products have been achieved with a p-nc-SiO$_X$:H/p-nc-Si:H bi-layer configuration. The question is however, if the relatively low E_{act} of the p-nc-Si:H is indeed the reason behind the improved electrical performance of the tandem devices, could a similar improvement be achieved by a p-nc-SiO$_X$:H/p-nc-SiO$_X$:H$^+$ bi-layer configuration, where the p-nc-Si:H contact layer is replaced by a heavily doped p-nc-SiO$_X$:H layer? Such an alternative bi-layer configuration could potentially yield higher current densities because of the higher optical transparency of the p-nc-SiO$_X$:H layer.

Fig.8.10 shows the relative improvement in FF (bottom) and V_{oc} (top) with respect to a single p-nc-SiO$_X$:H layer, as a function of F_{B2H6} of the p-nc-SiO$_X$:H$^+$ contact layer. The icons represent different series of cells. With a single outlier, strong improvements in performance with addition of a p-nc-SiO$_X$:H$^+$ layer can be observed, regardless of device architecture. For some samples, such as the nc-Si:H/a-SiGe:H tandems between 40-60sccm and the a-SiGe:H/a-Si:H tandem between 30-50sccm, the $V_{oc}*FF$ product improvement saturates, at which point there is a trade-off between V_{oc} and FF. For most series though the optimal F_{B2H6} is apparently located outside of the observed experimental range. The highest $V_{oc}*FF$ product of the devices with a p-nc-SiO$_X$:H/p-nc-SiO$_X$:H$^+$ bi-layer is comparable to that of the devices with a p-nc-SiO$_X$:H/p-nc-Si:H bi-layer. This would seem to indicate that the low E_{act} is the most important criteria for the contact layer in a bi-layer configuration.

It should be noted that in Fig.8.2, where the p-nc-SiO$_X$:H layer was not used in a bi-layer configuration, a significant decrease was observed in terms of $V_{oc}*FF$ product for $F_{B2H6} \geq$15-20sccm. This is likely a result of "side effects" of increasing the dopant gas flow rate to p-nc-SiO$_X$:H material growth. These effects include a more porous amorphous growth with lower crystallinity and a larger a-SiO$_X$ material phase fraction [159]. The results show however that for a 3-6nm contact layer these side-effects are minimal.

Since both bi-layer p-nc-SiO$_X$:H/p-nc-SiO$_X$:H$^+$ and p-nc-SiO$_X$:H/p-nc-Si:H bi-layer configurations yield similar $V_{oc}*FF$ products, the final question that remains is which bi-layer configuration should be used for optimal device performance. To answer this question,
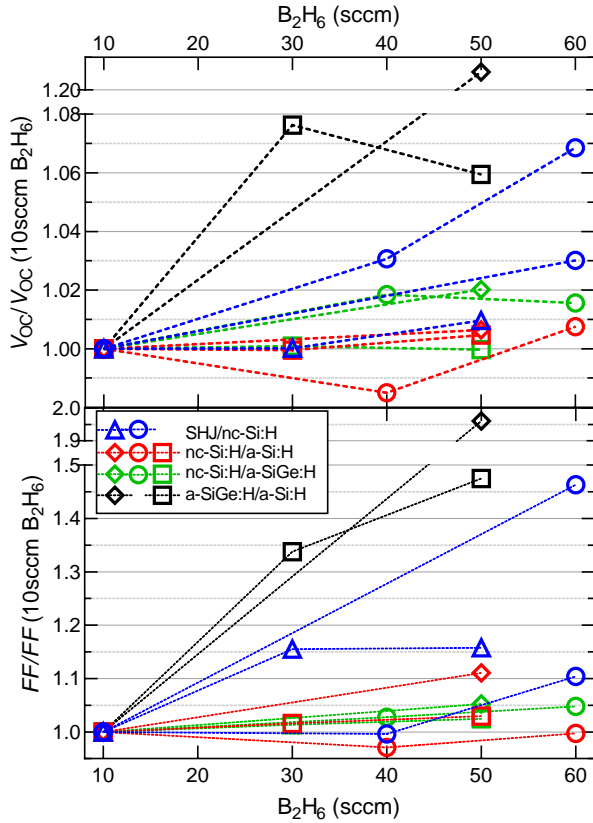
Figure 8.10: V_{oc} (top) and FF (bottom) improvement in bi-layer p-nc-SiO$_X$:H/p-nc-SiO$_X$:H$^+$ configurations. Improvement is determined with respect to a reference sample processed without 3-5nm p-nc-SiO$_X$:H$^+$ contact layer but of similar thickness. V_{oc} and FF improvements are plotted as a function of the diborane flow rate of the contact layer. The icons indicate series of samples processed at the same point in time with the exact same deposition conditions for all supporting layers. The colours indicates the multijunction architectures, namely SHJ/nc-Si:H (blue), nc-Si:H/a-Si:H (red), nc-Si:H/a-SiGe:H (green) and a-SiGe:H/a-Si:H (black).
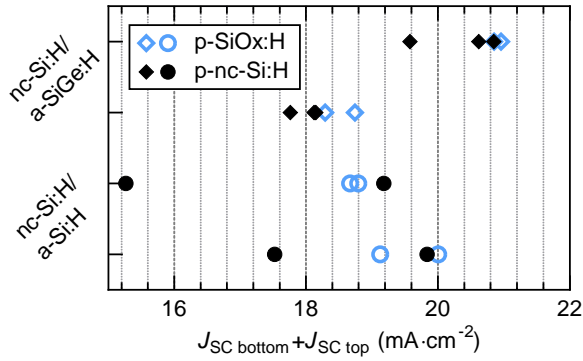
Figure 8.11: The sum of the J_{sc} of the bottom junction and the J_{sc} of the top junction for two different series of nc-Si:H/a-Si:H (circles) and nc-Si:H/a-SiGe:H (diamonds) device architectures. J_{sc} for each junction is determined by weighing the measured spectral EQE curve with the AM1.5g spectrum. All samples have a p-nc-SiO$_X$:H/p-Si:H bi-layer configuration, with p-nc-SiO$_X$:H (Blue, open symbols) and p-nc-Si:H (black, closed symbols) contact layers. The individual J_{sc}'s of the bottom and top junctions can be found in the supplementary information.

we consider the sum of the measured J_{sc}'s in the top and bottom junction of the tandem devices, as presented in Fig.8.11. The figure shows the sum of the current densities for two different experimental series of bi-layer configurations, indicated by the circles and diamonds, applied in two different device architectures. It can be observed that the p-nc-SiO$_X$:H/p-nc-SiO$_X$:H$^+$ bi-layer configurations overall result in higher current densities, likely resulting from less parasitic absorption. Ultimately though, the choice for a specific bi-layer configuration will depend on the intended device architecture. Indeed, parasitic absorption in a 3-6nm p-nc-Si:H layer positioned behind a 2000-3000nm i-nc-Si:H absorber, in reference to the incident light, will be negligible. Consequently, the obtained $V_{oc}*FF$ products could be considered to indicate a level of freedom of design for p-nc-SiO$_X$:H/low-E_{act} bi-layer configurations in which the transmission and reflection at the TRJ's can be taken into account.

8.1.4 Conclusion

In this work the experimental results of a large number of SHJ/nc-Si:H, nc-Si:H/a-Si:H, nc-Si:H/a-SiGe:H and a-SiGe:H/a-Si:H multijunction devices are presented. The fundamental mechanisms behind the observed phenomena are qualitatively demonstrated using energy band diagrams obtained through electrical simulations in TCAD Sentaurus. The influence of thickness and design of the p-layer in the TRJ of these tandems are observed across different device architectures. It was found that for optimal device performance in terms of $V_{oc}*FF$ product, the presence of a high bandgap p-nc-SiO$_X$:H layer is crucial, and the optimal thickness is in the range of 12-18nm. Moreover, a strong improvement was observed when a thin, low activation energy contact layer was used in combination with the p-nc-SiO$_X$:H layer. High $V_{oc}*FF$ products could be achieved both by p-nc-SiO$_X$:H/p-nc-SiO$_X$:H$^+$ and p-nc-SiO$_X$:H/p-nc-Si:H bi-layer configurations.

8.2 Application of metal, metal-oxide and silicon-oxide based intermediate reflective layers for current matching in autonomous high voltage multijunction photovoltaic devices

This section was recently accepted in *Progress in Photovoltaics*[†]

Abstract

A logical next step for achieving a cost price reduction per Watt peak of photovoltaics (PV) are multijunction PV devices. In two-terminal multijunction PV devices, the photo-current generated in each subcell should be matched. Intermediate reflective layers (IRL)'s are widely employed in multijunction devices to increase reflection at the interface between subcells to enhance current generation in the subcell(s) positioned before the IRL, in reference to the incident light.

In this work, the results of over 65 multijunction devices are presented, in order to explore the effect of different current matching approaches. The influence of variations in absorber thickness as well as thickness variations of different IRL's based on silicon-oxide, various transparent conductive oxides (TCO) and metallic layers on all-silicon multijunction PV devices is studied. Specifically, hybrid, 2-terminal, monolithically integrated silicon heterojunction (SHJ) and thin film nanocrystalline silicon (nc-Si:H) and amorphous silicon (a-Si:H) tandem and triple junction devices are processed. Based on these experiments, certain design rules for optimal current matching operation in multijunction devices are formulated.

Finally, taking these design rules into account, record all-silicon multijunction devices are processed. Conversion efficiencies close 15% and V_{oc} ≈2V are demonstrated for triple junction SHJ/nc-Si:H/a-Si:H devices. Such conversion efficiencies for a wireless, high-voltage wafer-based all-silicon 2-terminal multijunction PV device opens the way for efficient autonomous solar-to-fuel synthesis systems as well as other wireless innovative approaches in which the multijunction solar cell is used not only as a photovoltaic current-voltage generator, but also as an ion-exchange membrane, electrochemical catalysts and/or optical transmittance filter.

8.2.1 Introduction

Multijunction photovoltaic (PV) devices have the potential to enhance spectral utilization, thereby achieving increased PV yield per area as well as reduced heating and lower temperature coefficients. Additionally, multijunction PV devices can achieve high voltages without interconnection, facilitating autonomous solar-to-fuel applications.

Photo-generation of charge carriers occurs in each subcell in multijunction devices. For optimal operation, in two-terminal devices, the photo-current generated in each subcell should be matched. In multijunction devices, generally, the bottom cell is not current limiting as a reflective metallic layer can be positioned at the back of the devices. For the top or middle subcell(s), the simplest means of increasing the photo-generated current is increasing the absorber thickness. However, this generally results in an increase of the series resistance, and consequently decrease of the open circuit voltage (V_{oc}) and Fill Factor (FF), as the recombination probability increases with the average distance a photo-generated charge carrier has to travel for collection. Such a trade-off between the short circuit current density (J_{sc}) and V_{oc} has been demonstrated in silicon solar cells, including devices with hydrogenated (:H) nano-crystalline (nc-) silicon (Si) absorbers [72], amorphous (a-) Si-germanium (SiGe):H absorbers [156] and amorphous silicon-oxide (SiO_x):H absorbers [172].

For that reason, intermediate reflective layers (IRL's) are widely employed in multijunction devices [40], [46]–[48], [51], [405], [411], to enhance current generation and/or reduce the absorber thickness. IRL's are used to increase reflection at the interface between subcells to enhance current generation in the subcells(s) positioned before the IRL, in reference to the incident light. There are different materials that can be used for such an IRL. In certain device architectures, such as a perovskite/crystalline silicon (c-Si) [117] and a-Si:H/CIGS [75] transparent conductive oxides (TCO) are positioned in between subcells. In silicon based multijunction devices, silicon-oxide based IRL's are often employed [46], [48], [404], [405]. Generally an n-type (n-) SiO_x layer is used [416]. The properties of n-SiO_x layers are more easily adjusted to achieve characteristics desirable for an IRL, in reference to p-SiO_x properties, as the device performance is very sensitive to p-SiO_x characteristics like the oxide fraction and layer thickness [155]. In this work, in addition to silicon-oxide and TCO based IRL's, the use of a very thin metallic layer is explored.

In order to characterise the performance of the different IRL's, all-silicon multijunction PV devices are used. Specifically, a hybrid c-Si and thin film Si multijunction device is used, consisting of a silicon heterojunction (SHJ) subcell and one or two additional thin film silicon subcells based on nc-Si:H and a-Si:H absorbers. The advantage of these plasma enhanced chemical vapour deposition (PECVD) processed, 2-terminal, monolithically integrated devices, is that a $V_{oc} \approx 2$V can be achieved without external wiring. Given the inherent chemical stability of silicon in reference to other PV technologies [168], this allows for wireless, autonomous solar-to-fuel synthesis systems [29], [30], [417], [418], as well as other wireless innovative approaches in which the multijunction solar cell is used not only as a photovoltaic current-voltage generator, but also as an ion-exchange membrane [34], [35], electrochemical catalysts and/or optical transmittance filter.

First, in section 8.2.3, the influence of the nc-Si:H absorber thickness on 1J, SHJ/nc-Si:H (2J) and SHJ/nc-SI:H/a-Si:H (3J) device is characterized. In the following three sections, the influence of an IRL based on SiO_x, TCO and silver (Ag) are characterized. Using the
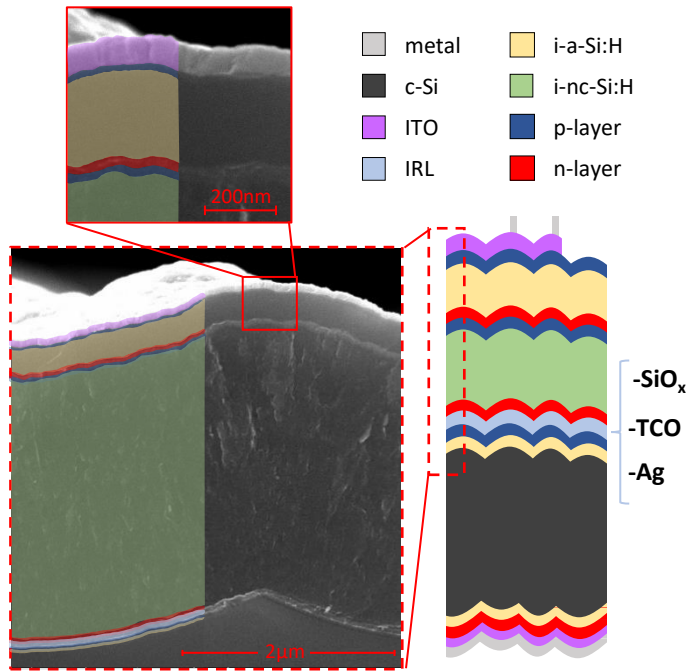
Figure 8.12: Schematic structure and SEM images of a typical SHJ/nc-Si:H/a-Si:H triple junction device presented in this work. The colours in the schematic structure, as well as those added to the left half of the SEM images, represent different materials, as indicated by the top-right legend. The position of the IRL, as well as the different materials used for the IRL, are indicated on the right of the schematic.

design rules obtained from these characterization, a champion autonomous high-voltage 2J and 3J device is processed, which is presented in section 8.2.3.

8.2.2 Experimental section

In this work, a number of tandem PV devices are presented, consisting of a wafer-based silicon heterojunction subcell and a thin film silicon subcell with a nc-Si:H absorber. For the 3J devices an additional thin film silicon junction was processed with an a-Si:H absorber. Scanning electron microscope (SEM) images as well as a simplified schematic structure of the triple junction device are presented in Fig.8.12. All hydrogenated silicon(oxide) layers,

Table 8.2: Conditions used for the p-layer depositions. Layers are processed at P_{RF}=83.3mW$\cdot$cm^{-2}, T_S=180$°$C and p=2.2mbar

	F_{SiH4} (sccm)	F_{B2H6} (0.02%) (sccm)	F_{CO2} (sccm)	F_{H2} (sccm)
p-nc-SiO$_X$:H	0.8	10	2.2	170
p-nc-SiO$_X$:H$^+$	0.8	50	2.2	170

doped and undoped, are processed using plasma enhanced chemical vapour deposition (PECVD). The exact configuration and deposition conditions of the PECVD processed layers, with exception of the p-layers, are reported in [155]. For the p-layers a bi-layer configuration was used, consisting of a 12nm p-nc-SiO$_X$:H and a more highly doped 4nm p-nc-SiO$_X$:H$^+$ layer. The deposition conditions of these layers are reported in table 8.2. Additionally, metals and TCO's are used at the front and back of the devices, as shown in Fig.8.12, as well as as a material for the IRL in sections 8.2.3 and 8.2.3. All TCO's are processed through RF magnetron sputtering. More information about the processing equipment and conditions of indium-oxide doped with tin (ITO) and tungsten (IWO) can be found in [419], while the sputtering conditions of AZO can be found in [156]. Aluminum contacts are processed using electron beam evaporation, while the Ag layers are evaporated using resistive heating.

300μm thick n-type mono-crystalline silicon wafers with <100> orientation are used for processing the SHJ devices. The wafers are textured using an approach consisting of alkaline etching step followed by an acidic etching step. Both the texturing approach [155] and the optical behaviour of the textured surface [153] are discussed in more detail elsewhere. The thin film silicon junctions are processed on top of the SHJ device, in n-i-p substrate configuration.

Additionally, in section 8.2.3, a series of single junction nc-Si:H devices are presented which are processed on textured glass. These devices are processed in n-i-p substrate configuration with a transparent aluminum-doped zinc oxide (AZO) back contact. The glass texturing procedure and processing flowchart of these single junction devices is similar to those used in [156]. No back reflector is used for these devices to better represent the situation when the nc-Si:H junction is used at the front or middle in a multijunction configuration.

The external quantum efficiency (EQE) of the multijunction device was obtained using an in-house EQE setup. The EQE of an individual junction in a multijunction device was obtained by saturating the other junction(s) with bias light. No bias voltage was applied during measurements. By weighing the EQE spectra with the AM1.5$_G$ solar spectrum, the short-circuit current density (J_{sc}) of the individual junctions was obtained. The J-V curves of the devices are measured at 25°C using an AM1.5$_G$ solar simulator. The open circuit voltage (V_{oc}), fill factor (FF), series resistance (R_s) and shunt resistance (R_{sh}) are obtained from these J-V curves. On each sample, 24 individual 16mm^2 cells are processed. All 24 cells are measured and the results presented in this work are the average of the five best cells. More detailed descriptions of these measurements can be found in [155]. The V_{oc}, FF, J_{sc}, R_s, R_{sh} and conversion efficiency (η) of all cells presented in this work can be found in the supplementary information. Finally, the reflectance measurements were performed using a LAMBDA 1050+ Spectrophotometer from PerkinElmer.

Figure 8.13: Multijunction device characteristics as a function of d_{nc-Si}. **A** presents the $V_{oc}*FF$. **B** presents the J_{sc} of all the individual junctions as well as the total J_{sc}-sum of the individual subcells for the 2J and 3J devices, as obtained from EQE. The 1J device are processed on transparent substrates without back reflector. The EQE diagram of the 1J devices are presented in **C**, while the relevant spectral part of the 2J devices are presented in **D**.

8.2.3 Results and Discussion

Varying the i-nc-Si:H absorber thickness

Among the various means of distributing current over junctions in a multijunction device, a change in absorber thickness is the most straightforward. The product of the V_{oc} and FF ($V_{oc}*FF$) and J_{sc} of a series of nc-Si:H single junction (1J) and SHJ/nc-Si:H (2J) and SHJ/nc-Si:H/a-Si:H (3J) multijunction devices are presented in Fig.8.13**A**-**B**. The J_{sc} of the nc-Si:H subcell shows the expected increases with nc-Si:H thickness ($d_{nc\text{-}Si}$). For the 1J and 2J devices, where the nc-Si:H subcell is positioned at the front of the device, the increase follows an exponential decay, as described by the Lambert-Beer law. The J_{sc}'s of the 1J and 2J devices are roughly similar, as the 1J devices are processed on transparent substrates, which means neither device has a back reflector positioned at the rear of the nc-Si:H junction. The EQE's of Fig.8.13**C** show that the increase in J_{sc} is a result of increased absorption in the 600nm-1050nm wavelength region, where the photon energy is closer to the bandgap energy of the nc-Si:H absorber and the absorption probability is lower. The same effect can be observed in the EQE's of the 2J device, in Fig.8.13**D**, where it can additionally be observed that the increased absorption in the nc-Si:H subcell results in a decrease of the EQE in the bottom junction in the same wavelength region. This is reflected in the J_{sc}'s of the 2J and 3J devices, where the J_{sc} increase in the nc-Si:H subcell results in a J_{sc} decrease in the SHJ. The sum of the J_{sc}'s remains relatively unchanged. The fact that the total current density of the 2J devices exceeds that of the 3J devices will be addressed in section 8.2.3.

The $V_{oc}*FF$ decreases continuously with increasing $d_{nc\text{-}Si}$ for the 1J and 3J devices. For the single junctions, this predominantly seems to be a result of Rsh, which continuously decreases from 5300Ωcm^2 to just under 2000Ωcm^2. The $V_{oc}*FF$ trends trends observed in the multijunction devices are the results of a subtle interplay between the single junction effects and the current matching conditions between the individual junctions. Under perfect current matching conditions, simplistically, the FF can be understood to be a result of the collective resistances in the different junctions (p-(i-)n junctions, tunneling junctions and metal-semiconductor junctions) and the FF can be expected not to exceed that of its constituent junctions. However, in the case of a current mismatch this does not hold. The influence of the current matching conditions, specifically the influence of the magnitude of the current mismatch on the FF, is exemplified by the >80% FF of the 3J devices. This FF is achieved despite the fact that the initial FF of world-record a-Si:H devices is around 76% [420], [421]. This is because the current limiting junction has a dominant influence on the FF of the overall device [411]. Moreover, the FF generally increases with increasing current mismatch between sub-cells [411], [412].
Such current matching related FF effects cause the $V_{oc}*FF$ trend to deviate from the near linear-relation observed in the 1J device. For both multijunction configurations, the nc-Si:H junction is current limiting for the smallest values for $d_{nc\text{-}Si}$. As $d_{nc\text{-}Si}$ is increased, the SHJ in the tandem configuration and the a-Si:H junction in the 3J configuration become current limiting. In the 3J the FF continues to decrease with $d_{nc\text{-}Si}$, as the current mismatch between subcells decreases and the a-Si:H subcell, with the poorest FF, becomes current limiting. In the tandem configuration, the FF increases with a $d_{nc\text{-}Si}$ increase from 2.5 to 4.5μm, as the current mismatch increases and the SHJ, the subcell

Table 8.3: External device characteristics of 1J, 2J and 3J devices with an $d_{\text{nc-Si}}$ difference of $\approx 2\mu m$. $\Delta_{V_{oc}}$ and $\Delta_{J_{sc}}$ indicate the change in V_{oc} and J_{sc}, respectively, for the $d_{\text{nc-Si}} \approx 2\mu m$ increase. For the 3J-$\Delta_{V_{oc}}$ (*), $d_{\text{nc-Si}}=2.2\mu m$ and $d_{\text{nc-Si}}=5\mu m$ are used, as the V_{oc} of $d_{\text{nc-Si}}=3\mu m$ was not indicative of the overall trend.

	1J		2J		3J	
$d_{\text{nc-Si}}$ (μm)	2	4	2.2	4.4	3	5
V_{oc} (mV)	512	489	1121	1092	1983	1983
FF (%)	67.1	61.3	75.4	75	80.8	76.6
J_{sc} (mA $\cdot$ cm^{-2})	17.1	20.4	16	19.3	9.1	10.9
η (%)	5.88	6.11	13.5	12.3	14.6	12.6
$\Delta_{V_{oc}}$ (mV)	-23.4		-29.6		-41.4*	
$\Delta_{J_{sc}}$ (%)	19.3		20.5		19.1	

with the highest FF, becomes the current limiting junction. At the same time, the V_{oc} continuously decreases with increasing $d_{\text{nc-Si}}$.

Qualitatively, the collective trends in Fig.8.13 suggest some design trends for the multijunction devices as a function of $d_{\text{nc-Si}}$. Most of the gains in J_{sc} are realized in the $d_{\text{nc-Si}} \leq 3\mu m$ range, while for $d_{\text{nc-Si}} > 4\mu m$ the gain in J_{sc} is minimal. Consequently, considering the $V_{oc}*FF$ trend of the 1J device, $d_{\text{nc-Si}}$ should be kept $\leq 4\mu m$ and preferably even $\leq 3\mu m$. Additionally, intentionally introducing a (small) current mismatch in which the junction with the highest FF is limiting can, in reference to a current matched design, positively affect overall device performance.

Quantitatively, the trade-off between voltage and current as a function of $d_{\text{nc-Si}}$ can also be expressed. In table 8.3 the device characteristics of the devices with the smallest $d_{\text{nc-Si}}$ are compared to the devices with an additional approx $2\mu m$. For the 3J, the devices with $3\mu m$ and $5\mu m$ are compared, as the device with $d_{\text{nc-Si}}=4.5\mu m$ did not result in a successful deposition.
The trade-offs in the 1J and 2J devices, both with the nc-Si:H junction positioned at the front, are remarkably similar. Roughly, starting with $d_{\text{nc-Si}}=2\text{-}2.2\mu m$, the J_{sc} increase is about 19.1-20.5% and the V_{oc} loss is about 11.7-13.8mV per additional μm $d_{\text{nc-Si}}$. Similarly, for the 3J, an increase of $2\mu m$, from $d_{\text{nc-Si}}=3\mu m$ to $5\mu m$, result in a J_{sc} increase of 19.1%. The V_{oc} is decreased by 16.4mV per per additional μm $d_{\text{nc-Si}}$ in the 2.5 to $5\mu m$ range. Additionally, the results from table.8.3 suggest that the highest conversion efficiencies are generally achieved for small $d_{\text{nc-Si}}$.

SiOx:H based intermediate reflective layer

In the preceding section the attractiveness of an intermediate reflective layer, which could potentially yield an increase in J_{sc} without a (significant) decrease in $V_{oc}*FF$, is demonstrated. In this section the effectiveness of an silicon-oxide based IRL is investigated.

In Fig.8.14**B**, the J_{sc} of the nc-Si:H junctions are shown to increase with increasing $d_{\text{n-SiOx}}$, for both the 2J and 3J series, while the J_{sc} of the SHJ decreases. The EQE curves of the 2J and 3J series, in Fig.8.14**D**-**E**, indicate that this is a result of an absorption shift from the SHJ to the nc-Si:H junction in the 650-900nm wavelength region, as reflection at the nc-Si:H/SHJ interface is increased with increasing $d_{\text{n-SiOx}}$. Note that the
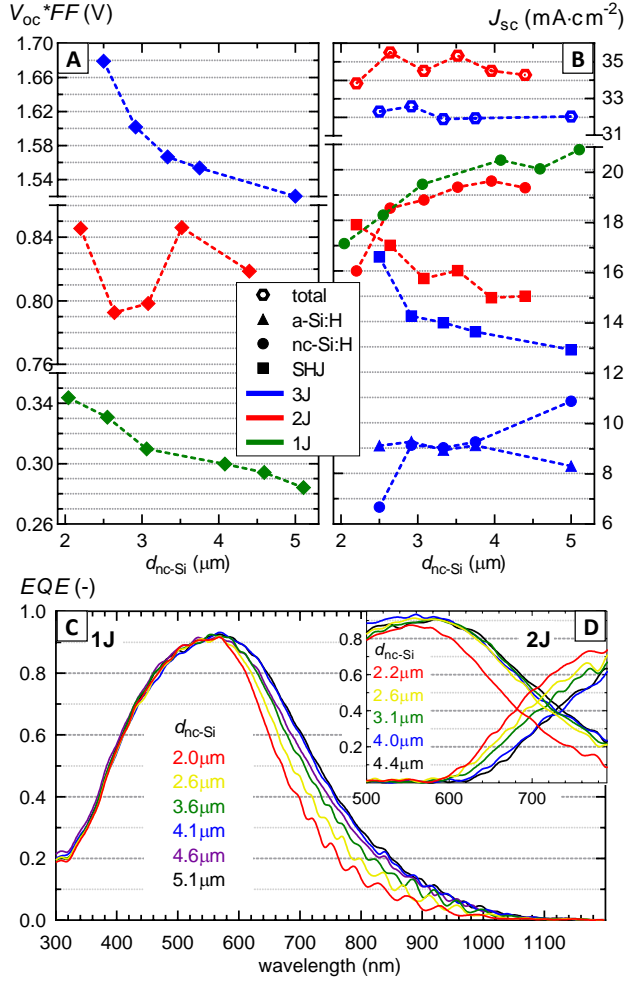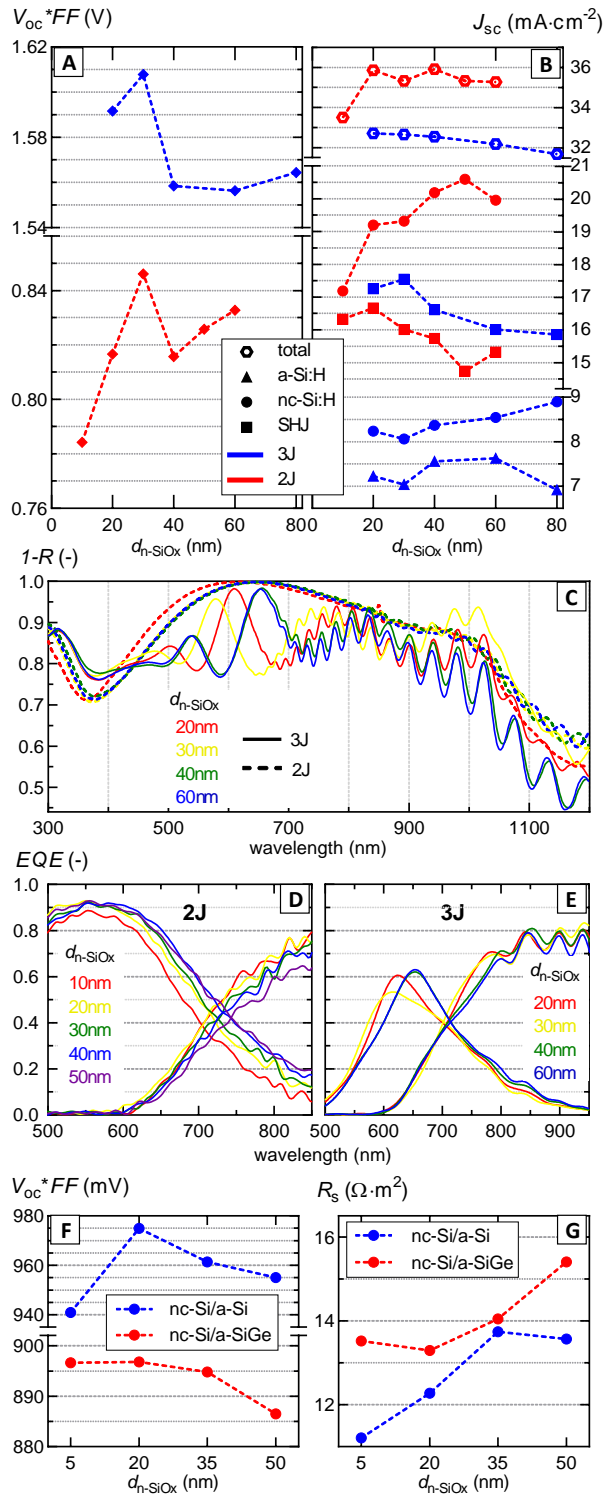
Figure 8.14: caption on next page

Figure 8.14: Multijunction device characteristics as a function of $d_{\text{n-SiOx}}$. **A** presents the $V_{\text{oc}}*FF$. **B** presents the J_{sc} of all the individual junctions as well as the total J_{sc}-sum of the individual subcells for the 2J and 3J devices, as obtained from EQE. The 1-R curves of the 2J and 3J devices are presented in **C**. The relevant spectral ranges of EQE diagrams of the 2J and 3J devices, including only the nc-Si:H junction and SHJ, are presented in **D-E**. The $V_{\text{oc}}*FF$ and R_{s} of two separate series of tandem devices, based on nc-Si:H/a-Si:H and nc-Si:H/a-SiGe:H device architectures, are shown in **F-G**.

green and blue curves in Fig.8.14**E** largely overlap. This absorption shift is in line with earlier reports [46], [48], [404], [405].

Interpretation of the $V_{\text{oc}}*FF$, in Fig.8.14**A**, is less straightforward. The n-nc-SiO$_x$:H layer is not exclusively an IRL, but also the n-layer in both an n-i-p subcell and p-n tunnel recombination junction. As a consequence, there are a large number of complex mechanisms involved that can have competing effects on the V_{oc} and FF of the overall device, as a function of $d_{\text{n-SiOx}}$. A detailed description of the relevant mechanisms that can influence the $V_{\text{oc}}*FF$, as a function of variations in a doped layer in Si-based multijunction devices, can be found in our earlier work [155].

The observed $V_{\text{oc}}*FF$ trends can approximately be divided into three regions. Initially, for $d_{\text{n-SiOx}} \leq$30nm the $V_{\text{oc}}*FF$ increases with increasing $d_{\text{n-SiOx}}$. This is likely the result of the increased R_{sh} in this range, independent of J_{sc}-mismatch, as the hole barrier functionality of the n-layer is improved with $d_{\text{n-SiOx}}$. A similar "minimum-thickness-requirement" has been observed in p-nc-SiO$_x$:H layers in TRJ's in silicon based multijunction devices [155]. Such an effect is in line with the observed EQE, and $J_{\text{sc-sum}}$, increase for the 2J device from $d_{\text{n-SiOx}}$=10-20nm. It should be noted that R_{s} and R_{sh}, that directly influence the FF, do not directly influence the EQE, which is measured under short circuit conditions. However, if the underlying mechanisms that causes the resistances to deteriorate introduces a barrier against charge carrier collection, this mechanism then can limit both the EQE and J_{sc} as well as influence the FF [155].

Notably, the initial $V_{\text{oc}}*FF$ increase for $d_{\text{n-SiOx}} \leq$30nm is consistent with two separate series of nc-Si:H/a-SiGe:H and nc-Si:H/a-Si:H tandem devices, processed at the same time undergoing the same change in $d_{\text{n-SiOx}}$ and exhibiting no significant change in current matching conditions. These two series also exhibit an optimum $V_{\text{oc}}*FF$ in 20-35nm range, as shown in Fig.8.14**F**.

Following this initial increase of $V_{\text{oc}}*FF$, a steep drop occurs for both devices in the $d_{\text{n-SiOx}}$=30-40nm range. This drop is predominantly FF related, caused by a sudden increase of R_{s} of about 50%. The origin of this R_{s} increase is not entirely clear.

Finally, for $d_{\text{n-SiOx}} \geq$40nm, the $V_{\text{oc}}*FF$ is observed to slightly increase again. It should be noted that in this range, for the 2J and 3J devices, the V_{oc} and FF trends are in competition. The V_{oc} decreases continuously, likely as a result of an increased resistance against carrier movement through the thicker n-SiO$_x$:H layer. This can also be observed in the aforementioned nc-Si:H/a-SiGe:H and nc-Si:H/a-Si:H devices, for which R_{s} increases continuously with $d_{\text{n-SiOx}}$, as shown in Fig.8.14**G**. For the 2J and 3J devices, FF increases in this range, likely as a result of the increased current mismatch.

Qualitatively, the observed trends can be translated into two distinct design rules. The J_{sc}'s of the sub cells show that varying $d_{n\text{-}SiOx}$ is an effective means of transferring current between sub cells. The collective results suggest that for optimal $V_{oc}*FF$ a minimal $d_{n\text{-}SiOx}$ is required in the range of 20-30nm. A further increase of $d_{n\text{-}SiOx}$ results in a trade-off between J_{sc} and $V_{oc}*FF$, although this effect can be mitigated to some extent when the current matching conditions are taken into account during device design.
For this reason, quantifying this trade-off for $d_{n\text{-}SiOx} > 20$nm is challenging. Keeping that in mind, increasing $d_{n\text{-}SiOx}$ from 30 to 60nm for the 2J and 3J devices, for instance, result in a J_{sc} increase in the nc-Si:H subcell of 2.8-5.6% and a $V_{oc}*FF$ decrease of 13-51mV. For the nc-Si:H/a-Si:H and nc-Si:H/a-SiGe:H devices of Fig.8.14**F** this decrease is 14-20mV for an $d_{n\text{-}SiOx}$ increase from 20-50nm.

An additional observation can be made regarding the J_{sc}'s of the devices presented in Fig.8.14**B**. The $J_{sc\text{-}sum}$ of the 3J devices is about 3mA $\cdot$ cm^{-2} lower with respect to the 2J devices. This same difference is observed in the multijunction devices with different d_{ncSi} and IRL's. Reflectance measurements presented Fig.8.14**C**, in which the front reflection of 2J and 3J devices is plotted as a function of $d_{n\text{-}SiOx}$, show that this J_{sc} loss is mainly an optical effect. With the introduction of the a-Si:H junction, given the typical layer thicknesses and the fact that no optimization has been performed regarding front-side anti-reflection, strong interference effects occur. these interference effect lead to the observed $J_{sc\text{-}sum}$ loss in the 3J devices in reference to the 2J devices.

TCO based intermediate reflective layer

Next the use of a TCO as an IRL is investigated. If we consider Fig.8.15**B**, an increase of d_{TCO} does not show the expected J_{sc} increase in the nc-Si:H junction, despite a J_{sc} decrease in the SHJ for both the 2J and 3J series. The EQE curves in Fig.8.15**C** provide more insight. It seems that with increasing d_{TCO} the reflection by the IRL does increase, as absorption in the 680-820nm wavelength range is shifted from the SHJ to the nc-Si:H. However, the overall EQE of the nc-Si:H junction is decreased. The EQE spectra of the three individual subcells, as well as the sum of the 3 EQE's and 1-R curve, of a 3J device with (Fig.8.15**E**) and without (Fig.8.15**F**) TCO as an IRL are plotted. The difference between 1-R and EQE-sum in the 650-1050nm is minimal for the device without TCO and significant for the device with TCO.
The difference between 1-R and EQE-sum is a result of either parasitic absorption in the TCO layer, or a reduced collection efficiency resulting from the TCO introduction. A reduced collection efficiency seems most likely, since: 1. the TCO is positioned between the nc-Si:H junction and SHJ, which means it is unlikely the parasitic absorption in the TCO would significantly reduce absorption in the nc-Si:H junction, which is positioned before the TCO layer in reference to the incident light. 2. the uniform EQE decrease of $\approx$0.2 occurs over the entire 650-1050nm wavelength region, where the nc-Si:H and SHJ are absorbing, is consistent with effects observed in tandems devices with a collection barrier introduced by a poorly performing TRJ [155]. 3. an electrical barrier against charge carrier collection is consistent with the deterioration of the electrical device characteristics observed in Fig.8.15**A** with TCO introduction. This $V_{oc}*FF$ decrease is predominantly the result of a strong decrease of the R_{sh} with increasing d_{TCO}. Fig.8.15**D** shows that

Figure 8.15: Multijunction device characteristics as a function of d_{TCO}. **A** presents the $V_{oc}*FF$. **B** presents the J_{sc} of all the individual junctions as well as the total J_{sc}-sum of the individual subcells for the 2J and 3J devices, as obtained from EQE. The EQE diagram of the 3J devices, including only the nc-Si:H junction and SHJ, are presented in **C**. The shunt resistance of three series of 2J devices, using an ITO, IWO and AZO IRL, are presented in **D**. An EQE diagram of a 3J device, including all three subcells as well as the sum of three subcells (dotted line) and 1-R curve dashed line is presented with (**F**) and without (**E**) TCO used as an IRL.

the R_{sh} decreased irrespective of whether ITO, room temperature IWO or AZO was used. Moreover, the low R_{sh} persists even when shunting paths at the edges of the substrate were eliminated, through additional masking steps or by physically isolating the cell from the edges by cutting the wafer.

As the use of a TCO does not result in the desired transfer of current transfer between subcells, and the V_{oc}*FF deteriorates when a TCO is introduced, the use of a TCO as an IRL in these monolithically integrated silicon-based multijunction devices does not appear to be a desirable option.

Silver based intermediate reflective layer

Finally, the use of a thin metallic layer as an IRL is considered. Ag is used for its favourable reflective and conductive properties. From Fig.8.16**A**-**B**, two things are apparent. First, for both series the V_{oc}*FF have clear optimum for d_{Ag}=2-3nm. This is predominantly a result of a strong increase of R_{sh} for very thin Ag layers up to 2-3nm. Following this initial improvement, the V_{oc}*FF decreases continuously. Secondly, the introduction of a thin silver film does not result in the desired shift of current from the SHJ to the nc-Si:H subcell. In fact, with increasing d_{Ag}, the J_{sc} of the SHJ strongly decreases, while the J_{sc} of the nc-Si:H subcell remains relatively constant, resulting in a strong decrease of J_{sc}-sum. Fig.8.16**C** show that this is a result of an overall decrease of the EQE of the SHJ with d_{Ag}.

Both these effects are related to the Ag growth. At the low intended thicknesses considered in this section, the Ag does not result in the formation of a uniform layer. Rather, Ag clusters are formed as can be observed in the SEM images in Fig.8.17. As a consequence, the reported thickness in this section are intended thicknesses. The factual average diameter (D), and standard deviation, of these clusters are indicated in Fig8.17. As a consequence of the size and shape of the Ag nanoparticles, plasmonic resonance occurs. The SEM images in Fig8.17 indicate that with increasing d_{Ag}, D increases and the particles become more ellipsoidal. This observation serves as an explanation for a number of the trends observed in the multijunction device characteristics.

For one, the plasmon resonance, so the position of maximum attenuation, is shifted to higher wavelengths with increasing D [422]–[424]. This red-shift reportedly also occurs for increasingly ellipsoidally shaped Ag nanoparticles [425], [426]. The absorption peak in the EQE plot of the nc-Si:H subcell in Fig.8.16**C** is observed to red-shift with increasing d_{Ag}. The 1-R inset shows that the shift of the EQE peak directly corresponds to a shift of reflection with d_{Ag}.

Additionally, considering the overall quantum efficiency decrease of the SHJ with d_{Ag}. A similar decrease has been observed before in the long-wavelength range for cells containing small nanoparticles [427]. The decrease can be attributed to reflection changes only to a small extent, as can be observed in Fig.8.16**C**. However, in the 750-950nm wavelength range, 1-R values are roughly similar, while the quantum efficiency for devices with d_{Ag} ≥2nm is significantly reduced. The decrease therefore is a result of either increased parasitic absorption, or decreased collection efficiency as a function of increasing d_{Ag}.

Most likely both effects have an influence on the observed device performance. It is widely reported that the scattering cross section in reference to the absorption cross section of the Ag nanoparticles increases with increasing D [423], [424], [426], [428]. A strong decrease
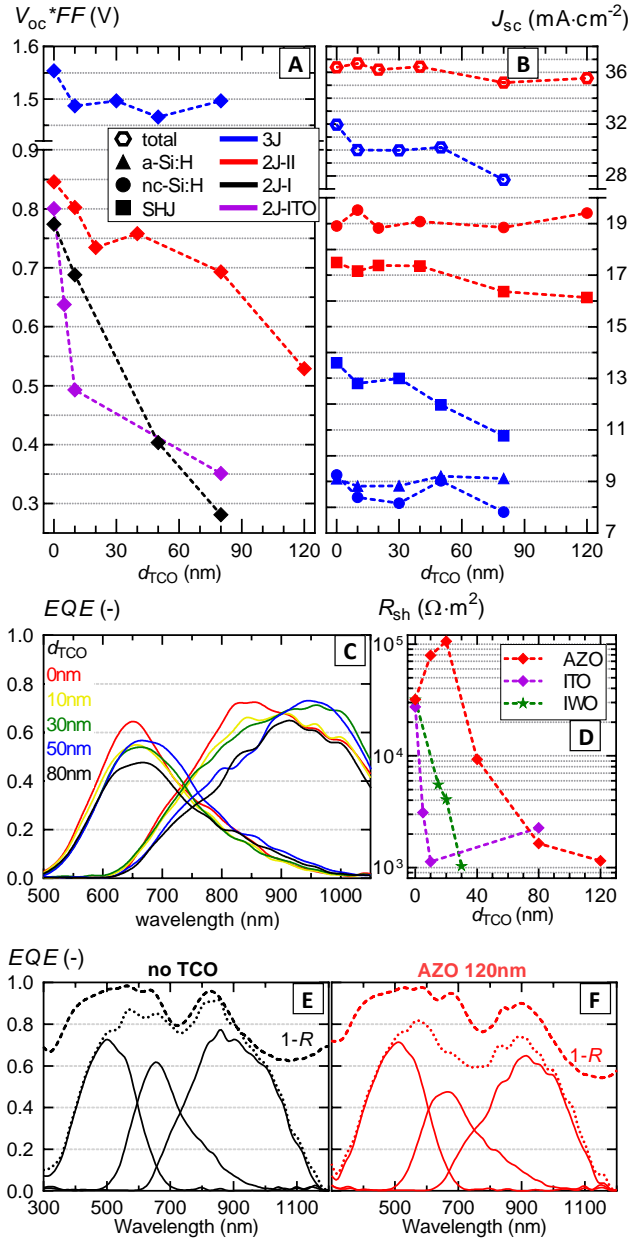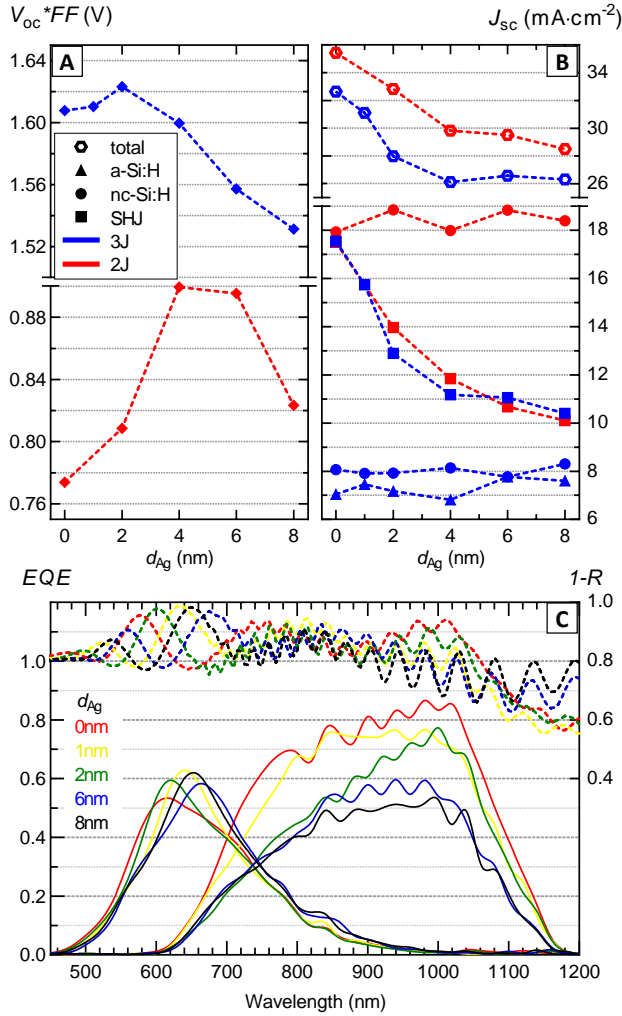
Figure 8.16: Multijunction device characteristics as a function of d_{Ag}. **A** presents the $V_{oc}*FF$. **B** presents the J_{sc} of all the individual junctions as well as the total J_{sc}-sum of the individual subcells for the 2J and 3J devices, as obtained from EQE. The EQE diagram of the 3J devices, including only the nc-Si:H junction and SHJ, are presented in **C**, The inset in **C** shows the 1-R curves of the 3J for the low-wavelength range.
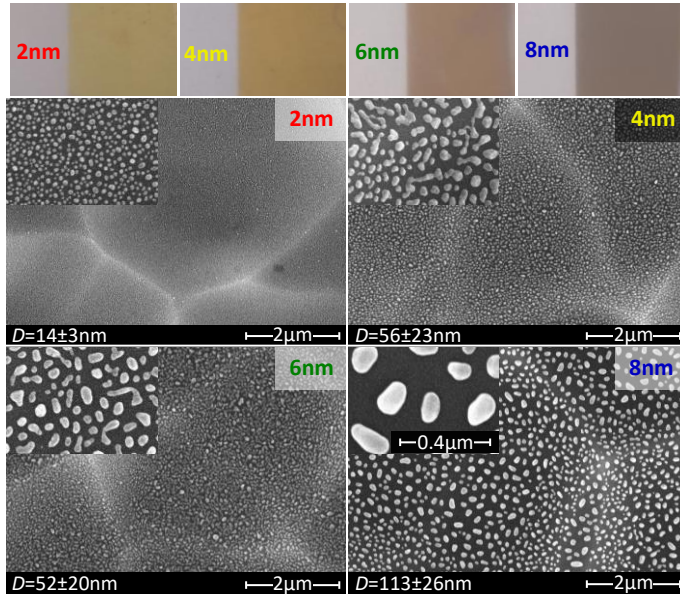
Figure 8.17: Optical images (top) of Ag on glass for different d_{Ag}. SEM images of Ag on textured Si wafers for different d_{Ag}. Insets show SEM images at different magnification, as indicated by the scale in the bottom-right inset. The average nanoparticle diameter (D) and standard deviation are indicated at the bottom of the SEM images.

of the optical transparency can also be observed for the thin Ag films on glass in Fig.8.17. Given these reports and the average particle size shown in Fig8.17, the nanoparticles will cause significant parasitic absorption in our devices. A decrease of the collection efficiency, on the other hand, is also likely considering both the strong decrease of the $V_{\mathrm{oc}}{*}FF$ in the d_{Ag}=4-8nm range as well as earlier reports of a FF decreases in thin films silicon devices with increasing Ag nanoparticle size [424], [426]. The mechanism through which the larger nanoparticles introduce the observed decrease in FF and collection efficiency is not entirely clear. The Ag particles could negatively affect the subsequent growth of the doped and intrinsic layers, which were not optimized to facilitate particles of such size. Alternatively, considering the decrease of R_{sh}, the large particles could create additional shunting paths. This could occur either through an increase of the average lateral conductivity, facilitating the connection of spatially distributed shunting paths, or through the creation of new shunting paths.

Regardless of the mechanisms involved, the design rules resulting from the experiments presented in this section are straightforward. Introduction of a thin Ag layer does not result in the desired IRL functionality. However, evidently, a TRJ-functionality could potentially be improved, realizing a $V_{\mathrm{oc}}{*}FF$ increase, by the introduction of a very thin Ag film, at the cost of current generation in the junctions positioned at the back of the device.
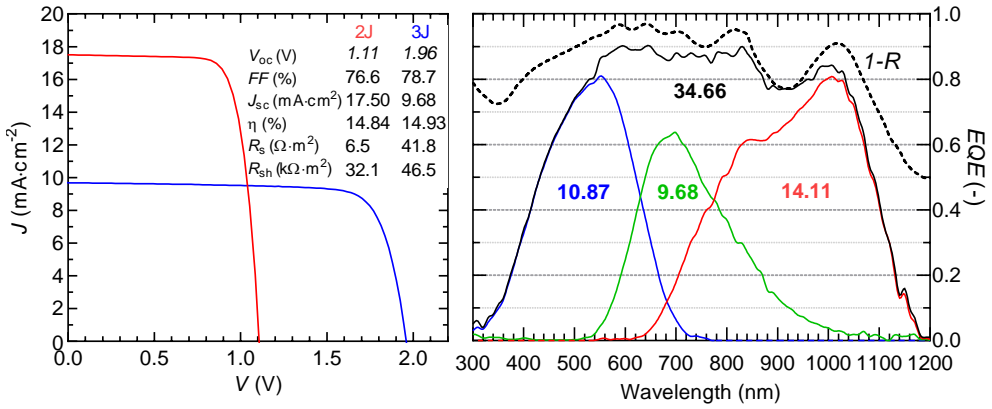
Figure 8.18: The J-V and EQE curves of the champion 2J and 3J devices. An EQE diagram of the champion device, including all three subcells as well as the sum of three subcells and 1-R curves dashed line is presented.

Champion autonomous high-voltage device

Finally, several 2J and 3J devices were processed with high voltage and champion conversion efficiency. The J-V curves of the 2J and 3J devices with the highest conversion efficiency, as well as the EQE curves of the 3J device are presented in Fig.8.18. Excellent FF's in the range of 76-79% and V_{oc}'s of over 1.1V and close to 2V are realized for the 2J and 3J devices, respectively. An SiO_x-based IRL was applied at the interface between the SHJ and nc-Si:H junction, with $d_{n\text{-}SiOx}$=40nm. The sub-optimal V_{oc} of the champion 3J device in Fig.8.18 is the result of a relatively thick wafer and relatively thick absorbers in the range of $d_{a\text{-}Si} \approx$350nm and $d_{nc\text{-}Si} \approx$4μm.
The sum of the J_{sc}'s of the individual junctions of the 2J device is around 36mA $\cdot$ cm^{-2}. For the 2J device the nc-Si:H junction is current limiting with a J_{sc} of 17.50mA $\cdot$ cm^{-2}. In the triple junction device, the nc-Si:H junction is also current limiting with a J_{sc} of 9.68mA $\cdot$ cm^{-2}. This results in conversion efficiencies in the range of η=14.84-14.93%. The conversion efficiency of 14.93% is a strong improvement over earlier reported conversion efficiencies of 10.5% [29] and 12.7% [30] for such hybrid 3J c-Si/nc-Si:H/a-Si:H devices that can be used for autonomous solar-to-fuel applications. In fact, to the best of the authors knowledge, it is the highest reported conversion efficiency for an all-silicon solar cell that generates at least 1V, for which the record initial efficiency is in the range of 14.3-14.8% [54], [171]. Note that this excludes the 3J device from United solar, which has an alloyed SiGe:H absorber [429].

Finally, considering the collective results presented in this work, we can reflect on the potential of the c-Si/nc-Si:H/a-Si:H multijunction device. Regarding the V_{oc}, the best V_{oc}'s recently achieved by the authors for single junction devices is around 700mv for the SHJ, 510mV for the nc-Si:H junction and 910mV for the a-Si:H junction, while using transparent rear-electrodes for the nc-Si:H and a-Si:H devices. The sum of the V_{oc}'s is round 2.13V. Considering a voltage loss of around 15mV per TRJ, a number that can be

considered a realistic voltage drop for a well engineered TRJ [430] but that does not take into account concessions in $d_{\text{nc-Si}}$ or $d_{\text{n-SiOx}}$ that might be required for current-matching, a V_{oc} of 2.1V could realistically be achieved.

In fact, among the champion devices processed a 3J was realized with V_{oc}=2.04V and a FF 80% for which unfortunately, due to technical difficulties, no EQE measurements could be obtained. Such 3J devices with V_{oc}*FF >1.6 are also presented in Fig.8.13 and Fig.8.16.

Moreover, the EQE's of the individual junctions in Fig.8.18 show that the photo-generated current density is not evenly distributed amongst the different junctions. Additionally, a large optical loss in the blue part of the spectrum in the 300-500nm wavelength region. The 1-R curve, and the difference between the EQE_{sum} curve and the 1-R curve, indicate this to be a result of both relatively high front reflection as well as parasitic absorption losses, presumably in the front TCO and p-doped window layer. Further optimization of these layers in combination with the use of an anti-reflection coating, as well as improved current matching, could yield a current limiting J_{sc} in the range of 11-12mA · cm^{-2}. Therefore, with further optimization, a hybrid all-silicon SHJ/nc-Si:H/a-Si:H 3J device with V_{oc} >2V and η >18% could realistically be achieved.

8.2.4 Conclusion

In this work, the results of over 65 silicon-based multijunction photovoltaic devices are presented, with the purpose to explore different current matching approaches. The influence of absorber thickness as well as the thickness of different intermediate reflective layers, based on silicon-oxide, various TCO's and Ag, on the tandem SHJ/nc-Si:H and triple junction SHJ/nc-Si:H/a-Si:H device performance was characterized. Based on these experiments certain design rules can be formulated.

An increase of the nc-Si:H absorber thickness results in a continuous decrease of V_{oc}*FF, while gains in J_{sc} are predominantly realized in the $d_{\text{nc-Si}} \leq 3\mu$m range. Consequently, it would be advisable to keep $d_{\text{nc-Si}} \leq 4$-3μm. Of the different IRL's, only the silicon-oxide based IRL resulted in the desired absorption shift from the SHJ to the nc-Si:H junction. For the TCO and Ag based IRL's no current gain was observed in the nc-Si:H junction, as the increased reflection by the IRL was counter-acted by a decreased charge carrier collection efficiency. However, for a very thin Ag IRL, an increase of V_{oc}*FF was realized for the multijunction devices, at the cost of J_{sc} in the SHJ. Additionally, it was observed that the FF is strongly influenced by the current matching conditions. For optimal device performance, it would be advisable to intentionally introduce a minor current mismatch in which the junction with the highest FF is current limiting.

Finally, taking these design rules into account, champion devices were processed. For the triple junction SHJ/nc-Si:H/a-Si:H device a $V_{\text{oc}} \approx$2V and $\eta \approx$15% are reported, which to the best of the author's knowledge is a record for an all-silicon multijunction device. Such a conversion efficiency for a high-voltage wafer-based all-silicon 2-terminal multijunction PV device opens the way for highly efficient autonomous solar-to-fuel synthesis systems.

9

Silicon alloys in multijunction devices

9.1 The versatile application of thin film silicon alloys in multijunction devices

Manuscript in preparation *

Abstract

Electricity is projected to account for only about 20% of the total global primary energy consumption in 2030. A logical next step is therefore the conversion of light into sustainable and clean chemical fuels. A prerequisite for the development of an autonomous solar-to-fuel synthesis device is a 2-terminal monolithically integrated multijunction PV component that generates sufficient voltage to drive the desired electrochemical reduction reaction.

In this work, the front p-type contact and nc-Si:H absorber, integrated into most all-silicon multijunction devices, are investigated and the flexible application of earth abundant and chemically inert silicon and silicon-germanium alloys is demonstrated in two distinct device architectures. In these architectures up to 4 different junctions are combined, yielding a V_{oc} range of 0.5V to 2.8V. This broad band of V_{oc}'s can facilitate the development of a range of wireless and stand-alone photo-electrochemical devices by fulfilling the voltage requirement for a range of electrochemical reduction reactions and electrocatalysts.

---

*Thierry de Vrijer, Ashish Binani, David van Nijen, Thijs Blackstone, Federica Saitta, Sander Miedema, Harsh Parasramka, Steven J. Roerink, Maik Wiering, Gianluca Limodio, Arno H.M. Smets, "*The versatile application of thin film silicon alloys in multijunction devices*" In preparation

9.1.1 Introduction

For the past decades, solar energy research has primarily focused on improving the light-to-electricity conversion efficiency of photovoltaic (PV) devices. As a result, the conversion efficiency achieved for a silicon solar cell in a research facility of 26.7% [431] is admirably close to the theoretical limit of about 29.4% [432] and PV is the cheapest source of electricity in many parts of the world [11]. However, electricity is projected to account for only about 20% of the total global primary energy consumption in 2030 [433].

A logical next step is therefore the conversion of light into sustainable and clean chemical fuels, which plays a dominant role in the primary energy consumption. Different architectures can be considered for such solar-to-fuel synthesis systems, ranging from a full decoupled PV-Electrolyser system to a fully integrated photoelectrochemical (PEC) device [29]. The latter can, while more complex, facilitate the development of compact, easily produced units that have less wiring and fewer parts, providing ease of installation and excellent scalability.

A prerequisite for such a PEC device is that the PV component generates sufficient voltage to drive the desired electrochemical reduction reaction. In addition to the PEC-reduction of H_2O to H_2, which has been demonstrated in lab scale devices [34], [434], increasing attention has been devoted recently to the electrochemical reduction of CO_2 (and H_2O) to hydrocarbon fuels like formaldehyde, formic acid, methanol and methane. These hydrocarbons have the benefit of a higher volumetric energy density and better compatibility with existing infrastructure and engines. The reduction of water requires fundamentally different reaction potentials in reference to each of the CO_2 reduction pathways [265]. In addition to the fundamental reaction potential, overpotentials associated with the particular device design [35], [435] and the J-V characteristics of the used electrocatalysts [436], [437] are required for efficient PEC operation. An open circuit voltage (V_{oc}) of around 2V has been demonstrated to be sufficient for a stand-alone PEC water splitting device [29], [35], but larger potentials are required for the various CO_2 reduction pathways.

Multijunction (MJ) PV devices can accommodate this need for a flexible output voltage. By combining 2 or more junctions with varying bandgap energies the output voltage can be tuned. In this work, using alloys based on silicon (Si), the most earth abundant and chemically inert of all materials used for PV applications [168], the V_{oc} of a range of single and multijunction PV devices is studied. These device include hybrid c-Si and thin film (TF) Si and silicon-germanium (SiGe) multijunction devices as well as devices exclusively based on TF-Si(Ge) alloys.

Several optimizations for these silicon-based monolithically integrated 2-terminal multijuction PV devices have been performed in earlier work. The textures used for the c-Si/TF-Si devices and all-TF-Si devices were developed in [153] and [438], respectively. The interfaces between the different junctions were studied extensively in [155] and [152], where the tunnel recombination junction and use of intermediate reflective layers were investigated. Moreover, the growth of SiGe and the optimal profiling of SiGe for use in PV devices was explored in [156]. In addition to these optimizations, in this work, an optimization of the front p-type (p-) contact and nanocrystalline (nc-) Si absorber are presented in section 9.1.3 and section 9.1.4, respectively. A wide range of V_{oc}'s for different MJ device architectures are presented in section 9.1.5,
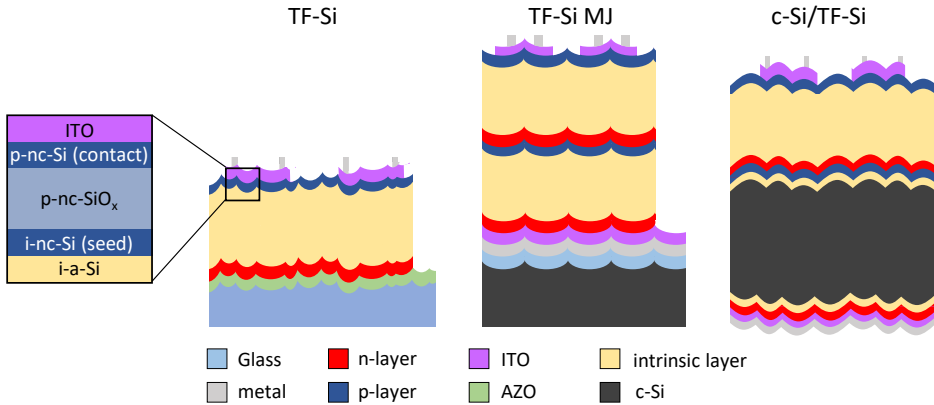
Figure 9.1: Schematic structure of the single junction thin film silicon devices on textured glass (TF-Si, left), multijunction TF-Si devices on textured Si wafers (TF-SI MJ, centre) and hybrid c-Si and TF-Si multijunction devices (c-Si/TF-Si, right).

Table 9.1: PECVD processing conditions

	P_{RF} (mW·cm⁻²)	p (mbar)	T_S (°C)	F_{SiH4} (sccm)	F_{GeH4} (sccm)	F_{H2} (sccm)	F_{CO2} (sccm)	F_{PH3} (2%) (sccm)	F_{B2H6} (0.02%) (sccm)
i-a-SiGe:H	27.8	3.6	180	30	0.2-4.3	200	-	-	-
i-a-Si:H(H)	62.5	10	120	2.4	-	200	-	-	-
i-a-Si:H(L)	19.5	0.7	180	40	-	-	-	-	-
i-nc-Si:H*	278	4	180	1.2/3.3	-	120	-	-	-
i-nc-Si:H (seed)†	243.1	2.2	180	0.8	-	170	-	-	-
p-nc-SiOₓ:H (window) †	83.3	2.2	180	0.8	-	170	2.2	-	25
p-nc-Si:H (contact) †	243.1	2.2	180	0.8	-	170	-	-	20
p-nc-SiOₓ:H‡	83.3	2.2	180	0.8	-	170	2.2	-	10
p-nc-SiOₓ:H⁺‡	83.3	2.2	180	0.8	-	170	2.2	-	50
n-nc-SiOₓ:H	76.4	1.5	180	1	-	120	1.6	2	-
n-nc-Si:H	76.4	1.5	180	1	-	120	-	3	-
n-a-Si:H	27.8	0.6	180	40	-	-	-	11	-

9.1.2 Experimental section

All devices in this work are process in n-i-p substrate configuration. The single junction devices presented in sections 9.1.3 and 9.1.4 are processed on a textured glass substrate with a transparent conductive oxide (TCO) back contact consisting of 700nm aluminium-doped zinc-oxide. These back reflector-less substrates are similar to those used in [156]. This situation with minimal back reflection provides the most straightforward relation between the variations in p-type contact and nc-Si:H absorber and the J-V characteristics of the PV cells. Moreover, it better represents the light absorption performance of the single junction used in a multijunction configuration.

For the TF-Si multijunction devices, textured c-Si wafers with a periodic honeycomb texture were used. 300 nm SiO_2 is processed on the honeycomb textured wafers to electrically isolate the wafer from the TF-Si solar cell followed by a back contact consisting of 500nm Ag and 150nm indium-doped tin-oxide(ITO). More detail about the development of the texture and substrates is provided in [438]. The hybrid c-Si/TF-Si devices are processed on textured 300μm thick n-type mono-crystalline silicon wafers. The wafers

are textured using consecutive alkaline and acidic etching steps. The device architecture is similar to the one used in [155] and [152]. The three different device architectures are schematically visualized in Fig.9.1.

The devices are processed using a radiofrequency PECVD cluster tool. Precursor gas flow rates are indicated by (F_{gas}). The PECVD processing conditions are reported in table9.1. Diborane (B_2H_6) and phosphine (PH_3), the precursors for p- and n-type doping respectively, are diluted in H_2 as indicated in table9.1. Silane (SiH_4) and carbon-dioxide (CO_2) are used as silicon and oxygen precursors, respectively. The germanium content in the a-SiGe:H absorbers is profiled in the growth direction by varying F_{GeH4} at a constant F_{SiH4}. In this work, the ratio of the i/p to the i/n region width is set at 0.25, with a plateau region of 25% of the absorber width and a peak flow rate of F_{GeH4}=4.3sccm. This profile is the results of an optimization performed in [156].

The external quantum efficiency (EQE) of the single junction devices was obtained using an in-house EQE setup. By weighing the EQE spectra with the AM1.5$_\mathrm{G}$ solar spectrum, the short-circuit current density (J_{sc}) of the individual junctions was obtained. The J-V curves of the devices are measured at 25°C using an AM1.5$_\mathrm{G}$ solar simulator. On each sample, 24 individual 16mm^2 cells are processed. All 24 cells are measured and the results presented in this work are the average of the five best cells. Finally, an inVia confocal Raman microscope with a laser operating at a wavelength of 514nm was used for the Raman measurements. The crystallinity was determined from the Raman measurements using the approach described in [159].

9.1.3 Window layer optimization

For optimal operation, the p-type layer at the front of the device should combine optical transparency with excellent transverse charge carrier conduction from the intrinsic absorber to the metal contact. p-type hydrogenated (:H) nanocrystalline silicon-oxide (p-nc-SiO$_\mathrm{x}$) has demonstrated this [49], [91], [439]. The SiO$_\mathrm{x}$ phase has a high bandgap energy (E_G), resulting in low parasitic absorption losses, and the crystalline phase facilitates transverse conductivity. In addition to these two properties, it has been demonstrated in silicon heterojunction devices that a low activation energy (E_{act}) is required for good energetic band alignment between the p-layer and transparent conductive oxide (TCO) [410]. Combining these different properties, high E_G, high crystallinity and low E_{act}, has proven challenging in a single layer [159], [406]. The use of a separate low-E_{act} contact layer between the p-nc-SiO$_\mathrm{x}$ layer and TCO could therefore provide a potential solution.

The challenges associated with processing high-performance p-nc-SiO$_\mathrm{x}$ layers are different for devices grown in a p-i-n superstrate architecture compared to a n-i-p substrate architecture. For p-i-n devices, where the intrinsic absorber layer growth follows that of the p-layer, unintentional doping of the intrinsic layer as a results of boron diffusion poses a significant challenge [440]. In n-i-p devices, where the p-layer is grown on top of the amorphous (a-) intrinsic layer, facilitating crystal nucleation in first nanometres of the p-nc-SiO$_\mathrm{x}$ layer growth, crucial for charge carrier conduction, is challenging [49], [441]. A separate nucleation layer, or seed layer, at the i/p-interface can promote crystal formation in the first nanometres.

To investigate the influence of these different layers in the p-layer stack on device
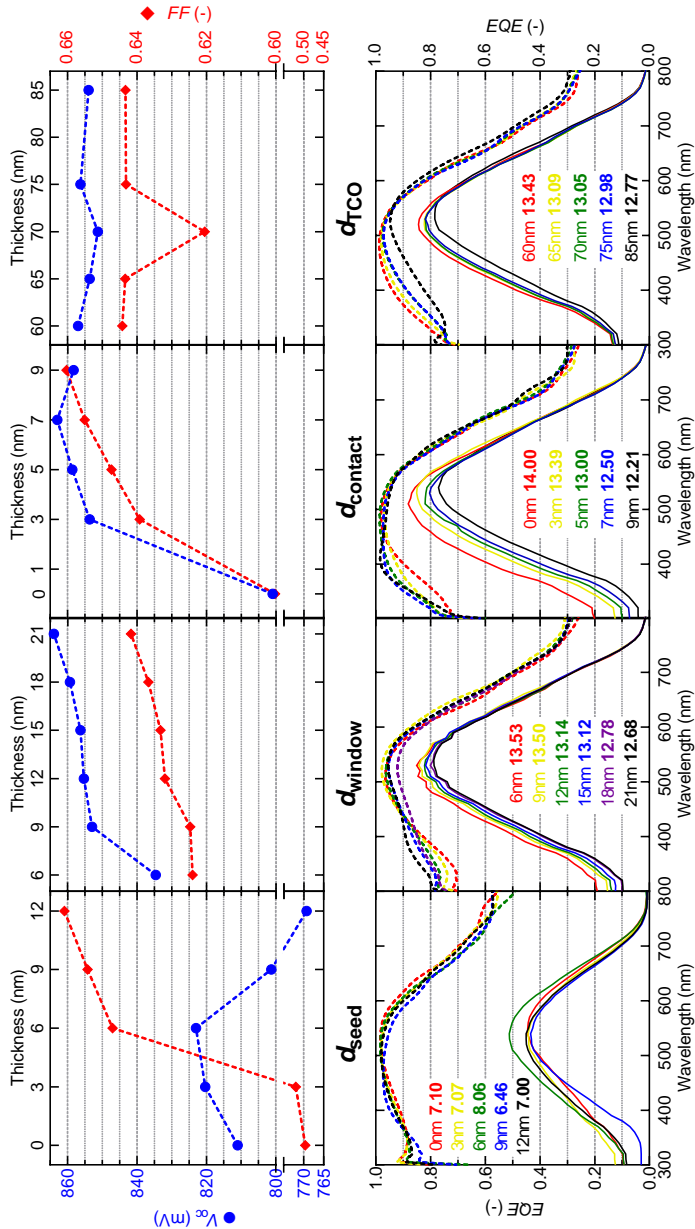
Figure 9.2: V_{oc} (top, blue circles), FF (top, red diamonds) and EQE curves (bottom) as a function of d_{seed} (left), d_{window} (centre-left), d_{contact} (centre-right) and d_{TCO} (right). J_{sc} values are indicated in the EQE plots. 1-R curves are indicated by the dashed lines in the EQE plots. When not varied, d_{seed}=5nm, d_{window}=12nm, d_{contact}=4nm and d_{TCO}=75nm.

performance, single junction a-Si PV devices are processed in which the thickness of the different layers are varied. The TF-Si devices, and p-layer stack specifically, are schematically visualized in in Fig.9.1. The V_{oc} and FF (top) as well as the EQE curves and J_{sc} values (bottom) as a function of the seed layer thickness (d_{seed}), p-nc-SiO$_{\mathrm{x}}$ thickness ($d_{\mathrm{p\text{-}SiOx}}$), contact layer thickness (d_{contact}) and TCO thickness (d_{TCO}) are presented in Fig.9.2. Several important observations can be made from the results.

1. The use of a seed layer is essential for achieving a high V_{oc}*FF product. A seed layer with d_{seed}=6nm increases the FF by over 14% absolute and V_{oc} by over 10mV, in reference to the device without contact layer. A further increase of d_{seed} results in an additional FF increase of about 1.5% but a significant V_{oc} decrease. It should be noted that, due to an issue with the n-nc-Si layer at the back of the device, no trend can be observed in the EQE curves and reported V_{oc}'s are lower than the other experimental series.

2. An increase of $d_{\mathrm{p\text{-}SiOx}}$ results in an continuous increase of FF and V_{oc}, within the experimental range. The V_{oc}*FF increase is accompanied by a decrease of J_{sc}. Considering the minimal differences in the 1-R curves as a function of $d_{\mathrm{p\text{-}SiOx}}$, and the continuous decrease in the 300-550nm wavelength range in the EQE curves, the loss in J_{sc} is likely the result of increased parasitic absorption. Over the entire $d_{\mathrm{p\text{-}SiOx}}$=6-21nm range, a loss of about 0.9 mA $\cdot$ cm^{-2} is observed. There are two main potential reasons for the V_{oc}*FF increase with $d_{\mathrm{p\text{-}SiOx}}$. First, from an energetic band alignment perspective, the improvement can be the result of improved band bending at the i/p-interface. Improved band bending and associated improvements in V_{oc} and FF, with increasing $d_{\mathrm{p\text{-}SiOx}}$, has been demonstrated for the use of p-nc-SiO$_{\mathrm{x}}$ in silicon heterojunction devices, through numerical simulations, assuming constant p-nc-SiO$_{\mathrm{x}}$ properties in the growth direction [410]. Alternatively, from a processing perspective, the improvement can be the result of the evolution of different material phase fractions in the growth direction. The crystalline filamental growth in p-nc-SiO$_{\mathrm{x}}$ develops in the growth direction [36], [59], [61], [109], improving transverse charge carrier conduction with increasing thickness [159]. Improved carrier conduction, especially an improvement in the transverse direction with respect to the lateral direction, can reduce recombination losses and increase V_{oc} and FF. Additionally, it has been suggested that higher active dopant concentrations are achieved for higher crystalline phase fractions [159], as the dopants favourable reside in, or on the surface of, crystalline grains in reference to the amorphous-Si phase [99], [100]. Higher dopant concentration results in lower E_{act}, which can improve V_{oc} and FF [410].

3. The use of a contact layer is essential for achieving high V_{oc}*FF product. The use of a 3nm contact layer, in reference to the device without contact layer, results in a 4% absolute FF increase and a V_{oc} boost of over 50mV. Further increasing d_{contact} to 7-9nm results in an additional, yet smaller, absolute FF increase of 2% and a maximum V_{oc} increase of up to 10 mV. Again the increase of V_{oc}*FF comes at the cost of J_{sc}, due to increased parasitic absorption losses. Over the entire range of d_{contact}=0-9nm, a significant J_{sc} loss of 1.8 mA $\cdot$ cm^{-2} is observed. This J_{sc} loss of about 0.2 mA $\cdot$ cm^{-2} per nm d_{contact} is significantly higher than the parasitic loss for the p-nc-SiO$_{\mathrm{x}}$ layer of approximately 0.06 mA $\cdot$ cm^{-2} nm^{-1}. This is to be expected, as the p-nc-Si contact layer has a significantly lower optical bandgap energy of E_{04}=1.95eV compared to the 2.3eV of the p-nc-SiO$_{\mathrm{x}}$ layer, as obtained from spectroscopic ellipsometry measurements.

4. Variations in d_{TCO}, within the experimental range, do not have a significant effect

on the V_{oc} and FF values. The J_{sc}, on the other hand, decreases continuously with increasing d_{TCO}, by about a total of 0.7 mA cm^{-2}, for a 60 to 85nm d_{TCO} increase. The change in J_{sc} seems to be predominantly related to a change in reflection, rather than parasitic absorption as with the $d_{p\text{-}SiOx}$ and $d_{contact}$ variations. The change in reflection with d_{TCO} is likely a result of a change in interference behaviour in the thin TCO film, with optimal destructive interference in the 300-500nm wavelength range observed for d_{TCO}=60nm. A similar thickness series with a indium-tungsten-oxide TCO, not presented here, showed a similar EQE-trend and an optimal thickness of d_{TCO}=65nm.

Considering these four observations, some design rules can be formulated for the front contact of n-i-p substrate devices. For optimal operation, d_{TCO} should be around 60-65nm and both a seed layer at the i/p-interface and contact layer at the p/TCO-interface should be included. A thickness of approximately d_{seed}=6nm appears optimal. $d_{contact}$ should be in the 2-3nm range, considering the steep J_{sc} loss and the large V_{oc} *FF gain in this range. In terms of maximum conversion efficiency, the optimal $d_{p\text{-}SiOx}$ is around 9nm, as the J_{sc}-loss for further increasing $d_{p\text{-}SiOx}$ outweighs the Voc*FF gain.
It should be noted that the observation regarding the optimal $d_{p\text{-}SiOx}$, and to a lesser extend the optimal $d_{contact}$, is valid only for single junction devices. The V_{oc} of a MJ device can be expected to be equal to the sum of the V_{oc}'s of the individual junctions, minus a V_{oc}-loss for each tunnel recombination junction. This means that a V_{oc} boost of a single junction device should result in a similar V_{oc} boost when that junction is integrated in a MJ device. The same is not true for the J_{sc} however. Light is divided over the different junctions in a MJ device. Simply put, under current matched conditions, the J_{sc} gain of a single junction device will only results 1 over the total number of junctions in the MJ device. Determining the effect of a FF gain in a single junction device on MJ device performance is more complex. The FF of a MJ device can, simplistically and under perfect current matching conditions, be understood to be a result of the collective resistances in the different junctions [152]. However, under current-mismatch conditions the current limiting junction has a dominant influence on the FF of the overall MJ device [411] and the FF generally increases with increasing current mismatch between junctions [411], [412]. This means that in a MJ configuration, in reference to a single configuration, thicker p-nc-SiO$_x$ layers might be favourable as the gain in V_{oc} and FF can outweigh the gain in J_{sc}. This effect will be stronger with an increasing number of junctions integrated in the MJ device.

9.1.4 nc-Si:H absorber optimization

Nano-crystalline silicon is a heterogeneous material in which silicon crystals are embedded in an amorphous silicon phase. It is widely reported that device quality nc-Si:H is obtained for plasma conditions near the crystalline-to-amorphous transition regime [145], [442]–[447], and, additionally, that this transition regime is usually found within a very narrow processing window [442], [443]. Most processing conditions can affect the transition from nc-Si:H to a predominantly amorphous material [74], including the deposition temperature [440], [446], pressure [446], excitation frequency [145], [416] and electrode gap [145]. The silane concentration (SC), the ratio of the silane flow rate (F_{SiH4}) to the hydrogen flow rate (F_{H2}), SC = $F_{SiH4}/(F_{SiH4} + F_{H2})$, and the deposition power (P_{RF}) are generally

Figure 9.3: EQE curves (top, left) and Raman shift plots (top, right) and device characteristics (bottom) as a function of F_{SiH4}. Crystallinity (χ_{C}) values as a function of F_{SiH4} are indicated in the Raman plot. All samples are processed at $P_{\text{RF}}=35\text{W}$.

reported to be most influential. For this reason, in this section, the influence of these two processing conditions on the performance of single junction nc-Si:H devices is investigated.

First, we consider the influence of silane concentration used during i-nc-Si:H absorber layer deposition on the performance of single junction n-i-p solar cells. The cells are processed on a transparent AZO back contact. A thin incubation layer (SC=1%) is used for all i-nc-Si:H depositions and the deposition times are adjusted such that all nc-Si:H absorber have a constant thickness of $\approx 3\mu\text{m}$. The results of variations in F_{SiH4}, processed at a constant F_{H2} of 120sccm, are presented in Fig.9.3. F_{SiH4} is varied from 2.9sccm (SC=2.36%) to 3.7sccm (SC=2.99%). The Raman spectra, measured from the p-side, show that the c-Si peak at 520cm⁻¹ continuously decreases in reference to the amorphous silicon transverse optic mode at 480cm⁻¹ with increasing F_{SiH4}. This continuous decrease of the crystallinity (χ_{C}) with increasing silane concentration crystallinity has been well established [90], [444], [446], [448], [449].

A significant change in χ_{C} can be observed when F_{SiH4} is varied from 3.3sccm to 3.5sccm. Even though ΔSC is only 0.15%, a significant change in the crystallinity of about 30%

absolute can be observed. This very sharp transition from a-Si:H to nc-Si:H for minor changes in the silane concentration is in line with earlier reports [444], [447], [450]. The transition of the dominant material phase fraction from crystalline to amorphous silicon strongly affects the characteristics of the nc-Si:H solar cells. It can be observed in Fig.9.3 that increasing F_{SiH4} beyond the crystalline to amorphous transition results in a significant J_{sc} drop of about 8 mA $\cdot$ cm^{-2}. The EQE spectra show that the J_{sc} loss occurs both in the blue (λ <600nm) and in the infrared (λ >700nm)part of the spectrum, which is in line with [444], [451]. The loss in the infrared is likely related to the higher bandgap energy of a-Si:H in reference to nc-Si:H, resulting in an average absorption probability decrease for the low energy infrared-photons with increasing amorphous phase fraction. The loss in the blue part of the spectrum is likely related to poor charge carrier collection. Generally, the defect density in the amorphous phase is relatively large in reference to the crystalline phase and consequently, the recombination probability in a-Si:H is relatively high. Considering that the majority of the high energy blue photons will be absorbed near the i/p-interface, the poor collection efficiency of electron-hole pairs generated upon blue-photon absorption can be understood to be significantly reduced in these relatively thick predominantly amorphous absorber layers. This poor collection efficiency translates into a high series resistances and the poor FF that is observed for F_{SiH4} >3.3sccm. The V_{oc} is the only parameter that does not show a significant change at the nc-Si:H to a-Si:H transition regime, but rather decreases continuously with crystalline volume fraction. The highest conversion efficiency is obtained at F_{SiH4} >3.3sccm, just before the nc-Si:H to a-Si:H transition.

We then consider the device characteristics as a function of P_{RF}, which are presented in Fig.9.4. The Raman spectra show that the χ_{C} increases with P_{RF}, which is in line with [69], [444]. Again a sharp transition from a predominantly crystalline to amorphous phase is observed. The χ_{C} decreases by approximately 30% for only a 3W change in P_{RF}. A similar 3W increment or decrement only yields a change of approximately χ_{C}=4%. This demonstrates the sensitivity of this transition threshold to minor variations in the processing window. Similar to the F_{SiH4} series, following the nc-Si:H to a-Si:H transition, significant losses in the blue and infrared red part of the spectrum are observed, resulting in a significant J_{sc} decrease. The FF also decreases strongly following the transition, by almost 20%(!) absolute.
Similar to the F_{SiH4} series, the V_{oc} is not as strongly affected by the transition. In fact, if we consider the combined results in Fig.9.5(left), the V_{oc} shows a near linear dependency on χ_{C}, as indicated by the dashed line, with the exception of the two samples from the P_{RF} series with very low χ_{C} <25%. This linear decrease of V_{oc} with crystallinity is in line with earlier reports [145], [444], [446], [450].
The highest conversion efficiency as a function of P_{RF} is again obtained near the crystalline-to-amorphous transition. If we consider the conversion efficiency as a function of χ_{C}, as presented in Fig.9.5(right), it can be observed that for both the F_{SiH4} series and P_{RF} series, the highest conversion efficiencies are achieved for χ_{C} $\approx$60%, which is in line with earlier reports [74], [145], [447].
While the best performance is obtained right at the nc-Si:H to a-Si:H transition, the consequences for passing the threshold are significant. A processing window should therefore be chosen as close to the transition regime as equipment dependent control over the
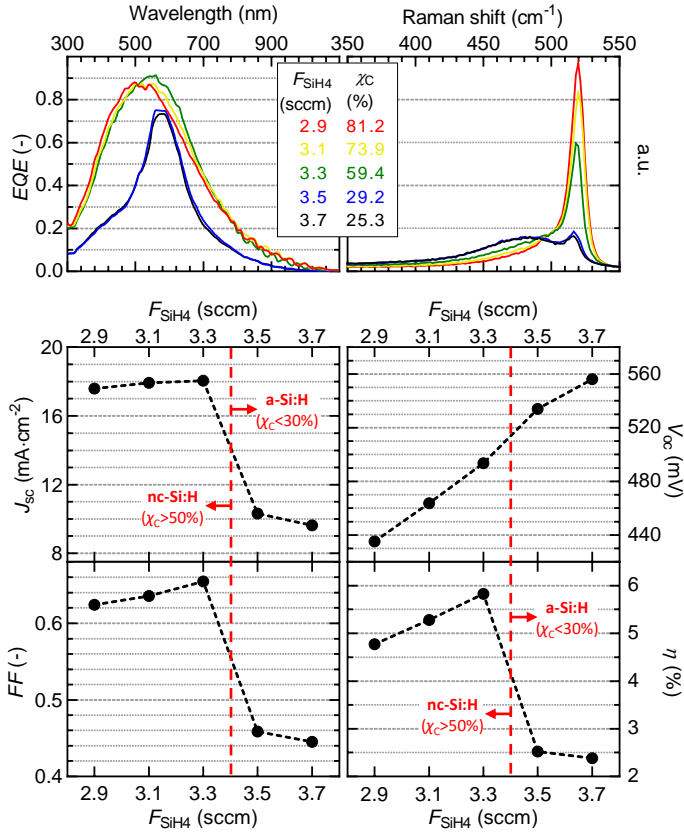
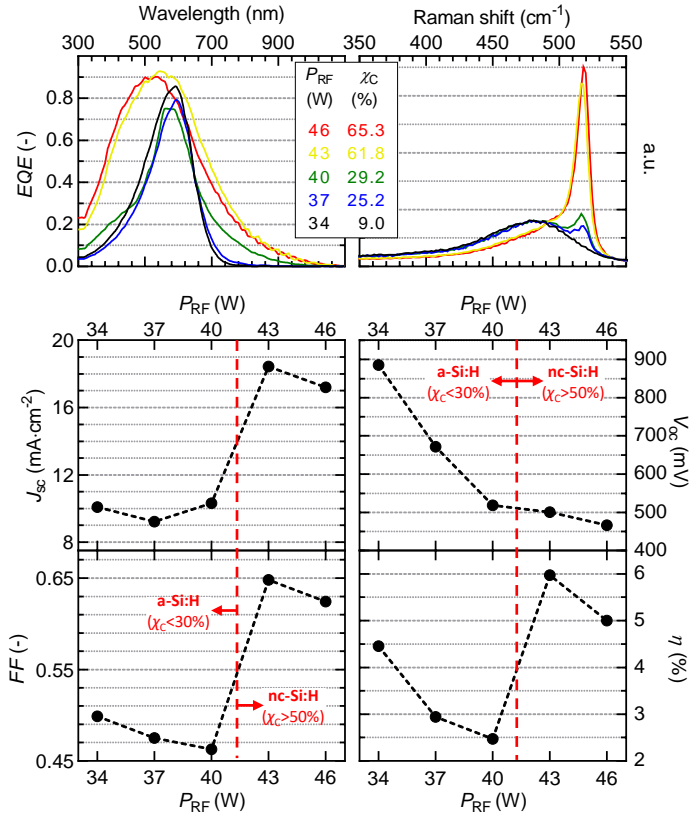Figure 9.4: EQE curves (top, left) and Raman shift plots (top, right) and device characteristics (bottom) as a function of P_{RF}. Crystallinity values as a function of P_{RF} are indicated in the Raman plot. All samples are processed at F_{SiH4}=3.3sccm.
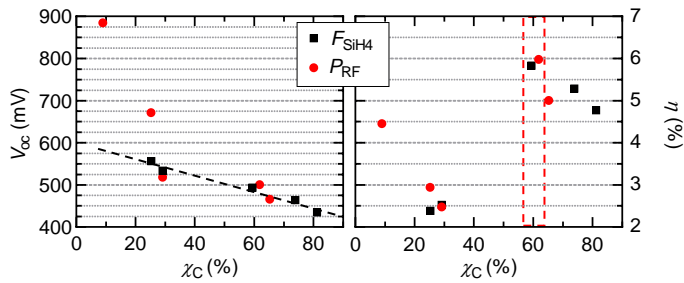

Figure 9.5: V_{oc} (left) and conversion efficiency (right) as a function of crystallinity. Black dashed line added as a guide to the eye.

process and sample to sample fluctuations allow.

9.1.5 Range of thin film devices

In this section the flexible application of thin film silicon alloys in a range of single and multijunction devices is demonstrated. The optimizations performed in sections 9.1.3 and 9.1.4, as well as those preformed in [152], [155], [156], [159], have resulted in the processing conditions reported in table.9.1. Two different silicon-based monolithically integrated 2-terminal multijuction PV device device architectures are presented in this section. The hybrid c-Si/ TF-Si devices are processed on significantly smoothened pyramidal features (the ¡111¿ crystal orientation) [153], while the TF-Si multijunction devices are processed on silicon wafers with honeycomb features with a 3 micron period [438]. The different MJ device architectures are schematically shown in Fig.9.1 and cross-sectional SEM images are presented in Fig.9.6. Colour has been partly added to the SEM images to highlight the different layers in the MJ stack.

Fig.9.6 shows a range of MJ devices processed in this work combining different silicon alloys in the c-Si/TF-Si (left) and TF-Si (right) device architectures. 3 lines are present for each device architecture. Of these, the two solid lines indicate the highest measured V_{oc} and the V_{oc} of the device with the highest $V_{\mathrm{oc}}*FF$ product processed in our lab. Highest measured V_{oc}'s are also indicated next to the device architectures. The dashed line indicates the V_{oc} of devices with the highest reported conversion efficiency, an overview of which is presented in table 9.2. Several observations can be made from this visual.

1. For this work, silicon alloys are used with different material phases. These range from c-Si wafers and a-Si:H layers to the nc-Si:H characterised in the preceding section. Additionally, a-SiGe:H absorbers as used. Fig.9.6 shows that, when used in single junction device, V_{oc}'s generated by these alloys vary from 520mV for nc-Si:H to 710mV for a c-Si SHJ device and 910mV for an a-Si:H single junction device. The V_{oc} of a single junction a-SiGe:H device depends strongly on the Ge-fraction.

2. By combining these 4 alloys and by extending the number of junctions from 1 to 4, a significant V_{oc} range of over 2.1V (0.71V-2.83V) has been achieved for the SHJ/TF-Si devices and 1.75V (0.52-2.27) for the TF-Si devices. If we consider the potential of the TF-Si 4j device, for which a 2.82V V_{oc} is reportedly achieved [452], a V_{oc} range of 2.31V (0.51-2.82V) can be realized with 4 Si(Ge)-based junctions.

3. Through the combination of a different number of junctions based on different Si(Ge)-alloys, a relatively continuous range of V_{oc}'s can be realized. The combinations presented in Fig.9.6 are by no means exhaustive. The gaps in the V_{oc} range could be bridged by different MJ architectures. The SHJ+a-Si could, for instance, easily generated a V_{oc} of 1.6V with some optimization. Additionally, if a V_{oc} is required between that of the triple junction (2.05V) and quadruple junction (2.83V) c-Si/TF-Si devices, a SHJ/nc-Si/nc-Si/a-Si device could be processed, which would approximately yield 2.5V.

4. A significant ΔV_{oc} can be observed between highest V_{oc} and V_{oc} of the device with highest $V_{\mathrm{oc}}*FF$, especially for the both quadruple junction and TF-Si 3J devices. Lacking dedicated optimization, relatively large J_{sc} mismatches occur for these devices. As a consequence, due to current mismatch related FF-compensation, the FF dominantly affects $V_{\mathrm{oc}}*FF$. Dedicated optimization of each particular device architecture should minimize
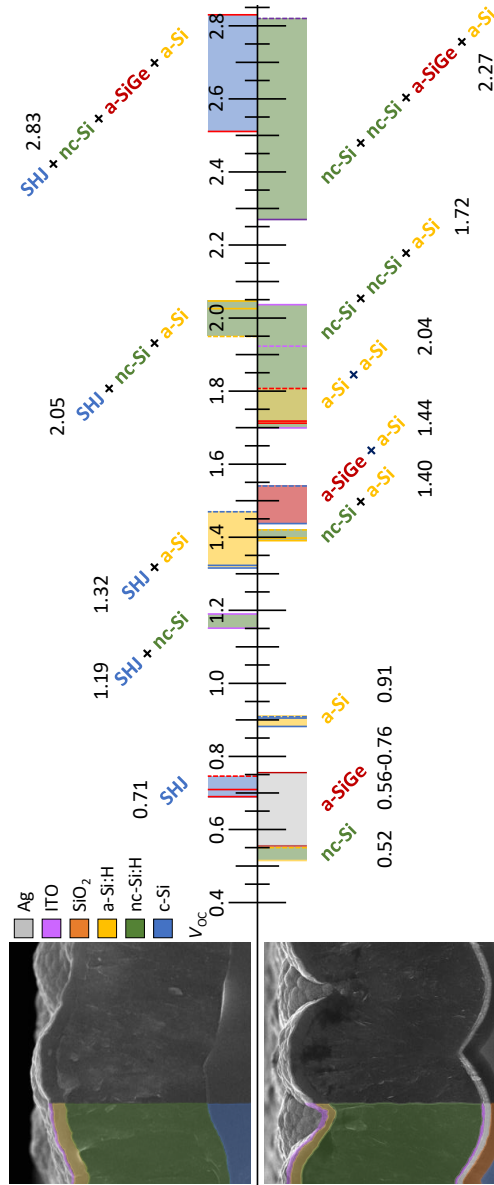
Figure 9.6: V_{oc} range of different single- and multijuction PV device architectures. Top row indicates SHJ and hybrid SHJ and thin film silicon (SHJ+) multijunction devices. Bottom row indicates thin film silicon devices. Cross-sectional SEM images indicate the device architectures of the SHJ+ and thin film silicon multijunction devices. Colours added in the SEM images represent different materials, as indicated by the legend. In the V_{oc} range, 3 lines are present for each device architecture. Of these, the two solid lines indicate the highest measured V_{oc} and the V_{oc} of the device with the highest $V_{oc}*FF$ product processed in our lab. Highest measured V_{oc}'s are also indicated next to the device architectures. The dashed line indicates the V_{oc} of devices with the highest reported conversion efficiency, an overview of which is presented in table 9.2. Dashed lines are absent from the SHJ/nc-Si and SHJ/nc-Si/a-SiGe/a-Si devices, which, to the best of the authors knowledge, have not been processed before. Dashed lines is also absent from the a-SiGe single junction devices, for which the V_{oc} strongly depends on the used stoichiometry, is reported in [156].

Table 9.2: Reported V_{oc}'s of the devices with the highest conversion efficiency. V_{oc} range of 1J a-SiGe devices does not present record V_{oc}'s, but rather the V_{oc} range as a function of Ge fraction.

	V_{oc}	Ref.
nc-Si	0.550	[453]
a-SiGe*	0.56-0.76	[156]
a-Si	0.910	[421]
nc-Si+a-Si	1.420	[54]
a-SiGe+a-Si	1.54	[454]
a-Si+a-Si	1.807	[455]
nc-Si+nc-Si+a-Si	1.922	[171]
nc-Si+nc-Si+a-SiGe+a-Si	2.82	[452]
SHJ	0.749	[456]
SHJ+nc-Si	1.19	[152]
SHJ+a-Si	1.47	[457]
SHJ+nc-Si+a-Si	2.05	[152]
SHJ+nc-Si+a-SiGe+a-Si	2.83	this work

the ΔV_{oc} between the two reported V_{oc} values, as the SHJ/nc-Si/a-Si device, optimized in [152], demonstrates.

Fig.9.6 demonstrates the range of V_{oc}'s that can be realized by combining earth abundant and chemically inert silicon-based alloys in different wireless MJ architectures. The figure and the V_{oc}'s presented therein, can be used as a framework for selecting a suitable device architecture for a range of prospective electrochemical reduction reactions and electrocatalysts.

9.1.6 Conclusion

A prerequisite for the development of stand-alone solar-to-fuel synthesis devices is a 2-terminal monolithically integrated multijunction PV component that generates sufficient voltage to drive the desired electrochemical reduction reaction.

In this work, the front p-type contact and nc-Si:H absorber, integrated into most all-silicon multijunction devices, are investigated. The influence of the p-type contact, consisting of an i-nc-Si:H seed layer, p-nc-SiO$_x$:H layer, p-nc-Si:H contact layer and TCO, on the performance of single junction amorphous silicon devices is characterized. It is demonstrated that the presence of each of these layers in the p-layer stack is crucial for performance, and that all layers exhibit a different degree of trade-off between the V_{oc} and FF on the one hand, and the J_{sc} on the other.

Moreover, the influence of the silane concentration and deposition power on the development of crystalline growth in nc-Si:H absorbers was characterized. It was demonstrated that optimal device performance is achieved for a processing window close to the nanocrystalline-to-amorphous transition regime, where crystallinity values of around 60% are obtained. The transition regime is rather abrupt and large changes in crystallinity and device performance are found for minor variations in the processing window.

Finally, the flexible application of earth abundant and chemically inert silicon and silicon-germanium alloys is demonstrated in two distinct device architectures, combining up to 4 different junctions, yielding a V_{oc} range of 0.5V to 2.8V. This broad band of V_{oc}'s can

facilitate the development of a range of wireless and autonomous photo-electrochemical devices by fulfilling the voltage requirement for a range of electrochemical reduction reactions and electrocatalysts.

10

From photovoltaic to photoelectrochemical device

10.1 From photovoltaic to photo-electrochemical device: a study of micropore processing, size and distribution

Manuscript in preparation *

Abstract

The synthesis of chemical fuels, using sustainably generated electricity, is essential for realizing a zero-emission energy system. For the most integrated photovoltaic (PV)-electrochemical applications a two-terminal, monolithically integrated multijunction PV device based on group-IV elements is the most realistic candidate. Converting such a multijunction PV device into a photoelectrochemical (PEC) device capable of continuous, autonomous stand-alone operation, requires the use of electrocatalytically active contacts and the development of micropores through the PV device to prevent large pH-gradient related overpotentials.

In this work the influence of the size and distribution of micropores on the photovoltaic performance and electrochemical performance of a PEC device is simulated. Additionally, the resolution and taper of mircopores processed through pulsed laser drilling and deep reactive ion etching are compared. Finally, the successful processing of Pt microdots with a 2μm diameter and 5% surface coverage is demonstrated.

10.1.1 Introduction

The synthesis of chemical fuels, using sustainably generated electricity, is an essential puzzle piece in the transition towards a zero-emission energy system. Solar photovoltaics (PV) is the cheapest source of electricity in many parts of the world [11], and is projected to play a dominant role in our future energy system[3]–[5]. Solar-to-fuel synthesis systems are therefore receiving increasing interest. Such systems can take many forms [29]. Fully decoupled PV-inverter-electrolyser systems can benefit from mature and readily available components that can be optimized separately. Fully integrated photoelectrochemical (PEC) devices, on the other hand, require more complex optimizations, but facilitate the development of compact, easily produced, potentially cheaper units that have less wiring and fewer parts, providing ease of installation and excellent scalability.

For the most integrated PV-electrochemical (EC) and PEC applications there is, realistically, only single candidate for the PV component. This is a *two-terminal, monolithically integrated multijunction PV* device based on *group IV* elements. A *monolithically integrated two-terminal* design facilitates the processing of catalyst materials on either side of the PV device to facilitate the respective EC oxidation and reduction reactions. A *multijunction PV* device is required to generate sufficient voltage to drive the EC-reactions. The PV device should be based on *group IV* elements like silicon and germanium, which possess an inherent chemical stability absent in all other semiconductor PV technologies. The chemical stability of III-V-, chalcogenide- and perovskite-based semiconductors is fundamentally limited, in reference to silicon, owing to the chemical complexity introduced by the use of elements from different groups and periods [168].

All-silicon multijunction PV devices have already demonstrated the ability to generate sufficient potential for water splitting [29], [30], [35], [417]. An open circuit voltage (V_{oc}) of over 2V and a PV conversion efficiency close to 15%[152] have been demonstrated for a hybrid crystalline silicon (c-Si)/thin film silicon triple junction PV device. The application of such a PV device is not limited to water splitting. In recent work, through the flexible use of different group IV alloys in different device architectures, V_{oc}'s has been demonstrated ranging from 0.5V to over 2.8V for thin film silicon and hybrid c-Si/thin film silicon device architectures [458]. Such voltages not only provide potential routes towards the (photo)electrochemical reduction of H_2O to H_2, but also of CO_2 (and H_2O) to chemical fuels like syngas, formaldehyde, formic acid, methanol and methane, which each require different reaction potentials [265].

A number of steps are required for the use of a PV cell in an integrated autonomous solar-to-fuel synthesis system. For one, the positive and negative contacts on the PV junctions should facilitate the oxidation and reduction reactions. This means that electrocatalytically active contacts should be used that require minimal overpotentials. As a consequence, rather than the Al or Ag contacts conventionally used for PV, Ir and Pt contacts should be used instead, in the case of water splitting operation under basic conditions [459]. Additionally, for continuous, autonomous stand-alone operation, pores should be developed through the PV device to prevent pH gradient formation due to long-distance ion transport [34], [35].
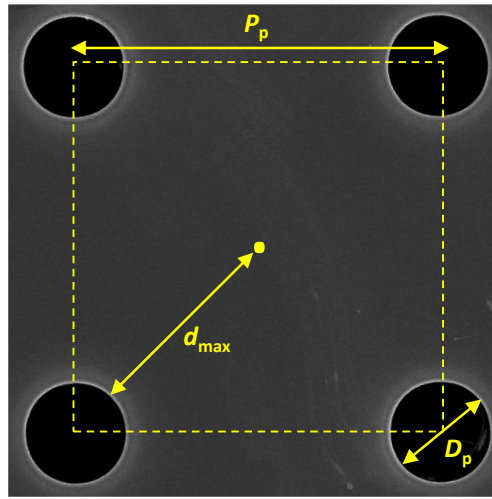
Figure 10.1: SEM image of the surface of a porous substrate with D_{p}, P_{p} and $d_{\max}$ schematically indicated.

In this work, the different considerations for the design and development of the micropores and electrocatalytic contacts for an all-silicon autonomous solar-to-fuel device are discussed. In section 10.1.2 simulations are performed to determine the optimal size and spacing of the micropores from both a PV and electrochemical perspective. Additionally, the advantages and limitations of different methods for pore processing are evaluated. In section 10.1.3 Pt contact design is discussed and the successful processing of the contacts is demonstrated.

10.1.2 Micropore design

In earlier work it was demonstrated that a monolithic 2-terminal design in which micropores were developed through the PEC cell can reduce the required overpotential by several hundreds of millivolts in reference to a wired PEC design or a wireless pore-free design [35]. This is because only for such a design are the ion transport distances and consequently ionic ohmic losses minimal, especially for technologies with low operational currents [34], [35], [435]. Additionally, a very strong dependence of the PEC performance on the period (P_{p}) and diameter (D_{p}) of pores was demonstrated [35].

The relation between pore design and PEC performance can best be understood by considering the influence of the pores on the PV performance and EC performance separately. For PV performance, the introduction of pores results in a loss of photoactive area and consequently a loss of generated photocurrent (J_{ph}). In fact, it was demonstrated that approximately 99% of the losses in J_{sc}, following the development of pores in in a PV device, were related to the loss in photoactive area [34]. This indicates that the losses in J_{ph} can be accurately approximated by the overall surface coverage of the pores (θ_{p}), assuming that the difference between the entry and exit diameter of the pores is

minimal. Under this assumption the loss in generated photocurrent of a porous device in reference to a non-porous device ($J_{\text{ph-porous}}/J_{\text{ph-max}}$) can therefore be assumed equal to $1-\theta_{\text{p}}$. Considering the schematic drawing in Fig.10.1, θ_{p} can be expressed as:

$$\theta_{\text{p}} = \left(\frac{\frac{1}{4}\pi D_{\text{p}}^2}{P_{\text{p}}^2} \right) \tag{10.1}$$

Using Eq.10.1, the effect of P_{p} and D_{p} on $J_{\text{ph-porous}}/J_{\text{ph-max}}$, as a function of pore size and distribution, is visualized in Fig.10.2.

The relation between pore size and distribution and EC performance is more complex. Proton transport can be considered a two-step process, where 1. a proton travels from its point of generation on the surface to a pore and 2. travels through the pore. The resistive losses associated with step 1, the surface transport step, can intuitively be understood to be related to the maximum distance (d_{max}) a generated proton has to travel to reach a pore. From Fig.10.1 it can be observed that d_{max} will decrease if either D_{p} is increased or P_{p} is decreased. On the other hand, losses resulting from the in-pore transport, step 2, are the results of resistance against transport in the pores. This resistance can, considering fluid dynamics, be understood to depend on D_{p} and the length of the pores. The pore-length in this work is mainly determined by the thickness of the wafer of $\approx 300\mu$m, as all supporting layers combined amount to $\leq 5\mu$m. It was demonstrated that in-pore transport losses can greatly be reduced at reduced thickness of the PEC cell [35]. In fact, the PV performance would also benefit from using thinner wafers, considering that the V_{oc} generally exhibits an inverse relationship to the wafer thickness and the J_{sc} of c-Si junction in the record 2-terminal silicon based multijunction device would likely not be current limiting at reduced thickness [152]. Nevertheless, a wafer thickness of 300μm is used in this study considering the reduced structural integrity of thinner wafers and the large number of steps and processing tools used to developed the porous PEC devices.

In order to assess the collective effects of the pore size and distribution on the EC performance, the PEC cells are modelled COMSOL Multiphysics, using the Tertiary Current Distribution Nernst-Planck Interface. The EC performance is evaluated from the pH gradient that evolves between the anode and the cathode for different hole patterns. The pH at the surface of each electrode is obtained from 2D simulations of the porous cells. As a 2D model is used, the pores are modelled as slits, through which the molar fluxes of chemical species are assessed. The modelling approach is similar to the one used in [34], which was based on approaches used in [460] and [35]. The assumptions and inputs for the model are discussed in great detail in [461] and are similar to those used in [34].

A few steps are involved in determining the EC current loss as a function of the pore dimensions. A detailed description of the steps can be found in [461]. First, using pH values obtained from the COMSOL model, the proton concentrations at the anode and cathode are determined. Using the Nernst equation, the proton concentrations are used to calculate the electrode potentials and determine the required overpotential (E_{loss}). E_{loss} is then used to evaluate the Butler-Volmer current density, which represents the losses in current density due to pH gradient-related over-potentials. The cathodic Butler-Volmer current density was found to be several orders of magnitude larger than the anodic current density in this PEC system. The EC current density loss ($J_{\text{EC-loss}}$) as a function of

pore morphology is therefore approximately equal to the cathodic Butler-Volmer current density loss:

$$J_{\text{EC-loss}} = J_0 \left(\exp(\frac{\alpha_a F E_{\text{loss}}}{RT}) - \exp(\frac{\alpha_c F E_{\text{loss}}}{RT}) \right) \qquad (10.2)$$

Here F and R are the Faraday constant and the universal gas constant, T is the temperature and α_a and α_c are the anodic and cathodic charge transfer coefficients, respectively. J_0 is the exchange current density, or operating current density. J_0 is set to $J_{\text{ph-max}}=8.13\text{mA} \cdot \text{cm}^{-2}$ in this study. This value is approximately the J_{sc} of the PV device developed for water splitting in [29] and used as J_0 for simulations in [34]. Use of this number therefore facilitates model comparison and validation. In Fig.10.2B a contour plot of the influence of P_p and D_p on the EC performance, specifically the fractional performance loss in reference to $J_{\text{ph-max}}$ ($\frac{(J_{\text{ph-max}}-J_{\text{EC-loss}})}{J_{\text{ph-max}}}$) is presented. It can be observed that, as expected, minimal current losses (red) are achieved for large D_p and small P_p values. However, $\frac{J_{\text{ph-porous}}}{J_{\text{ph-max}}}$ for this combination is minimal, as large D_p and small P_p result in relatively large θ_p values, so a surface largely covered by pores. Fig.10.2C therefore shows the combined effects of pore morphology on the PV and EC performance. It is clear that for this system, the influence of pore dimensions on EC and PV performance are similar in magnitude and opposite in trend. Optimal D_p-P_p combinations extend diagonally across the whole D_p range.

A final optimization was therefore performed to find the optimal pore dimensions. In this optimization, the optimal P_p was determined for a D_p of 20μm, 40μm, 60μm and 80μm. The result are indicated by the black dashed line in Fig.10.2C. The optimization additionally showed that the collective losses are minimal for the smallest of the studied combinations, with $D_p=20\mu$m and $P_p=70\mu$m. For this combination, a maximum of 83.4% of $J_{\text{ph-max}}$ can be retained, for the specific design and assumptions used in this study.

It should be noted that while small D_p-P_p combinations are favoured theoretically, technically they might prove challenging to achieve. For optimal operation the pores should be filled with a proton exchange material [34]. A uniform distribution of such a material inside the pores will prove challenging at relatively small pore diameters. Moreover, the taper, the fractional difference between the diameter of the exit or entry hole, for a given wafer thickness is generally larger for smaller pore diameters. As the EC losses associated to the effect of D_p on proton transport is limited by the smallest pore diameter, that of the exit or entry hole, a large taper results in a loss of photoactive bulk without loss reduction for proton transport.

Micropore processing

The results from the preceding section indicate that pores with a diameter several tens of microns should be developed for optimal PEC operation. Additionally, the taper should be minimal and development of the holes should not result in damage to the solar cell. Taking these criteria into consideration, several pore processing methods are considered in this section.

In earlier work, deep reactive-ion etching (DRIE) was used for pore development [34].
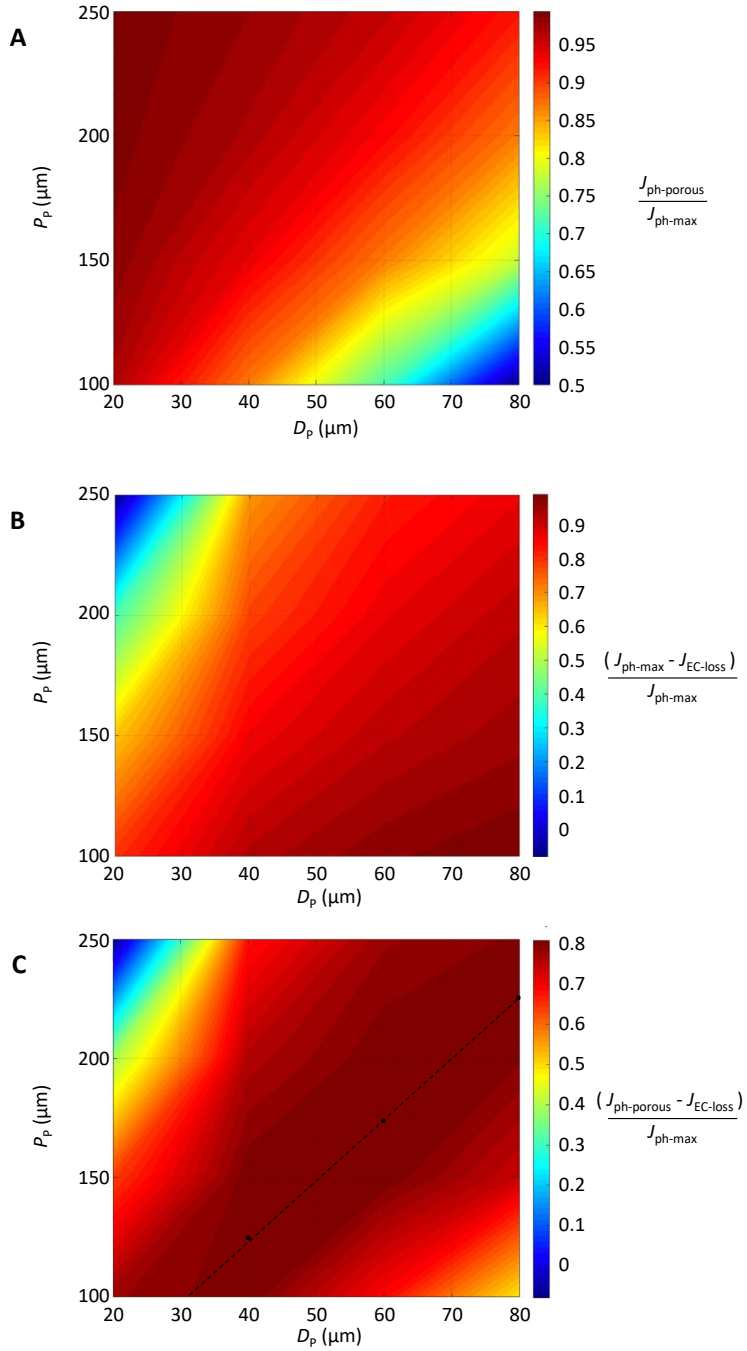
Figure 10.2: Contour plots of the influence of D_P and P_P on the current characteristics of a PEC device in reference to the current generated by a non-porous PV component. Plots indicate the effects on **A** exclusively the PV component, **B** exclusively the EC component and **C** the combined effect of pore dimensions on PEC behaviour. Black markers in **C** indicate individually optimized P_P for $D_\mathrm{P}{=}40\mu$m, 60μm and 80μm. Dashed line is added as a visual guide.
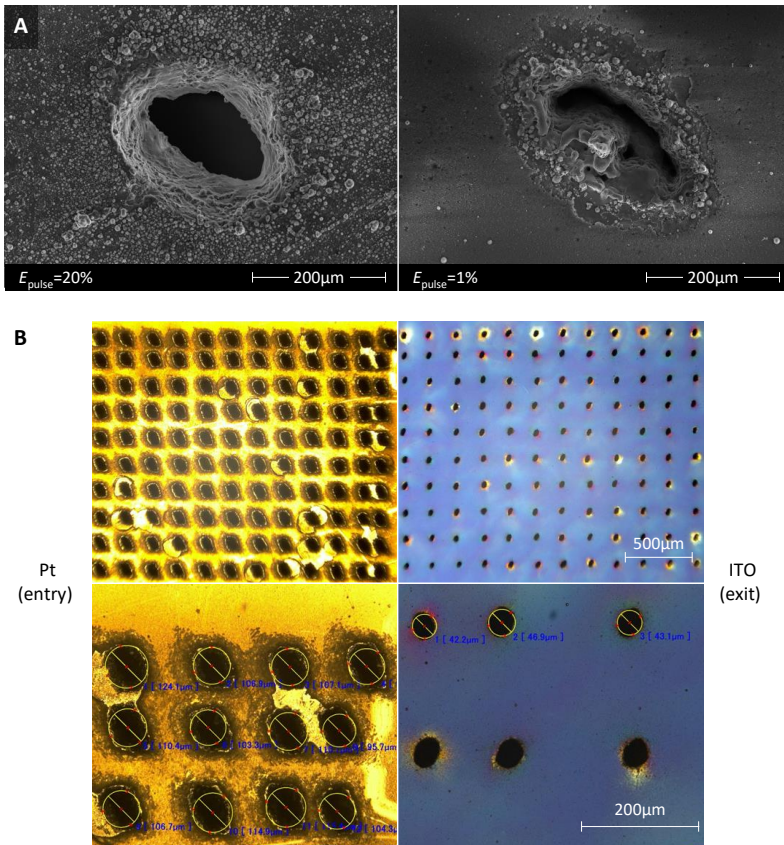
Figure 10.3: **A** SEM images of the substrate surface following PLD at E_{pulse}=20% (top, left) and E_{pulse}=1% (top, right). **B** Optical microscope images of a matrix of PLD-pores drilled from the PT side. Entry (left) and exit (right) holes are presented excluding (top) and including (bottom) analysis of the hole morphology.

DRIE is a pulsed process in which the development of holes with minimal taper is achieved through alternated steps of plasma etching and deposition of a passivation layer. While successfully applied to solar cells, the process is relatively complex and time consuming. For that reason, conventional micro drilling techniques are additionally considered. The increasing demand for holes with few-micron diameters has led to significant recent advances in the field of micro drilling [462]. Conventional mechanical rotary drilling, electro discharge machining (EDM) and pulsed laser drilling (PLD) are three of the most widely used microdrilling techniques, each able to develop holes with a diameter in the order of several (tens of) microns [462]. Of these, only laser drilling is a viable option for wafer based solar cells, since the thin wafer is too brittle for mechanical drilling and too resistive for EDM. In this section, an optimization is presented for the DRIE and PLD processing of pores in a silicon wafer.

Pulsed Laser Drilling PLD is the process of developing pores through evaporation of material induced by repeated focused laser pulses. For this work all PLD experiments are performed at the Sirius Laser Facility at the Aerospace Engineering department of TU Delft. A 300nm wavelength laser is used with a maximum intensity of 1000 W · cm^{-2} and 200ns pulse duration. The pulse frequency as well as the number of pulses (N_{pulse}) and (E_{pulse}) can be varied. Due to time considerations, only the latter two were varied in this study. Given the constant pulse duration, E_{pulse} is varied by attenuating the laser intensity with optical filters. E_{pulse} is therefore expressed as a fraction of the maximum laser intensity. A PI programmable XY stage is used to map out the hole patterns. A dedicated substrate holder was developed to prevent the substrate from touching the stage and minimize vibrations during PLD operation. The experiments were performed on 300μm c-Si wafers with 75nm ITO on the front and 75nm Pt at the back.

   An initial experiment was performed, with E_{pulse} =20%, 5% and 1% and N_{pulse} ranging from 2 to 400, to establish 1. a relation between E_{pulse} and N_{pulse} for processing a hole through the entire wafer and 2. a relation between E_{pulse} and the hole diameter, taper and potential surface damage. The results of the preliminary experiment can be observed in Fig.10.3A, where SEM images of PLD processed entry-holes are shown.
Through SEM and optical microscope imaging it was established that the relation between E_{pulse} and N_{pulse} is roughly inversely proportional. With E_{pulse}=20%, about 10-14 pulses are required to drill through the wafer. At E_{pulse}=5% the N_{pulse} required is about 4 times as large and at E_{pulse}=1% about 20 times as many pulses are required. Moreover, for E_{pulse} >1% the surface damage is quite significant with relatively large amounts of material redeposited around the entry hole. Additionally, it could be observed that the holes are not circular of shape, which indicates that the laser is not in optimal focus.
Considering these findings, a further experiment was designed. In this experiment a triangular matrix of laser setting was devised where N_{pulse} is decreased with increasing E_{pulse}. For these, E_{pulse} of 1% and lower was explored. Additionally, the laser operator made an effort to improve the laser focus and a 12μm thick AZ12XT photoresist layer was applied at the front of the wafer. This layer acts as a temporary protective layer during PLD and is removed after the process.
This optimization resulted in optimal PLD parameters for these pore dimensions are E_{pulse}= 0.58–0.6% and N_{pulse}=80–90. With these settings reproducible pores with an average entrance diameter on the Pt-coated side of 104.7±4.1 μm and an average exit diameter on the ITO-side of 46.7±2.6μm are measured, as shown in Fig.10.3B. With the use of the protective layer the holes could be drilled without significant damage to the platinum contact. However, even with optimized settings a significant taper persists for these 300μm thick wafers, with the average diameter of the exit hole less than twice the size of the entry hole. The achieved resolution in the range of 80-100μm is also sub-optimal.

Deep Reactive-ion Etching Deep reactive-ion etching (DRIE) is a process that allows for etching features in silicon with a very high aspect ratio and selectivity [463]–[465]. The DRIE-reactor consists of a low pressure plasma chamber with an inductive coil and a capacitive plate generator that directs ions from the plasma towards the sample. The power delivered by the coil and plate generators are referred to as the source and bias
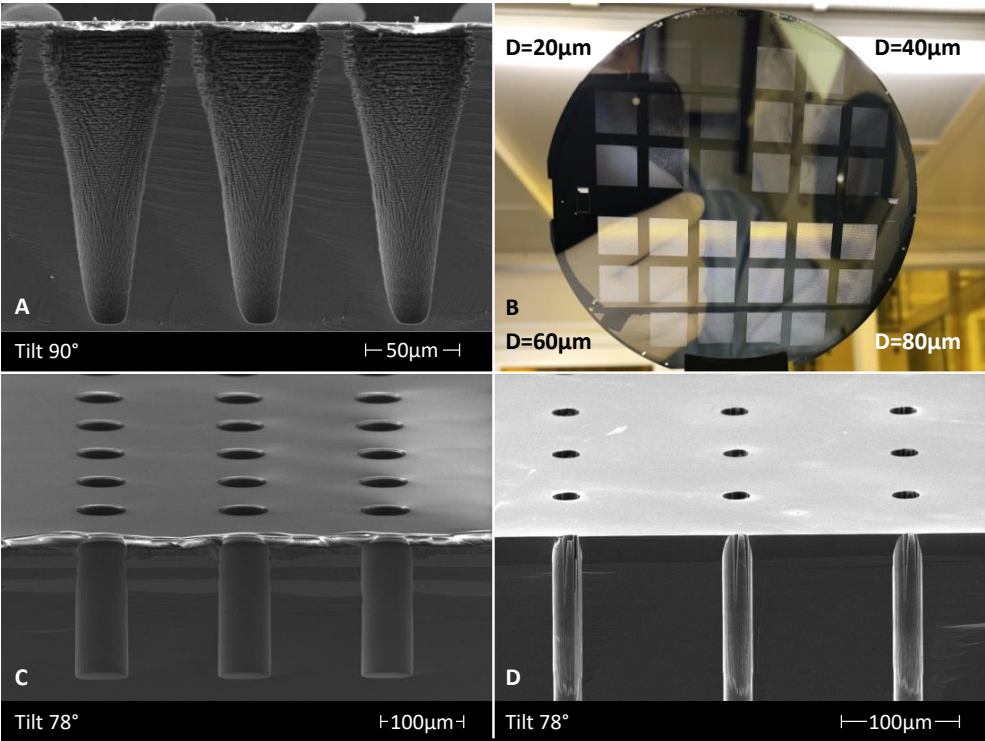
Figure 10.4: **A** Cross-sectional SEM image of pores processed at sub-optimal conditions resulting in a significant taper. **B** Porous substrate following successful application of the DRIE process. Substrate has quadrants with different P_p and D_p. **C-D** Cross-sectional SEM images of pores with $D_\mathrm{p}{=}60\mu$m (**C**) and $D_\mathrm{p}{=}20\mu$m (**D**) processed partly through the wafer.

Table 10.1: Optimal DRIE processing conditions

	etching step	passivation step
Source power (W)	600	
Bias power (W)	15	
Stage temperature (°C)	20	
Source-sample distance (mm)	120	
Time (s)	8	5
Pressure (μbar)	15	30
SF_6 flow rate (sccm)	150	0
C_4F_8 flow rate (sccm)	0	85
O_2 flow rate (sccm)	13	0

power. A 2-step DRIE process, known as the Bosch method, is used in this work. The pulsed process alternates between precursor gasses that have a passivating and etching effect. The ADIXEN AMS 110 systems was used for this work, which is a single wafer etcher with a 3kW ICP source and 300W bias power supply and helium backside cooling. SF_6 is used as the precursor gas for the etching step. The SF_6 is partially dissociated in the plasma into fluor radicals which react with silicon to form gaseous SiF_4. C_4F_8 is the passivating agent, which upon dissociation forms CF_{1-2} radicals that deposit as a teflonlike substance on the substrate [465]. The samples for DRIE consist of a 300μm silicon wafer and a 150nm and 75nm ITO layer on the front and back. To form the desired pore pattern, a SiO_2 hard mask was processed on the front of the wafer, using photolithography. The process of photolithographically developing the hard mask is similar to the approach used for developing a hard mask (Fig.3.11 step 1-5) for the honeycomb structure in section 3.2, with the exception of the mask used during the exposure step. SiO_2 is much more resistant against SF_x etching than the exposed Si wafer. Under the right processing conditions, the selectivity for Si-wafer etching in reference to mask etching can be as high as 300 to 1. Additionally, to protect the equipment from damage once the pores were etched through, a 500 μm carrier wafer was used, with a 15μm SiO_2 layer. Some Fomblin oil was used for improved adhesion between the two wafers.

There are a large number of DRIE processing conditions that affect the selectivity and directionality of the process. These include the source and bias power, pressure and precursor gas flow rates for both the etching and passivation step, as well as the duration of each step and the distance of the sample to the source. Using the standard Bosch recipe as a starting point, available on the ADIXEN AMS 110 system, the bias power and source power were varied. This yielded a number of samples with very poor selectivity and directionality, with extensive damage to the SiO_2 mask and no significant pore etching. A different recipe was then used, obtained from [466]. The use of this recipe resulted in excellent selectivity, but sub-optimal directionality, as shown in Fig.10.4A. It can be observed that the SiO_2 mask appears intact, but the developed pores have a significant taper. Further optimization of the distance between the source and the sample improved the directionality of the etching process. Fig.10.4C-D show that for both large and small pore diameters, the pores exhibit a cylindrical shape with no significant taper. The optimized DRIE processing conditions are reported in Table 10.1. However, none of the pores went through the entire wafer thickness. A final step therefore involved optimization of the etching time. This resulted in the pores through the wafer shown in Fig.10.4B, at just over 4 hours for the pores with D_p=40-80μm and 6,5hrs for the pores with D_p=20μm. The DRIE process can benefit from further optimization, as the etch rate, currently at $<1\mu$m $\cdot$ min^{-1}, should ideally be increased to reportedly achievable 5-8μm $\cdot$ min^{-1} [463], [464], [466], while maintaining good pore morphology.

Much better pore morphology is achieved using the DRIE process in reference to the PLD process. The minimum diameter achieved using DRIE is 20μm compared to 80-100μm for PLD. The taper for a pore though a 300μm-thick wafer is <2% for DRIE, while for PLD the exit hole diameter is less than twice that of the entry hole. Moreover, due to the pulsed etching and passivating nature of the DRIE process, the inner surface of the pores appear much smoother compared to the pore-surface resulting from the PLD process. Whether this observation translates to surface damage and an increase in electrical resistances could not be confirmed through J-V measurements on finished
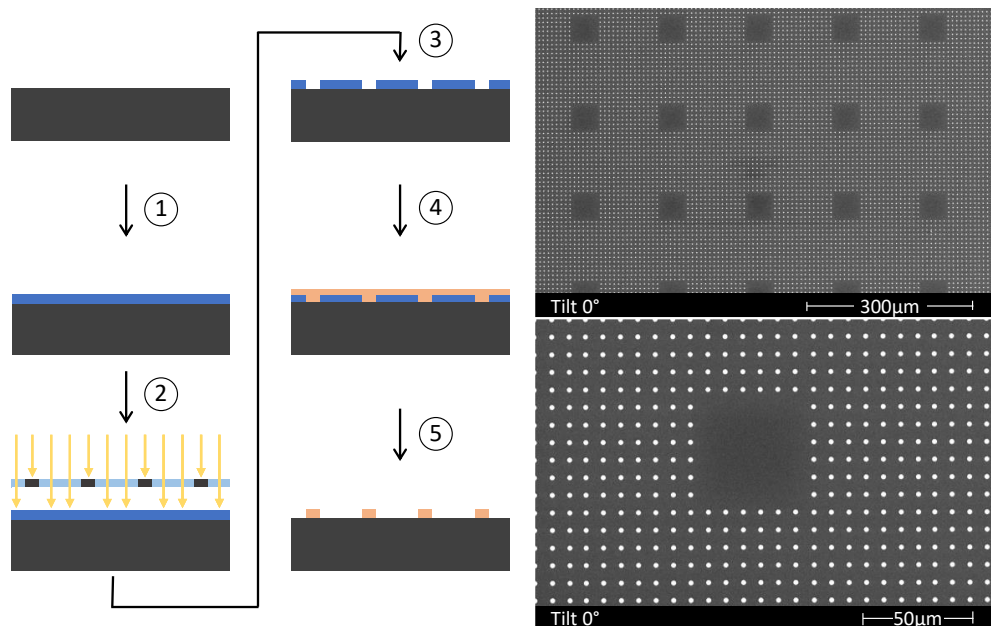
Figure 10.5: Flowchart of the microdot development process. Steps 1-5 are referenced in the text. SEM images of the substrate surface following successful microdot application.

porous PV devices however, due to constrains in time and equipment availability.

The DRIE process yields the best results for the application investigated in this work. It should be noted that, considering the large number of technically challenging and time-consuming steps involved in the DRIE process, the relative quick and simple PLD process could be the preferred pore processing method if the project parameters allow for it. Specifically, PLD could be preferable if larger pore diameters are acceptable, or if much thinner substrates of $<50\mu$m are used, which would result in much smaller tapers.

10.1.3 Microdot design and processing

The electrocatalyst processed at the back of the PEC device covers the entire surface, with exclusion of the micropores. However, at the front of the device a balance has to be found between facilitating catalytic activity and light transmission into the PEC device. Light transmission is diminished by surface area covered with a reflective and absorptive electrocatalyst material. It was demonstrated in earlier work that a good balance between these competing effects could be achieved using patterned electrocatalysts [467]. Using a microdot pattern, an optimization of the microdot spacing was performed in [34]. Using microdots with a 2μm diameter, the study demonstrated that an optimal balance between light transmission and catalytic activity for a 8μm period, corresponding to a surface coverage of about 5%.

A similar design was used in this work. The microdot pattern is shown in Fig.10.5. The squares formed by the absence of microdots indicate the position of micropore formation.

On each wafer there are 32 cells of 1x1cm that are covered with microdots. The microdot process consist of several steps, as schematically shown in Fig.10.5. The wafers are first heated in an oven at 110°C for 10 minutes to remove moisture, and treated with HMDS vapour for 10 minutes to improve resist adhesion. In step 1, a negative photoresist, AZ nLof 2020, is applied using a manually operated spincoater. The photoresists is then exposed using a SUSS MABA 8 mask aligner and developed in step 4 in AZ MF 322 developer. After the Pt deposition in step 5, the remaining photoresist is removed in step 6 by sonicating at high frequency in hot (75-80°C) Nmethyl2pyrrolidone (NMP) for 15 minutes.

Several optimizations are performed to achieve a uniform distribution of microdots across all cells on each wafer, as initially only 17 out of 32 cells featured microdots. The standard puddle method, in which a single dose of developer is decanted on the wafer with exposed resist, was compared to a multi dose approach and to the immersion method, in which the wafer is immersed in developer. Use of the immersion method resulted in a moderate improvement from 17 to 21 out of 32 cells. An increase of development time from 110s to 130s and 150s did not yield any changes. A significant improvement was realized when the photoresists thickness was reduced from 3.5μm to 2μm, through an increase of the spin speed. After fine-tuning of the exposure time for the reduced thickness a uniform distribution of microdots was achieved across all 32cells. The results of successful execution of these steps is presented in Fig.10.5.

10.1.4 Conclusion

Converting a multijunction PV device into a PEC device capable of continuous, autonomous stand-alone operation, requires the use of electrocatalytically active contacts and the development of micropores through the PV device to prevent large pH-gradient related overpotentials.

In this work the influence of the size and distribution of micropores on the photovoltaic performance and electrochemical performance of a PEC device is simulated. It is shown that the influence on PV and EC performance is opposite in trend and that current density losses can be limited to less than 20% for a range of pore diameter-period combinations. Minimal losses are theoretically realized for small pore diameters of $\leq 20\mu$m, but uniform filling of such micropores with a proton exchange material might prove technically challenging.

The processing of micropores was achieved using two different techniques: pulsed laser drilling and deep reactive ion etching. Much better resolution, reproducibility and taper were achieved using the DRIE process in reference to PLD. Using DRIE, micropores with a diameter of 20μm were successfully processed with a taper $<2\%$. For PLD, minimal entry diameters are in the range of 80-100um, with exit diameters of 40-50um. This makes DRIE the preferred method for the application considered in this work. Finally, the successful processing of Pt microdots with a 2μm diameter and 5% surface coverage is demonstrated.

11

Conclusion and Outlook

In this dissertation a framework is presented for the development of high voltage multi-junction photovoltaic devices. Specifically, wireless silicon-based monolithically integrated 2-terminal multijunction PV devices are investigated. Such devices can be used in autonomous solar-to-fuel synthesis systems, as well as other innovative approaches in which the multijunction solar cell is used not only as a photovoltaic current-voltage generator, but also as an ion-exchange membrane, electrochemical catalysts and/or optical transmittance filter. The framework presented in this dissertation encompasses all investigations performed in answering this thesis' central question:

To what extent can fundamental insight and device engineering reduce the opto-electrical losses in a hybrid wafer-based and thin film photovoltaic multijunction device, based on group IV elements?

This research questions is divided into three key-questions, relating to the investigation of I. textures, photovoltaic materials and single junction solar cells, II. a low bandgap Ge(Sn):H absorber and III. multijunction PV and PEC devices. In this section, each key-question will be considered in turn.

I. *How and to what extent can the processing conditions of individual layers and surfaces be tuned such that they result in desirable material properties for different functionalities for use in single junction photovoltaic devices?*

A photovoltaic device consist of a series of layers, doped and intrinsic, and the interfaces between these layers. In doped nanocrystalline silicon and silicon-oxide films the chemical stability has to be balanced with opto-electrical performance. In **Chapter 2.1** we demonstrate that deterioration of the p-SiO$_X$:H layer, under ambient exposure, is responsible for the degradation of single junction devices. Increasing the deposition pressure of doped SiO$_X$:H films increases its chemical stability, but at the cost of (initial) solar cell conversion efficiency. Moreover, a relation was established between the p-SiO$_X$:H degradation behaviour to both the crystallinity and position of the p-layer in a single junction device in reference to the ambient.
In addition to this balance between chemical stability and performance, a trade-off exists between the optical and electrical material properties. In **Chapter 2.2**, a material phase diagram is developed to visualize the relative crystalline silicon, amorphous silicon and amorphous silicon-oxide fractions as a function of the various precursor gas flow rates. The influence of the material phases, in combination with the density of the a-Si(O$_X$):H phase and the extent of doping, on the opto-electrical properties of a/nc-SiO$_{X \geq 0}$:H films is shown. Finally, we demonstrate that as the material phase fractions develop along the growth direction, opto-electrical properties as a function of film thickness evolve as well.

In **Chapter 3**, the substrates on which the photovoltaic devices are processed are investigated. As conventional flat and pyramidal textures are not compatible with the growth of device quality nano- to poly-crystalline materials, several novel texturing approaches were developed. In **Chapter 3.1**, three separate texturing approaches are presented involving one or more chemical etching steps and the use of a poly-crystalline sacrificial layer. For each of the texturing approaches, the influence of one or more of the processing steps on the silicon surface characteristics, optical behaviour and passivation quality is characterized. A strong correlation was established between the reflective behaviour of the surface, both in terms of light in-coupling and wide angle scattering, and the ability to facilitate crack-free nc-Si:H growth to the coverage and average slope of pyramidal features on the silicon surface.
In **Chapter 3.2**, the texturing approach involving a sacrificial poly-Si layer was optimized, through an investigation of the processing conditions of the sacrificial layer (the used ion type, ion dose, implantation energy, layer thickness, annealing time and temperature). Additionally, a texturing approach was presented involving a photolithographically developed honeycomb structure. The optical behaviour (reflection, haze, angular distribution intensity) of the textured surfaces is was investigated and the performance of the textures in PV cells was compared, both in optically simulated and experimental devices. Simulations demonstrate strong improvements in J_{sc}-sum ($\approx 45\%$), in reference to a flat surface, and high $V_{oc}*FF$s of over 1V are experimentally demonstrated for a-Si/nc-Si tandem devices.

In **Chapter 4**, an expedient semi-empirical approach for the optimal bandgap profiling of stoichiometric absorbers is presented, using a-SiGe:H as a model. In this approach

the J_{SC} and V_{OC} of cells as a function of the bandgap energy profile are simulated. First, the influence of i.a. the relative germane flow rate on the bandgap energy and conductivity of undoped a-SiGe:H films are characterized. Then a large number of solar cells with profiled a-SiGe:H absorbers are presented, in which 1. the absorber thickness, 2. minimum bandgap energy and 3. the introduction of a plateau at the minimum bandgap energy are investigated. Using the presented semi-empirical relations, the combination of thickness, minimum bandgap energy and plateau fraction resulting in the highest V_{OC}-J_{SC} product can be found. Additionally, for a certain required J_{SC}, or alternatively for a certain spectral range of absorption, the bandgap profile resulting in the highest V_{OC} can be found, which is particularly useful for multijunction applications.

II. *Through a fundamental opto-electrical optimization, can an intrinsic low bandgap energy (0.5-0.8eV) plasma enhanced chemical vapour deposition processed hydrogenated germanium or germanium-tin alloy be developed for use in photovoltaic devices?*

The processing of a group IV, low bandgap, intrinsic and stable material starts with the processing of Ge:H, a material that has not been processed for over a decade and never before in our group. In **Chapter 5.1** the processing window for Ge:H films in our reactor is identified by performing a full exploration of the processing conditions (precursor gas flow rates, temperature, pressure, power). A strong correlation was found between the refractive index and the presence of a GeO_X signature, indicating that a dense a-Ge:H network with a low void density is required to prevent the in-diffusion of water from the ambient and subsequent post-deposition oxidation. The oxidation strongly affects the opto-electrical properties of Ge:H films. Surprisingly it was found that oxidation can actually decrease the dark conductivity at room temperature, despite an activation energy decrease, as oxygen is suspected to passivate the Ge-dangling bonds and reduce the defect density.

In **Chapter 5.2** improved a/nc-Ge:H films are presented, by processing at elevated temperature and a reduced electrode gap, facilitating low power depositions. This results in plasma conditions of low-energetic ion bombardment, where densification is achieved through temperature induced restructuring of the growth zone. Under these conditions amorphous and nano-crystalline Ge:H films are processed with the highest refractive indices and lowest dark conductivity values reported in literature for chemical vapour deposition processed Ge:H.

In **Chapter 6** the structural and opto-electrical properties of Ge(Sn):H are compared to those of other group IV alloys. In **Chapter 6.1** infrared and Raman vibrational spectroscopy, as well as elemental analysis, is performed on a range of hydrogenated group IV alloys. The evolution of the vibrational spectra of these alloys is monitored over time while exposed to different ambient and illumination conditions. This unique and comprehensive overview provides a single work of reference for the identification of oxide and hydrides peaks across the group IV elements carbon, silicon and germanium for both amorphous and nano-crystalline materials. Moreover, the influence of the dielectric medium on the peak frequency of a vibrational mode, is illustrated using the experimentally observed

frequency shifts of X-O and X-H (X=C, Si, Ge) vibrational modes. Additionally, all experimentally observed frequency positions of silicon hydride stretching modes in silicon solids are identified considering all potential hydrogenated volume deficiencies within tetrahedrally coordinated amorphous and nanocrystalline lattice.

In **Chapter 6.2** the first ever evidence of the post deposition appearance of CH_yO_z vibrational modes in PECVD processed hydrogenated germanium is presented. It is proposed that the observed carbisation reaction involves the catalytic reduction of CO_2 in Ge:H films to products like CO, formic acid and formaldehyde. A two-step process is proposed, in which the reduction of CO_2 follows the post-deposition chemical transformation of a-Ge:H to a-GeO$_x$:H upon reaction with water. The reaction rate is demonstrated to be a function of the material porosity. A theory is presented in which the a-GeO$_x$:H phase is essential for energetic alignment of the valence band edge with the water oxidation reaction potential. Protons from water splitting are used for the catalytic CO_2 reduction reaction.

In **Chapter 6.3** the opto-electrical properties of over 400 PECVD processed films group IV alloys are presented, demonstrating a E_{04} range of over 1.3eV. Based on these results the fundamental relations between the material density, as a function of the stoichiometry, void fraction and crystalline phase fraction, and bandgap energy are discussed. Moreover, the relation between the bandgap energy and electrical materials characteristics such as the dark conductivity, activation energy and photoresponse are considered. Additionally, based on 230 a/nc-Ge:H films, three inherent challenges are identified related to the PECVD processing of hydrogenated germanium. These are related to the intrinsicity, chemical stability and photoresponse of the films. Two pathways for tackling these challenges are presented. The first involves a very specific processing window, while the second involves the alloying of Ge:H. Improved chemical stability is demonstrated for Ge:H films alloyed with O and C. While these alloys exhibit higher E_{04} than unalloyed Ge:H, a similar improvement in chemical stability could be achieved in GeCSn:H alloys.

In **Chapter 7** the first steps towards the PECVD processing of a GeSn:H alloy are presented. Some inherent challenges are identified for the processing of GeSn:H using a tetramethyltin precursor, involving i) the relatively low melting point of Sn, resulting in the formation of Sn-clusters, and ii) the fact that four CH_3 groups are introduced into the reactor for each Sn-atom. We demonstrate that managing the C and Sn integration into the material is crucial, as large CH_3 fluxes results in porous and chemically unstable films and high atomic fractions of Sn are essential for achieving low-E_G. A number of nc-GeSn(C):H films with a crystallinity of≈50% are processed with a highly heterogeneous nature, consisting of GeSn crystals with 15.5-17.5% Sn embedded in an a-GeC:H phase in which almost no Sn is present. Such heterogeneous nc-GeSnC:H films could provide a potential route towards a low bandgap energy group IV alternative for photovoltaic multijunction applications.

III. *How do different materials, variations in material properties and different device configurations affect the performance of multijunction photovoltaic and photo-electrochemical devices?*

The J-V characteristics of a multijunction device are a function of the substrate type and morphology, the device architecture (the number and position of junctions and used absorber materials), and the interfaces between the junctions.

In **Chapter 8.1** the influence of thickness and design of the p-type nc-Si(O$_X$):H based layer in the tunnel recombination junction (TRJ) of a large number of SHJ/nc-Si:H, nc-Si:H/a-Si:H, nc-Si:H/a-SiGe:H and a-SiGe:H/a-Si:H multijunction devices is observed across different device architectures. It was found that for optimal V_{oc}*FF product, the presence of a high bandgap p-nc-SiO$_X$:H layer is crucial, and the optimal thickness is in the range of 12-18nm. Moreover, a strong improvement was observed when a thin, low activation energy (E_{act}) contact layer was used in combination with the p-nc-SiO$_X$:H layer. This low-E_{act} layer can be both a p-nc-Si:H layer or more highly doped p-nc-SiO$_X$:H layer.

In **Chapter 8.2**, different current matching approaches are explored in tandem SHJ/nc-Si:H and triple junction SHJ/nc-Si:H/a-Si:H devices. The influence of absorber thickness as well as the thickness of different intermediate reflective layers (IRL), based on silicon-oxide, various transparent conductive oxides (TCOs) and Ag, on the tandem SHJ/nc-Si:H and triple junction SHJ/nc-Si:H/a-Si:H device performance is investigated. It is shown that both an increase of absorber thickness and an increase of IRL thickness (positioned at the back of a junction in reference to the incident light) result in an J_{sc} increase at the cost of V_{oc}*FF. The V_{oc}*FF dependence on layer thickness is approximately linear, while J_{sc} dependence is not. Understanding of reflective/absorptive behaviour (J_{sc} gain), as well as the resistive behaviour (V_{oc}*FF loss), of the different layers as a function of thickness is essential for optimal device performance. Moreover, considering the observed FF-dependence on current matching conditions, intentionally introducing a minor current mismatch in which the junction with the highest FF is current limiting is advisable. Additionally, a V_{oc} $\approx$2V and η $\approx$15% are reported for a triple junction SHJ/nc-Si:H/a-Si:H device , which is the highest reported conversion efficiency for an all-silicon solar cell that generates at least 1V.

In **Chapter 9** an optimization of the p-type front contact and i-nc-Si:H absorber are presented. It is demonstrated that an optimal p-contact, for an n-i-p device, consists of a stack of layers each fulfilling a different role (nucleation layer, window layer, contact layer, TCO) and that significant J_{sc}-V_{oc}*FF trade-offs are presented for minor thickness variations of each of the layers. Additionally, it is demonstrated that optimal conditions, in terms of device performance, for i-nc-Si:H are found near the nanocrystalline-to-amorphous transition regime (crystallinity$\approx$60%). This regime is very sensitive to minor variations in processing conditions. Finally, using the collective findings presented in this dissertation, the flexible application of earth abundant and chemically inert silicon and silicon-germanium alloys is demonstrated in a large number of 2-terminal monolithically integrated multijunction devices. Two distinct device architectures, on different substrate morphologies, are used for these multijunction devices, combining up to 4 different junctions, yielding a V_{oc}-range of 0.5V to 2.8V. This range of V_{oc}s demonstrates the potential of all-silicon multijunction devices for facilitating a range of prospective electrochemical reduction reactions and electrocatalysts in autonomous and wireless PEC devices.

In **Chapter 10** the design, optimization and processing of electrocatalytically active contacts and micropores through the PV device, steps required for converting a multi-junction PV device into a PEC device, are investigated. It is shown that the influence of micropore size and distribution on PV and EC performance is opposite in trend and that current density losses can be limited to less than 20% for a range of pore diameter-period combinations. Using deep reactive ion etching, for which much better resolution, reproducibility and taper are demonstrated compared to pulsed laser drilling, micropores with a diameter of 20μm were successfully processed with a taper $<2\%$. Finally, the successful processing of Pt microdots with a 2μm diameter and 5% surface coverage is demonstrated.

11.1 Outlook

Based on the collective results presented in this dissertation some recommendations can be made for future research. The experiments performed in part 1 are completed to satisfaction, so no further research is recommended there.

For part 2, two recommendations are made. The first is related to the further development of the Ge(C)Sn:H films for PV applications. In this dissertation only the first steps towards the processing of such an alloy were made. Particularly the use of a different Sn-precursor, such as SnD_4, is recommend, potentially with the addition of a separate CH_4 precursor such that both flows can be controlled independently. Additionally, the integration of a/nc-Ge(CSn):H films in photovoltaic devices is recommended to evaluate the PV potential of the low bandgap alloys.

For part 3, the recommendations are related to the processing of the stand-alone, wireless all-silicon photo-electrochemical device described in chapters 9 and 10. In Part III all the pieces are presented to develop a demonstrator. To achieve this, the micropore and microdot processing performed in chapter 10 should be applied to PV devices (rather than on bare silicon wafers) and a proton exchange material should be used to fill the micropores. If additionally the improvements described in chapter 8.2 to achieve a SHJ/nc-Si:H/a-Si:H 3J device with $\eta \approx 18\%$ are realized, a solar-to-hydrogen conversion efficiency of $\approx 11.6\%$ can be achieved, which would be a strong improvement over the current record of $\approx 7\%$ [34].

Bibliography

[1] United Nations Foundation, *Sustainable Development Goals*.

[2] World Bank Group, *Fertility rate, total (births per woman) — Data*.

[3] M. Ram, D. Bogdanov, A. Aghahosseini, A. Oyewo, A. Gulagi, M. Child, H. Fell, and C. Breyer, "Global energy system based on 100% renewable energy - power sector," Lappeenranta University of Technology and Energy Watch Group, Lappeenranta, Berlin, Tech. Rep., 2017.

[4] S. Teske, S. Sawyer, and O. Schafer, "Energy [r]evolution, 5th Edition 2015 world energy scenario," Greenpeace International, Global Wind Energy Council, SolarPowerEurope, Tech. Rep., 2015.

[5] K. Loffler, K. Hainsch, T. Burandt, P. Oei, C. Kemfert, and C. von Hirschhausen, "Designing a Global Energy System Based on 100% Rwables for 2050: GENeSYS-MOD: An Application of the Open-Source Energy Modelling System (OSeMOSYS)," *SSRN Electronic Journal*, 2017. DOI: 10.2139/ssrn.3028519.

[6] Bloomberg NEF, "New Energy Outlook 2022," Tech. Rep., 2020.

[7] International Energy Agency, "World Energy Outlook 2020," Tech. Rep., 2020.

[8] BP, "Statistical Review of World Energy 2020," p. 66, 2020.

[9] C. Breyer, D. Bogdanov, A. Gulagi, A. Aghahosseini, L. S. Barbosa, O. Koskinen, M. Barasa, U. Caldera, S. Afanasyeva, M. Child, J. Farfan, and P. Vainikka, "On the role of solar photovoltaics in global energy transition scenarios," *Progress in Photovoltaics: Research and Applications*, vol. 25, no. 8, pp. 727–745, 2017. DOI: 10.1002/pip.2885.

[10] S. P. Philipps, C. Kost, and T. Schlegl, "Up-To-Date Levelized Cost of Electricity of Photovoltaics.," Fraunhofer ISE, Tech. Rep., 2014.

[11] M. Victoria, N. Haegel, I. M. Peters, R. Sinton, A. Jäger-Waldau, C. del Cañizo, C. Breyer, M. Stocks, A. Blakers, I. Kaizuka, K. Komoto, and A. Smets, "Solar photovoltaics is ready to power a sustainable future," *Joule*, pp. 1–16, 2021. DOI: 10.1016/j.joule.2021.03.005.

[12] IRENA, *Electricity storage and renewables: Costs and markets to 2030*. 2017.

[13] J. Carlsson, "ETRI 2014 Energy Technology Reference Indicator projections for 2010-2050," European Commission, Joint Research Centre, Institute for Energy and Transport, Tech. Rep., 2014. DOI: 10.2790/057687.

[14] O. Schmidt, A. Hawkes, A. Gambhir, and I. Staffell, "The future cost of electrical energy storage based on experience rates," *Nature Energy*, vol. 2, no. 8, p. 17 110, 2017. DOI: 10.1038/nenergy.2017.110.

[15] Battery University, *Elevating Self-discharge*.

[16] P. Greim, A. A. Solomon, and C. Breyer, "Assessment of lithium criticality in the global energy transition and addressing policy gaps in transportation," *Nature Communications*, vol. 11, no. 1, p. 4570, 2020. DOI: 10.1038/s41467-020-18402-y.

[17] International Energy Agency (IEA), "The Role of Critical Minerals in Clean Energy Transitions," *IEA Publications*, 2021.

[18] Shell, "Meeting the goals of the Paris agreement (Sky scenario)," Tech. Rep., 2018, p. 72.

[19] R. R. Ikreedeegh and M. Tahir, "A critical review in recent developments of metal-organic-frameworks (MOFs) with band engineering alteration for photocatalytic CO_2 reduction to solar fuels," *Journal of CO_2 Utilization*, vol. 43, p. 101 381, 2021. DOI: 10.1016/j.jcou.2020.101381.

[20] I. I. Alkhatib, C. Garlisi, M. Pagliaro, K. Al-Ali, and G. Palmisano, "Metal-organic frameworks for photocatalytic CO_2 reduction under visible radiation: A review of strategies and applications," *Catalysis Today*, vol. 340, pp. 209–224, 2020. DOI: 10.1016/j.cattod.2018.09.032.

[21]   D. Ješić, D. Lašič Jurković, A. Pohar, L. Suhadolnik, and B. Likozar, "Engineering photocatalytic and photoelectrocatalytic CO_2 reduction reactions: Mechanisms, intrinsic kinetics, mass transfer resistances, reactors and multi-scale modelling simulations," *Chemical Engineering Journal*, vol. 407, p. 126 799, 2021. DOI: 10.1016/j.cej.2020.126799.

[22]   S. Fukuzumi, "Production of Liquid Solar Fuels and Their Use in Fuel Cells," *Joule*, vol. 1, no. 4, pp. 689–738, 2017. DOI: 10.1016/j.joule.2017.07.007.

[23]   B. Metz, O. Davidson, H. de Coninck, M. Loos, and L. Meyer, "Carbon dioxide capture and storage," IPCC, Tech. Rep., 2005. DOI: 10.1002/9783527818488.ch15.

[24]   International Energy Agency, *The Role of CO_2 Storage*, 2019.

[25]   P. Perez Rodriguez, "Photovoltaic-(photo)electrochemical devices for water splitting and water treatment," Ph.D. dissertation, Delft University of Technology, 2018. DOI: 10.4233/uuid.

[26]   W. J. Chang, K.-H. Lee, H. Ha, K. Jin, G. Kim, S.-T. Hwang, H.-m. Lee, S.-W. Ahn, W. Yoon, H. Seo, J. S. Hong, Y. K. Go, J.-I. Ha, and K. T. Nam, "Design Principle and Loss Engineering for Photovoltaic–Electrolysis Cell System," *ACS Omega*, vol. 2, no. 3, pp. 1009–1018, 2017. DOI: 10.1021/acsomega.7b00012.

[27]   C. Xiang, K. M. Papadantonakis, and N. S. Lewis, "Principles and implementations of electrolysis systems for water splitting," *Materials Horizons*, vol. 3, no. 3, pp. 169–173, 2016. DOI: 10.1039/C6MH00016A.

[28]   X. Li, L. Zhao, J. Yu, X. Liu, X. Zhang, H. Liu, and W. Zhou, "Water Splitting: From Electrode to Green Energy System," *Nano-Micro Letters*, vol. 12, no. 1, p. 131, 2020. DOI: 10.1007/s40820-020-00469-3.

[29]   P. Perez-Rodriguez, W. Vijselaar, J. Huskens, M. Stam, M. Falkenberg, M. Zeman, W. Smith, and A. H. Smets, "Designing a hybrid thin-film/wafer silicon triple photovoltaic junction for solar water splitting," *Progress in Photovoltaics: Research and Applications*, vol. 27, no. 3, pp. 245–254, 2019. DOI: 10.1002/pip.3085.

[30]   S. Kirner, H. Sarajan, A. Azarpira, T. Schedel-Niedrig, B. Stannowski, B. Rech, and R. Schlatmann, "Wafer Surface Tuning for a-Si:H/μc-Si:H/c-Si Triple Junction Solar Cells for Application in Water Splitting," *Energy Procedia*, vol. 102, pp. 126–135, 2016. DOI: 10.1016/j.egypro.2016.11.327.

[31]   W. A. Turner, S. J. Jones, D. Pang, B. F. Bateman, J. H. Chen, Y.-M. Li, F. C. Marques, A. E. Wetsel, P. Wickboldt, W. Paul, J. Bodart, R. E. Norberg, I. El Zawawi, and M. L. Theye, "Structural, optical, and electrical characterization of improved amorphous hydrogenated germanium," *Journal of Applied Physics*, vol. 67, no. 12, pp. 7430–7438, 1990. DOI: 10.1063/1.344533.

[32]   W. Paul, "Structural, Optical and photoelectronic properties of improved PECVD a-Ge:H," *Journal of Non-Crystalline Solids*, vol. 137&138, pp. 803–808, 1991.

[33]   M. Moreno, N. Delgadillo, A. Torres, R. Ambrosio, P. Rosales, A. Kosarev, C. Reyes-Betanzo, J. de la Hidalga-Wade, C. Zuniga, and W. Calleja, "Boron doping compensation of hydrogenated amorphous and polymorphous germanium thin films for infrared detection applications," *Thin Solid Films*, vol. 548, pp. 533–538, 2013. DOI: 10.1016/j.tsf.2013.08.102.

[34]   W. J. C. Vijselaar, P. Perez-Rodriguez, P. J. Westerik, R. M. Tiggelaar, A. H. M. Smets, H. Gardeniers, and J. Huskens, "A Stand-Alone Si-Based Porous Photoelectrochemical Cell," *Advanced Energy Materials*, vol. 9, no. 19, p. 1 803 548, 2019. DOI: 10.1002/aenm.201803548.

[35]   C. Trompoukis, A. Abass, J.-W. Schüttauf, T. Bosserez, J. Rongé, J. Lauwaert, J. A. Martens, and R. Baets, "Porous multi-junction thin-film silicon solar cells for scalable solar water splitting," *Solar Energy Materials and Solar Cells*, vol. 182, pp. 196–203, 2018. DOI: 10.1016/j.solmat.2018.03.041.

[36]   P. Cuony, D. T. L. Alexander, I. Perez-Wurfl, M. Despeisse, G. Bugnon, M. Boccard, T. Söderström, A. Hessler-Wyser, C. Hébert, and C. Ballif, "Silicon Filaments in Silicon Oxide for Next-Generation Photovoltaics," *Advanced Materials*, vol. 24, no. 9, pp. 1182–1186, 2012. DOI: 10.1002/adma.201104578.

[37] K. Ding, U. Aeberhard, F. Finger, and U. Rau, "Silicon heterojunction solar cell with amorphous silicon oxide buffer and microcrystalline silicon oxide contact layers," vol. 195, no. 5, pp. 193–195, 2012. DOI: 10.1002/pssr.201206030.

[38] V. Smirnov, W. Böttler, A. Lambertz, H. Wang, R. Carius, and F. Finger, "Microcrystalline silicon n-i-p solar cells prepared with microcrystalline silicon oxide (μc-SiO$_x$:H) n-layer," *physica status solidi (c)*, vol. 1056, no. 3, NA–NA, 2010. DOI: 10.1002/pssc.200982830.

[39] P. Delli Veneri, L. V. Mercaldo, and I. Usatii, "Silicon oxide based n-doped layer for improved performance of thin film silicon solar cells," *Applied Physics Letters*, vol. 97, no. 2, p. 023 512, 2010. DOI: 10.1063/1.3463457.

[40] L. V. Mercaldo, P. Delli Veneri, I. Usatii, E. M. Esposito, and G. Nicotra, "Properties of mixed phase n-doped silicon oxide layers and application in micromorph solar cells," *Solar Energy Materials and Solar Cells*, vol. 119, pp. 67–72, 2013. DOI: 10.1016/j.solmat.2013.05.030.

[41] K. Schwanitz, S. Klein, T. Stolley, M. Rohde, D. Severin, and R. Trassl, "Solar Energy Materials & Solar Cells Anti-reflective microcrystalline silicon oxide p-layer for thin-film silicon solar cells on ZnO," *Solar Energy Materials and Solar Cells*, vol. 105, pp. 187–191, 2012. DOI: 10.1016/j.solmat.2012.06.003.

[42] J. H. Shim, S.-w. Ahn, and H.-m. Lee, "Microcrystalline silicon oxide (μc-SiO:H) alloys as a contact layer for highly efficient Si thin film solar cell," *Current Applied Physics*, vol. 13, no. 7, pp. 1401–1403, 2013. DOI: 10.1016/j.cap.2013.04.014.

[43] R. Biron, C. Pahud, F.-j. Haug, and C. Ballif, "Origin of the V_{oc} enhancement with a p-doped nc-SiO$_x$:H window layer in n-i-p solar cells," *Journal of Non-Crystalline Solids*, vol. 358, no. 17, pp. 1958–1961, 2012. DOI: 10.1016/j.jnoncrysol.2012.01.058.

[44] T. Grundler, A. Lambertz, and F. Finger, "pss," no. 3, pp. 1085–1088, 2010. DOI: 10.1002/pssc.200982872.

[45] M. Despeisse, C. Battaglia, M. Boccard, G. Bugnon, M. Charrière, P. Cuony, S. Hänni, L. Löfgren, F. Meillaud, G. Parascandolo, T. Söderström, and C. Ballif, "Optimization of thin film silicon solar cells on highly textured substrates," *physica status solidi (a)*, vol. 208, no. 8, pp. 1863–1868, 2011. DOI: 10.1002/pssa.201026745.

[46] P. Buehlmann, J. Bailat, D. Dominé, A. Billet, F. Meillaud, A. Feltrin, and C. Ballif, "In situ silicon oxide based intermediate reflector for thin-film silicon micromorph solar cells," *Applied Physics Letters*, vol. 91, no. 14, p. 143 505, 2007. DOI: 10.1063/1.2794423.

[47] S.-t. Hwang, D. J. You, S. H. Kim, S. Lee, and H.-m. Lee, "Large area Si thin film solar module applying n-μc-SiO$_x$:H intermediate layer with low refractive index," *Solar Energy Materials and Solar Cells*, vol. 113, pp. 79–84, 2013. DOI: 10.1016/j.solmat.2013.01.042.

[48] M. Boccard, M. Despeisse, J. Escarre, X. Niquille, G. Bugnon, S. Hanni, M. Bonnet-Eymard, F. Meillaud, and C. Ballif, "High-Stable-Efficiency Tandem Thin-Film Silicon Solar Cell With Low-Refractive-Index Silicon-Oxide Interlayer," *IEEE Journal of Photovoltaics*, vol. 4, no. 6, pp. 1368–1373, 2014. DOI: 10.1109/JPHOTOV.2014.2357495.

[49] H. Tan, P. Babal, M. Zeman, and A. H. Smets, "Wide bandgap p-type nanocrystalline silicon oxide as window layer for high performance thin-film silicon multi-junction solar cells," *Solar Energy Materials and Solar Cells*, vol. 132, pp. 597–605, 2015. DOI: 10.1016/j.solmat.2014.10.020.

[50] A. Lambertz, T. Grundler, and F. Finger, "Hydrogenated amorphous silicon oxide containing a microcrystalline silicon phase and usage as an intermediate reflector in thin-film silicon solar cells," *Journal of Applied Physics*, vol. 109, no. 11, p. 113 109, 2011. DOI: 10.1063/1.3592208.

[51] S. Kirner, S. Calnan, O. Gabriel, S. Neubert, M. Zelt, B. Stannowski, B. Rech, and R. Schlatmann, "An improved silicon-oxide-based intermediate-reflector for micromorph solar cells," *physica status solidi (c)*, vol. 9, no. 10-11, pp. 2145–2148, 2012. DOI: 10.1002/pssc.201200243.

[52] S. Y. Myong and L. S. Jeon, "Improved light trapping in thin-film silicon solar cells via alternated n-type silicon oxide reflectors," *Solar Energy Materials and Solar Cells*, vol. 119, pp. 77–83, 2013. DOI: 10.1016/j.solmat.2013.05.033.

[53] S. Kim, H. Lee, J.-w. Chung, S.-w. Ahn, and H.-m. Lee, "n-Type microcrystalline silicon oxide layer and its application to high-performance back reflectors in thin-film silicon solar cells," *Current Applied Physics*, vol. 13, no. 4, pp. 743–747, 2013. DOI: 10.1016/j.cap.2012.11.017.

[54] H. Tan, E. Moulin, F. T. Si, J.-W. Schüttauf, M. Stuckelberger, O. Isabella, F.-J. Haug, C. Ballif, M. Zeman, and A. H. M. Smets, "Highly transparent modulated surface textured front electrodes for high-efficiency multijunction thin-film silicon solar cells," *Progress in Photovoltaics: Research and Applications*, vol. 23, no. 8, pp. 949–963, 2015. DOI: 10.1002/pip.2639.

[55] F. T. Si, O. Isabella, H. Tan, and M. Zeman, "Quadruple-Junction Thin-Film Silicon Solar Cells Using Four Different Absorber Materials," *Solar RRL*, vol. 1, no. 3-4, p. 1 700 036, 2017. DOI: 10.1002/solr.201700036.

[56] R. Vasudevan, Z. Thanawala, L. Han, T. Buijs, H. Tan, D. Deligiannis, P. Perez-Rodriguez, I. A. Digdaya, W. A. Smith, M. Zeman, and A. H. Smets, "A thin-film silicon/silicon hetero-junction hybrid solar cell for photoelectrochemical water-reduction applications," *Solar Energy Materials and Solar Cells*, vol. 150, pp. 82–87, 2016. DOI: 10.1016/j.solmat.2016.02.006.

[57] M. Boccard, P. Cuony, M. Despeisse, D. Dominé, A. Feltrin, N. Wyrsch, and C. Ballif, "Substrate dependent stability and interplay between optical and electrical properties in μc-Si:H single junction solar cells," *Solar Energy Materials and Solar Cells*, vol. 95, no. 1, pp. 195–198, 2011. DOI: 10.1016/j.solmat.2010.04.043.

[58] V. Smirnov, A. Lambertz, B. Grootoonk, R. Carius, and F. Finger, "Microcrystalline silicon oxide (μc-SiO$_x$:H) alloys: A versatile material for application in thin film silicon single and tandem junction solar cells," *Journal of Non-Crystalline Solids*, vol. 358, no. 17, pp. 1954–1957, 2012. DOI: 10.1016/j.jnoncrysol.2011.12.019.

[59] P. Babal, H. Lopez, L. Xie, B. van Veen, M. van Sebille, H. Tan, M. Zeman, and A. Smets, "Nanostructure Analysis of P-Doped Nanocrystalline Silicon Oxide," *28th European Photovoltaic Solar Energy Conference and Exhibition*,

[60] A. Richter, L. Zhao, F. Finger, and K. Ding, "Nano-composite microstructure model for the classification of hydrogenated nanocrystalline silicon oxide thin films," *Surface and Coatings Technology*, vol. 295, pp. 119–124, 2016. DOI: 10.1016/j.surfcoat.2015.09.016.

[61] V. Smirnov, A. Lambertz, S. Moll, M. Bär, D. E. Starr, R. G. Wilks, M. Gorgoi, A. Heidt, M. Luysberg, B. Holländer, and F. Finger, "Doped microcrystalline silicon oxide alloys for silicon-based photovoltaics: Optoelectronic properties, chemical composition, and structure studied by advanced characterization techniques," *physica status solidi (a)*, vol. 213, no. 7, pp. 1814–1820, 2016. DOI: 10.1002/pssa.201533022.

[62] M. Python, E. Vallat-Sauvain, J. Bailat, D. Dominé, L. Fesquet, A. Shah, and C. Ballif, "Relation between substrate surface morphology and microcrystalline silicon solar cell performance," *Journal of Non-Crystalline Solids*, vol. 354, no. 19-25, pp. 2258–2262, 2008. DOI: 10.1016/j.jnoncrysol.2007.09.084.

[63] H. Sai, K. Saito, N. Hozuki, and M. Kondo, "Relationship between the cell thickness and the optimum period of textured back reflectors in thin-film microcrystalline silicon solar cells," *Applied Physics Letters*, vol. 102, no. 5, p. 053 509, 2013. DOI: 10.1063/1.4790642.

[64] H. Sai, T. Koida, T. Matsui, I. Yoshida, K. Saito, and M. Kondo, "Microcrystalline Silicon Solar Cells with 10.5% Efficiency Realized by Improved Photon Absorption via Periodic Textures and Highly Transparent Conductive Oxide," *Applied Physics Express*, vol. 6, no. 10, p. 104 101, 2013. DOI: 10.7567/APEX.6.104101.

[65] A. H. M. Smets, W. M. M. Kessels, and M. C. M. van de Sanden, "Vacancies and voids in hydrogenated amorphous silicon," *Applied Physics Letters*, vol. 82, no. 10, pp. 1547–1549, 2003. DOI: 10.1063/1.1559657.

[66] ——, "Surface-diffusion-controlled incorporation of nanosized voids during hydrogenated amorphous silicon film growth," *Applied Physics Letters*, vol. 86, no. 4, p. 041 909, 2005. DOI: 10.1063/1.1853508.

[67] A. H. M. Smets and M. C. M. van de Sanden, "Relation of the Si-H stretching frequency to the nanostructural Si-H bulk environment," *Physical Review B*, vol. 76, no. 7, p. 073 202, 2007. DOI: 10.1103/PhysRevB.76.073202.

[68]   A. H. M. Smets, W. M. M. Kessels, and M. C. M. van de Sanden, "The effect of ion-surface and ion-bulk interactions during hydrogenated amorphous silicon deposition," *Journal of Applied Physics*, vol. 102, no. 7, p. 073 523, 2007. DOI: 10.1063/1.2786873.

[69]   A. H. M. Smets, T. Matsui, and M. Kondo, "High-rate deposition of microcrystalline silicon p-i-n solar cells in the high pressure depletion regime," *Journal of Applied Physics*, vol. 104, no. 3, p. 034 508, 2008. DOI: 10.1063/1.2961334.

[70]   A. H. M. Smets, M. A. Wank, B. Vet, M. Fischer, R. A. C. M. M. van Swaaij, M. Zeman, D. C. Bobela, C. R. Wronski, and M. C. M. van de Sanden, "The relation between the band gap and the anisotropic nature of hydrogenated amorphous silicon," in *2011 37th IEEE Photovoltaic Specialists Conference*, IEEE, 2011, pp. 003 342–003 342. DOI: 10.1109/PVSC.2011.6186662.

[71]   A. H. M. Smets, M. A. Wank, B. Vet, M. Fischer, R. A. C. M. M. van Swaaij, M. Zeman, D. C. Bobela, C. R. Wronski, and R. M. C. M. van de Sanden, "The Relation Between the Bandgap and the Anisotropic Nature of Hydrogenated Amorphous Silicon," *IEEE Journal of Photovoltaics*, vol. 2, no. 2, pp. 94–98, 2012. DOI: 10.1109/JPHOTOV.2011.2180701.

[72]   H. Tan, E. Psomadaki, O. Isabella, M. Fischer, P. Babal, R. Vasudevan, M. Zeman, and A. H. M. Smets, "Micro-textures for efficient light trapping and improved electrical performance in thin-film nanocrystalline silicon solar cells," *Applied Physics Letters*, vol. 103, no. 17, p. 173 905, 2013. DOI: 10.1063/1.4826639.

[73]   M. Fischer, H. Tan, J. Melskens, R. Vasudevan, M. Zeman, and A. H. M. Smets, "High pressure processing of hydrogenated amorphous silicon solar cells: Relation between nanostructure and high open-circuit voltage," *Applied Physics Letters*, vol. 106, no. 4, p. 043 905, 2015. DOI: 10.1063/1.4907316.

[74]   A. Bronneberg, M. v. de Sanden, and M. Creatore, "Remote plasma deposition of microcrystalline silicon thin-films: Film structure and the role of atomic hydrogen," *Journal of Non-Crystalline Solids*, vol. 358, no. 2, pp. 379–386, 2012. DOI: 10.1016/j.jnoncrysol.2011.10.005.

[75]   A. Blanker, P. Berendsen, N. Phung, Z. Vroon, M. Zeman, and A. Smets, "Advanced light management techniques for two-terminal hybrid tandem solar cells," *Solar Energy Materials and Solar Cells*, vol. 181, pp. 77–82, 2018. DOI: 10.1016/j.solmat.2018.02.017.

[76]   D. Y. Kim, E. Guijt, R. A. C. M. M. van Swaaij, and M. Zeman, "Development of a-SiO$_x$:H solar cells with very high V$_{oc}$×FF product," *Progress in Photovoltaics: Research and Applications*, vol. 23, no. 6, pp. 671–684, 2015. DOI: 10.1002/pip.2581.

[77]   P. Sichanugrist, T. Sasaki, A. Asano, Y. Ichikawa, and H. Sakai, "Amorphous silicon oxide and its application to metal / n-i-p / ITO type a-Si solar cells," *Solar Energy Materials and Solar Cells*, vol. 34, pp. 415–422, 1994.

[78]   M. Niwano, J.-i. Kageyama, K. Kurita, K. Kinashi, I. Takahashi, and N. Miyamoto, "Infrared spectroscopy study of initial stages of oxidation of hydrogen-terminated Si surfaces stored in air," *Journal of Applied Physics*, vol. 76, no. 4, pp. 2157–2163, 1994. DOI: 10.1063/1.357627.

[79]   A. Bronneberg, A. Smets, M. Creatore, and M. van de Sanden, "On the oxidation mechanism of microcrystalline silicon thin films studied by Fourier transform infrared spectroscopy," *Journal of Non-Crystalline Solids*, vol. 357, no. 3, pp. 884–887, 2011. DOI: 10.1016/j.jnoncrysol.2010.11.001.

[80]   T. Matsui and M. Kondo, "High-Efficiency Microcrystalline Silicon and Microcrystalline Silicon-Germanium Alloy Solar Cells," *MRS Proceedings*, vol. 1321, no. 5, pp. 11–1321, 2011. DOI: 10.1557/opl.2011.1149.

[81]   M. Izzi, M. Tucci, L. Serenelli, P. Mangiapane, M. Della Noce, I. Usatii, E. Esposito, L. V. Mercaldo, and P. Delli Veneri, "Doped SiO$_x$ emitter layer in amorphous/crystalline silicon heterojunction solar cell," *Applied Physics A*, vol. 115, no. 2, pp. 705–712, 2014. DOI: 10.1007/s00339-013-7858-1.

[82]   S. Rattanapan, T. Watahiki, S. Miyajima, and M. Konagai, "Improvement of Rear Surface Passivation Quality in p-Type Silicon Heterojunction Solar Cells Using Boron-Doped Microcrystalline Silicon Oxide," *Japanese Journal of Applied Physics*, vol. 50, no. 8, p. 082 301, 2011. DOI: 10.1143/JJAP.50.082301.

[83]   J. Cashmore, M. Apolloni, A. Braga, O. Caglar, V. Cervetto, Y. Fenner, S. Goldbach-Aschemann, C. Goury, J. Hötzel, T. Iwahashi, J. Kalas, M. Kitamura, M. Klindworth, M. Kupich, G.-F. Leu, J. Lin, M.-H. Lindic, P. Losio, T. Mates, D. Matsunaga, B. Mereu, X.-V. Nguyen, I. Psimoulis, S. Ristau, T. Roschek, A. Salabas, E. Salabas, and I. Sinicco, "Improved conversion efficiencies of thin-film silicon tandem (MICROMORPH™) photovoltaic modules," *Solar Energy Materials and Solar Cells*, vol. 144, pp. 84–95, 2016. DOI: 10.1016/j.solmat.2015.08.022.

[84]   F. Hou, C. Han, O. Isabella, L. Yan, B. Shi, J. Chen, S. An, Z. Zhou, W. Huang, H. Ren, Q. Huang, G. Hou, X. Chen, Y. Li, Y. Ding, G. Wang, C. Wei, D. Zhang, M. Zeman, Y. Zhao, and X. Zhang, "Inverted pyramidally-textured PDMS antireflective foils for perovskite/silicon tandem solar cells with flat top cell," *Nano Energy*, vol. 56, pp. 234–240, 2019. DOI: 10.1016/j.nanoen.2018.11.018.

[85]   T. de Vrijer, F. T. Si, H. Tan, and A. H. Smets, "Chemical stability and performance of doped silicon oxide layers for use in thin film silicon solar cells," *IEEE Journal of Photovoltaics*, vol. 9, no. 1, pp. 3–11, 2019. DOI: 10.1109/PVSC.2018.8548192.

[86]   P. Babál, "Doped nanocrystalline silicon oxide for use as (intermediate) reflecting layers in thin film silicon solar cells," Ph.D. dissertation, TU Delft, 2014.

[87]   C. M. Herzinger, B. Johs, W. A. McGahan, J. A. Woollam, and W. Paulson, "Ellipsometric determination of optical constants for silicon and thermally grown silicon dioxide via a multi-sample, multi-wavelength, multi-angle investigation," *Journal of Applied Physics*, vol. 83, no. 6, pp. 3323–3336, 1998. DOI: 10.1063/1.367101.

[88]   H. Tan, P. Babal, M. Zeman, and A. H. M. Smets, "Solar Energy Materials & Solar Cells Wide bandgap p-type nanocrystalline silicon oxide as window layer for high performance thin-film silicon multi-junction solar cells," *Solar Energy Materials and Solar Cells*, vol. 132, pp. 597–605, 2015. DOI: 10.1016/j.solmat.2014.10.020.

[89]   D. M. Zhigunov, G. N. Kamaev, P. K. Kashkarov, and V. A. Volodin, "On Raman scattering cross section ratio of crystalline and microcrystalline to amorphous silicon," *Applied Physics Letters*, vol. 113, no. 2, p. 023 101, 2018. DOI: 10.1063/1.5037008.

[90]   C. Smit, R. A. C. M. M. van Swaaij, H. Donker, A. M. H. N. Petit, W. M. M. Kessels, and M. C. M. van de Sanden, "Determining the material structure of microcrystalline silicon from Raman spectra," *Journal of Applied Physics*, vol. 94, no. 5, pp. 3582–3588, 2003. DOI: 10.1063/1.1596364.

[91]   P. Cuony, M. Marending, D. T. L. Alexander, M. Boccard, G. Bugnon, M. Despeisse, and C. Ballif, "Mixed-phase p-type silicon oxide containing silicon nanocrystals and its role in thin-film silicon solar cells," *Applied Physics Letters*, vol. 97, no. 21, p. 213 502, 2010. DOI: 10.1063/1.3517492.

[92]   C. Song, X. Wang, R. Huang, J. Song, and Y. Guo, "Effects of doping concentration on the microstructural and optoelectrical properties of boron doped amorphous and nanocrystalline silicon films," *Materials Chemistry and Physics*, vol. 142, no. 1, pp. 292–296, 2013. DOI: 10.1016/j.matchemphys.2013.07.017.

[93]   S. Kirner, O. Gabriel, B. Stannowski, B. Rech, and R. Schlatmann, "The growth of microcrystalline silicon oxide thin films studied by in situ plasma diagnostics," *Applied Physics Letters*, vol. 102, no. 5, p. 051 906, 2013. DOI: 10.1063/1.4790279.

[94]   O. Gabriel, S. Kirner, M. Klingsporn, F. Friedrich, B. Stannowski, and R. Schlatmann, "On the Plasma Chemistry During Plasma Enhanced Chemical Vapor Deposition of Microcrystalline Silicon Oxides," *Plasma Processes and Polymers*, vol. 12, no. 1, pp. 82–91, 2015. DOI: 10.1002/ppap.201400114.

[95]   S. Bishop and S. Carlos, "Studies of Hydrogenated Amorphous Silicon," Naval Research Laboratory, Solar Energy Research Institute, Colorado, Tech. Rep., 1984.

[96]   M. de Lima and F. Marques, "On the doping mechanism of boron-doped hydrogenated amorphous silicon deposited by rf-co-sputtering," *Journal of Non-Crystalline Solids*, vol. 299-302, no. PART 1, pp. 605–609, 2002. DOI: 10.1016/S0022-3093(01)01205-4.

[97]   D. Caputo, G. de Cesare, F. Irrera, A. Nascetti, and F. Palma, "On the relation between defect density and dopant concentration in amorphous silicon films," *Journal of Non-Crystalline Solids*, vol. 266-269, pp. 565–568, 2000. DOI: 10.1016/S0022-3093(99)00846-7.

[98] W. B. Jackson and N. M. Amer, "Direct measurement of gap-state absorption in hydrogenated amorphous silicon by photothermal deflection spectroscopy," *Physical Review B*, vol. 25, no. 8, pp. 5559–5562, 1982. DOI: 10.1103/PhysRevB.25.5559.

[99] R. Guerra and S. Ossicini, "Preferential Positioning of Dopants and Co-Dopants in Embedded and Freestanding Si Nanocrystals," *Journal of the American Chemical Society*, vol. 136, no. 11, pp. 4404–4409, 2014. DOI: 10.1021/ja5002357.

[100] S. H. Hong, Y. S. Kim, W. Lee, Y. H. Kim, J. Y. Song, J. S. Jang, J. H. Park, S.-H. Choi, and K. J. Kim, "Active doping of B in silicon nanostructures and development of a Si quantum dot solar cell," *Nanotechnology*, vol. 22, no. 42, p. 425 203, 2011. DOI: 10.1088/0957-4484/22/42/425203.

[101] J. Westra, "Solid phase crystallisation of hydrogenated amorphous silicon deposited by ETPCVD on glass," Ph.D. dissertation, 2018, p. 289. DOI: 10.4233/uuid:6b40384c-c139-4b7a-8080-fe883aa95628.

[102] S. Ray, P. Chaudhuri, A. Batabyal, and A. Barua, "Electronic and optical properties of boron doped hydrogenated amorphous silicon thin films," *Solar Energy Materials*, vol. 10, pp. 335–347, 1984.

[103] D. B. Saint John, H.-B. Shin, M.-Y. Lee, S. K. Ajmera, A. J. Syllaios, E. C. Dickey, T. N. Jackson, and N. J. Podraza, "Influence of microstructure and composition on hydrogenated silicon thin film properties for uncooled microbolometer applications," *Journal of Applied Physics*, vol. 110, no. 3, p. 033 714, 2011. DOI: 10.1063/1.3610422.

[104] H. Fujiwara and M. Kondo, "Real-time monitoring and process control in amorphouscrystalline silicon heterojunction solar cells by spectroscopic ellipsometry and infrared spectroscopy," *Applied Physics Letters*, vol. 86, no. 3, p. 032 112, 2005. DOI: 10.1063/1.1850612.

[105] J. Perrin, Y. Takeda, N. Hirano, Y. Takeuchi, and A. Matsuda, "Sticking And Recombination Of The SiH$_3$, Radical On Hydrogenated Amorphous Silicon: The Catalytic Effect Of Diborane," *Surface Science*, vol. 210, pp. 114–128, 1989.

[106] I. M. Pepperberg, T. A. Halgren, and W. N. Lipscomb, "Extended topological rules for boron hydrides. 1. Structures and relative energies for the transient boron hydrides diborane(4), triborane(7), triborane(9), tetraborane(8), and tetraborane(12)," *Inorganic Chemistry*, vol. 16, no. 2, pp. 363–379, 1977. DOI: 10.1021/ic50168a028.

[107] A. Morimoto, M. Matsumoto, M. Yoshita, M. Kumeda, and T. Shimizu, "Doping effect of oxygen or nitrogen impurity in hydrogenated amorphous silicon films," *Applied Physics Letters*, vol. 59, no. 17, pp. 2130–2132, 1991. DOI: 10.1063/1.106102.

[108] K. Jiranapakul, K. Shirakawa, and J. Shirafuji, "Photoelectric Properties of Oxygen-Doped a-Si:H Prepared by rf Sputtering," *Japanese Journal of Applied Physics*, vol. 25, no. Part 1, No. 10, pp. 1457–1464, 1986. DOI: 10.1143/JJAP.25.1457.

[109] M. Klingsporn, S. Kirner, C. Villringer, D. Abou-Ras, I. Costina, M. Lehmann, and B. Stannowski, "Resolving the nanostructure of plasma-enhanced chemical vapor deposited nanocrystalline SiO$_x$ layers for application in solar cells," *Journal of Applied Physics*, vol. 119, no. 22, p. 223 104, 2016. DOI: 10.1063/1.4953566.

[110] Z. P. Wang, H. X. Han, X. S. Zhao, and G. H. Li, "Si-Cl Bonds In A-Si:H:Cl Films," *Solid State Communications*, vol. 58, no. 10, pp. 709–711, 1986.

[111] K. Kawamura, S. Ishizuka, H. Sakaue, and Y. Horiike, "Diagnostics of Hydrogen Role in the Si Surface Reaction Processes Employing In-situ Fourier Transform Infrared-Attenuated Total Reflection," *Japanese Journal of Applied Physics*, vol. 30, no. Part 1, No. 11B, pp. 3215–3218, 1991. DOI: 10.1143/JJAP.30.3215.

[112] M. Mews, T. F. Schulze, N. Mingirulli, and L. Korte, "Hydrogen plasma treatments for passivation of amorphous-crystalline silicon-heterojunctions on surfaces promoting epitaxy," *Applied Physics Letters*, vol. 102, no. 12, p. 122 106, 2013. DOI: 10.1063/1.4798292.

[113] M. A. Wank, R. A. C. M. M. van Swaaij, P. Kudlacek, M. C. M. van de Sanden, and M. Zeman, "Hydrogenated amorphous silicon deposited under accurately controlled ion bombardment using pulse-shaped substrate biasing," *Journal of Applied Physics*, vol. 108, no. 10, p. 103 304, 2010. DOI: 10.1063/1.3505794.

[114] G. Yang, A. Ingenito, O. Isabella, and M. Zeman, "IBC c-Si solar cells based on ion-implanted poly-silicon passivating contacts," *Solar Energy Materials and Solar Cells*, vol. 158, pp. 84–90, 2016. DOI: 10.1016/j.solmat.2016.05.041.

[115] Y. Chen, D. Chen, C. Liu, Z. Wang, Y. Zou, Y. He, Y. Wang, L. Yuan, J. Gong, W. Lin, X. Zhang, Y. Yang, H. Shen, Z. Feng, P. P. Altermatt, and P. J. Verlinden, "Mass production of industrial tunnel oxide passivated contacts (i-TOPCon) silicon solar cells with average efficiency over 23% and modules over 345 W," *Progress in Photovoltaics: Research and Applications*, vol. 27, no. 10, pp. 827–834, 2019. DOI: 10.1002/pip.3180.

[116] J. Lehr, M. Langenhorst, R. Schmager, F. Gota, S. Kirner, U. Lemmer, B. S. Richards, C. Case, and U. W. Paetzold, "Energy yield of bifacial textured perovskite/silicon tandem photovoltaic modules," *Solar Energy Materials and Solar Cells*, vol. 208, p. 110 367, 2020. DOI: 10.1016/j.solmat.2019.110367.

[117] M. Jaysankar, S. Paetel, E. Ahlswede, U. W. Paetzold, T. Aernouts, R. Gehlhaar, and J. Poortmans, "Toward scalable perovskite-based multijunction solar modules," *Progress in Photovoltaics: Research and Applications*, pip.3153, 2019. DOI: 10.1002/pip.3153.

[118] J. Li, L. Jiang, M. Chen, X. Li, Y. Wei, Y. Ma, Z. Fu, and Y. Yan, "Structure and physical properties evolution of ITO film during amorphous-crystalline transition using a highly effective annealing technique," *Ceramics International*, vol. 45, no. 13, pp. 16 214–16 225, 2019. DOI: 10.1016/j.ceramint.2019.05.143.

[119] A. Hajijafarassar, F. Martinho, F. Stulen, S. Grini, S. López-Mariño, M. Espíndola-Rodríguez, M. Döbeli, S. Canulescu, E. Stamate, M. Gansukh, S. Engberg, A. Crovetto, L. Vines, J. Schou, and O. Hansen, "Monolithic thin-film chalcogenide–silicon tandem solar cells enabled by a diffusion barrier," *Solar Energy Materials and Solar Cells*, vol. 207, p. 110 334, 2020. DOI: 10.1016/j.solmat.2019.110334.

[120] M. Jošt, E. Köhnen, A. B. Morales-Vilches, B. Lipovšek, K. Jäger, B. Macco, A. Al-Ashouri, J. Krč, L. Korte, B. Rech, R. Schlatmann, M. Topič, B. Stannowski, and S. Albrecht, "Textured interfaces in monolithic perovskite/silicon tandem solar cells: advanced light management for improved efficiency and energy yield," *Energy & Environmental Science*, vol. 11, no. 12, pp. 3511–3523, 2018. DOI: 10.1039/C8EE02469C.

[121] M. Lozac'h, S. Nunomura, and K. Matsubara, "Double-sided TOPCon solar cells on textured wafer with ALD SiO$_x$ layer," *Solar Energy Materials and Solar Cells*, vol. 207, p. 110 357, 2020. DOI: 10.1016/j.solmat.2019.110357.

[122] M. Moreno, D. Murias, J. Martínez, C. Reyes-Betanzo, A. Torres, R. Ambrosio, P. Rosales, P. Roca i Cabarrocas, and M. Escobar, "A comparative study of wet and dry texturing processes of c-Si wafers for the fabrication of solar cells," *Solar Energy*, vol. 101, pp. 182–191, 2014. DOI: 10.1016/j.solener.2014.01.004.

[123] J. Hylton, "Light coupling and light trapping in alkaline etched multicrystalline silicon wafers for solar cells," Ph.D. dissertation, University of Utrecht, 2006.

[124] H. Seidel, "Anisotropic Etching of Crystalline Silicon in Alkaline Solutions," *Journal of The Electrochemical Society*, vol. 137, no. 11, p. 3612, 1990. DOI: 10.1149/1.2086277.

[125] K. Chen, J. Zha, F. Hu, X. Ye, S. Zou, V. Vähänissi, J. M. Pearce, H. Savin, and X. Su, "MACE nano-texture process applicable for both single- and multi-crystalline diamond-wire sawn Si solar cells," *Solar Energy Materials and Solar Cells*, vol. 191, pp. 1–8, 2019. DOI: 10.1016/j.solmat.2018.10.015.

[126] H. Zhang, B. Ding, and T. Chen, "A high efficiency industrial polysilicon solar cell with a honeycomb-like surface fabricated by wet etching using a photoresist mask," *Applied Surface Science*, vol. 387, pp. 1265–1273, 2016. DOI: 10.1016/j.apsusc.2016.07.039.

[127] Y. Saito and T. Kosuge, "Honeycomb-textured structures on crystalline silicon surfaces for solar cells by spontaneous dry etching with chlorine trifluoride gas," *Solar Energy Materials and Solar Cells*, vol. 91, no. 19, pp. 1800–1804, 2007. DOI: 10.1016/j.solmat.2007.06.009.

[128] D. Deligiannis, S. Alivizatos, A. Ingenito, D. Zhang, M. van Sebille, R. A. C. M. M. v. Swaaij, and M. Zeman, "Wet-chemical Treatment for Improved Surface Passivation of Textured Silicon Heterojunction Solar Cells," *Energy Procedia*, vol. 55, pp. 197–202, 2014. DOI: 10.1016/j.egypro.2014.08.117.

[129] K. Jäger, O. Isabella, L. Zhao, and M. Zeman, "Light scattering properties of surface-textured substrates," *physica status solidi (c)*, vol. 7, no. 3-4, 2010. DOI: 10.1002/pssc.200982695.

[130] S. De Wolf and M. Kondo, "Abruptness of a-Si:H/c-Si interface revealed by carrier lifetime measurements," *Applied Physics Letters*, vol. 90, no. 4, p. 042 111, 2007. DOI: 10.1063/1.2432297.

[131] Y. Yan, M. Page, T. H. Wang, M. M. Al-Jassim, H. M. Branz, and Q. Wang, "Atomic structure and electronic properties of c-Si/a-Si:H heterointerfaces," *Applied Physics Letters*, vol. 88, no. 12, p. 121 925, 2006. DOI: 10.1063/1.2189670.

[132] U. K. Das, M. Z. Burrows, M. Lu, S. Bowden, and R. W. Birkmire, "Surface passivation and heterojunction cells on Si (100) and (111) wafers using dc and rf plasma deposited Si:H thin films," *Applied Physics Letters*, vol. 92, no. 6, p. 063 504, 2008. DOI: 10.1063/1.2857465.

[133] H. Fujiwara and M. Kondo, "Impact of epitaxial growth at the heterointerface of a-Si:H/c-Si solar cells," *Applied Physics Letters*, vol. 90, no. 1, p. 013 503, 2007. DOI: 10.1063/1.2426900.

[134] S. Olibet, E. Vallat-Sauvain, L. Fesquet, C. Monachon, A. Hessler-Wyser, J. Damon-Lacoste, S. De Wolf, and C. Ballif, "Properties of interfaces in amorphous/crystalline silicon heterojunctions," *physica status solidi (a)*, vol. 207, no. 3, pp. 651–656, 2010. DOI: 10.1002/pssa.200982845.

[135] A. Descoeudres, L. Barraud, S. De Wolf, B. Strahm, D. Lachenal, C. Guérin, Z. C. Holman, F. Zicarelli, B. Demaurex, J. Seif, J. Holovsky, and C. Ballif, "Improved amorphous/crystalline silicon interface passivation by hydrogen plasma treatment," *Applied Physics Letters*, vol. 99, no. 12, p. 123 506, 2011. DOI: 10.1063/1.3641899.

[136] D. Deligiannis, R. Vasudevan, A. H. M. Smets, R. A. C. M. M. van Swaaij, and M. Zeman, "Surface passivation of c-Si for silicon heterojunction solar cells using high-pressure hydrogen diluted plasmas," *AIP Advances*, vol. 5, no. 9, p. 097 165, 2015. DOI: 10.1063/1.4931821.

[137] H. Fujiwara, M. Kondo, and A. Matsuda, "Real-time studies of amorphous and microcrystalline Si:H growth by spectroscopic ellipsometry and infrared spectroscopy," *Thin Solid Films*, vol. 455-456, pp. 670–674, 2004. DOI: 10.1016/j.tsf.2003.11.233.

[138] N. Layadi, P. Roca i Cabarrocas, B. Drévillon, and I. Solomon, "Real-time spectroscopic ellipsometry study of the growth of amorphous and microcrystalline silicon thin films prepared by alternating silicon deposition and hydrogen plasma treatment," *Physical Review B*, vol. 52, no. 7, pp. 5136–5143, 1995. DOI: 10.1103/PhysRevB.52.5136.

[139] C. C. Tsai, G. B. Anderson, R. Thompson, and B. Wacker, "Control Of Silicon Network Structure In Plasma Deposition," *Journal of Non-Crystalline Solids*, vol. 114, pp. 151–153, 1989.

[140] S. Sriraman, S. Agarwal, E. S. Aydil, and D. Maroudas, "Mechanism of hydrogen-induced crystallization of amorphous silicon," *Nature*, vol. 418, no. 6893, pp. 62–65, 2002. DOI: 10.1038/nature00866.

[141] M. Katiyar and J. R. Abelson, "Investigation of hydrogen induced phase transition from a-Si:H to μc-Si:H using real time infrared spectroscopy," *Materials Science and Engineering: A*, vol. 304-306, no. 1-2, pp. 349–352, 2001. DOI: 10.1016/S0921-5093(00)01528-8.

[142] T. F. Schulze, H. N. Beushausen, C. Leendertz, A. Dobrich, B. Rech, and L. Korte, "Interplay of amorphous silicon disorder and hydrogen content with interface defects in amorphous/crystalline silicon heterojunctions," *Applied Physics Letters*, vol. 96, no. 25, p. 252 102, 2010. DOI: 10.1063/1.3455900.

[143] J.-W. A. Schüttauf, K. H. M. van der Werf, I. M. Kielen, W. G. J. H. M. van Sark, J. K. Rath, and R. E. I. Schropp, "Excellent crystalline silicon surface passivation by amorphous silicon irrespective of the technique used for chemical vapor deposition," *Applied Physics Letters*, vol. 98, no. 15, p. 153 514, 2011. DOI: 10.1063/1.3579540.

[144] S. De Wolf, S. Olibet, and C. Ballif, "Stretched-exponential a-Si:H/c-Si interface recombination decay," *Applied Physics Letters*, vol. 93, no. 3, p. 032 101, 2008. DOI: 10.1063/1.2956668.

[145]   J. Hoetzel, O. Caglar, J. Cashmore, C. Goury, J. Kalas, M. Klindworth, M. Kupich, G.-F. Leu, M.-H. Lindic, P. Losio, T. Mates, B. Mereu, T. Roschek, and I. Sinicco, "Microcrystalline bottom cells in large area thin film silicon MICROMORPH™ solar modules," *Solar Energy Materials and Solar Cells*, vol. 157, pp. 178–189, 2016. DOI: 10.1016/j.solmat.2016.05.043.

[146]   G. Limodio, G. Yang, Y. De Groot, P. Procel, L. Mazzarella, A. W. Weber, O. Isabella, and M. Zeman, "Implantation-based passivating contacts for crystalline silicon front/rear contacted solar cells," *Progress in Photovoltaics: Research and Applications*, pip.3250, 2020. DOI: 10.1002/pip.3250.

[147]   F. Feldmann, T. Fellmeth, B. Steinhauser, H. Nagel, D. Ourinson, S. Mack, E. Lohmüller, J.-I. Polzin, J. Benick, A. Richter, A. Moldovan, M. Bivour, F. Clement, J. Rentsch, M. Hermle, and S. Glunz, "Large Area TOPCon Cells Realized by a PECVD Tube Process," in *36th European Photovoltaic Solar Energy Conference and Exhibition*, Marseille, 2019. DOI: 10.4229/EUPVSEC20192019-2EO.1.4.

[148]   A. Bag, R. Radhakrishnan, R. Nekovei, and R. Jeyakumar, "Effect of absorber layer, hole transport layer thicknesses, and its doping density on the performance of perovskite solar cells by device simulation," *Solar Energy*, vol. 196, pp. 177–182, 2020. DOI: 10.1016/j.solener.2019.12.014.

[149]   M. Elbar, S. Tobbeche, and A. Merazga, "Effect of top-cell CGS thickness on the performance of CGS/CIGS tandem solar cell," *Solar Energy*, vol. 122, pp. 104–112, 2015. DOI: 10.1016/j.solener.2015.08.029.

[150]   Fraunhofer ISE, "Photovoltaics Report," Tech. Rep., 2021.

[151]   Joint Research Centre, *Photovoltaics Technology Development Report 2020*. 2020, pp. 1–85. DOI: 10.2760/827685.

[152]   T. de Vrijer, S. Miedema, T. Blackstone, D. van Nijen, C. Han, and A. H. M. Smets, "Application of metal, metal-oxide and silicon-oxide based intermediate reflective layers for current matching in autonomous high voltage multijunction photovoltaic devices," *Progress in Photovoltaics: Research and Applications*, no. recently accepted, 2022.

[153]   T. de Vrijer and A. H. M. Smets, "Advanced textured monocrystalline silicon substrates with high optical scattering yields and low electrical recombination losses for supporting crack-free nano- to poly-crystalline film growth," *Energy Science & Engineering*, 2021. DOI: 10.1002/ese3.873.

[154]   H. Sai, K. Saito, and M. Kondo, "Enhanced photocurrent and conversion efficiency in thin-film microcrystalline silicon solar cells using periodically textured back reflectors with hexagonal dimple arrays," *Applied Physics Letters*, vol. 101, no. 17, p. 173 901, 2012. DOI: 10.1063/1.4761956.

[155]   T. de Vrijer, D. van Nijen, H. Parasramka, P. A. Procel Moya, Y. Zhao, O. Isabella, and A. H. Smets, "The fundamental operation mechanisms of nc-SiO$_{x \geq 0}$:H based tunnel recombination junctions revealed," *Solar Energy Materials and Solar Cells*, vol. 236, p. 111 501, 2022. DOI: 10.1016/j.solmat.2021.111501.

[156]   T. de Vrijer, H. Parasramka, S. J. Roerink, and A. H. Smets, "An expedient semi-empirical modelling approach for optimal bandgap profiling of stoichiometric absorbers: A case study of thin film amorphous silicon germanium for use in multijunction photovoltaic devices," *Solar Energy Materials and Solar Cells*, vol. 225, p. 111 051, 2021. DOI: 10.1016/j.solmat.2021.111051.

[157]   G. Yang, R. A. van Swaaij, H. Tan, O. Isabella, and M. Zeman, "Modulated surface textured glass as substrate for high efficiency microcrystalline silicon solar cells," *Solar Energy Materials and Solar Cells*, vol. 133, pp. 156–162, 2015. DOI: 10.1016/j.solmat.2014.11.013.

[158]   K. Jäger, O. Isabella, R. A. C. M. M. van Swaaij, and M. Zeman, "Angular resolved scattering measurements of nano-textured substrates in a broad wavelength range," *Measurement Science and Technology*, vol. 22, no. 10, p. 105 601, 2011. DOI: 10.1088/0957-0233/22/10/105601.

[159]   T. de Vrijer and A. H. Smets, "The Relation Between Precursor Gas Flows, Thickness Dependent Material Phases, and Opto-Electrical Properties of Doped a/nc-SiO$_{x \geq 0}$:H Films," *IEEE Journal of Photovoltaics*, vol. 11, no. 3, pp. 591–599, 2021. DOI: 10.1109/JPHOTOV.2021.3059940.

[160]   R. B. Iverson and R. Reif, "Stochastic model for grain size versus dose in implanted and annealed polycrystalline silicon films on SiO$_2$," *Journal of Applied Physics*, vol. 57, no. 12, pp. 5169–5175, 1985. DOI: 10.1063/1.335251.

[161] Y. Wada and S. Nishimatsu, "Grain Growth Mechanism of Heavily Phosphorus-Implanted Poly-crystalline Silicon," *Journal of The Electrochemical Society*, vol. 125, pp. 1499–1504, 1978. DOI: 10.1149/1.2131703.

[162] L. Mei, M. Rivier, Y. Kwark, and R. W. Dutton, "Grain-Growth Mechanisms in Polysilicon," *Journal of The Electrochemical Society*, vol. 129, no. 8, pp. 1791–1795, 1982. DOI: 10.1149/1.2124295.

[163] W. K. Hofker, D. P. Oosthoek, N. J. Koeman, and H. A. M. de grefte, "Concentration profiles of boron implantations in amorphous and polycrystalline silicon," *Radiation Effects*, vol. 24, no. 4, pp. 223–231, 1975. DOI: 10.1080/00337577508240811.

[164] K. Suzuki, Y. Tada, Y. Kataoka, and T. Nagayama, "Monte Carlo Simulation of Ion Implantation Profiles Calibrated for Various Ions over Wide Energy Range," *JSTS:Journal of Semiconductor Technology and Science*, vol. 9, no. 1, pp. 67–74, 2009. DOI: 10.5573/JSTS.2009.9.1.067.

[165] E. Manea, E. Budianu, M. Purica, D. Cristea, I. Cernica, R. Muller, and V. Moagar Poladian, "Optimization of front surface texturing processes for high-efficiency silicon solar cells," *Solar Energy Materials and Solar Cells*, vol. 87, pp. 423–431, 2005. DOI: 10.1016/j.solmat.2004.06.013.

[166] H. Sai, K. Maejima, T. Matsui, T. Koida, M. Kondo, S. Nakao, Y. Takeuchi, H. Katayama, and I. Yoshida, "High-efficiency microcrystalline silicon solar cells on honeycomb textured substrates grown with high-rate VHF plasma-enhanced chemical vapor deposition," *Japanese Journal of Applied Physics*, vol. 54, no. 8S1, 08KB05, 2015. DOI: 10.7567/JJAP.54.08KB05.

[167] R. Santbergen, T. Meguro, T. Suezaki, G. Koizumi, K. Yamamoto, and M. Zeman, "GenPro4 Optical Model for Solar Cell Simulation and Its Application to Multijunction Solar Cells," *IEEE Journal of Photovoltaics*, vol. 7, no. 3, pp. 919–926, 2017. DOI: 10.1109/JPHOTOV.2017.2669640.

[168] T. de Vrijer, B. Bouazzata, A. Ravichandran, J. van Dingen, P. Roelandschap, K. Roodenburg, S. Roerink, F. Saitta, T. Blackstone, and A. Smets, "Opto-electrical properties of group IV alloys: the inherent challenges of processing hydrogenated germanium," *Advanced Science*, p. 2200814, 2022. DOI: 10.1002/advs.202200814.

[169] H. B. Li, R. H. Franken, J. K. Rath, and R. E. Schropp, "Structural defects caused by a rough substrate and their influence on the performance of hydrogenated nano-crystalline silicon n–i–p solar cells," *Solar Energy Materials and Solar Cells*, vol. 93, no. 3, pp. 338–349, 2009. DOI: 10.1016/j.solmat.2008.11.013.

[170] H. Sai, K. Maejima, T. Matsui, T. Koida, K. Matsubara, M. Kondo, Y. Takeuchi, S. Sugiyama, H. Katayama, and I. Yoshida, "Impact of front TCO layer in substrate-type thin-film microcrystalline silicon solar cells," in *2015 IEEE 42nd Photovoltaic Specialist Conference (PVSC)*, IEEE, 2015, pp. 1–6. DOI: 10.1109/PVSC.2015.7355677.

[171] H. Sai, T. Matsui, and K. Matsubara, "Stabilized 14.0%-efficient triple-junction thin-film silicon solar cell," *Applied Physics Letters*, vol. 109, no. 18, p. 183506, 2016. DOI: 10.1063/1.4966996.

[172] D. Y. Kim, E. Guijt, F. T. Si, R. Santbergen, J. Holovský, O. Isabella, R. A. van Swaaij, and M. Zeman, "Fabrication of double- and triple-junction solar cells with hydrogenated amorphous silicon oxide (a-SiOx:H) top cell," *Solar Energy Materials and Solar Cells*, vol. 141, pp. 148–153, 2015. DOI: 10.1016/j.solmat.2015.05.033.

[173] J.-W. Schüttauf, B. Niesen, L. Löfgren, M. Bonnet-Eymard, M. Stuckelberger, S. Hänni, M. Boccard, G. Bugnon, M. Despeisse, F.-J. Haug, F. Meillaud, and C. Ballif, "Amorphous sili-con–germanium for triple and quadruple junction thin-film silicon based solar cells," *Solar Energy Materials and Solar Cells*, vol. 133, pp. 163–169, 2015. DOI: 10.1016/j.solmat.2014.11.006.

[174] J. Jiang, S. Yang, Y. Shi, R. Shan, X. Tian, H. Li, J. Yi, and J. Zhong, "Optimization bandgap gradation structure simulation of $Cu_2Sn_{1-x}Ge_xS_3$ solar cells by SCAPS," *Solar Energy*, vol. 194, pp. 986–994, 2019. DOI: 10.1016/j.solener.2019.11.014.

[175] D. Hironiwa, M. Murata, N. Ashida, Z. Tang, and T. Minemoto, "Simulation of optimum band-gap grading profile of $Cu_2ZnSn(S,Se)_4$ solar cells with different optical and defect properties," *Japanese Journal of Applied Physics*, vol. 53, no. 7, p. 071201, 2014. DOI: 10.7567/JJAP.53.071201.

[176] F. Ahmad, T. H. Anderson, P. B. Monk, and A. Lakhtakia, "Efficiency enhancement of ultrathin CIGS solar cells by optimal bandgap grading," *Applied Optics*, vol. 58, no. 22, p. 6067, 2019. DOI: 10.1364/AO.58.006067.

[177] J. Xia, J. Zou, X. Peng, W. Deng, and Y. Zhang, "Theoretical modeling and simulation-based assessment of graded-bandgap AlGaAs/GaAs electron-injection cathode," *Ultramicroscopy*, vol. 219, p. 113121, 2020. DOI: 10.1016/j.ultramic.2020.113121.

[178] S.-T. Hwang, S. Kim, H. Cheun, H. Lee, B. Lee, T. Hwang, S. Lee, W. Yoon, H.-M. Lee, and B. Park, "Bandgap grading and $Al_{0.3}Ga_{0.7}As$ heterojunction emitter for highly efficient GaAs-based solar cells," *Solar Energy Materials and Solar Cells*, vol. 155, pp. 264–272, 2016. DOI: 10.1016/j.solmat.2016.06.009.

[179] O. Ergen, S. M. Gilbert, T. Pham, S. J. Turner, M. T. Z. Tan, M. A. Worsley, and A. Zettl, "Graded bandgap perovskite solar cells," *Nature Materials*, vol. 16, no. 5, pp. 522–525, 2017. DOI: 10.1038/nmat4795.

[180] Y.-T. Liu, Y.-H. Chen, C.-C. Lin, C.-M. Fan, J.-C. Liu, Y.-L. Tung, and S.-Y. Tsai, "Modeling and simulation of band-gap profiling with planar heterojunction of hole-transporting layer-free perovskite solar cells," *Materials Research Express*, vol. 4, no. 7, p. 075505, 2017. DOI: 10.1088/2053-1591/aa77ee.

[181] C. Chen, Z. Song, C. Xiao, D. Zhao, N. Shrestha, C. Li, G. Yang, F. Yao, X. Zheng, R. J. Ellingson, C.-S. Jiang, M. Al-Jassim, K. Zhu, G. Fang, and Y. Yan, "Achieving a high open-circuit voltage in inverted wide-bandgap perovskite solar cells with a graded perovskite homojunction," *Nano Energy*, vol. 61, pp. 141–147, 2019. DOI: 10.1016/j.nanoen.2019.04.069.

[182] S. Kim, J.-W. Chung, H. Lee, J. Park, Y. Heo, and H.-M. Lee, "Remarkable progress in thin-film silicon solar cells using high-efficiency triple-junction technology," *Solar Energy Materials and Solar Cells*, vol. 119, pp. 26–35, 2013. DOI: 10.1016/j.solmat.2013.04.016.

[183] R. Stolk, H. Li, R. Franken, J. Schüttauf, C. van der Werf, J. Rath, and R. Schropp, "Improvement of the efficiency of triple junction n–i–p solar cells with hot-wire CVD proto- and microcrystalline silicon absorber layers," *Thin Solid Films*, vol. 516, no. 5, pp. 736–739, 2008. DOI: 10.1016/j.tsf.2007.06.110.

[184] X. Deng, X. Liao, S. Han, H. Povolny, and P. Agarwal, "Amorphous silicon and silicon germanium materials for high-efficiency triple-junction solar cells," *Solar Energy Materials and Solar Cells*, vol. 62, no. 1-2, pp. 89–95, 2000. DOI: 10.1016/S0927-0248(99)00139-7.

[185] O. Isabella, A. H. M. Smets, and M. Zeman, "Thin-film silicon-based quadruple junction solar cells approaching 20% conversion efficiency," *Solar Energy Materials and Solar Cells*, vol. 129, pp. 82–89, 2014. DOI: 10.1016/j.solmat.2014.03.021.

[186] O. Isabella, J. Krč, and M. Zeman, "Modulated surface textures for enhanced light trapping in thin-film silicon solar cells," *Applied Physics Letters*, vol. 97, no. 10, p. 101106, 2010. DOI: 10.1063/1.3488023.

[187] T. Matsui, K. Ogata, M. Isomura, and M. Kondo, "Microcrystalline silicon–germanium alloys for solar cell application: Growth and material properties," *Journal of Non-Crystalline Solids*, vol. 352, no. 9-20, pp. 1255–1258, 2006. DOI: 10.1016/j.jnoncrysol.2005.11.144.

[188] L. Chen, J. Tauc, J.-K. Lee, and E. Schiff, "Photomodulation spectroscopy of defects in hydrogenated amorphous silicon germanium alloys," *Journal of Non-Crystalline Solids*, vol. 114, no. PART 2, pp. 585–587, 1989. DOI: 10.1016/0022-3093(89)90658-3.

[189] L. Veldhuizen, C. van der Werf, Y. Kuang, N. Bakker, S. Yun, and R. Schropp, "Optimization of hydrogenated amorphous silicon germanium thin films and solar cells deposited by hot wire chemical vapor deposition," *Thin Solid Films*, vol. 595, pp. 226–230, 2015. DOI: 10.1016/j.tsf.2015.05.055.

[190] T. Unold and J. D. Cohen, "Electronic mobility gap structure and the nature of deep defects in amorphous silicon-germanium alloys grown by photo-CVD," *Journal of Non-Crystalline Solids*, vol. 164-166, pp. 23–26, 1993.

[191] S. Y. Moon, D. You, S. Lee, and H. Lee, "In-situ monitoring and control of hydrogenated amorphous silicon–germanium band-gap profiling during plasma deposition process," *Current Applied Physics*, vol. 13, no. 7, pp. 1502–1505, 2013. DOI: 10.1016/j.cap.2013.05.005.

[192] D. P. Pham, S. Kim, J. Park, A. T. Le, J. Cho, J. Jung, S. Iftiquar, and J. Yi, "Silicon germanium active layer with graded band gap and μc-Si:H buffer layer for high efficiency thin film solar cells," *Materials Science in Semiconductor Processing*, vol. 56, pp. 183–188, 2016. DOI: 10.1016/j.mssp.2016.08.011.

[193] M. Bhan, L. Malhotra, and S. Kashyap, "Electrical and Optical Properties of Ion-Beam Sputtered Amorphous Silicon-Germanium Alloy Films," *Thin Solid Films*, vol. 203, pp. 23–32, 1991.

[194] A. Fedala, R. Cherfi, M. Aoucher, and T. Mohammed-Brahim, "Structural, optical and electrical properties of hydrogenated amorphous silicon germanium (a-Si$_{1-x}$Ge$_x$) deposited by DC magnetron sputtering at high rate," *Materials Science in Semiconductor Processing*, vol. 9, no. 4-5, pp. 690–693, 2006. DOI: 10.1016/j.mssp.2006.08.016.

[195] K. D. Mackenzie, J. R. Eggert, D. J. Leopold, Y. M. Li, S. Lin, and W. Paul, "Structural, electrical, and optical properties of a-Si$_{1-x}$Ge$_x$:H and an inferred electronic band structure," *Physical Review B*, vol. 31, no. 4, pp. 2198–2212, 1985. DOI: 10.1103/PhysRevB.31.2198.

[196] Y.-P. Chou and S.-C. Lee, "Structural, optical, and electrical properties of hydrogenated amorphous silicon germanium alloys," *Journal of Applied Physics*, vol. 83, no. 8, pp. 4111–4123, 1998. DOI: 10.1063/1.367229.

[197] F. Zhong, C.-C. Chen, and J. Cohen, "Electronic structure and light induced degradation of amorphous silicon-germanium alloys," *Journal of Non-Crystalline Solids*, vol. 198-200, no. PART 1, pp. 572–576, 1996. DOI: 10.1016/0022-3093(95)00766-0.

[198] B. P. Nelson, Y. Xu, J. D. Webb, A. Mason, R. C. Reedy, L. M. Gedvilas, and W. A. Lanford, "Techniques for measuring the composition of hydrogenated amorphous silicon-germanium alloys," *Journal of Non-Crystalline Solids*, vol. 269, pp. 680–684, 2000.

[199] A. Bhaduri, P. Chaudhuri, S. Vignoli, and C. Longeaud, "Correlation of structural inhomogeneities with transport properties in amorphous silicon germanium alloy thin films," *Solar Energy Materials and Solar Cells*, vol. 94, no. 9, pp. 1492–1495, 2010. DOI: 10.1016/j.solmat.2010.02.043.

[200] W. Paul, D. Paul, B. von Roedern, J. Blake, and S. Oguz, "Preferential Attachment of H in Amorphous Hydrogenated Binary Semiconductors and Consequent Inferior Reduction of Pseudogap State Density," *Physical Review Letters*, vol. 46, no. 15, pp. 1016–1020, 1981.

[201] T. de Vrijer, A. Ravichandran, B. Bouazzata, and A. H. Smets, "The impact of processing conditions and post-deposition oxidation on the opto-electrical properties of hydrogenated amorphous and nano-crystalline Germanium films," *Journal of Non-Crystalline Solids*, vol. 553, p. 120 507, 2021. DOI: 10.1016/j.jnoncrysol.2020.120507.

[202] B. Yan, L. Zhao, B. Zhao, J. Chen, G. Wang, H. Diao, Y. Mao, and W. Wang, "Hydrogenated amorphous silicon germanium alloy with enhanced photosensitivity prepared by plasma enhanced chemical vapor deposition at high temperature," *Vacuum*, vol. 89, no. 1, pp. 43–46, 2013. DOI: 10.1016/j.vacuum.2012.09.004.

[203] J. Xu, S. Miyazaki, and M. Hirose, "High-Quality Hydrogenated Amorphous Silicon-Germanium Alloys for Narrow Bandgap Thin Film Solar Cells," *Journal of Non-Crystalline Solids*, vol. 208, pp. 277–281, 1996.

[204] R. A. C. M. M. V. Swaaij, M. Zeman, S. Arnoult, and J. W. Metselaar, "Performance Dependence On Grading Width Of a-SiGe:H Component Solar Cells," pp. 869–872, 2000.

[205] R. J. Zambrano, F. Rubinelli, J. Rath, and R. E. Schropp, "Improvement in the spectral response at long wavelength of a-SiGe:H solar cells by exponential band gap design of the i-layer," *Journal of non-crystalline solids*, vol. 302, pp. 1131–1135, 2002.

[206] J. Zimmer, H. Stiebig, and H. Wagner, "a-SiGe:H based solar cells with graded absorption layer," *Journal of Applied Physics*, vol. 84, no. 1, pp. 611–617, 1998. DOI: 10.1063/1.368088.

[207] B. Pieters, M. Zeman, R. van Swaaij, and W. Metselaar, "Optimization of a-SiGe:H solar cells with graded intrinsic layers using integrated optical and electrical modeling," *Thin Solid Films*, vol. 451-452, pp. 294–297, 2004. DOI: 10.1016/j.tsf.2003.11.029.

[208] A. H. Smets, K. Jäger, I. Olindo, M. Zeman, and R. A. van Swaaij, "Solar Energy: The physics and engineering of photovoltaic conversion, technologies and systems," in, UIT Cambridge, 2016.

[209] S. Fan, Z. J. Yu, Y. Sun, W. Weigand, P. Dhingra, M. Kim, R. D. Hool, E. D. Ratta, Z. C. Holman, and M. L. Lee, "20%-efficient epitaxial GaAsP/Si tandem solar cells," *Solar Energy Materials and Solar Cells*, vol. 202, p. 110 144, 2019. DOI: 10.1016/j.solmat.2019.110144.

[210] M. Valentini, C. Malerba, L. Serenelli, M. Izzi, E. Salza, M. Tucci, and A. Mittiga, "Fabrication of monolithic CZTS/Si tandem cells by development of the intermediate connection," *Solar Energy*, vol. 190, pp. 414–419, 2019. DOI: 10.1016/j.solener.2019.08.029.

[211] K. Jäger, J. Lenssen, P. Veltman, and E. Hamers, "Large-area production of highly efficient flexible light-weight thin-film silicon PV modules," in *Proc. of the 28th European Photovoltaic Solar Energy Conference*, 2013, pp. 2164–2169.

[212] S. Philipps and W. Warmuth, "Photovoltaics Report 2019.," Fraunhofer ISE, Tech. Rep., 2019, pp. 1–49.

[213] Y. Cao, X. Zhu, X. Tong, J. Zhou, J. Ni, J. Zhang, and J. Pang, "Ultrathin microcrystalline hydrogenated Si/Ge alloyed tandem solar cells towards full solar spectrum conversion," *Frontiers of Chemical Science and Engineering*, vol. 14, no. 6, pp. 997–1005, 2020. DOI: 10.1007/S11705-019-1906-0.

[214] J. R. Blanco, P. J. McMarr, J. E. Yehoda, K. Vedam, and R. Messier, "Density of amorphous germanium films by spectroscopic ellipsometry," *Journal of Vacuum Science & Technology A: Vacuum, Surfaces, and Films*, vol. 4, no. 3, pp. 577–582, 1986. DOI: 10.1116/1.573851.

[215] B. Schröder, A. Annen, T. Drüsedau, H. Freistedt, P. Deák, and H. Oechsner, "Influence of oxygen incorporation on the properties of magnetron sputtered hydrogenated amorphous germanium films," *Applied Physics Letters*, vol. 62, no. 16, pp. 1961–1963, 1993. DOI: 10.1063/1.109504.

[216] A. Scholz, B. Muller, B. Schroder, H. Oechsner, and H. Freistedt, "Photoconductivity spectroscopy (CPM) on a-Ge:H at low temperatures," *Journal of Non-Crystalline Solids*, vol. 164-166, pp. 375–378, 1993.

[217] V. Sorianello, L. Colace, G. Assanto, and M. Nardone, "Micro-Raman characterization of Germanium thin films evaporated on various substrates," *Microelectronic Engineering*, vol. 88, no. 4, pp. 492–495, 2011. DOI: 10.1016/j.mee.2010.10.028.

[218] F. H. Karg, H. Bohm, and K. Pierz, "Influence of plasma deposition on structural and electronic properties of a-Ge:H," *Journal of Non-Crystalline Solids*, vol. 114, pp. 477–479, 1989.

[219] T. Nakashita, A. Inoue, S. Hagiwara, F. Uehara, and K. Kohno, "Dependence of Electronic Properties of Hydrogenated Amorphous Ge on Deposition Condition," *Japanese Journal of Applied Physics*, vol. 31, no. Part 1, No. 6A, pp. 1730–1736, 1992. DOI: 10.1143/JJAP.31.1730.

[220] G. Lucovsky, S. S. Chao, J. Yang, J. E. Tyler, R. C. Ross, Czubatyj, and W., "Chemical bonding of hydrogen and oxygen in glow-discharge-deposited thin films of a-Ge:H and a-Ge:(H,O)," *Physical Review B*, vol. 31, no. 4, pp. 2190–2197, 1985. DOI: 10.1103/PhysRevB.31.2190.

[221] J. R. Doyle, D. A. Doughty, and A. Gallagher, "Germane discharge chemistry," *Journal of Applied Physics*, vol. 69, no. 8, pp. 4169–4177, 1991. DOI: 10.1063/1.348384.

[222] K. Eberhardt and G. Bauer, "Effect of H-content and H-bonding configuration on light and thermal induced metastability in amorphous hydrogenated germanium (a-Ge:H)," *Journal of Non-Crystalline Solids*, vol. 164-166, no. PART 1, pp. 19–22, 1993. DOI: 10.1016/0022-3093(93)90482-D.

[223] M. Stutzmann, J. Stuke, and H. Dersch, "Electron spin resonance of doped glow-discharge amorphous germanium," *physica status solidi (b)*, vol. 115, no. 1, pp. 141–151, 1983. DOI: 10.1002/pssb.2221150116.

[224] J. R. Doyle, D. A. Doughty, and A. Gallagher, "Plasma chemistry in silane/germane and disilane/germane mixtures," *Journal of Applied Physics*, vol. 71, no. 10, pp. 4727–4738, 1992. DOI: 10.1063/1.350663.

[225] K. Gruntz, L. Ley, M. Cardona, R. Johnson, G. Harbeke, and B. v. Roedern, "Photoemission spectroscopy of amorphous hydrogenated germanium," *Journal of Non-Crystalline Solids*, vol. 35 & 36, pp. 453–458, 1980.

[226] C. Li, J. Ni, X. Sun, X. Wang, Z. Li, H. Cai, J. Li, and J. Zhang, "Nanocrystalline germanium nip solar cells with spectral sensitivities extending into 1450 nm," *Journal of Physics D: Applied Physics*, vol. 50, no. 4, p. 045 108, 2017. DOI: 10.1088/1361-6463/AA4F93.

[227] G. Lucovsky, R. J. Nemanich, and J. C. Knights, "Structural interpretation of the vibrational spectra of a-Si: H alloys," *Physical Review B*, vol. 19, no. 4, pp. 2064–2073, 1979. DOI: 10.1103/PhysRevB.19.2064.

[228] M. Wojdyr, "Fityk : a general-purpose peak fitting program," *Journal of Applied Crystallography*, vol. 43, no. 5, pp. 1126–1128, 2010. DOI: 10.1107/S0021889810030499.

[229] M. S. Abo-Ghazala and S. Al Hazmy, "Hydrogen Bonding in Hydrogenated Amorphous Germanium," *Tsinghua Science and Technology*, vol. 9, no. 2, pp. 177–180, 2004.

[230] M. Cardona, "Vibrational Spectra of Hydrogen in Silicon and Germanium," *physica status solidi (b)*, vol. 118, no. 2, pp. 463–481, 1983. DOI: 10.1002/pssb.2221180202.

[231] D. Bermejo and M. Cardona, "Raman Scattering in Pure and Hydrogenated Amorphous," *Journal of Non-Crystalline Solids*, vol. 32, pp. 405–419, 1978.

[232] O. Madelung, U. Rossler, and M. Schulz, "Germanium (Ge) Raman phonon frequencies and wavenumbers," in *Group IV Elements, IV-IV and III-V Compounds. Part a- Lattice Properties*, 2, vol. 4, Berlin/Heidelberg: Springer-Verlag, 2001, pp. 1–17. DOI: 10.1007/10551045_228.

[233] V. A. Volodin, G. K. Krivyakin, G. D. Ivlev, S. L. Prokopyev, S. V. Gusakova, and A. A. Popov, "Crystallization of Amorphous Germanium Films and Multilayer a-Ge/a-Si Structures upon Exposure to Nanosecond Laser Radiation," *Semiconductors*, vol. 53, no. 3, pp. 400–405, 2019. DOI: 10.1134/S1063782619030217.

[234] P. Alfaro-Calderón, M. Cruz-Irisson, and C. Wang-Chen, "Theory of Raman Scattering by Phonons in Germanium Nanostructures," *Nanoscale Research Letters*, vol. 3, no. 2, pp. 55–59, 2008. DOI: 10.1007/s11671-007-9114-0.

[235] Z. Remes, R. Vasudevan, K. Jarolimek, A. H. Smets, and M. Zeman, "The Optical Spectra of a-Si:H and a-SiC:H Thin Films Measured by the Absolute Photothermal Deflection Spectroscopy (PDS)," *Solid State Phenomena*, vol. 213, pp. 19–28, 2014. DOI: 10.4028/www.scientific.net/SSP.213.19.

[236] G. Talukder, J. C. L. Cornish, P. Jennings, G. T. Hefter, B. W. Clare, and J. Livingstone, "Effects of annealing on infrared and thermal-effusion spectra of sputtered a-Si:H alloys," *Journal of Applied Physics*, vol. 71, no. 1, pp. 403–409, 1992. DOI: 10.1063/1.350723.

[237] Y. H. Shing, J. W. Perry, and C. E. Allevato, "Amorphous Silicon Germanium Alloy Film Deposition With In Situ Plasma Diagnostics," *Solar Cells*, vol. 24, pp. 353–362, 1988.

[238] Y. Cao, Y. Liu, J. Zhou, Y. Wang, J. Ni, and J. Zhang, "Non-uniform distribution in μc-Si$_{1x}$Ge$_x$:H and its influence on thin film and device performance," *Solar Energy Materials and Solar Cells*, vol. 151, pp. 1–6, 2016. DOI: 10.1016/J.SOLMAT.2016.02.009.

[239] T. Matsui, K. Ogata, C. Chang, M. Isomura, and M. Kondo, "Carrier collection characteristics of microcrystalline silicon–germanium p–i–n junction solar cells," *Journal of Non-Crystalline Solids*, vol. 354, no. 19-25, pp. 2468–2471, 2008. DOI: 10.1016/j.jnoncrysol.2007.09.026.

[240] T. A. Abtew and D. A. Drabold, "Ab initio models of amorphous Si$_{1-x}$Ge$_x$:H," *Physical Review B*, vol. 75, no. 4, p. 045 201, 2007. DOI: 10.1103/PhysRevB.75.045201.

[241] R. L. Redington and D. E. Milligan, "Infrared Spectroscopic Evidence for the Rotation of the Water Molecule in Solid Argon," *The Journal of Chemical Physics*, vol. 37, no. 10, pp. 2162–2166, 1962. DOI: 10.1063/1.1732982.

[242] X. Wang, J. Ni, C. Li, X. Sun, Z. Li, H. Cai, J. Li, and J. Zhang, "The microstructure evolution of hydrogenated microcrystalline germanium promoted by power gradient method," *Journal of Crystal Growth*, vol. 455, pp. 136–142, 2016. DOI: 10.1016/j.jcrysgro.2016.10.011.

[243] J. R. Weber, A. Janotti, and C. G. Van de Walle, "Dangling bonds and vacancies in germanium," *Physical Review B*, vol. 87, no. 3, p. 035 203, 2013. DOI: 10.1103/PhysRevB.87.035203.

[244] M. Krause, H. Stiebig, R. Carius, and H. Wagner, "Microcrystalline Germanium Photodetectors," *MRS Proceedings*, vol. 664, A26.5.1, 2001. DOI: 10.1557/PROC-664-A26.5.1.

[245] J. Weber, M. Hiller, and E. Lavrov, "Hydrogen in germanium," *Materials Science in Semiconductor Processing*, vol. 9, no. 4–5, pp. 564–570, 2006. DOI: `10.1016/j.mssp.2006.08.007`.

[246] S. W. King, J. Bielefeld, G. Xu, W. A. Lanford, Y. Matsuda, R. H. Dauskardt, N. Kim, D. Hondongwa, L. Olasov, B. Daly, G. Stan, M. Liu, D. Dutta, and D. Gidley, "Influence of network bond percolation on the thermal, mechanical, electrical and optical properties of high and low-k a-SiC:H thin films," *Journal of Non-Crystalline Solids*, vol. 379, pp. 67–79, 2013. DOI: `10.1016/j.jnoncrysol.2013.07.028`.

[247] K. Sangwal and W. Kucharczyk, "Relationship between density and refractive index of inorganic solids," *Journal of Physics D: Applied Physics*, vol. 20, no. 4, pp. 522–525, 1987. DOI: `10.1088/0022-3727/20/4/019`.

[248] H. N. Ritland, "Relation Between Refractive Index and Density of a Glass at Constant Temperature," *Journal of the American Ceramic Society*, vol. 38, no. 2, pp. 86–88, 1955. DOI: `10.1111/j.1151-2916.1955.tb14581.x`.

[249] S. Maj, "On the relationship between refractive index and density for SiO$_2$ polymorphs," *Physics and Chemistry of Minerals*, vol. 10, no. 3, pp. 133–136, 1984. DOI: `10.1007/BF00309648`.

[250] D. Mergel and M. Jerman, "Density and refractive index of thin evaporated films," *Chinese Optics Letters*, vol. 8, pp. 67–72, 2010. DOI: `10.3788/COL201008S1.0067`.

[251] Z. Remes, M. Vanecek, P. Torres, U. Kroll, A. Mahan, and R. Crandall, "Optical determination of the mass density of amorphous and microcrystalline silicon layers with different hydrogen contents," *Journal of Non-Crystalline Solids*, no. 227-230, pp. 876–879, 1998.

[252] I. Chambouleyron, C. F. Graeff, A. R. Zanatta, F. Fajardo, M. Mulato, R. Campomanes, D. Comedi, and F. C. Marque, "The Perspectives of Hydrogenated Amorphous Germanium as an Electronic Material," *phys. stat. sol. (b)*, vol. 192, pp. 241–251, 1995. DOI: `10.1016/S1369-7021(07)70349-8`.

[253] E. V. Johnson and P. Roca i Cabarrocas, "High Quality a-Ge:H Films and Devices Through Enhanced Plasma Chemistry," *MRS Proceedings*, vol. 989, pp. 04–04, 2007. DOI: `10.1557/PROC-0989-A04-04`.

[254] Y. Toyoshima, K. Arai, A. Matsuda, and K. Tanaka, "In situ characterization of the growing a-Si:H surface by IR spectroscopy," *Journal of Non-Crystalline Solids*, vol. 137-138, no. PART 2, pp. 765–770, 1991. DOI: `10.1016/S0022-3093(05)80233-9`.

[255] M. Zacharias and J. Blasing, "Preparation of a-GeO$_x$:H alloys: Vibrational, optical, and structural properties," vol. 52, no. 19, pp. 14 018–14 024, 1995.

[256] M. Li, L. Jiang, Y. Sun, T. Xiao, P. Xiang, and X. Tan, "Silicon content influence on structure and photoluminescence properties of carbon rich hydrogenated amorphous silicon carbide thin films," *Journal of Alloys and Compounds*, vol. 753, pp. 320–328, 2018. DOI: `10.1016/j.jallcom.2018.04.226`.

[257] Y. H. Chen, H. Y. Fang, and C. M. Yeh, "Raman scattering and electrical characterizations studies of hydrogenated amorphous silicon-germanium alloys prepared by 40 MHz plasma-enhanced CVD," *Journal of Non-Crystalline Solids*, vol. 357, no. 1, pp. 1–3, 2011. DOI: `10.1016/j.jnoncrysol.2010.09.060`.

[258] D. Bermejo and M. Cardona, "Infrared absorption in hydrogenated amorphous and crystallized germanium," *Journal of Non-Crystalline Solids*, vol. 32, no. 1-3, pp. 421–430, 1979. DOI: `10.1016/0022-3093(79)90086-3`.

[259] V. A. Volodin and D. I. Koshelev, "Quantitative analysis of hydrogen in amorphous silicon using Raman scattering spectroscopy," *Journal of Raman Spectroscopy*, vol. 44, no. 12, pp. 1760–1764, 2013. DOI: `10.1002/jrs.4408`.

[260] B. Najafov and V. Figarov, "Hydrogen content evaluation in hydrogenated nanocrystalline silicon and its amorphous alloys with germanium and carbon," *International Journal of Hydrogen Energy*, vol. 35, no. 9, pp. 4361–4367, 2010. DOI: `10.1016/j.ijhydene.2010.02.061`.

[261] J. Melskens, A. Schnegg, A. Baldansuren, K. Lips, M. P. Plokker, S. W. H. Eijt, H. Schut, M. Fischer, M. Zeman, and A. H. M. Smets, "Structural and electrical properties of metastable defects in hydrogenated amorphous silicon," *Physical Review B*, vol. 91, no. 24, p. 245 207, 2015. DOI: `10.1103/PhysRevB.91.245207`.

[262] T. de Vrijer, J. E. van Dingen, P. J. Roelandschap, K. Roodenburg, and A. H. Smets, "Improved PECVD processed hydrogenated germanium films through temperature induced densification," *Materials Science in Semiconductor Processing*, vol. 138, p. 106 285, 2022. DOI: 10.1016/j.mssp.2021.106285.

[263] M. Python, D. Dominé, T. Söderström, F. Meillaud, and C. Ballif, "Microcrystalline silicon solar cells: effect of substrate temperature on cracks and their role in post-oxidation," *Progress in Photovoltaics: Research and Applications*, vol. 18, no. 7, pp. 491–499, 2010. DOI: 10.1002/pip.956.

[264] T. de Vrijer, K. Roodenburg, F. Saitta, T. Blackstone, G. Limodio, and A. H. M. Smets, "PECVD processing of low bandgap-energy amorphous hydrogenated germanium-tin (a-GeSn:H) films for opto-electronic applications," *Applied Materials Today*, vol. 27, p. 101 450, 2022. DOI: 10.1016/j.apmt.2022.101450.

[265] T. de Vrijer and A. H. M. Smets, "Infrared analysis of catalytic CO_2 reduction in hydrogenated germanium," *Physical Chemistry Chemical Physics*, no. 24, pp. 10 241–10 248, 2022. DOI: 10.1039/D2CP01054B.

[266] M. Künle, T. Kaltenbach, P. Löper, A. Hartel, S. Janz, O. Eibl, and K.-G. Nickel, "Si-rich a-SiC:H thin films: Structural and optical transformations during thermal annealing," *Thin Solid Films*, vol. 519, no. 1, pp. 151–157, 2010. DOI: 10.1016/j.tsf.2010.07.085.

[267] T. Matsumoto, Y. Murata, and J.-i. Watanabe, "Study of silicon-hydrogen bonds at an amorphous silicon/silicon nitride interface using infrared attenuated total reflection spectroscopy," *Applied Physics Letters*, vol. 60, no. 16, pp. 1942–1944, 1992. DOI: 10.1063/1.107158.

[268] I. Omkaram, R. Sreekanth Chakradhar, and J. Lakshmana Rao, "EPR, optical, infrared and Raman studies of VO^{2+} ions in polyvinylalcohol films," *Physica B: Condensed Matter*, vol. 388, no. 1-2, pp. 318–325, 2007. DOI: 10.1016/j.physb.2006.06.134.

[269] E. Abdelrazek, A. Abdelghany, and A. Tarabiah, "Characterization and Physical Properties of Silver/PVA nano-composite," *Research Journal of Pharmaceutical, Biological and Chemical Sciences*, vol. 3, no. 4, pp. 448–459, 2012.

[270] I. Chambouleyron, F. C. Marques, J. P. de Souza, and I. J. R. Baumvol, "Structure and composition of amorphous $Ge_{1x}Sn_x$ thin films," *Journal of Applied Physics*, vol. 63, no. 11, pp. 5596–5598, 1988. DOI: 10.1063/1.340338.

[271] O. Madelung, M. Schulz, and H. Weiss, *Numerical Data and Functional Relationships in Science and Technology: Special Systems and Topics. Comprehensive Index for III/17*. Heidelberg, New York, Toky: Springer-Verlag Berlin, 1985, pp. 68–75.

[272] M. Gazicki, "Plasma Deposition of Thin CarbonGermanium Alloy Films from Organogermanium Compounds," *Chaos, Solitons & Fractals*, vol. 10, no. 12, pp. 1983–2017, 1999. DOI: 10.1016/S0960-0779(98)00246-X.

[273] W.-J. Sah, H.-K. Tsai, and S.-C. Lee, "Physical and electronic structure of amorphous silicon carbon hydrogen alloy," *Applied Physics Letters*, vol. 54, no. 7, pp. 617–619, 1989. DOI: 10.1063/1.100896.

[274] S. Ray, D. Das, and A. Barua, "Infrared vibrational spectra of hydrogenated amorphous silicon carbide thin films prepared by glow discharge," *Solar Energy Materials*, vol. 15, pp. 45–57, 1987.

[275] A. Lukianov, N. Klyui, B. Sha, M. Dusheiko, V. Lozinskii, A. Liptuga, V. Kasatkin, and B. Liu, "Nonstoichiometric amorphous silicon carbide films as promising antireflection and protective coatings for germanium in IR spectral range," *Optical Materials*, vol. 88, pp. 445–450, 2019. DOI: 10.1016/j.optmat.2018.12.012.

[276] A. Kozak, O. Porada, V. Ivashchenko, L. Ivashchenko, P. Scrynskyy, T. Tomila, and V. Manzhara, "Comparative investigation of Si-C-N Films prepared by plasma enhanced chemical vapour deposition and magnetron sputtering," *Applied Surface Science*, vol. 425, pp. 646–653, 2017. DOI: 10.1016/j.apsusc.2017.06.332.

[277] J. Xu, L. Yang, Y. Rui, J. Mei, X. Zhang, W. Li, Z. Ma, L. Xu, X. Huang, and K. Chen, "Photoluminescence characteristics from amorphous SiC thin films with various structures deposited at low temperature," *Solid State Communications*, vol. 133, no. 9, pp. 565–568, 2005. DOI: 10.1016/j.ssc.2004.12.036.

[278] Y. Catherine and G. Turban, "Infrared absorption of hydrogenated amorphous Si-C and Ge-C films," *Thin Solid Films*, vol. 70, no. 1, pp. 101–104, 1980. DOI: 10.1016/0040-6090(80)90416-2.

[279] C. Zoita, C. Grigorescu, I. Vasiliu, and I. Feraru, "Influence of process parameters on structure and optical properties of GeC thin films deposited by RF magnetron sputtering," *Thin Solid Films*, vol. 519, no. 12, pp. 4101–4104, 2011. DOI: 10.1016/j.tsf.2011.01.204.

[280] I. Vivaldo, M. Moreno, A. Torres, R. Ambrosio, P. Rosales, N. Carlos, W. Calleja, K. Monfil, and A. Benítez, "A comparative study of amorphous silicon carbide and silicon rich oxide for light emission applications," *Journal of Luminescence*, vol. 190, pp. 215–220, 2017. DOI: 10.1016/j.jlumin.2017.05.048.

[281] J. Szmidt, "Electrophysical properties of thin germanium/carbon layers produced on silicon using organometallic radio frequency plasma enhanced chemical vapor deposition process," *Thin Solid Films*, vol. 441, no. 1-2, pp. 192–199, 2003. DOI: 10.1016/S0040-6090(03)00884-8.

[282] J. Tyczkowski, P. Kazimierski, and H. Szymanowski, "Correlations between process parameters, chemical structure and electronic properties of amorphous hydrogenated Ge_xC_{1-x} films prepared by plasma-enhanced chemical vapour deposition in a three-electrode reactor," *Thin Solid Films*, vol. 241, no. 1-2, pp. 291–294, 1994. DOI: 10.1016/0040-6090(94)90444-8.

[283] R. Cross and F. Glockling, "Infrared spectra of organogermanes," *Journal of Organometallic Chemistry*, vol. 3, no. 2, pp. 146–155, 1965. DOI: 10.1016/S0022-328X(00)84744-0.

[284] N. Saito, I. Nakaaki, T. Yamaguchi, S. Yoshioka, and S. Nakamura, "Influence of deposition conditions on the properties of a-GeC:H and a-Ge:H films prepared by r.f. magnetron sputtering," *Thin Solid Films*, vol. 269, no. 1-2, pp. 69–74, 1995. DOI: 10.1016/0040-6090(95)06671-3.

[285] E. Abdelrazek, I. Elashmawi, A. El-khodary, and A. Yassin, "Structural, optical, thermal and electrical studies on PVA/PVP blends filled with lithium bromide," *Current Applied Physics*, vol. 10, no. 2, pp. 607–613, 2010. DOI: 10.1016/j.cap.2009.08.005.

[286] A. Tawansi, A. Oraby, H. Zidan, and M. Dorgham, "Effect of one-dimensional phenomena on electrical, magnetic and ESR properties of $MnCl_2$-filled PVA films," *Physica B: Condensed Matter*, vol. 254, no. 1-2, pp. 126–133, 1998. DOI: 10.1016/S0921-4526(98)00414-1.

[287] M. Martin, *Characteristic IR Band Positions*.

[288] H. Jamali, R. Mozafarinia, and A. Eshaghi, "Evaluation of chemical and structural properties of germanium-carbon coatings deposited by plasma enhanced chemical vapor deposition," *Journal of Alloys and Compounds*, vol. 646, pp. 360–367, 2015. DOI: 10.1016/j.jallcom.2015.06.091.

[289] N. Ojha, A. Bajpai, and S. Kumar, "Enriched oxygen vacancies of $Cu_2O/SnS_2/SnO_2$ heterostructure for enhanced photocatalytic reduction of CO_2 by water and nitrogen fixation," *Journal of Colloid and Interface Science*, vol. 585, pp. 764–777, 2021. DOI: 10.1016/j.jcis.2020.10.056.

[290] H. Zhang, Y. Li, J. Wang, N. Wu, H. Sheng, C. Chen, and J. Zhao, "An unprecedent hydride transfer pathway for selective photocatalytic reduction of CO_2 to formic acid on TiO_2," *Applied Catalysis B: Environmental*, vol. 284, p. 119 692, 2021. DOI: 10.1016/j.apcatb.2020.119692.

[291] S. W. Pyo, C. Manianglung, and Y. S. Ko, "In-situ IR study on stability of amine-impregnated CO_2 adsorbents to acidic gases," *Catalysis Today*, vol. 352, pp. 198–203, 2020. DOI: 10.1016/j.cattod.2020.01.036.

[292] L. Wang, H. Tan, L. Zhang, B. Cheng, and J. Yu, "In-situ growth of few-layer graphene on ZnO with intimate interfacial contact for enhanced photocatalytic CO_2 reduction activity," *Chemical Engineering Journal*, vol. 411, p. 128 501, 2021. DOI: 10.1016/j.cej.2021.128501.

[293] C. Pirim and L. Krim, "A neon-matrix isolation study of the reaction of non-energetic H-atoms with CO molecules at 3 K," *Physical Chemistry Chemical Physics*, vol. 13, no. 43, p. 19 454, 2011. DOI: 10.1039/c1cp21835b.

[294] Y. Yashiki, S. Kouketsu, S. Miyajima, A. Yamada, and M. Konagai, "Growth and Characterization of Germanium Carbon Thin Films Deposited by VHF Plasma CVD Technique," in *2006 IEEE 4th World Conference on Photovoltaic Energy Conference*, vol. 2, IEEE, 2006, pp. 1608–1611. DOI: 10.1109/WCPEC.2006.279794.

[295] J. Zhu, C. Jiang, J. Han, H. Yu, J. Wang, Z. Jia, and R. Chen, "Optical and electrical properties of nonstoichiometric a-$Ge_{1-x}C_x$ films prepared by magnetron co-sputtering," *Applied Surface Science*, vol. 258, no. 8, pp. 3877–3881, 2012. DOI: 10.1016/j.apsusc.2011.12.051.

[296] P. Klement, C. Feser, B. Hanke, K. V. Maydell, and C. Agert, "Correlation between optical emission spectroscopy of hydrogen/germane plasma and the Raman crystallinity factor of germanium layers," *Applied Physics Letters*, vol. 102, no. 15, p. 152 109, 2013. DOI: 10.1063/1.4802028.

[297] J. Coates, "Interpretation of Infrared Spectra, A Practical Approach," in *Encyclopedia of Analytical Chemistry*, 2004, pp. 1–23.

[298] A. B. D. Nandiyanto, R. Oktiani, and R. Ragadhita, "How to read and interpret ftir spectroscope of organic material," *Indonesian Journal of Science and Technology*, vol. 4, no. 1, pp. 97–118, 2019. DOI: 10.17509/ijost.v4i1.15806.

[299] C. Hu, L. Qiao, H. Tian, X. Lu, Q. Jiang, and W. Zheng, "Role of carbon in the formation of hard $Ge_{1-x}C_x$ thin films by reactive magnetron sputtering," *Physica B: Condensed Matter*, vol. 406, no. 13, pp. 2658–2662, 2011. DOI: 10.1016/j.physb.2011.01.077.

[300] C. Jiang, J. Zhu, J. Han, Z. Jia, and X. Yin, "Chemical bonding and optical properties of germanium–carbon alloy films prepared by magnetron co-sputtering as a function of substrate temperature," *Journal of Non-Crystalline Solids*, vol. 357, no. 24, pp. 3952–3956, 2011. DOI: 10.1016/j.jnoncrysol.2011.08.014.

[301] P. W. Morrison and J. R. Haigis, "In situ infrared measurements of film and gas properties during the plasma deposition of amorphous hydrogenated silicon," *Journal of Vacuum Science & Technology A: Vacuum, Surfaces, and Films*, vol. 11, no. 3, pp. 490–502, 1993. DOI: 10.1116/1.578761.

[302] A. H. M. Smets, T. Matsui, and M. Kondo, "Infrared analysis of the bulk silicon-hydrogen bonds as an optimization tool for high-rate deposition of microcrystalline silicon solar cells," *Applied Physics Letters*, vol. 92, no. 3, p. 033 506, 2008. DOI: 10.1063/1.2837536.

[303] H. J. Stein, S. M. Myers, and D. M. Follstaedt, "Infrared spectroscopy of chemically bonded hydrogen at voids and defects in silicon," *Journal of Applied Physics*, vol. 73, pp. 2755–2764, 1993. DOI: 10.1063/1.353050.

[304] J. Baum, K. K. Gleason, A. Pines, A. N. Garroway, and J. A. Reimer, "Multiple-Quantum NMR Study of Clustering in Hydrogenated Amorphous Silicon," *Physical Review Letters*, vol. 56, no. 13, pp. 1377–1380, 1986. DOI: 10.1103/PhysRevLett.56.1377.

[305] E. Gericke, J. Melskens, R. Wendt, M. Wollgarten, A. Hoell, and K. Lips, "Quantification of Nanoscale Density Fluctuations in Hydrogenated Amorphous Silicon," *Physical Review Letters*, vol. 125, no. 18, p. 185 501, 2020. DOI: 10.1103/PhysRevLett.125.185501.

[306] J. Melskens, A. H. M. Smets, M. Schouten, S. W. H. Eijt, H. Schut, and M. Zeman, "New Insights in the Nanostructure and Defect States of Hydrogenated Amorphous Silicon Obtained by Annealing," *IEEE Journal of Photovoltaics*, vol. 3, no. 1, pp. 65–71, 2013. DOI: 10.1109/JPHOTOV.2012.2226870.

[307] J. Melskens, A. Smets, S. Eijt, H. Schut, E. Brück, and M. Zeman, "The nanostructural analysis of hydrogenated silicon films based on positron annihilation studies," *Journal of Non-Crystalline Solids*, vol. 358, no. 17, pp. 2015–2018, 2012. DOI: 10.1016/j.jnoncrysol.2012.01.037.

[308] A. H. Mahan, Y. Xu, D. L. Williamson, W. Beyer, J. D. Perkins, M. Vanecek, L. M. Gedvilas, and B. P. Nelson, "Structural properties of hot wire a-Si:H films deposited at rates in excess of 100 Å/s," *Journal of Applied Physics*, vol. 90, no. 10, pp. 5038–5047, 2001. DOI: 10.1063/1.1407317.

[309] V. G. Bhide, R. O. Dusane, S. V. Rajarshi, A. D. Shaligram, and S. K. David, "Positron-lifetime studies of hydrogenated amorphous silicon," *Journal of Applied Physics*, vol. 62, no. 1, pp. 108–116, 1987. DOI: 10.1063/1.339167.

[310] H. Fritzsche, *Amorphous silicon and related materials*. Singapore: World Scientific Publishing Co.Pte. Ltd., 1989.

[311] D. Bermejo and M. Cardona, "Raman scattering in pure and hydrogenated amorphous germanium and silicon," *Journal of Non-Crystalline Solids*, vol. 32, no. 1-3, pp. 405–419, 1979. DOI: 10.1016/0022-3093(79)90085-1.

[312] Y. Maeda, "Visible photoluminescence from nanocrystallite Ge embedded in a glassy SiO_2 matrix: Evidence in support of the quantum-confinement mechanism.," *Physical Review B*, vol. 51, no. 3, pp. 1658–1670, 1995. DOI: 10.1103/PhysRevB.51.1658.

[313] V. A. Volodin, D. V. Marin, V. A. Sachkov, E. B. Gorokhov, H. Rinnert, and M. Vergnat, "Applying an improved phonon confinement model to the analysis of Raman spectra of germanium nanocrystals," *Journal of Experimental and Theoretical Physics*, vol. 118, no. 1, pp. 65–71, 2014. DOI: 10.1134/S1063776114010208.

[314] A. Zanatta, "Temperature-dependent Raman scattering of the Ge + GeO_x system and its potential as an optical thermometer," *Results in Physics*, vol. 19, p. 103 500, 2020. DOI: 10.1016/j.rinp.2020.103500.

[315] G. Fraysse, A. Lignie, P. Hermet, P. Armand, D. Bourgogne, J. Haines, B. Ménaert, and P. Papet, "Vibrational Origin of the Thermal Stability in the Highly Distorted α-Quartz-Type Material GeO_2: An Experimental and Theoretical Study," *Inorganic Chemistry*, vol. 52, no. 12, pp. 7271–7279, 2013. DOI: 10.1021/ic4009416.

[316] J. Scott, "Raman spectra of GeO_2," *Physical Review B*, vol. 1, no. 8, pp. 3488–3493, 1970.

[317] S. Y. Park, J. D'Arcy-Gall, D. Gall, Y.-W. Kim, P. Desjardins, and J. E. Greene, "C lattice site distributions in metastable $Ge_{1-y}C_y$ alloys grown on Ge(001) by molecular-beam epitaxy," *Journal of Applied Physics*, vol. 91, no. 6, pp. 3644–3652, 2002. DOI: 10.1063/1.1448677.

[318] M. Losurdo, M. Giangregorio, P. Capezzuto, G. Bruno, and F. Giorgis, "Structural and optical investigation of plasma deposited silicon carbon alloys: Insights on Si-C bond configuration using spectroscopic ellipsometry," *Journal of Applied Physics*, vol. 97, no. 10, p. 103 504, 2005. DOI: 10.1063/1.1899758.

[319] C. Srisang, P. Asanithi, K. Siangchaew, A. Pokaipisit, and P. Limsuwan, "Characterization of SiC in DLC/a-Si films prepared by pulsed filtered cathodic arc using Raman spectroscopy and XPS," *Applied Surface Science*, vol. 258, no. 15, pp. 5605–5609, 2012. DOI: 10.1016/j.apsusc.2012.02.036.

[320] N. Gupta, B. P. Veettill, G. Conibeer, and S. Shrestha, "Effect of substrate temperature and radio frequency power on compositional, structural and optical properties of amorphous germanium carbide films deposited using sputtering," *Journal of Non-Crystalline Solids*, vol. 443, pp. 97–102, 2016. DOI: 10.1016/j.jnoncrysol.2016.04.018.

[321] J. Hong, A. Goullet, and G. Turban, "Ellipsometry and Raman study on hydrogenated amorphous carbon (a-C:H) films deposited in a dual ECR-r.f. plasma," *Thin Solid Films*, vol. 352, no. 1-2, pp. 41–48, 1999. DOI: 10.1016/S0040-6090(99)00298-9.

[322] J. Schwan, S. Ulrich, V. Batori, H. Ehrhardt, and S. R. P. Silva, "Raman spectroscopy on amorphous carbon films," *Journal of Applied Physics*, vol. 80, no. 1, pp. 440–447, 1996. DOI: 10.1063/1.362745.

[323] L. Han, M. Zeman, and A. H. M. Smets, "Raman study of laser-induced heating effects in free-standing silicon nanocrystals," *Nanoscale*, vol. 7, no. 18, pp. 8389–8397, 2015. DOI: 10.1039/C5NR00468C.

[324] D. Rouchon, M. Mermoux, F. Bertin, and J. Hartmann, "Germanium content and strain in $Si_{1-x}Ge_x$ alloys characterized by Raman spectroscopy," *Journal of Crystal Growth*, vol. 392, pp. 66–73, 2014. DOI: 10.1016/j.jcrysgro.2014.01.019.

[325] P. Pearce, T. Wilson, A. Johnson, and N. Ekins-Daukes, "Characterization of SiGeSn for Use as a 1 eV Sub-Cell in Multi-Junction Solar Cells," in *2018 IEEE 7th World Conference on Photovoltaic Energy Conversion (WCPEC) (A Joint Conference of 45th IEEE PVSC, 28th PVSEC & 34th EU PVSEC)*, IEEE, 2018, pp. 0943–0948. DOI: 10.1109/PVSC.2018.8547764.

[326] N. von den Driesch, D. Stange, S. Wirths, G. Mussler, B. Holländer, Z. Ikonic, J. M. Hartmann, T. Stoica, S. Mantl, D. Grützmacher, and D. Buca, "Direct Bandgap Group IV Epitaxy on Si for Laser Applications," *Chemistry of Materials*, vol. 27, no. 13, pp. 4693–4702, 2015. DOI: 10.1021/acs.chemmater.5b01327.

[327] S. Su, W. Wang, B. Cheng, W. Hu, G. Zhang, C. Xue, Y. Zuo, and Q. Wang, "The contributions of composition and strain to the phonon shift in alloys," *Solid State Communications*, vol. 151, no. 8, pp. 647–650, 2011. DOI: 10.1016/j.ssc.2011.01.017.

[328] IPCC, "Climate Change 2021: The Physical Science Basis. Contribution of Working Group I to the Sixth Assessment Report of the Intergovernmental Panel on Climate Change," Tech. Rep., 2021.

[329] M. B. Ross, P. De Luna, Y. Li, C.-T. Dinh, D. Kim, P. Yang, and E. H. Sargent, "Designing materials for electrochemical carbon dioxide recycling," *Nature Catalysis*, vol. 2, no. 8, pp. 648–658, 2019. DOI: 10.1038/s41929-019-0306-7.

[330] Z. Guo, G. Chen, C. Cometto, B. Ma, H. Zhao, T. Groizard, L. Chen, H. Fan, W.-L. Man, S.-M. Yiu, K.-C. Lau, T.-C. Lau, and M. Robert, "Selectivity control of CO versus HCOO⁻ production in the visible-light-driven catalytic reduction of CO_2 with two cooperative metal sites," *Nature Catalysis*, vol. 2, no. 9, pp. 801–808, 2019. DOI: 10.1038/s41929-019-0331-6.

[331] H. Yuan, B. Cheng, J. Lei, L. Jiang, and Z. Han, "Promoting photocatalytic CO_2 reduction with a molecular copper purpurin chromophore," *Nature Communications*, vol. 12, no. 1, p. 1835, 2021. DOI: 10.1038/s41467-021-21923-9.

[332] J.-Y. Kim, D. Hong, J.-C. Lee, H. G. Kim, S. Lee, S. Shin, B. Kim, H. Lee, M. Kim, J. Oh, G.-D. Lee, D.-H. Nam, and Y.-C. Joo, "Quasi-graphitic carbon shell-induced Cu confinement promotes electrocatalytic CO_2 reduction toward C_{2+} products," *Nature Communications*, vol. 12, no. 1, p. 3765, 2021. DOI: 10.1038/s41467-021-24105-9.

[333] P. Stewart, "Abundance of the elements - a new look," *Education in Chemistry*, vol. 40, no. 1, pp. 23–24, 2003.

[334] Y. Y. Lee, H. S. Jung, and Y. T. Kang, "A review: Effect of nanostructures on photocatalytic CO_2 conversion over metal oxides and compound semiconductors," *Journal of CO_2 Utilization*, vol. 20, pp. 163–177, 2017. DOI: 10.1016/j.jcou.2017.05.019.

[335] L. Liu, S. Wang, H. Huang, Y. Zhang, and T. Ma, "Surface sites engineering on semiconductors to boost photocatalytic CO_2 reduction," *Nano Energy*, vol. 75, p. 104 959, 2020. DOI: 10.1016/j.nanoen.2020.104959.

[336] J. Feng, H. Huang, S. Yan, W. Luo, T. Yu, Z. Li, and Z. Zou, "Non-oxide semiconductors for artificial photosynthesis: Progress on photoelectrochemical water splitting and carbon dioxide reduction," *Nano Today*, vol. 30, p. 100 830, 2020. DOI: 10.1016/j.nantod.2019.100830.

[337] S. K. Estreicher and D. M. Maric, "What is so strange about hydrogen interactions in germanium?" *Physical Review Letters*, vol. 70, no. 25, pp. 3963–3966, 1993. DOI: 10.1103/PhysRevLett.70.3963.

[338] C. G. van de Walle and J. Neugebauer, "Universal alignment of hydrogen levels in semiconductors insulators and solutions," *Nature*, vol. 423, pp. 626–628, 2003.

[339] Q. Lu, Y. Yu, Q. Ma, B. Chen, and H. Zhang, "2D Transition-Metal-Dichalcogenide-Nanosheet-Based Composites for Photocatalytic and Electrocatalytic Hydrogen Evolution Reactions," *Advanced Materials*, vol. 28, no. 10, pp. 1917–1933, 2016. DOI: 10.1002/adma.201503270.

[340] C. Van de Walle, J. Weber, and A. Janotti, "Role of hydrogen at germanium/dielectric interfaces," *Thin Solid Films*, vol. 517, no. 1, pp. 144–147, 2008. DOI: 10.1016/j.tsf.2008.08.071.

[341] J. F. Binder, P. Broqvist, and A. Pasquarello, "Charge trapping in substoichiometric germanium oxide," *Microelectronic Engineering*, vol. 88, no. 7, pp. 1428–1431, 2011. DOI: 10.1016/j.mee.2011.03.133.

[342] A. Ohta, H. Nakagawa, H. Murakami, S. Higashi, and S. Miyazaki, "Photoemission Study of Ultrathin GeO_2/Ge Heterostructures Formed by UV-O_3 Oxidation," *e-Journal of Surface Science and Nanotechnology*, vol. 4, pp. 174–179, 2006. DOI: 10.1380/ejssnt.2006.174.

[343] M. Perego, G. Scarel, M. Fanciulli, I. L. Fedushkin, and A. A. Skatova, "Fabrication of GeO_2 layers using a divalent Ge precursor," *Applied Physics Letters*, vol. 90, no. 16, p. 162 115, 2007. DOI: 10.1063/1.2723684.

[344] M. Yang, R. Q. Wu, Q. Chen, W. S. Deng, Y. P. Feng, J. W. Chai, J. S. Pan, and S. J. Wang, "Impact of oxide defects on band offset at GeO_2/Ge interface," *Applied Physics Letters*, vol. 94, no. 14, p. 142 903, 2009. DOI: 10.1063/1.3115824.

[345] B. L. Ong, S. W. Ong, A. Rusydi, and E. S. Tok, "Important roles of native-oxides on the electronic band offsets at Ge-oxide/Ge(0 0 1) heterojunction in ambient environment," *Applied Surface Science*, vol. 530, p. 147 256, 2020. DOI: 10.1016/j.apsusc.2020.147256.

[346] S. Kreft, D. Wei, H. Junge, and M. Beller, "Recent advances on TiO_2-based photocatalytic CO_2 reduction," *EnergyChem*, vol. 2, no. 6, p. 100 044, 2020. DOI: 10.1016/j.enchem.2020.100044.

[347] S. Fadida, M. Eizenberg, L. Nyns, S. Van Elshocht, and M. Caymax, "Band alignment of Hf–Zr oxides on $Al_2O_3/GeO_2/Ge$ stacks," *Microelectronic Engineering*, vol. 88, no. 7, pp. 1557–1559, 2011. DOI: 10.1016/j.mee.2011.03.075.

[348] L. F. Garay-Rodríguez, L. M. Torres-Martínez, and E. Moctezuma, "Photocatalytic evaluation of composites of $Ba_3Li_2Ti_8O_{20}$-CuO in the reduction of CO_2 to formaldehyde under visible light irradiation," *Journal of Photochemistry and Photobiology A: Chemistry*, vol. 361, pp. 25–33, 2018. DOI: 10.1016/j.jphotochem.2018.05.003.

[349] T. Ando and X.-A. Fu, "Materials: Silicon and beyond," *Sensors and Actuators A: Physical*, vol. 296, pp. 340–351, 2019. DOI: 10.1016/j.sna.2019.07.009.

[350] M. Ordu and S. N. Basu, "Recent progress in germanium-core optical fibers for mid-infrared optics," *Infrared Physics & Technology*, vol. 111, p. 103 507, 2020. DOI: 10.1016/j.infrared.2020.103507.

[351] C. Mishra and G. Palai, "Optical nonlinearity in germanium and silicon semiconductor vis-a-vis temperature and wavelengths for sensing application," *Optik*, vol. 137, pp. 37–44, 2017. DOI: 10.1016/j.ijleo.2017.02.092.

[352] R. Soref, "Mid-infrared photonics in silicon and germanium," *Nature Photonics*, vol. 4, no. 8, pp. 495–497, 2010. DOI: 10.1038/nphoton.2010.171.

[353] D. Colombara, H. Elanzeery, N. Nicoara, D. Sharma, M. Claro, T. Schwarz, A. Koprek, M. H. Wolter, M. Melchiorre, M. Sood, N. Valle, O. Bondarchuk, F. Babbe, C. Spindler, O. Cojocaru-Miredin, D. Raabe, P. J. Dale, S. Sadewasser, and S. Siebentritt, "Chemical instability at chalcogenide surfaces impacts chalcopyrite devices well beyond the surface," *Nature Communications*, vol. 11, no. 1, p. 3634, 2020. DOI: 10.1038/s41467-020-17434-8.

[354] K. Pal, P. Singh, A. Bhaduri, and K. B. Thapa, "Current challenges and future prospects for a highly efficient (>20%) kesterite CZTS solar cell: A review," *Solar Energy Materials and Solar Cells*, vol. 196, pp. 138–156, 2019. DOI: 10.1016/j.solmat.2019.03.001.

[355] T. Ratz, G. Brammertz, R. Caballero, M. León, S. Canulescu, J. Schou, L. Gütay, D. Pareek, T. Taskesen, D.-H. Kim, J.-K. Kang, C. Malerba, A. Redinger, E. Saucedo, B. Shin, H. Tampo, K. Timmo, N. D. Nguyen, and B. Vermang, "Physical routes for the synthesis of kesterite," *Journal of Physics: Energy*, vol. 1, no. 4, p. 042 003, 2019. DOI: 10.1088/2515-7655/ab281c.

[356] J.-F. Guillemoles, L. Kronik, D. Cahen, U. Rau, A. Jasenek, and H.-w. Schock, "Stability Issues of $Cu(In,Ga)Se_2$-Based Solar Cells," *The Journal of Physical Chemistry B*, vol. 104, no. 20, pp. 4849–4862, 2000. DOI: 10.1021/jp993143k.

[357] H. J. Snaith and P. Hacke, "Enabling reliability assessments of pre-commercial perovskite photovoltaics with lessons learned from industrial standards," *Nature Energy*, vol. 3, no. 6, pp. 459–465, 2018. DOI: 10.1038/s41560-018-0174-4.

[358] T. Leijtens, K. A. Bush, R. Prasanna, and M. D. McGehee, "Opportunities and challenges for tandem solar cells using metal halide perovskite semiconductors," *Nature Energy*, vol. 3, no. 10, pp. 828–838, 2018. DOI: 10.1038/s41560-018-0190-4.

[359] W. Xiang, S. Liu, and W. Tress, "A review on the stability of inorganic metal halide perovskites: challenges and opportunities for stable solar cells," *Energy & Environmental Science*, vol. 14, no. 4, pp. 2090–2113, 2021. DOI: 10.1039/D1EE00157D.

[360] S. D. Stranks and H. J. Snaith, "Metal-halide perovskites for photovoltaic and light-emitting devices," *Nature Nanotechnology*, vol. 10, no. 5, pp. 391–402, 2015. DOI: 10.1038/nnano.2015.90.

[361] K. O. Brinkmann, T. Gahlmann, and T. Riedl, "Atomic Layer Deposition of Functional Layers in Planar Perovskite Solar Cells," *Solar RRL*, vol. 4, no. 1, p. 1 900 332, 2020. DOI: 10.1002/solr.201900332.

[362] W. Zhao and Y. Duan, "Advanced Applications of Atomic Layer Deposition in Perovskite-Based Solar Cells," *Advanced Photonics Research*, vol. 2100011, no. 2, 2021. DOI: 10.1002/adpr.202100011.

[363] S. Giraldo, Z. Jehl, M. Placidi, V. Izquierdo-Roca, A. Pérez-Rodríguez, and E. Saucedo, "Progress and Perspectives of Thin Film Kesterite Photovoltaic Technology: A Critical Review," *Advanced Materials*, vol. 31, no. 16, p. 1 806 692, 2019. DOI: 10.1002/adma.201806692.

[364] S. Delbos, "Kësterite thin films for photovoltaics : a review," *EPJ Photovoltaics*, vol. 3, p. 35 004, 2012. DOI: 10.1051/epjpv/2012008.

[365] Z. Fan, K. Sun, and J. Wang, "Perovskites for photovoltaics: a combined review of organic–inorganic halide perovskites and ferroelectric oxide perovskites," *Journal of Materials Chemistry A*, vol. 3, no. 37, pp. 18 809–18 828, 2015. DOI: 10.1039/C5TA04235F.

[366] Q. A. Akkerman, G. Rainò, M. V. Kovalenko, and L. Manna, "Genesis, challenges and opportunities for colloidal lead halide perovskite nanocrystals," *Nature Materials*, vol. 17, no. 5, pp. 394–405, 2018. DOI: 10.1038/s41563-018-0018-4.

[367] T. de Vrijer, B. Bouazzata, and A. H. M. Smets, "Spectroscopic review of hydrogenated , carbonated and oxygenated group IV alloys," *Vibrational Spectroscopy*, 2022. DOI: 10.1016/j.vibspec.2022.103387.

[368] R. L. Moon, G. A. Antypas, and L. W. James, "Bandgap and lattice constant of GaInAsP as a function of alloy composition," *Journal of Electronic Materials*, vol. 3, no. 3, pp. 635–644, 1974. DOI: 10.1007/BF02655291.

[369] M. A. Humayun, M. A. Rashid, F. A. Malek, and A. N. Hussain, "Effect of lattice constant on band-gap energy and optimization and stabilization of high-temperature $In_xGa_{1-x}N$ quantum-dot lasers," *Journal of Russian Laser Research*, vol. 33, no. 4, pp. 387–394, 2012. DOI: 10.1007/s10946-012-9294-7.

[370] S. Dinca, G. Ganguly, Z. Lu, E. A. Schiff, V. Vlahos, C. R. Wronski, and Q. Yuan, "Hole Drift-Mobility Measurements in Contemporary Amorphous Silicon," *MRS Proceedings*, vol. 762, A7.1, 2003. DOI: 10.1557/PROC-762-A7.1.

[371] J. Melskens, M. Schouten, R. Santbergen, M. Fischer, R. Vasudevan, D. van der Vlies, R. Quax, S. Heirman, K. Jäger, V. Demontis, M. Zeman, and A. Smets, "In situ manipulation of the sub gap states in hydrogenated amorphous silicon monitored by advanced application of Fourier transform photocurrent spectroscopy," *Solar Energy Materials and Solar Cells*, vol. 129, pp. 70–81, 2014. DOI: 10.1016/j.solmat.2014.03.022.

[372] S. J. Blanksby and G. B. Ellison, "Bond Dissociation Energies of Organic Molecules," *Accounts of Chemical Research*, vol. 36, no. 4, pp. 255–263, 2003. DOI: 10.1021/ar020230d.

[373] Y. Luo, "Handbook of Bond Dissociation Energies in Organic Compounds," *Journal of the American Chemical Society*, vol. 126, no. 3, pp. 982–982, 2004. DOI: 10.1021/ja0336224.

[374] M. Decouzon, J. Gal, J. Gayraud, P. Maria, G. Vaglio, and P. Volpe, "Fourier Transform-Ion Cyclotron Resonance Study of the Gas-Phase Acidities of Germane and Methylgermane; Bond Dissociation Energy of Germane," *Journal of the American Society for Mass Spectrometry*, vol. 4, pp. 54–57, 1993.

[375] I. Alkorta and J. Elguero, "Theoretical study of the bond energy in n-silanes and n-germanes: Comparison with n-alkanes," *Chemical Physics Letters*, vol. 429, no. 1-3, pp. 58–61, 2006. DOI: 10.1016/j.cplett.2006.08.012.

[376] S. Wirths, D. Buca, and S. Mantl, "Si–Ge–Sn alloys: From growth to applications," *Progress in Crystal Growth and Characterization of Materials*, vol. 62, no. 1, pp. 1–39, 2016. DOI: 10.1016/j.pcrysgrow.2015.11.001.

[377] Y. Zhou, W. Dou, W. Du, T. Pham, S. A. Ghetmiri, S. Al-Kabi, A. Mosleh, M. Alher, J. Margetis, J. Tolle, G. Sun, R. Soref, B. Li, M. Mortazavi, H. Naseem, and S.-Q. Yu, "Systematic study of GeSn heterostructure-based light-emitting diodes towards mid-infrared applications," *Journal of Applied Physics*, vol. 120, no. 2, p. 023 102, 2016. DOI: 10.1063/1.4958337.

[378] C. L. Senaratne, P. M. Wallace, J. D. Gallagher, P. E. Sims, J. Kouvetakis, and J. Menéndez, "Direct gap Ge$_{1-y}$Sn$_y$ alloys: Fabrication and design of mid-IR photodiodes," *Journal of Applied Physics*, vol. 120, no. 2, p. 025 701, 2016. DOI: 10.1063/1.4956439.

[379] R. Roucka, A. Clark, and B. Landini, "Si-Ge-Sn alloys with 1.0 eV gap for CPV multijunction solar cells," in *AIP Conference Proceedings*, vol. 1679, 2015, p. 040 008. DOI: 10.1063/1.4931519.

[380] S. Assali, J. Nicolas, and O. Moutanabbir, "Enhanced Sn incorporation in GeSn epitaxial semiconductors via strain relaxation," *Journal of Applied Physics*, vol. 125, no. 2, p. 025 304, 2019. DOI: 10.1063/1.5050273.

[381] M. Oehme, K. Kostecki, M. Schmid, F. Oliveira, E. Kasper, and J. Schulze, "Epitaxial growth of strained and unstrained GeSn alloys up to 25% Sn," *Thin Solid Films*, vol. 557, pp. 169–172, 2014. DOI: 10.1016/j.tsf.2013.10.064.

[382] W. Wang, L. Li, Q. Zhou, J. Pan, Z. Zhang, E. S. Tok, and Y.-C. Yeo, "Tin surface segregation, desorption, and island formation during post-growth annealing of strained epitaxial Ge$_{1-x}$Sn$_x$ layer on Ge(001) substrate," *Applied Surface Science*, vol. 321, pp. 240–244, 2014. DOI: 10.1016/j.apsusc.2014.10.011.

[383] R. Hickey, N. Fernando, S. Zollner, J. Hart, R. Hazbun, and J. Kolodzey, "Properties of pseudomorphic and relaxed germanium$_{1-x}$tin$_x$ alloys (x<0.185) grown by MBE," *Journal of Vacuum Science & Technology B, Nanotechnology and Microelectronics: Materials, Processing, Measurement, and Phenomena*, vol. 35, no. 2, p. 021 205, 2017. DOI: 10.1116/1.4975149.

[384] J. Bennett and R. Egerton, "Fabrication of Sn$_x$Ge$_{1-x}$ thin films with non-equilibrium composition," *Vacuum*, vol. 47, no. 12, pp. 1419–1422, 1996. DOI: 10.1016/S0042-207X(96)00219-9.

[385] J. Zheng, Z. Liu, Y. Zhang, Y. Zuo, C. Li, C. Xue, B. Cheng, and Q. Wang, "Growth of high-Sn content (28%) GeSn alloy films by sputtering epitaxy," *Journal of Crystal Growth*, vol. 492, pp. 29–34, 2018. DOI: 10.1016/j.jcrysgro.2018.04.008.

[386] L. Zhang, Y. Wang, N. Chen, G. Lin, C. Li, W. Huang, S. Chen, J. Xu, and J. Wang, "Raman scattering study of amorphous GeSn films and their crystallization on Si substrates," *Journal of Non-Crystalline Solids*, vol. 448, pp. 74–78, 2016. DOI: 10.1016/j.jnoncrysol.2016.07.007.

[387] J. Margetis, A. Mosleh, S. A. Ghetmiri, S. Al-Kabi, W. Dou, W. Du, N. Bhargava, S.-Q. Yu, H. Profijt, D. Kohen, R. Loo, A. Vohra, and J. Tolle, "Fundamentals of Ge$_{1-x}$Sn$_x$ and Si$_y$Ge$_{1-x-y}$Sn$_x$ RPCVD epitaxy," *Materials Science in Semiconductor Processing*, vol. 70, pp. 38–43, 2017. DOI: 10.1016/j.mssp.2016.12.024.

[388] J. Aubin, J. Hartmann, A. Gassenq, L. Milord, N. Pauc, V. Reboud, and V. Calvo, "Impact of thickness on the structural properties of high tin content GeSn layers," *Journal of Crystal Growth*, vol. 473, pp. 20–27, 2017. DOI: 10.1016/j.jcrysgro.2017.05.006.

[389] V. R. D'Costa, Y. Fang, J. Mathews, R. Roucka, J. Tolle, J. Menéndez, and J. Kouvetakis, "Sn-alloying as a means of increasing the optical absorption of Ge at the C - and L -telecommunication bands," *Semiconductor Science and Technology*, vol. 24, no. 11, p. 115 006, 2009. DOI: 10.1088/0268-1242/24/11/115006.

[390] M. Bauer, J. Taraci, J. Tolle, A. V. G. Chizmeshya, S. Zollner, D. J. Smith, J. Menendez, C. Hu, and J. Kouvetakis, "Ge–Sn semiconductors for band-gap and lattice engineering," *Applied Physics Letters*, vol. 81, no. 16, pp. 2992–2994, 2002. DOI: 10.1063/1.1515133.

[391] R. Temkin, G. Connell, and W. Paul, "Structural And Optical Properties Of Amorphous Ge$_x$Sn$_{1-x}$ Alloys," *Solid State Communications*, vol. 11, pp. 1591–1595, 1972.

[392] I. Chambouleyron and F. C. Marques, "Use of hydrogenation in the study of the properties of amorphous germanium tin alloys," *Journal of Applied Physics*, vol. 65, no. 4, pp. 1591–1597, 1989. DOI: 10.1063/1.342950.

[393] S. Sato, N. Yamaguchi, and H. Ozaki, "Pseudogap of Energy in Amorphous Ge-Sn Films," *Journal of the Physical Society of Japan*, vol. 33, no. 5, p. 1497, 1972. DOI: 10.1143/JPSJ.33.1497.

[394] K. Yoshioka, R. Yokogawa, and A. Ogura, "Anisotropic biaxial stress evaluation in metal-organic chemical vapor deposition grown Ge$_{1-x}$Sn$_x$ mesa structure by oil-immersion Raman spectroscopy," *Thin Solid Films*, vol. 697, p. 137 797, 2020. DOI: 10.1016/j.tsf.2020.137797.

[395] K. Suda, N. Sawamoto, H. Machida, M. Ishikawa, H. Sudoh, Y. Ohshita, I. Hirosawa, and A. Ogura, "Role of H$_2$ supply for Sn incorporations in MOCVD Ge$_{1-x}$Sn$_x$ epitaxial growth," *Journal of Crystal Growth*, vol. 468, pp. 605–609, 2017. DOI: 10.1016/j.jcrysgro.2016.12.085.

[396] A. Oliveira and M. Carreño, "Post thermal annealing crystallization and reactive ion etching of SiC films produced by PECVD," *Journal of Non-Crystalline Solids*, vol. 352, no. 9-20, pp. 1392–1397, 2006. DOI: 10.1016/j.jnoncrysol.2006.01.075.

[397] A. Morimoto, T. Miura, M. Kumeda, and T. Shimizu, "Glow Discharge a-Si 1- x C x : H Films Studied by ESR and IR Measurements," *Japanese Journal of Applied Physics*, vol. 21, no. Part 2, No. 2, pp. L119–L121, 1982. DOI: 10.1143/JJAP.21.L119.

[398] S.-Y. Lien, K.-W. Weng, J.-J. Huang, C.-H. Hsu, C.-T. Shen, C.-C. Wang, Y.-S. Lin, D.-S. Wuu, and D.-C. Wu, "Influence of CH4 flow rate on properties of HF-PECVD a-SiC films and solar cell application," *Current Applied Physics*, vol. 11, no. 1, S21–S24, 2011. DOI: 10.1016/j.cap.2010.11.009.

[399] M. Fathallah, R. Gharbi, G. Crovini, F. Demichelis, F. Giorgis, C. Pirri, E. Tresso, and P. Rava, "Light-soaking in a-SiC:H films grown by PECVD in undiluted and hydrogen diluted SiH$_4$ + CH$_4$ gas mixtures," *Journal of Non-Crystalline Solids*, vol. 198-200, no. PART 1, pp. 490–494, 1996. DOI: 10.1016/0022-3093(95)00754-7.

[400] H. Tran, W. Du, S. A. Ghetmiri, A. Mosleh, G. Sun, R. A. Soref, J. Margetis, J. Tolle, B. Li, H. A. Naseem, and S.-Q. Yu, "Systematic study of Ge 1x Sn x absorption coefficient and refractive index for the device applications of Si-based optoelectronics," *Journal of Applied Physics*, vol. 119, no. 10, p. 103 106, 2016. DOI: 10.1063/1.4943652.

[401] *TETRAMETHYLTIN, 99% — Gelest, Inc.*

[402] B. Ruscic, "Active Thermochemical Tables: Sequential Bond Dissociation Enthalpies of Methane, Ethane, and Methanol and the Related Thermochemistry," *The Journal of Physical Chemistry A*, vol. 119, no. 28, pp. 7810–7837, 2015. DOI: 10.1021/acs.jpca.5b01346.

[403] R. Cariou, J. Benick, F. Feldmann, O. Höhn, H. Hauser, P. Beutel, N. Razek, M. Wimplinger, B. Bläsi, D. Lackner, M. Hermle, G. Siefer, S. W. Glunz, A. W. Bett, and F. Dimroth, "III–V-on-silicon solar cells reaching 33% photoconversion efficiency in two-terminal configuration," *Nature Energy*, vol. 3, no. 4, pp. 326–333, 2018. DOI: 10.1038/s41560-018-0125-0.

[404] S. Kirner, M. Hammerschmidt, C. Schwanke, D. Lockau, S. Calnan, T. Frijnts, S. Neubert, A. Schopke, F. Schmidt, J.-H. Zollondz, A. Heidelberg, B. Stannowski, B. Rech, and R. Schlatmann, "Implications of TCO Topography on Intermediate Reflector Design for a-Si/μc-Si Tandem Solar Cells—Experiments and Rigorous Optical Simulations," *IEEE Journal of Photovoltaics*, vol. 4, no. 1, pp. 10–15, 2014. DOI: 10.1109/JPHOTOV.2013.2279204.

[405] S.-j. Jung, B.-j. Kim, and M. Shin, "Low-refractive-index and high-transmittance silicon oxide with a mixed phase of n-type microcrystalline silicon as intermediate reflector layers for tandem solar cells," *Solar Energy Materials and Solar Cells*, vol. 121, pp. 1–7, 2014. DOI: 10.1016/j.solmat.2013.10.036.

[406] Y. Zhao, L. Mazzarella, P. Procel, C. Han, G. Yang, A. Weeber, M. Zeman, and O. Isabella, "Doped hydrogenated nanocrystalline silicon oxide layers for high-efficiency c-Si heterojunction solar cells," *Progress in Photovoltaics: Research and Applications*, vol. 28, no. 5, pp. 425–435, 2020. DOI: 10.1002/pip.3256.

[407] Synopsys, "Sentaurus TCAD Datasheet," Tech. Rep., 2018.

[408] P. Procel, H. Xu, A. Saez, C. Ruiz-Tobon, L. Mazzarella, Y. Zhao, C. Han, G. Yang, M. Zeman, and O. Isabella, "The role of heterointerfaces and subgap energy states on transport mechanisms in silicon heterojunction solar cells," *Progress in Photovoltaics: Research and Applications*, vol. 28, no. 9, pp. 935–945, 2020. DOI: 10.1002/pip.3300.

[409] S. Schicho, *Amorphous and microcrystalline silicon applied in very thin tandem solar cells*. Forschungszentrum Jülich, 2011.

[410] P. Procel, G. Yang, O. Isabella, and M. Zeman, "Theoretical evaluation of contact stack for high efficiency IBC-SHJ solar cells," *Solar Energy Materials and Solar Cells*, vol. 186, pp. 66–77, 2018. DOI: 10.1016/j.solmat.2018.06.021.

[411] M. Bonnet-Eymard, M. Boccard, G. Bugnon, F. Meillaud, M. Despeisse, F.-J. Haug, and C. Ballif, "Current matching optimization in high-efficiency thin-film silicon tandem solar cells," in *2013 IEEE 39th Photovoltaic Specialists Conference (PVSC)*, IEEE, 2013, pp. 0184–0187. DOI: 10.1109/PVSC.2013.6744126.

[412] B. Yan, G. Yue, J. Yang, and S. Guha, "Correlation of current mismatch and fill factor in amorphous and nanocrystalline silicon based high efficiency multi-junction solar cells," in *33rd IEEE Photovolatic Specialists Conference*, IEEE, 2008, pp. 1–6. DOI: 10.1109/PVSC.2008.4922607.

[413] P.-W. Chen, P.-L. Chen, and C.-C. Tsai, "Development of wider bandgap n-type a-SiO$_x$:H and μc-SiO$_x$:H as both doped and intermediate reflecting layer for a-Si:H/a-Si$_{1-x}$Ge$_x$:H tandem solar cells," *Electronic Materials Letters*, vol. 12, no. 4, pp. 445–450, 2016. DOI: 10.1007/s13391-016-4004-1.

[414] M. Vukadinović, F. Smole, M. Topič, R. E. I. Schropp, and F. A. Rubinelli, "Transport in tunneling recombination junctions: A combined computer simulation study," *Journal of Applied Physics*, vol. 96, no. 12, pp. 7289–7299, 2004. DOI: 10.1063/1.1811375.

[415] Y. Zhao, P. Procel, C. Han, L. Mazzarella, G. Yang, A. Weeber, M. Zeman, and O. Isabella, "Design and optimization of hole collectors based on nc-SiO:H for high-efficiency silicon heterojunction solar cells," *Solar Energy Materials and Solar Cells*, vol. 219, p. 110 779, 2021. DOI: 10.1016/j.solmat.2020.110779.

[416] M. Stuckelberger, R. Biron, N. Wyrsch, F.-J. Haug, and C. Ballif, "Review: Progress in solar cells from hydrogenated amorphous silicon," *Renewable and Sustainable Energy Reviews*, vol. 76, pp. 1497–1523, 2017. DOI: 10.1016/j.rser.2016.11.190.

[417] L. Han, I. A. Digdaya, T. W. F. Buijs, F. F. Abdi, Z. Huang, R. Liu, B. Dam, M. Zeman, W. A. Smith, and A. H. M. Smets, "Gradient dopant profiling and spectral utilization of monolithic thin-film silicon photoelectrochemical tandem devices for solar water splitting," *Journal of Materials Chemistry A*, vol. 3, no. 8, pp. 4155–4162, 2015. DOI: 10.1039/C4TA05523C.

[418] J. Rongé, T. Bosserez, D. Martel, C. Nervi, L. Boarino, F. Taulelle, G. Decher, S. Bordiga, and J. A. Martens, "Monolithic cells for solar fuels," *Chem. Soc. Rev.*, vol. 43, no. 23, pp. 7963–7981, 2014. DOI: 10.1039/C3CS60424A.

[419] C. Han, Y. Zhao, L. Mazzarella, R. Santbergen, A. Montes, P. Procel, G. Yang, X. Zhang, M. Zeman, and O. Isabella, "Room-temperature sputtered tungsten-doped indium oxide for improved current in silicon heterojunction solar cells," *Solar Energy Materials and Solar Cells*, vol. 227, p. 111 082, 2021. DOI: 10.1016/j.solmat.2021.111082.

[420] T. Matsui, K. Maejima, A. Bidiville, H. Sai, T. Koida, T. Suezaki, M. Matsumoto, K. Saito, I. Yoshida, and M. Kondo, "High-efficiency thin-film silicon solar cells realized by integrating stable a-Si:H absorbers into improved device design," *Japanese Journal of Applied Physics*, vol. 54, no. 8S1, 08KB10, 2015. DOI: 10.7567/JJAP.54.08KB10.

[421] A. Lambertz, F. Finger, R. E. I. Schropp, U. Rau, and V. Smirnov, "Preparation and measurement of highly efficient a-Si:H single junction solar cells and the advantages of μc-SiO$_x$:H n-layers," *Progress in Photovoltaics: Research and Applications*, vol. 23, no. 8, pp. 939–948, 2015. DOI: 10.1002/pip.2629.

[422] S. K. Sardana, V. S. N. Chava, E. Thouti, N. Chander, S. Kumar, S. R. Reddy, and V. K. Komarala, "Influence of surface plasmon resonances of silver nanoparticles on optical and electrical properties of textured silicon solar cell," *Applied Physics Letters*, vol. 104, no. 7, p. 073 903, 2014. DOI: 10.1063/1.4866163.

[423] J. Chantana, Y. Yang, Y. Sobajima, C. Sada, A. Matsuda, and H. Okamoto, "Localized surface plasmon enhanced microcrystalline-silicon solar cells," *Journal of Non-Crystalline Solids*, vol. 358, no. 17, pp. 2319–2323, 2012. DOI: 10.1016/j.jnoncrysol.2011.12.038.

[424] H. Tan, L. Sivec, B. Yan, R. Santbergen, M. Zeman, and A. H. M. Smets, "Improved light trapping in microcrystalline silicon solar cells by plasmonic back reflector with broad angular scattering and low parasitic absorption," *Applied Physics Letters*, vol. 102, no. 15, p. 153 902, 2013. DOI: 10.1063/1.4802451.

[425] K. L. Kelly, E. Coronado, L. L. Zhao, and G. C. Schatz, "The Optical Properties of Metal Nanoparticles: The Influence of Size, Shape, and Dielectric Environment," *The Journal of Physical Chemistry B*, vol. 107, no. 3, pp. 668–677, 2003. DOI: 10.1021/jp026731y.

[426] C. Eminian, F.-J. Haug, O. Cubero, X. Niquille, and C. Ballif, "Photocurrent enhancement in thin film amorphous silicon solar cells with silver nanoparticles," *Progress in Photovoltaics: Research and Applications*, vol. 19, no. 3, pp. 260–265, 2011. DOI: 10.1002/pip.1015.

[427] E. Moulin, J. Sukmanowski, M. Schulte, A. Gordijn, F. Royer, and H. Stiebig, "Thin-film silicon solar cells with integrated silver nanoparticles," *Thin Solid Films*, vol. 516, no. 20, pp. 6813–6817, 2008. DOI: 10.1016/j.tsf.2007.12.018.

[428] H. R. Stuart and D. G. Hall, "Island size effects in nanoparticle-enhanced photodetectors," *Applied Physics Letters*, vol. 73, no. 26, pp. 3815–3817, 1998.

[429] B. Yan, G. Yue, L. Sivec, J. Yang, S. Guha, and C.-S. Jiang, "Innovative dual function nc-SiO$_x$:H layer leading to a ¿16% efficient multi-junction thin-film silicon solar cell," *Applied Physics Letters*, vol. 99, no. 11, p. 113 512, 2011. DOI: 10.1063/1.3638068.

[430] F. T. Si, O. Isabella, and M. Zeman, "Too Many Junctions? A Case Study of Multijunction Thin-Film Silicon Solar Cells," *Advanced Sustainable Systems*, vol. 1, no. 10, p. 1 700 077, 2017. DOI: 10.1002/adsu.201700077.

[431] K. Yoshikawa, H. Kawasaki, W. Yoshida, T. Irie, K. Konishi, K. Nakano, T. Uto, D. Adachi, M. Kanematsu, H. Uzu, and K. Yamamoto, "Silicon heterojunction solar cell with interdigitated back contacts for a photoconversion efficiency over 26%," *Nature Energy*, vol. 2, no. 5, p. 17 032, 2017. DOI: 10.1038/nenergy.2017.32.

[432] A. Richter, M. Hermle, and S. W. Glunz, "Reassessment of the Limiting Efficiency for Crystalline Silicon Solar Cells," *IEEE Journal of Photovoltaics*, vol. 3, no. 4, pp. 1184–1191, 2013. DOI: 10.1109/JPHOTOV.2013.2270351.

[433] European Environment Agency, *Share of electricity consumption in final energy consumption by region in 2004 and projections for 2030*.

[434] L. Han, F. F. Abdi, R. van de Krol, R. Liu, Z. Huang, H.-J. Lewerenz, B. Dam, M. Zeman, and A. H. M. Smets, "Efficient Water-Splitting Device Based on a Bismuth Vanadate Photoanode and Thin-Film Silicon Solar Cells," *ChemSusChem*, vol. 7, no. 10, pp. 2832–2838, 2014. DOI: 10.1002/cssc.201402456.

[435] T. Bosserez, L. Geerts, J. Rongé, F. Ceyssens, S. Haussener, R. Puers, and J. A. Martens, "Minimization of Ionic Transport Resistance in Porous Monoliths for Application in Integrated Solar Water Splitting Devices," *The Journal of Physical Chemistry C*, vol. 120, no. 38, pp. 21 242–21 247, 2016. DOI: 10.1021/acs.jpcc.6b06766.

[436] S. Wang, A. Lu, and C.-J. Zhong, "Hydrogen production from water electrolysis: role of catalysts," *Nano Convergence*, vol. 8, no. 1, p. 4, 2021. DOI: 10.1186/s40580-021-00254-x.

[437] B. You and Y. Sun, "Innovative Strategies for Electrocatalytic Water Splitting," *Accounts of Chemical Research*, vol. 51, no. 7, pp. 1571–1580, 2018. DOI: 10.1021/acs.accounts.8b00002.

[438] T. de Vrijer, M. Wiering, D. van Nijen, G. Padmakumar, S. Sambamurthy, G. Limodio, and A. H. M. Smets, "The optical performance of random and periodic textured crystalline silicon surfaces for photovoltaic applications," *Progress in Photovoltaics: under review*, 2022.

[439] R. Biron, C. Pahud, F.-j. Haug, J. Escarré, K. Söderström, and C. Ballif, "Window layer with p doped silicon oxide for high V$_{oc}$ thin-film silicon n-i-p solar cells," *Journal of Applied Physics*, vol. 110, no. 12, p. 124 511, 2011. DOI: 10.1063/1.3669389.

[440] T. Matsui, T. Fujibayashi, Y. Nasuno, H. Fukuhori, Y. Kanemitsu, M. Kondo, and a. Matsuda, "Impurity diffusion effect on p/i interface properties of p-i-n junction microcrystalline silicon solar cells," *3rd World Conference onPhotovoltaic Energy Conversion, 2003. Proceedings of*, vol. 2, pp. 1–4, 2003.

[441] G. Bugnon, G. Parascandolo, S. Hänni, M. Stuckelberger, M. Charrière, M. Despeisse, F. Meillaud, and C. Ballif, "Silicon oxide buffer layer at the p–i interface in amorphous and microcrystalline silicon solar cells," *Solar Energy Materials and Solar Cells*, vol. 120, pp. 143–150, 2014. DOI: 10.1016/j.solmat.2013.08.034.

[442] S. Agbo, J. Krč, R. van Swaaij, and M. Zeman, "Optimization of the p–i interface properties in thin film microcrystalline silicon solar cell," *Solar Energy Materials and Solar Cells*, vol. 94, no. 11, pp. 1864–1868, 2010. DOI: 10.1016/j.solmat.2010.06.034.

[443] B. Rech, T. Repmann, J. Hüpkes, M. Berginski, H. Stiebig, W. Beyer, V. Sittinger, and F. Ruske, "Recent Progress in Amorphous and Microcrystalline Silicon Based Solar Cell Technology," *20th European Photovoltaic Solar Energy Conference*, 2005.

[444] O. Vetterl, F. Finger, R. Carius, P. Hapke, L. Houben, O. Kluth, A. Lambertz, A. Möck, B. Rech, and H. Wagner, "Intrinsic microcrystalline silicon: A new materials for photovoltaics.," *Solar Energy Materials & Solar Cells*, vol. 62, no. 1/2, p. 97, 2000.

[445] P. Delli Veneri, P. Aliberti, L. V. Mercaldo, I. Usatii, and C. Privato, "Influence of microcrystalline silicon bottom cell on micromorph tandem solar cell performance," *Thin Solid Films*, vol. 516, no. 20, pp. 6979–6983, 2008. DOI: 10.1016/j.tsf.2007.12.032.

[446] S. Klein, F. Finger, R. Carius, and M. Stutzmann, "Deposition of microcrystalline silicon prepared by hot-wire chemical-vapor deposition: The influence of the deposition parameters on the material properties and solar cell performance," *Journal of Applied Physics*, vol. 98, no. 2, p. 024 905, 2005. DOI: 10.1063/1.1957128.

[447] M. van den Donker, B. Rech, R. Schmitz, J. Klomfass, G. Dingemans, F. Finger, L. Houben, W. Kessels, and M. van de Sanden, "Hidden parameters in the plasma deposition of microcrystalline silicon solar cells," *Journal of Materials Research*, vol. 22, no. 7, pp. 1767–1774, 2007. DOI: 10.1557/jmr.2007.0226.

[448] O. Astakhov, R. Carius, F. Finger, Y. Petrusenko, V. Borysenko, and D. Barankov, "Relationship between defect density and charge carrier transport in amorphous and microcrystalline silicon," *Physical Review B*, vol. 79, no. 10, p. 104 205, 2009. DOI: 10.1103/PhysRevB.79.104205.

[449] A. Shah, J. Meier, E. Vallat-Sauvain, N. Wyrsch, U. Kroll, C. Droz, and U. Graf, "Material and solar cell research in microcrystalline silicon," *Solar Energy Materials and Solar Cells*, vol. 78, no. 1-4, pp. 469–491, 2003. DOI: 10.1016/S0927-0248(02)00448-8.

[450] S. Guha, J. Yang, A. Banerjee, B. Yan, and K. Lord, "High quality amorphous silicon materials and cells grown with hydrogen dilution," *Solar Energy Materials and Solar Cells*, vol. 78, no. 1-4, pp. 329–347, 2003. DOI: 10.1016/S0927-0248(02)00441-5.

[451] M. N. van den Donker, S. Klein, B. Rech, F. Finger, W. M. M. Kessels, and M. C. M. van de Sanden, "Microcrystalline silicon solar cells with an open-circuit voltage above 600mV," *Applied Physics Letters*, vol. 90, no. 18, p. 183 504, 2007. DOI: 10.1063/1.2734375.

[452] F. T. Si, D. Y. Kim, R. Santbergen, H. Tan, R. A. C. M. M. v. Swaaij, A. H. M. Smets, O. Isabella, and M. Zeman, "Quadruple-junction thin-film silicon-based solar cells with high open-circuit voltage," *Applied Physics Letters*, vol. 105, no. 6, p. 063 902, 2014. DOI: 10.1063/1.4892890.

[453] H. Sai, T. Matsui, H. Kumagai, and K. Matsubara, "Thin-film microcrystalline silicon solar cells: 11.9% efficiency and beyond," *Applied Physics Express*, vol. 11, no. 2, p. 022 301, 2018. DOI: 10.7567/APEX.11.022301.

[454] E. Maruyama, S. Okamoto, A. Terakawa, W. Shinohara, M. Tanaka, and S. Kiyama, "Toward stabilized 10% efficiency of large-area (>5000 cm^2) a-Si/a-SiGe tandem solar cells using high-rate deposition," *Solar Energy Materials and Solar Cells*, vol. 74, no. 1-4, pp. 339–349, 2002. DOI: 10.1016/S0927-0248(02)00093-4.

[455] P.-K. Chang, C.-H. Lu, C.-H. Yeh, and M.-P. Houng, "High efficiency a-Si:H/a-Si:H solar cell with a tunnel recombination junction and a n-type μc-Si:H layer," *Thin Solid Films*, vol. 520, no. 9, pp. 3684–3687, 2012. DOI: 10.1016/j.tsf.2011.12.083.

[456] M. A. Green, E. D. Dunlop, J. Hohl-Ebinger, M. Yoshita, N. Kopidakis, and X. Hao, "Solar cell efficiency tables (Version 58)," *Progress in Photovoltaics: Research and Applications*, vol. 29, no. 7, pp. 657–667, 2021. DOI: 10.1002/pip.3444.

[457] G. Li, H. Li, J. Ho, M. Wong, and H.-S. Kwok, "Ultra-thin, high performance crystalline silicon tandem cells fabricated on a glass substrate," *Solar Energy Materials and Solar Cells*, vol. 141, pp. 225–231, 2015. DOI: 10.1016/j.solmat.2015.05.042.

[458] T. de Vrijer, A. Binani, D. van Nijen, T. Blackstone, F. Saitta, S. Miedema, H. Parasramska, S. J. Roerink, M. Wiering, G. Limodio, and A. H. Smets, "The versatile application of thin film silicon alloys in mutlijunction devices," *In preparation*, 2022.

[459] C. C. McCrory, S. Jung, I. M. Ferrer, S. M. Chatman, J. C. Peters, and T. F. Jaramillo, "Benchmarking Hydrogen Evolving Reaction and Oxygen Evolving Reaction Electrocatalysts for Solar Water Splitting Devices," *Journal of the American Chemical Society*, vol. 137, no. 13, pp. 4347–4357, 2015. DOI: 10.1021/JA510442P/SUPPL{_}FILE/JA510442P{_}SI{_}001.PDF.

[460] J. Jin, K. Walczak, M. R. Singh, C. Karp, N. S. Lewis, and C. Xiang, "An experimental and modeling/simulation-based evaluation of the efficiency and operational performance characteristics of an integrated, membrane-free, neutral pH solar-driven water-splitting system," *Energy Environ. Sci.*, vol. 7, no. 10, pp. 3371–3380, 2014. DOI: 10.1039/C4EE01824A.

[461] M. El Makkaoui, "Effect of Pore Size and Distribution on the PEC Properties of Si-Based Porous Monolithic Water-Splitting Devices," Ph.D. dissertation, TU Delft, 2020.

[462] M. Hasan, J. Zhao, and Z. Jiang, "A review of modern advancements in micro drilling techniques," *Journal of Manufacturing Processes*, vol. 29, pp. 343–375, 2017. DOI: 10.1016/j.jmapro.2017.08.006.

[463] B. Lips and R. Puers, "Three step deep reactive ion etch for high density trench etching," *Journal of Physics: Conference Series*, vol. 757, no. 1, p. 012 005, 2016. DOI: 10.1088/1742-6596/757/1/012005.

[464] H. V. Jansen, M. J. de Boer, S. Unnikrishnan, M. C. Louwerse, and M. C. Elwenspoek, "Black silicon method: X. A review on high speed and selective plasma etching of silicon with profile control: an in-depth comparison between Bosch and cryostat DRIE processes as a roadmap to next generation equipment," *Journal of Micromechanics and Microengineering*, vol. 19, no. 3, p. 033 001, 2009. DOI: 10.1088/0960-1317/19/3/033001.

[465] F. Laermer, S. Franssila, L. Sainiemi, and K. Kolari, "Deep Reactive Ion Etching," in *Handbook of Silicon Based MEMS Materials and Technologies*, Elsevier, 2010, pp. 349–374. DOI: 10.1016/B978-0-8155-1594-4.00023-1.

[466] T. Xu, Z. Tao, H. Li, X. Tan, and H. Li, "Effects of deep reactive ion etching parameters on etching rate and surface morphology in extremely deep silicon etch process with high aspect ratio," *Advances in Mechanical Engineering*, vol. 9, no. 12, p. 168 781 401 773 815, 2017. DOI: 10.1177/1687814017738152.

[467] Y. Chen, N. S. Lewis, and C. Xiang, "Operational constraints and strategies for systems to effect the sustainable, solar-driven reduction of atmospheric CO_2," *Energy & Environmental Science*, vol. 8, no. 12, pp. 3663–3674, 2015. DOI: 10.1039/C5EE02908B.

Acknowledgements

Naturally, this work would not have been possible without support. So here we go:

I want to start by thanking Arno, as all this started with Arno. I've come to know Arno as an enthousiastic lecturer and smart and insightful researcher. Arno's lectures about solar energy during the Sustainable Energy Technology minor, some 9 years ago, inspired me to pick up my game and get into the SET Masters program. Arno inspired me to do a Master thesis project involving fundamental PV material and device research, which did not fit, at all, my Technology, Policy and Management background. Arno hired me to work on the Solar Energy MicroMasters and only because of Arno did I choose to do a PhD. Arno is the guy that basically told me four years ago; this is the goal, here is a lab, do your thing. He gave me the freedom to take a somewhat different approach to doing a PhD project, resulting in this dissertation. For that I am grateful. He's also the guy who took 12 months reviewing my first paper and from whom it was near-impossible to get any feedback on research approach and experimental design. Two sides to each coin. I'm not sure anymore to what degree you shaped my way of thinking, or if I took an interest because your way of thinking reflected my own. Perhaps a bit of both. Anyway, an inspirational person you are; albeit one with almost as many cautionary characteristics as aspirational qualities. I could say that I owe you for the opportunities, but looking at the finished MicroMasters program (and its revenue stream) and the 13 papers with your name on them, I'd say we're even ;).

I was very lucky to work with a large number of (mostly) very gifted students. You provided a sounding board and a range of complementing skills. But most importantly, you guys allowed me to leech of your enthusiasm and excitement; the two properties most important to an effective 4-year research PhD. So a sincere thanks to Paolo, Taha, Steven, Ashish, Maik, Ashwath, Bilal, David, Harsh, Megan, Mohammed, Gino, Paul, Julian, Koos, Sander, Thijs and Federica. You guys are awesome!

I am grateful, and have nothing but respect for the efforts and support of our technicians. Martijn, Stefaan, Remko and Daragh; you guys are some very patient, nice and capable people indeed. I truly appreciate all your efforts in keeping the train running during these challenging couple of years, even as people fell off the wagon and the train kept getting bigger and even relocated at some point.

Then my long-time officemates. Nasim and Paul, in whom I found willing victims for all my baby photos and video game talk (guess who did what). Thanks, Nasim, Rita and Paula, for allowing me to vent about any and all things I find idiotic, of which there are many, and about all them bloody students. (yes those same students I praised a moment ago. Clever kids are still kids.). Moreover, I want to thank Paul for lending his simulating expertise and Nasim for the LaTeX template I have used for this thesis. Andres and Rita, our very own PVMD love story and two of the nicest people I know. Thanks for all the knitted woolen baby blankets and caps. I get it if you want to move some place sunny, but just don't go too far! Talking about nice, Paula, thanks for helping me getting started

in this project. More importantly, thanks for the incredible murals in my kids rooms, first in Rotterdam and then again in Schiedam, they're amazing!

Thanks Johan, partner in crime for defending Holland's pride and major selling point (Feyenoord and the city of Rotterdam of course). And Gianluca and Robin, with whom I spend two of the best weeks of my life in Hawaii, unforgettable. Presenting at the PVSC world conference and hopping on a boat to get close to an active volcano, barely escaping with our lives, according to Gianluca's account (ask Arno, he'll happily show you the footage). I also want to thank Juan Camilo, a great guy, who shares a passion for the ridiculous adventures of three former Top Gear presenters. Of course Klaas Bakker, who I assisted in beating all the other nerds during an amazing week in the Quantsol Summer school. Also thank you David van Nijen, easy going colleague and the only student of the almost 600 (give or take a few) I have supervised during the MicroMasters development and PhD research that asked me for a performance evaluation. This guy is going places! Thanks to my at-one-time roomies; Dimitris, always easy with one of his spirit-lifting laughs, and Dr. Luana Mazzarella and Dr. Malte Vogt. Also thanks to my former MSc supervisors and first co-authors, Fai Tong Si and Hairen Tan and to Can Han and Yifeng Zhao, for the discussions and professional contribution.

In fact there are many that have contributed in one form or another, at the very least in making the PVMD group into what it is, for better or worse. So a sincere thank you to Dr. René van Swaaij, Prof.Dr. Olindo Isabella, Prof.Dr. Miro Zeman, Prof.Dr. Arthur Weeber, Dr. Rudi Santbergen, Dr. Hesan Ziar, Dr. Patrizio Manganiello, Dr. Guangtao Yang, Dr. Engin Özkol, Dr. Daniele Scirè, Dr. Carlos Ruiz Tobon, Dr. Yilei Tian, Manvika Sing, Yifeng Zhao, Arturo Martinez, Yilong Zhou, Dr. Mirco Muttillo and Maarten Verkou

My special thanks go to the graduation committee, Prof.dr. Arthur Weeber, Dr. Tom Savenije, Prof.Dr. René Janssen, Prof.Dr. Pere Roca i Cabarrocas, Dr. Subhendu Guha, Dr. Hitoshi Sai, Prof.Dr.Olindo Isabella. I appreciate the time you spent on evaluating this thesis and providing me with helpful feedback.

The biggest thanks of all to my family. Pa, Ma, Gaabs, Pascallieballie, you were a source of unwavering support; indignant, proud and there to put things in perspective at all the right times, despite not making it past the first few words of any of the papers I published!

Thank you my smart and beautiful wife. Four years.. it feels like a month ago we were in Hawaii, finding out we were going to have a baby. Renovating our apartment, finishing weeks before Samuel was born, vowing to never combine construction with a pregnancy again. It feels like last week we found out we were going to have another baby. Looking for a bigger house and then completely renovating a bigger house. It feels like yesterday Rosa was born, about a week before we finished most of the house. Four years.. It's been a trying couple of years my love. Thanks for sharing them with me and supporting me, even at the cost of your own ambitions.

And finally my babies, Samuel and Rosa; it would not be right to say I did any of this for you. Thinking about your futures however, and that of your kids.. the state of this

place when you guys inherit it.. it has motivated me everytime research had me down (and there is a lot of downs in research) to get back at it full force. I love you.

List of Publications

Articles in peer-reviewed journals

1. **T. de Vrijer**, F.T. Si, H. Tan, A.H.M. Smets, "Chemical Stability and Performance of Doped Silicon Oxide Layers for Use in Thin-Film Silicon Solar Cells" *IEEE Journal of Photovoltaics*, **9, 3–11, 2019**
   DOI: 10.1109/jphotov.2018.2882650.

2. **T. de Vrijer**, A.H.M. Smets, "The relation between precursor gas flows, thickness dependent material phases and opto-electrical properties of doped a/nc-SiO$_{X\geq0}$:H films" *IEEE Journal of Photovoltaics*, **11, 3, 591–599, 2021**
   DOI: 10.1109/jphotov.2021.3059940.

3. **T. de Vrijer**, A.H.M. Smets, "Advanced textured monocrystalline silicon substrates with high optical scattering yields and low electrical recombination losses for supporting crack-free nano-to poly-crystalline film growth" *Energy Science & Engineering*, **9, 1080–1089, 2021**
   DOI: 10.1002/ese3.873.

4. **T. de Vrijer**, M. Wiering, D. van Nijen, G. Padmakumar, S. Sambamurthy, G. Limodio, A.H.M. Smets, "The optical performance of random and periodic textured crystalline silicon surfaces for photovoltaic applications" *EPJ Photovoltaics*, **under review**.

5. **T. de Vrijer**, H. Parasramka, S.J. Roerink, A.H.M. Smets, "An expedient semi-empirical modelling approach for optimal bandgap profiling of stoichiometric absorbers: a case study of thin film amorphous silicon germanium for use in multi-junction photovoltaic devices" *Solar Energy Materials & Solar Cells*, **225, 111051, 2021**
   DOI: 10.1016/j.solmat.2021.111051.

6. **T. de Vrijer**, A. Ravichandran, B. Bouazatta, A.H.M. Smets, "The impact of processing conditions and post-deposition oxidation on the opto-electrical properties of hydrogenated amorphous and nano-crystalline Germanium films" *Journal of Non-Crystalline Solids*, **533, 120507, 2021**
   DOI: 10.1016/j.jnoncrysol.2020.120507.

7. **T. de Vrijer**, J.E.C. van Dingen, P.J. Roelandschap, K. Roodenburg, A.H.M. Smets, "Improved PECVD processed hydrogenated germanium films through temperature induced densification" *Materials Science in Semiconductor Processing*, **138, 106285, 2022**
   DOI: 10.1016/j.mssp.2021.106285.

8. **T. de Vrijer**, K. Roodenburg, F. Saitta, T. Blackstone, G. Limodio, A.H.M. Smets, "PECVD processing of low bandgap-energy amorphous hydrogenated germanium-tin (a-GeSn:H) films for opto-electronic applications" *Applied Materials Today*, **27,**

101450, 2022
DOI: 10.1016/j.apmt.2022.101450.

9. **T. de Vrijer**, B. Bouazatta, A.H.M. Smets, "Spectroscopic review of hydrogenated, carbonated and oxygenated group IV alloys" *Vibrational Spectroscopy*, **2022**
DOI:10.1016/j.vibspec.2022.103387.

10. **T. de Vrijer**, A.H.M. Smets, "Infrared analysis of catalytic CO_2 reduction in hydrogenated germanium" *Physical Chemistry Chemical Physics*, **24, 10241–10248, 2022**
DOI: 10.1039/D2CP01054B.

11. **T. de Vrijer**, B. Bouazatta, A. Ravichandran, J.E.C. van Dingen, P.J. Roelandschap, K. Roodenburg, S.J. Roerink, F. Saitta, T. Blackstone, A.H.M. Smets, "Opto-electrical properties of group IV elements: the challenges of processing hydrogenated germanium" *Advanced Science*, **2200814, 2022**
DOI: 10.1002/advs.202200814.

12. **T. de Vrijer**, D. van Nijen, H. Parasramka, P.P.A. Procel Moya, Y. Zhao, O. Isabella, A.H.M. Smets, "The fundamental operation mechanisms of nc-SiO$_{X \geq 0}$:H based tunnel recombination junctions revealed" *Solar Energy Materials & Solar Cells*, **236, 111501, 2022**
DOI: 10.1016/j.solmat.2021.111501.

13. **T. de Vrijer**, S. Miedema, T. Blackstone, D.van Nijen, C. Han, A.H.M. Smets, "Application of metal, metal-oxide and silicon-oxide based intermediate reflective layers for current matching in autonomous high voltage multijunction photovoltaic devices" *Progress in Photovoltaics*, **recently accepted**.

14. **T. de Vrijer**, A. Binani, D. van Nijen, T. Blackstone, F. Saitta, S. Miedema, H. Parasramska, S. J. Roerink, M. Wiering, G. Limodio, Arno H.M. Smets, "The versatile application of thin film silicon alloys in multijunction devices" **in preparation**.

15. **T. de Vrijer**, M. El Makkaoui, S. Miedema, A.H.M. Smets, "From Photovoltaic to Photo-electrochemical device: a study of pore processing, size and distribution" **in preparation**.

16. **T. de Vrijer**, M. Atkins, G. Vis, M. Tamarzians, A.H.M. Smets, "A techno-economical feasibility study of a self-reliant PV-battery-hydrogen based system for a dutch neighbourhood " **in preparation**.

Conference contributions

1. **T. de Vrijer**, F.T. Si, H. Tan, A.H.M. Smets, "Chemical stability and performance of doped silicon oxide layers for use in thin film silicon solar cells" in *World Conference on Photovoltaic Energy Conversion (WCPEC-7)*, Waikoloa, Hawaii, June 2018

2. **T. de Vrijer**, A.H.M. Smets, "Sensitivity of opto-electrical properties of doped nanocrystalline silicon and silicon oxide layers to the precursor gas flow rates and thickness" in *46th IEEE Photovoltaic Specialist Conference (PVSC-46)*, Chicago, USA, June 2019.

3. **T. de Vrijer**, A.H.M. Smets, "Development of a novel smooth texture on crystalline silicon for processing polycrystalline materials" in *SPIE Photonics Europe 2020*, virtual, March 2020.

4. **T. de Vrijer**, A.H.M. Smets, "Novel Monocrystalline Silicon Texturing for supporting nano- to polycrystalline layers" in *47th IEEE Photovoltaic Specialist Conference (PVSC-47)*, virtual, June 2020.

5. **T. de Vrijer**, D. van Nijen, H. Parasramka, A.H.M. Smets, "The influence of contact layer properties and thickness on tunnel recombination junction performance in four different multijunction pv device architectures" in *48th IEEE Photovoltaic Specialist Conference (PVSC-48)*, virtual, June 2021.

Curriculum Vitae

Thierry de Vrijer was born in Rotterdam on 28 January 1990. In 2013, he received his B.Sc. degree in Technology, Policy and Management from TU Delft, with a minor in Sustainable Energy Technologies. Continuing down that path, he obtained a M.Sc. degree in Sustainable Energy Technologies in 2015 in the Photovoltaic Materials and Devices group. He spend over a year creating content for, and managing the development of, TU Delft's first online MicroMasters program, the DelftX Solar Energy Engineering MicroMasters; an online program consisting of 5 master-level courses.

In 2017, he continued in the PVMD group at Delft University of Technology to obtain his doctorate degree. The focus of his PhD project was on the development of high voltage multijunction photovoltaic devices for autonomous solar-to-fuel applications, with an additional focus on the development of a low bandgap group-IV alloy based on hydrogenated germanium(tin). In September 2021 he continued as a post-doctoral researcher at the TU Delft, working on the development of high efficiency thin film silicon devices on flexible foils in collaboration with HyET Solar.

Contact

Email: `thierrydevrijer@hotmail.com`

LinkedIn: `https://www.linkedin.com/in/thierry-de-vrijer-0b278993/`